UNIVERSITÀ DEGLI STUDI DI NAPOLI FEDERICO II

Doctorate in Earth, Environmental and Resource Sciences

"Cycle XXXIII"

PRE-ERUPTIVE MAGMATIC PROCESSES TRIGGERING TWO DIFFERENT SIZE ERUPTIONS OCCURRED IN RECENT VOLCANIC ACTIVITY OF THE PHLEGRAEAN DISTRICT AND THEIR TIMESCALES

TUTOR	PhD STUDENT
Prof.ssa Paola Petrosino	Dott. Carlo Pelullo
COTUTOR	HEAD OF DOCTORATE
Dott.ssa Lucia Pappalardo	Prof. Maurizio Fedi

INDEX

INTRODUCTION

Volcanic eruptions are triggered by magmatic processes occurring in subvolcanic plumbing systems, thus a better understanding of magma evolution rates and processes has implications for volcanic hazard forecasting (Blundy and Cashman, 2008; Saunders et al., 2012a; Kahl et al., 2013; Cashman and Giordano, 2014; Petrone et al., 2016; Sparks and Cashman, 2017; Astbury et al., 2018, Cooper, 2019). Petrology has long been used to study the evolution of magmatic systems. Over the past few decades, petrologic techniques have been increasingly applied to questions of pre-eruption magma storage, particularly those that may lead to eruptions (e.g. Cashman and Sparks, 2013). Combined mineralogical, textural and compositional characterization of rocks provides direct critical information for understanding differentiation processes in magmatic systems (e.g., Streck, 2008). Geochemical analysis of igneous rocks and their constituent minerals represents a powerful tool to investigate magma chamber processes and their timescales. A first-order observation relates to the complex growth histories and diverse origins of minerals. Importantly, widespread disequilibrium textures and diverse crystal compositions can record mixing of different magmas, disruption of mush, entrainment of refractory plutonic materials, and xenocrysts incorporated from surrounding country rock (e.g. Davidson et al., 2007). Many petrological and geochemical characteristics of volcanic products have been explained by processes within a magma chamber that as itself is at least transiently connected to a magma supply at depth. For example, replenishment by new magmas is widely postulated to trigger eruptions and explain various petrological characteristics of volcanic materials (Sparks and Cashman, 2017 and reference therein). Nowadays, the role of magma mingling/mixing as a mechanism for triggering volcanic eruptions is well known (Sparks et al. 1977; Folch and Martì 1998; Don Snyder 2000; Druitt et al. 2012). The presence of mafic enclaves showing isotopic/textural disequilibrium with the host intermediate/evolved lava in volcanic deposits from different tectonic settings provides strong support to this model (Bacon 1986; Leonard et al. 2002; Martin et al. 2006; Zellmer and Turner 2007; Andrews and Manga 2014). However, the petrogenetic relationship between mafic enclaves and their host lavas as well as the specific role of these “mafic inclusions” in triggering an eruption still remains unclear.

Analyses of whole-rocks, melt inclusions, residual glass matrix, and the isotopic composition of separated minerals and matrix allow the reconstruction of the pre-eruptive condition of the magma chamber and the definition of syn-eruptive mixing processes and their relationship with eruption dynamics (e.g. Sigurdsson, 2000). In this context, analysis of textures and chemical zoning in minerals is one of the most efficient tools aiming at the investigation of such kinds of plumbing system dynamics (e.g. Humphreys et al., 2006; Morgan and Blake, 2006; Davidson et al., 2007; Ginibre et al., 2007; Streck, 2008). Minerals can be highly sensitive to gradual or sudden changes in the volcanic system, and, for this reason, they are employed as archives of magmatic processes. As minerals respond texturally and compositionally to changing magmatic environments, they preserve in crystal growth stratigraphy a wealth of information regarding their past history of magmatic processes and compositions (e.g. Ginibre et al. 2007). In fact, since the mineral composition in a magma depends on crystallization conditions, crystals preserve evidence of parameters (e.g. pressure, temperature, oxygen fugacity and volatile content) of the environments where they formed. Thus, associating a set of conditions to a magmatic environment, it is possible to investigate the temporal change of magmatic environments over the lifetime of the crystal, from initial nucleation to final quenching upon eruption. In particular, investigations of mineral textures and zoning as evidence for open system processes during magmatic evolution have always been a centerpiece of petrological studies and have provided some of the best evidence for magma mixing and crustal contamination for many decades (e.g., Milch 1905; Kuno 1936; Eichelberger 1975; Anderson, 1984; Streck, 2008). In recent years, mineral studies are invigorated by the development of high-precision, high-resolution analytical instruments and techniques through which textural information and compositional data are combined (e.g., Ginibre et al. 2007; Jerram and Davidson

2007). Mineral microanalysis consists of high-precision, high spatial resolution analysis of major and trace elements of chemically zoned minerals and represents a powerful tool for investigating the magma chamber processes that preceded explosive eruptions of variable energy and their timescales. In fact, compositional data on various portions of chemically heterogeneous minerals have provided information both on pre-eruptive processes such as magma rising, recharge of a reservoir, differentiation and mingling/mixing or on the time the magma spent in the plumbing system before an eruption (residence time) and even on the timescales over which the processes that created the zoning occurred (e.g.Zellmer et al., 1999,2003; Costa and Chakraborty, 2004; Humphreys et al., 2006; Turner and Costa, 2007; Charlier et al., 2005; Alves et al., 2009; Kahl et al., 2011, 2013,2015,2017;Chamberlain et al., 2014; Ubide et al., 2015, 2019; Ubide and Kamber, 2018; Astbury et al., 2018, Cooper, 2019).

Estimating the timescales of magmatic processes is crucial for volcanic hazard assessment and risk mitigation at active volcanoes. In particular, for a dormant, though active and restless volcano, an estimate of the time required for magma to become eruptible, either by coalescence of separate shallow batches or mixing caused by deeper magma recharge, is of paramount importance (e.g. Iovine et al., 2017a).

Examples of such volcanoes, which are the subject of this thesis, are the Neapolitan volcanoes, in south Italy. The Neapolitan area, including the city of Naples, has a population of about four million people and has been growing over the past few millennia around, above and within three active volcanoes: Somma-Vesuvius, Campi Flegrei and Ischia (e.g. Orsi et al., 2003). Therefore, this area is prone to severe volcanic hazards if renewal of volcanism occurs at any of the three active volcanoes. In particular, this thesis focuses on two different size eruptions occurred at Campi Flegrei caldera (CFc) and Ischia island.

The CFc is the result of two highly explosive volcanic episodes (Campanian Ignimbrite: ca. 40 ka; Giaccio et al., 2017 and reference therein; Neapolitan Yellow Tuff: ca 15 ka; Deino et al., 2004) associated with minor eruptions from monogenic vents. Recently, explosive activity has been recognized between the Campanian Ignimbrite and Neapolitan Yellow Tuff (Masseria del Monte Tuff: 29 ± 0.7 ka; Albert et al., 2019). Explosive eruptions of the past 15 ka have been grouped into three size classes: low-, medium- and high-magnitude events (Orsi et al. 2004, 2007). Violent Strombolian, sub-Plinian and Plinian type eruptions correspond to the defined low-, medium-, and high-magnitude size classes. The CFc is currently in a persistent state of activity, as testified by the last eruption of Monte Nuovo, the recent unrest episodes, and the intense fumarolic activity (Orsi et al. 2004 and references therein). This current state of activity and the explosive character of the system make the potential for volcanic hazards very high. The expected resuming of explosive activity joined to the high population density makes the Campi Flegrei caldera one of the most hazardous and vulnerable volcanic areas on Earth (Orsi et al., 2004, 2009; Bevilacqua et al., 2015; Mastrolorenzo et al., 2017).

Ischia is an active volcanic island located in the Neapolitan area (south Italy) and is part of the Phlegraean Volcanic District (PVD) with the Campi Flegrei caldera and the Procida islet. Due to the mainly explosive character of its recent volcanism and the large population living or at least spending holidays at Ischia, the risk is extremely high. Currently, although expected to resume explosive activity in the next future, Ischia is the only active volcano in the Neapolitan area that still lacks a risk mitigation plan. Nevertheless, due to the large number of eruptive episodes (at least 47), the change in chemical and isotopic composition of magma with respect to the previous periods of activity (Civetta et al. 1991; Casalini et al. 2017), the concomitance of resurgence and explosive activity (e.g. de Vita et al. 2006), the last 10 ka is the reference time window for probabilistic volcanic hazard assessment (Selva et al. 2019).

Therefore, improving the knowledge of recent and different size complex volcanic events in the PVD could help refining the hazard framework for this area, supplying more information for risk mitigation.

Several attempts at assessing timescales of pre-eruptive processes for the PVD volcanic activity have been made through different approaches. Estimates of timescales of magma differentiation, transfer, recharge, accumulation and mixing have been obtained through isotope analyses (Arienzo et al., 2011), zircon geochronology (Gebauer et al., 2014; Wu et al., 2015), diffusion chronometry (Iovine et al., 2017a) and experimental petrology (Perugini et al., 2015). Timescale information based on textural analysis (e.g. Crystal Size Distribution – CSD - Piochi et al., 2005; Mastrolorenzo and Pappalardo, 2006; Pappalardo and Mastrolorenzo, 2012; Arzilli et al., 2016), historical, archaeological, geological and long-term geodetic record (Di Vito et al., 2016 and reference therein), numerical simulations (Montagna et al., 2015) and crystals growth rates (Astbury et al., 2018) have been already acquired. However, a precise reconstruction of pre-eruptive magma dynamics controlling the onset, evolution and magnitude of eruptions is still far from being attained. Moreover, mineral microanalysis on zoned crystals aimed at investigating chemical and physical changes of the Campi Flegrei and Ischia magmas is uncommon.

In this thesis, the volcanic products of two different size eruptions occurred in recent volcanic activity of the Phlegraean District have been investigated. The proposed case studies are the Plinian Agnano-Monte Spina (A-MS) eruption, at Campi Flegrei caldera, and the low-magnitude mainly effusive Zaro eruption, at Ischia island. This thesis presents a detailed study of the mineralogy and geochemistry of the A-MS and Zaro volcanic products, including petrographic observations, major and trace element compositions, mineral microanalysis on clinopyroxene crystals and Sr and Nd isotope ratio determinations, with the aim to understand the main pre-eruptive processes and timescale of magma storage in the plumbing system before the eruptions.

The A-MS eruption (4482-4625 cal. years BP; Smith et al., 2011) was the highest magnitude event occurring over the last 5 ka of the Campi Flegrei caldera volcanic history and it was characterized by complex eruptive dynamics with alternating plinian/subplinian purely magmatic and phreatomagmatic activity (Dellino et al., 2004). Furthermore, it can be considered as the the reference event for a future large-scale explosive eruption in the case of renewal of volcanism in short- to mid-terms at Campi Flegrei (Orsi et al., 2002). Previous studies (e.g. de Vita et al., 1999; Arienzo et al., 2010) established that the A-MS eruption was fed by two isotopically and chemically distinct magmas that mixed prior/during the eruption.

The Zaro eruption occurred less than 7 ka at Ischia (Vezzoli et al., 2009), when the island was already inhabited by Neolithic people, as testified by the findings of archaeological artefacts dated to the 4th millennium B.C. (Buchner, 1969). The eruption was characterized by an earlier, short explosive phase (Sbrana et al., 2011, 2018) and a later effusive phase that emplaced a 1 km long lava complex extruded from a NE–SW-striking eruptive fissure in the north-western part of the island (Vezzoli et al., 2009). Therefore, notwithstanding the relatively low energy, the mixed explosive-effusive character and the seismic activity that presumably accompanied the eruption might have caused casualties in the population of the age and damages to their settlements.

Interestingly, the products of the Zaro eruption are characterized by enclaves of mafic to felsic composition in a main felsic lava body, that suggest refilling of a preexisting magma reservoir and mingling/mixing processes occurred prior to the eruption. For both A-MS and Zaro eruptions, the chemical and isotopic compositions of whole rocks and minerals suggest the injection of mafic magmas in evolved reservoirs. In addition to the chemical and isotopic variability, the investigation of the complex zoning patterns of the A-MS and Zaro clinopyroxene crystals, carried out through mineral microanalysis, corroborates such hypothesis. Particularly, the measured zoning patterns of Fe–Mg and selected minor elements (e.g. Al, Ti) often consist of two or more compositional plateau with both sharp and/or slightly diffuse boundaries between them. The plateau composition has been interpreted to represent the growth of clinopyroxene under a constant set of intensive thermodynamic variables as pressure, temperature, composition, fugacity of volatile species, each characterizing a single magmatic environment. A systematic characterization of the chemical information recorded in such zoning patterns, performed through the quantification and the nature of connectivities among different magmatic environments, allowed to reconstruct the evolutionary history of crystals and to precisely recognize the magmatic components involved in the mixing/mingling processes occurred in the A-MS and Zaro plumbing systems.

The study of diffusive modifications detected in the chemical compositions of zoned minerals allows deciphering processes which create complex compositional relationship found in hybrid rocks and their minerals. The application of modeling of the kinetic modifications (diffusion modeling) can help to constrain the timescales of the several magmatic processes that are potentially able to lead to an eruption.

Therefore, after recognizing the number and the frequency of occurrence of magmatic environments in the whole A-MS and Zaro clinopyroxene compositional set, their connections were quantified in order to reconstruct the evolutionary history of crystals. Finally, diffusion modeling of the zoning patterns in clinopyroxene was used to constrain timescales of the processes that were identified from the previous analysis.

The whole dataset supports the injection of mafic magmas into reservoirs containing magma(s) of evolved composition that preceded the eruptions in monthly to decadal time span. This information is of crucial importance for volcanic hazard assessment in case of renewed volcanic activity and can be connected to monitoring data. In fact, the magmatic processes occurring in Campi Flegrei and Ischia deep reservoirs could have effects on the shallow magmatic and hydrothermal systems (e.g. Moretti et al., 2018) where the processes (e.g. fluid migration at shallow depths or sills/dykes intrusions; D’Auria et al., 2011; Woo and Kilburn, 2010) leading to ground deformation and seismicity take place.

1. MAGMATIC SYSTEMS AND MAGMATIC PROCESSES LEADING TO ERUPTIONS

The core questions of volcanology focus on how volcanoes work, that are, how magma forms and moves to the surface, and how the specific properties of the magma, and the lithosphere through which it moves, control eruptive activity. A critical control on eruption style is the pre-eruptive history of shallow magma storage in magma chambers (Cashmann and Sparks, 2013). The magmatic architecture and physicochemical processes inside volcanoes influence the style and timescale of eruptions (e.g. Cooper, 2019). A long-standing challenge in volcanology is to establish the rates and depths of magma storage and the events that trigger eruption. Magma feeder systems are remarkably crystal-rich, and the growth stratigraphy (the chemical sequence recorded in the zoning pattern during growth) of minerals sampled by erupted magmas can reveal a wealth of information on pre-eruptive processes (e.g. Ginibre et al., 2007; Streck, 2008; Kahl et al., 2011, 2013,2015; Ubide et al., 2015; Ubide and Kamber, 2018). Detailed textural and chemical data acquired on volcanic products and their minerals allow the investigation of the plumbing system prior to the onset of activity (e.g. Ubide et al., 2019).

1.1 Transcrustal magmatic system: magma reservoirs and magma chambers

Magma systems that supply volcanoes can extend throughout the crust and consist of mush (melt within a crystalline framework; Fig. 1) together with ephemeral magma accumulations.

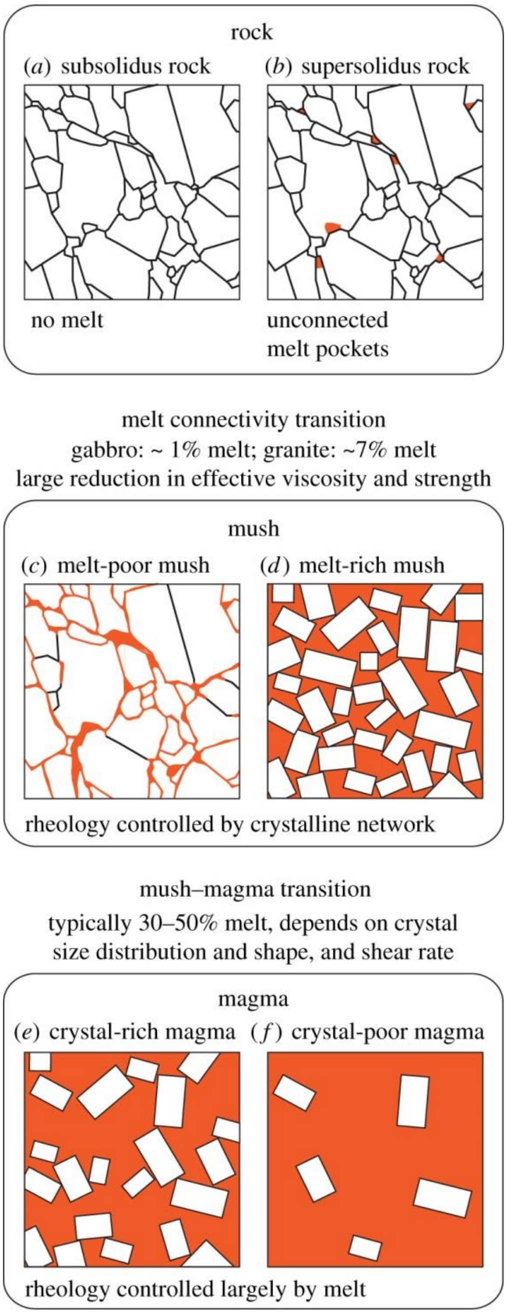

Fig. 1 Diagram depicting physical and rheological properties of major domains within magmatic systems (from Spark et al., 2019).

Within a crystal-rich mush, slow processes of melt segregation and heat loss alternate with fast processes of destabilization and magma transport. Within an active magmatic system, there can be multiple regions of mush and magma at different levels (Fig. 2; Sparks and Cashman, 2017).

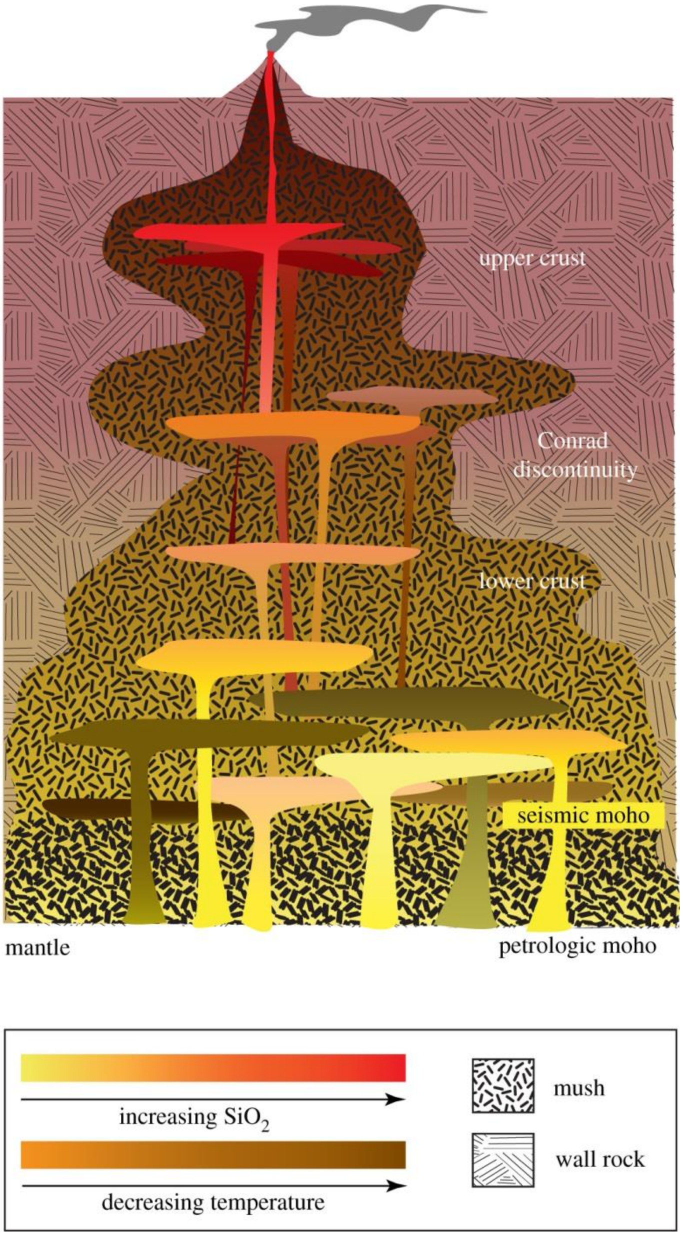

Fig. 2 Depiction of a thermally mature transcrustal magmatic system, where melt processing in a volumetrically dominant mush domain leads to the formation of multiple magma chambers in the middle and upper crust (from Spark et al., 2019).

The term “magma reservoir” was originally synonymous with the term “magma chamber”, but it is increasingly used to describe the entire transcrustal magmatic system (Sparks and Cashman, 2017). A magma reservoir may be defined as a region of partially or wholly molten rock with varying proportions of melt, crystals and exsolved volatiles (Bachmann & Bergantz, 2008). The knowledge of magma reservoirs is based on a range of experimental, observational and theoretical approaches. The study of magma reservoirs has wide implications not only for understanding geothermal and magmatic systems, but also for natural oil and gas reservoirs and for ore deposit formation (Edmonds et al., 2019). Magma chambers are regions of magma embedded within mush and, commonly, fully solidified plutons (Sparks and Cashman, 2017). Magma chambers can supply volcanic eruptions. Phenomena associated with volcanic unrest and eruptions, such as shallow earthquakes, ground deformation and gas emissions can be attributed to the internal processes within a magma chamber (Fig. 3).

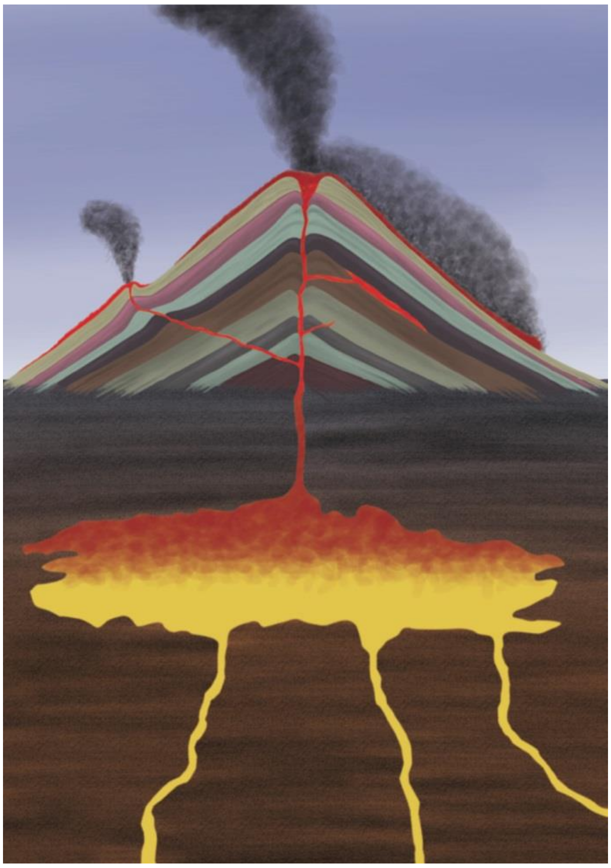

Fig. 3 Depiction of a classic magma chamber beneath a volcano in which the chamber is envisaged as a melt-dominated body recharged from below by new magma from depth and supplying volcanic eruptions (from Spark et al., 2019).

1.2 Magmatic processes

Within transcrustal magma systems, three types of igneous processes can be distinguished: vertical (upward) transport of magma; stalling in the crust (intrusion); internal (super-solidus) magma and mush processes (e.g. Sparks and Cashman, 2017). Vertical magma transport, which can occur by means of fast or slow mechanisms, consists of flow of magma and magmatic fluids along fractures and can be manifested in active volcanic systems as earthquakes, tremor and deformation. Interruption of magma ascent is necessary to form igneous intrusions and magma chambers. The geometry and location of magma accumulation depends on geological structures, strain, strain rate, causative stress systems and rheological properties (Menand, 2008). Once a magma chamber has formed, it determines both the nature of magmas that can erupt and the fate of new melt inputs. Internal magma and mush processes refer to igneous processes occurring in magma reservoirs. Processes active within central (and open) magma chambers can be complex, including magma compositional stratification, disruption of cumulates, assimilation of wall rock and mingling/mixing. When magma reaches crustal reservoirs it can change its chemical composition through different routes. The whole gamut of mechanisms for differentiation has been referred to as the FARM process (Grove and Brown, 2018), which stands for Fractional crystallization, Assimilation, Replenishment and magma Mixing (Fig. 4).

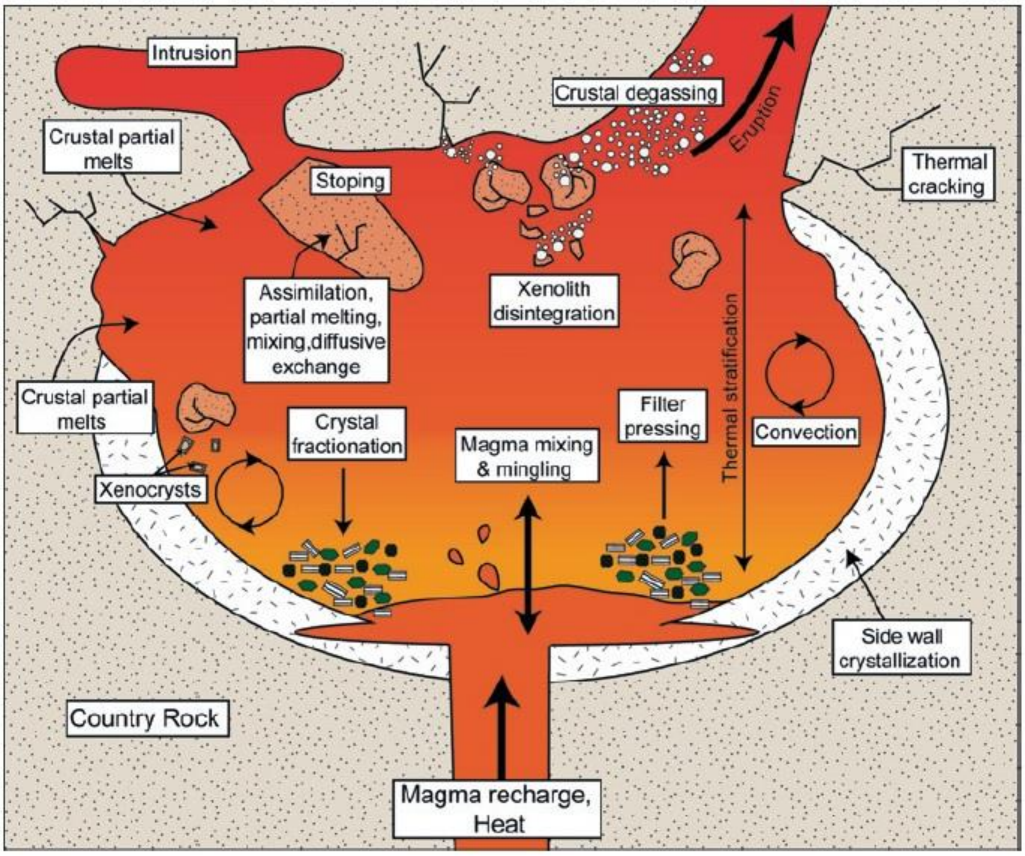

Fig. 4 Schematic sketch showing various magma chamber processes (not to scale; modified after Troll, 2001).

Magma body may cool through inward solidification, generating a progressive layering (from mafic to more evolved bulk compositions) by efficient separation of crystals from the remaining liquid (Wager et al., 1960; Marsh, 1989; Naslund and McBirney, 1996). There is no doubt whatsoever that chemical differentiation in igneous systems results from the physical separation of crystals and melt. Numerous mass balance calculations involving reasonable solid phases and derived melts show the great feasibility of crystal fractionation as a means of efficient chemical differentiation (Sigurdsson et al., 2000). While a simple fractional crystallization process, consisting of a mechanical separation of mineral phases (cumulitic assemblage) from a melt (residue liquid), is a closed-system process, the others processes occur in open-system conditions. However, fractional crystallization can be combined with one or more open-system processes (AFC: Assimilation and Fractional Crystallization, RAFC: Recharge, Assimilation and Fractional Crystallization etc.). Other mechanisms for magma differentiation concern expulsion of melt from the mush pile during compaction (McKenzie, 1985) or gas-driven filter pressing (Sisson and Bacon, 1999) and may be enhanced by partial melting of the mush during recharge by hotter magmas (Bachmann and Bergantz, 2006; Ruprecht et al., 2008; Huber et al., 2011). These processes can be responsible for the activation of eruptions. Several studies have proposed that magma reservoirs crystallized to near rigid crystal-mush can be partially remelted by diffusion of hot fluids and some volcanic eruptions have been interpreted as induced by this mechanism (e.g., Couch et al., 2001). Moreover, recent studies outlined that remelting can occur without a significant increase of the magma temperature, but simply by diffusion of H_2O by the magmatic gases feeding the system (Triglia et al., 2008). Assimilation refers to processes in which magma reacts with country rocks. Crustal assimilation is inextricably linked to the fractional crystallization: an important source of heat for melting wallrock is the latent heat of crystallization (resulting in cumulate formation; e.g. Taylor et al., 1979; Spera and Bohrson, 2001). Magma recharge events and subsequent mixing/mingling have been widely recognized in different tectonic setting. Nowadays, evidence of magma recharge (intrusion of new magma into a preexisting magma chamber) is commonplace and this process is considered able to trigger volcanic eruption. During/after replenishment by a new magma influx, a process of interaction between magmas can occur. It has become an accepted practice to apply the term magma mingling to indicate the process of acting to disperse physically (no chemical exchanges are involved) one or more magmas within a host magma, whereas the term magma mixing indicates that the mingling process is also accompanied by chemical exchanges (e.g. Flinders and Clemens, 1996). Rocks formed by mingling of magmas retaining their contrasting identity are evident on scales ranging from a thin section to large outcrops. After mingling, magmas may become mixed on an atomic scale by diffusion, if sufficient time and thermal energy are available, forming an essentially homogeneous melt. Magma mixing processes can occur potentially in any geological environment, from deep crustal magma chambers to volcanic conduits (Perugini and Poli, 2012). Homogenization and equilibration of crystals from the two batches of magma take a longer time.

Hybridizing magmas can be derived from different sources, such as basaltic magma from the upper mantle and silicic magma from the deep continental crust, or they may have a common parent magma but have followed different evolutionary tracks (Best, 2003), so differing by as little as a few weight percentages in major elements. Compositionally dissimilar magmas are usually also dissimilar in temperature and physical properties, particularly viscosity. Such contrasts are involved in many mechanisms of hybridization. It has been widely documented that magmas can mix efficiently only when their rheology is similar (e.g. Sparks and Marshall, 1986; Bateman, 1995).

1.3 Mixing processes as eruption trigger

There are many possible mechanisms of triggering explosive volcanic eruptions, most of which involve factors which ultimately lead to supersaturation of the melt with respect to volatiles. The eruption trigger may take place in response to a tipping point caused by the long-term processes of fractionation, settling, compaction, reactive flow and second boiling (Tait et al., 1989); or it may be due to recharge of the reservoir by mafic magmas from the lower parts of the crust, or from the mantle (e.g. Edmonds et al., 2010; Ruprecht and Bachmann, 2010; Bergantz et al., 2015). The instabilities generated from the interaction of chemically and thermally different magmas may give rise to scenarios whereby the reservoir may re-organize (Christopher et al., 2015) or overturn (Ruprecht et al., 2008; Woods and Cowan, 2009) on short timescales prior to, or during, eruption. A typical scenario is that of a primitive, hot magma rising from depth and intercepting on its way upwards an already established, more evolved batch of stalling magma.

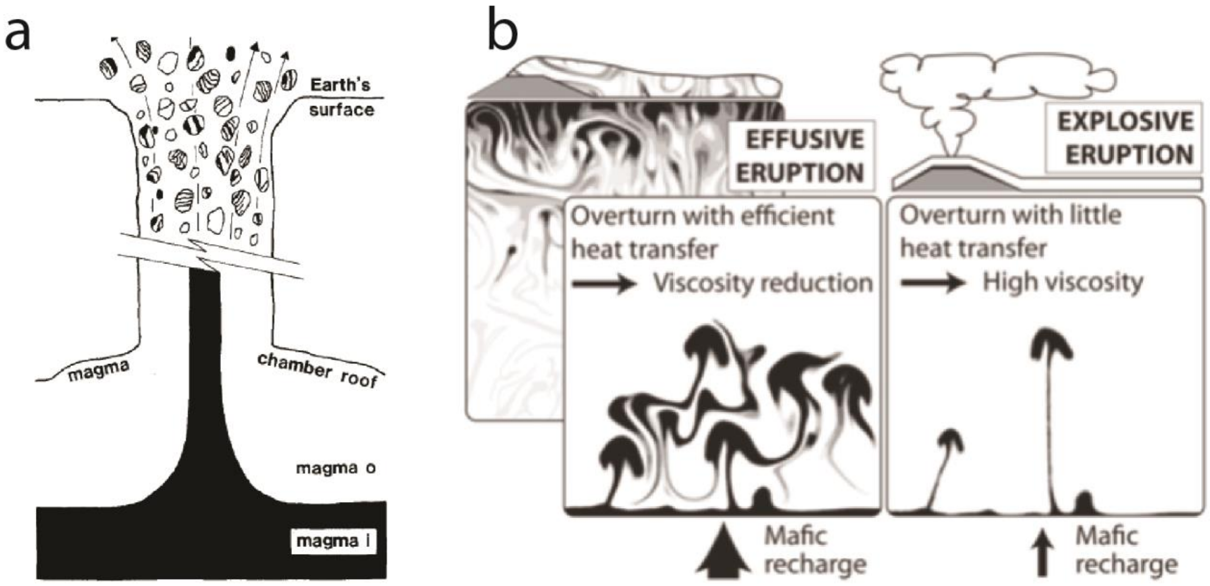

Fig. 5 a) Cartoon showing the flow and mixing of two magmas during their rise (from Blake and Campbell, 1986) b) Conceptual model for main control of effusive-explosive transition of volcanic eruptions (from Ruprecht and Bachmann, 2010).

Indeed, the two magmas typically can differ also in terms of volatile content. Such general scenario can have a variety of declinations: depending on the specific setting and physicochemical characteristics of the magmatic mixtures involved, on the timescales of the process and on the thermal conditions of the magmatic system, the two magmas can interact on a purely physical basis, so that a mingling (mechanical mixing) process occurs, or they can experience a chemical exchange, by which their original compositions are modified. Hence, the intrusion of mafic magma into a more evolved magma chamber has been recognized as one of the main processes responsible for triggering of highly explosive volcanic eruptions (Sparks et al. 1977; Folch and Martì 1998; Don Snyder 2000; Murphy et al., 2000; Leonard et al., 2002; Druitt et al. 2012). Injection of the more mafic magma into the felsic magma triggers convection dynamics and widespread mixing (Sparks et al., 1977). This process increases the volumetric stress in the chamber and may drive volatile transfer from the mafic to the felsic magma which, when coupled to the additional thermal input from the mafic magma, destabilizes the magmatic system and triggers rapid volatile exsolution and eruption (Kent et al., 2010; Mariño et al., 2017). Vesiculation induced by convection increases magma pressure and may fracture the volcanic edifice triggering an explosive eruption.

Moreover, recently new mechanisms to explain how this magmatic interaction at depth triggered rapid heterogeneous bubble nucleation and growth and could have enhanced eruption explosivity have been proposed (e.g. Mariño et al., 2017). The most violent and catastrophic volcanic eruptions on Earth have been triggered by the refilling of a felsic volcanic magma chamber by a hottest and more mafic magma (Murphy et al., 1998; Kent et al., 2010). Examples include Vesuvius 79 AD (Cioni et al., 1995), Krakatau 1883 (Self, 1992), Pinatubo 1991 (Kress, 1997), the Campanian Ignimbrite (Arienzo et al., 2009) and Eyjafjallajökull 2010 (Sigmundsson et al., 2010). Since magma mixing/mingling can be a key process during highly explosive eruptions, this has implications for hazard assessment for those volcanoes in which evidence of these processes exists. The hypotheses of a mixing/mingling process, due to input of new mafic magma into a more evolved magma chamber, able to destabilize the magmatic system and trigger the Agnano-Monte Spina and the Zaro eruptions lays the groundwork of the thesis. For both case studies evidences of mixing/mingling have relatively been investigated in previous works (Di Girolamo et al., 1995, de Vita et al., 1999; Arienzo et al., 2010, Moretti et al., 2019).

1.4 Evidence of mixing

1.4.1 Textural evidence: flow structures, banded pumices, magmatic enclaves

Evidence for mixing of distinct magmas is observed macroscopically and also at the crystal-scale with phenocryst heterogeneities and zoning (Eichelberger, 1980). Magma mixing processes can generate products with visible different structural features (texture, mineralogy, abundance of mineral phases etc.). If, in the initially stages of mixing, the magma were erupted, then we might expect to find rocks that show a "marble cake" appearance, with dark mafic rock intermingled with lighter colored sialic rock. From a structural point of view, several kinds of products can be recognized. For example, flow structures (Fig. 6) can be formed: the term refers to portions of a magma having a wide spatial continuity dispersed within a compositionally different host magma. Generally, these structures can be readily recognized in field outcrops as they show alternating light and dark colored bands constituted by magmas with different compositions (Perugini and Poli, 2012 and reference therein; Morgavi et al., 2017). Flow structures generated by interaction occur in lava flows outcropping on the island of Lesbos (North-Eastern Greece; Perugini et al., 2003), on the island of Salina and Vulcano (Aeolian islands, Southern Italy; Perugini et al., 2003), at Grizzly Lake (Yellowstone National Park; USA; Morgavi et al., 2016) and at Soufrière Hills volcano (Island of Montserrat, UK; Plail et al. 2014).

Fig. 6 Magma mixing structures in lava flows from the island of Lesbos. The dark flow structures consist of B magmas dispersed through light colored A magmas (from Perugini et al., 2003)

Similarly, another evidence of mixing is the occurrence, in some deposits of explosive eruptions, of the so-called banded pumices (Fig. 7). The bands in banded pumice are commonly of either silicic or mafic end-member composition, but a complete series of hybrid bands can also occur (Macdonald and Katsura, 1965).

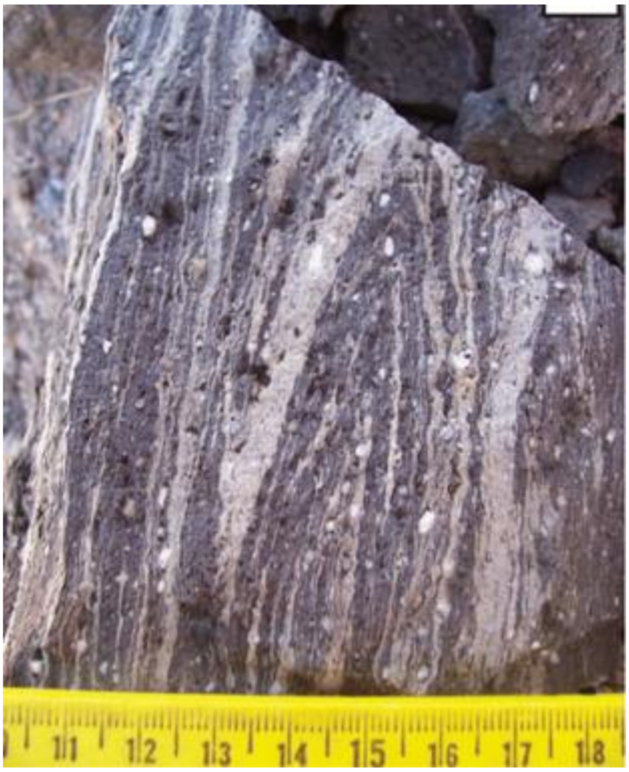

Fig. 7 Banded pumice from Lassen Peak shows fluid mixing of andesite and dacite magmas shortly before eruption. Scale at the base of photograph is in centimeter (from Andrews and Manga, 2014).

Freudt and Tait (1986) proposed, based on their experimental set-up, a model of banded pumice formation, in which mafic clasts represent uncontaminated inner portions of the central flow while banded pumice is formed at the margins by shear mixing with the silicic magma entrained into the central flow. However, banded texture is only preserved for a limited time, and eventually a homogeneous hydrid is formed (Kouchi and Sunagawa, 1985). Rapid hybridization may account for the formation of hybrid bands in banded pumice where viscosity and temperature contrasts were small (Andrews and Manga, 2014).

1.4.1.1 Magmatic enclaves

The structural evidence that probably, according to common thinking, mostly characterizes magma mixing processes is the occurrence of magmatic enclaves (Fig. 8): the term is used to identify a discrete portion of a magma occurring within a host magma with a different composition (e.g., Wilcox, 1944; Bacon, 1986, Didier and Barbarin, 1991).

Fig. 8 Mafic enclaves (dark) in rhyodacite host lava from Chaos Crags Dome C record brittle mixing of two magmas (from Andrews and Manga, 2014).

These solidified ‘blobs’ of injected magma are evidence of magma mixing, but the petrological and mechanical conditions during their formation are debated. Generally, enclaves display quite sharp contacts with the host rock, although it is not rare to observe that some enclaves display engulfment and disruption of their boundaries due to infiltration of the host magma (Morgavi et al., 2017). It is a common belief that magmatic enclaves represent regions where chemical exchange is less efficient (e.g. Poli and Perugini, 2012). Hence, they can play a crucial role as messengers of the initial composition of the mafic magma(s) that took part in the mixing process. However, as time passes during mixing, enclaves loose progressively their initial composition because: i) in the long term, chemical diffusion can represent a process that may alter their composition, in particular along the boundaries; ii) crystals belonging to the host magma are frequently observed within enclaves.

Enclave characteristics such as their physical appearance, petrographic texture, vesicularity, bulk composition, mineral heterogeneities, and groundmass textures can help constrain the magmatic properties during mixing. The physical properties of enclaves such as shape and size distributions provide evidence for mixing styles, or degree of mixing (Turner and Campbell, 1986; Ventura et al., 2006; Paterson et al., 2004). Enclave abundance provides insight into the volume of recharge magma present or able to mix with the host magma (Barclay et al., 2010). Enclaves that are compositionally and mineralogically similar to their respective host lavas suggest that variations in viscosity to form the enclaves must be driven by temperature, density, or crystallinity differences rather than compositional contrasts.

Textural evidence and petrologic analysis of chemical zoning within individual crystals assist in understanding whether crystal exchange occurred during mixing (Eichelberger, 1980; Tepley et al., 1999; Kent et al., 2010). The presence of enclaves either signifies mingling between the intruded and host magmas with no crystal exchange or represents partially mixed magma that did not reach complete hybridization. Therefore, investigating whether crystal exchange occurred between the host and intruding magmas to produce enclaves at Zaro lava complex is one of the purposes of this study. In cases where mechanical mixing dominates with little to no crystal exchange, the processes of enclave formation can be further distinguished according to whether the enclave magma cooled and crystallized before or after being entrained within the host magma (Marsh, 1981; Coombs et al., 2000). Essentially, enclave quenching is related to changes in temperature between the intruding magma and the preexisting magma. Enclave cooling may occur at the interface between a cooled host magma or country rock within a conduit or when the enclave cools once entrained within the host magma. Additionally, the intruding magma may cool in response to decompression-induced crystallization during rapid ascent from recharge events (Mollo and Hammer, 2017). Exsolved volatiles during crystallization may also play an important role in enclave formation, as bubbles may increase the viscosity while simultaneously decreasing the density of the intruding magma (Coombs et al., 2000; Browne et al., 2006). Textural indicators for enclave cooling, either after entrainment and dispersal within the host magma or prior to incorporation within the host magma, include degree of vesicularity, abundance of phenocrysts (>450 μm), groundmass crystals (450-200 μm), and microlites (<200 μm), presence of quenched margins, quenched glass, and signs of undercooling within the groundmass crystals and microlites. Therefore, not only the chemical identity and rheology of the intruding and host magmas is essential in deciphering enclave formation, but detailed analyses to determine timing of enclave cooling are also necessary.

The presence of mafic enclaves showing isotopic/textural disequilibrium with the host intermediate/evolved lava from different tectonic settings, provides strong support to processes of replenishment and subsequent mingling/mixing prior to the eruption (Bacon 1986; Leonard et al. 2002; Martin et al. 2006; Zellmer and Turner 2007; Andrews and Manga, 2014). There are several known examples worldwide of felsic volcanic rocks characterized by the occurrence of mafic enclaves. They include but aren’t limited to: Santa Barbara eruption at Sete Cidades volcano, São Miguel, Azores (Mariño et al. 2017); Pietre Cotte eruption at Vulcano, South Italy (Perugini et al. 2007); Kaharoa eruption at the Tarawera Volcanic Complex, New Zealand (Leonard et al. 2002); 1997-2007 lava flows eruptions at Soufriere Hills, Montserrat (Barclay et al., 2010): 1570–1573, 1925–1928, 1940–1941 and 1950 eruptions at the Kameni islands, Santorini, Greece (Martin et al. 2006); the 1991–1995 lava eruptions of Unzen volcano, Japan (Browne et al., 2006); Chaos Crags eruption at the Lassen Volcanic National Park, California (Andrews and Manga, 2014).

1.4.2 Geochemical evidences: chemical and isotopic composition

Flow structures, banded pumices and magmatic enclaves preserved in the volcanic products indicate a process of mixing/mingling presumably frozen at the moment (or shortly before) the eruption occurs. Nevertheless, if the interaction process proceeds to the point where any other evidence is erased (the physical identity of the two magmas is not preserved), evidence for mixing can still be detected in the chemical and/or isotopic composition of the mixed magmas. Combined with petrographic investigations and mineral chemistry, chemical and isotopic analyses on volcanic rocks have revealed compositional variations at different length scales pointing to a complex interplay of fractional crystallization, mixing/mingling and crustal assimilation during the evolution of several magmatic systems (e.g., De Paolo, 1979; James, 1982; Wörner et al., 1985; Thirlwall et al., 1996; Tepley et al, 1999; Hawkesworth et al., 2000; Maier et al., 2000; Waight et al., 2001; Peccerillo et al., 2004; Yang et al., 2004; Arienzo et al., 2009; Freymuth et al., 2015; Morgavi et al., 2017). In fact, structural and textural features are tightly connected with the modulation of geochemical composition of the mixing system. From the geochemical point of view, when two chemically different components mix in varying proportions, the chemical compositions of the resulting mixtures vary systematically depending on the relative abundances of the end members. It is a common belief that magma mixing processes must produce linear trends in inter-elemental binary plots for any couple of major or trace elements (Fig. 9; e.g. Fourcade and Allegre, 1981, Rollinson, 1993, Schiano et al., 2010).

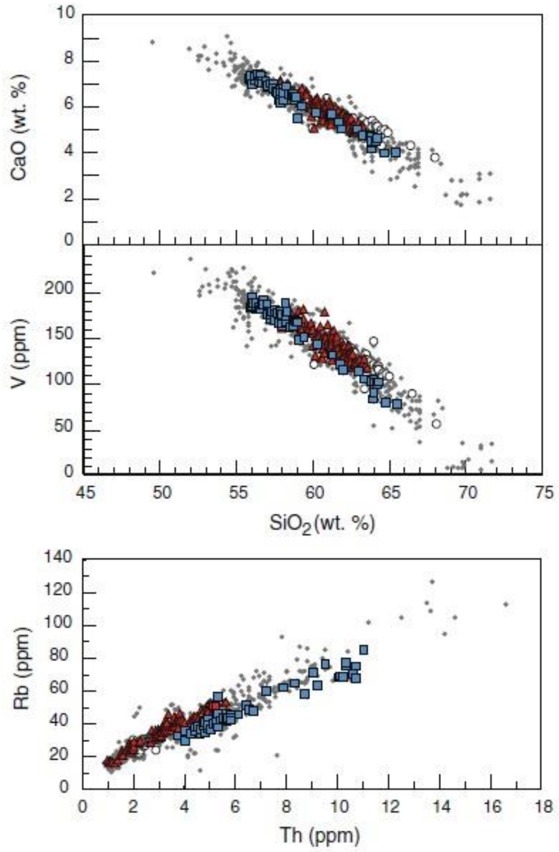

Fig. 9 Variation diagrams showing major (CaO) element and compatible trace element (Co and V) data for about 700 lavas from 16 Ecuadorian volcanic centres (from Schiano et al., 2010).

The mixing process is thus modeled using a simple linear equation relating the mass fraction of interacting end-member magmas and element concentrations. In this way, changing melt compositions (liquid lines of descent) during crystal-melt fractionation and proportions of two mixed magmas can be determined. Nevertheless, in some volcanic complexes the majority of the erupted products are chemically rather homogeneous, displaying a dominant composition. Despite the roughly homogenous composition, the isotopic features suggest that complex open system processes occurred and superposed upon the main fractional crystallization trend. In fact, isotopic analyses (e.g., Sr, Nd, Pd, B) have been proven to be an important tool for discriminating between closed-system fractional crystallization and open-system magma mixing/mingling or crustal contamination (e.g., James, 1982; Knesel et al., 1999; Turner and Foden, 2001). As well as for major and trace elements, the isotope compositions of the elements in a suite of binary mixtures vary progressively depending on the isotope compositions of the end members and on the proportions of mixing. The isotopic composition of two-component mixtures is related to their end members by characteristic hyperbolic patterns formed by their isotopic composition (Faure, 1992).

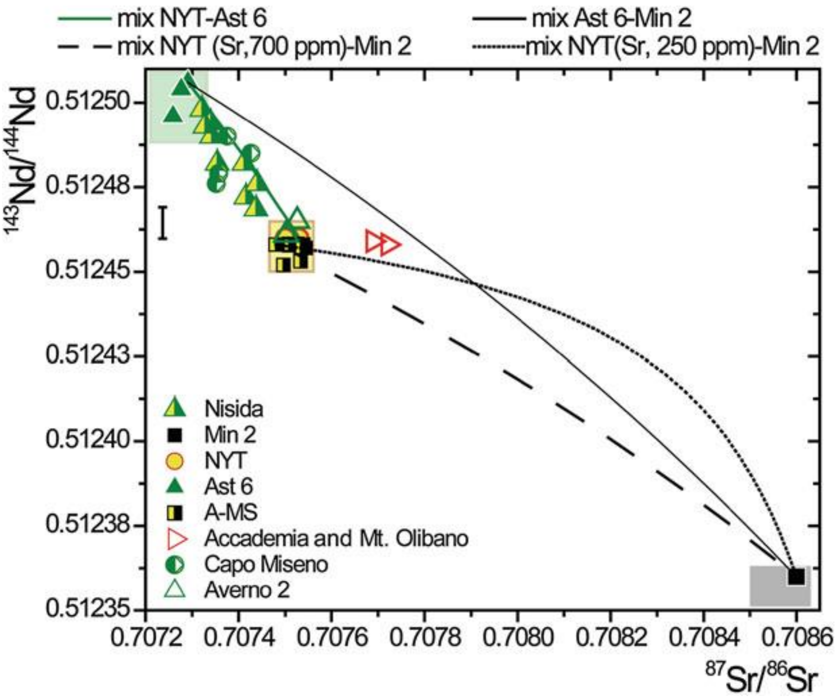

Fig. 10 Modelling of the Sr-Nd isotopic features of some of the Campi Flegrei volcanics of the past 5 ka, by assuming mixing among the Astroni 6 (Ast-6)-, Neapolitan Yellow Tuff (NYT)- and Minopoli 2 (Min 2)-like magmatic components. The green, yellow and black boxes represent the range of Sr and Nd isotopes of the products erupted during the Astroni 6, Neapolitan Yellow Tuff and the Minopoli 2 eruptions, respectively. Symbols inside the plot represent volcanic products belonging to the listed eruptions. The vertical error bar is the uncertainty in ^{143}Nd/^{144}Nd determination at the 2r level of confidence; that for ^{87}Sr/^{86}Sr is included in the symbols. Modified after Arienzo et al. (2016)

An alternative yet complementary approach is the determination of the isotopic compositions of individual mineral grains: the crystal isotope data provide fresh insights into the dynamics of open-system (e.g. Knesel et al., 1999). Isotopic disequilibrium between minerals and their host rocks suggests mixing between chemically and isotopically distinct batches of magma and/or crystal cargo from an earlier magmatic phase. In this context, combined with the chemical composition, the isotopic analysis of individual crystals belonging to the different lithotypes (chemically different enclaves and their host lava) of the Zaro lava complex has been very useful for the interpretation of their origin (Pelullo et al., 2020). Moreover, as consistently demonstrated by recent studies (Davidson & Tepley, 1997; Waight et al., 2000, 2001; Davidson et al., 2001; Gagnevin et al., 2005), isotope heterogeneity at the mineral scale is very common in volcanic and plutonic rocks of varied compositions. This allows for open-system processes to be identified and quantified in terms of end-members and products; in favorable cases, the timescale of the process can also be estimated (e.g. Davidson et al., 2007; Costa et al., 2008; Alves et al., 2009).

1.4.3 Disequilibrium textures of crystals

Besides the over mentioned macroscopic evidence, crystals involved in magma mixing can be affected by disequilibrium textures: the injection of a hot mafic magma into a felsic magma produces dramatic thermal and compositional disequilibria (e.g. Bateman, 1995, Sparks and Marshall, 1986) and minerals already present in the magmatic mass necessarily react to these disequilibria. Disequilibrium phases, such as coexisting quartz and Mg-olivine in a rock are often interpreted to be the result of interaction between different crystal-bearing magmas. Moreover, multiple lines of independent evidence can strengthen the mixing interpretation but are never sufficient to prove this process occurred. Disequilibrium textures in a rock that appears to be homogeneous but was produced by mixing of felsic and mafic magmas might still be preserved if the crystals present in one of the magmas does not completely dissolve or react. For instance, minerals occurring in the low-temperature felsic magma are expected to undergo a remelting/resorption process because of the increase in temperature (Poli and Perugini, 2012). Resorbing reaction relations are common in magmas, consuming, to varying degrees, previously precipitated phases. Examples are complex resorption and overgrowths in phenocrysts, such as spongy zones within plagioclase and rapakivi overgrowth of plagioclase on alkali feldspar (Fig. 11; e.g. Pearce, 1994; Renjith et al., 2013; O’Brien et al., 2019).

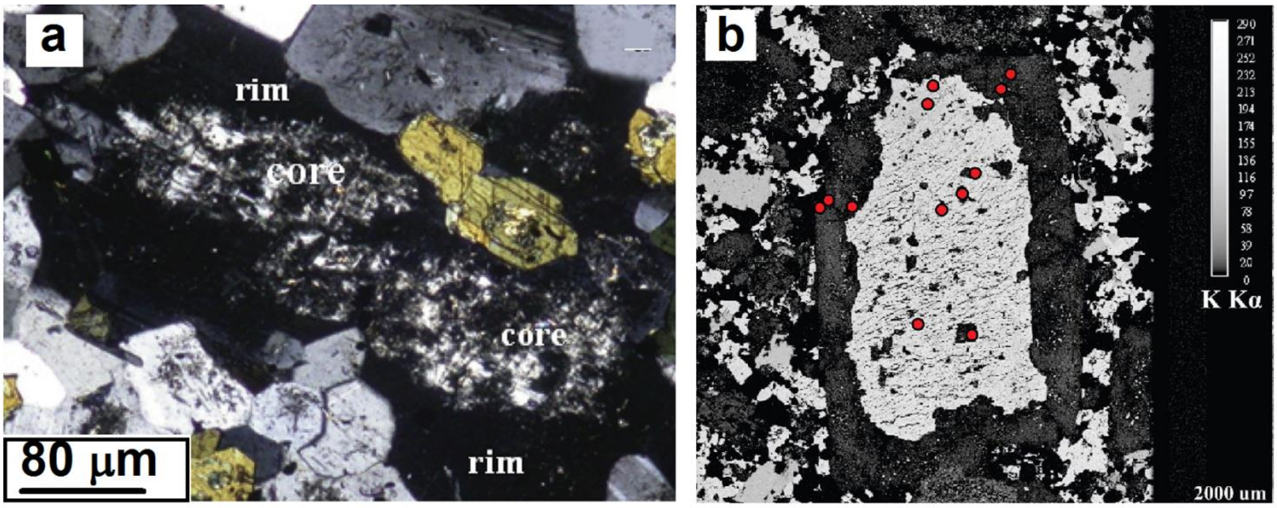

Fig. 11 a) Petrographic thin section of a plagioclase crystal with spongy core and clear plagioclase rim (under extinction; from Renjith et al., 2013); b) Gray-scale X-ray-element maps (K Kα) of rapakivi feldspar (from O'Brien et al., 2019)

However, overgrowth textures can possibly be produced also simply by changes in pressure or water fugacity in the magma system. Dissolution of crystals occurs during mixing of dissimilar crystal-bearing magmas that are striving to reach a state of internal equilibrium. Resorption processes lead to removal of previously crystallized material and they occur in different forms. In one case, resorption leads to dissolution of crystal material progressively from the exterior of euhedral crystals leading to various degrees of rounded, anhedral appearances (Edwards and Russell, 1996). Pervasive resorption may affect the entire crystal leading to an open, cellular mineral structure (e.g. sieve texture; Stewart and Pearce, 2004). Cellular textures can have a boxy or a spongy appearance that are typically related to rapid growth and to pervasive dissolution, respectively (Lofgren, 1980; Nakamura and Shimakita, 1998).

Disequilibrium textures are typically considered as good indicators of magma mixing processes but, as pointed out above, caution should be exerted to interpret them as a univocal evidence of magma mixing. Mineral disequilibria are extraordinary probes for magma mixing and helpful petrological tools only when additional features can be recognized in the rocks. For example, the association with mafic enclaves and/or flow structures makes mineral disequilibria excellent tools to investigate the small length-scale propagation of compositional heterogeneity in the igneous system during mixing (e.g. Ginibre et al., 2002).

1.5 Zoned minerals as a tool for detecting magmatic processes and magmas physical conditions: zoning pattern, magmatic environments and thermobarometry

1.5.1 Crystal zoning

Another expression of disequilibrium in crystals is represented by crystal zoning. Crystal zoning is a systematic pattern of chemical variation within a solid solution mineral (Streck, 2008). It is a record of incomplete continuous reaction relations between a melt and the crystallizing solid solution as intensive parameters were changing in the magma system faster than kinetic rates could maintain equilibrium (Best, 2003). To maintain a constant state of equilibrium between crystals and melt there is an exchange reaction between coupled ions. Exchange must occur by migration (diffusion) of these ions across the interface between the melt and already formed crystals as intensive variables change. If there is a change in the environment in which the crystal is growing, it can lead to different growth bands in the crystal having different color tones (Fig. 12; that are a reflection of different compositions in the mineral).

Fig. 12 Backscattered electron image of a vesuvianite sample showing the fine-scale chemical zoning. The white bar is in microns. (from Bellatreccia et al., 2006)

Zoning can be of several types. In normal or continuous zoning the outer portions of the crystal have a lower-temperature composition than the core. Normal zoning usually reflects continuing re-equilibration of a crystal to progressive changing melt composition as the host magma cools and evolves during the growth history of the phenocryst in a magma chamber. In reverse zoning the outer portions of the crystal have a higher temperature composition than the core. Reverse zoning indicates disequilibrium conditions and a return to less evolved compositions. Usually it reflects mixing between host magma and a more primitive magma during crystal growth. Oscillatory zoning is a repetitive, more or less periodic variation in mineral composition, resulting in concentric growth zones usually from a few to tens of microns in width. Oscillatory zoning can be explained as a crystal's response to fluctuating external conditions. For example, it can be attributed to recycling of phenocrysts through zones of cooler, more evolved melt and hotter, more primitive melt in a convecting magma chamber. It can otherwise record a crystal's reaction to repeated influxes of fresh magma and its mixing with a more evolved resident magma. Oscillatory zoning can be explained also in terms of local effects. Patchy zoning is characterized by irregular areas of contrasting composition. Usually patchy zoning consists of irregular corroded portions having been filled and surrounded in crystallographic continuity by a different mineral composition. Morphologies of crystals and growth zones reflect the kinetics of growth (Lofgren, 1974) or dissolution (Tsuchiyama, 1985).

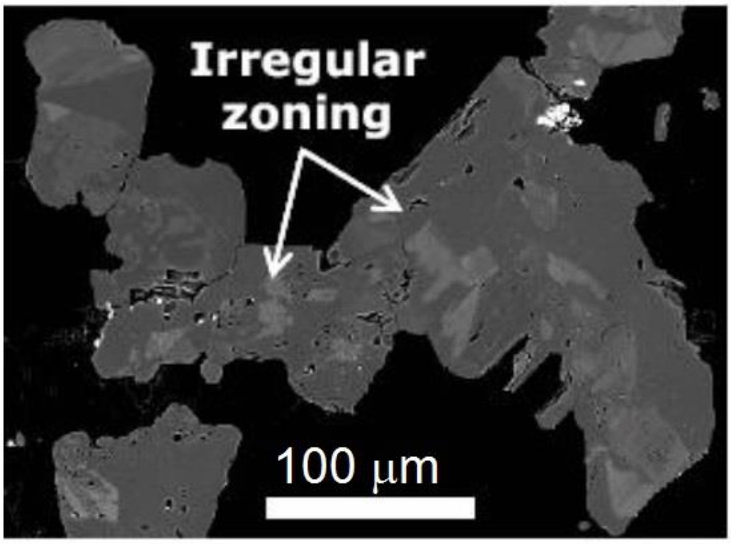

Fig. 13 Backscattered electron image of rutile crystals showing irregular or patchy zoning (from Rabbia and Hernandèz, 2012)

1.5.2 Zoning patterns and magmatic environments

The study of the zoning patterns, by the investigation of the relations among compositional populations, can provide details on the evolution of magma(s) and growth history of crystals. As the zoning pattern can be well preserved in minerals, these latter become messengers of information about physical conditions operating in the magmatic system during the development of magmatic processes (e.g. Eichelberger, 1980). As the change in composition is due to change of intensive variables, spatial compositional variations in magmatic minerals record chemical and physical changes in the magma from which they grew (Anderson, 1984; Helz, 1987; Hibbard, 1981; Humphreys et al., 2006; Singer et al., 1995; Wallace & Bergantz, 2002, 2004, 2005; Ginibre et al., 2007; Streck, 2008).. As an example, using experimentally determined phase relationships, e.g. compositions of minerals in equilibrium with a melt as a function of pressure, temperature and water content, the chemical composition of mineral assemblages allows the reconstruction of the conditions of crystallization. Conversely, crystal populations out of equilibrium can be identified. In this way, zoned crystals can provide a record of the processes (such as crystallization, recharge of a magma chamber, crustal assimilation, convection in the magma chamber) and conditions (pressure, temperature and volatile content) in the magma chamber and may also contain clues about the mechanisms triggering eruption (e.g. Ginibre et al., 2007). The use of compositionally zoned minerals, including plagioclase (Vance, 1962, 1965; Pearce and Kolisnik, 1990; Ginibre et al., 2002), olivine (Clark et al., 1986; Kohn et al., 1989; Kahl et al., 2011, 2013, 2015) and clinopyroxene (Downes, 1974; Clark et al., 1986; Streck et al., 2002) to unravel the sequence of events that occurred in a magmatic system is well established. Investigations of mineral textures and zoning have provided evidence for open system processes during magmatic evolution (Streck, 2008). Magma mixing often leaves a marked record in the texture and zoning of single minerals and in the observed mineral populations of the resident magmas as crystals and melts are added from recharging magma. Multiple subsets of crystal populations, and multiple zones inside crystals, may allow the reconstruction of complex series of mixing events that involve different populations of crystals (e.g. Martin et al., 2008; Kahl et al., 2013, 2015).

The zoning patterns of major and/or trace elements of a mineral which experienced open system processes often consists of two or more compositional plateaux with diffuse or sharp boundaries between them. Progressive changes, such as cooling or differentiation, would produce continuous variations in composition rather than plateaux separated by sudden jumps. Instead, the occurrence of several compositional plateau between the core and the rim of crystals indicates that the compositional zonings were not produced by simple fractionation during growth (e.g. Costa et al., 2008). In case the zoning patterns of elements consist of two or more compositional plateau, the composition of the latter likely represents growth of the crystal under a constant set of intensive thermodynamic variables (pressure, temperature, composition, fugacities of volatile species). A set of such variables characterizes a magmatic environment (ME; Kahl et al., 2015), which may also represent a physical reservoir (e.g. a sill) or be a part of a larger physical reservoir (e.g. a portion of a zoned magma reservoir). The chemical record preserved within a crystal allows an ME to be identified; the nature of the physical reservoir can sometimes also be inferred, but this is a matter of interpretation. The compositional variation from core to rim in a crystal can be assumed to represent a sort of chemical stratigraphy; that is, the ME recorded by the core of a crystal is interpreted to be an environment experienced by the crystal earlier than the ME recorded by compositions closer to the rim (Kahl et al., 2015). The change in zoning pattern from one plateau composition to another is then equivalent to the transfer of the crystal from one magmatic environment to another. This can be accomplished either by the crystal physically moving (with some melt) from one environment to another, or by the environment itself changing around the crystal (e.g. by cooling or degassing). The successive superimposition of two plateau compositions therefore can represent the mixing of magmas from two different MEs, either by the magma containing the crystal entering a new ME or by magma with different characteristics entering the environment of the crystal and modifying the ME. In this way, associating a set of conditions to a magmatic environment, it is possible to investigate the change of magmatic environments over the lifetime of the crystal, from initial nucleation to final quenching upon eruption.

The zoning patterns of clinopyroxene crystals belonging to the volcanic products of the Zaro and the Agnano-Monte Spina eruptions have been characterized from this point of view. A population-based approach has been used in order to investigate the different magmatic environments in which clinopyroxenes grew. The chemical composition of the crystals, combined with the determination of intensive variables (temperature, pressure) experienced by crystals, allowed to identify the number of magmatic environments recorded in such zoning patterns. The chemical information recorded in the zoning patterns has been systematically organized in order to quantify the number of connectivity between different magmatic environments. This allowed to reconstruct the evolutionary history of the clinopyroxene crystals.

Moreover, recently, the study of compositional zoning in minerals in volcanic systems characterized by magma mixing has been successfully utilized as a proxy to estimate the residence time of magma in subvolcanic reservoirs prior to eruption (e.g. Martin et al., 2008; Costa and Morgan, 2011), further highlighting the importance of disequilibrium in crystals and providing information about volcanic systems that would be otherwise inaccessible.

1.5.3 Geothermometry and geobarometry

As already mentioned, since the crystal composition in a magma depends on crystallization conditions, crystals can provide details of the physical conditions (temperature, pressure) during storage and prior to eruption of the magmatic system (e.g. Eichelberger, 1980).

Determination of intensive parameters in magma systems using equilibrium assemblages of coexisting minerals is a major endeavor of modern petrology. Geothermobarometry allows to estimate crystallization pressure and temperature by applying calibrated equations to geochemical data of various mineral phases, glasses, melt inclusions and whole rock compositions, or a combination thereof. The fundamental premise of geothermobarometry is that mineral assemblage of a rock and mineral compositions are sensitive to pressure and temperature conditions of formation and that the events subsequent to mineral equilibration have not significantly modified these rock properties. The theoretical basis for most geothermobarometers involves determining the equilibrium constant for a reaction and estimating the conditions of sample equilibration based on that value (Mihaljevic, 1999; Putirka, 2008). Reactions that have been used as geothermometers and geobarometers include, but are not restricted to, univariant equilibria, multivariant or net transfer equilibria, exchange reactions, and solvus equilibria (Bohlen and Lindsley, 1987).

Calculated pressures in combination with bedrock density provide a means of calculating depths of crystallisation and hence estimate potential magma storage depth. Determining magma storage depths is essential for various reasons. For example, understanding the distribution of magma storage depths within the lithosphere provides information about crustal formation mechanisms in both oceanic and continental settings (Henstock et al., 1993; Kelemen et al., 1997; Annen et al., 2006). Estimating pre-eruptive magma storage depths is also essential for integrating petrological records of magmatism with expressions of ongoing unrest such as seismicity, ground deformation and gas emission in volcanically active regions (Edmonds, 2008; Sigmundsson et al., 2010; Tarasewicz et al., 2014).

Many quantitative mineral geothermometers and geobarometers have been calibrated by experiments and thermodynamic models. Commonly these models either make use of exchange reactions between minerals and co-existing melt (Putirka et al., 1996, 2003; Putirka, 2005, 2008; Masotta et al., 2013; Neave and Putirka, 2017), cation content in minerals and co-existing melt (Johnson and Rutherford, 1989; Henry et al., 2005), pressure-sensitive variations in crystal lattice structure (Nimis 1995, 1999; Nimis and Ulmer 1998), or phase relations of a set of minerals (Yang et al. 1996; Benisek et al., 2004).

The choice of a thermobarometric model is dependent on the mineral content and the geochemical composition of the analyzed magmatic products as the models are calibrated for certain mineral phases and restricted magma compositional ranges. For mafic magmas, for example, ‘OPAM’ (Olivine-Plagioclase-Augite-Melt) barometry uses the melt composition that is in equilibrium with plagioclase, clinopyroxene and olivine to estimate a pressure of ‘last equilibration’ (Yang et a., 1996; Bali et al., 2018). It is therefore possible to determine the pressure at which the melt was last in equilibrium with olivine, plagioclase and augite. Current barometric methods range from exploiting volatile solubility laws (e.g., Newman and Lowenstern, 2002; Moore et al., 2008) or equations of state (Hansteen and Klügel, 2008) to determine melt and fluid inclusion entrapment pressures, through to calibrating pressure-sensitive phase equilibria relations using experimental data (e.g., Putirka 2008). A geobarometer for determination of pressure during crystallization of some felsic magma systems relies on the equilibrium concentration of Al in hornblende and calibration is sensitive to temperature, oxygen fugacity, and the crystalline phases coexisting with a water-saturated melt (Anderson and Smith, 1995). A commonly used geobarometer uses clinopyroxene components: since the incorporation of jadeite ($NaAlSi_2O_6$; Jd) into clinopyroxene is strongly pressure dependent, Putirka et al. (1996) presented a series of equations describing the pressure-dependent Jd-liquid (liq) reaction, as well as the strongly temperature-dependent Jd into diopside-hedenbergite ($Ca(Mg,Fe)Si_2O_6$; Di-Hd) and calcium Tschermak's component ($CaAlAlSiO_6$; Ca-Ts) into Di-Hd exchange reactions. These thermobarometric equations were subsequently reformulated in 2003 to extend their applicability to felsic and hydrous systems (Putirka et al., 2003), before being reviewed further five years later (Putirka, 2008). However, these various barometric methods are subject to numerous assumptions and unavoidably return pressure estimates with considerable uncertainties. Oxygen fugacity and temperature can be determined from equilibrium coexisting magnetite and ilmenite solid solutions (Carmichael, 1967; Powell and Powell, 1977; Spencer and Lindsley, 1981; Anderson and Lindsley, 1985; Rao et al., 1991). Temperature can be determined from coexisting alkali feldspar and plagioclase (Kroll et al., 1993; Benisek et al., 2004) and from clino- and orthopyroxene solid solutions (Lindsley and Andersen, 1983).

Most of the commonly used current geo-thermometers are based on the modeling of entropy and volume changes occurring in equilibrium reactions between melts and crystals (Putirka, 2018). Clinopyroxene-melt (Putirka, 2003) and plagioclase-melt (Putirka, 2005) geothermobarometers are well known and commonly used by petrologists. The typical calibration procedure for thermometers and barometers consists in five main steps: i) to identify chemical equilibria associated with large variations of entropy and volume, respectively (Putirka, 2005, 2008); ii) to retrieve a consistent experimental dataset with known temperature and pressure; iii) to calculate the mineral components from chemical analyses; iv) to define a regression strategy; v) model validation (Putirka, 2005, 2008).

Clinopyroxene-liquid equilibria have also been used to specific cases, such as to define transcrustal magma plumbing systems under Mt. Etna amongst other locations (Giacomoni et al., 2016). Moreover, to improve the suitability of clinopyroxene-liquid thermobarometers for evolved alkaline systems, a series of recalibrated thermobarometric expressions has been developed and applied to Nemrut in Turkey (Macdonald et al., 2015) , as well as to Mt. Vesuvius and Campi Flegrei in Italy (Masotta et al., 2013). When applicable, multiple thermobarometric models can be employed in order to provide independent tests.

In this thesis, the geaothermobarometers of Putirka (2008) and Masotta et al. (2013) have been used to detect pressure and temperature of crystallization of clinopyroxenes crystals belonging to volcanic products of Zaro and Agnano-Monte Spina. Moreover, the determination of temperature is essential into apply diffusion modelling, which allows to obtain information on timescales (see Chapter 2). In particular, the obtained duration is exponentially dependent on the temperature value.

1.5.3.1 Mineral-melt thermobarometers: equilibrium conditions

In order to produce robust pressure and temperature estimates, equilibrium of mineral-melt pairs is of crucial importance for most thermobarometric models. Generally, before applying thermobarometric models, it is necessary to verify the equilibrium conditions through the compositional dependence between a melt and a coexisting mineral phase. The “tests for equilibrium” are predictive models obtained via regression analysis of crystal-melt pairs in equilibrium conditions, by using both experimental and natural datasets. These predictive models show the theoretical equilibrium field of a melt and a coexisting mineral, through the Kd (defined as the molar ratio between selected elements of the liquid divided by the molar ratio between the same elements of coexisting minerals). Hence, for clinopyroxene- and olivine-melt thermobarometry, the recommended procedure of assessing equilibrium, at the time of crystallization, between clinpyroxene/olivine and a possible nominal melt is evaluation of the $Kd_{(Fe\text{-}Mg)}$ exchange coefficient. This practice has a long history for both olivine and clinopyroxene; authors have indeed suggested that, at the equilibrium condition, $^{(ol–melt)}$ Kd $_{(Fe–Mg)}$ and $^{(cpx–melt)}$ Kd $_{(Fe–Mg)}$ yield constant values of 0.30 ± 0.02 (Roeder and Emslie, 1970; Matzen et al., 2011) and 0.27 ± 0.03 (Grove and Bryan, 1983; Sisson and Grove, 1993; Putirka et al., 2003), respectively. In case of plagioclase-melt thermobarometry, suitable plagioclase-melt pairs were chosen through the $KD_{(An\text{-}Ab)}$ equilibrium test (Putirka, 2005). These equilibrium test approaches ensure that only equilibrium mineral-melt pairs are considered for further thermobarometric calculations.

However, it has also long been known that Fe–Mg exchange has certain limitations. For example, Gee and Sack (1988) highlighted that $^{(ol–melt)}$ Kd $_{(Fe–Mg)}$ is sensitive to melt composition, which implies that fixed values for such coefficients cannot be applied. Similarly, Putirka (2008) showed that $^{(cpx–melt)}$ Kd $_{(Fe–Mg)}$ is not a reliable indicator of clinopyroxene–liquid equilibrium for a wide range of compositions. Therefore, the best test for assessing whether or not a mineral and co-existing melts were in equilibrium at the time of crystallization is based on the deviation of mineral components, i.e., for clinopyroxene, Di, Hd, En, Fs, CaTs, CaTiTs, CaCrTs and Jd, between crystal and melt from equilibrium values. The degree of disequilibrium is determined through the comparison between components "predicted" for a mineral phase via regression analyses of mineral–liquid pairs in equilibrium conditions, with those "measured" in the analyzed crystals. Using this model, Putirka (2008) and Mollo et al. (2010) suggested that the difference between "predicted" and "observed" components provides a more robust test for equilibrium than the Kd.

2. TIMESCALES OF MAGMATIC PROCESSES

Important questions about the behavior of magma reservoirs concern the timescales of various processes. These timescales are important in evaluating volcanic hazards, interpreting volcano monitoring data and, on longer time spans, developing models of likely repose periods for large volcanic systems. The timescales of magma supply, fractionation, mixing and recharge events also have relevance for broader questions relating to the timescale of crustal growth and of the creation of ore deposits in the crust (Edmonds et al., 2019). One might ask: on what timescale are magmas remobilized and ‘assembled’ prior to eruptions? How fast are melts extracted from mushy regions to form eruptible volumes? Progress in developing methods and models to generate timescale data in magmatic petrology, is reviewed, along with their limitations, in several papers (e.g. Hawkesworth et al., 2000; Morgan and Blake, 2006; Dohmen et al., 2017; Cooper, 2019).

Magmatic timescales can be constrained primarily by three methods: observational, radiometric and diffusive (e.g. Dohmen et al., 2017). Other methods (e.g. CSD; crystal size distribution), based on textural and kinetics approaches, have been recently employed to generally infer magma ascent rates shortly before eruption. Observational methods are limited to active magmatic systems, such as volcanoes that are erupting or degassing. For example, the growth of lava domes or inter-eruption gas discharge have been documented with unprecedented detail over the course of more than two decades. These observations provide precise timescales that can be used to refine physical understanding of sub-volcanic processes (e.g. Melnik and Sparks, 2005; Pistolesi et al., 2011; Christopher et al., 2015) and are nowadays supplemented by geodesy, tiltmeters, seismology and measurements of gas chemistry. The drawback of quantitative observational timescales is that they are limited to the modern era and to extend the observational timescale further back in time requires the availability of historical records.

As for the other two main methods, generally, radiometric ages allow quantification of crystallization ages whereas diffusion modelling constrains storage durations within the magma reservoir, and collectively they can capture processes such as long-term magma storage, mixing, and assembly of erupted magma bodies (Edmonds et al., 2019). The timescales obtained through these approaches range from minutes to hours for syn-eruptive magma ascent to years to centuries for magma mixing within the upper crust, to tens of thousands to hundreds of thousands of years of crystal storage and recycling in a long-lived magma reservoir (Cooper, 2019). This diverse sampling of timescales records different aspects of the system.

2.1 Textural and kinetics methods

Some methods use textural observation and growth rates of crystals (Cashman and Marsh, 1988; Eberl et al., 2002; Brugger and Hammer, 2010) in order to obtain information on magmatic processes and their timescales. The occurrence of microlites in pumice and scoria provides potential information on the timescale of magma migration within the crust, specifically from the magma chamber to the fragmentation level (Cashman and Marsh 1988; Marsh, 1998). This information may be unraveled by studying the size distribution of microlites pre- and syn-eruptively crystallized and quenched in the matrix of juvenile magma fragments (Fig. 14).

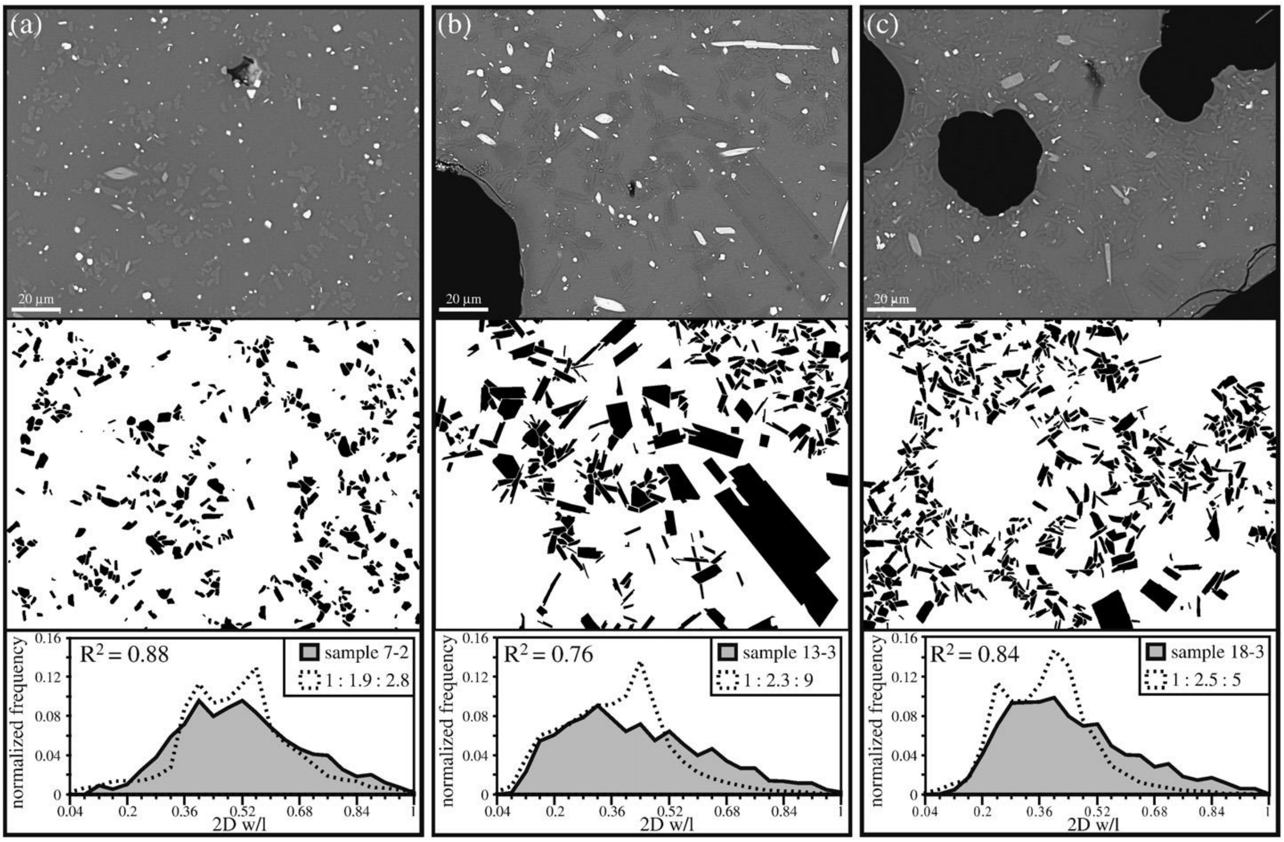

Fig. 14 Examples of BSE and binary images from decompression experiments. Two dimensional width/length distributions for each sample are shown along with their best fit crystal habit as determined by CSD Slice (Morgan and Jerram, 2006). (a) Sample decompressed at 0.5 MPa h^{-1} and quenched at 87 MPa. (b) Sample decompressed at 0.5 MPa h^{-1} and quenched at 5 MPa. (c) Sample decompressed at 2 MPa h^{-1} and quenched at 5 MPa (from Brugger and Hammer, 2010).

The observed variations in both composition and texture of crystals from igneous rocks reflect the integrated pressure–temperature–composition–time history of the magma from which they formed. As a result, it is possible to link textural observations on rocks with experimentally derived data for rates of crystal growth and crystal number density for specific mineral phases to the undercooling values of the parental melt. Crystal size and number density are intricately linked to the rates of crystal growth and nucleation, which change in response to variations in magma temperature, vapor pressure, and melt composition (e.g. Marsh, 1998). Thus, temporally-constrained studies of crystal textures provide insight into magma crystallization kinetics under changing thermobarometric conditions such as those imposed during magma transport, ascent, and eruption. The most commonly used quantitative measure of crystal textures is the crystal size distribution (CSD) technique, initially developed to study industrial crystallization in chemical engineering by Randolph and Larson (1971), and subsequently employed in the study of magmatic systems by Cashman and Marsh (1988) and Marsh (1988). Although it is possible to adopt any of a variety of models describing the time-, crystal size- or even melt composition-dependence of crystal growth rate (e.g., Jancic and Garside, 1976; Janse and deJong, 1976; Marsh, 1998; Eberl et al., 2002;) in order to extract kinetic information from a CSD, the vast majority of practitioners (e.g., Cashman, 1988, 1992; Hammer et al., 1999; Cashman and McConnell, 2005; Piochi et al., 2005; Armienti, 2008; Bindeman, 2003; Blundy and Cashman, 2008; Salisbury et al., 2008) assume constant crystal growth rate. This simplifying assumption allows nucleation rate and characteristic crystal size to be extracted directly from the y-intercept and slope, respectively, of a plot of the natural log of the population density versus crystal size (Fig. 15).

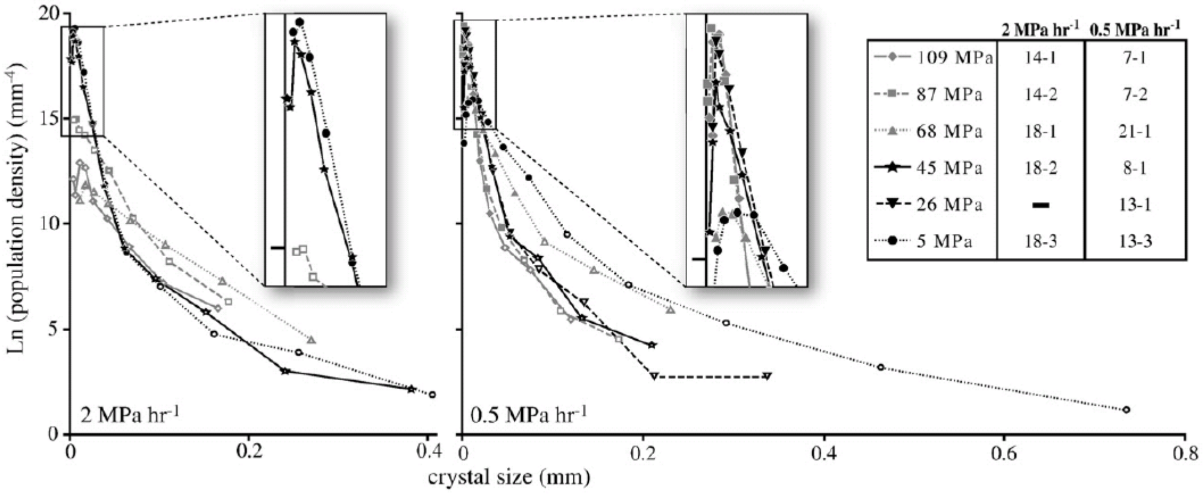

Fig. 15 Crystal size distributions calculated using CSD Corrections (from Brugger and Hammer, 2010).

Additionally, when magma residence time is independently known, CSDs may be used to determine crystal growth rates. Volcanological applications of CSDs include determining crystal growth mechanisms (Kile and Eberl, 2003; Kile et al., 2000), magma cooling rates (Cashman, 1993; Garrido et al., 2001; Lentz and McSween, 2000), and the timing of magma mixing events (Higgins, 1996b), and to calculate magma ascent time and/or residence time in a magma chamber (Mangan, 1990; Higgins, 1996a; Turner et al., 2003; Piochi et al., 2005; Noguchi et al., 2006; Salisbury et al., 2008). CSDs have also been used as evidence to support models of magmatic processes such as polybaric crystallization (Armienti et al., 1994), crystal settling (Bindeman, 2003), textural coarsening (Higgins, 1998, 1999; Higgins and Roberge, 2003) and mixing of distinct crystal populations in a batch of magma (Bindeman, 2003; Higgins, 1996b).

Anyway, CSD theory relies on many assumptions that are often clearly not fulfilled in natural systems: crystal growth rates are assumed to be constant. Experimental growth rates are not very well calibrated and depend, for example, on the degree of undercooling. Therefore, caution should be exerted into applying this approach, for example, to crystals showing complex zoning patters.

2.2 Radiometric methods

Radiometric dating systems, such as U-Pb and U-series of accessory minerals such as zircon and titanite (Hawkesworth et al., 2000; Cooper and Reid, 2008; Cooper, 2015), record long ages, corresponding to the time the mineral fractionated parent isotopes and became closed. The radiometric chronometers commonly applied to volcanic crystals are the U-Pb and ^{238}U-^{230}Th-^{226}Ra systems. The so-called uranium-series (U-series) nuclides provide unique timescale information on magmatic processes ranging from melt production, differentiation and ascent to magmatic degassing prior to eruption (e.g., Bennett et al., 1982, Gill and Williams, 1990, Turner et al., 2000, Condomines et al., 2003, Peate and Hawkesworth, 2005, Bourdon et al., 2006, Reagan et al., 2006, Handley et al., 2008, Reagan et al., 2008, Berlo and Turner, 2010, Sims et al., 2013, Bragagnia et al., 2014) as the nuclides have varied geochemical properties that cause them to be fractionated in distinct ways by different magmatic processes (see Peate and Hawkesworth, 2005 for a review). At secular equilibrium the activities of the nuclides are equal, for example, $(^{230}\mathrm{Th}/^{238}\mathrm{U}) = 1$. If the decay chain is affected by chemical fractionation of a parent/daughter elemental ratio, restoration of equilibrium by radioactive decay is determined by the half-life of the daughter nuclide involved.

Excess ^{238}U (^{238}U/^{230}Th > 1) and ^{226}Ra (^{226}Ra/^{230}Th > 1) values in volcanic rocks from subduction zone are typically attributed to fluid addition from the subduction slab on timescales of less than ~380,000 years and less than ~8000 years, respectively (e.g., Gill and Williams, 1990, Hawkesworth et al., 1997) although there may be some modification of ratios by crustal-level processes (e.g., Handley et al., 2008, Reubi et al., 2014, Huang et al., 2016). The U-series dating method (e.g., Cooper and Reid 2008) has also proven especially valuable in constraining magmatic timescales of processes occurring shortly before or during an eruption. For example, radon is a gas whose loss from the decay chain can provide valuable insights into degassing processes (e.g., Gauthier and Condomines, 1999; Berlo et al., 2006; Kayzar et al., 2009). The short-lived ^{210}Pb nuclide is produced by decay of the gas ^{222}Rn (half-life = 3.8 days), which readily enters the volatile phase in magmas (Lambert et al., 1985, Gill et al., 1985). Persistent loss or gain of ^{222}Rn via magmatic degassing or volatile accumulation will therefore result, in an open, degassing system (where ^{222}Rn is efficiently lost in the gas phase) in a deficit of ^{210}Pb. Thus, ^{210}Pb deficits can constrain the duration of degassing (e.g., Gauthier and Condomines, 1999). Alternatively, if gas is supplied from underlying fresh (and probably more mafic) magma, it is possible to create a ^{210}Pb excess (e.g., Kayzar et al., 2009, Condomines et al., 2010). Other daughter isotopes are preferentially sequestered by specific minerals, thereby constraining the onset of crystallization of those minerals in an evolving magmatic system. The uptake of radium by plagioclase is a case in point (e.g., Cooper and Reid, 2003; Turner et al., 2003).

The wide variety of half-lives of U-series radionuclides means that, in principle, a wealth of timescales from seconds to millennia can be recovered. However, once secular equilibrium between parent decay and daughter in growth is established, typically after about 5 daughter half-lives, all chronometric information is lost. Thus, what is dated is a time of decoupling (or cessation of secular equilibrium). A further limitation of the U-series approach is that the analytical techniques used do not lend themselves to high spatial resolution. Consequently, it may be difficult to disentangle multiple timescales from zoned crystals, especially where crystal cores and rims differ greatly in age (e.g., Cooper and Reid, 2003; Dohmen et al., 2017).

2.3 Diffusion chronometry

A family of geochronometers relies on the time-dependent flux (diffusion) of elements in response to chemical potential gradients established during magmatic processes. These gradients are most readily manifest in zoned crystals of common minerals in magmatic systems (e.g., Costa et al. 2008; Kahl et al., 2011). As a crystal grows, it takes up major and trace elements in response to changes in the melt with which it is bathed. Perturbations to the melt chemistry or the physical parameters that control uptake, such as pressure, temperature and redox, result in chemical changes between one layer (zone) and the next in the growing crystal. At the instant of growth, each layer has some simple relationship to the melt from which it grew, but no such relationship to the previous layer. The relationship between each layer and the melt may be one of chemical equilibrium or, if growth is relatively rapid, kinetic factors may dominate (e.g., Watson and Liang, 1995; Watson, 1996). Foremost amongst these is the rate at which chemical components can be supplied diffusively to the boundary layer around the growing crystal (Albarède and Bottinga, 1972) and the relative preference of trace species for the surface of growing crystals relative to their interior (Pinilla et al., 2012). What is important is that the growth of zoned magmatic crystals sets up chemical potential gradients between successive zones. Diffusion strives to eliminate such gradients by moving chemical components from one layer to another (Fig. 16).

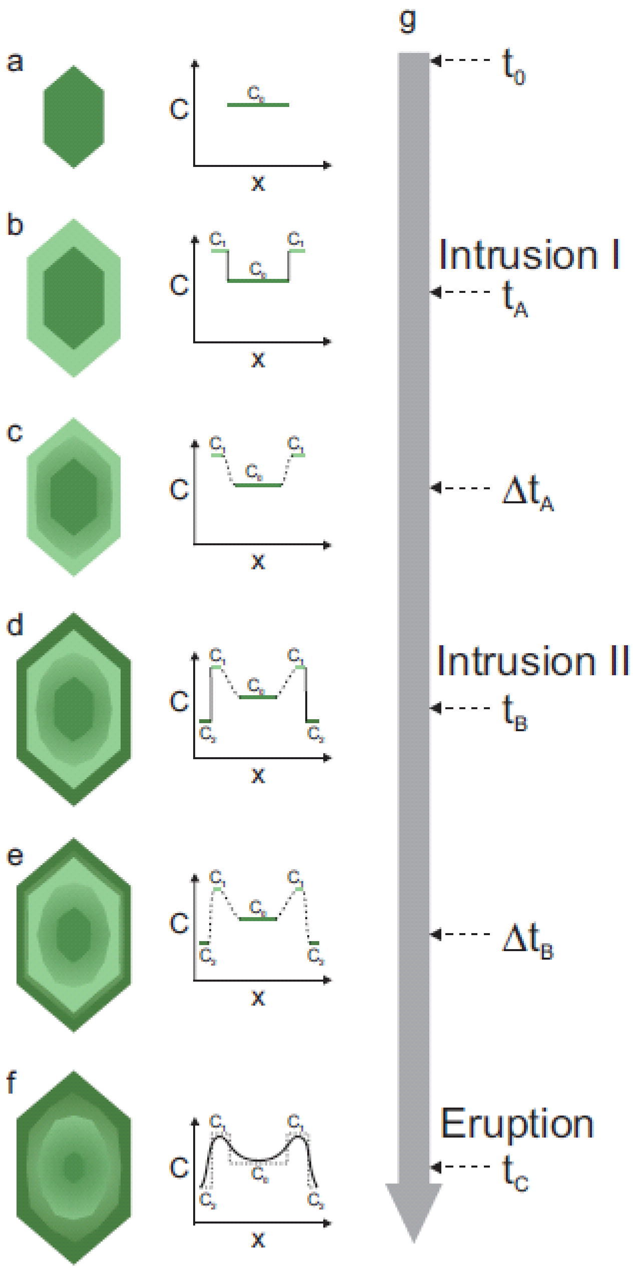

Fig. 16 Illustration of the concept to reconstruct the growth history and residence times in different magmatic environments of a phenocryst by sequential diffusion modelling. (a)–(f) illustrate concentration profiles (x denotes distance) induced sequentially by magmatic events during time line (g): (a) At some time t_0 a homogeneous crystal with composition C_0 was formed; (b) After the crystal came into contact with a different magmatic environment at time t_A (e.g., a new batch of melt arrived) a new rim with composition C_1 was formed; (c) After the formation of the rim, a diffusive flux starts to smooth the initial step profile; (d) At time t_B a second magmatic event (intrusion, magma mixing) changes the local thermodynamic conditions and a second rim is formed with composition C_2; (e) Concentration gradients between C_0, C_1 and C_2 tend to homogenize the entire concentration profile by chemical diffusion. (f) The eruption cools the magma quickly and freezes the concentration profile, which is eventually a product of growth and diffusion zoning (black solid line). The black dashed line represents the concentration profile produced only by growth without

diffusion (the initial profile used for diffusion modelling). The duration of diffusion at different stages before eruption, here Δt_A and Δt_B, are the quantities that can be obtained by simulating the observed concentration profiles (from Kahl et al. 2011).

The rate at which this happens, the chemical diffusivity, is a complex function of the diffusion mechanism, the point defect chemistry of the crystal, the temperature at which diffusion occurs and the geometry of the interface across which diffusion takes place. The significance of these various parameters is relatively well established through experiment and theory for a range of both crystals and melts, and the diffusivity of many trace species has been determined experimentally. Diffusion is, ultimately, a thermally mediated process; such that it occurs most rapidly at high (magmatic) temperatures and is effectively quenched once a system cools below a characteristic closure temperature (e.g., Dodson, 1986; Kohn and Penniston-Dorland, 2017). Consequently, diffusion chronometry is a very effective means to constrain the timescale between the event that caused the chemical perturbation responsible for a zone to form in a crystal and the moment at which this system cooled below some closure temperature when diffusion was effectively arrested. For explosive volcanic systems closure occurs upon eruption such that diffusion chronometry is a valuable tool for recovering the timescales of pre-eruptive processes that are responsible for modifying the chemistry of volcanic crystals.

2.3.1 The theory of diffusion

Mass is transported in magmatic systems by bulk flow (advection) and by diffusion. Diffusion (from the Latin word “diffundere” which means to pour out or spread out) can be defined as the relative motion of one or more particles of a system relative to other particles of the same system (Onsager, 1945). Diffusion arises from random motions of particles in a fluid or solid. Here the particles can be neutral molecules or atoms, or charged cations or anions. Random motions result from the thermal energy contained in a system, and they occur in all materials at all times at temperatures above the absolute zero. Hence, the existence of a concentration gradient or driving force of any kind is not necessary for diffusion. In order to describe diffusion in gases, liquids and solids, through a quantitative law, it is necessary to consider the quantity called flux. It is defined as the amount of material (expressed as the number of moles, mass of a substance, volume of a substance, and so forth) that crosses a plane of unitary surface area in a given direction per unit time. To obtain a net flux or directed motion due to diffusion, a driving force that coaxes particles to preferentially move in one direction is required. In transport of matter, the commonly applicable driving force is a chemical potential gradient-matter flow in the direction of decreasing chemical potential. Chemical potential is directly related to concentration in most cases, and diffusion can be considered usually as a process related to concentration gradients. In geochemistry, diffusion is defined as the process by which, under the influence of a chemical potential gradient, atoms, molecules, ions or lattice vacancies move from one position to another in a solvent phase.

The theory of diffusion was first developed for the description of energy transfer in the theory of heat conduction (Fourier, 1822). Several solutions of the heat conduction equation, also known as Fourier's law, have been provided by Carslaw and Jaeger (1959) and have been widely used for the modeling of thermal processes in the Earth's crust. The analogy of Fourier's theory to the diffusion of matter was first recognized by Fick (1855) and, accordingly, Fourier's principles applied to mass diffusion are called Fick's law. Fick's law has been widely accepted as a description for many geomorphological and petrochemical processes (e.g. Beaumont et al., 1992; Chakraborty and Ganguly, 1991). Solutions of Fick's law for a large number of boundary and initial conditions have been provided by Crank (1975).

Onsager (1945) assumed that the flux, J_i, of a diffusing component *i*, is proportional to the gradient of the corresponding chemical potential, $\partial\mu_i/\partial x$ (diffusion in one dimension), and the two are related to each other via a proportionality constant, L_i:

$$J_i = -L_i \frac{\partial \mu_i}{\partial x}$$

Chemical potentials can be related to measurable concentrations by the definition of a reference state and its associated reference chemical potential, $\mu°$: $\mu_i = \mu° + RT \ln(\gamma_i C_i)$, where γ_i is the activity coefficient. In the case of an ideal solution or a diluted component, where the derivative $\partial\ln(\gamma_i)/\partial x$ is zero, this relationship can be shown to be equivalent (e.g., Schmalzried, 1981; Ganguly, 2002) to the empirical relationship observed by A. Fick about 100 years earlier (Fick, 1855). It connects the flux, J_i, to the concentration gradient of the species, $(\partial C_i/\partial x)$:

$$J_i = -D_i \frac{\partial C_i}{\partial x}$$

In this equation, D_i is the diffusion coefficient or diffusivity of component *i*, C_i is the concentration of component *i* and $\partial C_i/\partial x$ is the concentration gradient of component *i* along the *x* direction.

The units of the diffusive flux are mass per unit area per unit time (such as $\mathrm{mol \cdot m^{-2} \cdot s^{-1}}$). The concentration has the units of mass per unit volume. The diffusion coefficient has the units of length-squared per unit time (for example, $\mathrm{m^2 \cdot s^{-1}}$). The diffusive flux is a vector (along x direction in this case) and the negative sign is to ensure that material diffuses from regions of high concentration to low concentration, that is, along the direction of decreasing concentration gradient. Fick's first law states that the diffusional flux of matter, J, is proportional to the spatial concentration gradient. In other words, flow by diffusion is driven by a spatial change in concentration, C. This relationship, often referred to as Fick’s first law, is analogous to other laws relating fluxes of different kinds to relevant driving forces (e.g., electrical current to electrical potential gradient: Ohm’s Law; heat flux to the gradient of temperature: Fourier’s Law) and is of practical use because concentration is an easily measurable quantity. The connection to the chemical potential gradient is the reason why Fick’s law is applicable to diffusion in gases, liquids, and solids, even though the mechanisms of diffusion in these media are entirely different. The homogenization of a concentration gradient is usually the result of a directed flux and not just random diffusion. Diffusion is ubiquitous, directed flux occurs only in the presence of a suitable driving force. Fick's first law has been used to define the diffusion coefficient and to study steady-state diffusion along a concentration gradient. The variable time does not appear explicitly in any of the equations shown above. Time is introduced by employing one of two universal constraints that any process must follow—the requirement of mass balance (the second being the requirement that total entropy must increase in any natural process). In terms of fluxes, this is stated most simply as: when a specified system is observed over any given length of time, the difference between what comes in and what goes out is the net change in the amount contained in that system. Fick's second law of diffusion is a statement of mass conservation for diffusive mass transfer in a medium. In one dimension, the diffusion equation can be written as:

$$\frac{\partial c_i}{\partial t} = \frac{\partial}{\partial x}\left(D_i \frac{\partial c_i}{\partial x}\right)$$

where *t* is the diffusion time. When the diffusion coefficient is independent of concentration or spatial coordinate (such as in the case of minerals and melts), the combination of a constitutive equation related to fluxes with the continuity equation leads to the following equation:

$$\frac{\partial c_i}{\partial t} = D_i \frac{\partial^2 c_i}{\partial x^2}$$

which relates the change of concentrations in time to the concentration gradients in the form of a partial differential equation: this is often described as the diffusion equation, or Fick's second law. This equation describes the evolution of concentration, *C*, as a function of time, *t*, at different spatial coordinates, *C(x,t)*, in one dimension. To obtain the specific concentration distribution (= concentration profile), *C(x)*, at any time after the initiation of diffusion, we need to define initial and boundary conditions for each medium (e.g., crystal, melt) in which diffusion occurs. Firstly, a diffusion model needs to be defined by describing the element fluxes and geometry for the real system. The model has to be translated to partial differential equations that must be solved for the given initial conditions (the concentration distributions at some defined point in time) and boundary conditions (the element fluxes at the geometric boundaries of the system). The boundary conditions define the interaction of the system (typically a chemically zoned crystal) with the exterior, thermodynamic environment (e.g., a silicate melt). Once the initial and boundary conditions have been specified, if the diffusion coefficient is known, the concentration at any position *(x)* and time *(t)* can be calculated.

For diffusion in three-dimensional isotropic media, the diffusion equation takes on the more general form in a Cartesian coordinate:

$$\frac{\partial c_i}{\partial t} = D_i\left(\frac{\partial^2 c_i}{\partial x^2} + \frac{\partial^2 c_i}{\partial y^2} + \frac{\partial^2 c_i}{\partial z^2}\right)$$

For diffusion in an axisymmetric sphere, the diffusion equation takes on the special form:

$$\frac{\partial c_i}{\partial t} = D_i\left(\frac{\partial^2 c_i}{\partial r^2} + \frac{2}{r}\frac{\partial c_i}{\partial r}\right)$$

where *r* is the radial coordinate. This equation can be used to model diffusion in and around mineral grains and fluid or melt inclusions. These laws are directly applicable to diffusion in isotropic media such as melts, glasses, and minerals of isometric crystal system.

It is possible to obtain other kinds of mathematical relationships between directed flux and the concentration. Some examples are:

(i) diffusion in an anisotropic medium (e.g., a non-cubic crystal):

$$\begin{aligned}
J_i^x &= -D_i^{xx}\frac{\partial C_i}{\partial x} - D_i^{xy}\frac{\partial C_i}{\partial y} - D_i^{xz}\frac{\partial C_i}{\partial z} \\
J_i^y &= -D_i^{yx}\frac{\partial C_i}{\partial x} - D_i^{yy}\frac{\partial C_i}{\partial y} - D_i^{yz}\frac{\partial C_i}{\partial z} \\
J_i^z &= -D_i^{zx}\frac{\partial C_i}{\partial x} - D_i^{zy}\frac{\partial C_i}{\partial y} - D_i^{zz}\frac{\partial C_i}{\partial z}
\end{aligned}$$

Total flux, J_i^x, along a direction x is not just proportional to the concentration gradient along this direction. These principal axes may coincide with the crystallographic symmetry axes in some crystal classes, as is the case for orthorhombic olivine;

(ii) diffusion accompanied by growth or dissolution:

$$J_i = -D_i \frac{\partial C_i}{\partial x} + v \cdot C_i$$

Here the total flux, J_i, is the result of flux due to diffusion plus another flux due to the net growth or dissolution of a crystal in the surrounding medium (e.g., melt) at a rate, ν. This equation describes flux of matter in a growing/dissolving crystal if the x-axis is defined to be such that the origin (x = 0) is always at the surface of the growing/dissolving crystal.

2.3.1.1 Type of diffusion

Depending on the chemical state of the system, the nature of the diffusants, the initial and boundary conditions, and simplifications involved, several types of diffusion can be identified: self-diffusion, chemical diffusion, multicomponent diffusion, effective binary diffusion, thermal diffusion and grain boundary diffusion (Ganguly, 2002; Chakraborty, 2008). Self-diffusion or tracer diffusion takes place when the system of interest is at chemical, but not isotopic, equilibrium. There is no concentration or chemical potential gradient of any elements in the system. This would be related to the random motions of atoms. Chemical diffusion or multicomponent diffusion takes place when the system of interest is out of chemical equilibrium. Many geological systems are made of two or more components. A silicate magma, for example, typically has seven or more major oxide components. During chemical diffusion, the concentration gradient of one component may affect the diffusive flux of another component. An alternative and much simplified approach is to treat chemical diffusion in magmas as an effective binary process. This is possible when chiefly the component of interest varies in concentration relative to all other components in the system. Here the multicomponent system is treated as a pseudo-binary system in which the component of interest is taken as the independent variable and all other components are taken together as the dependent variable (Cooper, 1968). Thermal diffusion is a general case of chemical diffusion in that the flow of heat drives a flow of matter. This transport phenomenon is often referred to as the “Soret effect”. The driving force for thermal diffusion involves temperature gradient. Grain boundary diffusion is a general case of diffusion in crystalline solids in which the boundaries between neighboring grains and dislocation pipes within the crystals serve as fast-pathways or short-circuits for the spreading of diffusant. Diffusion in polycrystalline materials is multipath and consists of both lattice diffusion (also called volume diffusion) and grain boundary diffusion. The mathematical treatment of diffusion in polycrystalline materials generally requires two independent diffusivities, one for diffusion in the crystal lattice and the other for diffusion along grain boundaries or dislocation pipes (Fisher, 1951; Le Claire, 1963). The structure of grain boundaries is relatively open compared to the structure of the crystal lattice. Diffusion along grain boundaries is typically orders of magnitude faster than diffusion within the crystal lattice.

2.3.1.2 Diffusion coefficient

The diffusion coefficient, D, is an example of material constant. The mathematical form of these equations describes the nature of the process; the values of the material constants are the causes of different behavior in different systems. The diffusion coefficients are expressed as a function of time, *D(t),* through their dependence on temperature, *T*. This is accomplished via an Arrhenius-type equation with activation energy, *Q* (e.g. Chakraborty, 2008), i.e.:

$$D(t) = D_0 \exp\left(\frac{-Q}{RT(t)}\right)$$

where D_0 is related to the vibration frequency and jumping distance of the diffusing species in the medium. This equation describes diffusion that occurs in any thermal event, i.e., along any temperature–time path, $T(t)$. As already seen, this time-dependent diffusion coefficient is used in the diffusion equation, which lets to describe how concentration gradients (i.e., concentration profiles) evolve as a function of time. In general, both self-diffusion and chemical diffusion coefficients in a substance or medium vary systematically with temperature, pressure, and composition. Pressure, water fugacity, oxygen fugacity, composition and crystallographic direction also play a role, depending on their values and the mineral and elements of interest. The effects of oxygen or water fugacity, the composition or crystallographic orientation, are typically incorporated in the pre-exponential factor D_0, although they may also have an effect in the activation energy (Costa et al., 2008). The crystallographic orientation influences the diffusion coefficient: in an isotropic medium it is independent of direction or orientation and can be treated as a scalar. For diffusion in anisotropic media, such as minerals of crystal systems other than isometric, the diffusion coefficient will depend on the direction of diffusion in the crystals. Diffusivities measured along different directions in the crystal may be different depending on the symmetry of the crystal (e.g., for Fe–Mg interdiffusion in olivine, where the D along c axis is 6 times greater than D along a and b axes, in the T range 700–1250 °C; diffusion anisotropy changes at higher temperatures; Tachibana et al., 2013).

Diffusion coefficients for earth and planetary materials reported in the literature are mostly obtained from laboratory experiments. The methods for measuring diffusivities vary considerably, depending on physical state of the matter (fluid, melt, glass, or solid) and availability of analytical methods. Regardless of experimental complexity and sophistication, the basic idea of all diffusion experiments remains the same: given an initial perturbation in concentration or isotopic ratio on the surface or in part of the specimen of interest, to monitor the spread of the diffusant in the specimen as a function of diffusion time by measuring concentration and/or isotopic ratio profile(s) in the experimental charge using a suitable analytical instrument, and to retrieve diffusion coefficient(s) from the measured concentration profiles using solutions to diffusion equations pertinent to the experimental setup.

2.3.1.3 The power of diffusion chronometers: general strengths and advantages

Empirical equations combining nucleation and growth have been used to determine timescales. Examples include crystal size distribution (CSD) analysis. For these kinetic approaches, many assumptions occur, that are often clearly not fulfilled in natural systems: crystal growth rates are assumed to be constant. Moreover, nucleation and crystal growth can occur through different mechanisms and, consequently, the first step of modeling these processes is to identify the law (i.e., the equation) they obey in a given case. The radiometric dating method (e.g. U-series) has proven especially valuable in constraining many magmatic timescales (e.g. Turner and Costa, 2007). Nevertheless, the central problem of radiometric dating persists; the parent and daughter isotopes can become decoupled, such that what is dated is a time of decoupling (or cessation of secular equilibrium). A further limitation of the U-series approach is that the analytical techniques used do not lend themselves to high spatial resolution. Consequently, it may be difficult to disentangle multiple timescales from zoned crystals, especially where crystal cores and rims differ greatly in age (e.g., Cooper and Reid, 2003). Within this context, Chakraborty (2006) has discussed why diffusion is a powerful tool for determining durations or timescales:

(a) It is a ubiquitous process. Natural minerals are typically solid solutions and so thermodynamics requires that the composition of the reactant and the product in an elementary step of any chemical transformation is different. Obtaining a product with a different chemical composition from that of the reactant requires diffusion of atoms to occur on some scale somewhere.

(b) The process is governed by one well-defined, quantitative law. A combination of conventional petrographic skills (to identify suitable initial and boundary conditions) combined with modern numerical methods for solution of differential equations is necessary for usefully applying this law.

(c) Under favorable circumstances, the durations/timescales are determined by modeling diffusion of the same elements that are also used to determine the pressure/temperature/dates of various events affecting the rocks. This allows the durations to be related to specific processes.

(d) Diffusion modeling yields durations directly. Radiogenic isotopes date events accurately, but it is by combining several such dates, with some consideration of closure of a system (typically dependent on consideration of diffusion), that one can conclude anything about durations or rates. By using diffusion chronometry we can determine a timescale of the respective process (duration) that is independent of the absolute age of the crystal. Thus, the same methodology can be applied to crystals in volcanic rocks from any age, i.e., Archean to the present day.

(e) There is no limit on the timescale that can be investigated, from seconds up to billions of years. Short-lived processes can be determined in old crystals. For example, with diffusion modelling the cooling rate of refractory high temperature condensates in the solar nebula or the peak temperature of metamorphism were determined for chondrite parent bodies at the onset of our solar system (Simon et al., 2011; Schwinger et al., 2016).

(f) Diffusion rates of different elements in the various minerals are spread over many orders of magnitudes at any given condition. In this connection, the rapidly increasing capability of measuring trace element and isotopic concentration gradients with increasing spatial resolution is of immense importance.

(g) The increased speed and resolution of analytical equipment means that it is possible to measure multiple compositional profiles/maps from the same sample. This affords the possibility of numerous cross checks between information obtained from the diffusion modeling of the same elements in different grains (including the use of effects resulting from anisotropy of diffusion), different elements in the same mineral, and different elements in different minerals. This ability to obtain multiple measurements allows statistics to outweigh uncertainties that stem from lack of knowledge of initial or boundary conditions during diffusion. The same procedure helps to identify compositional gradients that have been produced by processes other than diffusion.

2.3.2 Diffusion modelling

Compositional zoning in a crystal may be used to obtain time if: (i) one or more of the magmatic environmental variables such as temperature, pressure, volatile fugacities, or the composition of the liquid change (creating zoning) are known, and (ii) the diffusion of the elements of interest in the mineral is fast enough to partially erase the zoning, but slow enough for the crystal to not fully equilibrate to the new set of conditions. Once a zoning pattern is established in a crystal it is possible, under certain conditions, to obtain a time constraint and correlate this directly to the process that is recorded in the crystal (e.g. Chakraborty, 2008; Costa et al., 2008; Kahl et al., 2011, 2013, 2015). The first thing is to consider what magmatic processes the crystals are recording. The same type of zoning in different samples can be modeled in different ways, depending on the geological context. This means that a detailed petrological study must be conducted before to launch into the models. For example, diffusion modelling of compositional steps in volcanic crystals has emerged as a critical method to establish the age of ‘young’ (10^{-1}–10^{3} years) mixing events in magmas (e.g. Costa and Morgan, 2011), made possible by advances in microanalysis as well as in modelling diffusional processes.

With the diffusion equation, to obtain robust timescales of magmatic processes, we need to consider the following points: (i) how well the values of the diffusion coefficient are know; (ii) how well the concentration gradients have been characterized, paying special attention to the precision and spatial resolution of the analytical technique that is used.

The initial and boundary conditions are crucial aspects. The initial condition refers to how to determine or infer the initial shape of the profile used to start the calculation (e.g. homogenous, ladder type, oscillatory). The boundary conditions refer to the type of boundary between the crystal and the surrounding media (e.g. at the crystal rim). This means it is necessary an appropriate diffusion model, which includes geometry (e.g., simplified geometry vs. real crystal shape; 1D vs. 2D vs. 3D models), initial condition (e.g., homogenous concentration vs. step-like zoning vs. complex zoning), and boundary condition (e.g., fixed rim composition vs. variable rim composition as controlled by a temperature-dependent exchange reaction, a geothermometer, or by variable element fluxes from the environment; open system vs. closed system; Chakraborty and Ganguly, 1991). This is not always straightforward and, depending on the crystal growth and diffusion rates of the elements of interest, the observed profile is a combination of both growth and diffusion. Different initial profiles would yield different timescales as a result, although a detailed analysis of the most common end-member possibilities shows that the effects on absolute times are not so large as we would anticipate (Costa et al., 2008). There have been different approaches to assessing the initial conditions; these fall mainly into three categories: (i) use the profile shapes of the slow-diffusing elements, combined with a consideration of melt chemistry and partitioning, as a proxy for the initial profile shape of faster-diffusing elements. A perfect candidate for this approach is plagioclase, where the slow diffusivities of the anorthite component involving coupled diffusion of NaSi-CaAl (Grove et al., 1984) are a good indicator of the profiles created during magmatic processes and thus can be used to model the initial condition for the faster diffusing elements such as Mg or Sr (Costa et al., 2003. 2010). In clinopyroxene crystals from the Agnano-Monte Spina eruption, used to infer timescales estimation in this thesis, the Al (slow diffusive element) has been used to model the initial condition for Fe-Mg interdiffusion (faster diffusing elements); (ii) assume a very sharp profile as the initial condition, in which case the time obtained is a maximum. This has been shown to be useful for modeling Fe-Mg in clinopyroxene (Morgan et al., 2004) or Ti diffusion in quartz (Wark et al., 2007); (iii) use a homogenous initial profile and prove a posteriori that this is a good assumption by the consistency of the results obtained by modeling multiple elements and multiple traverses along different orientations. Olivine has been a good candidate for such an approach because of the diffusion anisotropy of many elements (Costa & Chakraborty, 2004; Costa and Dungan, 2005). The other important decision is the type of boundary that is applicable to the problem that we want to model. The boundary conditions arise from the nature of exchange of the elements of interest at the boundary of the crystal with its surrounding matrix. Two end-member cases are an isolating boundary where the crystal does not exchange matter or equilibrate with its surroundings (e.g. liquid), and an open boundary where re-equilibration of the crystal with its host liquid occurs. In the case of magmatic rocks and crystals that are freely set in a liquid of a much larger mass than the crystals, it is likely that the boundary of the crystal will be open to exchange with the liquid. Open boundaries are expected to be far more common in magmatic systems where minerals are in diffusive communication via melts. This open boundary condition has been applied in many studies and is mainly of two types: the concentration is constant along time, or the concentration at the boundary changes because of crystallization, mixing or changes in temperature and the partition coefficients. These considerations allow isothermal diffusion models to be evaluated, and these are often adequate for volcanic systems. Such models yield the duration of time that a heterogeneous crystal experienced high temperatures; i.e., prior to quenching by eruption: this is the case of clinopyroxene crystals studied in this thesis.

Once the initial and boundary conditions have been adequately chosen for the specific diffusion model, the key parameter in such model is the diffusion coefficient. The value of the diffusion coefficient strongly depends on temperature (D exponentially increases with temperature), which is the main parameter affecting the diffusion process, other than on pressure, water fugacity, oxygen fugacity, composition and crystallographic direction which also play a role. Anyway, the advancements in experimental and analytical equipment based on thin film technology and nanometer-sized diffusion zones allow the determination of diffusion coefficients in many cases directly at the relevant P, T, and other environmental variables (e.g., Dohmen et al., 2002). Moreover, the number and the quality (e.g., exploring the full range of environmental variables) of diffusion coefficients has increased dramatically, and it is possible to better understand the mechanisms of diffusion.

Once the form of the constitutive equation appropriate for modeling the relevant continuity equation (the initial and boundary conditions and the diffusion coefficient have been defined) has been identified the diffusion equations may be solved numerically or analytically. For the analytical solution, where concentration is given as an analytical function of space and time, two methods are used: solution by integration and solution by Fourier transform. Integrated solutions, namely those of infinite half-space and step function type problems, often contain *x* and *t* inside a term of the form:

$$\operatorname{erf}\left(\frac{x}{\sqrt{4Dt}}\right)$$

where *erf* is the error function (Crank, 1975; Carslaw and Jaeger, 1959). The error function is the name given to the unsolvable integral:

$$\operatorname{erf}(n) \equiv 2/\sqrt{\pi} \int_0^n \mathrm{e}^{-n^2}\,\mathrm{d}n$$

for which tabular listings and numerical solutions are provided by many software packages (e.g. Costa et al., 2008) and textbooks (e.g. Crank, 1975). The error function is used to model the variation of concentration as a function of time. Analytical solutions are typically in the form of an error function, Bessel function or exponentials and it is necessary to have a different solution for given initial conditions, boundary conditions and geometry (plane sheet, cylinder or sphere). The analytical solutions for many different initial and boundary conditions for different geometries can be found in Crank (1975) and Carslaw and Jaeger (1959). An alternative to analytical solutions is to discretize the continuity equations using numerical methods. Numerical solution to the diffusion equation can be found using the techniques of finite differences (Crank, 1975; Press et al., 2007).

The technique uses an approximate solution to the partial derivatives with a Taylor series approximation and algebraic manipulations (e.g. Costa et al., 2008). Numerical solutions have the disadvantage that the algorithms need to be written and that depending on the scale of the problems and the desired resolution, a significant amount of computer time could be necessary.

For both analytical and numerical solutions, a forward model is used to infer the solution of the equation: the measured distributions of concentration are fitted by this solution, where time (or the temperature–time path) is the only unknown. In such model, the time term of the diffusion equation is varied until the shapes of calculated profiles closely match those of the measured profiles. The difference between the initial and the final (measured) concentration distribution (or, more correctly, the chemical potential distribution) of the element/isotope of interest is the measure of the total extent of diffusion, which basically contains the time information. These steps need to be applied to multiple crystals from single and multiple thin sections in order to obtain a suitable statistics and confidence in the retrieved timescales. In fact, the validity of the resulting timescales is invigorated by the use of multiple profiles in a crystal and by the use of multiple crystals yielding similar time estimates. If these conditions are satisfied, it is possible to consider reliable the obtained time span. If two profiles of the same crystal yield different time estimates, the crystal can be considered to be affected by processes other than diffusive modifications (e.g. Costa et al., 2008).

2.3.2.1 Applications of diffusion modelling in natural crystals

Diffusion chronometry can be applied to different elements/isotopes in different mineral phases, in order to investigate time of magma assimilation, metasomatism, magma mixing or mingling, and mafic intrusion into a reservoir and the subsequent eruption. The relatively large number of modeling studies devoted to this subject probably reflects the importance of such processes for understanding magma differentiation (e.g., Eichelberger, 1978) and their potential for eruption triggering and volcanic hazards (e.g., Sparks et al., 1977).

Many studies have used Fe-Ti zoning in magnetite (e.g., Nakamura, 1995; Venezky and Rutherford 1999; Coombs et al. 2000; Chertkoff and Gardner 2004). Other studies have used major (e.g. Fe-Mg) and minor (e.g. P) element zoning in olivine (e.g. Coombs et al. 2000; Pan and Batiza 2002; Costa and Chakraborty 2004; Costa and Dungan, 2005). Diffusion in olivine is well constrained (e.g. Chakrabory and Ganguly, 1991; Costa et al., 2008) and diffusion data for many elements, including the effects of different environmental variables are known. Fe-Mg zoning in clinopyroxene has been used for determining the time between magma intrusion and eruption (e.g., Costa and Streck, 2004; Morgan et al. 2004). Zoning of trace elements (Sr, Mg, Ba) in plagioclase has also been applied (e.g., Costa et al. 2003, 2008) and there exists a number of recent determinations of diffusion coefficients which have been reported for a large range of thermodynamic variables and numbers of elements. Morgan and Blake (2006) and Zellmer and Clavero (2006) have used Sr and Ba zoning in sanidine. Morgan and Blake (2006) modeled magma residence and differentiation times for a large silicic magma to be ca. 100 ka. There is significant diffusion data on sanidine (e.g., Cherniak 1996, 2002), but the difficulty is to model a suitable differentiation history. This requires a model that considers changing composition at the crystal boundary with time, as well as growth during diffusion. Morgan and Blake (2006) exploited the different diffusion rates of Sr and Ba to partly overcome such complexities. Wolff et al. (2002) and Bindeman et al. (2006) used the disequilibrium between oxygen isotope composition of feldspars and quartz or olivines to obtain timescales for assimilation. A recent development is the use of Ti zoning in quartz (Wark et al., 2007), which is also based on new determinations of Ti diffusion coefficients (Cherniak et al., 2007), and the development of a new geothermometer (Wark and Watson, 2006). This should open new pathways for understanding the time-temperature histories of silica-rich magmas. A recent new finding is that H is zoned in mantle olivines (Demouchy et al., 2006; Peslier and Luhr, 2006). Such crystals also have been used to infer mantle-to-surface transport rates of several hours to days. Timescale for the generation of silica-rich magmas by partial melting or remobilization of crustal rocks have also been estimated with oxygen isotopes in quartz and zircon (Bindeman and Valley, 2001), and Sr and Ba zoning in plagioclase (Zellmer et al. 1999, 2003).

2.3.2.2 Diffusion modelling in pyroxene

For nearly one century pyroxenes have been used as geological archives of magmatic processes (Larsen et al., 1938; Tomkeieff, 1939) and due to the relatively low diffusivity, the interpretation of compositional zoning patterns enables the quantification of the duration of igneous processes (Müller et al., 2013) such as the residence time of crystals by measuring the width of the diffused rims (Morgan et al., 2004). In the last decades a wide range of cations were subject to diffusion studies in Ca-rich clinopyroxene mainly focusing on the self-diffusion and interdiffusion (Freer et al., 1982; Brady and McCallister, 1983; Sautter et al., 1988; Béjina and Jaoul, 1996; Dimanov and Jaoul, 1998; Zhang et al., 2010; Müller et al., 2013). Pyroxenes have been generally used to constrain timescales of processes in silicic systems that lack olivine (Dohmen et al., 2017). BSE imaging (for Fe–Mg, e.g., Morgan et al. 2004, Saunders et al. 2012a) or other higher resolution methods have been used (TOF-SIMS: Saunders et al. 2012b; NanoSIMS: Saunders et al. 2014) to resolve in detail the chemical zoning. Fast processes can be determined using Li diffusion in clinopyroxene. For example, concentration profiles of Li in clinopyroxene from Martian meteorites (nakhlites) were modelled to determine cooling rates of the respective magmatic system (Beck et al. 2006).

Pyroxenes in silicic volcanic rocks typically show a diversity of zoning styles, with normal, reversed, multiple, or patchy zoning. However, it is quite common that a final, outermost rim with a thickness of 10–100 μm is formed at some point before the magma erupts. The compositional jump at the interface between the outermost rim and the interior of the crystal is typically very sharp and hardly can be resolved using electron microprobe analysis without convolution effects (Ganguly et al., 1988; Morgan et al., 2004). Therefore, Morgan et al. (2004) inferred variations in the Fe content using the grey scale of BSE images of clinopyroxene, since the contribution to the changes in the grey scale by variations of other elements, Al or Si, are minor. For clinopyroxene it must also be assumed that the variation of Ca was small enough to not affect the grey scale at all. The linear correlation of the grey scale with the Mg# = Mg / (Fe + Mg) was demonstrated by Allan et al. (2013). BSE imaging allows for a spatial resolution down to 100 nm or less (e.g., Saunders et al. 2012b) and is a very time efficient way to map Fe in pyroxene crystals. The appropriate diffusion coefficient depends on the magmatic temperature, which Morgan et al. (2004) determined based on the composition of melt inclusions in clinopyroxene using the geothermometer of Cioni et al. (1999). Using the diffusion data of Dimanov and Sautter (2000) to calculate the diffusion coefficient for Fe-Mg in clinopyroxene, Morgan et al. (2004) determined residence times in multiple clinopyroxene crystals (following growth of the final rim) from the 1944 eruption of Vesuvius and obtained a range from 0.4 to 9 yr with a distribution skewed to young ages. Instead, the diffusion coefficient used in this thesis, to calculate timescales of magmatic processes, by modelling diffusional profiles in clinpyroxene crystals from the Zaro and Agnano-Monte Spina eruptions, is that (more recent) of Müller et al. (2013).

3. GEOLOGICAL AND VOLCANOLOGICAL BACKGROUND OF THE PHLEGRAEAN VOLCANIC DISTRICT: A FOCUS ON TWO DIFFERENT SIZE ERUPTIONS OF THE MOST RECENT PERIOD OF ACTIVITY: AGNANO-MONTE SPINA, IN THE CAMPI FLEGREI CALDERA, AND ZARO, AT ISCHIA ISLAND

3.1 Regional geologic setting: the Campania Plain and the volcanoes of the Neapolitan district

Among the active volcanic areas worldwide the volcanic hazard posed by the Phlegraean Volcanic District (PVD) is extremely high, due to its explosive character. Both the high volcanic hazard and the intense urbanization result in an extreme volcanic risk in this area (e.g. Orsi et al., 2004, 2009; Selva et al., 2012, 2019; Bevilacqua et al., 2015,2017; Mastrolorenzo et al., 2017), leading to a considerable interest in understanding which processes might contribute to trigger eruptions and control eruptive dynamics.

The PVD, located within the Campania Plain (southern Italy; Fig. 17), is constituted by the Campi Flegrei caldera and the islands of Ischia and Procida (Orsi et al., 1996a). Except for Procida, whose activity ended ca 22 ka (Morabito et al., 2014), Ischia island and Campi Flegrei volcanic field are still active and pose a very high potential volcanic hazard. Together with the still active Somma-Vesuvius strato-volcano, these volcanic complexes make up the Neapolitan district (e.g. Conticelli et al., 2010).

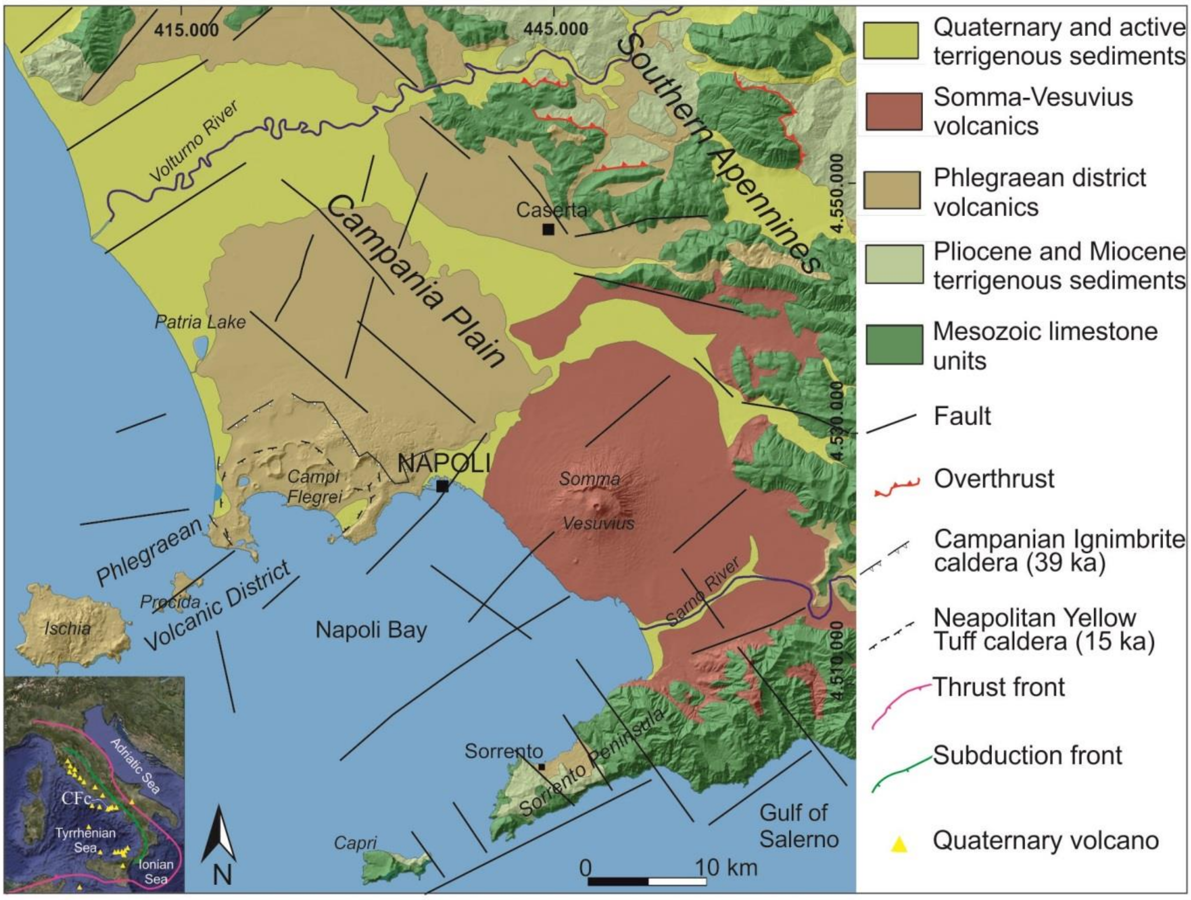

Fig. 17 Geological and structural sketch map of the Southern Campania Plain (modified after Orsi et al., 2003) showing the location of the Neapolitan volcanoes and the main tectonic features.

The PVD formed in response to the Pliocene-Quaternary extensional processes that generated the Campania Plain graben, along the Tyrrhenian margin of the Apennine thrust belt (Acocella and Funiciello, 2006). The latter results from the deformation of the African continental margin: Southern Apennines consist of a number of thrusts, locally covered by Plio-Quaternary autochthonous shallow marine and continental sediments. The crust, beneath the Apennine chain, is about 25-30 km thick (e.g. Locardi and Nicolich, 1988; Piromallo and Morelli, 2003) and the pile of tectonic thrusts overlies a crystalline-metamorphic basement. The Apennine thrust belt is composed of a variety of Mesozoic and Palaeogenic palaeogeographic domains (e.g. D’Argenio et al., 1973). Tectonic units (Sicilide, Liguride, Alburno-Cervati, Lagonegro, etc.; Ippolito et al., 1975; Grasso, 2001; Vitale and Ciarcia, 2013) consist of a wide variety of rock types (e.g. limestones, dolostones, flysch sequences, sandstones, marls, ophiolitic rocks, in order of abundance) ranging in age from

Upper Triassic to Miocene. They mostly represent basinal sequences formed on the border of the African plate, which were delaminated and superimposed over the Apulia foreland. The latter is located east of the Apennine chain and consists of Mesozoic to Tertiary platform carbonates (e.g. Grasso 2001; Patacca and Scandone 2001; Vai and Martini 2001). The geodynamic evolution of the whole area is controlled by the interaction among two major plates, the European Plate and the African Plate. The extensional tectonics, linked to the opening of the Tyrrhenian basin during the Upper Tortonian and the compressional tectonics leading to the chain development are consequent to the subduction and roll-back of the Adriatic plate under the Sardinia-Corsica plate (e.g. Patacca and Scandone, 2007). Overthrusting of tectonic units occurred during Upper Oligocene to Lower Pleistocene compressional phases. These were followed by intensive extensional tectonic phases, in turn due to the complex stress field produced by the great collision between African and Tyrrhenian plates in the Mediterranean area (e.g. Mantovani et al., 1990; Mazzoli and Helman, 1994; Mazzoli et al., 2001, 2008; Handy et al., 2010). These extensional tectonic phases generated fault systems (both parallel and normal to the Apennine chain) which have downthrown the western Apennines at least during Quaternary times (Brancaccio et al., 1991; Cello and Mazzoli, 1999). The activation of NW-SE normal and NE-SW normal to strike-slip transfer fault systems have generated the present setting of the Campania Plain (e.g. Acocella and Funiciello, 2006), in which the active volcanoes lie. The middle-southern part of the Plain is featured by two principal orographic elements: Campi Flegrei volcanic field, west of Napoli, and Somma-Vesuvius strato-volcano, east of Napoli (Fig. 17).

The Campania Plain is ca 3000 km^2 wide and it is composed of ca 3.000 m thick sequences of Plio-Quaternary continental, deltaic, and marine sediments, intercalated with volcanic deposits. The nearly rectangular flat plain is elongated in a NW-SE direction for about 100 km, and occupies a wide, graben-like structural depression. The regional stress regime, which has determined the formation of the plain, has also favoured generation of volcanism (along all the Tyrrhenian margin of the Italian peninsula) because the NW-SE and NE-SW trending normal faults represent a preferential structure for magma upwelling and fluids emissions (Acocella et al., 1999; Brocchini et al., 2001; Piochi et al., 2005a; Acocella and Funiciello, 2006).

The geological evolution of the Campanian plain and the relationships with volcanic activity have been studied in detail by several authors (Ippolito et al., 1973; Cinque et al., 1987, 1993; Albore Livadie et al., 1989; Brancaccio et al., 1991; Romano, 1992; Acocella et al., 1999; Acocella and Funiciello, 2006; Torrente et al., 2010). The volcanic complexes are made up mainly of pyroclastic rocks with subordinate lava flows but their structures and morphological appearance vary widely. The volcanic rocks cover an area as large as the entire Campanian plain, and some tephra levels originated from the largest eruptions of the Campi Flegrei and Ischia can be found throughout the Mediterranean basin and over (e.g. Munno and Petrosino, 2004; Engwell et al., 2014; Giaccio et al., 2017; Sevink et al., 2020).

Most of the volcanoes of the Neapolitan district developed during the Upper Pleistocene but with an intense volcanic activity piercing the Pleistocene-Holocene boundary (Brocchini et al., 2001; De Vivo et al., 2001; Deino et al., 2004). A wealth of data regarding the recent phases of activity of these volcanoes is available, but little is known about the Middle Pleistocene history of Neapolitan volcanoes, because most of these products are buried by Holocene volcanic activity, or just beneath the sea level. The absence of Pliocene marine sediments in the drills of the Campanian Plain, indicates that the southern part of the plain was above sea level during the Middle Pleistocene (Brancaccio et al., 1991; Cinque et al., 1993), the period to which date back the older potassic and ultrapotassic rocks of the district (ca 330 ka; Brocchini et al., 2001).

During the last 50 ka, an intense explosive activity, with recurrent intervals, dispersed both primary and secondary pyroclastic products over an area as wide as 10.000 km^2, which includes the entire plain and the surroundings. Stratigraphic studies reveal that from prehistory to the present time, both the Campi Flegrei and Somma-Vesuvius areas, including the area of Napoli and the mountain reliefs, have been affected by volcano-tectonic events (subsidence, bradyseism, and rapid caldera collapse), as well as the coupled primary deposition of volcanic products and secondary deposition of volcanically induced mass flows.

3.2 Campi Flegrei volcanic field

The Campi Flegrei volcanic field, the main feature of the PVD, together with the Somma–Vesuvius strato-volcano and Ischia volcanic island, is one of the three active volcanoes of the Neapolitan area. Campi Flegrei includes a continental and a submerged part. The Campi Flegrei volcanic field (Fig. 18) is dominated by a quaternary 12 km wide caldera depression, outlined on land by a discontinuous ring-shaped hilly morphology with inward-facing scarps enclosing the volcanic field.

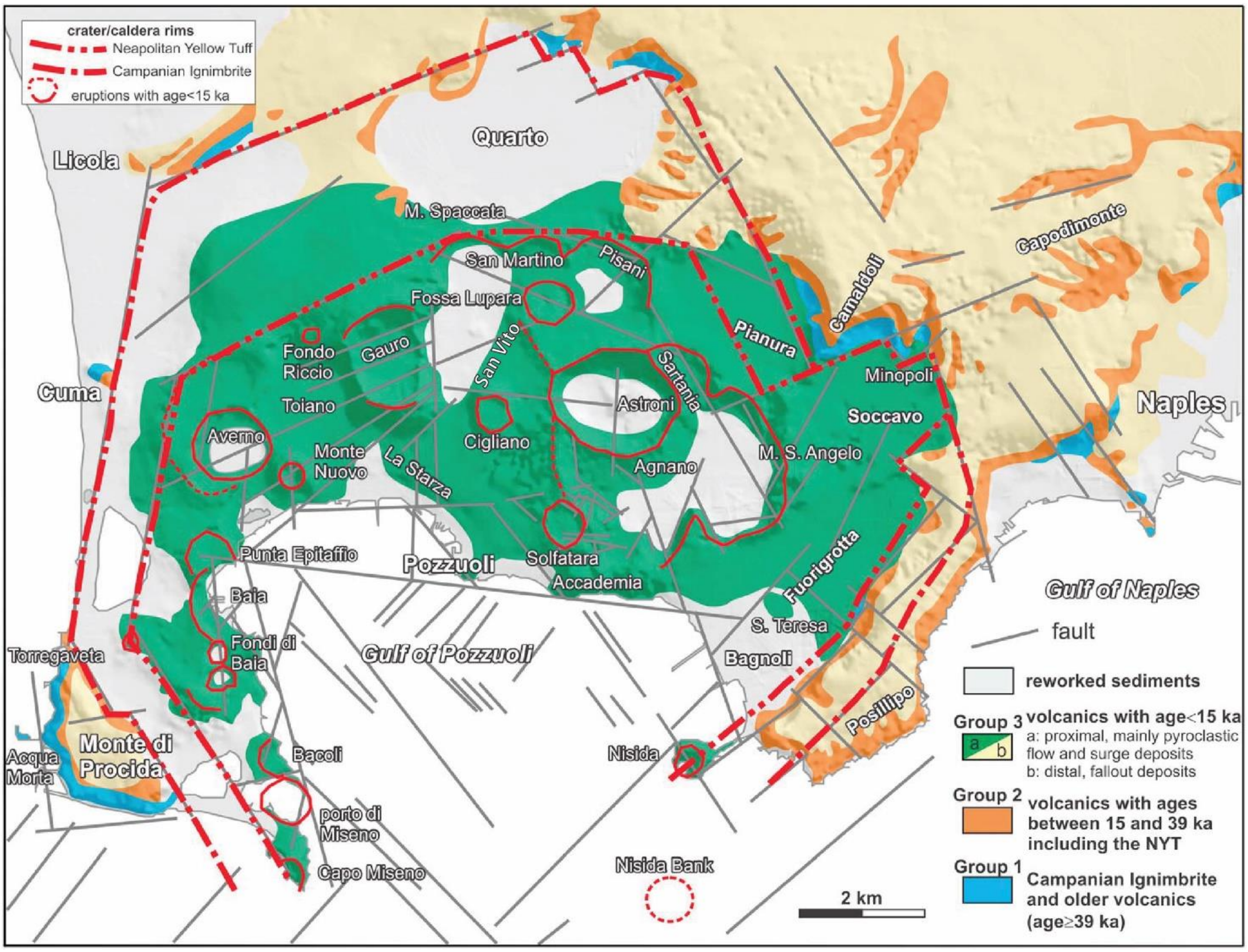

Fig. 18 Simplified geological map of Campi Flegrei caldera showing the traces of regional faults and main morphological structures such as caldera and crater rims and faults derived from deep sea seismic profiles (modified after Vitale and Isaia, 2014).

The caldera results by multiple collapses occurred during two highly explosive volcanic eruptions: the Campanian Ignimbrite (CI) occurred ca 40 ka (Gebauer et al., 2014; Giaccio et al., 2017) and the Neapolitan Yellow Tuff (NYT) occurred ca 15 ka (Deino et al., 2004). The Campanian Ignimbrite eruption and caldera collapse was the earliest event to profoundly influence the present geological setting of the area. The Neapolitan Yellow Tuff eruption and caldera collapse was the last dramatic event in the history of the caldera. The geometry and dynamics of both large calderas, as well as of smaller volcano-tectonic collapses, were deeply influenced by both local and regional stress regimes (Orsi et al., 1996a, 2003). Each large collapse affected the structural conditions of the system, and constrained the foci of later volcanism (Orsi et al., 2009). The caldera rim ranges in elevation between about 450 meters and a few tens of meters, and one third of it continues below sea level, forming Pozzuoli Bay. A few submerged volcanic relicts represent the submerged part of the volcanic field (Fig. 18). The southern limits of the caldera are poorly known and mainly inferred by the geophysical investigations. A vertical fault system defines the geometry of the central depression, which characterizes the nearly perfect circular caldera structure. The intracalderic area of Campi Flegrei shows the typical features of a volcanic field characterized by different land forms. It includes closely-grouped volcanic hills, coalesced craters, depressions bordered by steep, eroded volcano flanks, and fault scarp faces, crater-filling lakes, and relicts of ancient marine terraces (Fig. 18). The few major intracalderic plains of Fuorigrotta, Soccavo, Pianura, S.Vito, Quarto, and La Starza, are associated with localized subsidence areas, due to local ground movement following eruptive episodes (De Natale et al., 2006). The present, intracalderic landform of Campi Flegrei is dominated by a closely grouped assortment of pyroclastic cones, tuff rings and tuff cones spanning the entire range of hydromagmatic activity at shallow depth, and occurred after the emplacement of the Neapolitan Yellow Tuff. Apart from scoria cones and spatter cones, which were formed through Strombolian activity, cinder cones, tuff cones, and tuff rings result from the increasing efficiency of magma/water interaction (Di Girolamo et al, 1984; Di Vito et al, 1985; Rosi and Sbrana, 1987; Mastrolorenzo, 1994; Mastrolorenzo et al. 2001). The surface distribution of the monogenetic volcanoes reflects the tectonic and volcano-tectonic evolution of the caldera that, in turn, controlled the magma conduit position and the main ground collapses (Rosi et al, 1996).

Volcanic products of the Campi Flegrei caldera (CFc) are mostly pyroclastic rocks and subordinate lava flows and domes, and volcanic activity has been dominantly explosive through time, with several minor volcano-tectonic collapse episodes. The volcanic history of Campi Flegrei has been extensively investigated in scientific studies in the past decades (e.g. Rittman et al., 1950; Rosi and Sbrana, 1987; Orsi et al., 1996a; Di Vito et al., 1999, 2016; Isaia et al., 2004, 2009; Smith et al., 2011; Scarpati et al., 2013; Mastrolorenzo et al., 2017). The age of the beginning of volcanism in the area is not known. Many authors recognized early volcanism (e.g., Di Girolamo et al., 1984; Orsi et al., 1996a; Pappalardo et al., 1999) prior to the CI eruption. Barbieri et al. (1979) describe calc-alkaline lavas below 1550 m from the Parete 2 well, 20 km northwest of Napoli, that were dated at 2.0 ± 0.4 Ma. Old ignimbrites, even if highly altered, at Durazzano (116.1 ka), Moschiano (184.7 ka), Seiano Valley (245.9 and 289.6 ka), and Taurano — Acqua Feconia (157.4, 183.8, 205.6, and 210.4 ka) localities, in the north-eastern Campania Plain, have been recently characterized by Belkin et al. (2016). A deep borehole at Camaldoli della Torre (Somma-Vesuvius) penetrated 10 pre-CI units whose eruption ages fall between the CI event and Marine Isotope Stage 5 - ca.126 ka (Di Renzo et al., 2007). Lithified pre-caldera pyroclastic deposits, named the Ancient Tuffs, have been ascribed to the volcanic activity (ca 80-50 ka) which predates the CI eruption. These deposits were generated by monogenic vents (San Martino, Parco Margherita, Parco Grifeo, Funicolare di Chiaia, San Sepolcro) mostly located in the west part of the city of Napoli (Scarpati et al., 2013). At least twelve pre-CI units are recognized at the Trefola Quarry (Orsi et al., 1996a) spanning the 59–39 ka period (Pappalardo et al., 1999). Volcanics older than the CI also include the lava domes of Punta Marmolite (47 ka; Cassignol and Gillot, 1982; 62.4+3.9 ka, Wu et al., 2015) and Cuma (37 ka; Cassignol and Gillot, 1982, 41 ka in Lirer et al., 2011; 45.9+3.6 ka, Wu et al., 2015) and the Tufi di Torre Franco pyroclastic deposits (> 42 ka; Alessio et al., 1973).

The ca 40 ka Campanian Ignimbrite (CI; Gebauer et al., 2014), emplaced during a catastrophic explosive event having a magnitude of 7.2 (Scarpati et al., 2014), is considered the most powerful eruption ever occurred in the Neapolitan area. The CI plinian eruption emplaced a large volume of pyroclastic fall and pyroclastic density current (PDC) products, which resulted in a very complex sequence in proximal, medial and distal outcrops (Barberi et al., 1978; Di Girolamo et al., 1984; Rosi and Sbrana 1987; Fisher et al., 1993; Perrotta and Scarpati 1994, 2003; Civetta et al., 1997; Orsi et al., 1996a; Rosi et al., 1996, 1999; Cappelletti et al., 2003; Perrotta et al., 2006; Fedele et al., 2008; Scarpati and Perrotta 2012, 2016; Engwell et al., 2014; Scarpati et al., 2015a, 2015b, 2016). Stratigraphic data suggest that the eruption began with phreatomagmatic explosions, followed by the formation of a sustained Plinian eruption column that was fed by simultaneous emission of both trachytic and phonolitic magmas (Pappalardo et al. 2002a, 2008). With the onset of a sustained plinian plume, up to 39-50 km high, the eruption produced a stratified pumice lapilli fall deposit dispersed toward the east (Martì et al., 2016; Scarpati and Perrotta, 2016). The plinian phase was followed by a collapsing column phase during which impressive PDCs were generated, spreading over an area of more than 30000 km^2 and able to surmount mountain ridges up to 1000 m high (Fisher et al., 1993). This phase produced a massive, mostly welded, grey ignimbrite sheet in medial areas (e.g., Barberi et al., 1978; Fisher et al., 1993; Scarpati and Perrotta, 2012; Scarpati et al., 2015a) and a proximal accumulation of lithic breccias, welded horizons and unconsolidated pumiceous deposits along the caldera rim (the Breccia Museo; e.g., Rosi et al., 1993; Perrotta and Scarpati, 1994; Melluso et al., 1995; Fedele et al., 2008). Reported estimates for the total volume of erupted magma have historically oscillated from ca 80 up to 300 km^3 DRE (dense rock equivalent; Keller et al., 1973; Thunnel et al., 1979; Cornell et al., 1983; Fisher et al., 1993; Civetta et al., 1997; Fedele et al., 2008, 2016; Scarpati et al., 2014; Silleni et al., 2020). About 16 km^3 of co-plinian ash and 100 km^3 of cogenetic co-ignimbrite ash fall (Perrotta and Scarpati, 2003) were dispersed and emplaced in the eastern Mediterranean Sea and eastern Europe (e.g., Keller et al., 1973; Thunnel et al., 1979; Cornell et al., 1983; Perrotta and Scarpati, 2003; Pyle et al., 2006; Costa et al., 2012; Engwell et al., 2014). The lithology and depositional characteristics (lithofacies) of the CI change both laterally and vertically, especially due to variations in emplacement mechanisms, degree of welding and post-depositional processes, i.e. glass recrystallization and zeolitization (Cappelletti et al., 2003; Langella et al., 2013). This gives origin to the superposition of different units, with different areal distribution and large variability from proximal to distal sites. Along and close to the caldera rims, the CI deposits occur in scattered outcrops mainly representing the proximal facies of this formation.

The post-CI, pre-NYT volcanic activity is characterized by a thick succession of pyroclastic deposits. This activity was confined inside the CI caldera and the majority of the rocks were produced by explosive, mostly hydromagmatic eruptions (Orsi et al., 1996a). Their deposits occur in scattered outcrops across the central part of the city of Napoli, and along the northwestern and southwestern scarps of the Posillipo hill (Monte di Procida, Cuma, Punta Marmolite, Trefola, Masseria del Monte, Vallone del Verdolino, Moiariello, Ponti Rossi, Sant'Arpino, Monte Echia, San Martino hill, Villanova, Coroglio, and Trentaremi; Orsi et al., 1996a, Pappalardo et al., 1999). $^{40}Ar/^{39}Ar$ dated eruptions range in age from 30.3 ka to 14.6 ka (Pappalardo et al., 1999). These pre-NYT units are known collectively as Tufi Biancastri (Rittman et al., 1950). The stratigraphic relationships between these deposits are not well constrained owing to their limited distribution. At least 10 pre-NYT tephra layers are also recorded in the Lago Grande di Monticchio core (Wulf et al., 2004). Moreover, recently, Albert et al. (2019), based on tephrostratigraphic studies revealed the high magnitude (M 6.6 or VEI 6) of one of the Pre-NYT deposit: the Masseria del Monte Tuff, otherwise known as Y-3 tephra in the tephrostratigraphic record of the Mediterranean area (dated at 29.3 ± 0.7 ka); the authors concluded that during this event ca17 km^3 (DRE) of magma were erupted, based largely on the distal ash fall covering an area >150000 km^2.

The NYT was produced during one of the largest eruptions of the CFc, and it is by far the largest trachytic phreatoplinian deposit known. The NYT outcrops in scattered localities over an area of ca1000 km^2, with a conservatively estimated volume of ca 40 km^3 (DRE; Orsi et al., 1992b, 1995; Scarpati et al. 1993). In the caldera depression, the thickness varies between a few meters to more than 100 m, and is mostly covered by younger pyroclastic deposits. The NYT pyroclastic sequence consists of two main units called Lower and Upper Member according to the nomenclature of Orsi et al. (1992b, 1995). The Lower Member consists of a sequence of pumice-and-ash fallout deposits and dilute PDC deposits which extend up to a distance of ca 35 km from the vent and make ca 1/3 of the total erupted volume (Orsi et al., 1992b). The Upper Member comprises both massive and thick pumice-and-ash deposits from highly concentrated PDCs and stratified ash beds from dilute PDCs which were recognized up to a distance of ca 14 km from the vent (Wohletz et al., 1995). A coarse lithic breccia corresponding to the onset of the caldera collapse phase was identified at the base of the Upper Member in the proximal areas (Scarpati et al., 1993). No paleosoils have been recognized between the two members in the field and ^{40}Ar/^{39}Ar dating confirms that the two units have the same age (14.9 ka; Deino et al., 2004). The NYT formation consists of two main diagenetic facies; a yellow, lithified, unwelded facies rich in zeolite, and a gray, non-lithified facies called “Pozzolana” (Scherillo, 1955). The NYT deposits show lateral and vertical variations of the degree of lithification and zeolitization, which mostly depend upon the thermal conditions of deposition and the amount of phreatomagmatic water involved during eruption. The most lithified and zeolitized rocks are concentrated in the inner portions of the pyroclastic sequence in the proximal areas where the ignimbrite shows its maximum thickness. Here, relatively high temperatures within the wet deposits were maintained long enough to trigger the hydration-dissolution processes in the volcanic glass (de’ Gennaro et al., 2000).

During the last 15 ka, the caldera has been the site of intense volcanism and deformation, characterized by about 70 eruptions grouped into three epochs of activity: epoch 1: ca 15-10.6 ka;

epoch 2: ca 9.6-9.1 ka; and epoch 3: ca 5.5-3.5 ka (Smith et al., 2011) during which eruptions have followed one another at mean time intervals of a few tens of years.

During the epoch 1, at least 32 explosive eruptions took place, with a mean frequency of one eruption every 70 years (Di Vito et al., 1999). All the eruptions of this epoch were explosive, varying from magmatic to phreatomagmatic. Most of the eruptive vents were located along the structural margin of the caldera (Lirer et al, 1987; Orsi et al., 1996a). Near the end of this phase, the activity migrated toward the center of the caldera and the Plinian deposit of the Pomici Principali was erupted from the Agnano area (11.9-12.1 ka; Smith et al., 2011). During the last 15 ka only the Pomici Principali and the Agnano-Monte Spina, occurred during the epochs 1 and 3 of activity, respectively, were Plinian eruptions.

The epoch 2 of activity began with the Fondi di Baia eruption (9.5-9.5 ka; Smith et al., 2011). During this epoch, six explosive eruptions, all low magnitude, took place with a mean frequency of 65 years (Di Vito et al., 1999). All the eruption vents were located along the northeastern sector of the structural boundary of the NYT caldera (Fig. 18). Only the Fondi di Baia eruption took place along its western segment. The magmatic and phreatomagmatic eruptions produced deposits mostly distributed over the emerged part of the caldera floor (Di Vito et al. 1999; Orsi et al. 2004).

Epoch 3 was characterized by numerous eruptions in a short time interval. 28 low-to medium-magnitude eruptions occurred from vents mostly located in the NE part of the NYT caldera in the 12-km^2 Agnano-San Vito area (Fig. 18; Smith et al., 2011; Bevilacqua et al., 2017). This includes the Astroni, Solfatara, and Agnano craters, and is considered to be one of the sites of highest probability of vent opening in the case of future eruptions (Orsi et al., 2004; Selva et al., 2012; Bevilacqua et al., 2016, 2017). This portion of the NYT caldera has been subjected to extensional tectonics since at least ca 5 ka (Capuano et al., 2013) through NW-SE- and NE-SW-trending regional faults, favoring the ascent of the trachytic and latitic magmas which fed the eruptions. During this epoch an intense monogenetic explosive and subordinate effusive activity took place from vents located within the central part of the caldera: Solfatara (4.1-4.3 ka; Smith et al., 2011), Astroni (4.1-3.8 ka; Tonarini et al., 2009; Smith et al., 2011), Averno (5.4-4.1 ka; Di Vito et al., 2011; Smith et al., 2011; Fourmentraux et al., 2012), and Monte Nuovo (1538 AD; Piochi et al., 2005b; Guidoboni and Ciuccarelli, 2011; Di Vito et al., 2016; Liedl et al., 2019) pyroclastic cones, Agnano Monte Spina (4.4-4.6 ka; deVita et al., 1999; Dellino et al., 2001, 2004; Arienzo et al., 2010; Smith et al., 2011; Romano et al., 2020) Plinian to phreatomagmatic eruption, and Monte Olibano and Accademia lava domes (4.36+1.13 ka, Wu et al., 2015) are the principal events that modified the inner part of the volcanic field (Fig. 18). Isaia et al. (2009) noted there was significant ground deformation (associated with hydrothermal activity) between the Santa Maria della Grazie (4.3-4.5 ka; Smith et al., 2011) and Agnano-Monte Spina eruptions, and separated the epoch into two subgroups (3a and 3b). The explosive eruptions before the largest Agnano-Monte Spina event varied from magmatic to phreatomagmatic and produced pyroclastic-fall and -flow deposits mostly distributed in the northeastern part of the CFc and over an area which extends few kilometers from the caldera boundary (Di Vito et al., 1999). After Agnano-Monte Spina there were many small events, including the emission of a lava domes and the occurrence of strombolian activity. The last event took place in 1538 AD with the formation of Monte Nuovo scoria cone (Guidoboni and Ciuccarelli, 2011; Di Vito et al., 2016).

The intense fumarolic activity and the unrest episodes that occurred in recent decades (Del Gaudio et al., 2010) testify to the persistent activity of the CFc system. The caldera was affected by two main uplift phases in 1970–1972 and 1982–1984, events which were accompanied by seismicity and increase in heat fluxes and fumarolic activity (Del Gaudio et al., 2010). The current occurrence of long lasting fumarolic activity, widespread manifestations of hydrothermal springs, and ongoing ground deformation, started in 2005, suggests that the CFc magmatic system remains in a state of unrest (Vilardo et al. 2010; Chiodini et al. 2012, 2015, 2016). The Pozzuoli district has been the main epicentral region for local seismicity, especially during the uplift phases (e.g., De Natale et al., 2001; Troise et al., 2008, 2019), as well as an area of degassing, including the emission of as much as 1500 tons of CO_2 per day (Chiodini et al., 2001). The presence of 350000 inhabitants in the central part of the caldera raises the risk level to very high (Neri et al., 2015; Mastrolorenzo et al., 2017; Charlton et al., 2020).

3.3 The Agnano-Monte Spina eruption

The Agnano-Monte Spina (A-MS) eruption, dated 4482-4625 cal. years BP (Smith et al., 2011), is the highest-magnitude eruption in the CFc during its last epoch of activity (Orsi et al. 2004, 2009) and it is considered as the reference event for a future medium-size explosive eruption (Mele et al., 2015). The eruption was characterized by a magmatic/phreatomagmatic activity (de Vita et al., 1999; Dellino et al., 2001) that lead to the emplacement of alternating fall and PDC deposits, distributed over an area of about 1000 km^2 (Fig. 19a). Thickness of the tephra varies from a maximum estimated value of about 70 m in the Agnano plain, the inferred vent area for the eruption, to a few centimeters over a distance of about 50 km. Estimations based on distribution and thickness of A-MS products yield a volume of ejected magma of about 0.9 km^3 (DRE; Orsi et al., 2009).

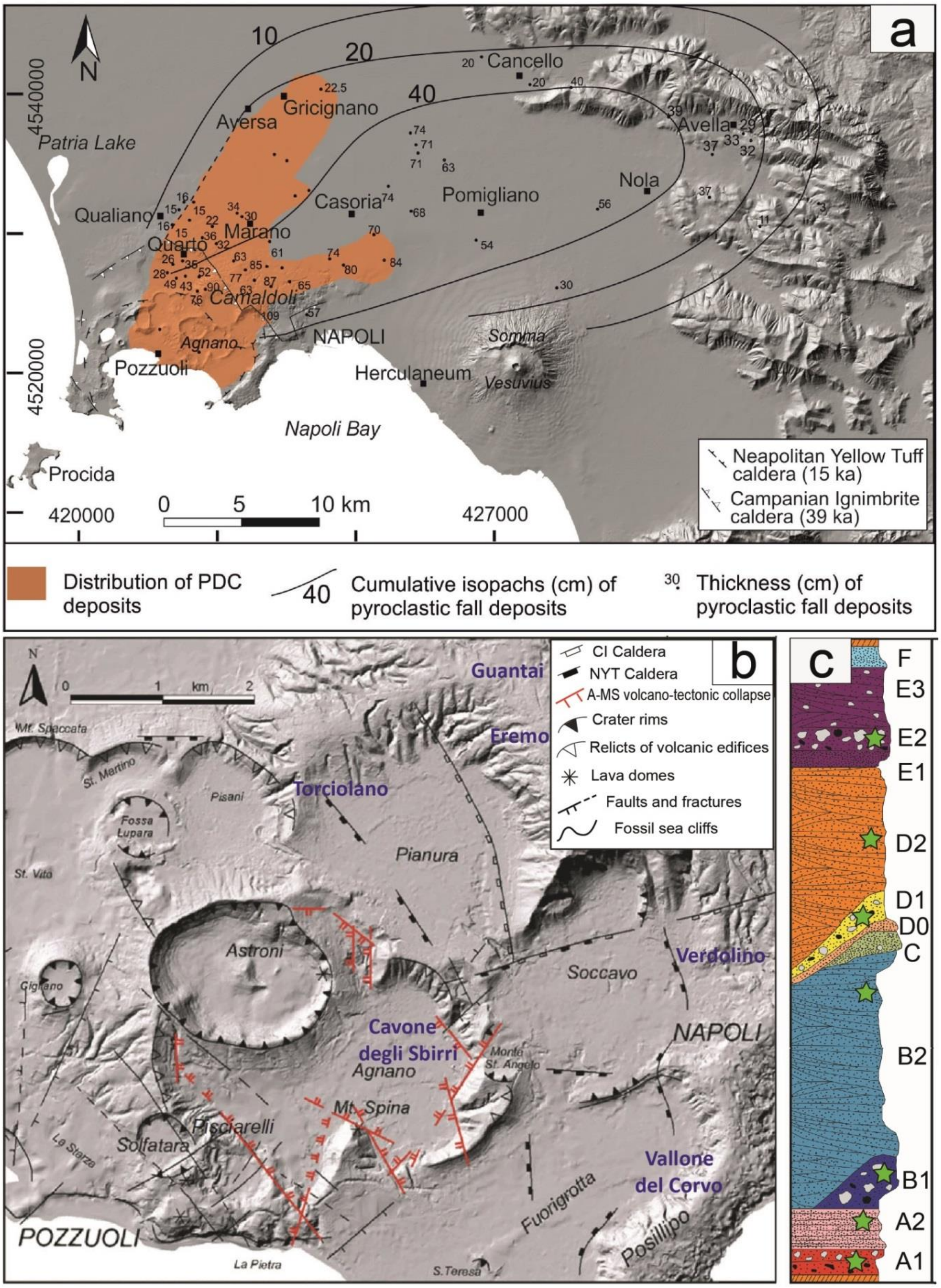

Fig. 19 a) Areal distribution of the Agnano–Monte Spina volcanic deposits (redrawn from de Vita et al., 1999); b) Detail of the Agnano-San Vito area (modified after Iovine et al., 2017a); c) Schematic stratigraphic column of the A-MS members (modified after Iovine et al., 2017a).

The Agnano-Monte Spina unit was first defined by Rosi et al. (1983) and later described by Di Girolamo et al. (1984), Rosi and Santacroce (1984) and Rosi and Sbrana (1987). Di Girolamo et al. (1984) described the products of this eruption as a sequence of pumice- and scoria-flows confined inside the Agnano plain, underlain by an associated lag–breccia deposit, and characterized by the presence of a welded scoria deposit in the upper part. Rosi and Santacroce (1984) and Rosi and Sbrana (1987), based on 15 sections measured over an area of about 400 km^2, identified four main phases in the A-MS eruption. The authors, on the basis of the areal distribution of the basal breccia deposit, suggested that the area of Monte Spina hill, in the Agnano plain (Fig. 19b), was the vent area for this eruption. Later, the A-MS deposits and stratigraphy were characterized in detail by de Vita et al. (1999). On the base of the sedimentological features of the A-MS deposits, these authors suggested that the eruption was characterized by five phases with variable dynamics and dispersal of the pyroclastic products. The authors were able to characterize the type of magma withdrawal and fragmentation (for example if magma-water interaction occurred) in each phase. De Vita et al. (1999) measured stratigraphic sequences of the A-MS tephra in 80 sections over an area of about 1000 km^2. The most distal studied exposure is 44 km northeasterly of the eruption vent. The distribution of the unit inside the caldera has also been investigated by interpreting the logs of 67 boreholes drilled in variable morphological settings. The unit has been recognized in 43 of the 67 examined logs. The borehole data allowed to define the thickness variations of the A-MS deposit and the vertical movements of the Agnano plain. Variations of sedimentological characteristics and presence of a significant erosional unconformity have allowed the subdivision of the A-MS deposit in six members, named A through F, from base up section (Fig. 19c). Many of the members have been subdivided in layers due to the occurrence of second-order sedimentological variations. Analysis of lateral facies variations and vertical facies associations of correlated layers reveals that during some eruptive phases (e.g. during the emplacement of layers B2, D2 and E2) the contrasting eruptive dynamics were almost contemporaneous (Dellino et al., 2004). Dellino et al. (2001), based on deposit structures and grain size have recognized six main lithofacies, which allowed to infer the transportation and deposition dynamics of the various members, also elucidating the magmatic and phreatomagmatic fragmentation mechanisms operating during the various explosive events. Based on these stratigraphic and sedimentological investigations (de Vita et al., 1999; Dellino et al., 2001, 2004) it is possible to precisely reconstruct the phases and dynamics of the A-MS eruption as follow. The eruption began with phreatomagmatic explosions that produced a highly expanded ash cloud (basal part of A1). Member A, subdivided in two layers, named A1and A2, is exposed over an area of about 800 km^2 which covers almost the entire outcrop area of the A-MS tephra. The upper fallout bed of A1 was deposited from a relatively low eruption column (about 5 km) produced by a magmatic explosion. Isopleths of the maximum lithic clasts show an easterly directed dispersal axis, but they are elliptical in the distal areas, while distorted and widened in the proximal areas. This member is interpreted as the product of an initial phase of the eruption, during which an efficient water–magma interaction caused extreme magma fragmentation, formation of an expanded cloud, formation and collapse of a low eruption column with a high particle concentration. Sub-member A2 is a sequence of ash to lapilli surge and fallout beds generated by eruption column collapse and phreatomagmatic explosions. Within the CFc, layer A2 represents mainly the product of deposition of pyroclastic currents; outside the CFc, in those sites where they were channeled along morphological saddles, it is the product of simultaneous deposition of pyroclastic surges and fallout. Member B is subdivided in two layers, named B1 and B2. Layer B1 is a pumice fallout deposit, which covered an area larger than 500 km^2 with a dispersal axis oriented toward the east–north-east. This pumice fallout bed spread up to about 45 km eastward from the vent area. It was deposited from an unsteady column, which reached a maximum height of about 23 km, and was generated by magmatic explosions. Partial collapses of the column generated the basal pyroclastic surge deposits of B2. Pyroclastic flow and surge deposits were distributed over an area of about 100 km^2, while fallout deposits blanketed an area larger than 600 km^2. Layer B2 is interpreted to be generated by two interplaying phenomena: collapse of the eruption column and the intermittent water–magma interaction that generated base-surges, strombolian scoria-fallout and pumice- and scoria-flows. This phase was followed by a pause in the eruption and it is inferred to record the initiation of a volcano-tectonic collapse. Heavy rains caused erosion along steep slopes and ash suspended in the atmosphere was deposited to form member C: a fine-ash bed with abundant accretionary lapilli. This member represents fallout of particles suspended in the atmosphere after the emplacement of member B. Consisting mainly of east-to-northeast dispersed ash beds, this member occurs in all distal exposures, but it is missing in proximal areas. It covered an area larger than 600 km^2. The A-MS eruption was accompanied and followed by a volcano-tectonic collapse that affected the area of Agnano. The Agnano plain (Fig. 19b) has an elongated polygonal shape and is bordered by rectilinear high-angle scarps trending northwest–southeast and northeast–southwest. The volcano-tectonic collapse affected an area of about 6 km^2 and was of about 60 m. Therefore, the volume of the collapsed area is of about 0.4 km^3 (de Vita et al., 1999). During the initial phase of the collapse, fracturing of the roof rocks of the magma reservoir, which was related to re-activation of faults within the Agnano area, caused lowering of the lithostatic pressure with consequent volatile exsolution and magma migration toward the surface. Interaction of the rising magma with the geothermal system caused resumption of the eruption, recorded by the pyroclastic surge beds at the base of member D (D0). Member D has been subdivided in three layers, named D0, D1, and D2. Layer D0 is exposed only in few sections in proximal areas. The following event involved magmatic explosions and the formation of a Plinian eruption column that reached a maximum height of 27 km. This explosive phase generated a fallout deposit (D1) dispersed toward the north-east up to a distance of 45 km from the vent. Layer D1 is a pumice fallout deposit with a northeastward oriented dispersal axis. Isopachs are quite regular elliptical curves. Layer D1 covered an area of at least 700 km^2. The main episode of volcano-tectonic collapse took place during this phase. D2 is made up of discontinuous pumice lapilli and fine-ash beds probably generated by intermittent magma/water interaction and/or collapse of the eruption column that formed D1. Layer D2 usually thickens in preexisting valleys of the Campi Flegrei morphologic allow and thins toward the slopes that border the Agnano, Fuorigrotta, Soccavo and Pianura lowlands. Member E is made up of pyroclastic surge deposits with minor fallout beds mainly dispersed northward. Layer E1 represents the product of a phreatomagmatic phase, which produced an expanded cloud, accompanied by base surges. Layer E2 is punctuated by the presence of a magmatic pumice fallout bed, mainly dispersed northward, that was generated by a short-lived eruption column. Sub-member E3 is the product of a series of phreatomagmatic explosions that generated PDCs and minor fallout deposits. The final phase of the eruption was also phreatomagmatic, producing ash deposits (member F). Settling of particles suspended in the atmosphere, favored also by rainfall, marked the end of the eruption.

The lithofacies investigation (Dellino et al., 2001) helped to define the end-member involved in the dynamic of fallout events and PDCs of the A-MS eruption. The presence of highly vesiculated pumice lapilli in some deposits (e.g. sub-members A1, D1) suggests, on one hand, that exsolution of magmatic gas played a significant role in fragmentation during the eruption. On the other hand, the occurrence in other deposits (e.g. members C, E and F) of conspicuous amounts of fine ash and accretionary lapilli suggests the importance of phreatomagmatic processes and the formation of surge deposits (e.g. sub-member B2), at least during some phases of the eruption. For other deposits, which show variable proportions of highly vesiculated pumice lapilli and fine ash, the fragmentation processes were probably more complex. Also the study of ash particles using SEM (Dellino et al., 2001) elucidated the mechanism of magmatic and phreatomagmatic fragmentation processes.

The AMS juvenile fragments are potassic alkaline rocks, ranging in composition from trachyte to phonolite. Glass in pumice and scoria fragments is trachytic (de Vita et al., 1999) according to the TAS (Le Bas et al., 1986). Pumice and scoria fragments are porphyritic, with phenocrysts of plagioclase and alkali–feldspar, clinopyroxene, black mica, apatite and opaques in order of decreasing abundance (de Vita et al., 1999; Arienzo et al., 2010). SiO_2, Na_2O, Zr, Nb, Rb, and to a lesser extent Y contents show positive correlation with degree of chemical evolution (e.g. increasing differentiation index; D.I. = normative Ab+Or+Ne), whereas MgO, FeO_{tot}, CaO, P_2O_5, TiO_2, Sr, Ni and Cr contents show negative correlation. K_2O content increases in trachytes, at D.I. values from 74 to 79, then decreases in alkali–trachytes; Al_2O_3 and MnO contents are constant, although scattered (de Vita et al., 1999). The Sr-isotopic composition of whole-rock samples ranges from 0.70746 to 0.70756 showing a slightly negative correlation with degree of chemical evolution.. The alkali–trachytic products of the lower and middle portions of the stratigraphic sequence have a Sr-isotopic ratio of about 0.70748 (de Vita et al., 1999). The trachytic products of the upper portion of the sequence have a larger variability with $^{87}Sr/^{86}Sr$ ratio ranging from 0.70750 to 0.70756. De Vita et al. (1999) reported a general decreasing differentiation from bottom to top of A-MS sequence. They also noticed that the total range of variation for several trace elements is large despite the limited variation of major oxide contents and found evidence for Sr-isotopic disequilibria among whole rocks and minerals. The authors concluded that the A-MS eruption was fed by two isotopically and chemically distinct magma batches that mixed during the eruption. The first erupted alkali–trachyte is characterized by $^{87}Sr/^{86}Sr$ of 0.70750 and the last erupted trachyte characterized by $^{87}Sr/^{86}Sr$ of 0.70755. The occurrence of mixing between a trachytic and a phonolitic magma was suggested by Roach (2005) and Arienzo et al. (2010), on the bases of melt inclusions (MI) studies. MI data highlight the pre-eruption storage conditions of two magmatic end-members. By examining degassing trends and providing geobarometry estimation, Arienzo et al. (2010) depichted a scenario of the A-MS feeding system: the magma feeding the A–MS eruption was stored in a vertically extended plumbing system, that was continuously subject to volatile addition of a CO_2-dominated gas. This allowed the magmatic system to switch progressively from the relatively H_2O-rich background conditions of the system to the relatively dehydrated and CO_2-enriched ones, typical of a gas-buffered system which becomes nearly insensitive to gas–melt chemical exchanges. Under these gas-rich conditions more primitive magmas rose from depths ≥ 8 km and mixed with the evolved trachy-phonolite that fed the B phase of eruption. Moreover, Moretti et al. (2019) and Romano et al. (2020) also supported the mixing hypothesis of the previous authors and investigated the role of the volatile phases (H_2O, CO_2) involved prior to/during the eruption, linking them to the magmatic components and to the eruption dynamics.

3.4 Ischia island volcanic complex

The island of Ischia, part of the PVD, is the emerged part of an extensive volcanic system, which rises over 1000 m from the sea level, in the north-western sector of the Gulf of Napoli (Orsi et al., 1999; Bruno et al., 2002; Paoletti et al., 2013) and is located about 9 km from Campi Flegrei (Fig. 18). Ischia covers an area of 46.4 km^2 and is morphologically dominated by the central high of Mt. Epomeo (787 m above sea level), and by the NE-SW Mt. Vezzi–Mt. Cotto alignment of peaks in the southeastern corner (Fig. 20). The coastline is characterized by steep cliffs with interposed promontories on the southern side, and by slopes gently dipping towards the sea elsewhere.

Volcanism develops through the building of a volcanic field mainly made up of monogenic volcanoes (tuff cones, scoria cones, spatter cones and spatter ramparts, lava domes and lava flows) spread over an area of 250 km^2 (e.g. Sbrana et al., 2018). The geology of Ischia has attracted the attention of many scientists since the end of the eighteenth century (e.g. Breislak, 1798, 1801; von Buch, 1809; Fonseca, 1847, 1870; Scacchi, 1841; Johnston-Lavis, 1885; Deecke, 1901; De Lorenzo, 1904; Rittmann, 1930). More recent studies have contributed to a better definition of the behavior of the magmatic system through time (Poli et al., 1987; Poli and Civetta, 1987; Crisci et al., 1989; Poli et al., 1989; Civetta et al., 1991b; Piochi, 1994; Di Girolamo et al., 1995; Piochi et al., 1999; D'Antonio et al., 2013; Moretti et al., 2013; Brown et al., 2014; Melluso et al., 2014; Iovine et al., 2017b), the complex stratigraphic and structural setting (Chiesa et al., 1985a, 1985b, 1986, 1987; Orsi and Chiesa, 1988; Vezzoli, 1988; Fusi et al., 1990; Orsi et al., 1991, 1992a, 1994; Luongo et al., 1995; Tibaldi and Vezzoli, 1998, 2000, 2004; Acocella and Funiciello, 1999; Carlino et al., 2006; Brown et al., 2008; de Vita et al., 2010, Sbrana, 2018), the characteristics of seismicity, short-term ground deformation, and magnetic and gravimetric field (e.g. Cubellis, 1985; Del Gaudio and Sepe, 1998; Nunziata and Rapolla, 1987; Alessio et al., 1996; Paoletti et al., 2013; Troise et al., 2019; Trasatti et al., 2020) of the island, and the age of recent eruptions (Orsi et al., 1996b; Vezzoli et al., 2009; de Vita et al., 2010),. The results of archaeological investigations of the past 6 ka (Friedlander, 1927; Buchner, 1943, 1954, 1986; Buchner and Rittmann, 1948; Monti, 1980; Gialanella, 1994; Vezzoli et al., 2009) have been used to precisely date volcanic events that were too closely spaced to be discriminated with radiometric dating methods.

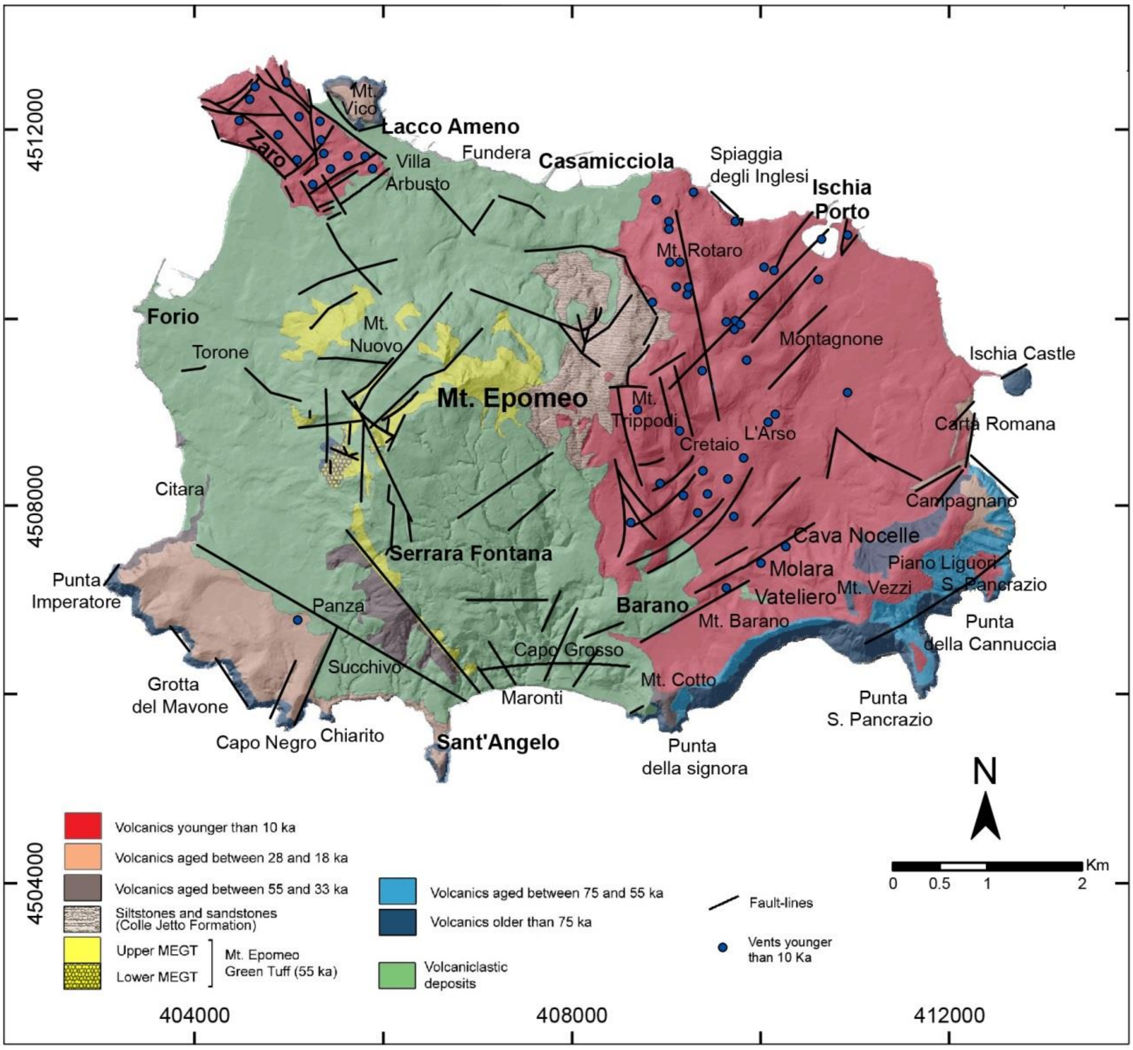

Fig. 20 Geological sketch map of Ischia (modified after D’Antonio et al., 2013).

The onset of the activity at Ischia dates back at least to about 150 ka, even though the oldest rocks are not exposed: these derive from a volcanic complex, formed by pyroclastic deposits, lava flows and trachytic and phonolithic lava domes, mostly located in the southeastern part of the island and which has been partially eroded and/or covered by more recent products (Fig. 20; Vezzoli, 1988); among these, the most studied is the Mt. Epomeo Green Tuff.

During its activity, several volcanic phenomena and/or volcanic related events affected the island: formation of calderas, Plinian or sub-Plinian eruptions, phreatomagmatic activity, PDCs, soil deformations (e.g. caldera resurgence) and landslides. The island has always exhibited discontinuous activity over time, alternating phases of explosive and effusive volcanism with long periods of quiescence (Gillot et al., 1982; Vezzoli 1988; Orsi et al., 1996b; de Vita et al. 2006, 2010).

The evolutionary history of the island is divided into different main phases (e.g. Vezzoli et al., 1988; Sbrana et al., 2018).

The volcanic products belonging to the first cycle mostly outcrop along the south-eastern coasts (between P.ta della Signora and Carta Romana); these outcrops in few localities on the south-western coasts (Caponegro, P.ta Chiarito and P.ta Imperatore) and in other areas (Mt. Vico and Castello d'Ischia; Fig. 20).This first phase of activity (> 150 ka) is mainly represented by large pyroclastic eruptions: the Scarrupata di Barano sequence shows PDCs and fall deposits interspersed with lava flows (Carrozza Formation and Scarrupata di Barano Formation) showing an overall thickness of about 100 m (Vezzoli et al., 1988). The Carrozza Formation, which formed a pyroclastic deposit due to Plinian eruptions, represents the bottom of the stratigraphic sequence of Ischia and emerges only at S. Pancrazio. The deposits are covered by thick lava fountains deposits, related to eruptive fractures (Torone, Monte di Vezzi, 130 ka; Fig. 20; Sbrana et al., 2018). Around 117 and 100 ka ago, lava flows and lava domes were emplaced (Sbrana et al., 2018).

The second phase occurred between ca 150 and 75 ka with mainly trachytic and trachyphonolitic lava flows and domes, along with minor pyroclastic rocks (e.g., Gillot et al. 1982; Vezzoli 1988; Crisci et al. 1989; Brown et al. 2014; Melluso et al. 2014): these deposits outcrop at P.ta Imperatore, Caponegro, P.ta Chiarito, Sant'Angelo, P.ta della Signora, Capo Grosso, La Guardiola, Monte di Vezzi, Monte Vico and Castello d'Ischia (Fig. 20).

Only recently an activity between ca 75 and 50 ka has been discovered (Brown et al., 2008), through the recognition of some pyroclastic layers that had previously been included within more recent deposits. Among these, the Sant'Angelo, Mago, Olummo, Tischiello and Porticello tephra were previously included in the activity associated with the Pignatiello Formation (ca 60 ka; Vezzoli, 1988; Sbrana et al., 2018). This phase was marked by a change of the eruptive style from mainly effusive to highly explosive eruptions with emplacement of complex successions of trachytic pumice falls interlayered with PDCs and breccias (Orsi et al. 1991; Brown et al. 2008). The volcanic rocks of this phase outcrop continuously along the southeastern sector of the island overlaying the rocks of the second phase. Around 60 ka, several layers of pumice-rich deposits intercalated to paleosoils, the Pignatiello Formation (Rosi et al., 1988) blanketed the southern and eastern sectors of Ischia, Vivara, and Procida islands and reached the continental Campi Flegrei volcanic field.

The Pignatiello Formation was followed by high magnitude explosive eruptions that formed an ignimbrite plateau: among these, the Mt. Epomeo Green Tuff paroxysmal eruption that marks the beginning of the third cycle of activity lasted between .ca 55 and 33 ka. The Mt. Epomeo Green Tuff eruption formed a ca 10 × 7 km large caldera and erupted ca 40 km^3 of pyroclastic products (e.g., Vezzoli, 1988; Tibaldi and Vezzoli, 1998; Tomlinson et al., 2014). The Mt. Epomeo Green Tuff consists of trachytic ignimbrites that partially filled a submerged depression, which now makes up the central part of the island. The Mt. Epomeo Green Tuff outcrops, with its maximum thickness, at the base of the western flank of the horst of Mt. Epomeo. The deposits show a welded ignimbritic facies, deposited in an underwater environment, with dense pumices, lithic clasts and crystals, in a green matrix (due to the alteration of sea water; Di Napoli et al., 2013) and a non-welded facies, yellowish-white in color, with vesiculated pumice and less lithics and crystals, in a fine matrix.

The caldera collapse was followed by the Mt. Epomeo block resurgence, in the central portion of the caldera (Acocella & Funiciello, 1999; Tibaldi and Vezzoli, 2004; Carlino et al., 2006; Orsi et al., 1991; Sbrana et al., 2009 and references therein). The resurgence determined a net uplift of about 900 m (Orsi et al., 1991). SW of Mt Epomeo the resurgent block, tilted southward and fragmented in smaller blocks, is delimited by conjugate systems of faults. The resurgence deeply influenced the morphology and geology of the volcanic field also with the formation of an epiclastic and volcanic apron all around Mt Epomeo. Several authors (Rittmann, 1930; Carlino et al., 2006; Sbrana et al., 2009) link the resurgence of Mt Epomeo and the volcanic activity around the block to a laccolith-shaped shallow magma body. Other authors explain the structure of the resurgence by an increase in pressure in a shallow magma chamber using a trapdoor model (Acocella & Funiciello, 1999) or a simple shear model (Orsi et al., 1991).

Resumption of volcanism after the caldera collapse occurred around 45 ka with the Citara tuff cone located in the western offshore area of the volcanic field after about 11 ka of stasis in volcanism (Sbrana et al., 2018). Minor trachytic hydromagmatic to magmatic eruptions from small vents along the southwestern and northwestern sectors of the island prolonged this phase up to 33 ka (de Vita et al. 2010).

The following phase (ca 28-13 ka) started after 5 ka of quiescence, with the arrival of shoshonitic magma into the main reservoir, which triggered the Mt. Epomeo caldera resurgence of ca. 900 m (Poli et al. 1989; Civetta et al. 1991b; Orsi et al. 1991; de Vita et al. 2006). Around 28 ka (Vezzoli, 1988) the eruption of Grotta di Terra, along the southeastern coastline, marked the beginning of this period of activity, which continued with sporadic eruptions until 18 ka. The dike (neck) of Grotta di Terra, exposed on the homonymous promontory, is formed by trachibasaltic/shoshonitic lava. Later, phreatomagmatic and magmatic explosive eruptions mostly emitted alkalitrachytic magmas, while effusive eruptions generated trachytic lava flows. The activity was mainly concentrated in the south-western sector of Ischia (Panza area); a few eruptive vents were located in the eastern sector (e.g. Scogli di S. Anna lava). The products of this period have been originated mostly by monogenic vents. Predominantly, this phase has been characterized by effusive activity: at the Pilaro promontory, the sequence is formed by the lava domes of Grotta del Mavone covered by the flows of the volcanic center of Pilaro, which overlaps pumice and slag levels of the Scarrupo di Panza Formation. In the south-eastern sector, the pyroclastic cones of Monte Cotto and Monte Vezzi lie on the Mt Epomeo Green Tuff. The activity of this phase was fairly constant, without prolonged periods of inactivity, as evidenced by the lack of paleosoils or erosion surfaces (e.g. Sbrana et al., 2018).

The last phase of activity started about 10 ka and is still in progress, with the last historic lava flow recorded at Arso in 1302 AD (de Vita et al. 2010 and references therein). This period has been characterized by extrusion of trachytic and subordinately latitic magmas through effusive eruptions and magmatic and phreatomagmatic explosive eruptions, mostly sourcing in the eastern sector of the island (Vezzoli 1988; de Vita et al., 2010). Many of them (11 out of 24) were characterized by both magmatic and phreatomagmatic explosions, whereas some were purely magmatic (6 out of 24) or phreatomagmatic (7 out of 24; Vezzoli et al. 2009). The effusive activity was characterized by lava domes and high aspect ratio lava flows, whereas magmatic and phreatomagmatic explosive eruptions generated tuff-cones, tuff-rings, and variably dispersed pyroclastic fall and pyroclastic current deposits (de Vita et al. 2010, and references therein). Most of the eruptive vents were located within the morphological depression to the east of Monte Epomeo. Lava domes and lava flows formed at east, north-east: Selva del Napolitano, Fundera, and Zaro complex. Only a few occurred in the northwestern corner, and at Punta Chiarito promontory, in the southwestern corner of the island. Tuff cone activity occurred at Casamicciola, Cava del Puzzillo, and Villa Arbusto, where explosive hydromagmatic centers, tuff cones, are activated. The Piano Liguori phreatoplinian eruption (5.6 ka) caused the emplacement of a thick cover of ashy layers (Sbrana et al., 2018) which mantle all the southeastern reliefs of the island.

This phase is also characterized by ongoing Mt. Epomeo caldera resurgence (e.g., Orsi et al. 1991, 1996b; Buchner et al., 1996; de Vita et al. 2006, 2010). Caldera resurgence restricted eruptions to the eastern sector of the island with only a few vents located outside this sector, along regional fault systems. The volcanism at Ischia volcanic field was very intense in Greek and Roman times, up to the Middle Ages; at least 15 volcanic edifices located mainly in the eastern sector of the island were identified (Sbrana et al., 2018). They are represented by complexes of lava domes and flows (Rotaro and Montagnone) with associated pyroclastics, scoria and spatter cones of Vateliero, Molara, Cava Nocelle, Punta della Cannuccia, Ischia Porto, and Spiaggia degli Inglesi (Fig. 20). Other mapped pyroclastic units are not referable to a well-identified volcanic edifice. This is the case of the pumice sheet of Cretaio sub-Plinian eruption deposits that were dated to 150 A.D. (Sbrana et al., 2018 and reference therein). The last volcanic episode of Ischia is represented by the Arso spatter and lava flow (1302 AD; Vezzoli, 1988; Piochi et al., 1999; Iovine et al., 2017b). This originated from the eastern side of Monte Epomeo, starting from a N-S directed fracture. It shows a scoriaceous blocky-shaped surface and is rich in centimeter-sized sanidine phenocrysts engulfed in a black to reddish groundmass (Vezzoli et al., 1988).

Archaeological findings reveal that Ischia has been discontinuously inhabited since Neolithic time (Buchner, 1986). Nowadays, the island is characterized by an active hydrothermal system (Chiodini et al. 2004; Di Napoli et al. 2011) that, along with its favourable position within the Neapolitan gulf and its beaches, makes it one of Italy’s major touristic hubs (Selva et al., 2019). The island is densely populated, with more than 60,000 inhabitants distributed in less than 50 km^2. In touristic seasons this population increases substantially. This makes the volcanic and related risks at Ischia very high (Selva et al., 2019), also for relatively small events, as demonstrated by the recent 3.9 magnitude volcano-tectonic earthquake occurred at Casamicciola in late August 2017 (De Novellis et al., 2018) that caused 2 fatalities, several tens of injured, and severe damages mainly to the village of Casamicciola Terme, located in the northern part of the island.

3.5 The Zaro eruption

During the last 10 ka volcanism on Ischia island has generated several effusive and explosive eruptions (magmatic and phreatomagmatic), mostly in the eastern sector of the island (Vezzoli et al., 1988; de Vita et al., 2010). Among these, the Zaro lava complex (<7 ka) was extruded from a NE-SW-striking eruptive fissure in the north-western part (Fig. 20) of the caldera floor and it represents the largest volume of lava (0.12 km^3) erupted during the post-caldera volcanism on Ischia (Vezzoli et al., 2009).

The Zaro peninsula, in the northwestern corner of the island, is characterized by the superposition of several lava domes and flows, likely emplaced in a short time span, along a complex network of N–S, NE–SW, and NW–SE trending faults (Fig. 21a; de Vita et al. 2010).

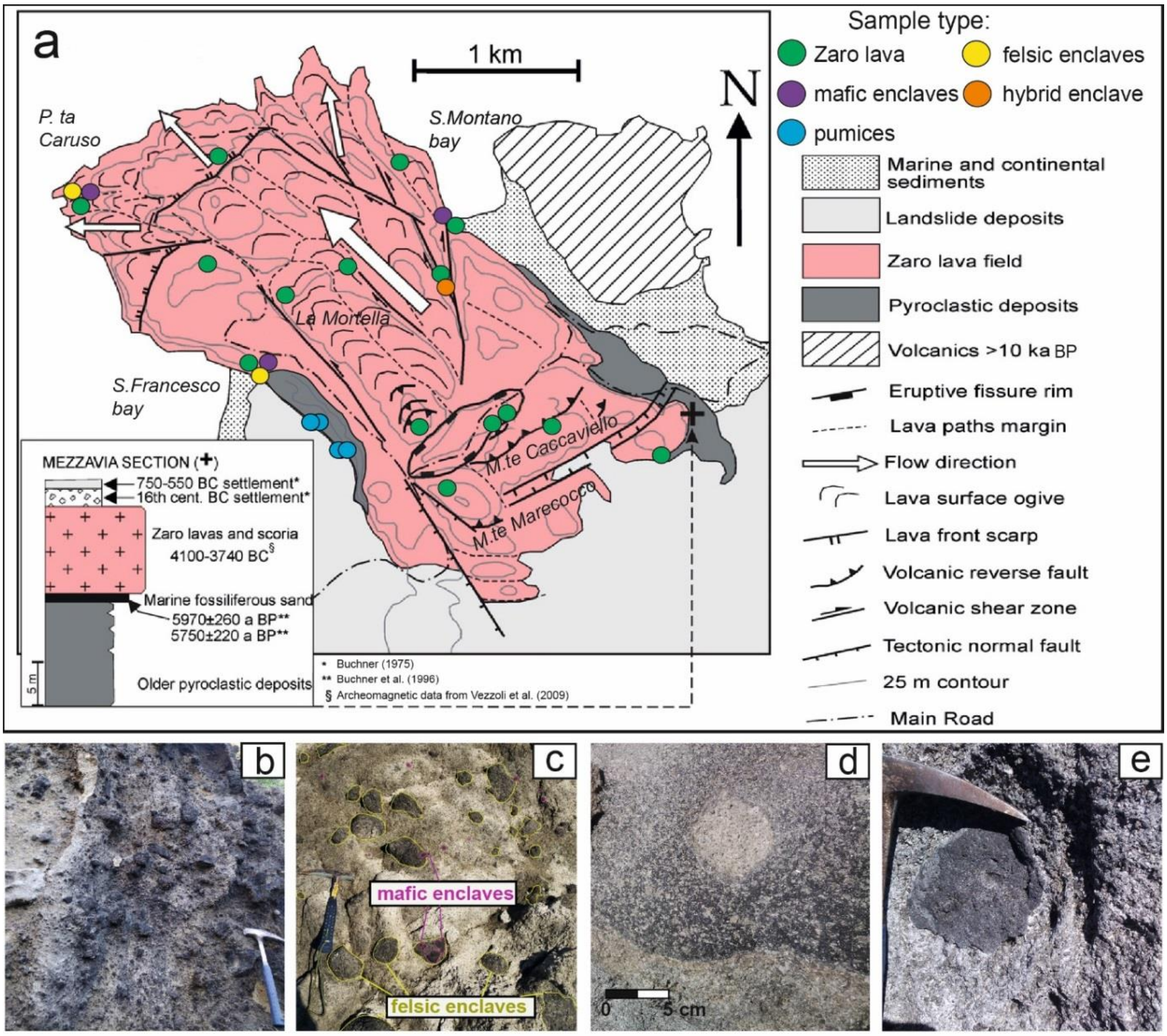

Fig. 21a) Geologic map of the Zaro volcanic complex at the north-western edge of the Ischia Caldera, showing the location of the sampled sites (modified after Vezzoli et al., 2009). Exact locality of samples is listed in Table 1-Supplementary Material 2. See Chapter 3 for a detailed description of the lava facies; Field photographs of b) Zaro pyroclastic deposit; c) Felsic and mafic enclaves hosted in Zaro lava; d) Zaro lava blob hosted in felsic enclave in Zaro lava; e) Mafic inclusion with cuspate borders.

The lava complex overlies an heterogeneous and heterometric undefined pyroclastic sequence. This deposit is a ca 25 m-thick massive to roughly stratified, poorly sorted, breccia-like deposit, containing juvenile elements and heterogeneous lithic clasts in a coarse-grained matrix (Fig. 21b). The juvenile elements are represented by poorly vesicular to very dense, feldspar-rich pumiceous clasts (up to 15 cm in size). The lithic clasts are heterogeneous and heterometric fragments: yellowish to green lapilli tuff, cm- to dm-sized, highly porphyritic to aphyric, angular to strongly flattened and rounded lava blocks, cm-sized vesicular scoriae and shallow-origin crystalline clasts

(Pelullo et al., 2020). This sequence was interpreted as the initial explosive activity of the Zaro eruptive center (Vezzoli et al., 2009; Sbrana et al., 2011, 2018), whereas de Vita et al. (2010) attribute this deposit to an older activity (> 10 ka). Below the lava complex, in the Mezzavia locality, there is a bed of coastal sand with marine fauna: two different species of shells from this deposit yielded a radiocarbon ages of 5970±260 and 5750± 220 years BC. Zaro lava flows are locally covered by a debris-flow deposit that partially buried the remnants of a Bronze Age village, dated to the 14th century BC (Vezzoli et al., 2009 and reference therein). Those deposits allow to constrain the emplacement of Zaro lavas between 4100 and 3740 years BC. In some cases, the extrusion occurred along the sides of pre-existing hills, producing asymmetric domes and very viscous, low-mobility and high-aspect ratio lava flows.

The lavas are trachytic in composition and show a very high crystal content (with a porphyricity index of 50%), of mainly (85%) sanidine phenocrysts, up to 15 mm in size. Lava domes (Mt. Marecocco and Mt. Caccaviello) have similar petrographic and textural features compared to the lavas. The flow surface is very irregular with extruded spines, domal structures of thickening flow, concentric transversal ridges (ogives), and longitudinal scarps and lineaments (interpreted as volcanic strike-slip faults; Vezzoli et al. 2009). A fingered flow front, with folded and brecciated internal structures, radiates from a 50 m high sub-vertical lava front scarp. The vent area is a prominent crease (500 m long, 50–100 m wide and 50 m deep), from which the lava outpoured and spread laterally, accumulated near the vent area in domes, and developed volcanic reverse faults (Tibaldi, 1996; Vezzoli et al. 2009). The petrographic texture, high aspect ratio (1/13), surface morphologies, internal structure, and strike-slip and reverse volcanic faulting indicate that the Zaro lavas were extremely viscous and had very high yield strengths at their emission (Vezzoli et al. 2009). The ogives formed during the first stages of lava cooling in response to compression parallel to flow. The longitudinal shear zones formed due to differential flow velocity of different lava sectors (Tibaldi, 1996).

NE trending faults, perpendicular to the flow direction, and SW trending tectonic features dominate the morphology of the lava complex, followed, in order of abundance, by NNW- (in the northwestern part of the flow face) and ENE- (in the northeastern part of the front) trending tectonic lineaments (Fig. 20). The NW trending faults dislocate the NNW and ENE trending faults, along the termination of the lava complex towards the sea (Tibaldi, 1996). The two sets of ancient faults border two hills (ca 90 m high) that are higher than the central lava body and therefore indicate local thickening areas of the lavas flow. Other NW trending fault planes in the vent area have been interpreted as reverse faults. Some faults coincide with brecciated areas. Some NE trending lineaments, which also cut the deposits above the lava complex, have been recognized as tectonic lines not due to the emplacement of the lavas, but associated with Quaternary regional deformation (Tibaldi, 1996).

The main lava body (hereafter referred to as Zaro lava) hosts several kinds of enclaves, from mafic to felsic in composition (Fig. 21c-e). In this thesis, different lithotypes have been collected and analyzed from both the pyroclastic sequence and the lava complex.

3.6 Magma genesis, magmatic evolution and architecture of the Campi Flegrei and Ischia feeding system

The knowledge of the magmatic system beneath the PVD, where magmas stagnate and rise to surface, is important for a better understanding of both magmatic and volcanic processes which occurred in the past, for inferring the present state of the magmatic feeding system, and assessing volcanic hazards. The scientific interest and the civil protection concern, due to the hazard in such a populated area, have stimulated multi-disciplinary researches, which allowed to investigate the architecture of the Campi Flegrei and Ischia magmatic system. In past decades, geochemical and geophysical investigation allowed a better understanding of the PVD magmatic system. Petrological and geochemical characterization of the erupted products provided direct critical information for understanding differentiation processes of magmas deriving from heterogeneous mantle sources and feeding the Ischia and Campi Flegrei plumbing systems.

The Campania volcanic rocks belong to the potassic series (KS) of Appleton (1972), whereas at Somma-Vesuvius, mildly to highly undersaturated rocks belonging to high-potassium series (HKS) also occur. The magmas erupted at Campi Flegrei range in composition from trachybasalt to phono-trachyte, with a predominance of trachyte (D’Antonio et al., 1999b; Pappalardo et al., 1999; Melluso et al., 2012). Minor less differentiated magmas (trachybasalt and latite) were erupted at Campi Flegrei at the end of the first epoch of the last period of activity, along NE-SW regional tectonic structures (Orsi et al., 1996a). The Campi Flegrei magmas exhibit a wide range of ^{87}Sr/^{86}Sr (0.7068-07086), but limited ranges of ^{143}Nd/^{144}Nd (0.51240-0.51266) and Pb-isotope ratios (e.g. ^{206}Pb/^{204}Pb: 18.85-19.25; Civetta et al., 1991a; Pappalardo et al., 2002b; D’Antonio et al., 2007; Arienzo et al., 2010, 2015, 2016). Ischia volcanic rocks belong to the low-K-series, showing affinities with sodic series and peralkaline conditions and range in composition from trachybasalt to latite, trachyte, alkali-trachyte and phonolite, the latter two being the most abundant rock types (Vezzoli, 1988; Crisci et al. 1989; Civetta et al. 1991b; Orsi et al. 1992a; Di Girolamo et al., 1995; Piochi et al. 1999; D’Antonio et al. 2007; Brown et al. 2008, 2014; Melluso et al., 2014). The Ischian rocks never reach typical phonolitic compositions, as in the Campi Flegrei (Melluso et al., 2014). At Ischia, such as at Campi Flegrei, slightly differentiated magmas, i.e., shoshonite and latite, have been erupted mostly by vents located along faults of the NE–SW system during the last period of activity (e.g. Arso, Vateliero and Cava Nocelle eruptions; D’antonio et al., 2013 and reference therein). The magmas erupted at Ischia have a wide range of isotopic values: ^{87}Sr/^{86}Sr ratio varies between 0.7050 and 07073, while ^{143}Nd/^{144}Nd ratio varies between 0.51246 and 0.51268 (Civetta et al., 1991b; D’Antonio et al., 2013; Iovine et al., 2017b; Pelullo et al., 2020); ^{206}Pb/^{204}Pb ratio varies between 18.88 and 19.05 (D’Antonio et al., 2007). The Sr isotopic ratios are generally less radiogenic than those of Somma-Vesuvius and Campi Flegrei, while the Nd, Pb and

B isotopic ratios are similar (Tonarini et al., 2004, 2009; D'Antonio et al., 2007). The geochemical variability of Campi Flegrei and Ischia magmas results from mantle source heterogeneity, fractional crystallization and open-system processes (e.g., Civetta et al., 1991a, 1991b; D'Antonio et al., 1999b, 2007, 2013; Pappalardo et al., 1999, 2002b; 2008; Tonarini et al., 2004, 2009; Di Renzo et al., 2007, 2011; Fedele et al. 2008; Mangiacapra et al., 2008; Arienzo et al. 2009, 2015, 2016; D'Antonio, 2011; Melluso et al., 2012, 2014; Tomlinson et al., 2012; Pappalardo and Mastrolorenzo, 2012; Brown et al., 2014; Forni et al., 2018b).

The source of the magmatism in the Neapolitan area has been located in a mantle, variably enriched in incompatible elements, radiogenic Sr and unradiogenic Nd (e.g. D'Antonio et al., 2007). The composition of the pre-enrichment mantle sector underlying the Neapolitan volcanic area is still poorly known. Actually, many are the hypotheses about magma genesis of the Italian volcanic rocks (e.g., Peccerillo and Lustrino, 2005), but most of the Italian orogenic magmatism might reasonably be the result of partial melting of mantle sources modified by slab materials during and/or after subduction event(s). This hypothesis is supported by a considerable amount of studies that highlight its post-collisional character (e.g., Peccerillo, 1999; Beccaluva et al., 1991; Conticelli et al., 2002, 2004, 2007, 2009; D'Antonio et al., 1996, 1999a, 2007, 2013; Francalanci et al., 2004, 2007; Tonarini et al., 2004; Duggen et al., 2005; Harangi et al., 2006; Avanzinelli et al., 2008, 2009; Prélevic et al., 2008; Nikogosian and van Bergen, 2010; Lustrino et al., 2011; Moretti et al., 2013). Furthermore, the Italian magmatism has been related to the subduction of the Ionian oceanic lithosphere, being part of the wider Tethys Ocean (Gvirtzman and Nur, 1999; Faccenna et al., 2007). Indeed, all the rocks from the Neapolitan district show island-arc geochemical signatures: it is known that worldwide subduction-related mafic volcanic rocks have distinctive incompatible elements patterns, such as strong enrichment in LILE (Large Ion Lithofile Elements) and Pb with respect to HFSE (High Field Strenght Elements), and REE. In fact, the mafic rocks of the Neapolitan volcanoes show negative anomalies of HFSE (noticeable the Nb, Ta and Ti), in their incompatible element patterns, and high LILE/HFSE ratios. Moreover, volcanic rocks from the

Neapolitan volcanoes show variable enrichment in radiogenic Sr and Pb and unradiogenic Nd. All these characteristics are reconducted to sediment recycling within the upper mantle via subduction. Experimental petrology constraints indicate that an amphibole-bearing spinel peridotite is the best candidate to generate mildly potassic arc magmas (e.g., Foley, 1992; Melzer and Foley, 2000; Conceição and Green, 2004) such as those of Campi Flegrei and Ischia. However, the nature of the pre-enrichment mantle source in Central-Southern Italy, including the Neapolitan area, is strongly debated. On the basis of isotopic and geochemical features of mafic volcanic rocks, some authors have proposed an OIB-like mantle (e.g., Ellam et al., 1989; Peccerillo and Panza, 1999; Peccerillo et al., 2008), others a MORB-like mantle (e.g., Serri, 1990; D’Antonio et al., 1999a, 2007; Conticelli et al., 2004; Schiano et al., 2004; Paone, 2006; Francalanci et al., 2007; Mazzeo et al., 2014), or a MORB-OIB mixture (Beccaluva et al., 1991; Gasperini et al., 2002; De Astis et al., 2006). Anyway, it is postulated that the original mantle has been modified by subduction-derived components. Debate also exists about the time of the enrichment (e.g. Avanzinelli et al., 2008; Mazzeo et al., 2014).

Thus, petrographic observations, as well as geochemical and isotopic data on large datasets of PVD volcanic rocks of variable age suggest that the magmas feeding the Ischia and Campi Flegrei magmatic systems originated from mantle-derived, K-basaltic parent melts. However, both at CFc and Ischia, very few rocks are possibly representative of near-primary melts (Beccaluva et al., 1991; Di Girolamo et al., 1995; D’Antonio et al., 1999a; Melluso et al., 2014) and most of the erupted magmas are chemically evolved. K-basaltic melts produced by partial melting of the mantle sources beneath the Neapolitan area have thus evolved through prolonged fractional crystallization processes which occurred in the crust (e.g., D'Antonio et al., 2007, and references therein). Hence, the occurrence of crustal storage region(s) within which the magmas evolve to trachyte and phonolite is necessary to explain their chemical composition. It is now well known that the magma feeding system of the Neapolitan volcanoes consists of a permanent, large molten body in the form of a wide (> 200 km^2) and thin (about 1 km) sill, located in the 7–10 km depth range and extending below the whole Neapolitan volcanic area, which includes Vesuvius, Campi Flegrei and, probably, Ischia volcanoes (Zollo et al., 1996, 2008). The extent of such layers at 7-10 km depth suggests some lateral continuity between the magma storage systems within the Neapolitan volcanic area (Pappalardo and Mastrolorenzo, 2012; Moretti et al., 2013).This reservoir is recharged by mantle derived magmas, that at this level stagnate, differentiate and eventually are contaminated by continental crust (Pappalardo et al., 2002b; Pappalardo et al., 2008; Pappalardo and Mastrolorenzo, 2010, 2012). From this long-lasting main reservoir, magmas can rise to shallow depth, where, occasionally magma accumulation can occur. However, there is no consensus on the structure of the plumbing system at shallower level (<7 km). In fact, some authors hypothesized the presence of permanent smaller magma chambers feeding the last 5000 years of activity including the last Monte Nuovo event (e.g. Di Vito et al., 2016, Asbury et al., 2018; Stock et al., 2018); while other authors suggested the development of ephemeral localized storage zone during magma ascent, where magma shortly resides until erupting or cooling (so called failed eruptions) (e.g. Liedl et al., 2019). The presence of deep magma reservoirs of regional extension, fed by mantle-derived fluids and magmas infiltrating from mantle depths is consistent with previous geochemical-petrologic hypotheses (e.g., Pappalardo and Mastrolorenzo, 2012; Moretti et al., 2013) and with strong geophysical evidences of a low-velocity crustal layer at around 7–10 km of depth (Zollo et al., 1996, 2008; De Natale et al., 2001, 2006; Guidarelli et al., 2006; Nunziata et al., 2006). At Campi Flegrei, the distribution of 3D gravimetric anomalies confirms the recurrent occurrence of small and shallow high-density bodies consistent with intrusions along faults periphery and the main structural lineaments, which have been preferential pathways for migration of aqueous fluids, gases, and magmas (Capuano et al., 2013). The distribution of anomalous bodies agrees well with previous and independent results from surface wave tomography that found a low shear velocity layer at a depth around 10 km (crustal reservoir), fed by a deeper mantle reservoir (Guidarelli et al., 2002, 2006). Melt inclusion data in Campi Flegrei minerals indicate crystallization between ~9 and ~3–5 km (e.g., Marianelli et al., 2006; Mangiacapra et al. 2008; Arienzo et al. 2010, 2016). However it is largely demonstrated that glass inclusions data can be affected by post-entrapment modification as well as the inclusion-bearing crystals can have a wide range of origins and ages, further complicating the interpretation of magmatic processes (Ruth et al., 2018). Thus melt inclusions volatile content does not univocally record pre-eruptive storage depth but can follow syn-eruption degassing paths. The deep structure of the Ischia caldera is poorly constrained from a geophysical point of view. Modeling of magnetic data (Orsi et al., 1999) points to a large magma body at ca. 7 km depth. However, in the absence of seismic data, the role of petrology in assessing the characteristics of the deep magma storage system and magma crystallization depth is of fundamental importance. Eruption of shoshonitic to latitic magmas at the margin of the caldera and of differentiated magmas within it testifies to the ascent of weakly differentiated, CO_2-rich magmas of deep provenance along regional faults and the occurrence of a shallow magma storage region beneath the caldera, in which the magmas evolve to trachyte and phonolite. Phenocryst-hosted melt inclusions studies from the Ischia volcanic products suggest that the trachyte and phonolite storage region is relatively shallow with respect to the reservoir from which the shoshonitic and latitic magmas come (Sbrana et al., 2009; Moretti et al., 2013). This deep reservoir is volatile-rich and acts as a valve controlling the upward transfer of magmas and fluids, giving rise to shallower magma chambers that feed both hydrothermal systems and surface eruptions (Moretti et al., 2013). Below Ischia and Campi Flegrei ascent and emplacement of magmas at shallower depth, where they evolve to trachyte and phonolite, could be controlled by the intersection of NE–SW transverse and NW–SE normal regional fault systems (Acocella and Funiciello, 2006). The structural conditions generated by the intersection of the NW-SE normal faults and NE-SW transfer faults are suitable for the formation of large magma chambers and large residual crystal mushes (e.g. De Natale et al., 2006; D’Antonio, 2011) in which interaction with deep fluid and new magma batches can explain why the Ischia and Campi Flegrei products record strong mineralogical and isotopic disequilibria (Civetta et al., 1991a, 1991b; Di Renzo et al., 2011).

Detailed geochemical analysis on Campi Flegrei and Ischia volcanic products allowed to investigate magmatic processes acting in the PVD magmatic system and its evolution through time.

At CFc, trachytic magmas were predominantly erupted in the last 100 ka (e.g. Civetta et al., 1997; Pappalardo et al., 2002b; Di Renzo et al., 2007). During the initial 100-44 ka period, trachytic magmas were erupted preferentially from vents located along NE-SW tectonic lineaments, and this first magmatic stage culminated in the formation of the caldera at ca 39 ka, with the catastrophic eruption of the voluminous trachytic Campanian Ignimbrite deposits (Civetta et al., 1991a; Pappalardo et al., 2002a, 2002b). Following this eruption, volcanism continued inside the caldera rim, with emplacement of trachytic and subordinately latitic products. Trachybasaltic magmas were erupted only during the last period of activity, through vents located on a NE-SW regional fault system that probably tapped the deeper least-evolved reservoir (e.g. D'Antonio et al., 1999; Moretti et al., 2013). A ciclicity in the Campi Flegrei magmatic system has been observed by Forni et al., 2018b. According to this theory, during the caldera forming eruptions, both highly differentiated, relatively cold, and water-rich extracted melts and less evolved, hotter, and drier magmas were erupted, generating zoned ignimbrites (CI and NYT). The caldera stage is characterized by large volume magma withdrawal involving the crystal-poor cap and part of the cumulate mush remobilized after more mafic recharge. This represents the main mechanisms responsible for the generation of gradients in the pyroclastic sequences of caldera-forming eruptions at Campi Flegrei. Forni et al., 2018aDuring the early post caldera stage, small and frequent eruptions were fed by mafic magmas of deeper origin (e.g., Torregaveta, Minopoli) and more evolved crystal-rich magmas recycling portions of the residual crystal mush (e.g., Trentaremi, Pomici Principali). This early post-caldera stage is associated with frequent injections of more mafic magmas of deeper origin into the upper crustal reservoir. Magmas can be erupted along the caldera ring faults or stall into the crust where they interact with the residual cumulate mush triggering remobilization and eruption of crystal-rich material. During this stage, eruption frequency is high and the vents concentrate within the caldera. During late post- or pre-caldera stage, less frequent eruptions involved highly evolved, water-rich, and relatively cold magmas (e.g., S. Severino, Verdolino). The transition to the late post-caldera/pre-caldera stage is thus marked by a decrease of the eruption frequency, which allows magmas to stall in the crust and evolve via fractional crystallization (Forni et al, 2018b).

At Ischia, temporal variations of the isotopic composition of the erupted products emplaced in the past 55 ka indicate complex behavior of the magmatic system, characterized by phases of magma evolution under closed-system conditions and by arrivals of new, isotopically distinct magmas that show evidence for contamination and mixing processes (Civetta et al., 1991b; Piochi et al., 1999; D’Antonio et al., 2013; Iovine et al., 2017b). Geochemical and isotopical variations through time have evidenced that the magmatic system between ca 55 and 33 ka acted as a closed system (Civetta et al., 1991b). Before the 28-13 ka period of activity, it was refilled by a deeper less evolved magma, which progressively mixed with the more-evolved resident magma. The last period of activity (<10 ka) was characterized by arrival of new magma: products of the last period of activity were fed by latitic to phonolitic magmas with a wide range of Sr-isotope compositions (ca. 0.70504–0.70700; Di Girolamo et al., 1995; D'Antonio et al., 2007, 2013). They show petrochemical disequilibria and a complex geochemical trend which suggest mingling/mixing processes between magmas with distinct chemical and isotopic composition (Crisci et al, 1989; Civetta et al., 1991b; Di Girolamo et al., 1995; Piochi et al., 1999; D’Antonio et al., 2013). Complex mingling/mixing processes operated till the last eruption, as testified by isotopic and mineralogical disequilibria (Piochi et al., 1999; Iovine et al., 2017b).

The magmatic system architecture and physicochemical processes occurring beneath the Neapolitan volcanoes influence the style and timescale of eruptions. Establishing the rates of magma storage and the events that precede eruptions, which is ultimately the aim of the thesis, is crucial to get information about the past and present of activity of these volcanoes as key to forecast their future behavior.

4. SAMPLES AND METHODS

4.1 Strategy of investigation

The primary targets of the present work is a detailed investigation of the pre-eruptive physical conditions of the A-MS and Zaro magmatic systems and a comprehensive definition of the magmatic processes leading to these eruptions different both as to size and eruptive mechanism. In order to accomplish these goals, after detailed field observations and sampling, the present study first focused on relevant petrographic and mineralogical characteristics of the sampled A-MS and Zaro volcanic products. A detailed chemical and isotopic characterization has been performed on whole rocks, matrix-glasses and mineral phases representative of the various units/members and sub-members of both the A-MS and Zaro sequences. Chemical analyses on rocks and minerals have been comprehensively useful for the characterization of pre-eruptive magma storage conditions. On selected samples, attention has been mainly focused on textural and in-situ compositional analysis of minerals sensitive to chemical and physical variations of the magmatic system, mainly clinopyroxene. Crystals from representative samples of the A-MS and Zaro sequences have been analyzed using multiple in-situ analytical approaches (i.e. SEM-EDS, EMPA) with the aim to detect major and minor element concentrations. This allowed a precise characterization of the clinopyroxene zoning patterns, which revealed the occurrence of different compositional populations. The isotopic characterization of rocks and minerals allowed to i) strongly constrain mineral-melt disequilibria, ii) identify open-system processes and iii) quantify these in terms of end-members. Lastly, timescales of magma residence and open-system magmatic processes have been constrained through the application of different diffusion modelling approaches on the chemical zoning of clinopyroxene crystals.

4.2 Sampling and selection of the volcanic products

The main difference to keep in mind about the A-MS and Zaro volcanic rocks is that, since the A-MS and Zaro rocks are the products of two different size eruptions, with very different eruptive dynamics, as described in previous chapters, their deposits are constituted by different lithotypes. On the one hand, since A-MS eruption was a magmatic to phreatomagmatic Plinian explosive event, the A-MS rocks are mainly made up of pumice and scoria fragments: these are the typical lithotypes representing the juvenile elements of the deposits; on the other, the Zaro eruption has been mainly characterized by an effusive activity with the emplacement of a lava complex. Based on the above, different criteria have been used for the selection of the samples for the two case studies. The main criteria for selection of the samples include petrological differences between lava rocks (i.e. porphyritic index, proportions of any single mineral phase within thin sections, groundmass texture), for the different lithotypes of the Zaro lava complex, as well as differences in the specific weight of juvenile fragments, for the A-MS pumices and scoria.

A-MS pumice and scoria fragments were collected from representative localities of the A-MS sequence (Cavone degli Sbirri, Guantai, Torciolano, Vallone del Corvo, Verdolino and Eremo; Fig. 19b) within and nearby the Agnano plain. In each locality, a part of the overall A-MS sequence outcrops. Samples, which correspond to the different sub-members A1, A2, B1, B2, D1, D2 and E2, belonging to both fall and PDC deposits were collected, from all localities. A general description of the sub-member sampled in such proximal and intermediate areas (ca. 2-5 km from the inferred vent) is the following: the A1 fallout deposit is constituted by a basal ash bed overlain by a coarse pumice-fallout deposit. The A2 sub-member consists of ash-to-lapilli size base-surge and fallout beds. The B1 member is a fallout deposit made of sub-angular, highly vesiculated pumices with subordinately hydrothermally altered lithic fragments. B2 sub-member is a PDC deposit showing a massive appearance, with centimeter-sized pumice inversely graded embedded in a fine matrix. At the base it is cineritic and massive, while upwards it is coarser with traction planar structures, crosslaminations and sand-waves structures. D1 sub-member is a fallout deposit consisting of centimetric highly vesiculated pumices. This layer shows abundance in reddish lithic fragments. D2 sub-member consists of an alternation of thin ash beds and thicker reverse graded layers of centimetric highly vesiculated pumice clasts. The E2 sub-member is a fallout deposit composed by millimetric to centimetric thick laminae consisting of fine to coarse-ash particles at the base and by a massive to slightly reversely graded deposit composed by angular pumiceous fragments at the top.

Samples belonging to the same sub-member, but outcropping in different localities were collected; as an example, samples belonging to sub-member B1 were collected both at Eremo and Guantai (Fig. 19b), in order to have a broad representativeness of the sampled sub-members, belonging to both proximal and intermediate areas. In this way, through successive matrix-glass chemical analysis, possible differences have been tested. Similarly, at Zaro lava complex, since the Zaro lava hosts different lithotypes, both enclaves and the host lava have been sampled in different localities (P.ta Caruso, S.Francesco bay, La Mortella, Mt. Marecocco, Mt. Caccaviello, S.Montano bay; Fig. 21a; Table 1-Supplementary Material 2). 6 enclaves, 15 Zaro lava (from the lava complex) and 4 pumiceous clasts (from the underlying pyroclastic sequence) whole rocks samples, representative of the whole facies variability, have been analyzed.

In order to choose populations of different density clasts for geochemical analysis, density analyses were performed on pumiceous clasts from the A1, A2, B1, B2, D1, D2 and E2 (Fig. 22) representative sampled members of the A-MS deposit. Sets of 100 clasts for each grain-size class, ranging from -4 to -2ϕ (where $\phi = -\mathrm{Log}_2\, d$; d = particle diameter), were weighted and coated with a thin film of paraffin wax, then their density was determined using a water pycnometer: clasts belonging to both the modal and the upper and lower 5% percentile classes values were chosen and, successively, their matrix-glass composition were analyzed: this allowed to test the possible chemical variability of pumiceous clasts showing different porosity or degree of vesicularity.

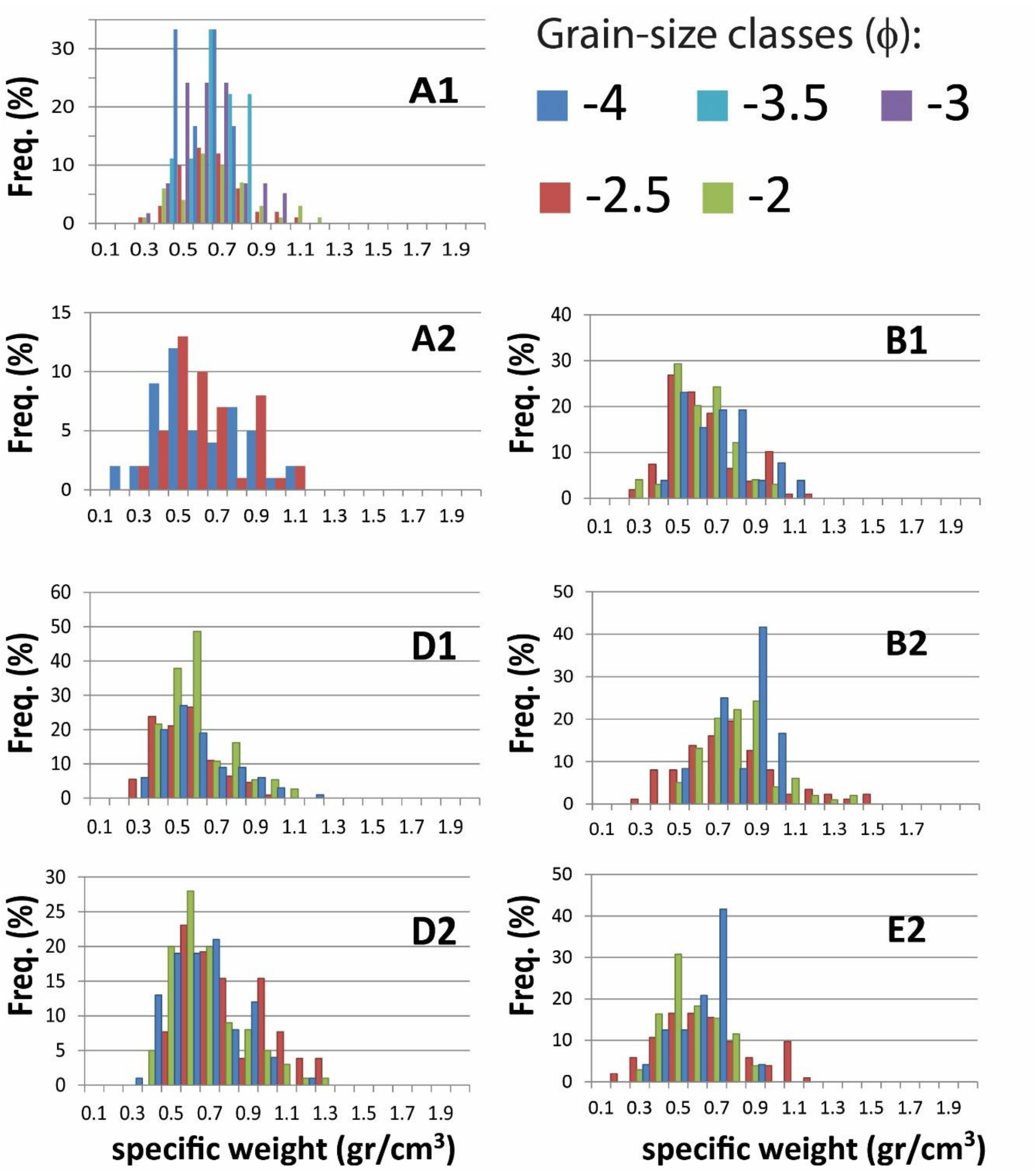

Fig. 22 Density analyses of pumiceous clasts for different grain-size classes of the A-MS sub-members.

4.3 Analytical procedures

4.3.1 Samples preparation for geochemical analysis

An aliquot of Zaro lava samples were sent at Laboratorio Sezioni Sottili of the Dipartimento di Scienze della Terra of the Università degli Studi di Roma "La Sapienza", to obtain polished thin sections for petrographic analysis. Instead, polished thin sections of the A-MS pumiceous clasts belonging to the sample collection of Dott.ssa Lucia Pappalardo were already available. Polished thin sections of the Zaro and A-MS samples have been used i) for textural, petrographic and mineralogical characterization of the rocks and ii) to obtain in-situ major and minor element chemical compositions of glass and minerals.

The selected samples of the A-MS and Zaro deposits were gently crushed to lapilli-size grains through a jaw crusher. Particles were previously washed in an ultrasonic bath (to remove sea water salts) and then dried at 60°C for 24 h. These samples were successively prepared, in different ways, for the different analytical acquisitions.

1. About 200 g of crushed rock for each sample belonging to the Zaro lava complex were powered in agate ball mill and sent at the Centres Científics i Tecnològics de la Universitat de Barcelona (CCiTUB), in order to perform whole rocks analysis (X-ray fluorescence for major and minor elements and Inductively Coupled Plasma-Mass Spectrometry for trace elements, respectively; see 4.3.2 section).
2. Another aliquot (ca 500 g) of crushed rock for each Zaro and A-MS sample were sieved using a stack of sieves with meshes ranging from 1ϕ to -1ϕ. From the sieved aliquots, clinopyroxene, K-feldspar, olivine, phlogopite phenocrysts and glass fragments were hand-picked under a binocular microscope. An aliquot (ca 0.2 g for each sample) of mineral grains were separated for isotopic analysis (see 4.3.5 section). Another aliquot of hand-picked minerals and glass grains were loaded in sample holders with epoxy resin and suitably polished with decreasing grain-size paste. In this way, glass and mineral grains were prepared for in-situ compositional analysis (see 4.3.3 section). Moreover, about 100 clinopyroxene crystals for each sample were loaded in sample holders in order to obtain detailed in-situ analytical data along core-to-rim transects of the crystals (see 4.3.4 section). Glass fragments and crystals were carefully studied with optical microscope (reflected and transmitted light), before to obtain compositional data.

3. About 200 g of crushed and washed whole rock samples were powdered in an agate ball mill for isotopic analyses. Whole rock powders (ca 0.1 g) and minerals were leached with warm HCl for 10 min before dissolution. Selected minerals (ca 0.2 g) were washed with 7% HF and Milli Q ® H_2O to remove any potentially remaining groundmass/glass film before dissolution. Sr and Nd were separated using standard column chromatographic methods, using Dowex AG50WX-8 (200–400 mesh) and Ln Spec cation exchange resins for Sr and Nd, respectively (Arienzo et al., 2013) and measured in static mode by thermal ionization mass-spectrometry (TIMS) using a Thermo Finnigan Triton TI.

Different types of geochemical analyses have been performed on different samples of the A-MS and Zaro rocks and minerals.

4.3.2 Whole rock analyses

Major, minor and trace elements compositions have been acquired on whole rock samples belonging to different lithotypes of the Zaro lava complex (Table 2-Supplementary Material 2). Major elements were analyzed by X-ray fluorescence using a sequential X-ray spectrometer Philips PW2400 at the CCiTUB. Concentrations of the major elements are expressed as weight percentages of oxides and elements determined were SiO_2, TiO_2, Al_2O_3, $Fe_2O_{3(t)}$, MnO, MgO, CaO, Na_2O, K_2O, P_2O_5. Concentrations of trace elements were determined by High Resolution-Inductively Coupled Plasma-Mass Spectrometry (HR-ICPMS, Element XR, Thermo Scientific), by using the Perkin Elmer Elan 6000 spectrometer. The detected trace elements are Sc, V, Cr, Co, Ni, Cu, Zn, Ga, Rb, Sr, Y, Zr, Nb, Ag, Cs, Ba, La, Ce, Pr, Nd, Sm, Eu, Gd, Tb, Dy, Ho, Er, Tm, Yb, Lu, Hf, Ta, Pb, Th, U and their concentrations are expressed as part per million (ppm). Whole-rock analysis by HR-ICP-MS was performed on a split (0.1 g) of each sample. This was digested with HNO_3:$HClO_4$:HF (2.5:2.5:5 ml, v/v), doubly evaporated to incipient dryness with addition of HNO_3, and finally made up to 100 ml with 1% (v/v) HNO_3. The precision and accuracy of analytical determinations, in the order of 1-2% for major oxides and 5-10% for trace elements, respectively, were monitored using reference materials of the Geological Survey of Japan (rhyolite JR-3 and basalt JB-3). Loss on ignition (LOI) was determined on 1 g sample at 1000 °C.

4.3.3 Matrix-glass and minerals analysis

In–situ major and minor elements composition of glass and minerals has been performed on both polished petrographic thin sections and sample holders. An overall chemical characterization of glass and mineral phases (Supplementary Materials 1-2) from all the aforementioned A-MS eruptive sub-members (A1, A2, B1, B2, D1, D2, E2) and all the Zaro lithotypes (enclaves and host lava from the Zaro lava complex, and pumiceous clasts from the underlying pyroclastic deposit) was performed by acquiring major and minor element compositions at DiSTAR - University of Napoli Federico II, by a JEOL-JSM 5310 electronic scanning microscope (SEM) equipped with an INCA X-Act detector using Energy Dispersion System (EDS) microanalysis technique. The following standards were used for calibration: diopside (Mg), wollastonite (Ca), anorthoclase (Al, Si), albite (Na), rutile (Ti), almandine (Fe), Cr_2O_3 (Cr), rhodonite (Mn), orthoclase (K), apatite (P), fluorite (F) and sodium chloride (Cl).

4.3.4 In-situ mineral microanalysis

Detailed mineral composition (examples are reported in Supplementary Material 3) have been obtained along transects of length varying from 20 µm to 800 µm on zoned clinopyroxene crystals. This kind of specific analysis was performed on selected samples belonging to A1, B1 and D1 sub-members of the A-MS sequence and on selected samples of the Zaro lava complex (the host lava and three chemically different types of enclaves), representative of the overall chemical variability of the investigated products. A selection of zoned clinpyroxene crystals from the A-MS (41 crystals; 2084 spot analyses) and Zaro (36 crystals; 1785 spot analyses) eruptions were thus analyzed by acquiring major and minor element compositions along core-to-rim or rim-to rim transects crosscutting the centers of crystals. The data were collected at the HP-HT Laboratory of Experimental Volcanology and Geophysics of the Istituto Nazionale di Geofisica e Vulcanologia in Rome (Italy), using a Jeol-JXA8200 electron microprobe equipped with five wavelength dispersive spectrometers. Crystals in carbon-coated resin mounts were analyzed under high vacuum conditions, using an accelerating voltage of 15 kV. Crystals were traversed using spots with constant separation of 1-2.5-3.5-5-7-10 μm and variable beam diameter of 1-2.5-3.5-5 μm, both depending on the transect length. Two transects, perpendicular to each other, of analysis spots were acquired. The electron beam current was set at 7.5 nA. Elemental counting times were 10 s on the peak and 5 s on each of two background positions. Corrections for inter-elemental effects were made using a ZAF (Z: atomic number; A: absorption; F: fluorescence) routone. Calibration used a range of standards from Micro-Analysis Consultants (MAC; http://www.macstandards.co.uk): albite (Si-PET, Al-TAP, Na-TAP), forsterite (Mg- TAP), augite (Fe-LIF), apatite (Ca-PET), orthoclase (K-PET), rutile (Ti- PET), and rhodonite (Mn-LIF). Smithsonian augite (Jarosewich et al.,1980) and MAC augite were used as quality monitor standards and for the calculation of accuracy and precision. Accuracy was better than 1–5% except for elements with abundances below 1 wt%, for which accuracy was better than 5–10%. Precision was typically better than 1–5% for all analyzed elements.

4.3.5 Sr- and Nd-isotopic analyses on whole rocks and separated minerals

Whole rocks Sr and Nd isotopic composition was acquired on all the Zaro lava complex lithotypes (Table 9-Supplementary Material 2). ^{86}Sr/^{88}Sr isotopic ratios have been acquired on whole rocks samples and mineral concentrates of K-feldspar, clinopyroxene and phlogopite, belonging to sub-member A1, A2, B1, B2, D1, D2 and E2 of the A-MS eruption (Table 8-Supplementary Material 1) and on separated minerals from all the Zaro lithotypes (Table 9-Supplementary Material 2).

Sr and Nd isotopic analyses were performed at the Radiogenic Isotope Laboratory of the Istituto Nazionale di Geofisica e Vulcanologia, sezione di Napoli-Osservatorio Vesuviano (INGV-OV) on the samples after dissolution. Sr and Nd isotopic ratios were measured by thermal ionization mass-spectrometry (TIMS) using a Thermo Finnigan Triton TI. Average 2σ mean, i.e., the standard error with N = 175, was ± 0.000009 for Sr, and ± 0.000007 for Nd measurements. During the time of isotopic data acquirement, NIST-SRM 987 and La Jolla standards gave mean values of ^{86}Sr/^{88}Sr = 0.710231 ± 0.000019 (2σ, N = 169) and ^{143}Nd/ ^{144}Nd = 0.511845 ± 0.000010 (2σ, N = 55), respectively. External reproducibility (2σ) during the period of measurements was calculated according to Goldstein et al. (2003). During acquisition, Sr and Nd isotopic ratios were normalized for within-run isotopic fractionation to ^{86}Sr/^{88}Sr = 0.1194, and ^{143}Nd/ ^{144}Nd = 0.7219, respectively. The measured Sr and Nd isotopic ratios were normalized to the accepted values of NIST-SRM 987 (^{86}Sr/^{88}Sr = 0.71025) and La Jolla (^{143}Nd/ ^{144}Nd = 0.51185) standards.

4.4 The connectivity system analysis

The chemical variations recorded in compositional (e.g. Mg#) zoning patterns can be used to track the evolution of different populations of crystals through distinct magmatic environments in which they grew. Following Kahl et al. (2011, 2015), a population-based approach has been used to investigate the different magmatic environments.

This method was applied in volcanology for the first time to Etna, in order to define, from olivine zoning pattern, the main active magmatic environments prior eruption, their connections (by heating, decompression, mixing, mingling, crystal settling, etc) and the pre-eruptive processes occurring at depth (Kahl et al., 2011; 2015). The method has also recently been applied to orthopyroxenes (Solaro et al., 2020), but has not been applied to clinopyroxenes yet to the best of our knowledge, although Mangler et al (2020) interpreted compositional zoning in a similar manner.

The compositions of unzoned, simple zoned and complex zoned clinopyroxenes along rim-to-rim or core-to-rim traverses allow to identify compositional plateau (Mg#). The occurrence of plateau in the zoning patterns of minerals, such as clinopyroxene, indicates that compositional zoning is not produced by pure fractionation (e.g. Costa et al., 2008), but that growth occurred for certain periods of time under stable conditions in response to fast changes of thermodynamic variables (pressure, temperature, oxygen fugacity or water fugacity). Consequently, plateau with different composition represent several episodes of overgrowth of the crystals under different sets of P-T-X conditions. Each set of such thermodynamic variables characterizes a single magmatic environment. It is therefore possible to associate each compositional population, detected in the whole set of crystals, to a specific magmatic environment. As explained by Kahl et al. (2015), a magmatic environment does not necessarily represent a physical magmatic reservoir. Two magmatic environments could be parts of a single physical reservoir as, for example, portion of a zoned magma reservoir that differ from other parts of the same reservoir only because, for instance, the temperature is different while other variables remain fixed.

In this way, being the crystal growth occurred sequentially from core to rim, cores represent the first magmatic environment recorded by crystals while outer rims represent the last magmatic environment. Analysis of compositional plateau from core to rim allows to track either movements of crystals and their carrying melts among different magmatic environments or modification of storage conditions by external processes (heating, decompression event, mixing, etc.) through the plumbing system until eruption. This procedure has to be repeated on all analyzed crystals in order to define crystal populations, proportions, and the frequently-travelled crystal transfer pathways (Solaro et al., 2020).

The approach uses connectivity diagrams to systematically organize the chemical information and identify the number of magmatic environments recorded in such zoning patterns. It is therefore possible to quantify the connections among the various magmatic environments (henceforth, ME), through the entire set of zoning pattern, in order to reconstruct the evolutionary history of crystals. This approach has been applied to A-MS and Zaro clinopyroxene, in order to investigate transfers of crystals among the different MEs, which characterized the A-MS and Zaro plumbing systems.

5. GEOCHEMICAL AND PETROLOGICAL CHARACTERIZATIONS OF A-MS AND ZARO VOLCANIC ROCKS

5.1 Texture, petrography, mineral chemistry and Sr-isotopic composition of the A-MS products

Chemical and isotopic compositions of A-MS minerals and whole rocks are listed in Supplementary Material 1.

The petrographic and mineralogical features of the A-MS products have been widely described in previous work (e.g. de Vita et al., 1999; Arienzo et al., 2010). For this reason, this work mainly focus on i) the matrix-glass compositional variability, ii) whole rocks and separated minerals Sr-isotopic signature and iii) especially on a detailed chemical characterization of the A-MS clinopyroxene crystals, extensively defined, for the first time, due to the large set of acquired data (> 2100 analytical spots).

Observations under polarized light petrographic microscope allowed a characterization of the A-MS samples. Pumice and scoria fragments from all the sampled sub-members (A1, A2, B1, B2, D1, D2, E2) are porphyritic (porphyricity index: P.I. 5-10%), with phenocrysts of alkali–feldspar (Fig. 23a) and clinopyroxene, plagioclase (Fig. 23b), black mica (Fig. 23c), opaque oxides (Fig. 23d) and apatite (Fig. 23e) in order of decreasing abundance. Feldspar, clinopyroxene and black mica phenocrysts occur as single crystals or sometimes as aggregates (Fig. 23b). The groundmass is glassy and contains rare microlites of clinopyroxene, K-feldspar, plagioclase and black mica. All the sub-members show similar textural and petrographic features. Some difference among different sub-members can be observed in the crystal content: notably, samples from sub-member E2 show a high crystal content with respect to samples from all the others sub-members. Moreover some difference can be identified also in the degree of vesicularity. Highly vesicular clasts (Fig. 23f), with vesicles separated by thin glass walls, are present in sub-members A1, B1 and D1. Pumiceous fragments from these sub-members show on average higher vesicles contents with respect to fragments of the other sub-members. The shape of vesicles is quite variable: these can be tubular, contorted or spherical.

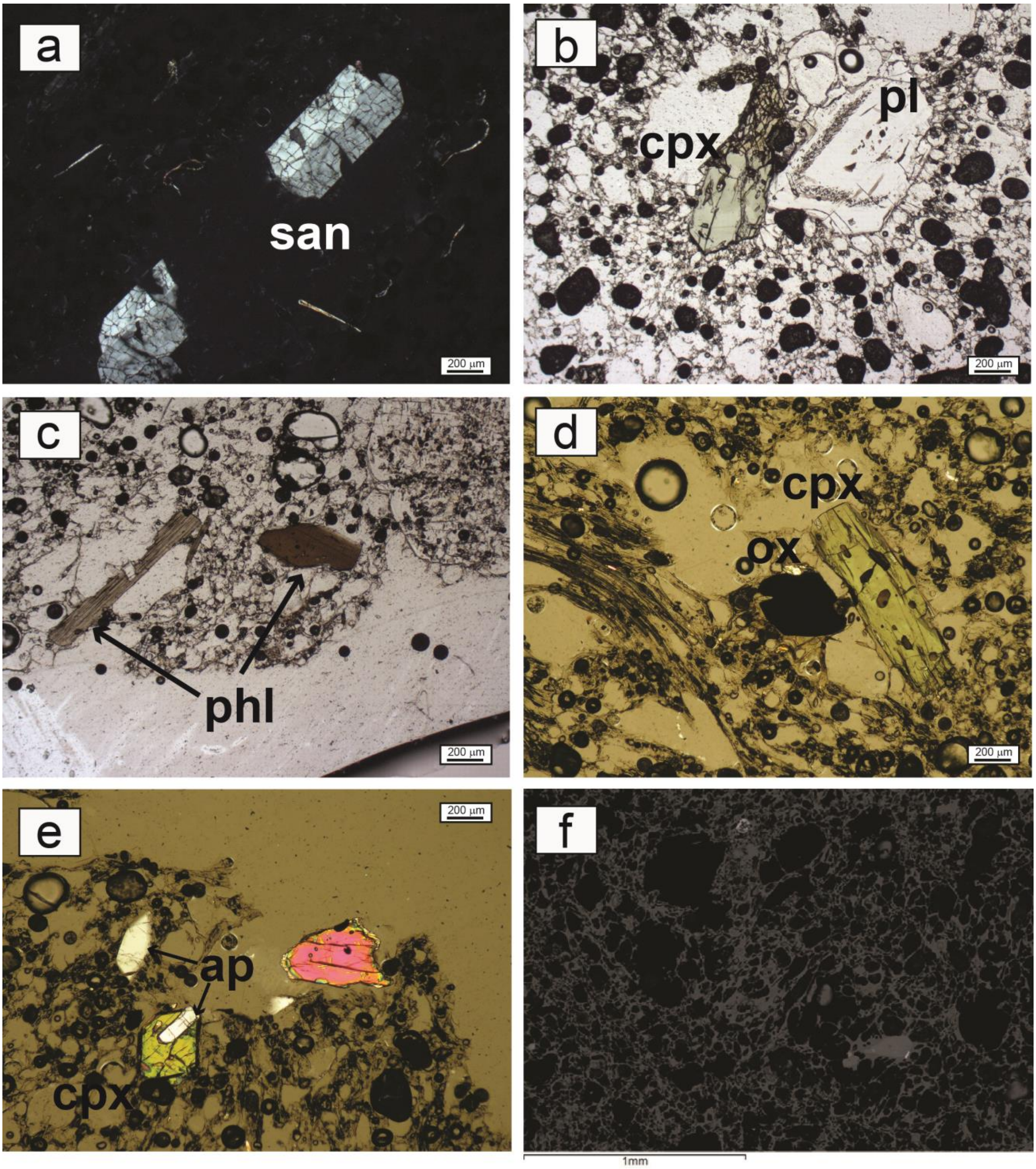

Fig. 23 Photomicrographs and BSE images of A-MS rocks showing the main textural and mineralogical features. a) microphotograph of a A-MS pumice from B1 member showing a sanidine phenocryst; b) microphotograph showing a plagioclase and clinopyroxene aggregate in a pumice clast from the A1 member; c) microphotograph showing brown mica crystals in a pumice clast from the B2 member; d) microphotograph showing clinopyroxene and opaque oxide crystals in a pumice clast from the A2 member; e) microphotograph showing apatite microcrysts in the matrix-glass and in clinopyroxene of a pumice clast from the D2 member; f) BSE image of a pumiceous clast from D1 sub-member showing the network of vesicles. Abbreviations: cpx = clinopyroxene; pl = plagioclase; san =sanidine; phl = phlogopite; ap = apatite; ox = opaque oxide

5.1.1 Mineral chemistry

5.1.1.1 Feldspar

Feldspar in the A-MS rocks occurs both as plagioclase and K-feldspar, the latter being the most abundant phase as phenocrysts. Both phases occur as phenocrysts, microphenocrysts or rarely as groundmass phase. Plagioclase and K-feldspar phenocrysts up to 1-cm long are often present. Plagioclase ranges from anorthite ($An_{91}Ab_8Or_1$) to andesine ($An_{44}Ab_{50}Or_6$), and bytownite is the most abundant component (Fig. 24). Plagioclase crystals from member A-B show on average a more sodic composition with respect to those from member D-E. K-feldspar is a quite homogeneous sanidine ($An_{3-3}Ab_{29-17}Or_{68-80;}$ Table 2-Supplementary Material 1).

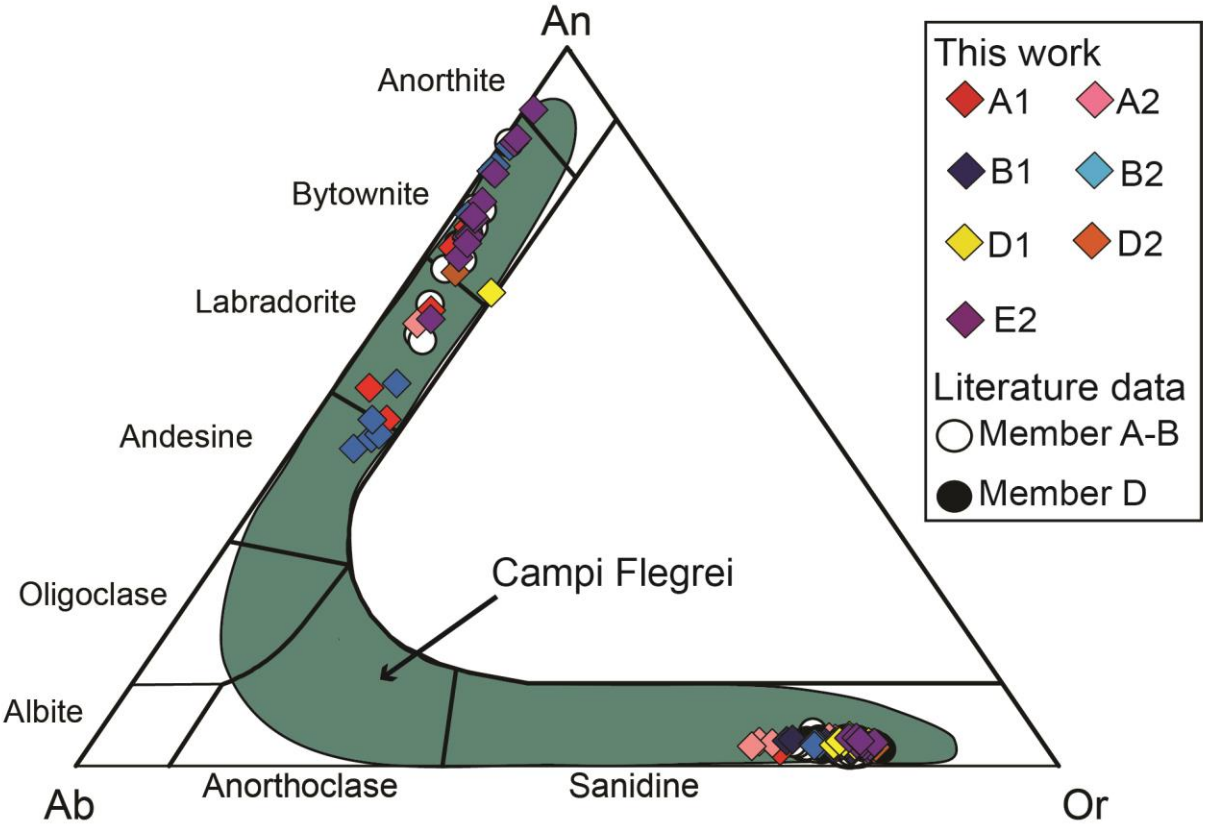

Fig. 24 An-Ab-Or classification diagram of feldspars from the A-MS rocks (data on A-MS and Campi Flegrei feldspar from literature for comparison are taken from de Vita et al., 1999; Melluso et al., 2012; Iovine et al., 2017a).

Plagioclase and sanidine crystals show different types of zoning. Plagioclase can show normal zoning (An_{82} in the core – An_{78} in the rim) or reverse zoning featured by rim composition more Ca-rich (An_{76}) with respect to that of the core (An_{62}). Both plagioclase and sanidine crystals show also more complex types of zoning such as oscillatory zoning, resulting in concentric zones usually from a few to tens of microns in width; some plagioclase crystals exhibit irregular zoning in the core, which is mantled by alternate concentric zones in the rim (Fig. 25a). The detected compositions in the different colored areas of one patchy zoned core of a plagioclase crystal result quite different, ranging from $An_{48}Ab_{46}Or_{6}$ in light zones to $An_{86}Ab_{13}Or_{1}$ in dark zones (Fig. 25b).

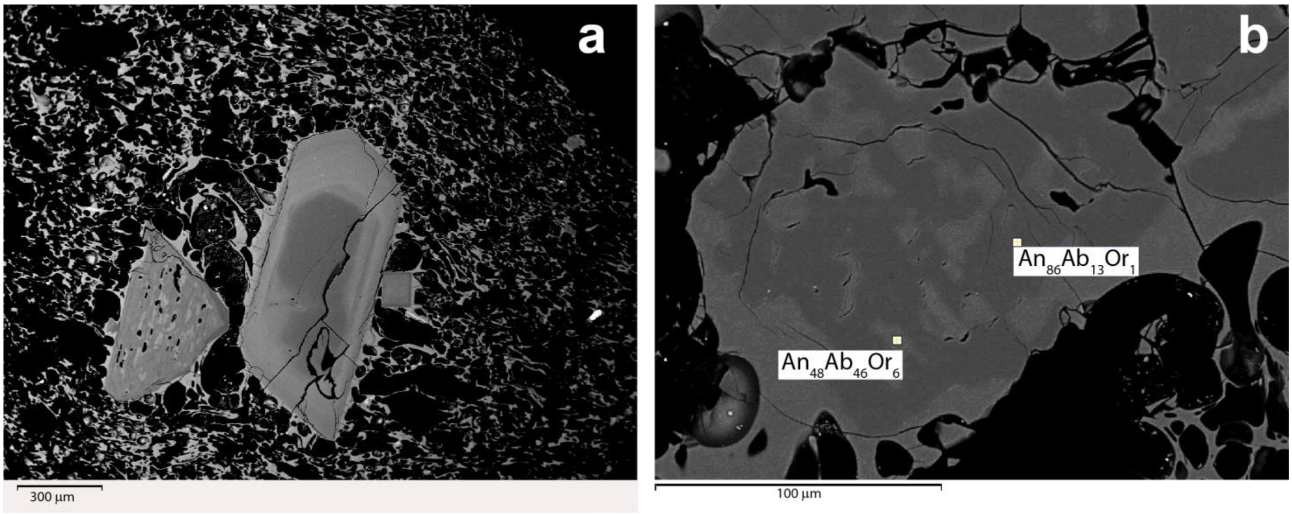

Fig. 25 a) Plagioclase crystals with a sponge texture (on the left) and with diffused zoned core and oscillatory zoned rim (on the right) b) Patchy zoned plagioclase crystal showing a different composition in the irregular areas.

5.1.1.2 Clinopyroxene

Previous works reported a characterization of the A-MS clinopyroxene: in de Vita et al. (1999) and Arienzo et al. (2010), 7 and 41 analytical spots, respectively, were acquired on clinopyroxene crystals from B and D members of the A-MS eruption. In this work, 58 analytical spots have been acquired on core, rim and groundmass clinopyroxene crystals belonging to sub-members A1, A2, B1, B2, D1, D2 and E2 for a preliminary characterization of the chemical variability of this mineral phase within the A-MS sequence. Moreover, 2084 analytical spots were acquired along core-to-rim traverses of clinopyroxene crystals belonging to sub-members A1, B1 and D1. A large number (ca. 300) of separated clinopyroxene crystals have been observed under polarized microscope. Only those showing evidence of compositional variations, representing however a minor percentage (ca. 15%), have been analyzed along zoning profiles. Detailed concentration profiles in zoned clinopyroxenes (major and minor elements: Si, Ti, Al, Fe, Mg, Mn, Ca, Na, K, Ni and Cr) were measured along two traverses, perpendicular to each other, with a spacing between individual points varying in the range 1-10 µm (Supplementary Material 3). A total of 41 clinopyroxene crystals belonging to members A1, B1 and D1, that are representative of the compositional variation of the A-MS deposits were studied in detail. The whole set of acquired data allowed to enlarge the already known compositional range of clinopyroxene from A-MS.

Clinopyroxene from A-MS deposit occurs as idiomorphic to allotriomorphic dark green phenocrysts and microcrysts in the groundmass. The A-MS clinopyroxene can be optically unzoned or optically zoned. Both kinds of clinopyroxene have a diopsidic/Fe-diopsidic composition that is Wo_{50-46}-En_{45-27}-Fs_{23-8} for the unzoned clinopyroxenes and Wo_{51-44}-En_{49-22}-Fs_{28-4} for the zoned ones (Fig. 26a). On the other hand, both kinds of clinopyroxenes show a significant compositional heterogeneity well reflected in the Mg# [molar Mg^{2+}/ (Mg^{2+} +Fe_{tot}) *100], which ranges from 87 to 55 in the unzoned crystals and from 92 to 45, in the zoned ones (Fig. 26b-f). The two kinds of clinopyroxene show quiet similar compositional ranges, although the optically unzoned crystals show narrower ranges with respect to those of the zoned crystals (Fig. 26a-g), as described below.

As for the unzoned clinopyroxenes, TiO_2 and Al_2O_3 contents range from 1.14 to 0.32 wt% and from 6.1 to 1.93 wt%, respectively (Fig. 26b-c). Na_2O and Cr_2O_3 content ranges from 0.71 to 0.15 wt% and from 0.58 to < 0.1 wt% (Fig. 26d-e). MnO content ranges from 0.75 to < 0.1 wt%.

As for the zoned clinopyroxenes, TiO_2 and Al_2O_3 contents range from 1.29 to 0.27 wt% and from 7.17 to 1.39 wt%, respectively (Fig. 26b-c). Na_2O and Cr_2O_3 content ranges from 0.77 to 0.10 wt% and from 1.26 to < 0.1 wt% (Fig. 26d-e). MnO content ranges from 0.80 to < 0.1 wt%.

In both kinds of clinopyroxenes, FeO, Al_2O_3 (Fig. 26b), TiO_2 (Fig. 26c) and Na_2O (Fig. 26d) contents increase with decreasing Mg#. Cr_2O_3 content decreases with decreasing Mg# (Fig. 26e). MnO content increases with Mg# decreasing from 92 to 60, then decreases (Fig. 26f).

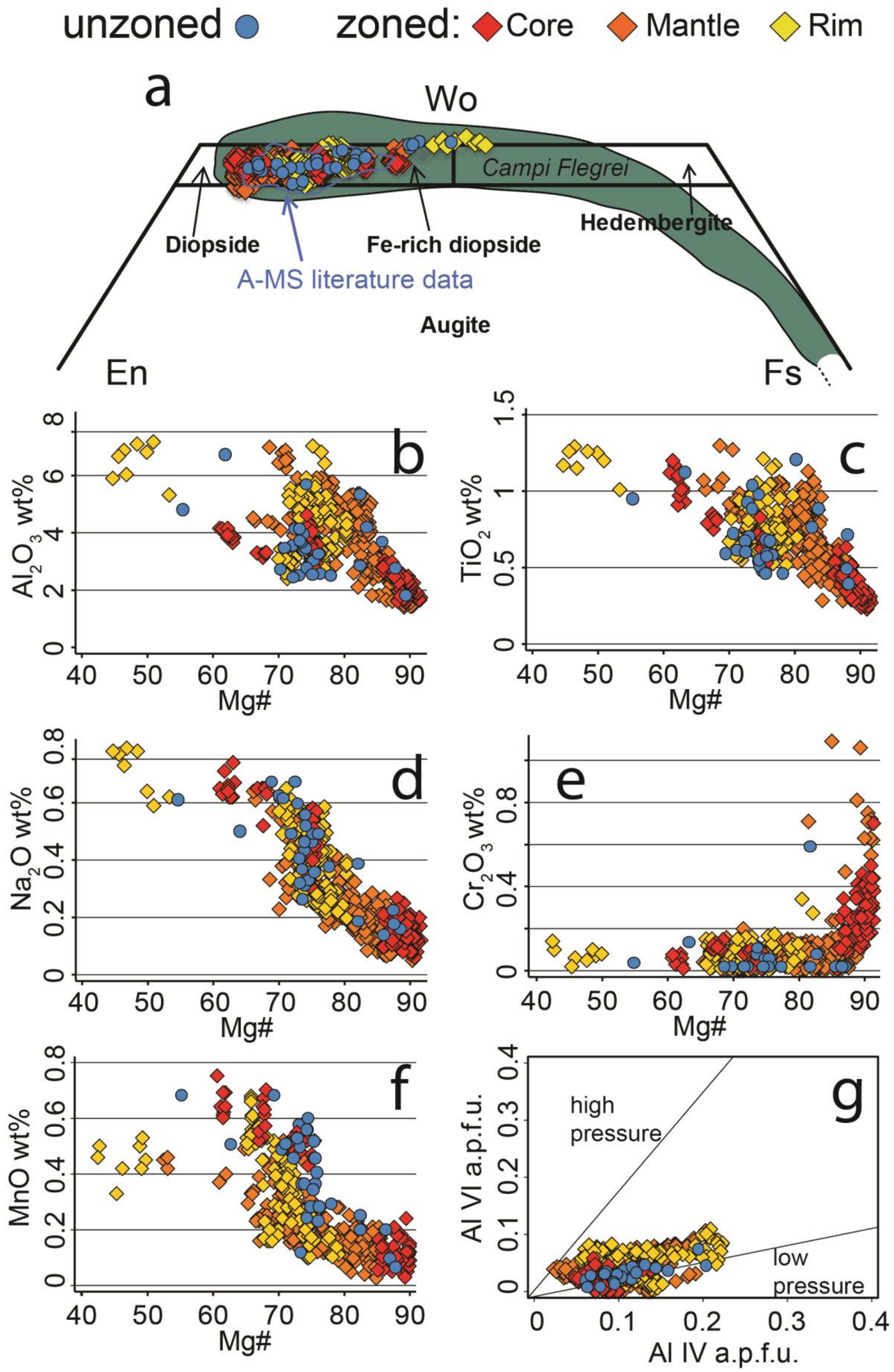

Fig. 26 a) Di-Hd-En-Fs classification diagram of the A-MS clinopyroxenes (data on A-MS and Campi Flegrei clinopyroxenes from literature for comparison are taken from de Vita et al., 1999; Melluso et al., 2012; Iovine et al., 2017a). b) Mg# vs Al_2O_3, c) Mg# vs

TiO_2, d) Mg# vs Na_2O, e) Mg# vs Cr_2O_3, f) Mg# vs MnO and g) Al IV vs Al VI (a.p.f.u.) variation diagrams of the analyzed zoned A-MS clinopyroxenes showing the wide compositional range in the different zoning sectors (core, mantle and rim).

5.1.1.2.1 Clinopyroxene compositional populations

By looking in detail to the composition of the clinopyroxene crystals it is possible to discretize different compositional populations.

Although the unzoned and zoned clinopyroxenes show similar compositional ranges, the main difference occurs in the abundance/frequency of certain compositional populations. The optically unzoned clinopyroxene crystals show a quite homogeneous composition: their Mg# mostly (40 out of 46 unzoned crystals) ranges between 78 and 70, with an average of 75 (Fig. 27a). Only four (out of the 46 analyzed homogeneous clinopyroxenes) crystals show higher (Mg# in the range 87-82) values. Other two unzoned crystals exhibit lower (Mg#=64 and 55) values.

On the counterpart, as for the zoned crystals, frequency histograms (Fig. 27a-c) of core, mantle and rim compositions show that there are different types of compositional populations.

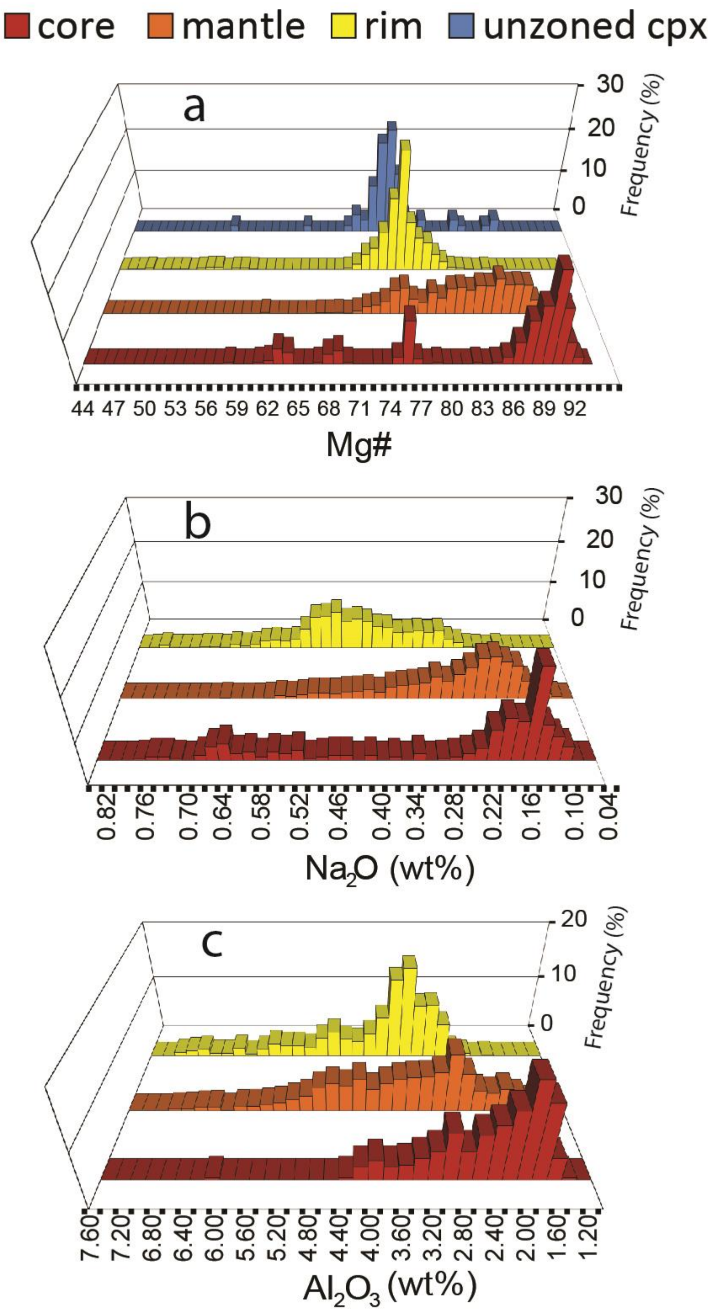

Fig. 27 a) Mg#, b) Na_2O and c) Al_2O_3 frequency histograms of core, mantle and rim of the zoned A-MS clinopyroxenes that allow different populations to be identified.

In particular, it is possible to well distinguish, through the Mg# parameter (Fig. 27a; Table 1): 1) a population of compositions (occurring in the 70% of the analyzed crystals, hereafter referred to as ME0) characterized by high Mg#, in most cases represented by cores; 2) a population of compositions (occurring in all the analyzed clinopyroxenes, hereafter referred to as ME2) with Mg# ranging between 78 and 70 and with an average value of 75, typical of the rims; 3) a population (occurring in the 34% of the analyzed clinopyroxenes, hereafter referred to as ME1) with Mg# intermediate between populations 1 and 2, which mostly constitutes the optically discriminable bands between cores and rims (mantles), and 4) another population (occurring in the 7% of the analyzed crystals, hereafter referred to as ME3) represented by few crystal cores and mantles with low Mg# (69-60). Moreover a single crystal rim shows very low Mg# (55-45). These populations are well discernible in the core of the clinopyroxene crystals.

Table 1

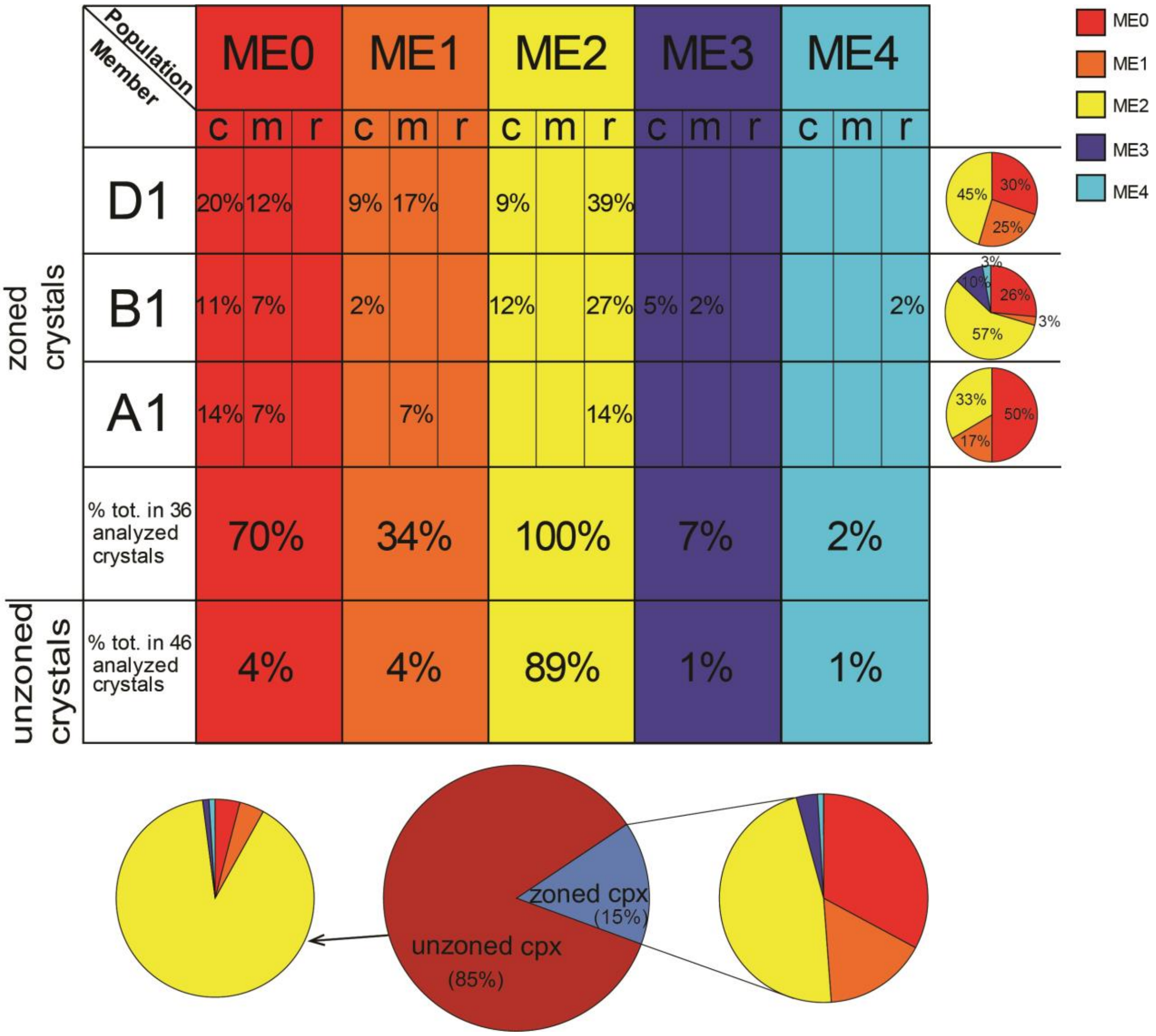

	Population / Member	ME0			ME1			ME2			ME3			ME4		
		c	m	r	c	m	r	c	m	r	c	m	r	c	m	r
zoned crystals	D1	20%	12%		9%	17%		9%		39%						
	B1	11%	7%		2%			12%		27%	5%	2%				2%
	A1	14%	7%			7%				14%						
	% tot. in 36 analyzed crystals	70%			34%			100%			7%			2%		
unzoned crystals	% tot. in 46 analyzed crystals	4%			4%			89%			1%			1%		

Table 1. Percentage of a compositional population occurring in a zoning sector (core, mantle or rim) in a total of 36 (out of 41) analyzed zoned clinopyroxene crystals of the A-MS deposit; c=core; m=mantle; r=rim. Percentages have been calculated considering

clinopyroxenes with plateau (zoning type I to type VII). Percentage of compositional populations occurring in the homogeneous clinopyroxene crystals is also reported.

In summary, ME0 and ME2 make up most of the zoned clinopyroxene population, with the most mafic compositions (Mg#> 85) recorded mostly in the cores of clinopyroxene crystals (Table 1). Although there are subtle variations in the distribution patterns of Al_2O_3, TiO_2 and Na_2O contents of the pyroxene crystals, the classification into different groups is largely corroborated by these compositional parameters as well (Fig. 28a-d).

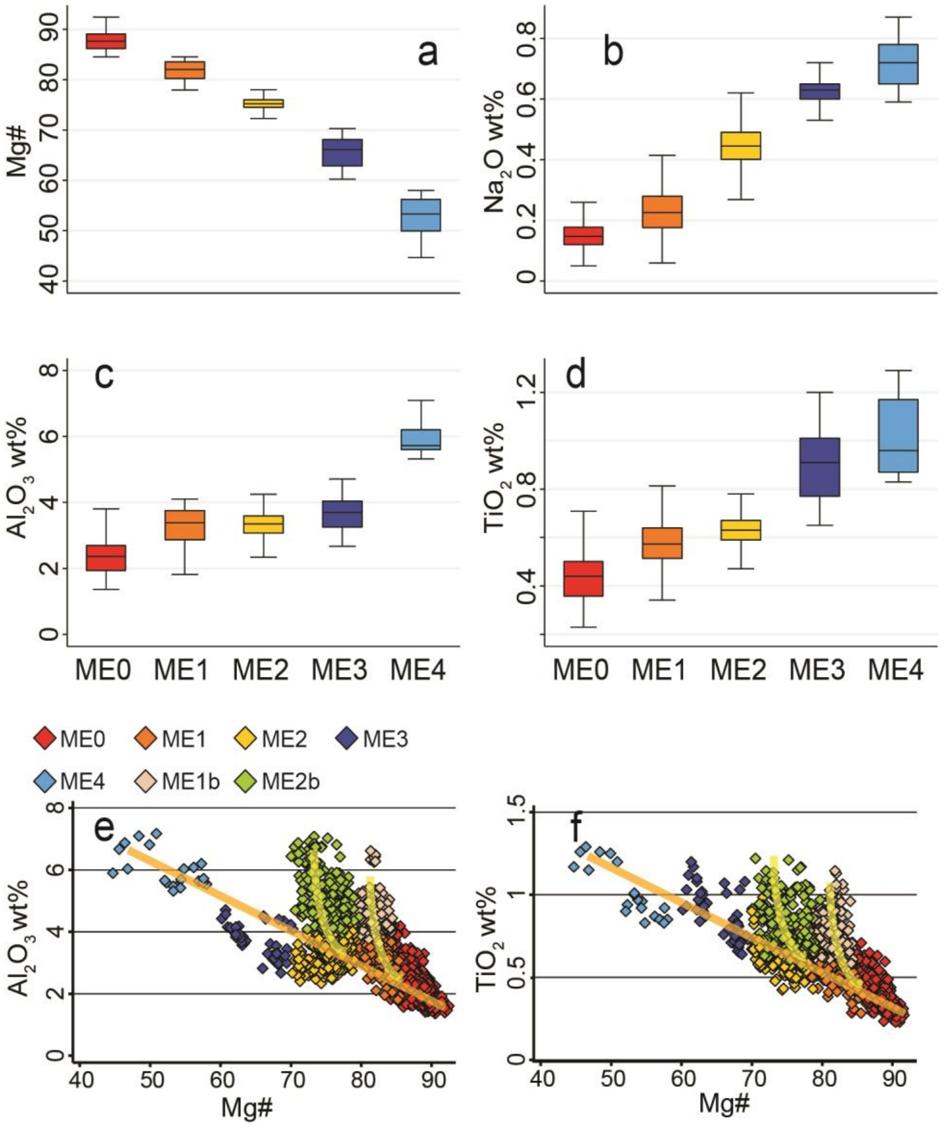

Fig. 28 a) Mg#- b) Na_2O- c) Al_2O_3- and d) TiO_2 box plot statistical diagrams showing the distinct clinopyroxene compositional populations; the upper and lower lines indicate the maximum and minimum values, respectively; the box encompasses the 95% of confidence intervals; the line within the box is the average of the values; e) Mg# vs Al_2O_3- and f) Mg# vs TiO_2 variation diagrams of the overall analyzed A-MS clinoyroxene crystals showing all the distinguishable populations and subpopulations. Note that all clinopyroxenes of different compositions lie on a trend defined by the orange line, with the exception of the ME1b and ME2b trends, which are shown in yellow. The significance of these trends will be discussed in Chapter 6.3.

The main difference between the three analyzed members is that only member B1 has a significant number (9 out of 15 analyzed crystals) of clinopyroxene crystals with cores showing intermediate compositions (Mg# 75-60); in clinopyroxene from member A1, cores have only high Mg# (all 6 analyzed crystals), while in those from member D1 only few cores (4 out of 20 analyzed crystals) show an intermediate composition. Indeed, member D1 has the highest number of clinopyroxenes (15 out of 20 analyzed crystals) with high Mg#, according to the less differentiated composition of its matrix-glass.

An important observation is that despite the wide compositional variability of cores and mantles, crystal rims show a homogeneous composition: except the crystal with the ME4 rim composition, all crystal rims show Mg# between 78 and 70 (ME2). Nevertheless, Al_2O_3 and TiO_2 show an overlap in the populations distinguishable with the Mg# and Na_2O contents (Fig. 28a-b). In particular, these elements show a wide compositional range in the populations of rims (ME2) and mantles (ME1) (Fig. 28c-d), so it is possible to discriminate two other subpopulations (ME1b and ME2b), which, at similar Mg# values, are characterized by high content of Al_2O_3 and TiO_2 (Fig. 28e-f). Thus, a compositional heterogeneity characterizes mantles and rims, despite these latter have homogeneous MgO, FeO and Na_2O contents. This aspect will become relevant in the construction of the diffusion models (Chapter 6.3).

5.1.1.2.2 Clinopyroxene zoning pattern

The complex zoning pattern of the A-MS clinpyroxene has been fully characterized. In most cases (36 out of 41 crystals), the zoning pattern of the main elements consists of two or more plateau with a constant composition separated by either sharp or gradual boundaries (Fig. 29a-g). Based on the chemical composition and the type of variation shown by plateau, various types of zoning have been identified, i.e. normal, reverse or complex. Normal zoning is defined by decreasing of the Mg# from core to rim and, on the other hand, reverse zoning by the increasing of the Mg# from core to rim of the clinopyroxene.

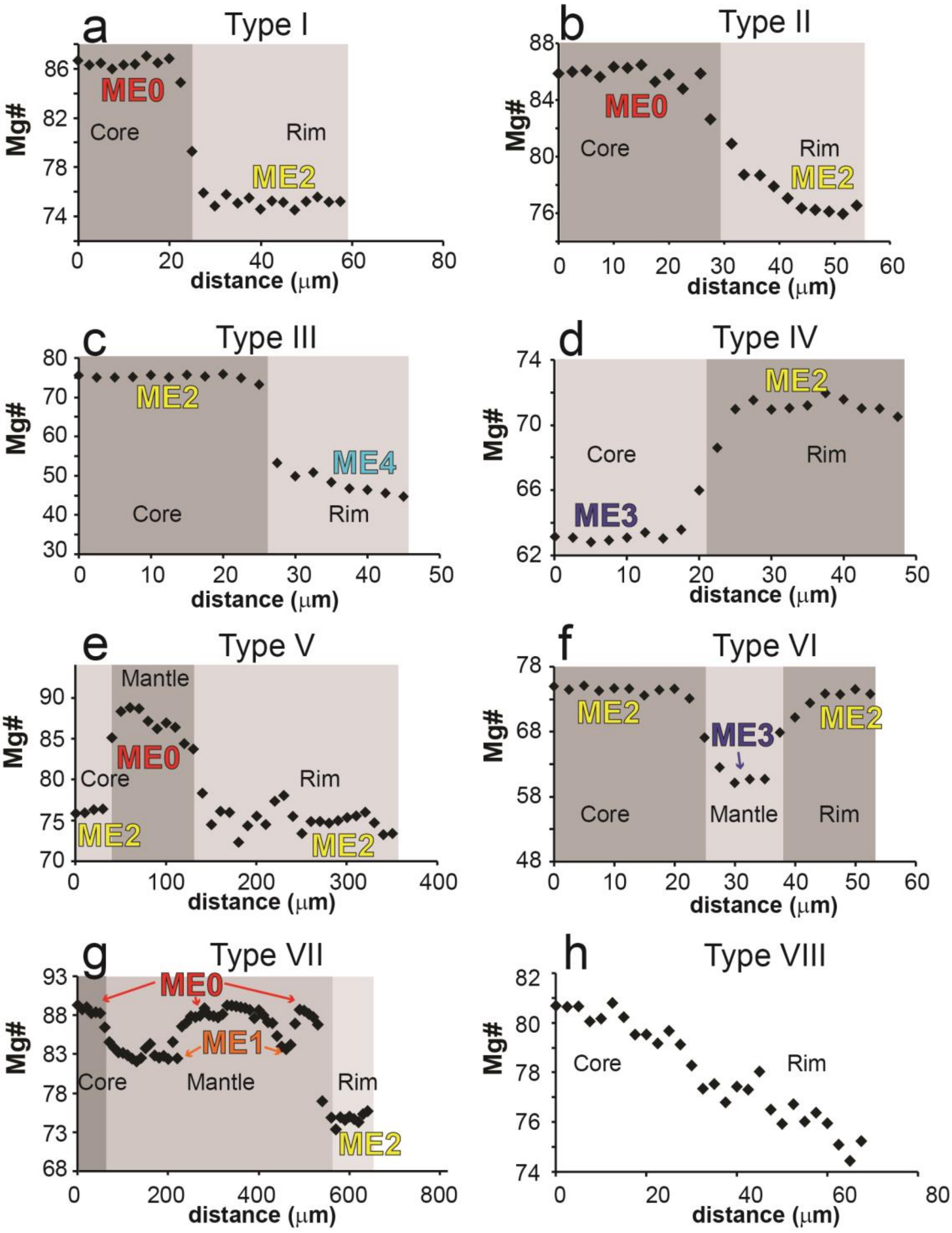

Fig. 29 Types of zonation of the A-MS clinopyroxenes. Black diamonds are measured analysis along the crystal traverses showing concentration profiles [Mg# = molar $Mg^{2+}/(Mg^{2+} + Fe_{tot})$].

The most common (44%) is normal zoning (type I), consisting of cores with high Mg# (92-80; ME0-ME1) and rims with intermediate composition (Mg# = 78-70; ME2) showing sharp variation (Fig. 29a). Another type of zoning is type II (5%), that is very similar to type I (normal zoning), but differ in that the variation is gradual (Fig. 29b). Only one normally zoned crystal (type III; Fig. 29c) shows a core with intermediate composition (Mg# = 75-73; ME2) and rim with low Mg# (55-45; ME4). Another less common zoning type (type IV; Fig. 29d; ca. 5%) is represented by reversely zoned crystals in which cores with Mg# of 68-63 (ME3) are surrounded by rims with less differentiated composition (Mg# = 75-73; ME2). Several types of complex zoning are also common. Most crystals have a reverse to normal zoning (type V; Fig. 29e; ca. 22%), with a core characterized by intermediate composition (Mg# = 81-72; ME1 or ME2), a mantle with higher Mg# (82-92; ME0 or ME1) and a rim with Mg# of 75-72 (ME2). An individual (type VI; Fig. 29f) from member B1 shows a variation from Mg# = 75 (ME2) in the core, through Mg# = 63 (ME3) in the mantle, to Mg# = 75 (ME2) in the rim. Finally, oscillatory zoned (type VII; Fig. 29g; ca. 7%) crystals are also present, showing an alternation of bands consisting of several plateau with composition ranging from Mg# = 92-88 (ME0) to 84-82 (ME1) and a rim with Mg# = 75 (ME2). Moreover, a few crystals (type VIII; Fig. 29h; ca. 12%) show normal or oscillatory zoning with gradual variation (Mg# from 81 to 71) without plateau.

5.1.1.2 Other mineral phases

The black mica in the A-MS rocks is phlogopite (Fig. 30a) in all the sampled sub-members. Mg# ranges from 69 to 66. The A-MS phlogopite shows a restricted compositional variation with TiO_2 and Na_2O contents varying from 5.74 to 3.53 wt% and from 0.64 to 0.32 wt%, respectively. Its composition is similar to that of phlogopite of other Ischia and Campi Flegrei products. Cl and F contents range from 0.18 to 0.01 wt% and from 1.85 to 0.89 wt%, respectively (Table 4-Supplementary Material 1).

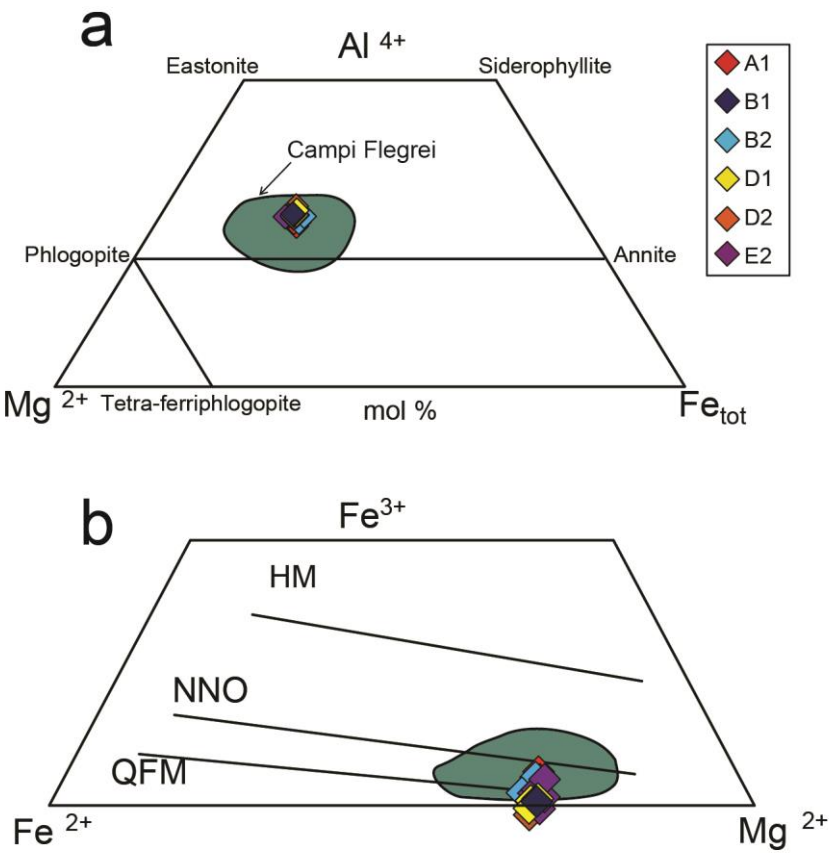

Fig. 30 a) Classification diagram of brown mica found in the A-MS products and b) compositional variation in the Fe^{2+}-Mg^{2+}-Fe^{3+} diagram. The HM (hematite-magnetite), NNO (nickel-nickel-oxide) and QFM (quartz-fayalite-magnetite) oxygen buffers indicate the oxidation state of the system (Wones and Eugster, 1965). Data on Campi Flegrei brown mica from literature for comparison are taken from Iovine et al., 2017b.

Magnetite is the only Fe-Ti oxide in our samples. Magnetite occurs as phenocryst or as inclusion in clinopyroxene or phlogopite phenocrysts. The analyzed phenocrysts from the sampled A-MS sub-members show a homogenous composition, with ulvöspinel component in the range 24-21(Fig. 31). The TiO_2 content ranges from 8.7 to 6.8 wt% and the MnO content is relatively low (1.2-0.7 wt%; Table 5-Supplementary Material 1).

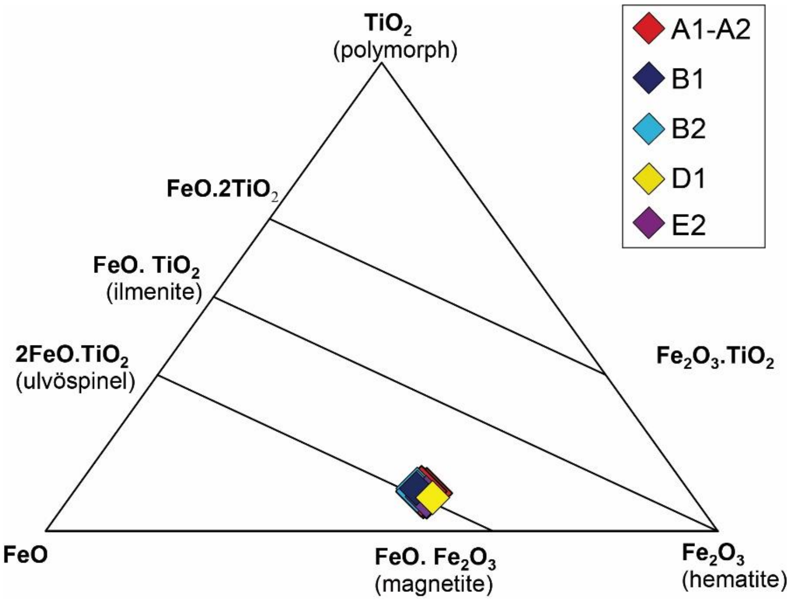

Fig. 31 Fe^{2+}-Fe^{3+}-Ti^{2+} classification diagrams of A-MS opaque oxides

Apatite is a rare accessory phase of the A-MS rocks. This phase mostly occurs as inclusion in clinopyroxene or phlogopite phenocrysts. BaO and F contents range from 0.42 to 0.15 wt% and from 2.9 to 2.0 wt%, respectively (Table 6- Supplementary Material 1).

5.1.2 Matrix-glass

A great number (118 analytical spots; Table 1-Supplementary Material 1) of matrix-glass analytical data has been acquired on representative samples belonging to sub-members A1, A2, B1, B2, D1, D2, E2 of the A-MS sequence. Matrix-glasses classify mostly as trachyte and subordinately as phonolite (Fig. 32) and show an alkaline affinity (Na_2O+K_2O = 13.6-10.5 wt% and SiO_2 = 60.0-55.7 wt%; Fig. 33a-c).

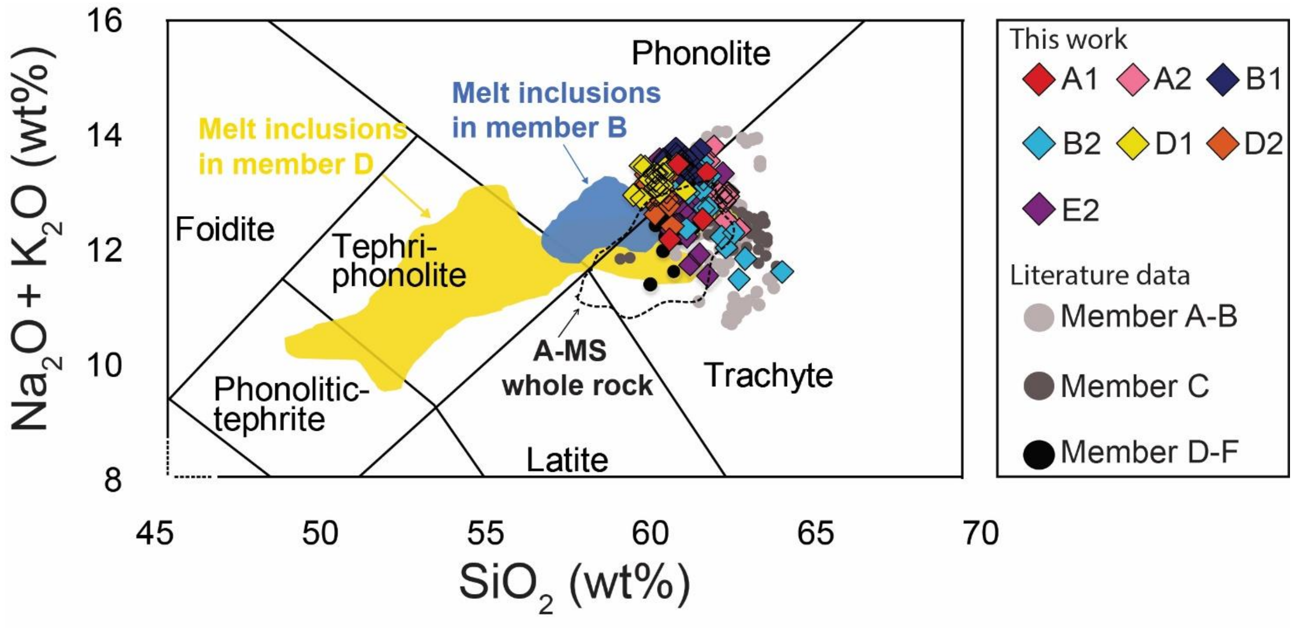

Fig. 32 Glass compositions of A-MS products plotted in the Total Alkali vs. Silica diagram. A-MS whole rocks (de Vita et al., 1999) and melt inclusions (Arienzo et al., 2010)compositional fields from literature are also reported.

The analyzed A-MS matrix-glasses are Ne-normative and their Mg# [molar $Mg^{2+}/(Mg^{2+}+Fe^{2+})*100$] varies from 42 to 23. The Mg# of the whole-rocks taken from literature (de Vita et al., 1999) for comparison, ranges from 45 to 31, thus is slightly shifted toward less evolved compositions. The agpaitic index [A.I. molar $(Na^{+}+K^{+})/ Al^{3+}$] of A-MS glasses ranges from 0.97 to 0.75. Na_2O and K_2O contents range from 5.55 to 3.24 wt% and from 9.99 to 7.50 wt%, respectively. The Na_2O/K_2O ratio ranges from 0.70 to 0.33 while the CaO/Al_2O_3 ratio ranges from 0.19 to 0.09. TiO_2 and Al_2O_3 contents of the analyzed A-MS matrix-glasses range from 0.75 to 0.17 wt% and from 19.8 to 18.1 wt%, respectively (Fig. 33e,g). $Fe_2O_{3(tot)}$ and MgO contents range from 4.27 to 2.58 wt% and from 1.12 to 0.33 wt%, respectively (Fig. 33d,i).

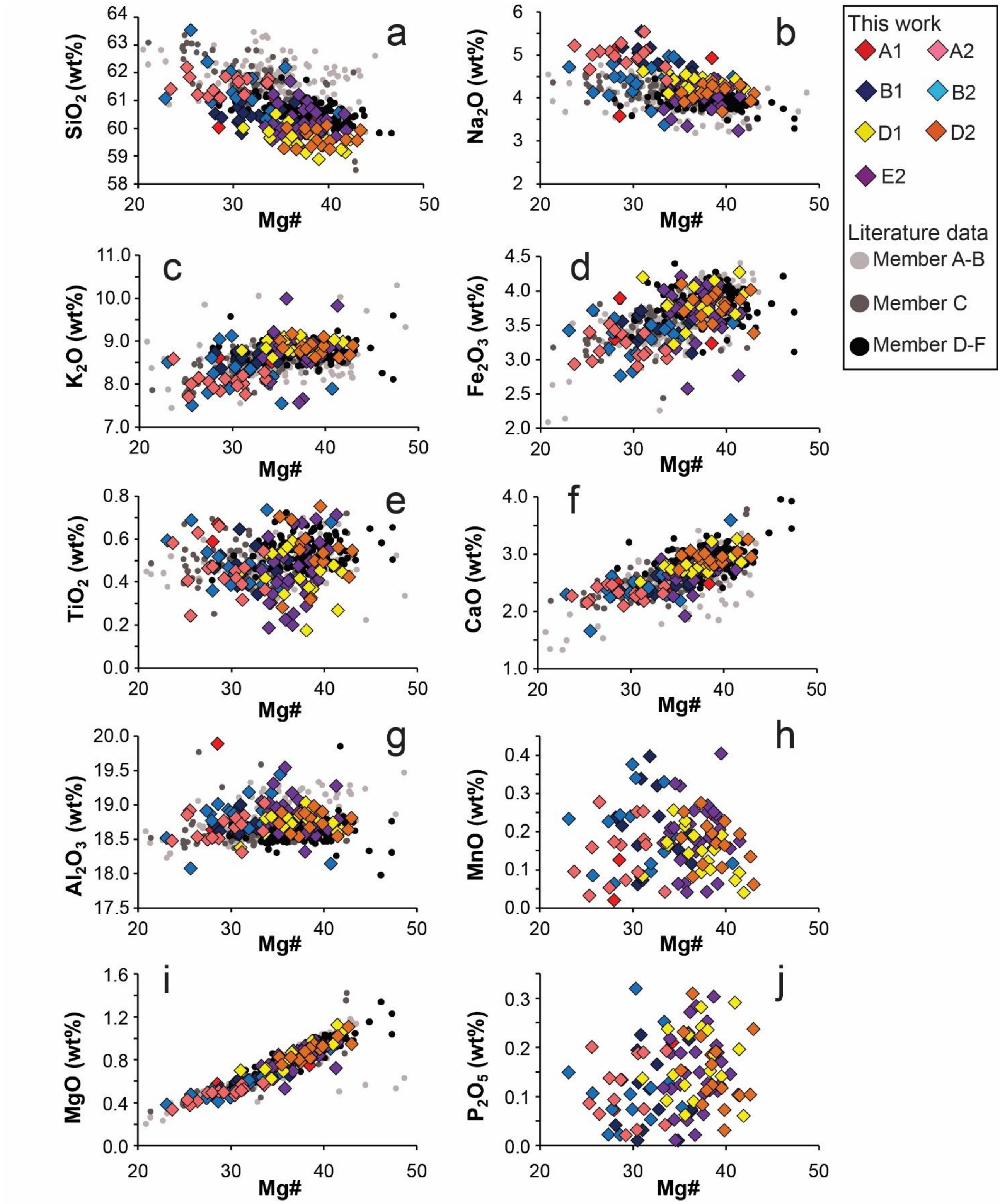

Fig. 33 Matrix-glass major and minor element variation diagrams of A-MS rocks.

SiO_2 and Na_2O contents show positive correlation with the degree of chemical evolution (decreasing Mg#; Fig. 33a-b), whereas CaO, MgO, $Fe_2O_{3(tot)}$, P_2O_5 and TiO_2 contents show negative correlation (Fig. 33d-f,i-j). K_2O content increases in trachytes and then decreases in more evolved rocks (Fig. 33c); $Al_2O_{3,}$ and MnO contents are constant, although scattered (Fig. 33g, h). The degree of differentiation generally decreases from the bottom to the top of A-MS deposits. In fact, even if partially overlapped, there is a remarkable difference in the major oxide contents of the A-MS juvenile clasts sampled in the different sub-members. In particular, matrix glasses from sub-members A1, A2, B1 and B2 show on average a slightly more differentiated composition than those from members D1, D2 and E2 (Fig. 32-33), as already reported in literature (de Vita et al., 1999; Roach, 2005; Romano et al., 2020).

5.1.3 Whole rock and minerals Sr isotopes

The studied whole-rock samples show similarities for the A-MS sub-members A1, A2 and B2 having $^{87}Sr/^{86}Sr$ isotopic ratios = 0.70749-0.70747, whereas samples from sub-members D2 and E2 show enriched $^{87}Sr/^{86}Sr$ isotopic ratios = 0.70753-0.70750 (Fig. 34; Table 7-Supplementary Material 1). Feldspars from all the A-MS members show a Sr-isotopic signature in the range 0.70750-0.70745. The Sr-isotopic signature of clinopyroxenes shows a huge range of variation, ranging from 0.70745, in clinopyroxenes from member A1, to 0.70755, in clinopyroxenes from member D2. Black mica crystals E2 have been analyzed only from member and they show a $^{87}Sr/^{86}Sr$ value of 0.70753. The new isotopic data acquired on whole rocks and mineral phases of the analyzed samples are reported in Supplementary Material 1 and result in the range of those detected in literature (Fig. 34).

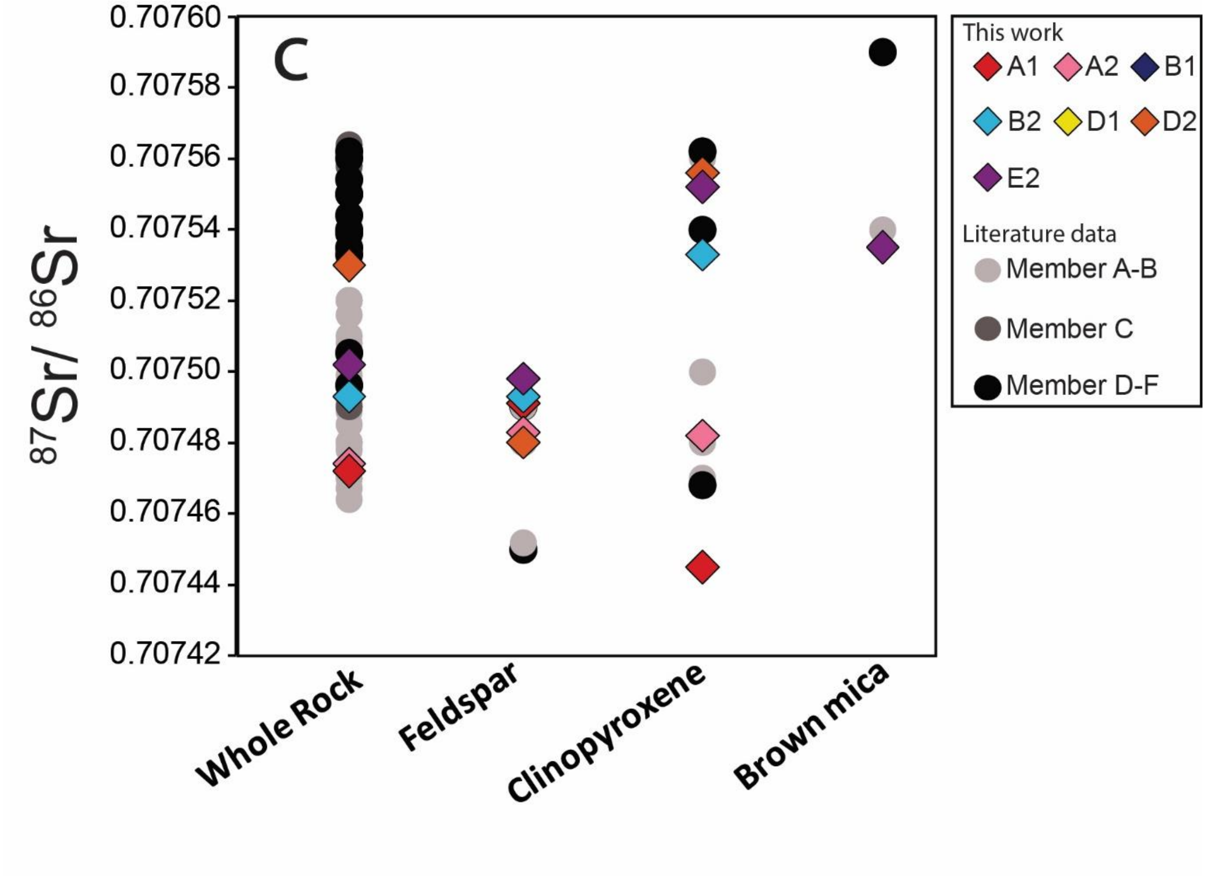

Fig. 34 Sr-isotopic composition of A-MS whole rocks and minerals. Literature data are from de Vita et al. (1999) and Arienzo et al. (2010).

5.2 Texture, petrography, mineral chemistry and Sr-Nd isotopic composition of the Zaro products

Chemical and isotopic compositions of Zaro minerals and whole rocks are listed in Supplementary Material 2.

5.2.1. Texture, petrography and mineral chemistry

5.2.1.1 The Zaro pumices

Four samples of pumiceous clasts have been collected from the breccia-like deposit underlying the lava complex (Fig. 21a-b). These pumices represent the juvenile fragments of the pyroclastic deposit of the early phase of the eruption. They are dense, porphyritic (P.I. ca. 20%) pumice clasts made up of K-feldspar phenocrysts (up to 85%) together with minor clinopyroxene, brown mica and opaque oxide immersed in a hypocrystalline groundmass.

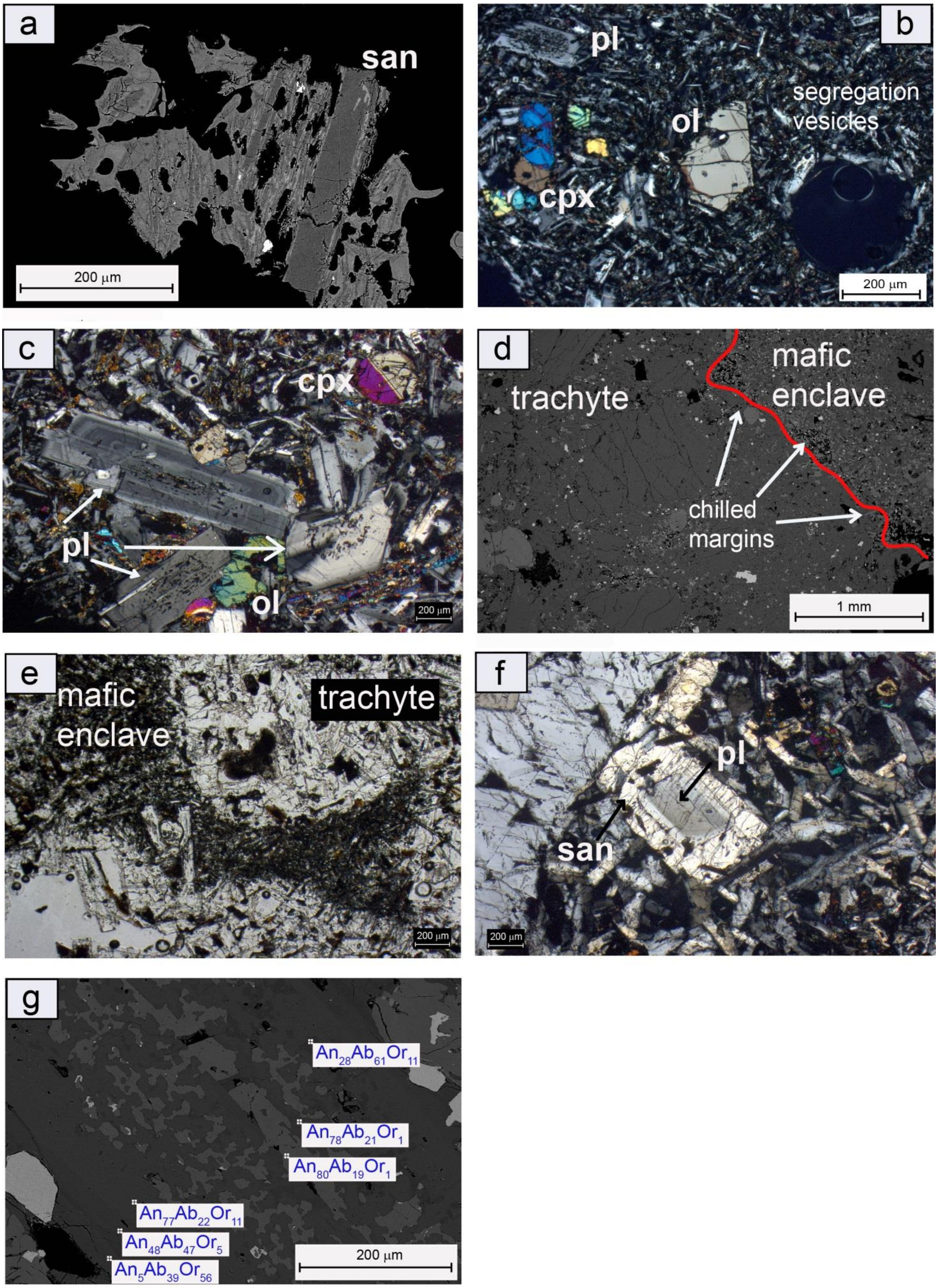
a
san
200 μm
b
pl
ol
segregation vesicles
cpx
200 μm
c
cpx
pl
ol
200 μm
d
trachyte
mafic enclave
chilled margins
1 mm
e
mafic enclave
trachyte
200 μm
f
pl
san
200 μm
g
$An_{28}Ab_{61}Or_{11}$
$An_{78}Ab_{21}Or_{1}$
$An_{80}Ab_{19}Or_{1}$
$An_{77}Ab_{22}Or_{11}$
$An_{48}Ab_{47}Or_{5}$
$An_{5}Ab_{39}Or_{56}$
200 μm

Fig. 35 Photomicrographs and BSE images of Zaro rocks showing the main textural and mineralogical features. (a) BSE image of a Zaro pumice showing a sanidine phenocryst and microlites in the groundmass; b) microphotograph showing the texture of a mafic enclave, made up of phenocrysts and microphenocrysts of olivine, clinopyroxene and plagioclase in a fine grain size groundmass; the enclave hosts segregation vesicles; c) mafic enclave with a coarse grain-size groundmass; d) BSE image showing chilled margins at the contact between the Zaro lava and a mafic enclave; e) filaments of mafic enclave intruded in the host trachyte; f) plagioclase phenocryst with a K-feldspar rim in the very coarse grain-sized groundmass of the hybrid enclave; g) BSE image showing a sieve texture in a plagioclase phenocryst from the hybrid enclave. Abbreviations: ol = olivine; cpx = clinopyroxene; pl = plagioclase; san =sanidine; phl = phlogopite.

The pumices show low vesicularity with spherical vesicles. SEM observation shows a high abundance of feldspar microlites in the groundmass (Fig. 35a). K-feldspar ($An_{5-4}Ab_{67-52}Or_{44-28}$) crystals from the pumices are notably more sodic in composition with respect to those of the overlaying lava flow (Fig. 36).

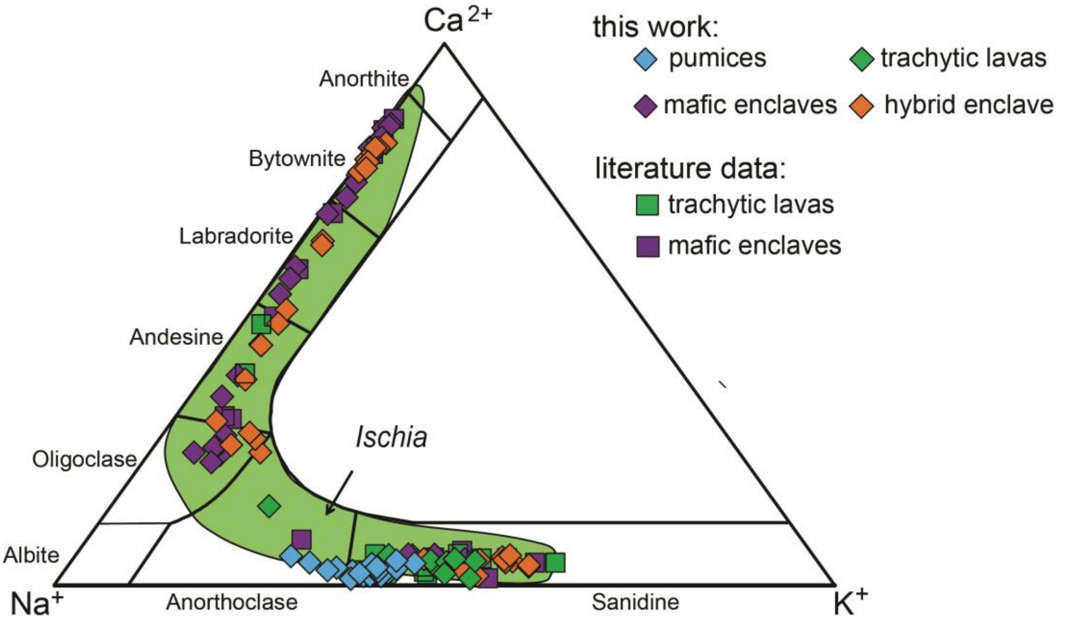

Fig. 36 An-Ab-Or classification diagram of feldspars found in Zaro rocks (data on Zaro and Ischia feldspars from literature for comparison are taken from Di Girolamo et al., 1995 and Melluso et al., 2014).

Clinopyroxenes are Fe-diopsidic in composition (Fig. 37a). Their Mg# [molar $Mg^{2+}/(Mg^{2+}+Fe_{tot})*100$] range from 76 to 57. Their Al_2O_3 and TiO_2 contents range from 2.38 to 1.22 wt% and from 0.88 to 0.46 wt%, respectively (Fig. 38a-b; Table 5-Supplementary Material 2).

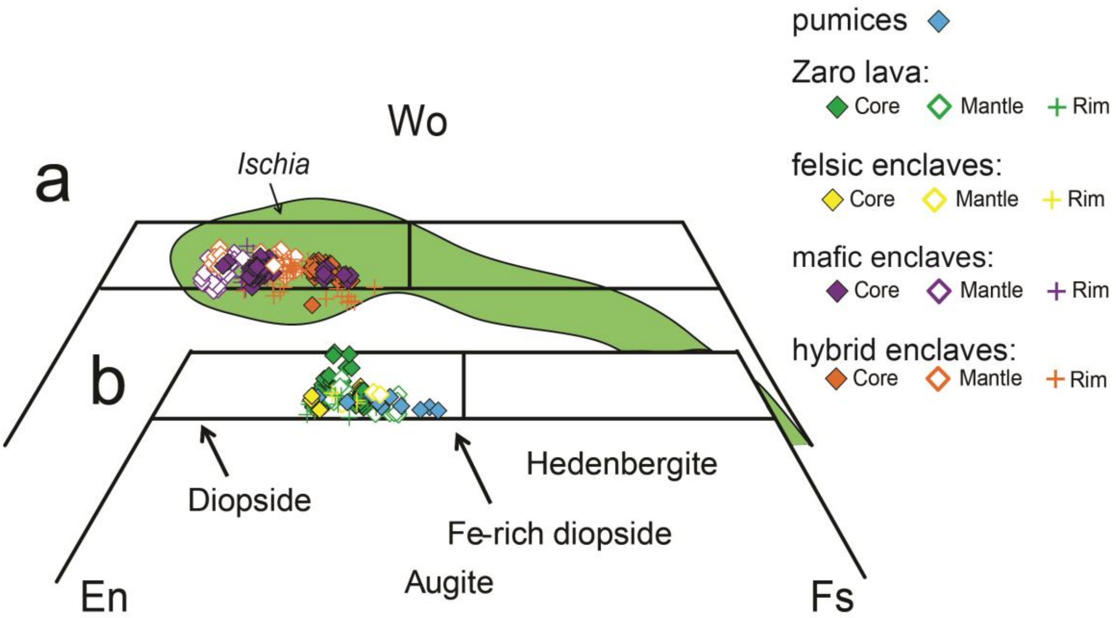

Fig. 37 Di-Hd-En-Fs classification diagram for the Zaro clinopyroxenes (data on Ischia clinopyroxene from literature are taken from Melluso et al., 2014).

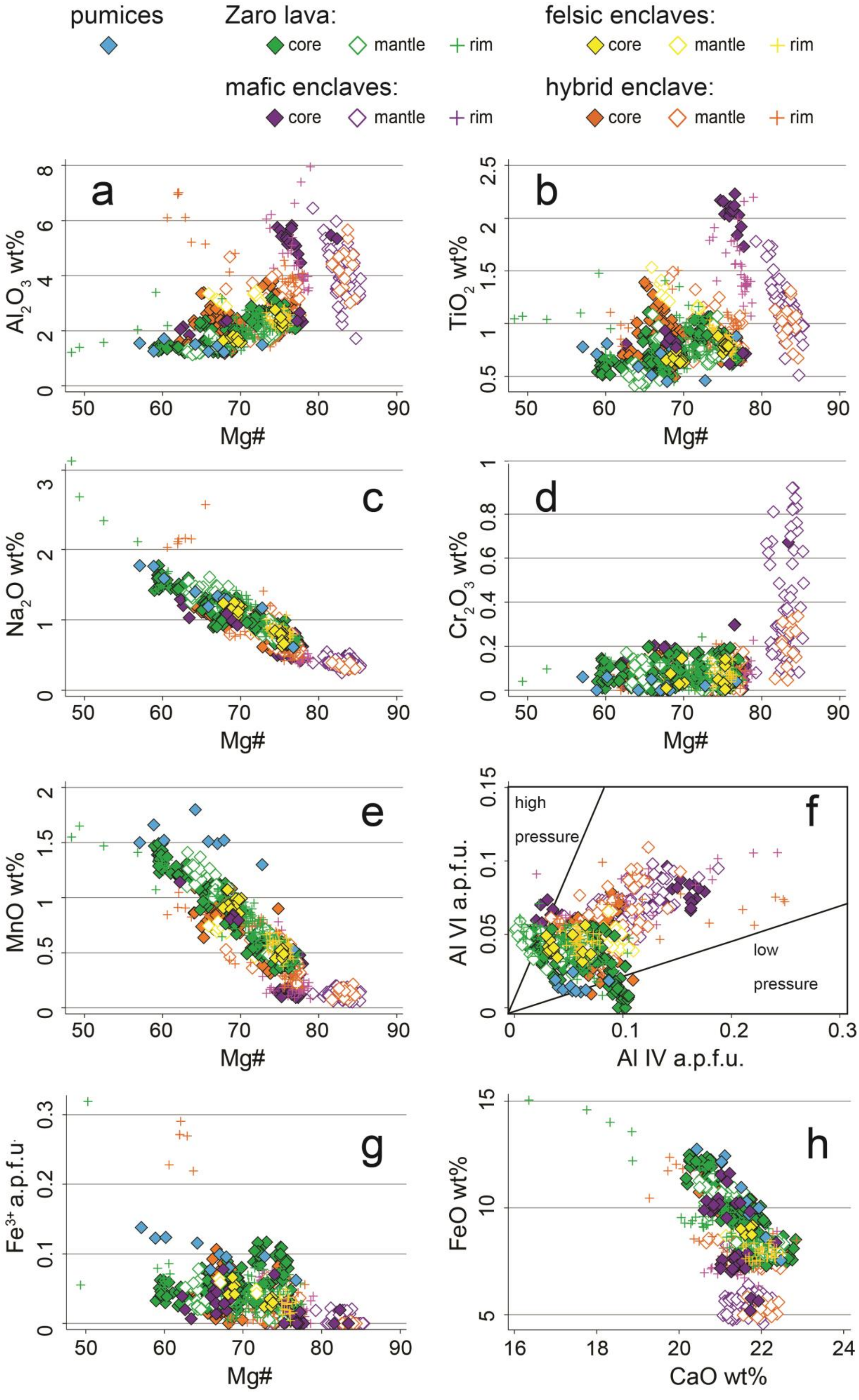
pumices
Zaro lava:
core
mantle
rim
felsic enclaves:
core
mantle
rim
mafic enclaves:
core
mantle
rim
hybrid enclave:
core
mantle
rim
a
Al_2O_3 wt%
b
TiO_2 wt%
c
Na_2O wt%
d
Cr_2O_3 wt%
e
MnO wt%
f
Al VI a.p.f.u.
Al IV a.p.f.u.
high
pressure
low
pressure
g
Fe^{3+} a.p.f.u.
h
FeO wt%
CaO wt%
Mg#
50
60
70
80
90

Fig. 38 Chemical variation diagrams showing differences between clinopyroxenes of the Zaro rocks

Mg# and Cr_2O_3, Al_2O_3 and TiO_2 contents are on average low compared to those of clinopyroxenes from all the lava lithotypes (Fig. 38a,-b, d). MnO contents of clinopyroxenes from pumices are high with respect to those of clinopyroxene from the other lithotypes (Fig. 38e). Moreover, lower Al^{VI} contents suggest crystallization at lower pressure conditions (Fig. 38f), compared to those from other Zaro rocks.

The black micas from Zaro pumices, like those of all the other Zaro products, can be classified as phlogopite (Fig. 39a). Ti-magnetite and titanite are commonly found in the groundmass of the Zaro pumices.

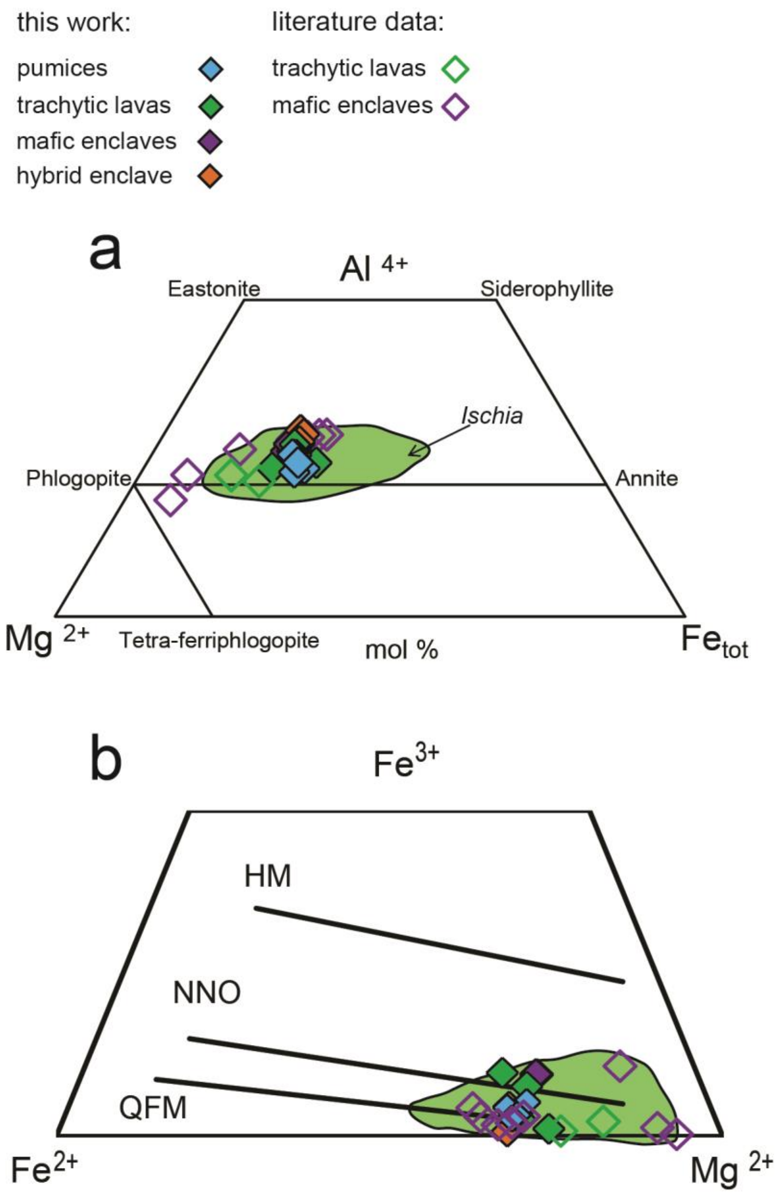

Fig. 39 a) Classification diagram of brown mica found in the Zaro products and b) compositional variation in the Fe^{2+}-Mg^{2+}-Fe^{3+} diagram (literature data on Zaro and Ischia brown mica are taken from Di Girolamo et al., 1995 and Melluso et al., 2014).

5.2.1.2 The Zaro lava

The Zaro lava facies is a white to grayish lava, showing a porphyritic to seriate texture with very high crystal content (P.I. ca. 50%). In total, 15 samples of Zaro lava have been collected for this study (Fig. 21). Phenocrysts of sanidine (up to 1 cm in size), making up to 85 % of the crystals, together with minor black mica, clinopyroxene, plagioclase and opaque oxide are immersed in a microcrystalline to hypocrystalline groundmass. Textures include overgrowth of alkali feldspar on plagioclase, zoning of clinopyroxenes and sanidines, and partial resorption of feldspars, clinopyroxenes and mica. Acicular microlites of alkali feldspar describe a typical trachytic/fluidal texture (Fig. 1a-Supplementary Material 2).

Zaro lava rarely exhibits a plagioclase core in alkali feldspar phenocrysts, sanidine ($An_{15-4}Ab_{65-34}Or_{62-20}$; Fig. 36) being the most common feldspar phase (both as phenocryst and microphenocryst in the groundmass). Most part of clinopyroxenes from Zaro lava is diopsidic/Fe-diopsidic ($Wo_{50-45}En_{42-30}Fs_{24-13}$; Fig. 37a) in composition, with Mg# ranging from 77 to 57 (Fig. 38). Omphacite and aegirin-augite components have been detected in the rims of three clinopyroxene crystals from the Zaro lava. These Na-rich components (with Na_2O up to 2.0 wt%) show significantly lower Mg# (from 57 to 48) compared to those of all the other clinopyroxenes. Their CaO content is lower and their FeO content (and hence also Fe^{3+}content) is higher, respectively, with respect to those of the diopsidic/Fe-diopsidic clinopyroxenes (Fig. 38g-h). They also show low Al_2O_3 and high MnO contents (Fig. 38a, c) with respect to those of the other clinopyroxenes. Aegirine-rich pyroxene (which is the most reliable indicator of the transition to peralkaline conditions) is found in nearly all trachytic rocks of all cycles of the Ischia activity (Melluso et al., 2014). The black micas of the Zaro lavas are phlogopitic in composition (Fig. 39a).

Groundmass of the Zaro lava contains subordinate phlogopite, clinopyroxene, opaque oxide and plagioclase microlites. Some samples host microcrystalline aggregates made up of alkali feldspar, plagioclase, phlogopite and clinopyroxene.

5.2.1.3 Enclaves

Paragenesis and textures of felsic enclaves are like those of Zaro main lava, including the fluidal texture and resorbed crystals but differing for a dark-grayish color of the groundmass due to a higher amount of glass (Fig. 1a-b in Supplementary Material 2). This facies is found in rounded and dimly flattened, centimeter- to decimeter-large enclaves, embedded in the lava along the sides and front of the complex (Fig. 21c). In some outcrops such felsic enclaves host in turn rounded decimeter-sized Zaro lava blobs, showing sharp contact (Fig. 21d). Two samples have been collected for this study (Fig. 21).

Sanidine ($An_{4-3}Ab_{49-44}Or_{57-52}$; Fig. 36), clinopyroxenes ($Wo_{47-45}En_{41-34}Fs_{24-13}$; Fig. 37a) and phlogopite (Fig. 39) from felsic enclaves are very similar in composition to those from Zaro lava.

Mafic enclaves are embedded both in Zaro lava and felsic enclaves (Fig. 21c). Three mafic enclaves have been sampled (Fig. 21a). Mafic enclaves consist of dark gray/blackish, round-shaped, vesicular, centimeter-to decimeter-large lava blobs (Fig. 21e). Enclaves are ellipsoidal, have a sharp contact with host rocks, often with cuspate borders. Mafic enclaves are porphyritic rocks (P.I. < 15 %) with phenocrysts and microphenocrysts of olivine, plagioclase and clinopyroxene (Fig. 35b) forming glomeroporhyritic clusters. The groundmass is variable, from very-fine grained microcrystalline with acicular crystals (Fig. 35b), to coarse-grained holocrystalline (Fig. 35c). It is made up of alkali-feldspar, plagioclase, clinopyroxene, olivine, opaque oxide and rare phlogopite, apatite and titanite. One sample (Fig. 35c) has a coarse grain size, holocrystalline groundmass, and contains more plagioclase phenocrysts compared to other samples of the same lava facies. Some enclaves show chilled margins at the contact with the host trachyte, i.e. fine-grained edges along the borders, possibly representing quenching of magma along contacts with cooler material (Fig. 35d). Segregation vesicles (from few millimeters up to one centimeter in size) are very common in the enclaves (Fig. 35b). Most of these are filled with feldspar microlites. One of the samples shows inter-fingering of the mafic enclaves with the host trachyte: Figure 35e shows filaments of mafic material intruded in the host trachyte. Moreover, the enclave displays disruption of its boundary due to infiltration and engulfment of the host trachyte (Fig. 1c-Supplementary Material 2).

Plagioclase phenocrysts, often optically zoned, range from $An_{86}Ab_{13}Or_1$ to $An_{24}Ab_{70}Or_6$ (Fig. 36). Generally, plagioclase cores have higher anorthite content, often falling in the bytownite field. Microphenocrysts in the groundmass range from bytownite ($An_{79}Ab_{21}Or_1$) to sanidine ($Ab_{39}Or_{56}An_4$). Clinopyroxene ($Wo_{51-42}En_{46-31}Fs_{21-8}$; Fig. 37b) occurs as idiomorphic to allotriomorphic dark green phenocrysts and microphenocrysts in the groundmass. Their Mg# ranges from 85 to 62   and their Cr_2O_3 content, which varies from 0.91 to 0.22 wt%, shows a huge variation compared to that of clinopyroxene from the other Zaro rocks. The Al_2O_3 and TiO_2 contents, ranging from 7.95 to 1.14 wt% and from 2.32 to 0.22wt% (Fig. 38a-b), respectively, can be significantly higher than those of clinopyroxenes from evolved rocks. Several optically zoned clinopyroxene crystals have been analyzed (see 5.2.2 section for a detailed characterization of the zoning pattern). Olivine hosted in mafic enclaves occurs as idiomorphic to allotriomorphic phenocrysts and microphenocrysts with forsterite (Fo) contents variable from 87 to 71 (Fig. 40).

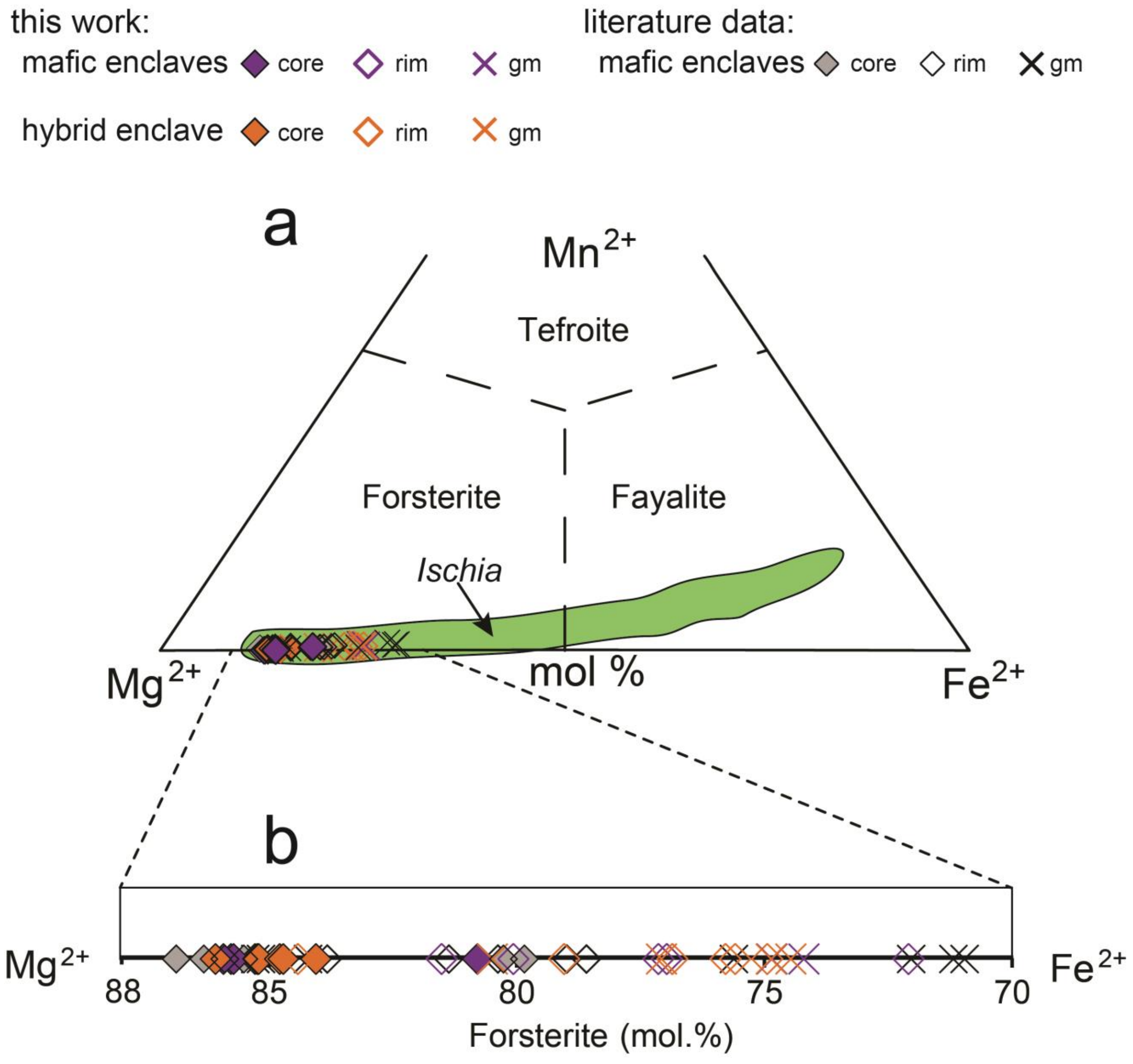

Fig. 40 Classification diagram of olivines found in the Zaro mafic and hybrid enclaves (literature data on Zaro olivine for comparison are from Di Girolamo et al., 1995 and Melluso et al., 2014).

Typically, phenocrysts cores are Mg-rich (Fo = 87-81) while rims and microlites have a lower amount of forsterite. Olivine phenocrysts show abundant Cr-Al-spinel inclusions. Spinel Cr# [molar Cr/(Cr+Al)*100] ranges from 51 to 30, while Al_2O_3 ranges from 37 to 23 wt%. The new data confirm that the Ischian chromiferous spinels hosted in olivine are the most Al-rich among those found in the Roman Magmatic Province (Melluso et al., 2014). Phlogopite generally occurs as euhedral phenocrysts and microphenocrysts. MgO, Al_2O_3, Fe^{2+} and Fe^{3+} contents of phlogopites from mafic enclaves show larger compositional variations with respect to those of phlogopites from evolved rocks (Fig. 39a-b). F in phlogopite crystals can be > 4 wt% (Table 4-Supplementary Material 2) indicating a F-rich environment in the Ischia magmas. Some phlogopite and olivine phenocrysts show partial resorption (Fig. 1d-Supplementary Material 2). Sodalite is an accessory phase found in the groundmass of the mafic enclaves. Melluso et al. (2014) found also phosphates and Zr-Ca-Na-REE-F-rich disilicates in the groundmass.

The hybrid enclave (Fig. 35f) is a peculiar kind of enclave showing mineralogical (but also chemical and isotopic; see text below) characteristics intermediate between those of the mafic enclaves and those of the felsic lavas, characterized by a lower abundance of mafic and felsic minerals compared with mafic and felsic rocks, respectively. It was found at the contact between a mafic enclave and the host trachyte. The contact between the mafic enclave and the hybrid one is gradational. The crystal assemblage is composed of phenocrysts of plagioclase, sanidine, clinopyroxene, olivine and phlogopite (in order of decreasing abundance). The groundmass is holocrystalline, made up of sanidine and subordinate plagioclase, clinopyroxene and opaque oxide. This enclave shows a coarser groundmass, a greater abundance of sanidine and plagioclase, a lower amount of olivine (always showing partial resorption; Fig. 1e in Supplementary Material 2) and no vesicles with respect to the mafic enclaves. It shows a lower abundance of K-feldspar with respect to the felsic lava facies. Feldspars from hybrid enclaves are both plagioclase ($An_{82-24}Ab_{61-17}Or_{14-2}$) and sanidine ($An_{4-2}Ab_{61-39}Or_{57-37}$) with a chemical range similar to those of feldspar from mafic enclaves. Plagioclase, often optically zoned, frequently shows sieve texture with an inclusion-free rim (Fig. 35g), both in mafic and hybrid enclaves. Moreover, some plagioclase crystals show a reversely zoned core (Fig. 1f in Supplementary Material 2). Some plagioclase phenocrysts show a K-feldspar rim, a common feature in volcanics of mildly potassic series. Clinopyroxene from hybrid enclave ranges from $Wo_{54}En_{44}Fs_{21}$ to $Wo_{44}En_{32}Fs_{8}$ (Fig. 37b). Na-rich clinopyroxenes, aegirin-augitic and omphacitic in compositions, are also present in few crystal rims of the hybrid enclave. Clinopyroxenes from mafic and hybrid enclaves have larger variations and higher contents in Cr_2O_3, TiO_2, Al_2O_3 and Mg# compared to those from felsic rocks (Fig. 38a,b,d). Moreover, higher Al^{VI} contents of clinopyroxenes from mafic and hybrid enclaves suggest crystallization at higher pressure conditions (Fig. 38d), compared to those from felsic rocks. Olivine from hybrid enclave ranges from Fo_{86} to Fo_{72} (Fig. 40). Similarly to olivine from mafic enclaves, generally phenocrysts cores are Mg-rich (Fo = 86-84) while rims and microlites have a lower amount of forsterite. Cr-Al-rich spinel has also been found in olivine from hybrid enclaves (Fig. 41a). Ilmenite ($FeTiO_3$) is another opaque oxide occasionally found in the groundmass of the hybrid enclave (Fig. 41b). Ti-magnetite is the most common opaque oxide found in both mafic and felsic compositions, showing a continuous compositional range between magnetite and ulvöspinel (Fig. 41b). It occurs as microphenocrysts and microlites in the groundmass or as frequent inclusions mostly in clinopyroxene and less in olivine and biotite phenocrysts. Ti-magnetite from the mafic and hybrid enclaves shows larger variations in the ulvöspinel content, with respect that of magnetite from felsic rocks. Apatite is a rare accessory phase of Zaro rocks.

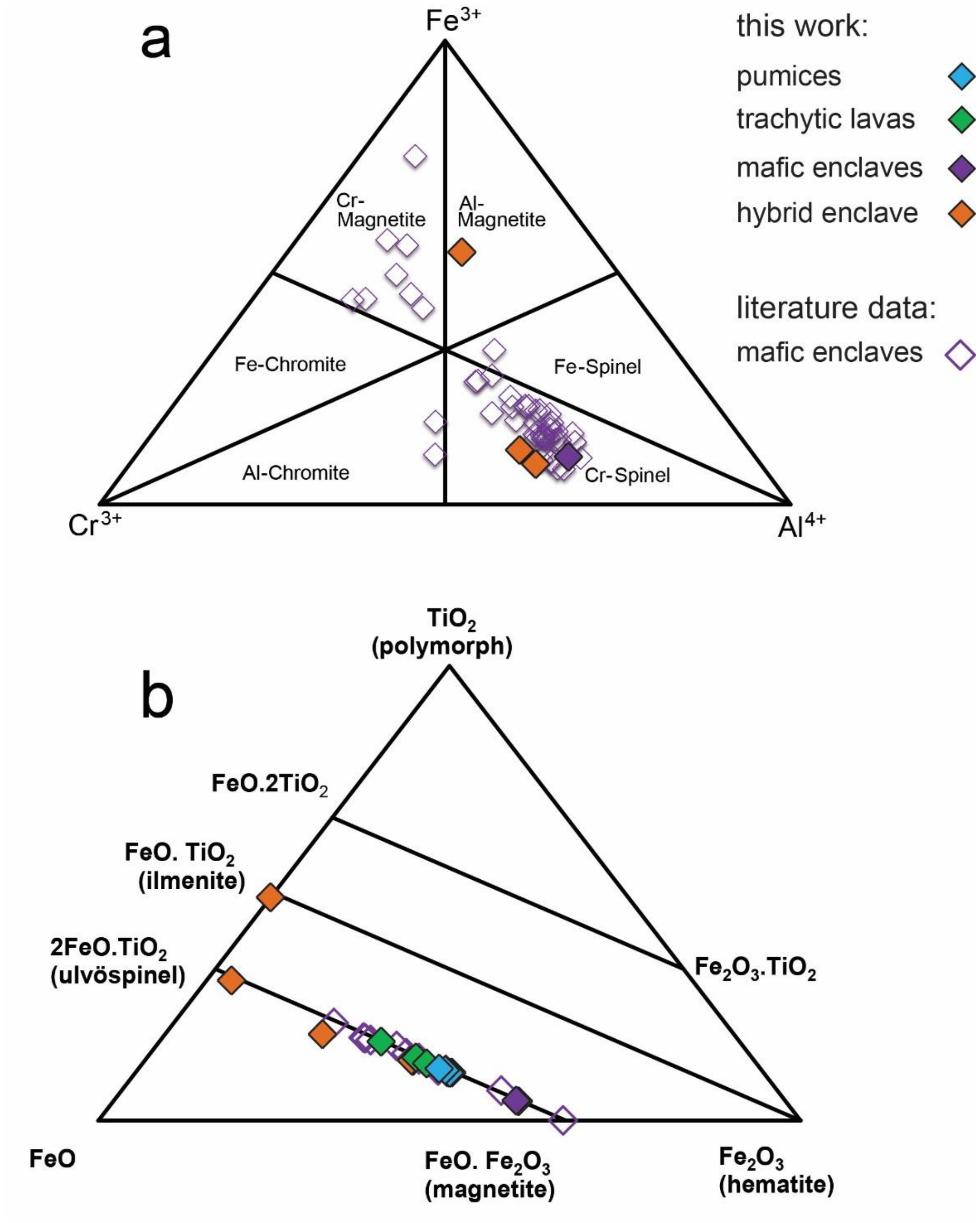

Fig. 41 a) Cr^{3+}-Al^{4+}-Fe^{3+} and b) FeO-TiO$_2$-Fe$_2$O$_3$ classification diagrams of Zaro opaque oxides. (literature data on Zaro opaque oxides are from Di Girolamo et al., 1995 and Melluso et al., 2014).

5.2.2 Zaro clinopyroxene: compositional populations and zoning pattern

Major and minor elements (Si, Ti, Al, Fe, Mg, Mn, Ca, Na, K, Ni and Cr) compositions were measured along detailed concentration profiles in zoned clinopyroxenes of the Zaro rocks. A total of ca 400 crystals were hand-picked and observed under both binocular and scanning-electron microscope. 68 analytical spots have been also acquired on optically unzoned crystals. 36 optically zoned clinopyroxene crystals (13 from Zaro lava, 3 from felsic enclaves, 11 from the hybrid enclave and 9 from mafic enclaves) have been analyzed. On these crystals the major and minor element composition was measured along i) a core-to-rim traverse with a spacing between individual points varying in the range 10-50 μm and ii) detailed traverses, with a spacing between individual points varying in the range 1-5 μm, crosscutting the boundaries between two zoning sectors of the crystals. The core-to-rim profile has been useful to characterize the chemical composition of the whole of the crystal and hence to investigate the zoning pattern of the Zaro clinpyroxene. The other traverses have been mostly used for diffusion modelling.

Zaro clinopyroxene occur as optically zoned or unzoned crystals. Different kinds of zoning have been recognized, as described in detail below. The optically unzoned clinopyroxenes (Fig. 42a) make up the ca. 70% of the whole investigated crystals.

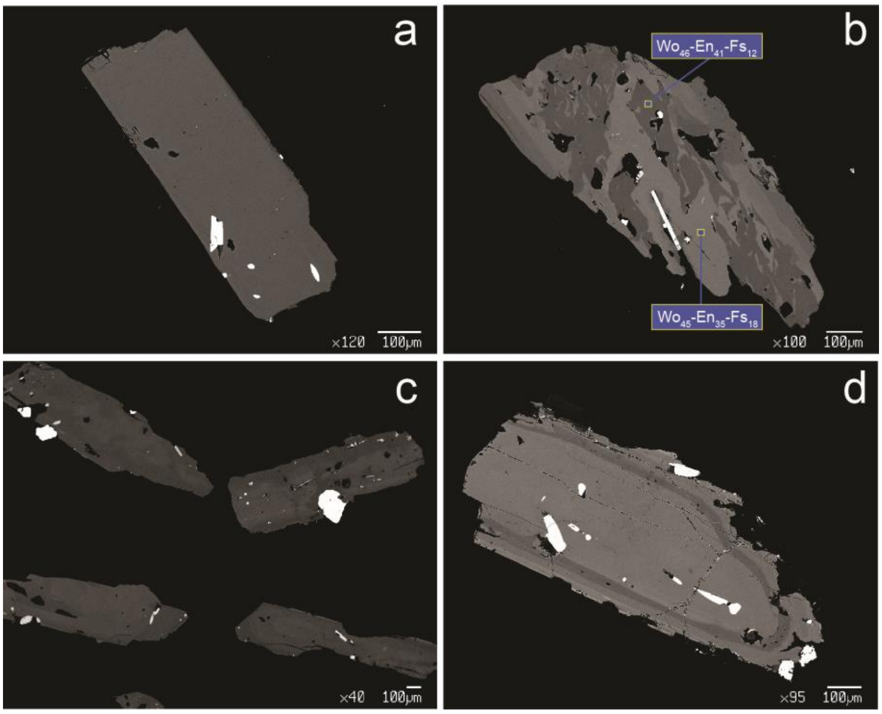

Fig. 42 BSE images of Zaro clinopyroxenes showing unzoned and different kinds of zoning crystals. a) optically unzoned clinopyroxene crystal from Zaro lava; b) patchy zoning in a clinopyroxene crystal from felsic enclaves, characterized by different compositions in the different colored areas; c) irregular zoning in several clinopyroxene crystals from the hybrid enclave; d) regular zoning in a clinopyroxene crystal from mafic enclaves.

Anyway the percentages are different for the different Zaro lithotypes (Table 2). Moreover, the zoned crystals can be divided into two main groups depending on the texture of the zoning: about 70% of the zoned clinopyroxenes show a patchy zoning, characterized by irregular areas, with different color tones and compositions (Fig. 42b-c). The remaining 30% of zoned clinopyroxenes, instead, show regular zoning mostly characterized by concentric sectors (Fig. 42d).

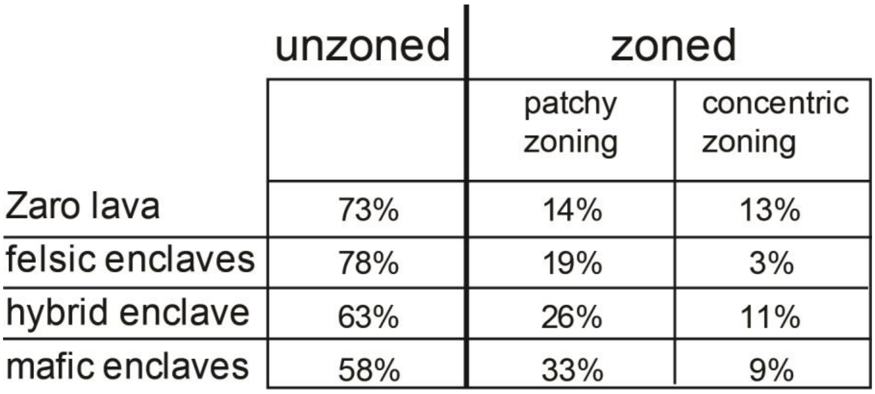

	unzoned	zoned	
		patchy zoning	concentric zoning
Zaro lava	73%	14%	13%
felsic enclaves	78%	19%	3%
hybrid enclave	63%	26%	11%
mafic enclaves	58%	33%	9%

Table 2 Percentages of unzoned and different kinds of zoned clinopyroxenes from the Zaro lithotypes.

5.2.2.1 Clinopyroxene zoning pattern

The zoning pattern of the Zaro clinpyroxenes characterized by regular zoning sectors (i.e. Fig. 42d) consists of two or more plateau with a constant composition separated by either sharp or gradual boundaries. Based on the Mg# parameter, it is possible to define normal zoning (Mg# decreases from core to rim), reverse zoning (Mg# increases from core to rim) or complex zoning, i.e. normal-to-reverse (Mg# decreases from core to mantle and increases from mantle to core). Different zoning types have been defined: reverse zoning has been classified as type I, reverse-to-normal zoning as type II, normal-to-reverse zoning as type III and normal zoning as type IV. Additionally, four crystals show a reverse zoned core surrounded by a reverse zoned mantle: thus, the zoning type V is defined by increasing of Mg# from core to mantle and from mantle to core. Moreover, the types I, II and III can be divided into two different categories, by taking into account the type of boundary. The latter can be characterized by sudden (sharp boundary) or progressive (gradual boundary) compositional variations. In this way, different types of zoning have been recognized in more detail.

12 out of 36 clinopyroxenes (ca 33%; Table 3) are characterized by simple reverse zoning (type I). In particular, 6 out of 36 crystals show a sharp variation (type I-a; Fig. 43), whereas other 6 show a gradual variation (type I-b; Fig. 43b).

Table 3

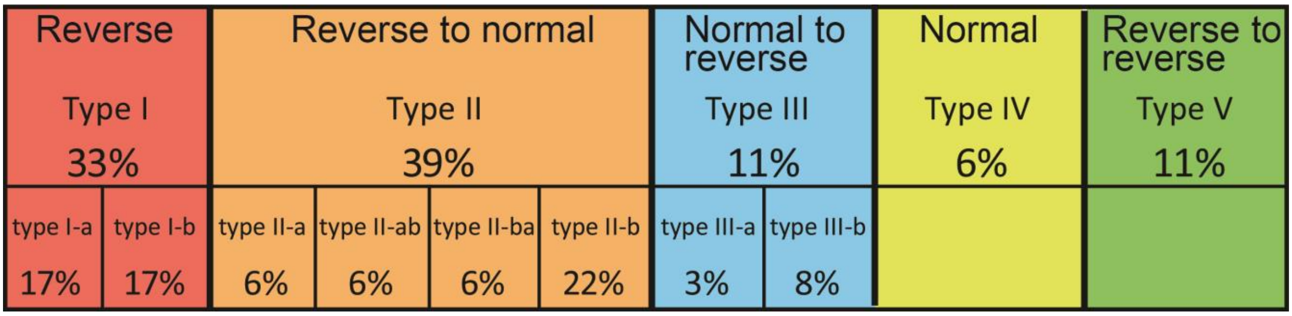

Reverse Type I 33%		Reverse to normal Type II 39%				Normal to reverse Type III 11%		Normal Type IV 6%	Reverse to reverse Type V 11%
type I-a 17%	type I-b 17%	type II-a 6%	type II-ab 6%	type II-ba 6%	type II-b 22%	type III-a 3%	type III-b 8%		

Table 6 Percentages of zoning types in the Zaro clinopyroxenes

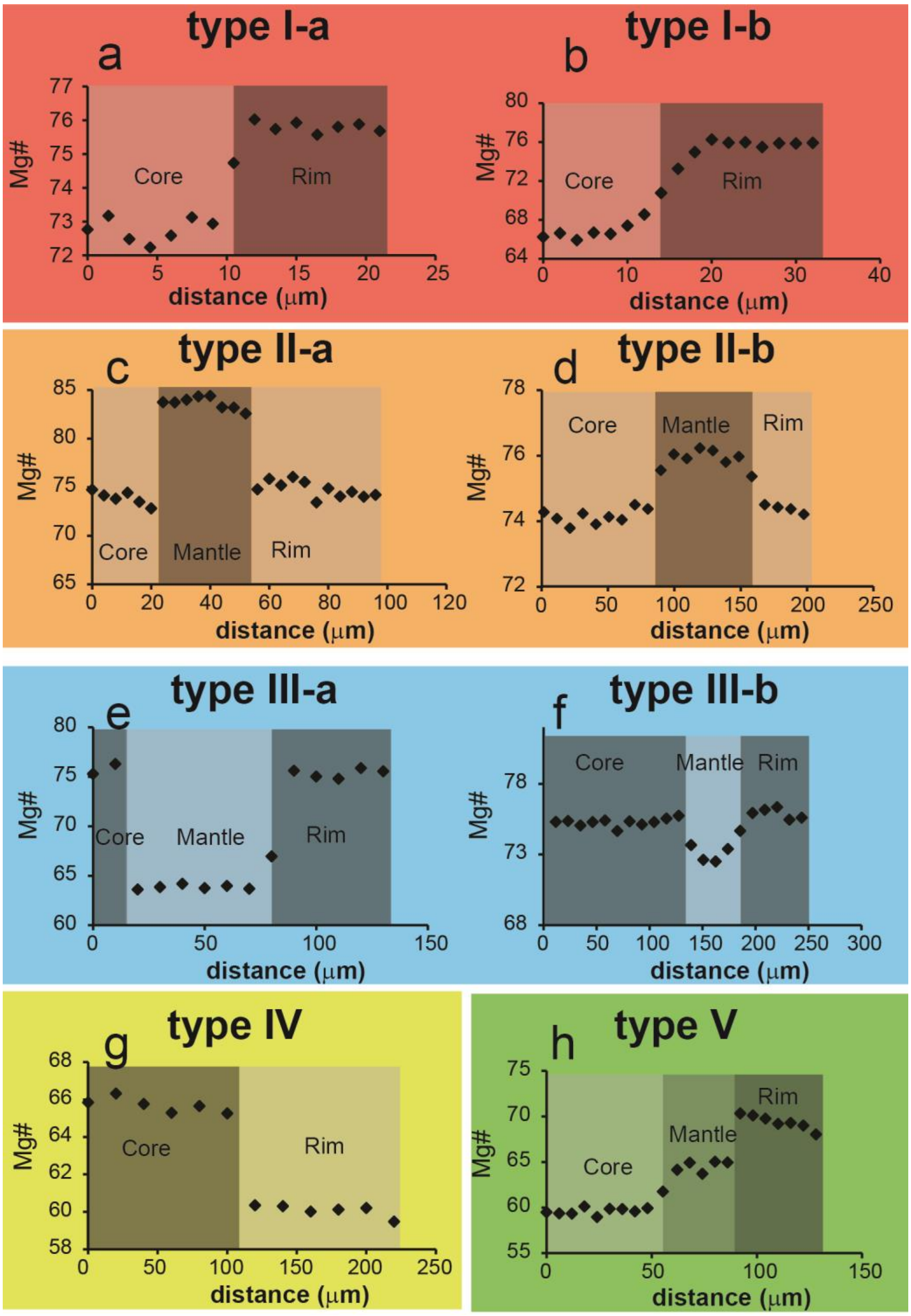

Fig. 43 Types of zonation of the Zaro clinopyroxenes. Black diamonds represent measured analysis along the crystal traverses showing concentration profiles from core to rim [Mg# = molar $Mg^{2+}/(Mg^{2+} + Fe_{tot})$].

The most common (ca 39%) zoning type is type II, constituted by a reverse zoned core surrounded by a normal zoned mantle. Being characterized by more than one boundary, the zoning types II-a and II-b are the end-members of four types of reverse-to-normal zoning: type II-a (Fig. 43c) consists of both boundaries characterized by sharp variations and occurs in two out of the 36 crystals; 8 out of 36 crystals have a type II-b zoning (Fig. 43d), characterized by two gradual boundaries; 2 out of 36 crystals show a gradual variation between the core plateau and mantle plateau and a sharp variation between the mantle plateau and the rim plateau (type II-ab); other 2 crystals vice-versa (type II-ba). 4 out of 36 zoned clinopyroxenes (11%) show a normal zoned core surrounded by a reverse zoned mantle (type III): of these, an individual shows both sharp variations at the boundaries (type III-a; Fig. 43e) and 3 crystals have both gradual variations at the boundaries (type III-b; Fig. 43f). 2 out of 36 clinopyroxenes (6%) show simple normal zoning (type IV; Fig. 43g), characterized by abrupt Mg# variations between the plateau. Lastly, 4 out of 36 crystals (11%) show an increase of Mg# from core to mantle and from mantle to rim plateau: zoning type V (Fig. 43h) only shows gradual boundaries and, in particular, the boundary between the core plateau and mantle plateau has a lower slope with respect to the that of the boundary between the mantle plateau and the rim plateau. An important observation is that most (30 out of 36) of the Zaro clinopyroxenes is characterized by a reverse zoned core. Significant relations between the zoning type and the chemically different Zaro rocks have not been detected: each zoning type is homogeneously distributed among the various lithotypes.

5.2.2.2 Clinopyroxene compositional populations

By looking in detail the chemical composition of the Zaro clinopyroxenes, different compositional populations can be recognized in their whole variation. The optically unzoned clinopyroxene crystals show a very homogeneous composition: the Mg# of clinopyroxene from both evolved (Zaro lava and felsic enclaves) and less evolved (mafic and hybrid enclaves) rocks ranges between 77 and 72, with an average at 75, for both crystals cores and rims (Fig. 44a).

Also the zoned clinopyroxene crystals characterized by patchy zoning show narrow compositional ranges: in clinopyroxenes from evolved rocks, the Mg# ranges from 70 to 67, in the light colored zones, and from 77 to 72, in dark zones, respectively, whereas in clinopyroxenes from less evolved rocks, Mg# ranges from 73 to 72, in light zones and from 83 to 82, in dark zones, respectively (Fig. 44b).

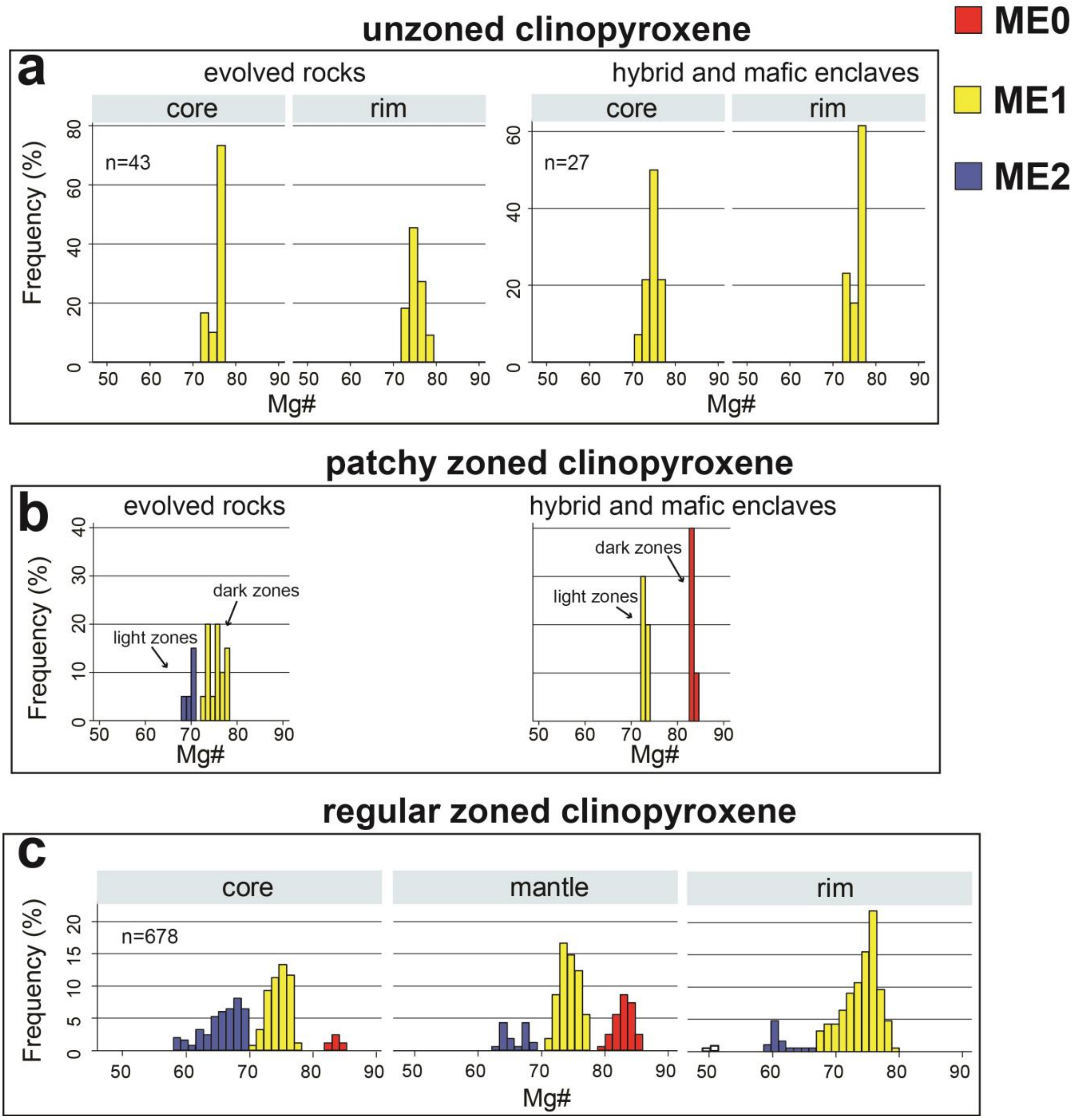

Fig. 44 a-b) Mg# frequency histograms of core and rim of optically unzoned Zaro clinopyroxene crystals and c) Mg# frequency histograms of core, mantle and rim of the zoned Zaro clinopyroxenes. These allow different populations to be identified.

Mg# frequency histograms (Fig. 44c) of core, mantle and rim compositions of the regular zoned crystals show that there are different types of compositional populations. In particular, the Mg# parameter allows distinguishing well: 1) a population of compositions (occurring in the 11% of the analyzed zoned clinopyroxenes, hereafter referred to as ME0) with Mg# in the range 79-86 and with an average value of 83; 2) a population (occurring in the 56% of the analyzed zoned clinopyroxenes, hereafter referred to as ME1) with Mg# between 79 and 71 and with an average value of 74; 3) a population of compositions (occurring in the 33% of the analyzed zoned crystals, hereafter referred to as ME2) characterized by Mg# in the range 70-58 with an average value of 66.

Table 4

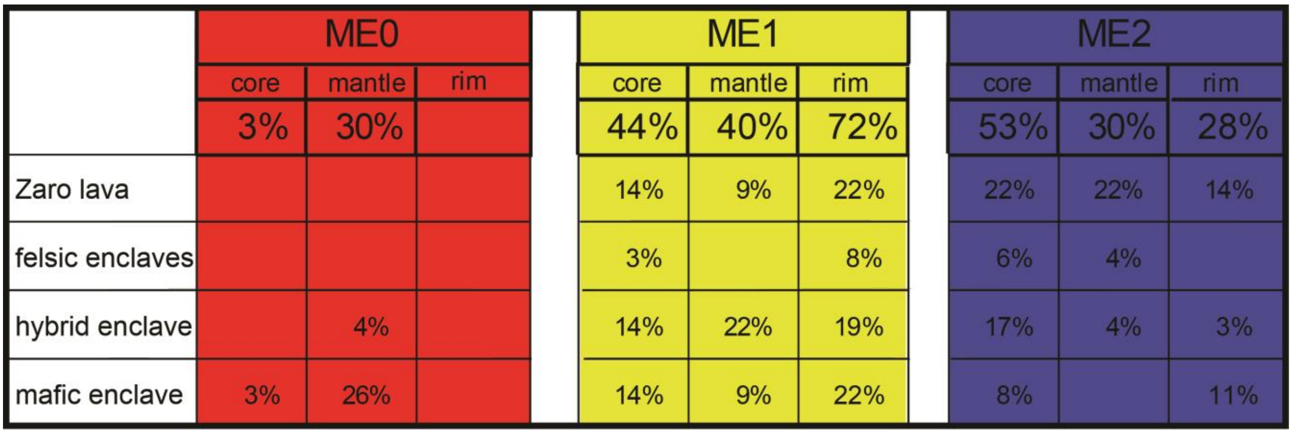

	ME0			ME1			ME2		
	core	mantle	rim	core	mantle	rim	core	mantle	rim
	3%	30%		44%	40%	72%	53%	30%	28%
Zaro lava				14%	9%	22%	22%	22%	14%
felsic enclaves				3%		8%	6%	4%	
hybrid enclave		4%		14%	22%	19%	17%	4%	3%
mafic enclave	3%	26%		14%	9%	22%	8%		11%

Table 4 Percentages of compositional populations in the zoning sectors of clinopyroxene crystals from the different Zaro lithotypes

ME0 occurs in only one out of 36 crystal cores and represents the mantle composition in 30% of the crystals. This population never occurs in crystal rims. ME1 is the composition of 16 out of 36 clinopyroxene cores and occurs in most (26 out of 36) of crystal rims. This population also occurs in the mantles in 40% of the crystals. ME2 is the composition of 19 out of 36 crystal cores and 10 out of 36 crystal rims. ME2 also represents the composition of clinopyroxene mantles, in 30% of the crystals. Besides these main populations, few analytical points show very low Mg# (48-53) and have only been detected in the most external rims of 5 crystals (3 crystals belonging to the Zaro lava and 2 crystals to the hybrid enclave): these represent the compositions of the Na-rich (aegirin-augitic) clinopyroxenes. In term of Mg#, the rims of the crystals are frequently (> 72%) characterized by the ME2 population, thus apparently indicating a homogeneous composition (similarly to the A-MS clinopyroxenes). Nevertheless, some elements, in particular Al_2O_3 and TiO_2 contents (Fig. 38a-b) show strong heterogeneities in the rims of the clinopyroxenes.

In addition to Mg#, other elements allow to well discriminate the compositional populations. In particular, by considering the Al_2O_3, Na_2O and MnO contents, the populations are completely distinct from each other in their 95% of confidence intervals (Fig. 45; populations can partially overlap each other only in the 5% of confidence intervals).

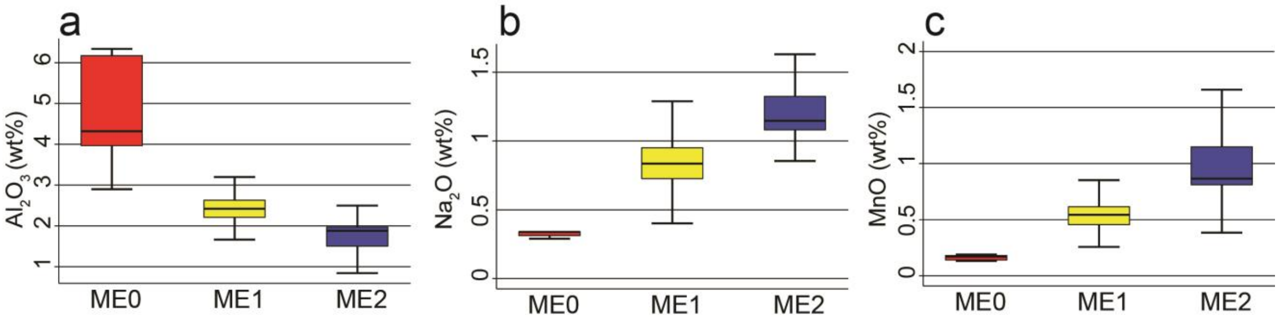

Fig. 45 a) Al_2O_3- b) Na_2O- and c) MnO box plot statistical diagrams showing the distinct clinopyroxene compositional populations; the upper and lower lines indicate the maximum and minimum values, respectively; the box encompasses the 95% of confidence intervals; the line within the box is the average of the values.

Furthermore, by looking in detail the composition in the cores of crystals, the over mentioned elements (e.g. MnO and Na_2O) largely corroborate the classification into different families (Fig. 46). Indeed, in the core of clinopyroxenes, noticeable difference can be view through the MnO and Na_2O contents.

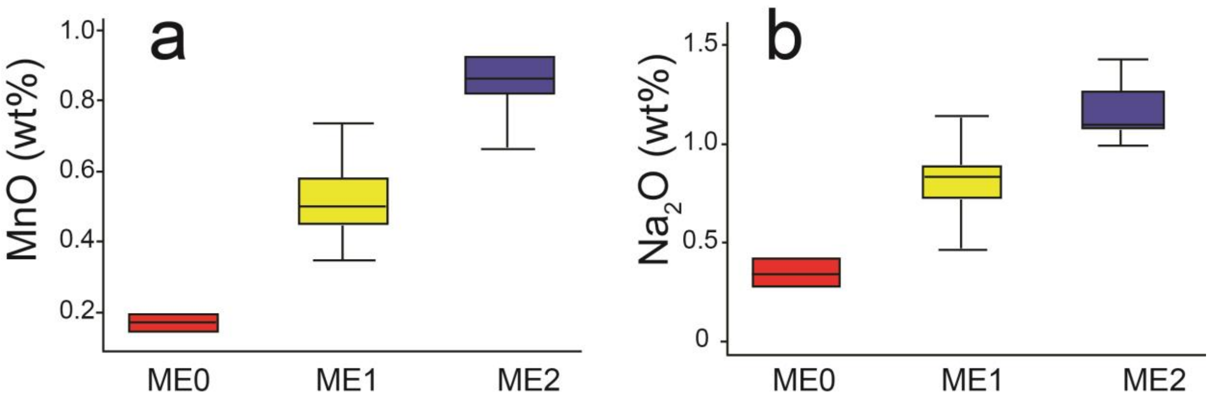

Fig. 46 a) MnO- and b) Na_2O box plot statistical diagrams of core of clinopyroxene crystals

Significant differences can be noticed among clinopyroxenes of the various lithotypes of the Zaro lava complex (Fig. 47). Also the clinopyroxene crystals characterized by patchy zoning show differences between the more and less evolved rocks (Fig. 44b).

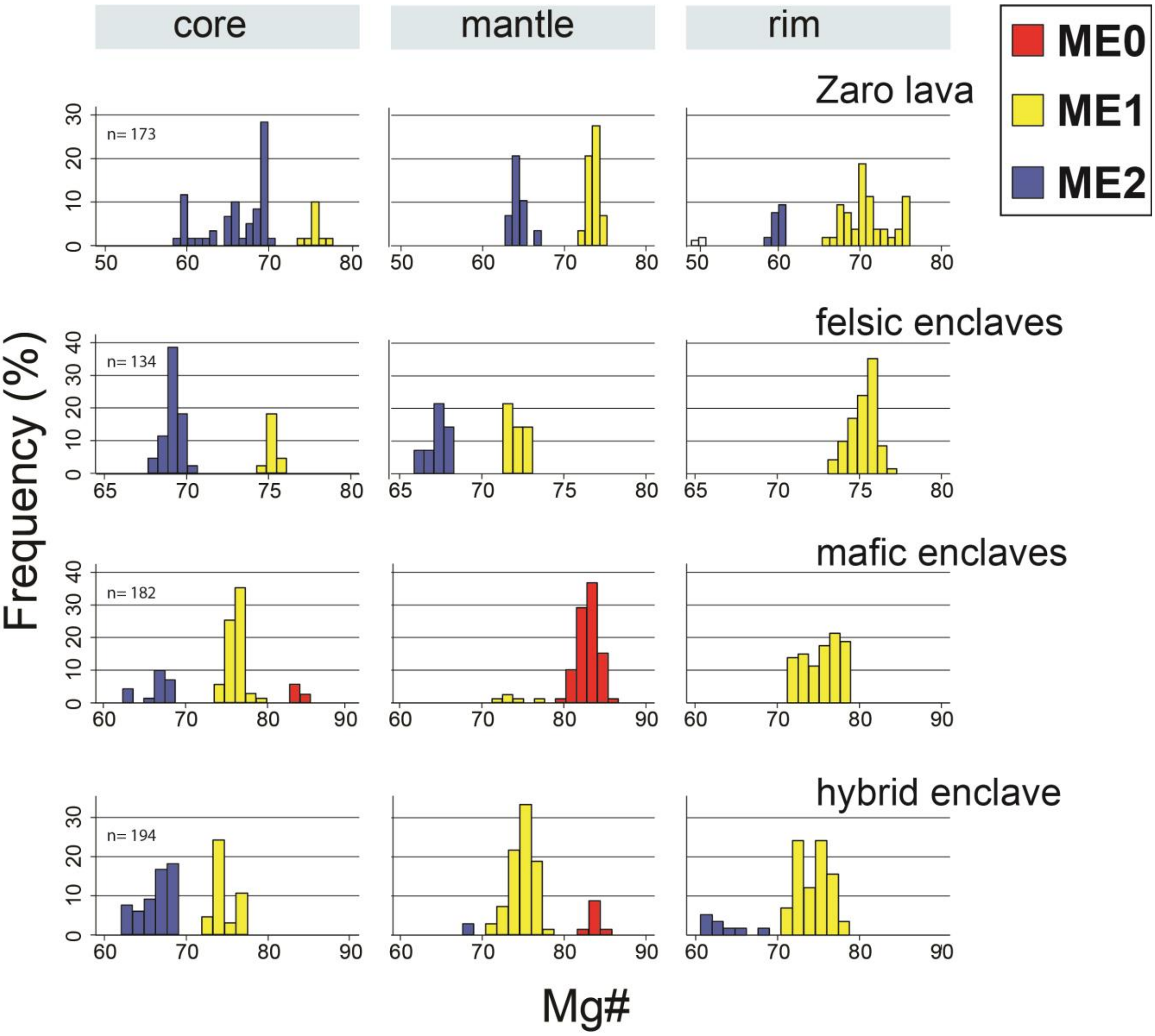

Fig. 47 Mg# frequency histograms of core, mantle and rim of the clinopyroxene crystals from the various Zaro lithotypes

In Figure 47, first of all, we can clearly see that clinopyroxenes from mafic and hybrid enclaves record less evolved compositions with respect to those of clinopyroxenes from evolved rocks: ME0 (which includes the highest Mg# values and, hence, represents the most mafic component) doesn't occur in the clinopyroxenes of the evolved rocks; this composition only occurs in mafic and hybrid enclave clinopyroxenes. ME2 population, which represents the most evolved component, is more frequent in clinopyroxenes from evolved rocks than in clinopyroxenes from the hybrid enclave and, even more, than in clinopyroxenes from mafic enclaves. Moreover, ME2 is more frequent than

ME1 in the core of clinopyroxene from evolved rocks. Clinopyroxenes from Zaro lava and felsic enclaves are characterized by populations (ME1 and ME2) showing similar ranges in crystal cores and mantles.

Some differences can be also noted between mafic enclaves and hybrid enclave clinopyroxenes. In particular, clinopyroxene from mafic enclaves records more mafic compositions with respect to these of clinopyroxene from the hybrid enclave. In the cores of clinopyroxenes from mafic enclaves, ME1 is more frequent than ME2 composition: 5 out of 9 crystal cores have a ME1 composition and 3 out of the 9 crystal cores have a ME2 composition. In the mantles of clinopyroxenes from the hybrid enclaves, ME1 is more frequent than ME2. Moreover, ME0 is more frequent in mantles of crystals from mafic enclaves than in mantles of crystals from the hybrid enclave. Similarly, crystal rims of the hybrid enclave, show more evolved compositions with respect to those of the rims of clinopyroxenes from mafic enclaves: ME2 doesn’t occur in clinopyroxenes rims of the mafic enclaves (see Table 4 for a synoptic view).

5.2.3 Whole-rock composition

Geochemical composition of the Zaro volcanic rocks is presented below considering new analyses carried out in the frame of this research (Table 2-Supplementary Material 2) and literature data (Di Girolamo et al., 1995; Melluso et al., 2014). The chemical and isotopic composition of other Ischia and Procida volcanic rocks is also illustrated in some diagrams below, since it will be compared to that of Zaro rocks and discussed in the context of the evolution of magmas feeding the PVD volcanoes plumbing systems (see Chapter 7).

In the TAS (total alkali vs silica) classification diagram (Fig. 48), the Zaro lava and felsic enclaves are trachytes.

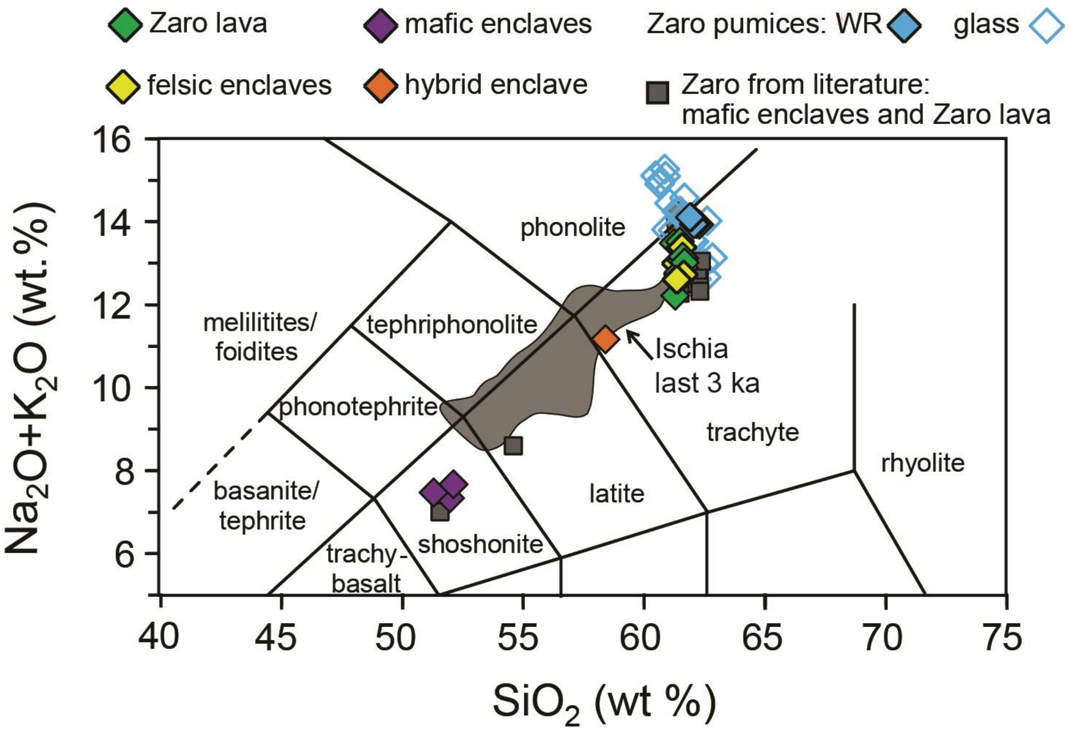

Fig. 48 TAS (total alkali vs silica) classification diagram of Zaro rocks.WR=whole rock; literature data for comparison are from Di Girolamo et al. (1995), D'Antonio et al. (2013), Melluso et al. (2014) and Iovine et al. (2017b).

The mafic enclaves are classified as shoshonites and latites whereas the hybrid enclave plots at the boundary between latite and trachyte. The Zaro pumice whole rocks straddle the boundary between trachyte and phonolite and pumice glass is in the phonolite field. In the Zaro lavas and felsic enclaves, Mg# [molar Mg^{2+}/ (Mg^{2+}+Fe^{2+})*100] varies from 39 to 30. Evolved lavas are generally silica rich (61.9-60.2 wt %), as they are composed by a large amount of feldspar and have alkali content (Na_2O+K_2O) up to 13 wt % (Fig. 49).

Mafic enclaves (SiO_2 = 55-51.5 wt %; Na_2O = 4.4-3.7 wt% and K_2O = 4.1-2.8 wt %) have MgO and CaO ranging from 5.4 to 3.9 wt %, and from 8.2 to 6.2 wt %, respectively. Mg# varies from 63 to 59. The hybrid enclave exhibits values intermediate between those of the mafic enclaves and those of the felsic lavas (Mg# = 48; SiO_2 = 58.1 wt %; MgO = 1.8 wt %; CaO = 3.6 wt %; Na_2O = 5.1 wt % and K_2O = 5.9 wt %). The Zaro pumices are more evolved rocks (Mg# = 26-23) when compared to felsic lavas.

All samples are CIPW Ne-normative (7.8-0.6 wt%; Table 8-Supplementary Material 2). At increasing differentiation degree (decreasing CaO content), the major and trace elements of Zaro samples increase in SiO_2, Na_2O, K_2O, Al_2O_3, Rb, Zr, Nb, Hf, Ta, Th, U, Pb and REE and decrease in MgO, $FeO_{(t),}$ P_2O_5, Sr, Ba, Cr, Ni, Co, Sc and V (Fig. 49; Table 2-Supplementary Material 2).

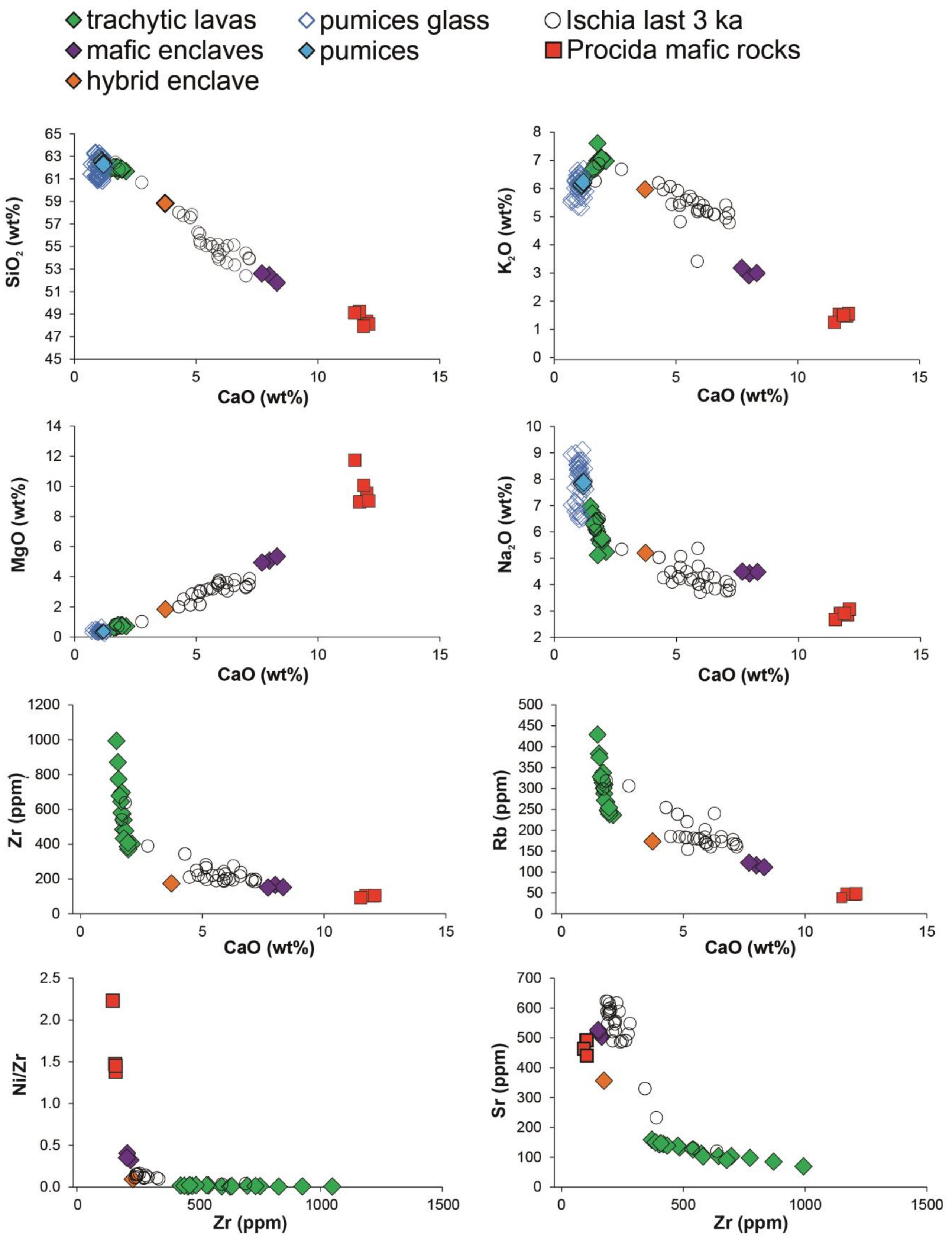

Fig. 49 Major and trace element variation diagrams of Zaro rocks compared to Procida mafic rocks and to the last 3 ka Ischia products (Molara, Vateliero, Cava Nocelle and Arso; literature references from D’Antonio et al., 1999a, 2013; Mazzeo et al., 2014; Iovine et al., 2017b).

Even though the trachytic lithotypes keep homogenous SiO_2 values, they display notable variation as to some trace elements (e.g., Rb, Y, Yb, Zr, Th, Hf) due to the high phenocryst amount of the lava (especially feldspar). Mafic enclaves exhibit higher Ni (74-40 ppm), Cr (145-60 ppm), V (181-130 ppm), Sc (20-13 ppm), Sr (557-453 ppm) and Ba (811-708 ppm) concentrations compared to felsic rocks (Ni $<$ 11 ppm, Cr $<$ 36 ppm, V $<$ 56 ppm, Sc $<$ 4, Sr = 69-158 ppm, Ba = 143-327 ppm). Rb ranges from 428 to 236 ppm in the evolved rocks and from 166 to 111 ppm in mafic enclaves. As for major elements, the hybrid enclave exhibits intermediate values between those of the mafic enclaves and those of the felsic lavas (Ni = 16 ppm; Cr = 40 ppm; Rb = 173 ppm; Sr = 356 ppm).

Chondrite normalized REE patterns (Fig. 50a) show enrichment in light REE compared to heavy REE (La/Lu_N = ~10 for mafic, and from 18 to 11 for evolved rocks). The Eu negative anomaly in trachytes and trachyphonolites is due to crystallization of feldspar during magma evolution. In the Primordial Mantle-normalized trace elements diagram (Fig. 50b), mafic enclaves are characterized by smooth patterns, showing enrichment in some incompatible elements (Rb, Th and K), positive picks at Pb and U, and slightly negative Nb, Ta and Ti anomalies.

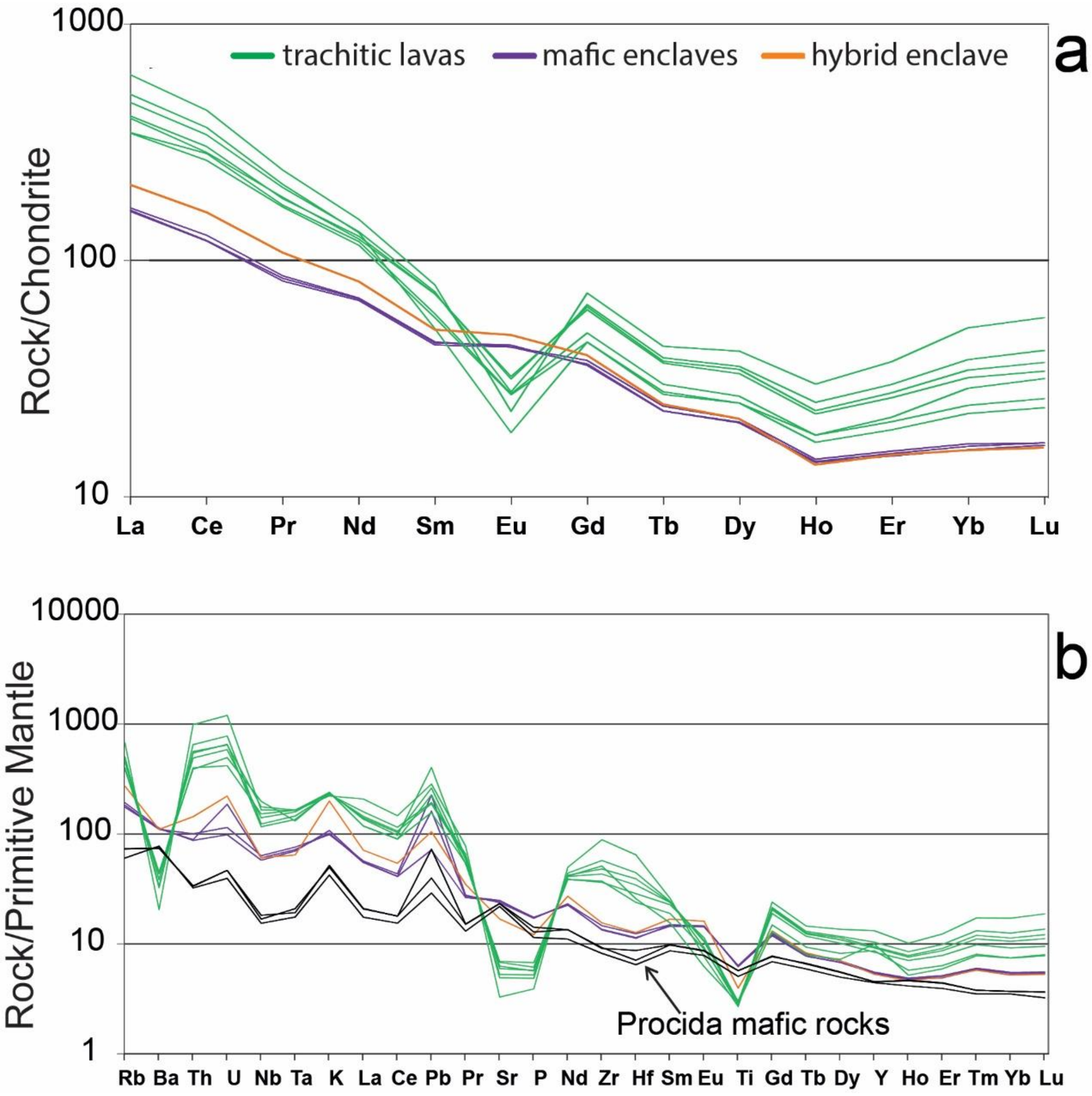

Fig. 50 Chondrite normalized REE patterns of Zaro rocks (normalization values from Boynton, 1984) and (b) Primordial Mantle normalized (normalization values from Sun and McDonough, 1989) trace elements distribution for Zaro rocks compared to mafic Solchiaro lithics from Procida (D’Antonio et al, 1999a)

5.2.4 Isotope compositions

The isotopic range of Zaro products is very variable (Table 9- Supplementary Material 1). However, all samples plot into the PVD isotopic field (Fig. 51).

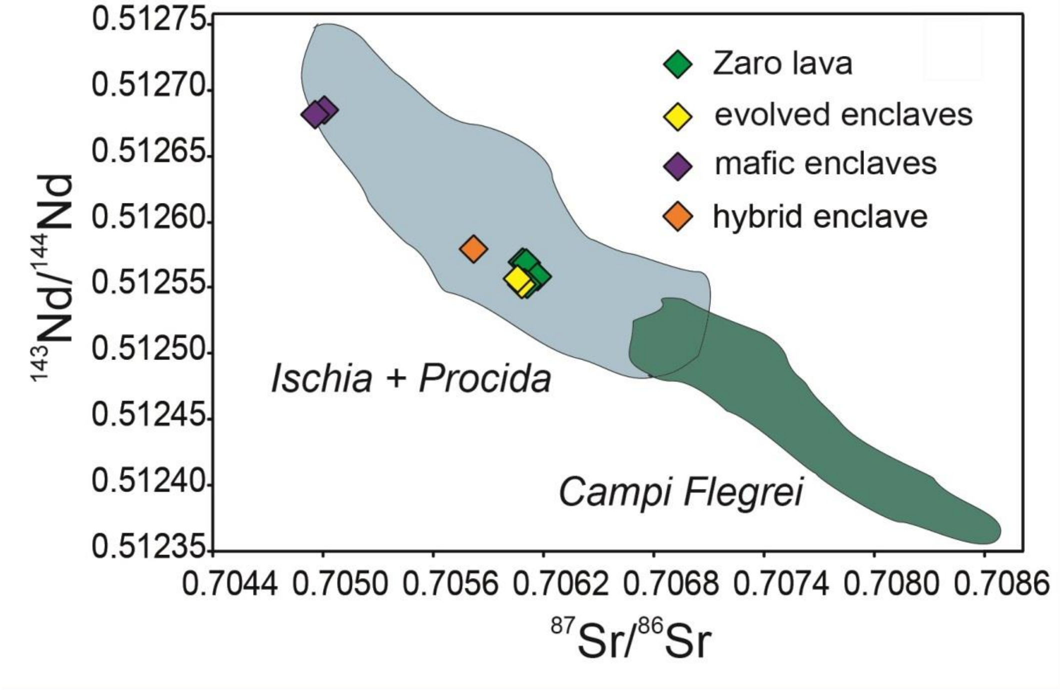

Fig. 51 Sr-Nd isotopic composition of Zaro samples within Ischia, Procida and Campi Flegrei isotopic fields, modified after Brown et al. (2014).

Zaro lavas and felsic enclaves are isotopically homogenous and show a small range of isotopic composition. They are more enriched in radiogenic Sr (0.70607-0.70615) and show lower ^{143}Nd/^{144}Nd (0.51255-0.51256) ratios compared to mafic enclaves. The hybrid enclave shows isotopic features (^{87}Sr/^{86}Sr = 0.70584 and ^{143}Nd/^{144}Nd = 0.51258) intermediate between those of the mafic and those of the felsic rocks, but closer to the felsic ones (Fig. 51).

The Sr-isotopic signature of minerals separated from Zaro products shows wide variations (Fig. 52). Olivines exhibit very low Sr isotopic compositions (0.70485-0.70493), whereas clinopyroxenes have a wider range (from 0.70560 to 0.70623) that is slightly correlated with the degree of magma evolution of their host rock. Feldspars have the highest and most homogeneous ^{87}Sr/^{86}Sr ratios (0.70602-0.70623).

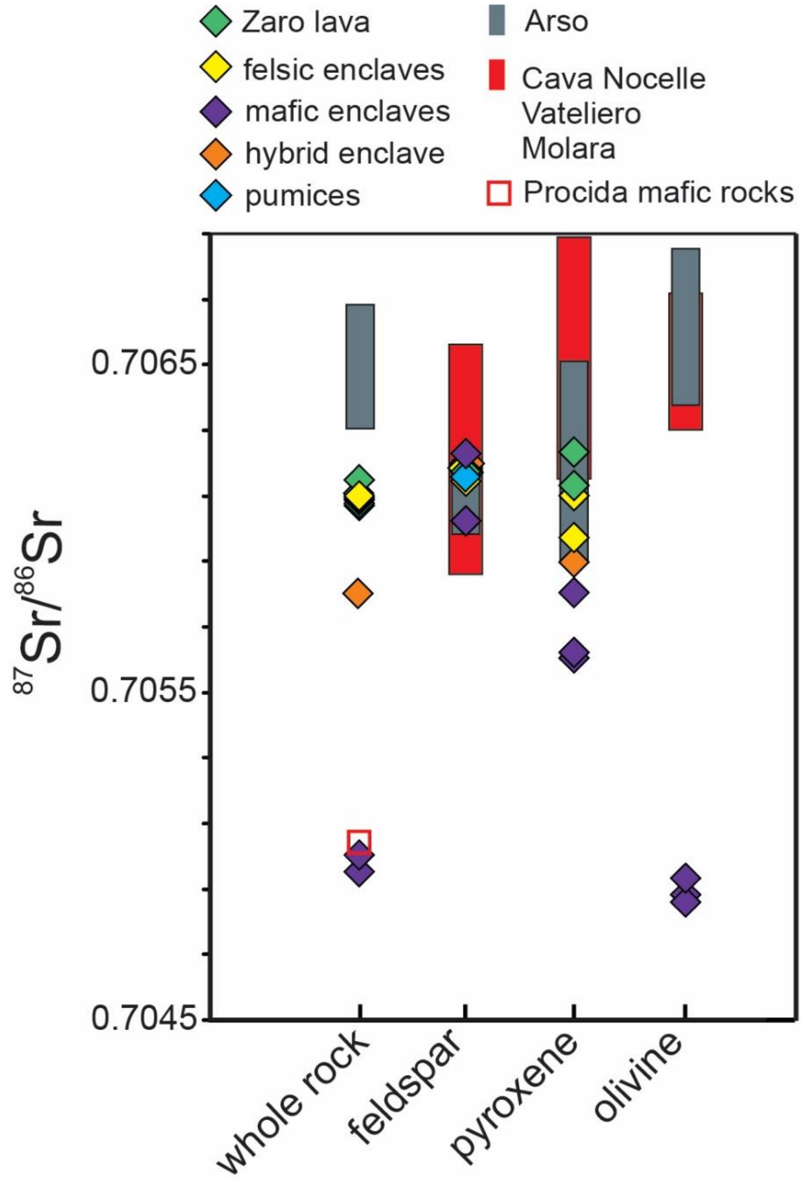

Fig. 52 Sr-isotopic composition of Zaro whole rocks and minerals compared to isotopic fields of Ischia last 3ka eruptions. Literature data are from D'Antonio et al. (2013), Mazzeo et al. (2014) and Iovine et al. (2017b).

6. DATA ELABORATION AND MODELLING

6.1 P-T crystallization conditions of A-MS clinopyroxene

Clinopyroxene-liquid thermometers and barometers specific for alkaline magmas (Masotta et al., 2013) have been used in order to investigate the crystallization conditions of the A-MS clinopyroxenes. However, only few clinopyroxenes have passed the compositional test for equilibrium (Fig. 53a; Putirka 2008), implying that the majority of the crystals, mostly those belonging to ME0 and ME1, grew in a more mafic melt and were subsequently trapped in the A-MS trachytic magma. Nevertheless, some of these clinopyroxenes are in equilibrium with whole rocks and/or melt inclusions representative of poorly evolved trachybasaltic to latitic Campi Flegrei magmas (Beccaluva et al., 1991; Civetta et al., 1991a; D'Antonio et al., 1999b; Lustrino et al., 2002; Mastrolorenzo and Pappalardo, 2006; Cannatelli et al., 2007).

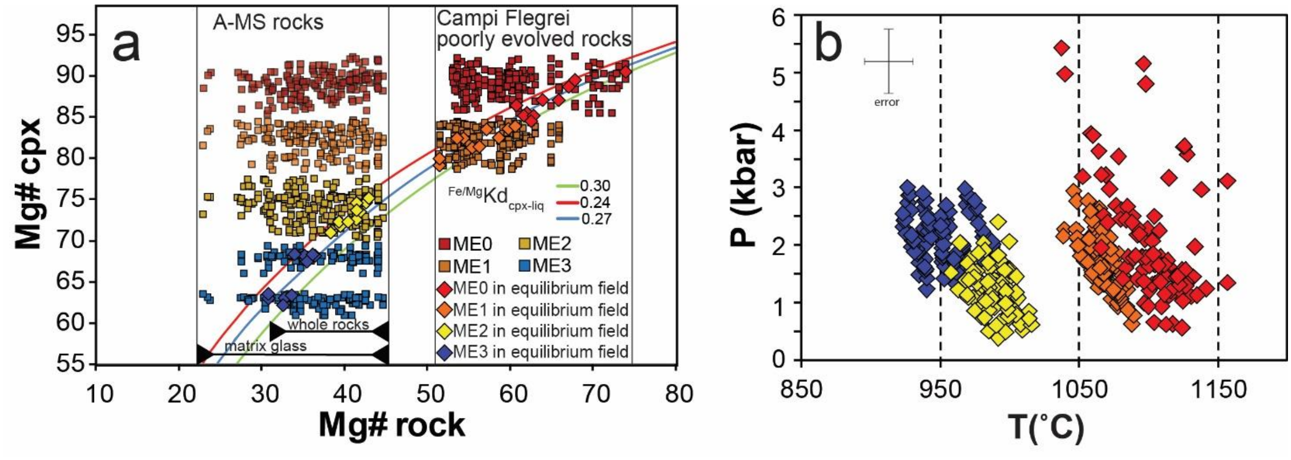

Fig. 53 a) Fe-Mg partitioning between clinopyroxene and host rock ($^{Fe/Mg}Kd_{Cpx\text{-}liq}$ = 0.27±0.03; Grove and Bryan, 1983; Putirka et al., 2003); square symbols represent the whole set of A-MS clinopyroxenes, belonging to different magmatic environments, compared to host rocks; the transparent small square symbols refer to clinopyroxenes with high Mg# (ME0 and ME1) compared to A-MS whole rocks and matrix glass compositions: these clinopyroxenes are out of equilibrium with respect to their host rocks; some of these clinopyroxenes are in equilibrium with more mafic rocks; diamond symbols refers to some clinopyroxenes which passed the compositional test for equilibrium and have been used for geothermobarometry. b) Output temperatures and pressure estimate for the different magmatic environments of the A-MS clinopyroxenes obtained by the clinopyroxene-liquid thermometers (equation Talk2012) and barometers (equation Palk2012) specific for alkaline magmas (Masotta et al., 2013).

Only clinopyroxene crystals in equilibrium with hypothetical melts, i.e. crystals from the ME0 and ME1 in equilibrium with Campi Flegrei poorly evolved volcanic products, and crystals from ME2 and ME3 in equilibrium with A-MS matrix-glass compositions (Fig. 53a) have been considered for the application of thermobarometry. As also explained in Masotta et al. (2013), since Mg# of clinopyroxenes and coexisting melts progressively increases with increasing temperature and H_2O content, the volatile(s) contents as input parameters can affect the output T-P estimates. Hence, in case melt inclusion compositions have been used as melts in equilibrium with ME0 and ME1 clinopyroxenes, the volataile contents used are exactly that detected in melt inlclusions representative of the poorly evolved Campi Flegrei magmas (Cannetelli et al., 2007); instead, in case the whole rock compositions have been used as melts in equilibrium with ME0 and ME1 clinopyroxenes, the H_2O composition analyzed in the whole rock or the H_2O by difference has been used. As for melts in equilibrium with ME2 and ME3 clinopyroxene, the H_2O by difference of the A-MS glasses analyzed in this thesis have been used: it seems reasonable since these H_2O contents are in the range of that detected in the A-MS melt inclusions by Arienzo et al. (2010).

Different ranges of temperature have been obtained for the variable clinopyroxene populations (Fig. 53b; Supplementary Material 4). The most mafic compositions yield the highest temperatures, with averages of 1104±24 °C for ME0 and 1066±11 °C for ME1. Average temperatures for ME2 and ME3 are 990±13 °C and 952±18 °C, respectively. ME4 was not considered because it is represented only by one crystal rim that possibly formed during the very final stage of crystallization (see Chapter 7). The estimated pressure is similar for all the populations ranging between 3.0 and 0.5 kbar, with an average value of ca. 1.7 kbar. Only a few output data show pressures >3 kbar, implying that some clinopyroxenes from ME0 could have started crystallizing at higher pressures. These values also fit with estimates obtained from previous studies on the A-MS (Roach, 2005;

Arienzo et al., 2010; Iovine et al., 2017a) and the PVD crystallization pressures (Perinelli et al., 2019; Bonechi et al., 2020). With the exception of a few clinopyroxenes from ME0, the obtained pressure range is the same for the different magmatic environments, which likely indicates that the resolution in pressure is not good enough to discriminate reservoirs at different depths.

6.2 Magmatic environments recorded in the A-MS clinopyroxenes

As previously described (Chapter 4.4), the occurrence of plateau in the zoning patterns of clinopyroxene indicates that growth occurred for certain periods of time under stable conditions. Consequently, plateau with different composition represent several episodes of overgrowth of the crystals under different sets of P-T-X conditions. Since the entire compositional range detected in the clinopyroxenes can be divided into different populations, each plateau belonging to a population with a certain composition represents the growth of crystals under a specific set of intensive thermodynamic variables (temperature, pressure, bulk composition, fugacity of volatile species), identified as a magmatic environment. Associating each population of clinopyroxene to a specific magmatic environment, it is possible to track the evolution of different crystals through distinct magmatic environments in which they grew.

In the systems connectivity diagram (Fig. 54) each box represents a distinct magmatic environment and each arrow represents the zoning type, i.e. the path, in terms of Mg#, from core to rim of each crystal.

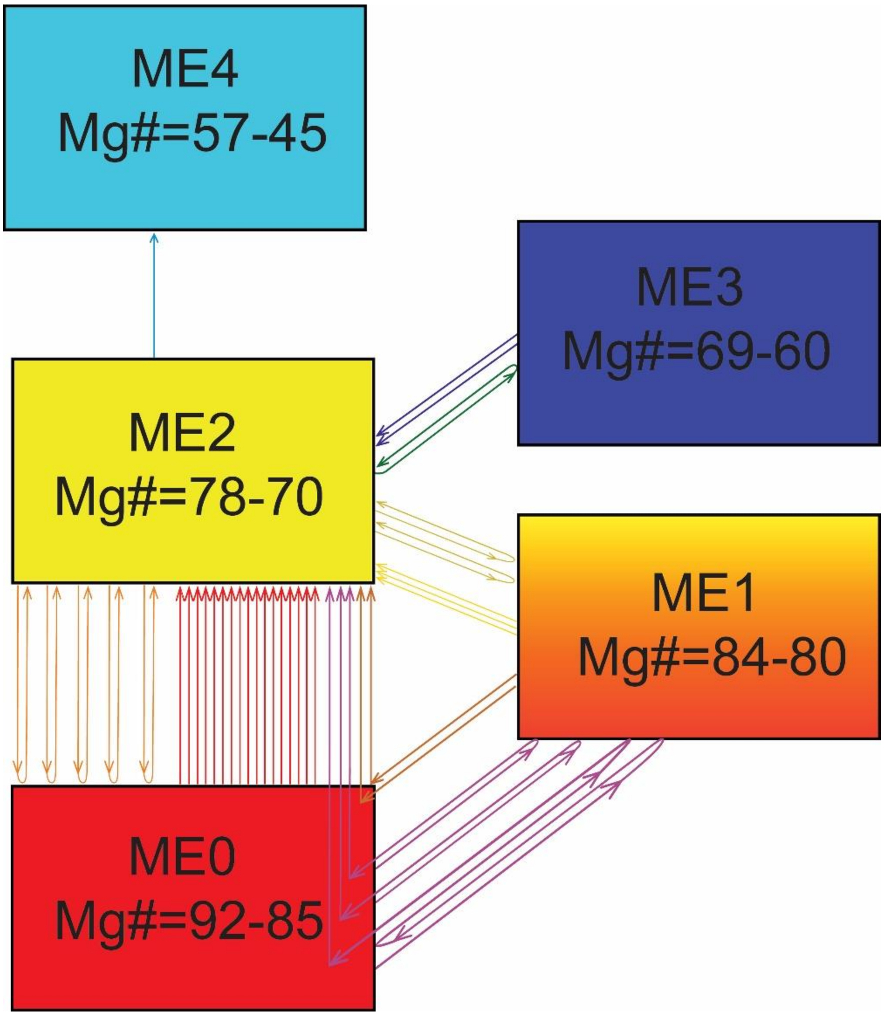

Fig. 54 Systems analysis of the zoning patterns of A-MS clinopyroxene crystals. Each box represents a magmatic environment. Each route/connection line indicates the composition of a crystal from core to rim; a single arrow represents the passageway of a crystal (or a magma in which the crystal was forming), from one magmatic environments to another with different conditions; a whole connection line (consisting of one or more arrows) represents the zoning type (each represented by different color, e.g. the orange routes represent clinopyroxene crystals with core formed in ME2, mantle formed in ME0 and the rim formed in ME2). The density of the connection lines can be used to infer the dominant passageways of crystals in different environments.

Such analysis reveals that, despite the complex diversity of zoning patterns, certain evolutionary tracks are recurrent in the history recorded by the clinopyroxene populations. It can be noted that there are many connections, depicted as arrows in Fig. 54, between the ME0 and ME2 environments. The connections often pass also through ME1 that represents an environment compositionally intermediate between ME0 and ME2. Finally, there is a much smaller number of connections between ME2 and ME3. Based on the available data, there are no connections between either ME0 or ME1 and ME3; this allows us to divide the evolutionary history of A-MS clinopyroxene phenocrysts in two steps: one involves the interaction among the magmatic environments ME0, ME1 and ME2, the other involves ME2 and ME3. Moreover, as also visible in the frequency histograms (Fig. 27), it is worth noting that both crystal cores with high Mg# (ME0) and crystal cores with low Mg# (ME3) converge toward an intermediate composition (ME2) at the rim, which means that the final stage of crystallization occurred in a compositionally homogeneous magmatic environment that was shared by crystals with different previous histories. At this point it is worth recalling that this distinction in different magmatic environments is supported by other compositional variables such as Na_2O, Al_2O_3 and TiO_2 contents, with the exception of the ME1b and ME2b groups of Al_2O_3 and TiO_2 contents that occur in the rim and mantle regions of the zoned clinopyroxenes. These will be discussed in detail in the following section on diffusion modeling.

6.3 Diffusion modelling for the A-MS clinopyroxenes

Kinetic modeling of the zoning patterns in clinopyroxene, which record fluctuations through the different magmatic environments, can yield information on the timescales over which the processes that created the different types of zoning took place. The well preserved plateau found in most profiles can be used to infer the initial profile shapes before diffusion occurred. Given the different kinds of zoning profiles, two different approaches for modeling can be taken here. I. Most of the profiles, characterized by compositional plateau and sharp gradients show little evidence of diffusive modification of growth zoning. In these cases, it is possible to calculate the relaxation of growth zoning timescales (e.g. see Chakraborty and Ganguly, 1991; Trepmann et al., 2004) to infer maximum possible durations that the crystals may have spent in a magmatic reservoir at a given temperature without perceptible, within the analytical resolution of this study, diffusive modification of the profiles. II. In a small subset of profiles (e.g. Type II) diffusive gradients are observed and these can be modelled to fit the observed profiles and yield durations of residence of the crystals in a particular magmatic environment. In both cases, solutions to the diffusion equation

$$\frac{dC}{dt} = \frac{d}{dx}\left(D(t)\frac{d}{dx}\right) \qquad (1)$$

are sought with an appropriate choice of initial and boundary conditions. The equation describes how concentration gradients (i.e., concentration profiles: dC/dx), evolve as a function of time and this aspect is utilized to obtain information on timescales from measured concentration profiles (e.g. Chakraborty et al., 2008). Diffusion modeling has been carried out at temperatures corresponding to that of the ME2 environment (990 °C) because, in most cases, this is the final temperature at which clinopyroxenes grew and resided before eruption, at least for ca. 98% of the zoned crystals, as well as the homogeneous crystals, which make up 85% of the clinopyroxene population. The diffusion coefficient has been calculated using the expression provided by Müller et al. (2013):

$$D^{\mathrm{Fe-Mg}} = 2.77 \pm\ 4.27\ * 10^{-7} \mathrm{exp}\left(\frac{-320.7 \pm \frac{16\mathrm{kJ}}{\mathrm{mol}}}{RT}\right) \mathrm{m}^2/s \qquad (2)$$

where R is the gas constant and T is the temperature in Kelvin.

In approach I, the measured profiles are taken as the initial profiles and equation (1) and (2) are used to numerically calculate evolution of the profile shapes as a function of time. The boundary conditions for these calculations may be either constant composition or no flux at the rims of crystals, with little difference in the results. Timescales on which the calculated profiles deviate measurably from the initial profiles are considered to be upper limits of residence times of crystals in a particular magmatic environment. Fig. 55 shows examples for different kinds of profiles (except Type II) modeled with method I.

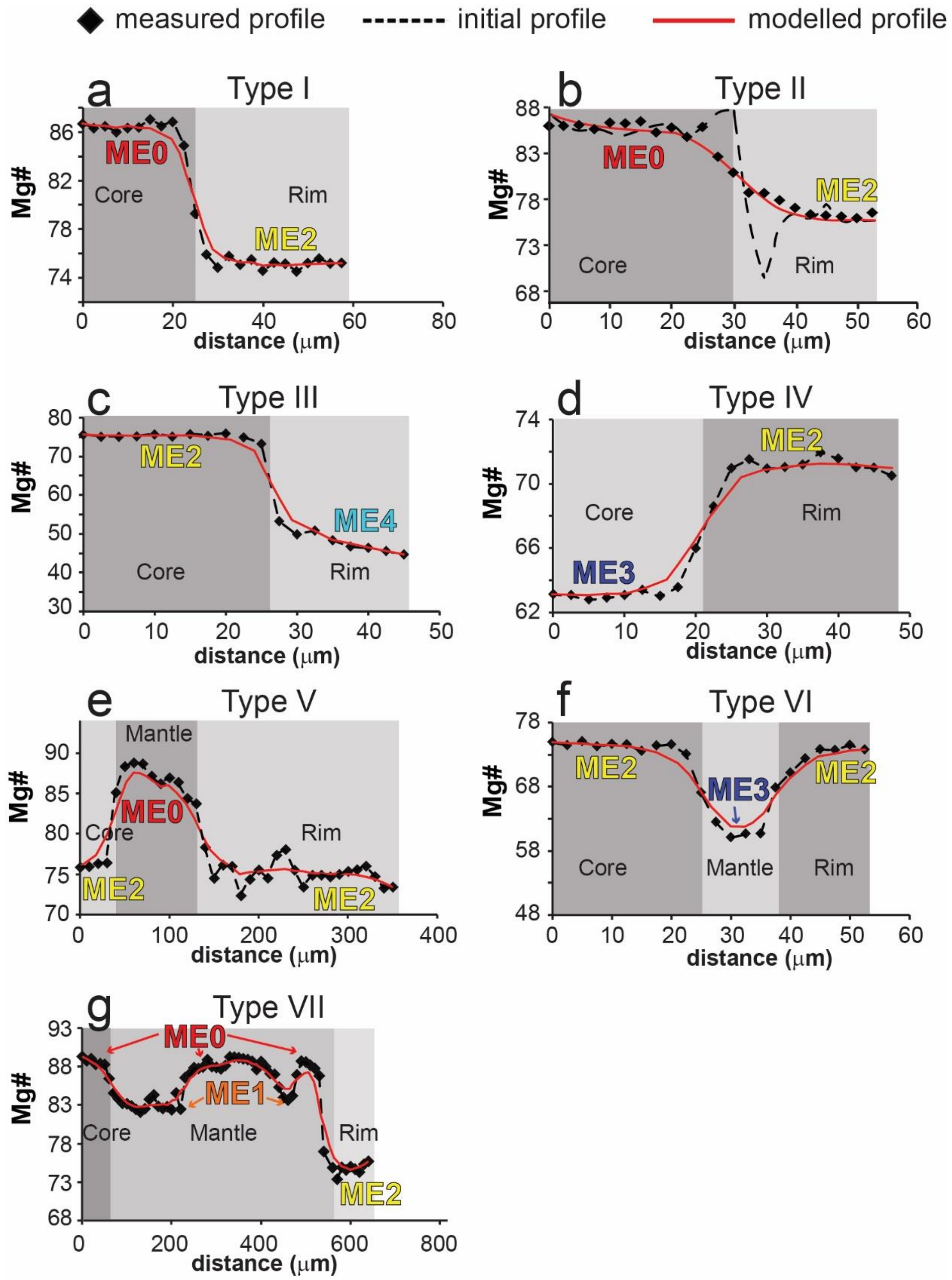

Fig. 55 Diffusion modelling for the A-MS clinopyroxenes. Black diamonds are measured analysis along the crystal traverses showing concentration profiles from core to rim [Mg# = molar $Mg^{2+}/(Mg^{2+} + Fe_{tot})$]. Black dashed lines indicate the initial profile shapes. In Fig. 55a,c,d,e,f.g the modelled profiles (red lines) show the permissible diffusive smoothing that a concentration gradient may have experienced; in Fig 55b, instead, the modelled profile (red line) indicates effective diffusive smoothing (see text for details).

The upper limit residence times for different plateau compositions in the various types of zoning profiles are listed in Table 5 and plotted in Fig. 57. These are found to be < 25 years, with durations < 15 years being the most common.

Table 5

Member	cpx n°-traverse n°	Method I	Method II
A1	cpx1-1	14.3	
	cpx1-2	15.5	
	cpx2-1	6.7	
	cpx2-2	6.7	
	cpx3-1		48.2
	cpx3-2		37.8
	cpx5-1		68.2
	cpx5-2		61.0
B1	cpx1-1	8.9	
	cpx1-2	8.9	
	cpx2-1	8.9	
	cpx2-2	7.1	
	cpx4-1		48.3
	cpx4-2		52.6
	cpx5-1	12.7	
	cpx5-2	9.5	
	cpx6-1	4.8	
	cpx6-2	4.8	
	cpx7-1	14.3	
	cpx7-2	4.8	
	cpx8-1	9.5	
	cpx8-2	12.7	
	cpx9-1	20.9	
	cpx9-2	7.6	
	cpx10-1	11.4	
	cpx10-2	8.6	
	cpx11-1		47.2
	cpx11-2		52.5
D1	cpx2-1	14.3	
	cpx2-2	6.8	
	cpx5-1		43.8
	cpx5-2		50.6
	cpx7-1	10.5	
	cpx7-2	11.1	
	cpx8-1	14.3	
	cpx8-2	9.5	
	cpx9-1	6.1	
	cpx9-2	8.6	
	cpx10-1	20.3	
	cpx10-2	6.7	
	cpx11-1	18.0	
	cpx11-2	6.7	
	cpx13-1	24.7	
	cpx13-2	7.9	
	cpx14-1	8.6	
	cpx14-2	5.2	
	cpx18-1	9.4	
	cpx18-2	7.9	
	cpx19-1	12.9	
	cpx19-2	5.3	

Table 5 Timescale estimates for Agnano-Monte Spina clinopyroxene crystals derived from Fe-Mg diffusion modeling across selected transects, calculated at T = 990 °C

In the approach II, on the other hand, it is necessary to define the shapes of the initial profiles and then model their diffusive modification. To do that, element concentrations that are correlated with each other through petrogenetic processes but diffusing at different rates are useful. Here Mg# and Al_2O_3 content, which are anti-correlated with each other (e.g. Fig. 26b) in the clinopyroxene crystals have been used, because Mg# decreases as Al_2O_3 content increases during fractional crystallization as well as partial melting processes (e.g. Jagoutz et al., 1979). As discussed above (see caption of Fig. 28), there are two groups of compositions, ME1b and ME2b, that deviate from this trend. It is possible to reliably infer the initial profile shapes of crystals which exhibit this characteristic: by plotting Al_2O contents vs Mg# in a profile it is possible to obtain a linear correlation. Most of crystals show a good correlation, as shown by the fit of the data by a linear trendline (in Fig. 56a, $R^2=0.94$), which can be then used to infer the hypothetical initial Mg# profile, which is plotted in figure 56b. Within the accuracy of the data, hardly it is possible to see difference between the measured profile and the theoretical profile, in particular, in the region with the sharp compositional gradient. That indicates that the Mg# profile was little or no affected by Fe-Mg interdiffusion. For these crystals, it has been possible to estimate a maximum timescale as explained above for approach I: in this case, since the inferred profile is very similar to the measured profile, the latter has been used as initial profile in the modeling. It is then possible to deduce that where Mg# and Al_2O_3 are correlated according to the overall general trend, the profiles of Mg# and Al_2O_3 track each other completely and the shapes overlap with each other. Conversely, when Al_2O_3 content is higher at a given Mg# compared to the value expected from the overall correlation trend, such as for crystals showing ME1b and ME2b trends (Fig. 28e-f), the Al_2O_3 preserves a sharper gradient whereas the Mg# shows more smoothed concentration patterns (e.g. zoning Type II). In this case, the correlation between Mg# and Al_2O_3 content is not good (in Fig. 56c, $R^2=0.74$), indicating that the original trend was overprinted by Fe-Mg interdiffusion. It is possible to estimate an original trend by taking the Mg# and Al_2O_3 contents of the two plateau regions, which is plotted as blue line in Fig. 56c. This original correlation has been used to estimate a growth zoning of Mg#, that is the initial profile in Fig. 56d. It is possible to observe that the Mg# theoretical initial profile noticeably deviate from the measured profile and the difference is strongest in the region with the large compositional gradient of Al_2O_3.This indicates that Mg has diffused to some extent in these situations and is consistent with known experimentally measured diffusion behavior of these elements (Mg vs. Al) in clinopyroxenes (e.g. Fe-Mg: Müller et al., 2013; Al: Sautter et al., 1988). Thus, the shape of the Al_2O_3 profile can be taken as the initial profile shape for Mg# (i.e. as a grown profile) and diffusion modeling may be used to try to reproduce the measured, diffused concentration profile shape of Mg#. At both ends of the profile concentrations, the system has been modeled as an infinite diffusion couple, i.e. boundary conditions are $C = C_{initial}$ at $\pm\infty$. Furthermore, since two compositional traverses were acquired across each clinopyroxene crystal, if modeling of both profiles did not yield the same time estimates, the concentration profiles were considered to be affected by processes other than diffusion and the obtained values were discarded (Costa et al., 2008). On the other hand, the fact that in many cases the same timescales were obtained from profiles that are oriented in mutually perpendicular directions may point to a limited anisotropy of Fe-Mg diffusion in clinopyroxene; that indeed has not been measured experimentally yet. An example of such a profile, with the initial and the final modelled profile shapes is shown in Fig. 55b and Fig. 56c-d.

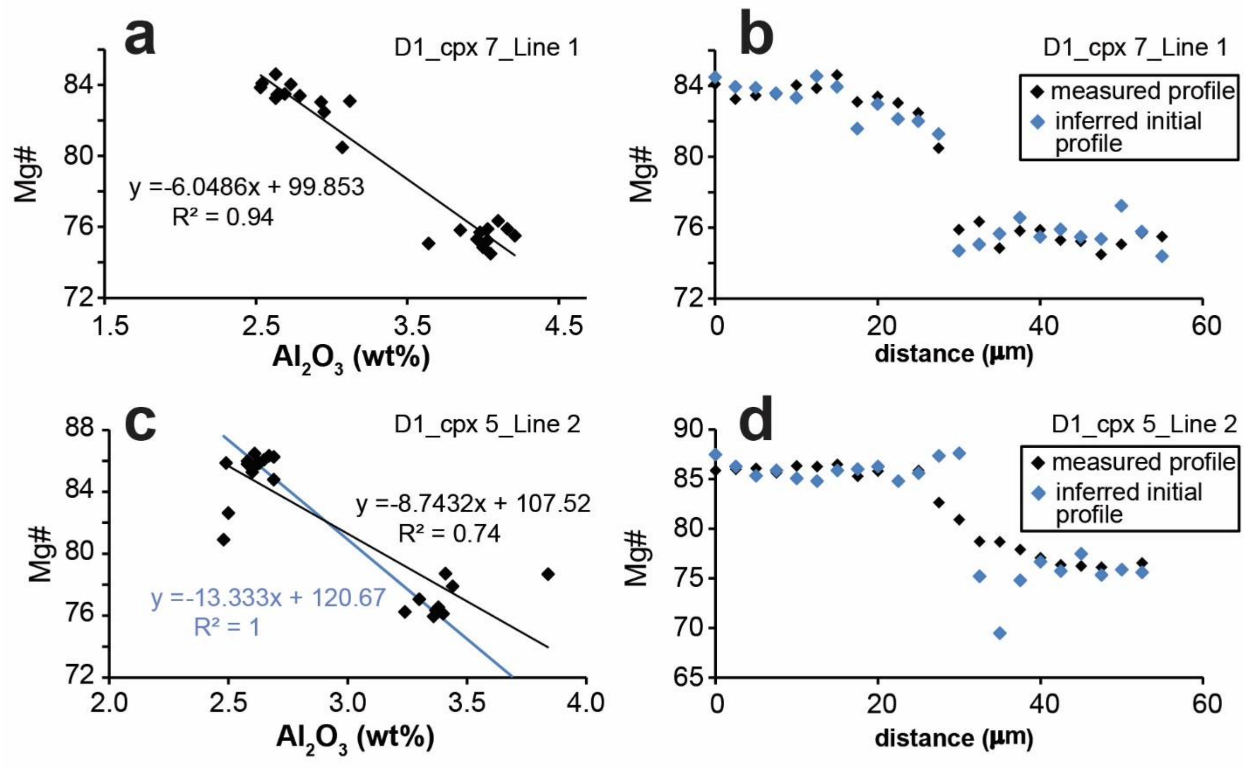

Fig. 56 a-c) Mg# vs Al_2O_3 (wt%) relation of two selected crystal profiles. In Fig. 55c, the blue trend-line fit is estimated by taking into account the Mg# and Al_2O_3 (wt%) pairs of the two plateau regions. b-d) measured and inferred initial Mg# profiles. The inferred theoretical profiles are calculated based on the relations assessed by best fit of the linear trend-lines of Fig. 55a, c.

Timescale information has been extracted only from crystals showing concentration profiles suitable for diffusion modeling using one of the two approaches described above: for example, crystals with profiles belonging to zoning type VIII (Fig. 29h) have not been used for the modeling. Altogether, diffusion modelling has been applied on 25 crystals with 50 measured profiles of different Types (Table 5). All calculated timescales are shown in Fig. 57 where it should be borne in mind that timescales obtained using approach I are upper limits of residence times in the magmatic environment ME2, while those obtained using approach II are residence times themselves. As seen in the figure, most crystals were amenable to modeling using the relaxation of growth zoning approach I, while 10 profiles from 5 crystals, i.e. 2 profiles in mutually perpendicular directions, were suitable for modeling using approach II. All of the profiles modelled using approach II yielded timescales that were consistent with each other from the mutually perpendicular profiles. These timescales range between 38 and 68 years. Stratigraphically, two of these crystals come from members A1 and B1, respectively, and one from member D1. These results explain why diffusive modification can be seen in some crystals and not in others even though they are compositionally almost identical: some of these crystals have resided longer in the magma reservoir (ME2 environment). The implications of these results for the nature of the plumbing system are discussed in Chapter 7.

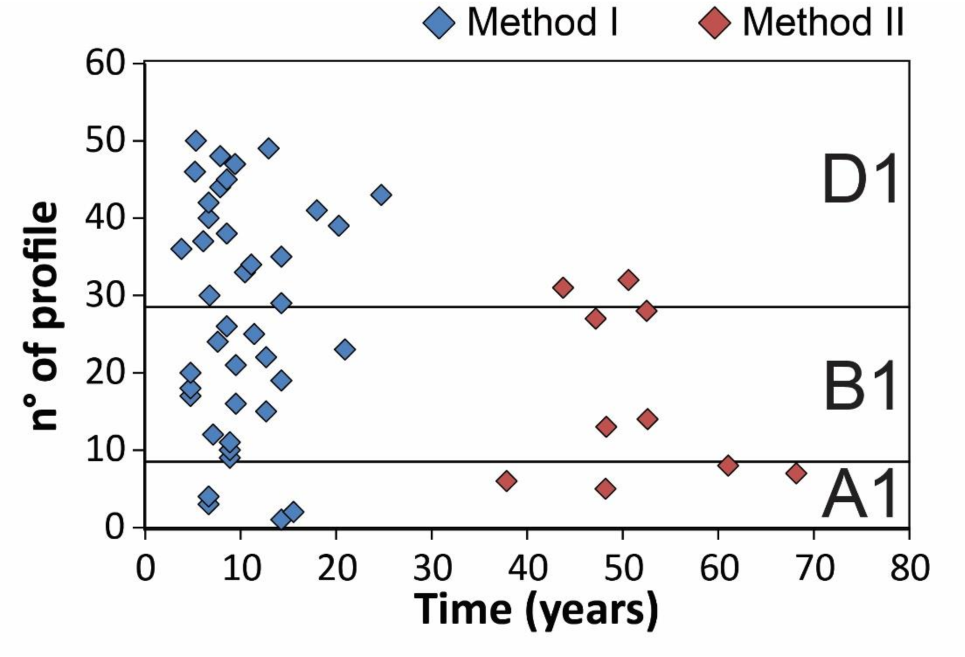

Fig. 57 Output values of times obtained by diffusion modeling on 50 out of 82 analyzed profiles on clinopyroxene crystals.

6.4 Zaro mineralogical disequilibria

Similarly to the A-MS clinopyroxenes, chemical equilibrium between minerals and their host rocks has been tested, also in order to apply geothermobarometry.

Based on the compositional dependence between a liquid and a coexisting mineral phase, the tests for equilibrium show the equilibrium field (comprised within the dotted lines in Fig. 58a-d), through the distribution coefficients (K_D), defined as the molar ratio between selected elements of the liquid divided by the molar ratio between the same elements of a coexisting mineral.

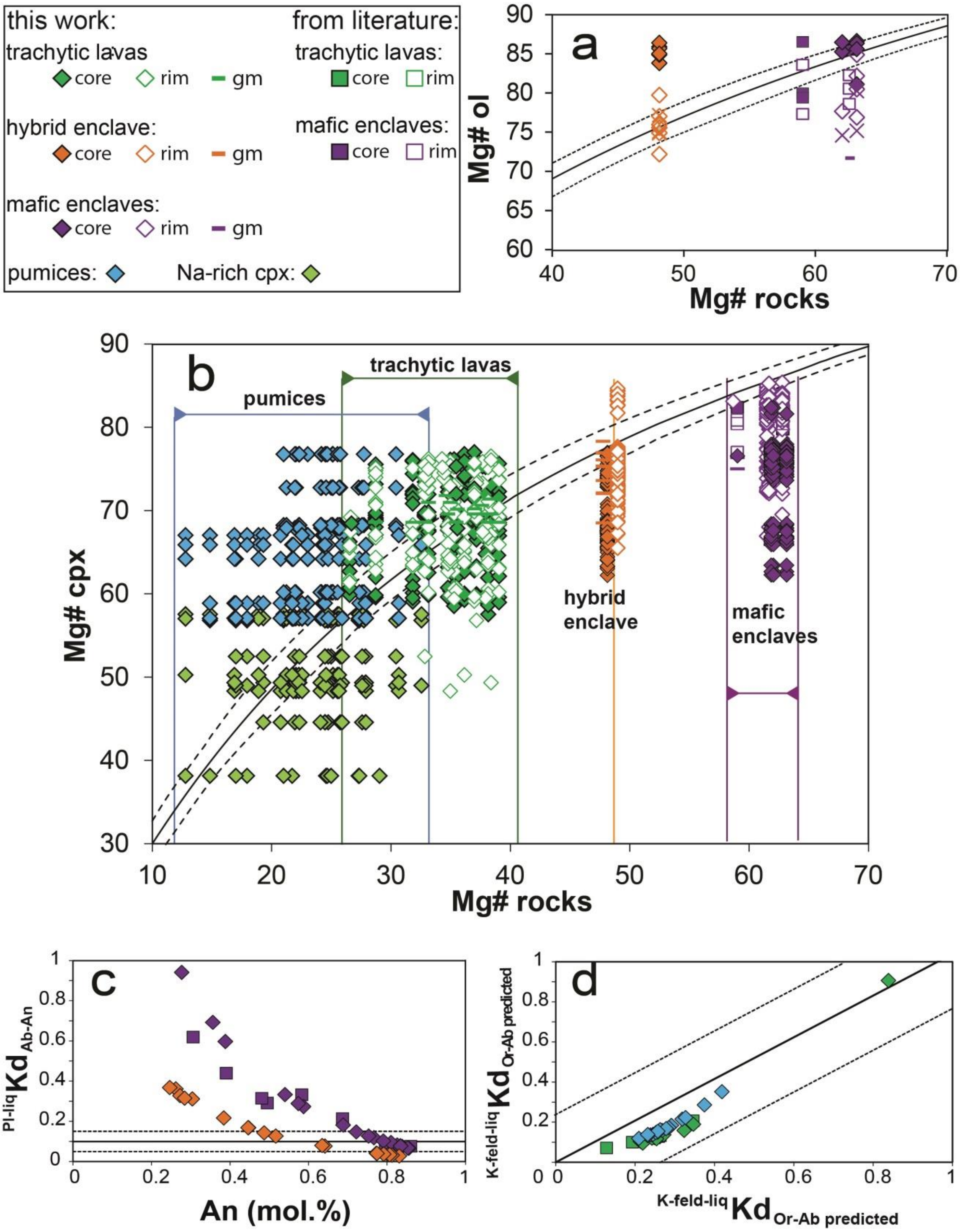

Fig. 58 Tests for equilibrium for olivine (a), clinopyroxene (b), plagioclase (c) and K-fledspar (d) crystals. (a) Fe-Mg partitioning between olivine and host rock ($^{Fe/Mg}Kd_{Ol-liq}$ = 0.30 ± 0.03;; Roeder and Emslie, 1970 ; Matzen et al., 2011); continuous line is $^{Fe/Mg}Kd_{Ol-liq}$ = 0.27; dotted lines = ± 0.03. (b) Fe-Mg partitioning between clinopyroxene and host rock ($^{Fe/Mg}Kd_{Cpx-liq}$ = 0.27 ± 0.03;

Grove and Bryan, 1983; Putirka et al., 2003; Mollo et al., 2013); continuous line is $^{Fe/Mg}Kd_{Ol\text{-}liq}$ = 0.30; dotted lines = ± 0.03. (c) variation diagram of An (mol%) vs calculated $^{pl\text{-}melt}Kd_{Ab\text{-}An.}$ The plagioclase-melt stability field was drawn using a value for $^{pl\text{-}melt}Kd_{Ab\text{-}An}$ of 0.1 (continuous line) ± 0.05 (dotted lines; Putirka, 2008). (d) $^{kfeld\text{-}liq}Kd_{Or\text{-}Ab}$ test for equilibrium based on Or-Ab exchange between K-feldspar and liquid (Mollo et al., 2015); the equilibrium field is inside the 1:1 line ± 0.25; gm= groundmass; in Fig. 58b rim= mantle and rim.

Given the published (K_D), only few olivines, ($^{Fe/Mg}Kd_{Ol\text{-}liq}$ = 0.30 ± 0.03; Roeder and Emslie, 1970; Matzen et al., 2011; Fig. 58a) and pyroxenes ($^{Fe/Mg}Kd_{Cpx\text{-}liq}$ = 0.27 ± 0.03; Grove and Bryan, 1983; Putirka et al., 2003; Fig. 58b) can be considered in equilibrium with their host rocks. In particular, the cores of olivines from mafic enclaves are in equilibrium with the host rock. The olivine cores from the hybrid enclave are xenocrystic, whereas the rim is in equilibrium with the host rock. Notably, most of clinopyroxenes from mafic enclaves have low Mg# and fall outside the equilibrium field; on the other hand, several clinopyroxenes of evolved rocks exhibit higher Mg# than expected if supposed in equilibrium with the host rocks (Fig. 58b). As to feldspar, most of the plagioclase phenocrysts, particularly those with An < 70 mol.%, plot outside the equilibrium range ($^{Plag\text{-}melt}Kd_{Ab/An} = Na_{Plag} * XAl_{liq} * XCa_{liq}/XCa_{Plag} * XNa_{liq} * XSi_{liq} = 0.1 \pm 0.05$; Putirka, 2008; Fig. 58c). Sanidine from trachytes is in equilibrium with its host rock (1:1 line of measured $^{K\text{-}feld\text{-}melt}Kd_{Or\text{-}Ab} = Na_{Feld} * XAl_{liq} * XCa_{liq}/XCa_{Feld} * XNa_{liq} * XSi_{liq}$ vs predicted $^{K\text{-}feld\text{-}melt}Kd_{Or\text{-}Ab} = -0.67+ (K_{liq}/K_{Feld}{}^{2} + \ln (\exp (K_{liq}{}^{2}/ Na_{liq} + K_{liq}) /10$; Fig. 58d) whereas several K-feldspars of mafic enclaves in the groundmass are in equilibrium with a much more evolved magma. The implications on disequilibrium are discussed in Chapter 7.4.

6.5 P-T crystallization conditions of Zaro minerals

In order to investigate the crystallization conditions of the Zaro clinopyroxenes, clinopyroxene-liquid thermometers and barometers specific for alkaline magmas (Masotta et al., 2013) have been used only for the points plotting in the theoretical equilibrium field of a liquid and a coexisting clinopyroxene (Fig. 58b). The equilibrium test shows that only clinopyroxenes with Mg#> 82 are in equilibrium with the composition of the mafic enclaves; having Mg#> 82, these crystals belong to ME0. The temperature estimated for this population ranges between 1142°C and 1092°C, with an average of 1120±11°C. Their pressure estimates range between 3.8 and 2.1 kbar, with an average of 3.1±0.4 kbar (Fig. 59).

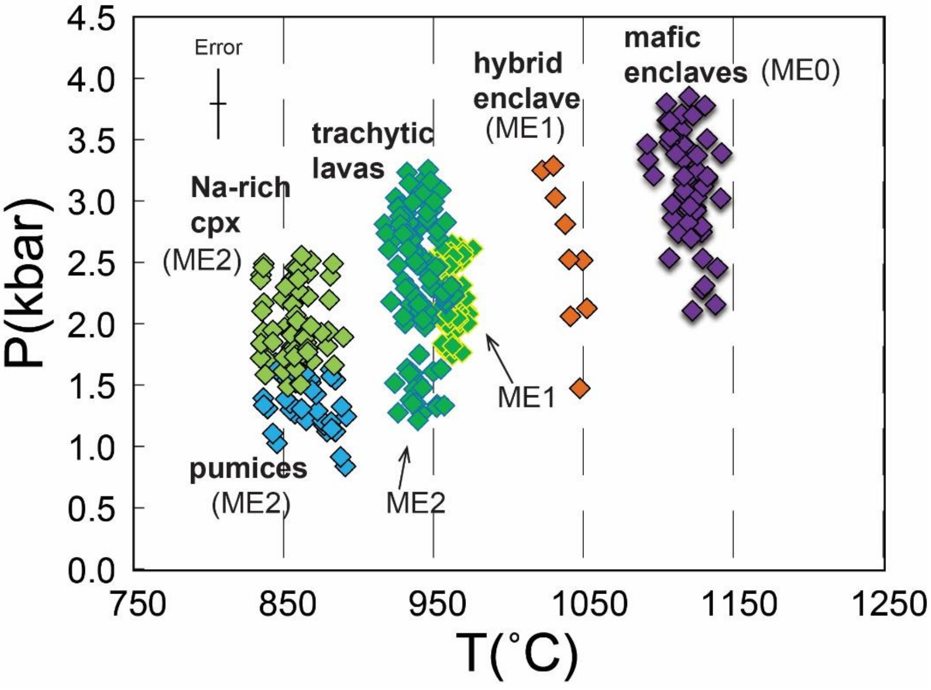

Fig. 59 Output temperatures and pressure estimates for the different magmatic environments of the Zaro clinopyroxenes obtained by the clinopyroxene-liquid thermometers (equation Talk2012) and barometers (equation Palk2012) specific for alkaline magmas (Masotta et al., 2013).

The ME0 clinopyroxenes from the hybrid enclave (Mg#>79), on the counterpart, are out of the equilibrium field. Only few clinopyroxenes, belonging to ME1, from the hybrid enclave are in equilibrium with its host rock (Fig. 58b). The output values of temperature of these crystals are in the range 1052-1022°C, with an average value of 1038±9°C, whereas the estimated pressure values are in the range 3.3-1.5 kbar, with an average value of 3±0.6 kbar (Fig 59). Several clinopyroxene crystals from trachytic lithotypes (Zaro lava and felsic enclaves) are in equilibrium with their host rocks (Fig. 58b). Moreover, it has been possible to discriminate the P-T crystallization conditions of clinopyroxenes belonging to ME1 and those of clinopyroxenes belonging to ME2. In fact, some of the ME1 clinopyroxenes which exhibit Mg# in the range 73-70 are in equilibrium with trachytic rocks (Zaro lava and felsic enclaves) with Mg# in the range 39-37. Also some ME2 clinopyroxenes with Mg# in the range 67-63 are in equilibrium with trachytic rocks which exhibit Mg# in the range 37-33. The estimated P-T condition are similar for the two populations: the output temperatures of ME1 clinopyroxenes of the trachytic rocks are in the range 976-947°C, with an average value of 962±6°C, whereas for ME2 clinopyroxenes of the trachytic rocks the values are in the range 963-917°C, with an average value of 930±10°C. The output pressures values of ME1 clinopyroxenes of the trachytic rocks are in the range 2.7-1.7 kbar, with an average value of 2±0.2 kbar, whereas the values of ME2 clinopyroxenes of the trachytic rocks are in the range 3.3-1.2 kbar, with an average value of 2±0.5 kbar (Fig. 59). Na-rich clinopyroxenes have Mg# in the range 52-48 and they are in equilibrium with pumice compositions that show Mg# in the range 22-19. The estimated temperature for these mineral-melt couples varies from 890 to 835°C, with an average value of 857±13°C. Their estimated pressures are in the range 2.6-1.5 kbar, with an average value of 2±0.3 kbar. Also the P-T crystallization conditions of clinopyroxenes from the pumices belonging to the Zaro pyroclastic deposit have been estimated. Clinopyroxene crystals with Mg# in the range 67-57, belonging to ME2, are in equilibrium with the trachyphonolitic composition of the pumices which exhibit Mg# in the range 32-24 (Fig. 58b). The estimated temperature values are the lowest detected for the Zaro products, being in the range 892-837°C, with an average value of 863±15°C. The estimated pressure ranges from 1.7 to 0.8 kbar, with an average value of 1±0.2 kbar (Fig. 59).

A part clinopyroxene-melt couples, other mineral-melt couples have been used to characterize the crystallization temperatures of Zaro minerals. In both cases, the volatile contents of melts in equilibrium with clinopyroxenes, which can affect the output T-P estimates, used as input parameters is the LOI (loss on ignition) detected in the whole rock compositions (Supplementary Material 2) of the Zaro lithotypes. A synoptic view of the whole estimated temperatures by using different mineral-melt couples is given in Fig. 60.

As shown before, few olivine cores of mafic enclaves are in equilibrium with the compositions of their host rocks and few olivine rims of the hybrid enclave are in equilibrium with the compositions of its host rock (Fig. 58a). The olivine-liquid thermometer of Putirka et al. (2007) has been used for these two set of couples. The output values of temperature of olivine from mafic enclaves are in the range 1132-1091°C, with an average value of 1109±11°C, hence very similar to the temperature range of clinopyroxene from mafic enclaves. The estimated temperatures of olivine rims from the hybrid enclave are in the range 1011-998°C, with an average value of 1007±4°C, thus, although slightly lower, the estimated temperature range is similar with respect of those estimated with clinopyroxene-hybrid enclave couples; however only 8 estimated values are available.

Moreover, feldspar-liquid thermometers (Putirka, 2005) have been used to estimates the crystallization temperature for the few plagioclase crystals in equilibrium with mafic and hybrid enclaves (Fig. 58c) and for K-feldspar crystals in equilibrium with trachytic lavas and pumices (Fig. 58d). Plagioclase-liquid thermometer yield temperature in the range 1154-1145°C, with an average value of 1152±2°C, for plagioclase crystals of mafic enclaves, and in the range 1080-1062°C, with an average value of 1076±6°C, for plagioclase crystals of the hybrid enclave (Fig. 60). These values are similar to the ranges of temperature estimated with clinopyroxene-liquid thermometer, for the respective lithotypes. The temperature estimates for K-feldspar of the trachytic lavas show a wide range, that is 1001-797°C, with an average value of 911±42°C. This range includes that of clinopyroxenes from the same lithotypes (Fig. 60). The temperature estimates for K-feldspar of the pumices are in the range 915-783°C, with an average value of 855±30°C, thus including the range of temperature estimated by using clinopyroxenes-pumices couples.

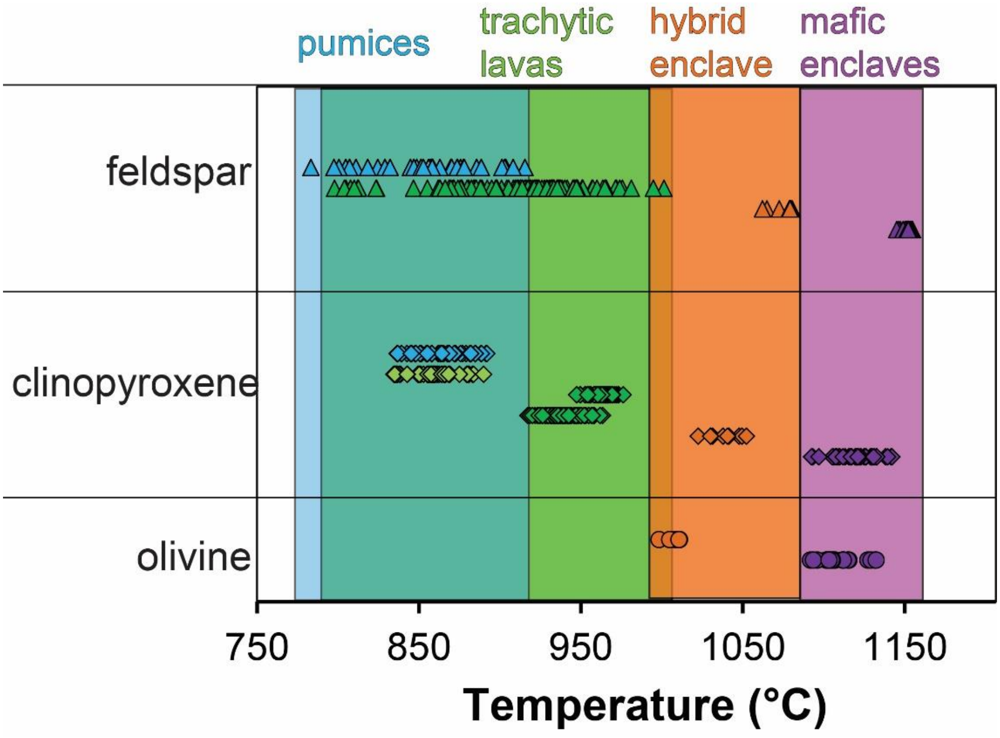

Fig. 60 Output temperature estimates for the different Zaro mineral phases obtained by olivine liquid barometer (Putirka et al., 2007; equation 22), clinopyroxene-liquid thermometer (Masotta et al., 2013; equation Talk2012), plagioclase-liquid thermometer (Putirka, 2005; equation 24) and K-feldspar-liquid thermometer (Putirka, 2005; equation 24).

6.6 Magmatic environments recorded in the Zaro clinopyroxenes

Similarly to what done for the A-MS clinopyroxene, the chemical variations recorded in compositional (e.g. Mg#) zoning patterns have been used to track the evolution of different populations of crystals through distinct magmatic environments in which they grew. The kinds of connections between the various magmatic environments recorded in the zoning patterns and their quantification are shown in the systems connectivity diagrams (Fig. 61).

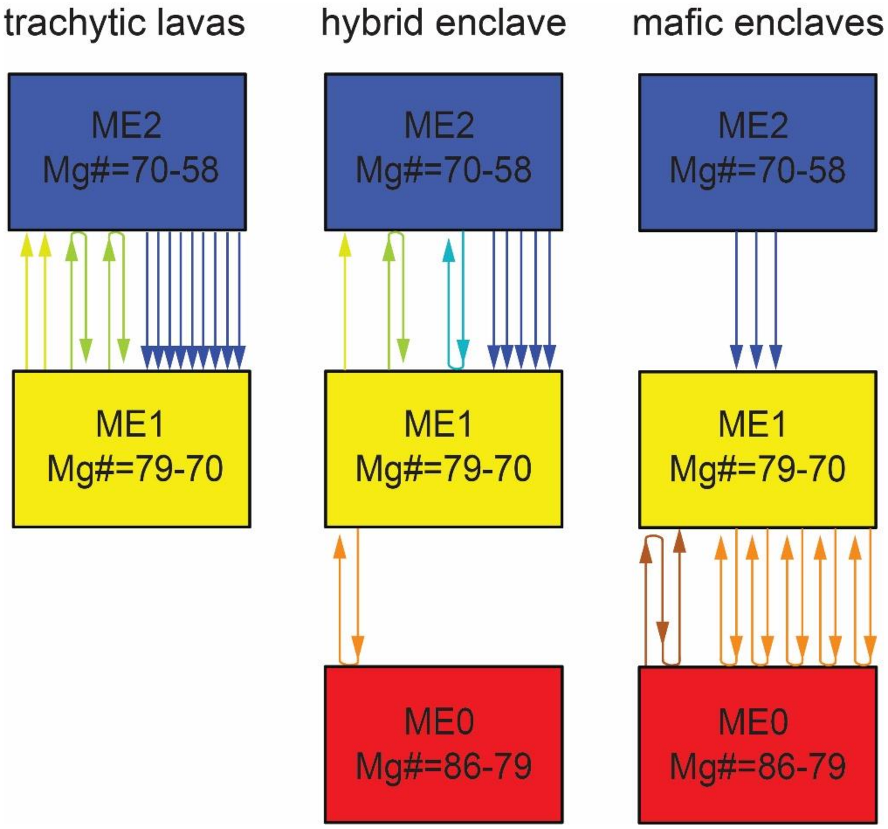

Fig. 61 Systems analysis of the zoning patterns of Zaro clinopyroxene crystals. Each box represents a magmatic environment. Each route/connection line indicates the composition of a crystal from core to rim; a single arrow represents the passageway of a crystal (or a magma in which the crystal was forming), from one magmatic environment to a different magmatic environment; a whole connection line (consisting of one or more arrows) represents the zoning type. The density of the connection lines can be used to infer the dominant passageways of crystals in different environments.

Despite the complex diversity of zoning patterns, certain evolutionary tracks are recurrent in the history recorded by the clinopyroxene populations. It can be noted that, apart few exceptions, most of the connections are characterized by the last passageway in ME1 environment: the latter represents the dominant composition of rims of most crystals from all the Zaro lithotypes (e.g. Fig 44c). The most frequent passageways are those from ME2 to ME1. This is the case for crystal cores with both ME2 and ME1 compositions, characterized by simple and complex zoning, respectively.

Substantial differences can be noted among the various Zaro lithotypes. First of all, in the trachytic lavas (Zaro lava and evolved enclaves), the interactions among the different magmatic environments do not include ME0, that represent the least evolved clinopyroxene compositions. In the trachytic rocks, most of the crystal cores have a ME2 composition converging toward ME1 (blue connection lines in Fig. 61). Crystals with a ME1 core composition showing complex zoning (green connection lines) tend toward ME1 in their rims as well. The connections among the magmatic environments in clinopyroxenes from the hybrid enclave show similarities with those of clinopyroxenes from the trachytic lavas, both as to kinds and frequency of the passageways. Nevertheless, here the connections involve also ME0. In clinopyroxenes of mafic enclaves, most of the connections concern ME0 and ME1, which are always in the form of reverse to normal zoning (orange connection lines in Fig. 61). Less frequent connections in the form of simple reverse zoning concern ME2 and ME1 in the mafic enclaves, too.

6.7 Diffusion modelling for the Zaro clinopyroxenes

Kinetic modeling of the diffusive modification of the zoning patterns provides information on the timescale of the magmatic processes occurred in the Zaro plumbing system. Similarly to the A-MS clinopyroxenes, the initial conditions depend, case by case, on the characteristics of the concentration profile shapes. The compositional plateau found in most profiles can be used to infer the initial profile shapes before diffusion occurred. Depending on the profile shapes, two different approaches for modeling have been used. It has been noticed that some crystals are characterized by compositional plateau and sharp gradients (zoning type I-a, type II-a, type III-a and type IV; Fig. 43), thus showing little evidence of diffusive modification of growth zoning. These profiles have been modeled in the same way used in method I for the A-MS clinopyroxenes: the relaxation of growth zoning timescales (e.g. see Chakraborty and Ganguly, 1991; Trepmann et al., 2004) has been calculated to infer maximum possible durations of the time spans that the crystals may have spent in a magmatic environment at a given temperature without perceptible diffusive modification of the profiles, within the analytical resolution of this study.

The remaining profiles (zoning type I-b, type II-ba, type II-b, type III-b and type V) show diffusive gradients and these have been modelled through method II, by fitting the observed profiles. This approach yields durations of residence of the crystals in a particular magmatic environment.

In both cases, solutions to the diffusion equation (1) (Chapter 6.3) are sought with an appropriate choice of initial and boundary conditions.

Different temperatures have been used for clinopyroxene crystals belonging to the chemically different Zaro lithotypes. By considering the averages of the output values obtained from the clinopyroxene-liquid thermometer, different temperatures should be used for the clinopyroxenes from the different rocks (Fig. 59). A temperature of 1120°C should be used for clinopyroxenes of the mafic enclaves, a temperature of 1038°C for the clinopyroxenes of the hybrid enclave and the average (951±6°C) of the output values of clinopyroxenes belonging to both ME1 and ME2, for clinopyroxenes of Zaro lava and felsic enclaves. Due to the large ranges of temperatures obtained through the various thermometers (Fig. 60), timescales for all the clinopyroxene crystals of the different Zaro rocks have been calculated at 950°C, 1050°C and 1100°C. This seems reasonable, since a temperature of 950°C is practically identical to the average value (951±6°C) of the temperature of clinopyroxenes of both Zaro lava and felsic enclaves, a temperature of 1050°C is similar to the average value (1038±9°C) of the temperatures of clinopyroxenes of the hybrid enclave, a temperature of 1100°C is similar to the average value (1120±11°C) of the temperatures of clinopyroxenes of mafic enclaves; the latter is slightly lower than the average, but it is still in the range 1142-1092°C.

The diffusion coefficient based on Fe–Mg interdiffusion rates in clinopyroxene (equation 2 in Chapter 6.3) obtained by Müller et al. (2013) has been calculated.

In the method I, the boundary conditions for these calculations may be either constant composition or no flux at the rims of crystals, with little difference in the results. Likewise the approach I used for the A-MS clinopyroxenes, the measured profiles are taken as the initial profiles. A forward modeling has been followed to obtain the maximum duration of thermal events by using a numerical method in which the time (t) term of the equation (1) has been varied until the modeled profile slightly oversteps the matching with the measured profile. Some examples of such modeled profiles are shown in Fig. 62a,c,e,g.

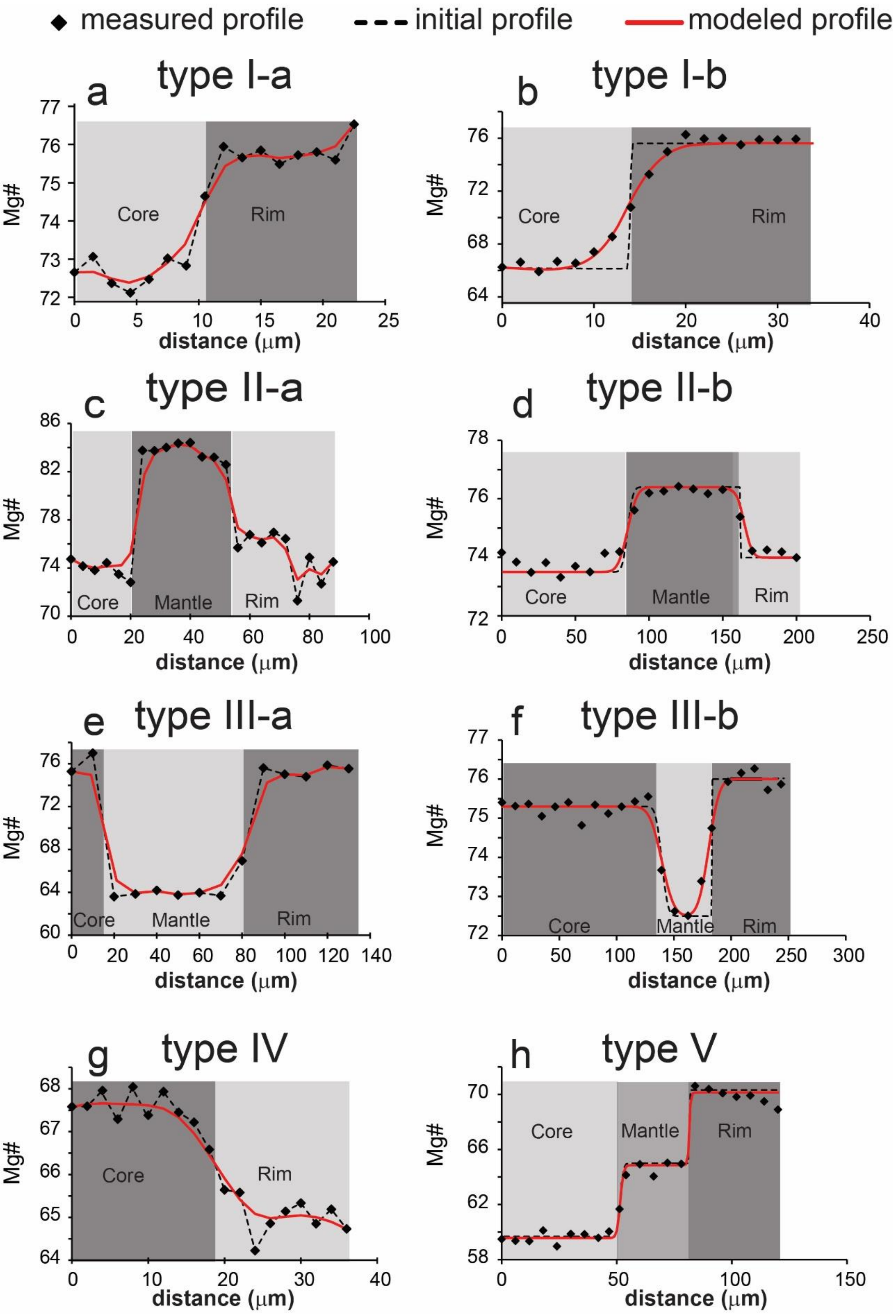

Fig. 62 Diffusion modelling for the Zaro clinopyroxenes. Black diamonds are measured analysis along the crystal traverses showing concentration profiles from core to rim [Mg# = molar $Mg^{2+}/(Mg^{2+} + Fe_{tot})$]. Black dashed lines indicate the initial profile shapes. In Fig. 62a,c,e,g the modelled profiles (red lines) show the permissible diffusive smoothing that a concentration gradient may have experienced; in Fig 62b,d,f,h, instead, the modelled profile (red line) indicates effective diffusive smoothing (see text for details).

In this case, the modelled profiles show the permissible diffusive smoothing that a concentration gradient may have experienced. Timescales on which the calculated profiles deviate measurably from the initial profiles are considered to represent the upper limits of residence times of crystals in a magmatic environment.

In the method II, on the other hand, it is necessary to define the shapes of the initial profiles and then model their diffusive modification. In this case, it is not possible to have a good constrain on the initial profile shape, by using relationships between fast and slow diffusive elements, such as in the case of the approach II used for the A-MS clinopyroxenes, because of the complex relations shown by these elements (e.g. Fig. 38). For this reason, the initial concentration profile is defined by a step-function zoning, in which the initial conditions are defined by the homogeneous measured concentration found at the core of crystals and the boundary conditions are defined by the homogeneous measured concentrations at the rim of crystals. This allows the evaluation of the evolution through time of the initial concentration profile that can be traced until the modeled profile fits the measured concentration profile.

In both approaches, timescales information has been extracted only from crystals showing concentration profiles suitable for diffusion modelling: crystals having a zoning type II-ab, which exhibit a sharp variation between the core and mantle plateau and a gradual variation between the mantle and the rim plateau, have not been used. Moreover, profiles in which the spacing between analytic points is large (e.g. 15 μm -25 μm -50 μm -70 μm) have not been used.

Furthermore, it has been possible to discern 1) the timescales of all the zonation events which affected the crystal: in this case, the measured Mg# profile has been sequentially modeled from core to rim, and 2) the timescales of the Mg# variation relating to the last growth event and subsequent diffusional modification. All the resulting timescales are reported in Table 6.

Table 6

Lithotype	cpx	transect	T (°C)	Method I (entire zoning)	Method I (last step)	Method II (entire zoning)	Method II (last step)
Zaro lava	cpx5	line1	950	2.9			
	cpx6	line1	950	3.9			
	cpx7	line1	950			4.3	
		line2	950			4.3	
		line3	950				1.1
	cpx8	line1	950			12.4	
		line2	950			18.3	
	cpx9	line1	950			10.5	
	cpx11	line1	950	3.9			
			950				
felsic enclaves	cpx1	line1	950			20.6	
		line2	950			25.1	
	cpx2	line1	950				20.3
	cpx3	line1	950			20.3	
		line2	950			23.1	
hybrid enclave	cpx1	line1	1050	2.3			
		line2	1050		0.2		
	cpx2	line1	1050			5.4	
		line2	1050				1.8
	cpx3	line1	1050		1.2		
	cpx4	line1	1050			7.0	
	cpx5	line1	1050			2.7	
	cpx6	line1	1050			4.0	
	cpx8	line1	1050		0.6		
	cpx9	line1	1050			1.1	
	cpx10	line1	1050	1.1			
	cpx11	line1	1050			1.7	

mafic enclaves	cpx1	line1	1100	0.2		
		line2	1100	0.2		
		line3	1100		7.2	
	cpx3	line1	1100			1.7
		line2	1100			1.1
	cpx4	line1	1100	0.5		
		line2	1100	0.4		
	cpx8	line1	1100		0.8	
		line2	1100		0.4	
	cpx9	line1	1100		3.6	
		line2	1100			0.9

Table 6 Timescale estimates for Zaro clinopyroxene crystals derived from Fe-Mg diffusion modeling across selected transects, calculated with different temperature, depending on the lithotypes.

As for the timescales of the entire zonation events (Fig. 63), 6 out of 13 crystals of the Zaro lava have been modeled at 950°C: the obtained ages are in the ranges 3.8-2.8 years for profiles modeled by using method I and 18-4.3 years for profiles modeled by using method II. 3 out of 3 crystals belonging to the felsic enclaves have been modeled at 950°C by using method II and the obtained ages are in the range 25-20 years. 10 out of 11 crystals belonging to the hybrid enclave have been modeled at 1050°C: the obtained ages are in the ranges 2.3-1.1 years for profiles modeled by using method I and 7.3-1.1 years for profiles modeled by using method II. 5 out of 9 crystals belonging to the mafic enclave have been modeled at 1100°C by using method II and the obtained ages are in the ranges 7.2-0.4 years.

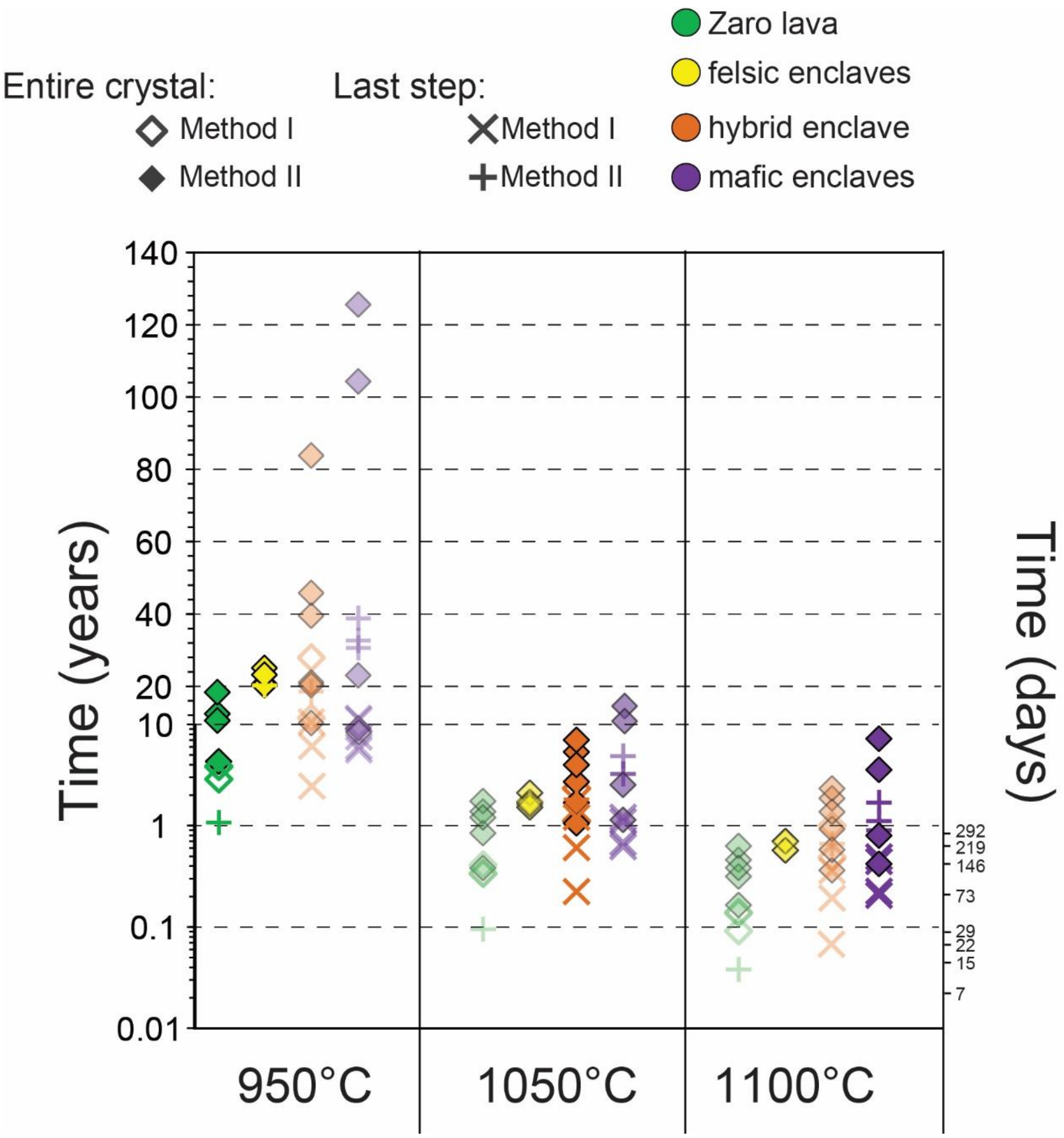

Fig. 63 Output values of times obtained through diffusion modeling on the analyzed profiles of the Zaro clinopyroxene crystals by using different temperatures. Timescales calculated from all the suitable profiles by arbitrarily using all the temperatures are also reported (transparent colored symbols; see Chapter 7.6 for details)

The Mg# profiles of transects crosscutting the boundary between the two most external plateau compositions of the crystals have been also used in order to obtain timescales related to the last growth event and subsequent diffusional modification that affected the Zaro clinopyroxenes. 1 out of the 6 suitable crystals of the Zaro lava has been modeled at 950°C by using method II and the obtained age is 1 year. 1 out of the 3 suitable crystals belonging to the felsic enclaves has been modeled at 950°C by using method II and the obtained age is 20 years. 2 out of the 10 suitable crystals belonging to the hybrid enclave have been modeled at 1050°C: the obtained ages are 438 - 81 days for profiles modeled by using method I and 1.8 years for profiles modeled by using method II. 2 out of the 5 suitable crystals belonging to the mafic enclave have been modeled at 1100°C: the obtained ages are in the ranges 162-72 days for profiles modeled by using method I and 1.7 years-329 days for profiles modeled by using method II.

The timescales obtained using method I represent upper limits of residence times in the various magmatic environments; as for the sequence of events relating to the entire zoning pattern, these range between 3.8 and 1.1 years. The timescales obtained using method II are residence times themselves. These range between 25 and 0.4 years, for the sequence of events relating to the entire zoning pattern (Fig. 63). Timescales obtained by modeling the Mg# profiles of transects crosscutting the boundary between the two most external plateau compositions of the crystals refers to the last event which created the zoning. Timescales obtained with method I ranges between 1.2 years and 72 days, whereas those obtained with method II range between 20 years and 329 days. All of the modeled profiles yielded timescales that were consistent with each other by using different temperatures as input parameter in the calculation of the diffusion coefficient (2), subsequently used to apply kinetic modeling on clinopyroxenes belonging to different Zaro rocks. The implications of such results are discussed in Chapter 7.6.

7. DISCUSSIONS

7.1 The magmatic plumbing system of Agnano-Monte Spina eruption

Taking into account the composition and temperature, the magmatic environment ME0, found in the A-MS clinopyroxene, can be associated with primitive magmas, especially for the high Mg# (> 91), while ME2 is ascribable to a crustal stationing layer of the Campi Flegrei magmatic system (see Chapter 3), in which clinopyroxenes with Mg# 78-72 formed. The composition of the ME2 population is the most widespread, making up the 89 % of the homogeneous clinopyroxenes as well as the final, rim compositions of almost all (98 %) zoned crystals (Fig. 27a; Table 1). On this basis it is reasonable to interpret the ME2 environment as the physical reservoir in which most of the magmatic interaction(s) leading to eruption took place. The chemical composition of environment ME3, more evolved with respect to ME2, has been found in only 3 out of the total 41 analyzed crystals; hence ME3 could represent the most evolved, less-abundant portion of the ME2 magmatic reservoir. Therefore, the history recorded in the A-MS clinopyroxene chemical compositions may be read as: one or more inputs of mafic magma(s) (ME0), originating from partial melting of the mantle, refilled a crustal reservoir already hosting a more evolved resident magma (dominantly ME2, minor ME3) and consequent formation of intermediate compositions (ME1) were caused by mingling of ME0 and ME2 melts. The isotopic disequilibrium between several A-MS mineral phases and their host rocks (Fig. 34), as already reported in the literature (de Vita et al., 1999; Arienzo et al., 2010), supports such a mixing/mingling process. A schematic diagram that illustrates the behavior of such a plumbing system is shown in Fig. 64.

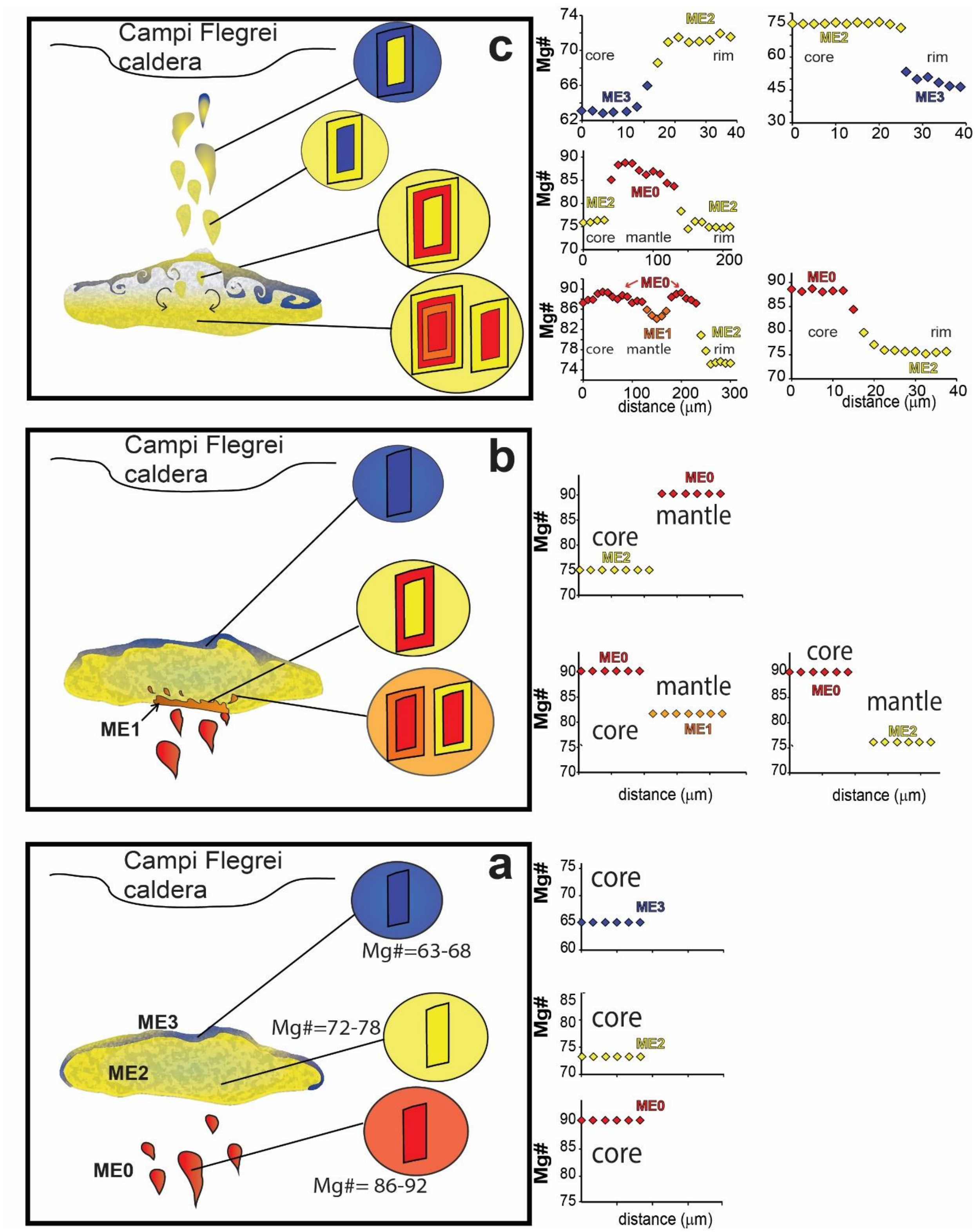

Fig. 64 Schematic sketch illustrating the magmatic processes occurred in the A-MS plumbing system. a) three distinct magmatic environments there were at a T = 0: one (ME0), in red, in which core of clinopyroxenes with high Mg# (92-85) were formed, is associated with primitive magmas; an environment (ME2), in yellow, ascribable to a crustal stationing layer of the Phlegraean magmatic system, in which core of clinopyroxenes with Mg#78-70 were formed and an environment (ME3), in blue, identifiable with a less abundant, most differentiated magma portion of the ME2 reservoir. b) The interaction between ME0 and ME2 explains

the normal zoning for clinopyroxenes of ME0 and, conversely, the reverse zoning for clinopyroxenes of ME2, leading also to the formation of intermediate compositions (ME1). c) The interaction between ME2 and ME3 justifies the whole set of observed zoning patterns in the A-MS clinopyroxene.

Since the whole rock and glass composition of A-MS products ranges from trachyte to phonolite, the amount of mafic magma that might have interacted with the evolved resident magma(s) must have been limited. This is also supported by the correlations between major or trace elements and Sr-isotopes of the analyzed A-MS products, which have been modeled using a binary mixing equation (Langmuir et al., 1978). The magmatic components commonly used (e.g. Arienzo et al., 2016) to explain the chemical and isotopic variability of CF magmas erupted during the last 5 ka have been taken into account. Mixing between Astroni 6-like magma, a more radiogenic, more evolved NYT-like magma and the least radiogenic, least evolved Minopoli 2-like magma, may account for the detected chemical and isotopic variability of the A-MS rocks. The calculated mixing curves (Fig. 65) are able to reproduce the Sr-CaO-composition and Sr-isotopic ratios measured on A-MS rocks. Moreover, these models allow inferring that the amount of mafic magma (e.g. Minopoli 2) must have been limited.

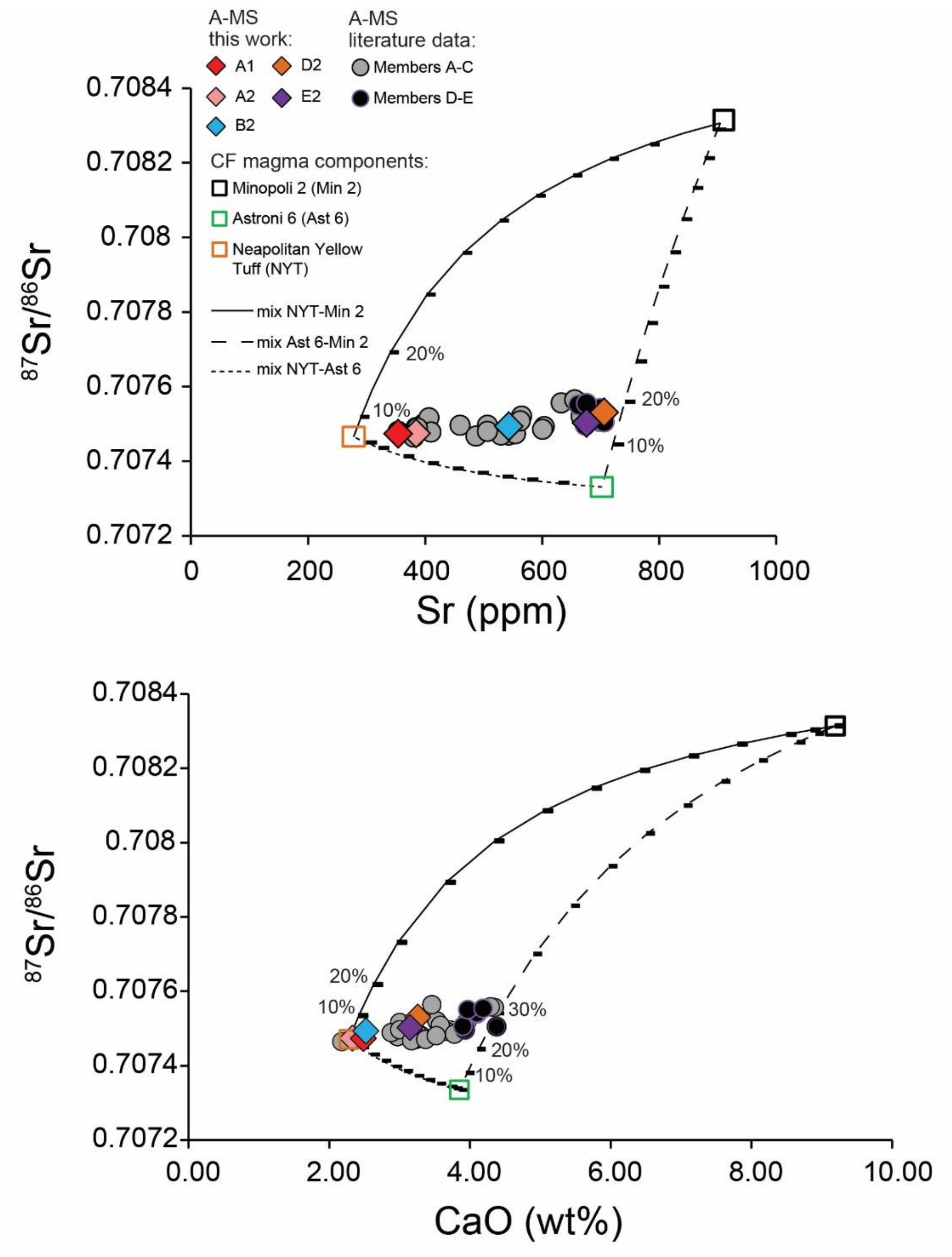

Fig. 65 Modeling of the Sr–Nd isotopic features of the A-MS rocks, by assuming mixing among the Astroni 6 (Ast-6), Neapolitan Yellow Tuff (NYT) and Minopoli 2 (Min 2) magmatic components. Literature data are from D'Antonio et al. (1999), de Vita et al. (1999), Tonarini et al. (2009) and Di Renzo et al. (2011).

This is in good agreement with what already suggested by Arienzo et al. (2010), who modeled the mixing process and proved that less than 10% of a mafic magma with average $^{87}Sr/^{86}Sr \approx 0.70754$ mixed with an evolved one with average $^{87}Sr/^{86}Sr \approx 0.70749$ would explain the occurrence of melt inclusions with less differentiated composition in the A-MS clinopyroxenes. Such a hypothesis also explains the Sr-isotopic signature of the analyzed A-MS rocks and minerals: both matrix-glass and clinopyroxene crystals from the D-E members, which show a less evolved composition with respect to those from A-B members (Fig. 33; Table 1 in Supplementary Material 1), are characterized on average by ^{87}Sr/^{86}Sr values higher than those of whole rocks and clinopyroxenes from A-B members (Fig. 34; Table 7 in Supplementary Material 1). Moreover, the ^{87}Sr/^{86}Sr values of feldspars from all the A-MS members are in the range of that of whole rocks and glasses from members A-B (Fig. 34); such a Sr-isotopic ratio is the typical Sr-signature of the evolved Campi Flegrei magma component (e.g. Neapolitan Yellow Tuff) identified by Arienzo et al. (2016). Since this is the most evolved magma component, it can be associated with our ME2 and ME3, while the more mafic magma could be represented by our ME0. This kind of mixing behavior is consistent with the nature of the clinopyroxene population as well, where ME0 and ME1, that represent the mafic magma, are statistically far less abundant than clinopyroxenes with ME2 composition.

The hypothesized mixing process is also consistent with the observed chemical zoning patterns in the clinopyroxenes. Injection of ME0 mafic magma into the ME2 environment/physical reservoir would produce crystals with cores of ME0 composition (Mg# 92-85) and rims of ME2 composition (Mg# 78-70) as shown by the most common Type I zoning pattern. Mixing of these two melts would produce a magma with intermediate composition, from which clinopyroxenes of composition ME1 (Mg# 84-80) might have grown, as testified by the somewhat less common Type VII and Type VIII zoning patterns. Oscillations between these compositions (e.g. Type VII) would suggest long lasting connectivity between the reservoirs such that crystals may be transferred from one environment to another, sometimes back and forth. Moreover, since ME3 has been found only in member B1, it probably represents the most evolved least-abundant portion of the A-MS magmas erupted during the first Plinian phase of the eruption.

Based on the above, it is possible to hypothesize that batches of high temperature (ca. 1100 °C) mafic magma (ME0) with primitive composition, i.e. very high Mg#, low Ti, Al and Na, arrived in a magma reservoir (Fig. 64a) where they partially mixed with a pre-existing more evolved magma (ME2), leading to the formation of intermediate compositions (ME1; Fig. 64b). The mafic input could have caused perturbation in a zoned reservoir and promoted interaction between the chemically different magmatic portions (ME2-ME3; Fig. 64c).

Furthermore, as a greater number of high Mg# core crystals are present in D1 compared to A1 and B1 members, it is plausible that the magma which led to the eruption of the second main fallout deposit (D1) was dominated by the mafic component. This could occur, for example, if the first phase of eruption (A-B) considerably emptied out the ME2 reservoir and a more direct connection was established between the eruptive conduit and the ME0 reservoir (likely deeper, although good barometric constraints are not available; see Chapter 7.7 as well).

7.2 Timescales of processes in the Agnano-Monte Spina plumbing system

Diffusion modeling of the chemical zoning profiles provides temporal constraints on magmatic processes. The occurrence of plateau can be interpreted as a result of crystal growth in different, stable magmatic environments, with residence times in each environment long enough to be recorded by crystal growth, but also short enough that the compositional gradient has not been erased by diffusional equilibration. Overall, the plumbing system that led to the A-MS eruption appears to have been active on decadal timescales. Most types of zoning patterns observed in the clinopyroxene crystals show little or no evidence of diffusive modification at the spatial resolution at which the compositions were studied in this thesis. This allows an upper limit to the duration of their residence in the ME2 magmatic reservoir to be placed, on the order of 10 – 15 years for the majority of the crystals. For a few crystals, a longer time range may be permissible. More specific constraints are provided by a small subset (5) of crystals that record diffusive modification. These indicate that a timescale of ca. 40 – 70 years elapsed between the entrapment of the ME0 crystals into the ME2 reservoir and the eruption. The rarity of such crystals, and the fact that back-and-forth transmission between ME0 and ME2 is recorded (see previous section and Fig. 61), suggest the following scenario: a long lived connectivity existed between the ME0 and ME2 environments over several decades such that crystals could be transferred back and forth, with a few crystals residing in the ME2 reservoir for several decades, until the extent of ME0 magma input increased considerably, as recorded by the major population of zoned crystals, within 10 – 15 years before the eruption.

Fig. 64 also explains the systematics of zoning pattern shown in Table 1 and Fig. 61. At the start of the eruption (member A), likely triggered by increased input of mafic magma, crystals from the main ME2 reservoir with cores of ME0 and rims of ME2 are erupted. Subsequently, as the reservoir is gradually emptied, more and more crystals with cores of ME2, mantles of ME0-ME1 and rims of ME2 are erupted (member B). At this stage, increased degassing may have produced more ME3 crystals as well. With progressive eruption, magma from the deeper, less evolved reservoir makes its way directly to the surface, with an increased contribution of less evolved melts as well as clinopyroxene crystals (member D). In the course of the eruption then the ME2 reservoir was partially or completely emptied, establishing a direct link between the more primitive environment and the eruptive conduit during the later stages of the eruption (i.e. D1).

7.3 Magmatic components in the Zaro magmatic system: a comparison with Procida and Ischia mafic rocks and implications for the feeding systems

The Zaro mafic enclaves are among the few poorly evolved igneous products of the whole Phlegraean Volcanic District, although some of them are intermediate in terms of silica content. They display major and trace elements, and especially isotopic similarity with high-Mg, K-basaltic scoriae and lithic lava fragments dispersed within the hydromagmatic tuff of the Solchiaro eruption from Procida Island (ca. 22 ka; Morabito et al., 2014). These lava fragments are alkaline, nepheline normative K-basalts with shoshonitic affinity, and show near primary characters (MgO up to 11 wt.%, Ni up to 200 ppm, Cr up to 500 ppm), representing the least-evolved magma of the whole PVD (D'Antonio et al., 1999a). Mazzeo et al. (2014) demonstrated that the Procida primitive melts were produced by partial melting of an amphibole/phlogopite-bearing enriched source derived from addition of slab-derived components (subducted melt and fluid from the Tethys Ocean) to an enriched MORB-like mantle wedge. Having $^{87}Sr/^{86}Sr$ in the range 0.70505-0.70515 and $^{143}Nd/^{144}Nd$ from 0.51270 to 0.51275, these products are similar to the Zaro mafic enclaves, which in comparison exhibit slightly less radiogenic Sr and more unradiogenic Nd signatures.

$\Delta^{18}O$ isotopic composition of whole rocks and separated minerals from Zaro lava, felsic and mafic enclaves and from the products of other eruptions from the Neapolitan area, have been recently published by Iovine et al. (2018). Even in terms of O-isotopic composition, the olivine from Procida mafic lithics (6.27-6.38 ‰; Iovine et al., 2018) is comparable to the olivine from the Zaro mafic enclaves (6.43 ‰). A mass balance calculation (Table 1 in Supplementary Material 5) suggests that Zaro mafic magmas could have been derived from ca. 50 % fractional crystallization of a primitive magma having the composition of Procida K-basaltic lithic fragments. Starting from a parental magma represented by Procida mafic whole rocks (D'Antonio et al., 1999a), the removal of a mineral assemblage, made up of 7 % of olivine (Fo_{86}), 23% of clinopyroxene ($Wo_{47}En_{45}Fs_{8}$), 16% of plagioclase ($An_{83}Ab_{16}Or_{1}$) and 3 % of Ti-magnetite, matches well ($\Sigma R^2 = 0.21$) the composition of the Zaro mafic enclaves.

The Zaro trachytes show Sr- and Nd-isotopic compositions ($^{87}Sr/^{86}Sr > 0.70607$ and $^{143}Nd/^{144}Nd < 0.51257$) significantly different compared to the mafic enclaves ($^{87}Sr/^{86}Sr < 0.70505$ and $^{143}Nd/^{144}Nd > 0.51267$). Thus, a simple fractional crystallization process appears to be unlikely. In order to establish a genetic link between mafic and felsic Zaro magmas (mafic enclaves and trachytes, respectively), a process of crustal assimilation, able to change the isotopic signature, has been hypothesized. The EC-AFC (energy-constrained assimilation plus fractional crystallization; Spera and Bohrson, 2001) process has been modeled to explain the evolution of Zaro lava and felsic enclaves (Sr = ~150 ppm; $^{87}Sr/^{86}Sr > 0.7060$; Nd = ~55 ppm; $^{143}Nd/^{144}Nd = 0.51255$; $\delta^{18}O > 5.5$ ‰; Iovine et al., 2018) starting from a parental magma with isotopic and chemical composition of the mafic enclaves (Sr = 519 ppm; $^{87}Sr/^{86}Sr = 0.7050$; Nd = 55 ppm; $^{143}Nd/^{144}Nd = 0.51268$; $\delta^{18}O = 5.19$ ‰). The results (Table 2 in Supplementary Material 5) suggest that such an open-system process can be ruled out because, assuming a granodiorite crust as the local deep basement, as suggested by many authors (Pappalardo et al., 2002b; Di Renzo et al., 2007; D'Antonio et al., 2013; Gebauer et al., 2014; Mazzeo et al., 2014), it would require more than 24 % of the assimilant. Such a high percentage is completely unrealistic because it would imply drastic changes in the chemical composition of the evolved lavas (e.g., towards a metaluminous composition). Therefore, the mafic enclaves cannot represent the parental magma from which the Zaro trachytes evolved; hence two distinct components with different origin must have fed the Zaro magmatic system. At Ischia, besides the Zaro mafic enclaves, mafic components have been found in products of recent eruptions (< 3 ka) resulting from interaction between chemically and isotopically distinct batches of magma (Cava Nocelle, Vateliero, Molara and Arso eruptions; Piochi et al., 1999; D'Antonio et al., 2013; Iovine et al., 2017b). These products, latitic to trachytic in composition, were emplaced in different zones of the island, mostly located in the eastern sector. Among these products, the mafic ones show compositional features comparable to those of Zaro mafic enclaves: Cava Nocelle and some Molara whole rocks are shoshonitic to latitic in composition; glass in olivines and clinopyroxenes from Vateliero Tephra show trachybasalt to shoshonite compositions (D'Antonio et al., 2013; Moretti et al., 2013). Despite the chemical similarities, the isotopic compositions of Zaro mafic enclaves are completely different from those of all the other products, as well as those of olivine: the Zaro olivines have $^{87}Sr/^{86}Sr$ ratios from 0.70485 to 0.70493 while those of the other < 3 ka eruptive centers of Ischia vary from 0.7062 to 0.7068. Also, the $\delta^{18}O$ values of olivines from Zaro mafic enclaves is slightly higher (6.43 ‰) than that of olivines from all other < 3 ka products. These isotopic differences between magmas with similar degree of evolution can be explained by either different mantle sources or open system shallow evolution processes.

On the other hand, the whole-rock Sr isotope compositions of Zaro lava and felsic enclaves (Fig. 52) are similar to the lowest values recorded by the Cava Nocelle, Vateliero and Molara products ($^{87}Sr/^{86}Sr$ ranging from 0.7061 to 0.7064), while Arso lavas are more enriched in radiogenic Sr (0.7063-0.7066). The $^{87}Sr/^{86}Sr$ values of feldspars from all Zaro facies, on the other hand, overlap those of feldspars from the other < 3 ka Ischia products, but show a narrower range. Previous works (D'Antonio et al., 2013; Iovine et al., 2017b) explained the isotopic signature of Cava Nocelle, Molara, Vateliero and Arso products through modeling an open-system evolution process in which primary magmas (Sr = 500 ppm; $^{87}Sr/^{86}Sr = 0.7063$), derived from an enriched mantle source previously modified by the addition of 0.5-2.5 % subducted sediments, assimilate a maximum of ~7 % of granodiorite crust. Here similar evolution processes can be hypothesized for the magma(s) leading to the formation of Zaro lava and felsic enclaves. Thus, the Zaro trachytes, similarly to the products of the Ischia eastern sector, may result from the evolution of a mafic magma already enriched in radiogenic Sr and unradiogenic Nd by source processes and later arrived in a shallower magma chamber. Mafic enclaves instead, being depleted in radiogenic Sr and unradiogenic Nd, could derive from a less enriched source, similar to the one that generated the Solchiaro melt at Procida, in which the Sr- and Nd- signature was less considerably modified. Probably, the magma that generated the mafic enclaves has changed its isotopic signature very little in the upper crust, suggesting that this magma stationed for a short time at a mid-low storage region, as also suggested for Solchiaro mafic magmas (Moretti et al., 2013; Perinelli et al., 2019; Bonechi et al., 2020). Ascent and emplacement of magmas at shallower depth, where they evolve to trachyte and phonolite, could be controlled by the intersection of NE-SW transverse and NW-SE normal regional fault systems (Acocella and Funiciello, 2006; Moretti et al., 2013). In the PVD, slightly differentiated magmas, i.e. shoshonite and latite, have been erupted mostly by vents located along faults of the NE-SW system (Arso, Vateliero and Cava Nocelle eruptions at Ischia, and Minopoli and Fondo Riccio eruptions at Campi Flegrei). Conversely, the Procida volcanic field has erupted relatively small volumes of mainly poorly evolved magma (K-basalt to shoshonite) through vents aligned along faults of the NW-SE transfer system (Moretti et al., 2013). The latter are the prevailing, although not the sole, tectonic lineaments affecting the Zaro peninsula. These structures can be responsible for the uprising of a small volume of mafic magma in an area characterized by a high vertical permeability, just as hypothesized for the Procida feeding system. At Zaro peninsula, as well as in the eastern sector of Ischia, the presence of such deep tectonic structures can justify the emission of mafic magmas; in all other sectors of the island these deep structures are lacking and fast rising of mafic magmas does not occur.

7.4 Mineralogical and isotopic disequilibria

Chemical disequilibrium between mafic and felsic mineral phases, and between them and host rocks at Ischia, particularly for the last eruptive phase (< 3 ka), is well documented (Di Girolamo et al., 1995; Piochi et al., 1999; D'Antonio et al., 2013; Iovine et al., 2017b). Similar disequilibria occur in the investigated Zaro products. As previously shown (Fig. 58a), olivine cores from the hybrid enclave are xenocrystic, whereas the rims of phenocrysts and the microcrysts of the groundmass are in equilibrium with the host rock; this implies that cores of olivines were probably inherited from a more mafic magma and have grown later in a more evolved one.

Most of clinopyroxenes from mafic enclaves have low Mg# and fall outside the equilibrium field (Fig. 58b); on the other hand, most of clinopyroxenes of evolved rocks exhibit higher Mg# than expected if supposed in equilibrium with the host rocks.

Similar observations concern the feldspars of Zaro mafic and hybrid enclaves. Most of the plagioclase phenocrysts, particularly those with An < 70 mol.%, plot outside the equilibrium range (Fig. 58c), whereas several K-feldspars of mafic enclaves in the groundmass are in equilibrium with a much more evolved magma.

Another indication of disequilibrium is the frequent reverse zoning of clinopyroxenes from both trachytes and less evolved lithotypes: 83% of crystals show a reverse zoning (section 5.2.2; Fig. 38; Fig. 61), that can be simple or complex. Similarly, plagioclase crystals are reversely zoned (e.g. Fig. 1f in Supplementary Material 2) and most plagioclase phenocrysts from mafic and hybrid enclaves show a sieve texture (Fig. 35g), commonly interpreted to represent open-system processes (Streck, 2008).

These features suggest that many of these minerals (outside the equilibrium field) crystallized from magmas different from that represented by the host rock. Since equilibrium tests have well known limits (e.g. Matzen et al., 2011; for example, K_D values are also temperature and pressure dependent) mineral-melt equilibrium has been also tested through Sr-isotopic data. Notwithstanding the partial chemical disequilibria observed in several clinopyroxenes from trachytes (Fig. 58b), they show isotopic values similar to those of their host rocks (Fig. 52). Similarly, mafic enclaves have olivine containing melt inclusions featured by $^{87}Sr/^{86}Sr$ ratios like those of the host rocks suggesting mineral-melt isotopic equilibrium; clinopyroxene and feldspar from this lava facies, instead, show $^{87}Sr/^{86}Sr$ values higher than those of their host rock. $^{87}Sr/^{86}Sr$ ratios of feldspars from mafic enclaves are similar to those of the trachytic rocks, while not all the clinopyroxenes show $^{87}Sr/^{86}Sr$ values within the range of trachytes (Fig. 52). These characteristics suggest that clinopyroxene and feldspar of mafic enclaves were inherited at least partly from magma(s) with Sr isotopic ratio higher than that of host magma.

7.5 Magmatic processes inside the Zaro plumbing system

Mafic enclaves hosted in the Zaro lava flows show an ellipsoidal shape, cuspate margins (Fig. 21e), a high grain size variability of the groundmass (Fig. 35b-c), occurrence of chilled margins (Fig. 35d), segregation vesicles (Fig. 35b) and inter-fingering with the trachytic host lava (Fig. 35e; Fig.

1c in Supplementary Material 2). All these textural features provide evidence of a magmatic origin: presumably, these mafic inclusions were in a partially molten state when they were incorporated in the trachyte. Additionally, they hardly have been entrapped and transported as lithic clasts during the lava flowing, as they are not engulfed within the pyroclastic deposit outcropping below the Zaro lava complex.

Moreover, most of clinopyroxenes from mafic enclaves are in chemical disequilibrium with the hosted liquid and show an isotopic range (0.7056-0.7058) intermediate between that of mafic and felsic rocks (Fig. 52), thus they presumably formed as a consequence of the mingling/mixing process. The Zaro zoned clinopyroxenes are characterized by reverse zoning patterns in the 83% of the cases, which strongly suggests input of mafic magma.

Likewise clinopyroxenes, feldspars from mafic enclaves are chemically similar to those included in trachytes and exhibit the same Sr-isotopic signature as that of the trachytic whole rocks, so they may have originally grown within the host trachyte and subsequently been taken up into the mafic enclaves.

All these features are indications of open system behavior of the magma bodies. Indeed, the enclaves themselves behave as an open system providing evidence of mixing/mingling processes occurred inside the Zaro magmatic system. Mechanical transport of crystals (mingling) indicates that hybridization was not extensive, and that mixing affected the magmas only to a limited extent. In particular, one of the sites where the mixing process between mafic and trachytic end-members occurred with the highest efficiency is probably represented by the hybrid enclave. This sample, showing chemical, mineralogical and isotopic features intermediate between those of mafic enclaves and those of trachytes, provides strong evidence that a process of hybridization must have occurred among magmas at various evolution degrees determining variable isotopic signatures.

Concerning the trachytic end-member(s), few considerations can be made. The Zaro pumices are representative of a magma more differentiated with respect to the lavas: this is evident from the whole rock, the glass composition (Fig. 48; Fig. 49) and the mineral chemistry of these products that show more sodic composition (e.g. clinopyroxene; Fig. 38c). The Zaro pumices and even more the Zaro lavas show very abundant phenocrysts content (e.g. PI of Zaro lava ca. 50%). This observation suggests that the trachytic and trachyphonolitic magmas were already partially crystallized before eruption occurred.

Thus, it is possible to hypothesize a zoned magma reservoir (Fig. 66a) that was composed by a trachytic crystal-rich (mushy) magma (the Zaro lava) and a more differentiated layer (the Zaro pumices): these magmas represents, respectively, the magmatic environments in which ME1 and ME2 compositions of clinopyroxene cores could have formed. The frequent occurrence of their reverse zoning well reflects the response of minerals to the input of mafic magma; this latter, on the other side, represents the magmatic environment in which ME0 plateau formed in clinopyroxenes of hybrid and mafic enclaves. As previously mentioned (Chapter 4.4), the occurrence of plateau in the zoning pattern of minerals indicates that growth occurred for certain periods of time under stable conditions in response to fast changes of thermodynamic variables (pressure, temperature, oxygen fugacity or water fugacity). Due to the input of hot mafic magma, clinopyroxene compositions instantaneously adapt to the new set of condition, e.g. higher temperature. Indeed, temperature estimated for ME0 clinopyroxenes (ca. 1120°C) is higher than those of the trachytic (ME1) and trachyphonolitic (ME2) magmas (Fig. 59; Fig. 60). Heating of the preexisting magmas explains the high Mg# plateau composition (ME0-ME1) found in mantles and/or rims of clinopyroxene crystals, due to their arrangement to the new set of conditions. In particular, the ME1 plateau developed as mantles and/or rims of clinopyroxene cores with ME2 composition, belonging to the Zaro lava and felsic enclaves (Fig. 61) indicate the local increasing temperature, experienced by trachytic magma, due to mafic recharge (Fig. 66b). The ME0 plateau composition developed as mantles of clinopyroxenes from the hybrid and mafic enclaves indicates a change of thermodynamic variables towards very high temperatures and mafic compositions experienced by crystals. This suggests that part of clinopyroxenes with ME1 cores and ME0 mantles were engulfed from trachytic magmas in hybrid and mafic enclaves (Fig. 66c). It cannot be ruled out that at this stage, hybrid clinopyroxenes, represented by cores with ME1 composition, crystallized.

The input of hot mafic magma could have caused perturbation of the system and remobilizing the cool magma (e.g. Murphy et al. 2000; Couch et al. 2001). Heating and remobilization of the trachyte may have caused a mechanical separation of different parts of the same magma. According to Burgisser and Bergantz (2011), when a stiff mushy magma is reheated from below, a reduction in crystallinity leads to the growth of a subjacent buoyant mobile layer (the felsic enclaves in our case; Fig. 66c). When the thickening mobile layer becomes sufficiently buoyant, it penetrates the overlying viscous crystal mush. This stage rapidly exports homogenized material from the lower mobile layer to the top of the system (Fig. 66d), and leads to a partial overturn within the viscous mush itself as an additional mechanism of mixing. Such mechanism promotes the formation of magma blobs. At this stage, crystals adapt again to a new set of conditions, e.g. decreasing temperature and/or changing composition toward more evolved ones. This can occur because temperature tends to partially homogenize and/or because crystals, due to overturn, are set in zones in which there is a prevalent amount of evolved magma. This explains the reverse to normal zoning pattern of several clinopyroxene crystals (Fig. 61; Fig. 66d).

This model perfectly explains the occurrence of felsic enclaves in the Zaro lava flows, their texture (higher amount of glass in the groundmass) and the frequent occurrence of mafic enclaves and Zaro lava blobs in the felsic enclaves (Fig. 21c-d). Moreover, this model explains the clinopyroxene zoning pattern and the chemical and isotopic signature of clinopyroxene and feldspar crystals due to their entrapment from trachytic magmas into the mafic enclaves.

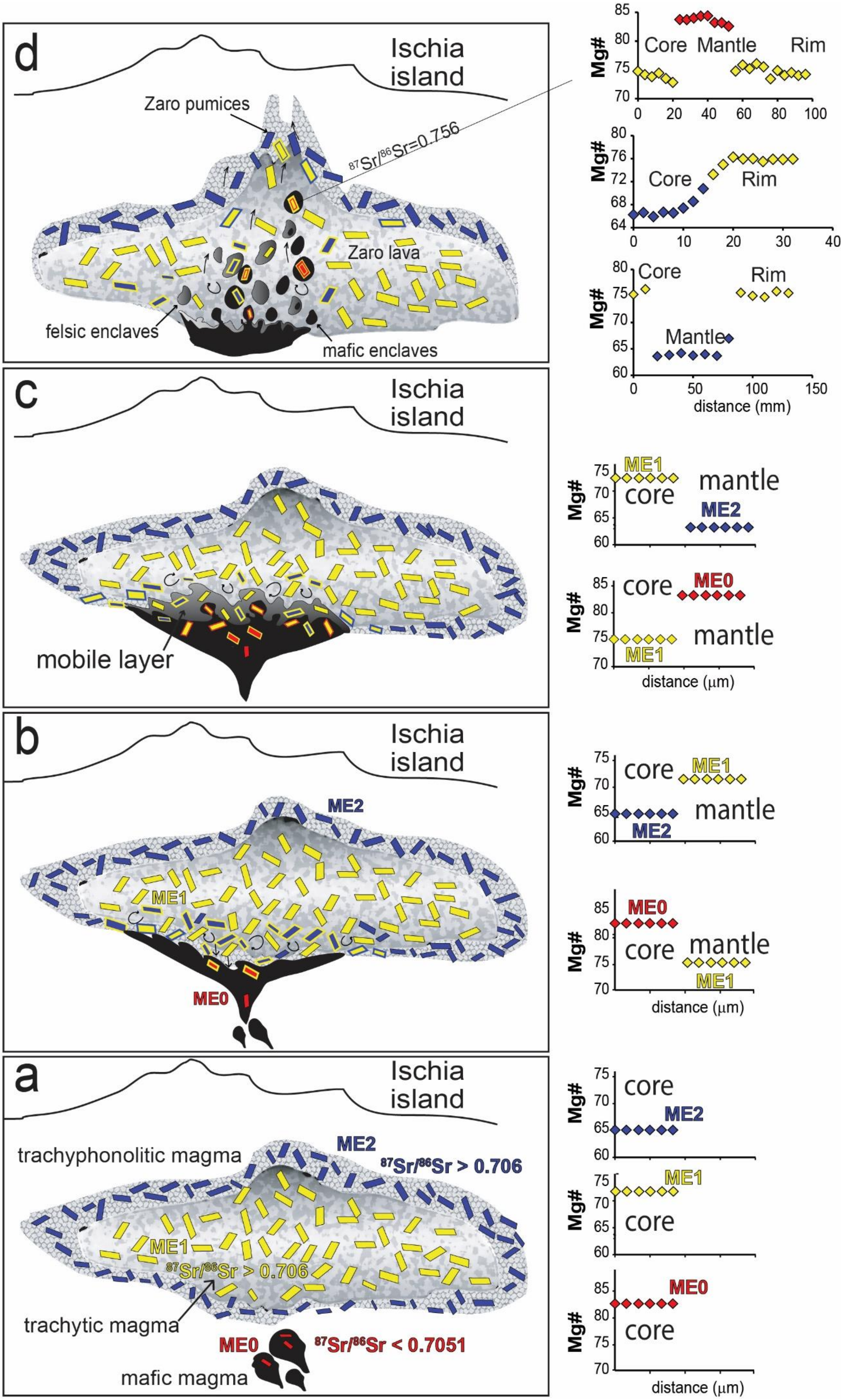
d
Ischia island
Zaro pumices
^{87}Sr/^{86}Sr=0.756
Zaro lava
felsic enclaves
mafic enclaves
Mg#
85
80
75
70
Core
Mantle
Rim
0
20
40
60
80
100
Mg#
80
76
72
68
64
Core
Rim
0
10
20
30
40
Mg#
80
75
70
65
60
Core
Mantle
Rim
0
50
100
150
distance (mm)
c
Ischia island
mobile layer
Mg#
75
70
65
60
ME1
core
mantle
ME2
Mg#
85
80
75
70
core
ME0
mantle
ME1
distance (μm)
b
Ischia island
ME2
ME1
ME0
Mg#
75
70
65
60
core
ME1
mantle
ME2
Mg#
85
80
75
70
ME0
core
mantle
ME1
distance (μm)
a
Ischia island
trachyphonolitic magma
ME2
^{87}Sr/^{86}Sr > 0.706
ME1
^{87}Sr/^{86}Sr > 0.706
trachytic magma
ME0
^{87}Sr/^{86}Sr < 0.7051
mafic magma
Mg#
75
70
65
60
core
ME2
Mg#
75
70
65
60
ME1
core
Mg#
85
80
75
70
ME0
core
distance (μm)

Fig. 66 Schematic sketch illustrating the magmatic processes occurred in the Zaro plumbing system. a) three distinct magmatic environments there were at a T = 0: one (ME0) is associated with mafic magmas, in which core of clinopyroxenes with high Mg# (86-79) were formed; the others environments, ME1 and ME2, are ascribable to a trachytic and a trachyphonolitic magmas, making up zoned reservoir. b) The input of hot mafic magma (ME0-mafic enclaves), which causes local heating, explains the most common reverse zoning pattern of clinopyroxenes showing ME2 compositions in their cores; at this stage, partial overturn could also have promoted the less frequent normal zoning shown by few ME0 and ME1 clinopyroxene cores. c) The mafic magma engulfs ME1 crystals from the trachytic magmas, subsequently causing overgrowth of ME0 compositions at the mantles/rims of crystals, thus explaining the frequent occurrence of this reverse zoning pattern; during this stage, heating of the preexisting trachytic magma can also cause the growth of a subjacent buoyant mobile layer, thus explaining the occurrence of felsic enclaves. d) the mobile layer penetrates the overlying mushy magma, with subsequent partial overturn. Such mechanism promotes the formation of magma blobs and their migration to the top of the system. This also justifies the whole set of observed zoning patterns in the A-MS clinopyroxene.

Heating of the resident magma and/or migration of blobs toward the top may also have resulted in a volatile release that could represent the driving force for fragmentation and rise of the more evolved magma layer (recorded in pumice fragments) thus triggering the early explosive phase of the Zaro eruption, which generated the breccia-like pyroclastic density current deposit. Once the volatiles were released from the system, the transition to an effusive phase, with emplacement of the lava flows and domes, was favored.

Despite the small volumes of magmas involved, the Zaro eruption could have caused casualties to the prehistoric population that inhabited that area of Ischia. Archaeological artefacts dated to the 4th millennium B.C. (Buchner, 1969) have been found exactly in the Zaro peninsula. In particular, the early explosive phase of the eruption, in which pyroclastic density current where emplaced, with the seismic activity that presumably accompanied the eruption, should have produced the greatest damages to Neolithic people and their settlements.

7.6 Timescales of processes in the Zaro plumbing system

Through the Fe-Mg diffusion model, the timescales of crystal residence at the new magmatic conditions, after intrusion of the mafic magma in the trachytic-trachyphonolitic reservoir, have been estimated. Reverse zoning at the rim and mantles of the identified populations well reflects mixing/mingling resulting from input of mafic magma, which produced chemical gradients. Diffusion modeling of the reverse zoning patterns leads, then, to define timing of the mixing/mingling events between compositionally different magmatic end-members. As previously explained, method I is applied to crystals that show little evidence of diffusion and it yields timescales that are upper limits of residence in a magmatic environment; method II, being applied to crystals which show evidence of diffusional modifications, gives more efficient time constrains. The timescales of the events which created the whole zoning patterns of the Zaro clinopyroxenes ranges between 3.8 and 1.1 years, for crystals modeled with method I and between 25 and 0.4 years for crystals modeled with method II. Such difference can be due to the fact that crystals can differently record the number of events of a same process: repeated input of mafic magma can be recorded by some crystals and not by others. In this context, crystals modeled with method II, which yield longer timescales, could have record more magma inputs with respect to crystals modeled with method I. These, showing little or no evidence of diffusion in their zoning pattern, could have recorded only the last input of magma, thus implying that time between recharge and eruption was not enough to undergo diffusive modification. The occurrence of more inputs would also explain the finding of chemically intermediate enclaves (hybrid enclave) that suggests that mafic and trachytic end-members had time enough to partially homogenize.

All of the modeled profiles yielded timescales that were consistent with each other. Moreover all crystals belonging to a certain lithotype, modeled at a specific temperature, yield timescales that were consistent with timescales obtained from crystals of other lithotypes, modeled at other temperatures. Hence, residence times estimated by modeling Zaro lava clinopyroxenes at 950°C are consistent with times estimated by modeling hybrid enclave clinopyroxenes at 1050°C and mafic enclaves' clinopyroxenes at 1100°C (Fig. 63; Table 6). Fig. 63 also shows the obtained timescales if kinetic modeling had been applied by using temperatures of 950°C, 1050°C and 1100°C to all the suitable profiles of crystals belonging to all the different lithotypes. Modeling crystals from different lithotypes at the same temperature would have yielded timescales inconsistent with each other. For example, by modeling diffusion of clinopyroxene of mafic enclaves at 950°C, the obtained timescales would have ranged from 125 to 8 years. These values are an order of magnitude higher than the values (18-4 years) obtained by modeling clinopyroxenes of the Zaro lava at 950°C. Likewise, kinetic modeling applied to clinopyroxenes of the Zaro lava at 1100°C would have yielded timescales in the range 230-33 days, which are lower than the presumable time span. On the other side, by using very different temperature (950-1050°C-1100°C) in diffusion modeling, very similar ranges of time have been obtained for clinopyroxenes of the different Zaro rocks. This implies that the processes which created the zoning occurred in the same time span, for crystals characterized by different previous histories: clinopyroxenes characterized by different compositions and crystallizing at different temperatures experienced diffusive modifications, in response to their tendency to equilibrate and to adapt to the local magmatic environment (e.g. new P-T etc.), over the same duration. This statement further supports the evidence of the mixing/mingling process itself.

The coexistence of magmas at different temperatures within the magma reservoir places additional constraints on the mixing/mingling process from thermal considerations. The evidence of coexistence of different temperature implies that the temperatures were not completely homogenized before eruption, thus suggesting that the mixing affected the magmas only to a limited extent, without attaining a complete homogenization, as also provided by the above mentioned textural evidences (Chapter 7.5).

Timescales obtained by modeling the Mg# profiles of transects crosscutting the boundary between the two most external plateau compositions of the crystals refer to the last event which created the zoning. Those obtained with method I range between 1.2 years and 72 days, whereas those obtained with method II range between 20 years and 329 days. Apart three results yielding very fast times span, in the range 81-72 days, all the timescales of the last event, although on average lower, are in the range of timescales of the events which created the whole zoning pattern. This suggests that almost all these timescales presumably represent the duration of the mixing/mingling process, or at least, of the last input recorded by crystals. Nevertheless, some of these can represent duration of processes occurred in the conduit or after the lava emplacement (e.g syn-eruptive mixing, degassing, cooling).

7.7 Magmatic environments detected in the A-MS and Zaro clinopyroxenes in the context of the PVD magmatism: a comparison with results of other timescales calculations

It is well known that the eruptive dynamics can be strongly affected by magmatic processes occurring in crustal reservoirs. Different methods can help to constrain the timescales of the different magmatic processes that are potentially able to lead to an eruption. Studies on timescales estimations of magmatic processes possibly leading to different-size eruptions in the PVD, of which Campi Flegrei and Ischia are part, are still poorly employed. In particular, at Ischia these kinds of investigations are missing.

The timescales of different processes that occurred in the plumbing system of Campi Flegrei have been determined using a variety of methods (e.g. Arienzo et al., 2011; Pappalardo and Mastrolorenzo, 2012; Montagna et al., 2015; Perugini et al., 2015; Wu et al., 2015; Arzilli et al., 2016; Di Vito et al., 2016; Iovine et al., 2017; Astbury et al., 2018). These may be considered in the context of the plumbing system connectivity and timescales inferred above from the A-MS clinopyroxene zoning pattern to develop an integrated knowledge. Although constraints are poor on depths of the magmatic environments that were identified based on the systems analysis of compositional zoning in the A-MS clinopyroxenes, results from other studies (e.g. Zollo et al., 2008; Arienzo et al., 2010; Pappalardo and Mastrolorenzo, 2012; Moretti et al., 2013; Di Vito et al., 2016; Fedi et al., 2018) that used different geological, geochemical or geophysical information, can be used to tentatively associate the magmatic environments to reservoirs at different depths. It is possible that the deeper reservoir at >10 km depth inferred in those studies is primarily associated with the less evolved ME0 environment while the shallower reservoir at < 8 km is primarily associated with the dominant ME2 reservoir. Connectivity between these reservoirs, as suggested from the systems analysis diagrams (Fig. 54), could at least be partially responsible for the smearing of the barometric record seen in Fig. 53b.

The overall assembly of eruptible magma which fed large eruptions at the CFc occurs over relatively long timescales (e.g. ca. 6.4 kyr in the case of the Campanian Ignimbrite eruption; Arienzo et al., 2011) but processes within magmatic plumbing systems occur on a hierarchy of shorter timescales. Mingling/mixing processes, involving mafic and evolved magmas that fed recent eruptions of the PVD have been investigated in some detail. Several studies (Montagna et al., 2015; Perugini et al., 2015; Astbury et al., 2018) concerning the interaction between mafic and evolved end-members, provided short (minutes to days) timescales of mixing processes leading to historical eruptions occurred in the Campi Flegrei caldera. As an example, the Astroni eruption, being featured by the emplacement of five lava domes during the final phases of explosive episodes (Isaia et al., 2004), was characterized by eruptive dynamics comparable with those of the Zaro eruption. Based on K-feldspar growth rates, Astbury et al. (2018) assessed the timescales of recharge event in the shallow plumbing system over a few hours to days before the Astroni 6 eruption.

Various lines of evidence point to the fact that degassing of rising magma plays an important role in the system (Montagna et al., 2015; Chiodini et al., 2016; Astbury et al., 2018; Forni et al., 2018) and that a short-lived episode of enhanced degassing occurs over hours to days before an eruption (e.g. Arzilli et al., 2016; Astbury et al., 2018; microlite based CSD in Pappalardo and

Mastrolorenzo, 2012; Montagna et al., 2015). Such a transient (and hence less frequently recorded), degassed magmatic environment could be represented by ME3 compositions detected in the A-MS clinopyroxenes, for example. Such degassing promotes crystallinity (e.g. Moretti et al., 2014; Arzilli et al., 2016), which may have produced the ME3 and ME4 compositions as well as the microlites that record a history of a few hours to days. Comparable or even more rapid timescales have been obtained for magma mingling processes in the Campi Flegrei magmatic system (e.g. tens of minutes; Perugini et al., 2015). As melts move between these reservoirs, they adapt to the local magmatic environment (i.e. new P, T etc.) almost instantaneously. However, the crystal cargo of such melts would require much longer to adapt to the new conditions, and the residence times of crystals of different minerals have been consistently found to be on the order of decades or even longer using a variety of minerals and methods, e.g. < 60 years based on Ba-zoning in sanidine (Iovine et al., 2017); few centuries for the coarsest feldspar crystals based on CSD (Pappalardo and Mastrolorenzo, 2012); few years to decades based on CSD of some microlites (Wu et al., 2015) and zoning in clinopyroxene (this thesis).

Taken together, this information would be consistent with a system below the CFc where a long-lived magma reservoir at depths of >10 km (Pappalardo and Mastrolorenzo, 2012) containing a shoshonitic-latitic magma, corresponding to ME0 of this thesis, is connected to a shallower (<. 8 km) reservoir containing a more evolved magma (e.g. trachyte), corresponding to ME2 of this thesis, over decadal, or even century, timescales. Entry of the more mafic magma in the more evolved reservoir/mush zone could lead to melting/assimilation and mixing, leading to the formation of a reservoir such as ME1 (Fig. 64). Melts transported from one environment to another mingle rapidly on timescales of minutes (Perugini et al., 2015) while their crystal cargoes retain their identities in the form of compositional zoning. Progressive degassing, the rate of which increases a few hours to days before eruption, may lead to the formation of a transient environment ME3 (and perhaps ME4). Such a scenario could be consistent, for example, with the record of unrest from 1251 AD – 1538 AD before the 1538 AD eruption at Campi Flegrei (Di Vito et al.,

2016) where the system evolved over ca. 300 years, with major changes occurred a couple of years before the eruption.

Hence, it is clear that different methods allow investigating timescales concerning different aspects of the whole transcrustal magmatic system (e.g. Chapter 1-2). In this context, kinetic modeling of diffusive modifications experienced by crystals reveals to be particularly efficient into reconstruct timescales of processes, such as mixing/mingling, which causes sudden changes of thermodynamic variables of the magmatic system.

In the larger context of the Neapolitan volcanic region of the Campania Plain, it is often considered that the underlying deeper plumbing system is similar (e.g. Pappalardo and Mastrolorenzo, 2012, Moretti et al., 2013) in the PVD and the Somma-Vesuvius volcanic system. In both areas, the different eruptive styles, e.g. effusive-Strombolian to highly explosive-Plinian eruptions, can be affected by magmatic processes, such as mixing/mingling and recharge, occurring over different times span before eruption. Information from clinopyroxene zoning patterns tends to support such an inference: Morgan et al. (2004) studied zoning in clinopyroxene from the products of the 1944 AD eruption of Vesuvius and found timescales of magma recharge of less than one decade (0.45 – 9 years). This eruption can be comparable with the size and the eruptive dynamics of the Zaro eruption and the inferred timescales are remarkably similar. Anyway, Morgan et al. (2004) used Fe-Mg zoning inferred from grayscales profiles of BSE images and used the diffusion data of Dimanov and Sautter (2000). Their timescales were skewed to shorter values and some of the small differences with this study could also arise from the use of different diffusion coefficients and methods for determination of compositional gradients. Anyway these months-to-years timescales are slightly lower than the decadal timescales inferred for large-scale eruptions of the PVD, such as A-MS (this thesis) and the famous 79 AD eruption of Vesuvius (Morgan et al., 2006). As for the latter, Morgan et al. (2006), through Ba diffusion in sanidine crystals, estimated that episodic recharge events occurred for several decades (ca. 20-80 years) prior to the Plinian eruption. These timescales are very similar to the ca. 40-70 years inferred, in this thesis, for the A-MS eruption, which was also characterized by the same intensity (Volcanic Explosivity Index; VEI=5; e.g. Mastrolorenzo et al., 2017) and similar eruptive dynamics compared to the 79 AD eruption. Morgan et al. (2006) also highlighted the occurrence of complex zoning pattern in sanidine which, similarly to A-MS (e.g. Fig. 54; Chapter 7.1-7.2), suggests a long lived connectivity between deep and shallow reservoirs.

Identifying the magmatic end-members and the magmatic environments involved in the mingling/mixing processes becomes hence fundamental for a better understanding of pre-eruptive magmatic processes and their timescales. This investigation has been particularly efficient through the systematic characterization of clinopyroxene zoning patterns, associated with isotopic signature of rocks and minerals. Moreover, element diffusion applied to clinopyroxene crystals efficiently allowed an assessment of the timescale of the magmatic processes that preceded both small-scale almost effusive (Zaro, Vesuvius 1944 AD) and big-scale explosive (A-MS, Vesuvius 79 AD) recent eruptions occurred in the PVD. This knowledge is vital for predicting the future behavior of the volcanoes and for a correct evaluation of volcanic hazard especially in densely populated area such as the CFc and Ischia island, in which a detailed a reconstruction of pre-eruptive magma dynamics and their timescales controlling the onset, evolution and magnitude of eruptions is still far from being attained.

CONCLUSIONS

In this thesis, the volcanic products of A-MS and Zaro, two recent different size eruptions, occurred at Campi Flegrei caldera and Ischia island, respectively, have been studied. Particularly the chemical and isotopic composition of whole rock and minerals have been characterized and the complex zoning pattern shown by clinopyroxene crystals from the A-MS and Zaro eruptions have been investigated. The chemical and isotopic disequilibria of whole rocks and minerals suggest that the magmas which fed both the A-MS and Zaro plumbing systems experienced open-system evolution processes. A detailed characterization of the chemical compositions recorded in the clinopyroxene zoning pattern allowed to reconstruct the physical conditions (e.g. T, P) of the chemically and isotopically different magmas in which clinopyroxenes grew. Despite the complex sequential zoning testified by the wide chemical variation and the great variability of zoning types, some transitions inside the zoning pattern of both A-MS and Zaro clinopyroxenes are prevalent suggesting a common late evolutionary history. A population-based approach allowed to identify several magmatic environments in which clinopyroxenes have grown sequentially. Quantification of connectivities in the systems connectivity diagrams allow to infer the pattern of crystals growing among the different magmatic environments and its frequencies. The timescales of such movement have been constrained by diffusion modeling.

The textural features and the chemical composition of the A-MS clinopyroxenes record the existence of at least two main, likely physically separated, magmatic environments that make up the A-MS plumbing system: the first (ME0), identified in clinopyroxene crystals with very high Mg# (>91), is representative of mafic magma presumably directly originated from partial melting of the local mantle source; while the second, dominant magmatic environment is represented by clinopyroxene crystals showing more evolved compositions (ME2: Mg# = 78-70) associated with trachytic and phonolitic magmas stationing in a shallower crustal reservoir. Mingling of magma from these two environments could have produced an intermediate environment (ME1; Mg # 80 – 84). These magmatic environments were connected to each other with transfer of magma between them over decadal, and perhaps even centennial, timescales. More evolved environments (e.g. ME3: Mg# = 69-60) could have appeared as a result of degassing-induced crystallization shortly (e.g. days to hours) before eruption.

In this thesis, geochemical and isotopic features of pumices and lava types (mafic enclaves, felsic enclaves, hybrid enclave and main felsic lava body) of the Zaro volcanic complex were explored also in the context of the last 10 ka volcanic activity at Ischia, which is the reference period for the current state of the volcano and the assessment of the related hazards. The whole set of acquired data allows a better understanding of the magmatic processes that occurred before and during the Zaro eruption.

- The strong isotopic difference between mafic enclaves and trachytes rules out a simple crystallization process for linking the various facies of the Zaro lava complex. Moreover, a process of crustal assimilation appears to be unlikely, since it requires a too high percentage of assimilant (more than 24%) in order to match the large isotopic gap between Zaro mafic enclaves and trachytes, hence these magmas are not genetically related. A small amount of crust assimilation for the mafic magma(s), however, cannot be ruled out.

- Therefore, distinct magmatic components result to have fed the Zaro magmatic system:

  - one is represented by the Zaro trachytes (whole rocks; $^{87}Sr/^{86}Sr > 0.706$, $^{143}Nd/^{144}Nd < 0.51257$) and feldspars from all the Zaro facies ($^{87}Sr/^{86}Sr > 0.706$) which exhibit an isotopic signature comparable to the Ischia products of the last 3 ka (Cava Nocelle, Vateliero, Molara and Arso eruptions; D'Antonio et al., 2013; Iovine et al., 2017b). According to the hypotheses formulated for the latter, these magmas were probably derived from partial melting of a mantle wedge previously enriched in variable proportions by subducted slab-derived components, and subsequent evolution through fractional crystallization processes occurred at mid-lower depths.

- another magmatic component is represented by the mafic enclaves (whole rocks; $^{87}Sr/^{86}Sr < 0.7051$ and $^{143}Nd/^{144}Nd > 0.51268$) and their olivines ($^{87}Sr/^{86}Sr < 0.7050$). This component, displaying significantly lower Sr and higher Nd isotopic ratios compared to the Ischia mafic products of the last 3 ka, shows the lowest evidence of mantle source contamination. It is possible to hypothesize an origin from a magma similar to that represented by the Solchiaro primitive products of Procida island, sharing similar Sr- and O- isotopic signatures (Iovine et al., 2018).

These two components are mingled inside the Zaro mafic and hybrid enclaves. Moreover the two components are clearly distinguishable in the clinopyroxene zoning patterns. The different magmatic environments detected in the clinopyroxene compositions provide evidences of the coexistence of compositionally different magmas, characterized by different set of thermodynamic variables. The ME1 and ME2 compositional populations (relatively low Mg#) represent the first component, which is ascribable to a zoned reservoir in which trachytic-trachyphonolitic magmas were partially crystallized at relatively low temperature. The ME0 compositions and its occurrence along the mantles of clinpyroxene further corroborate the injection in the system of the second magmatic component: this is the high-temperature mafic magma(s) which mixed/mingled with the trachytic one. The frequent occurrence of reverse zoning in the clinopyroxene zoning pattern well reflects the response of minerals to the input of mafic magma. In fact, the latter causes that clinopyroxene composition instantaneously adapts to the new set of condition, e.g. higher temperature, with overgrowth of high Mg# plateau (ME0) at the mantles of crystals. The diffusive modifications developed in response to the tendency of minerals to equilibrate the two chemical components have been modeled trough different methods and constrain over months to few decades the time span of the mixing/mingling processes.

-The mafic enclaves and ME0 clinopyroxenes might represent mafic magma that rapidly raised, due to the high vertical permeability of this sector of the island and reached a shallower reservoir filled by trachytic-trachyphonolitic magmas (ME1-ME2). Here the mafic magma induced thermo-chemical instability, possibly favoring the exsolution of a volatile phase, thus triggering the eruption. The mafic intrusion has caused a mechanical interaction and a mineral cargo entrapment from trachytes into the mafic blobs, thus explaining the chemical and isotopic features of clinopyroxenes and feldspars of the mafic enclaves and the clinopyroxene zoning patterns.

The two felsic lava facies do not display isotopic disequilibria between phenocrysts and host rocks. Nevertheless, field and textural (resorbed crystals and a lower degree of crystal content in the groundmass) observations suggest they could be the product of an auto-mingling process between slightly different physical layers of the same magma body. They could represent the result of a sort of segregation, in the slightly zoned trachytic reservoir, induced by the input of mafic magma.

Such a process of disaggregation of mafic inclusions and transfer of crystals from mafic to felsic magmas has been described in other volcanic systems. Irrespective of the details of the processes, these data imply that the timescales between intrusion of mafic magma and eruption are on the order of several hundreds of days to few decades.

Therefore, the knowledge of the pre-eruptive magmatic processes and their inferred timescales that occurred prior to the A-MS and Zaro eruptions can be efficiently integrated with that provided by other case-studies worldwide to build a unique behavioral model of similar active volcanoes useful for risk assessment. The proposed scenario, in which big size (A-MS) and small size (Zaro) eruptions are preceded by magmatic processes occurring over several decadal and possibly monthly to decadal timescales, respectively, can provide guidance for evaluating future volcanic hazards based on monitoring systems, e.g. by geophysical methods, of magma transfer to the shallower reservoirs.

.

References

Acocella V, Funiciello R, (1999) The interaction between regional and local tectonics during resurgent doming: the case of the island of Ischia, Italy. Journal of Volcanology and Geothermal Research. 88, 109-123

Acocella V, Salvini F, Funiciello R, Faccenna C (1999) The role of transfer structures on volcanic activity at Campi Flegrei (southern Italy). Journal of Volcanology and Geothermal Research. 91, 123 – 139

Acocella V, Funiciello R, (2006) Transverse systems along the extensional Tyrrhenian margin of central Italy and their influence on volcanism. Tectonics. 25, 1-24. TC2003. doi:10.1029/2005TC001845

Aiuppa A, Tamburello G, Di Napoli R, Cardellini C, Chiodini G, Giudice G, Grassa F, Pedone M, (2013) First observations of the fumarolic gas output from a restless caldera: implications for the current period of unrest (2005-2013) at Campi Flegrei. Geochemistry, Geophysics, Geosystems. https://doi.org/10.1002/ggge.20261

Albarède F, Bottinga Y, (1972) Kinetic disequilibrium in trace element partitioning between phenocrysts and host lava. Geochimica and Cosmochimica Acta. 36, 141–156

Albert PG, Giaccio B, Isaia R, Costa A, Niespolo EM, Nomade S, Pereira A, Renne PR, Hinchliffe A, Mark DF, Brown RJ, Smith VC, (2019) Evidence for a large-magnitude eruption from Campi Flegrei caldera (Italy) at 29 ka. Geology. 47, 595–599 doi: https://doi.org/10.1130/G45805.1

Albore Livadie C, Barra D, Beneduce G, Brancaccio L, Cinque A, Ortolani F, Pagliuca S, Russo F, (1989) Evoluzione geomorfologica, neotettonica e vulcanica della pianura costiera del Fiume Sarno (Campania) in relazione agli insediamenti anteriori all'eruzione del 79 d.C.. Vulcan. Paleog. Archeol. PACT 10, 237-256

Alessio G, Esposito E, Ferranti L, Mastrolorenzo G, Porfido S, (1996) Correlazione tra sismicitià ed elementi strutturali nell’isola di Ischia: Il Quaternario: Italian Journal of Quaternary Sciences. 9, 303–308.

Alessio M, Bella F, Improta S, Belluomini G, Cortesi C, Turi B, (1973) University of Rome carbon-14 dates X. Radio-carbon 15. 1, 165–178

Allan ASR, Morgan DJ, Wilson CJN, Millet M-A, (2013) From mush to eruption in centuries: assembly of the super-sized Oruanui magma body. Contribution to Mineralogy and Petrology. 166, 143–164

Alves A, Janasi VD, Simonetti A, Heaman L, (2009) Microgranitic enclaves as products of self-mixing events: a study of open-systemprocesses in the Mauà granite, São Paulo, Brazil, based on in situ isotopic and trace elements in plagioclase. Journal of Petrology. 50, 2221-2247 doi:10.1093/petrology/egp074

Anderson AT, (1984) Probable relations between plagioclase zoning and magma dynamics, Fuego volcano, Guatemala. American Mineralogist. 69, 660–676

Anderson AT, Lindsley DH, (1985) New (and Final ?) model for the Ti-magnetite/ilmenite geothermometers and oxygen barometers (abst.): Trans. Geophysical Union. 66, 416

Anderson JL, Smith DR, (1995) The effects of temperature and f on the Al-in-hornblende barometer. American Mineralogist. 80, 549–559

Andrews BJ, Manga M (2014) Thermal and rheological controls on the formation of mafic enclaves or banded pumice. Contribution to Mineralogy and Petrology. 167, 961. https ://doi.org/10.1007/s0041 0-013-0961-7

Annen C, Blundy JD, Sparks RSJ, (2006) The genesis of intermediate and silicic magmas in deep crustal hot zones. Journal of Petrology. 47, 505-539

Appleton JD, (1972) Petrogenesis of potassium rich lavas from the Roccamonfi na Volcano, Roman Region, Italy. Journao of Petrology. 13, 425-456

Arienzo I, Civetta L, Heumann A, Wörner G, Orsi G, (2009) Isotopic evidence for open system processes within the Campanian Ignimbrite magma chamber. Bulletin of Volcanology. 71, 285–300

Arienzo I, Moretti R, Civetta L, Orsi G, Papale P, (2010) The feeding system of Agnano-Monte Spina eruption (Campi Flegrei, Italy): dragging the past into the present activity and future scenarios. Chemical Geology. 270, 135–147

Arienzo I, Neumann A, Wörner G, Civetta L, Orsi G, (2011) Processes and timescales of magma evolution prior to the Campanian ignimbrite eruption (Campi Flegrei, Italy). Earth and Planetary Science Letters. 306, 217–228

Arienzo I, Carandente A, Di Renzo V, Belviso P, Civetta L, D'Antonio M, Orsi G, (2013) Sr and Nd isotope analysis at the Radiogenic Isotope Laboratory of the Istituto Nazionale di Geofisica e Vulcanologia Sezione di Napoli - Osservatorio Vesuviano. Rapporti Tecnici INGV. 260, 1–18. (available online at http://istituto.ingv.it/lingv/produzionescientifica/rapporti-tecnici-ingv/archivio/rapporti-tecnici-2013/).

Arienzo I, D'Antonio M, Di Renzo V, Tonarini S, Minolfi G, Orsi G, Carandente A, Belviso P, Civetta L, (2015) Isotopic microanalysis sheds light on the magmatic end members feeding volcanic eruptions: the Astroni 6 case study (Campi Flegrei Italy) Journal of Volcanology and Geothermal Research. 304, 24–37

Arienzo I, Mazzeo FC, Moretti R, Cavallo A, D'Antonio M, (2016) Open-system magma evolution and fluid transfer at Campi Flegrei caldera (Southern Italy) during the past 5 ka as revealed by geochemical and isotopic data The example of the Nisida eruption. Chemical Geology. 427, 109–124

Armienti P, (2008) Decryption of igneous rock textures: crystal size distribution tools In: Minerals, Inclusions and Volcanic Processes. Reviews in Mineralogy and Geochemistry. 69, 623–648

Astbury RL, Petrelli M, Ubide T, Stock MJ , Arienzo I, D'Antonio M, Perugini D, (2018) Tracking plumbing system dynamics at the Campi Flegrei caldera Italy: high-resolution trace element mapping of the Astroni crystal cargo. Lithos. 318–319, 464–477

Avanzinelli R, Elliot T, Tommasini S, Conticelli S, (2008) Constraints on the genesis of potassium-rich Italian volcanic rocks from U/Th disequilibrium. Journal of Petrology. 49, 195-223

Avanzinelli R, Lustrino M, Mattei M, Melluso L, Conticelli S, (2009) Potassic and ultrapotassic magmatism in the circum-Tyrrhenian region: significance of carbonated pelitic vs. pelitic sediment recycling at destructive plate margins. Lithos. 113, 213-227

Bachmann O, Bergantz GW, (2008) Rhyolites and their source mushes across tectonic settings. Journal of Petrology. 49, 2277–2285. doi:10.1093/petrology/egn068

Bachmann O, Bergantz GW, (2006) Gas percolation in upper-crustal silicic crystal mushes as a mechanism for upward heat advection and rejuvenation of near-solidus magma bodies. Journal of Volcanology and Geothermal Research. 149, 85–102. (doi:10.1016/j.jvolgeores.2005. 06.002)

Bacon CR, (1986) Magmatic inclusions in silicic and intermediate volcanic rocks. Journal of Geophysical Research. 91, 6091–6112

Bali E, Hartley M, Halldórsson S, Gudfinnsson G, Jakobsson S, (2018) Melt inclusion constraints on volatile systematics and degassing history of the 2014–2015 Holuhraun eruption, Iceland. Contribution to Mineralogy and Petrology. 173, 9 doi:10.1007/s00410-017-1434-1

Barberi F, Innocenti F, Lirer L, Munno R, Pescatore TS, Santacroce R, (1978) The Campanian Ignimbrite: a major prehistoric eruption in the neapolitan area (Italy). Bulletin of Volcanology. 41, 10–22

Barbieri M, Di Girolamo P, Locardi E, Lombardi G, Stanzione D, (1979) Petrology of the calcalkaline volcanics of the Parete 3 well (Campania, Italy). Periodico di Mineralogia – Roma. 48, 53–74

Barclay J, Herd R, Edwards BR, Christopher T, Kiddle EJ, Plail M, Donovan A, (2010) Caught in the act: implications for the increasing abundance of mafic enclaves during the recent eruptive episodes of the Soufrière Hills Volcano, Montserrat. Geophysical Research Letters. 37, 1–5 doi: 10.1029/2010GL042509

Bateman R, (1995) The interplay between crystallization, replenishment and hybridization in large felsic magma chambers. Earth-Science Reviews. 39, 91–106

Belkin HE, Rolandi G, Jackson JC, Cannatelli C, Doherty AL, Petrosino P, De Vivo B, (2016) Mineralogy and geochemistry of the older (> 40 ka) ignimbrites on the Campanian Plain, southern Italy. Journal of Volcanology and Geothermal Research. 323, 1-18

Beaumont C, Fullsack P, Hamilton J, (1992) Erosional control of active compressional orogens, in Thrust Tectonics (ed. K.R. McClay). London: Chapman and Hall. 1-18

Beccaluva L, Di Girolamo P, Serri G, (1991) Petrogenesis and tectonic setting of the Roman Volcanic Province, Italy. Lithos. 26, 191-221

Beck P, Chaussidon M, Barrat JA, Gillet Ph, Bohn M, (2006) Diffusion induced Li isotopic fractionation during the cooling of magmatic rocks: the case of pyroxene phenocrysts from nakhlite meteorites. Geochimica and Cosmochimica Acta. 70, 4813–4825

Béjina F, Jaoul O, (1996) Silicon self-diffusion in quartz and diopside measured by nuclear micro-analysis methods. Physics of the Earth and Planetary Interiors. 97, 145-162

Bellatreccia F, Ottolini L, Della Ventura G (2006): Microanalysis of hydrogen, boron and fluorine in vesuvianite by means of SIMS, EPMA and FTIR. Microchimica Acta. 155, 91-94

Belkin HE, Rolandi G, Jackson JC, Cannatelli C, Doherty AL, Petrosino P, De Vivo B, (2016) Mineralogy and geochemistry of the older (> 40ka) ignimbrites on the Campanian Plain, southern Italy. Journal of Volcanology and Geothermal Research. 323, 1-18

Benisek A, Kroll H, Cemic L, (2004) New developments in two-feldspar thermometry. American Mineralogist. 89, 1496-1504 doi: 10.2138/am-2004-1018

Bennett JT, Krishnaswami IS, Turekian KK, Melson WG., Hopson CA, (1982) The uranium and thorium decay series nuclides in Mt. St. Helens effusives. Earth and Planetary Science Letters. 60, 61–69

Bergantz G, Schleicher J, Burgisser A, (2015) Open-system dynamics and mixing in magma mushes. Nature Geoscience. 8, 793–796. (doi:10.1038/ngeo2534)

Berlo K., Turner S, (2010) ^{210}Pb–^{226}Ra disequilibria in volcanic rocks. Earth and Planetary Science Letters. 296, 155–164

Bevilacqua A, Isaia R, Neri A, Vitale S, Aspinall WP, Bisson M, Flandoli F, Baxter PJ, Bertagnini A, Esposti Ongaro T, Iannuzzi E, Pistolesi M, Rosi M, (2015) Quantifying volcanic hazard at Campi Flegrei caldera (Italy) with uncertainty assessment: I Vent opening maps. Journal of Geophysical Research. 120, 2309–2329. doi:101002/2014JB011775

Bevilacqua A, Flandoli F, Neri A, Isaia R, Vitale S, (2016) Temporal models for the episodic volcanism of Campi Flegrei caldera (Italy) with uncertainty quantification. Journal of Geophysical Research. 121, 7821–7845 doi:101002/2016JB013171

Bevilacqua A, Neri A, Bisson M, Esposti Ongaro T, Flandoli F, Isaia R, Rosi M, Vitale S, (2017) The effects of vent location, event scale and time forecasts on pyroclastic density current hazard maps at Campi Flegrei caldera (Italy). Frontiers in Earth Sciences. 5, 72 doi:103389/feart201700072

Bindeman IN, Valley JW, (2001) Low δ^{18}O rhyolites from Yellowstone: magmatic evolution based on analyses of zircons and individual phenocrysts. Journal of Petrology. 42, 1491-1517

Bindeman IN, (2003) Crystal sizes in evolving silicic magma chambers. Geology 31, 367–370

Bindeman IN, Sigmarsson O, Eiler J, (2006) Time constraints on the origin of large volume basalts derived from O-isotope and trace element mineral zoning and U-series disequilibria in the Laki and Grímsvötn volcanic system. Earth and Planetary Science Letters. 245, 245-259

Blake S, Campbell IH, (1986) The dynamics of magma-mixing during flow in volcanic conduits. Contributions to Mineralogy and Petrology. 94, 72-81

Blundy J, Cashman K, (2008) Petrologic reconstruction of magmatic system variables and processes. Review in Mineralogy and Geochemistry. 69, 179–239. https://doiorg/102138/rmg2008696

Bohlen SR, Lindsley DH, (1987) Thermometry and barometry of igneous and metamorphic rocks. Annual Review of Earth and Planetary Science. 15, 397-420

Bonechi B, Perinelli C, Gaeta M, (2020) Clinopyroxene growth rates at high-pressure: Constraints on magma recharge of the deep reservoir of the Campi Flegrei Volcanic District (south Italy). Bulletin of Volcanology. 82, 5

Bourdon B, Ribe NM, Stracke A, Saal AE Turner SP, (2006) Insights into the dynamics of mantle plumes from uranium-series geochemistry. Nature. 444, 713–717

Brady JB, McCallister RH, (1983) Diffusion data for clinopyroxenes from homogenization and self-diffusion experiments. American Mineralogist. 68, 95-105

Bragagnia A, Avanzinelli R, Freymuth H Francalanci L, (2014) Recycling of crystal mush-derived melts and short magma residence times revealed by U-series disequilibria at Stromboli volcano. Earth and Planetary Science Letters. 404, 206–219

Brancaccio L, Cinque A, Romano P, Rosskopf C, Russo F, Santangelo N, Santo A, (1991). Geomorphology and Neotectonic Evolution of a Sector of the Tyrrenian Flank of the Southern Apennines, (Region of Naples). Z. Geomorph N. F. 82, 47-58

Breislak S, (1798) Topografi a Fisica della Campania. 8: Firenze, 368 p.

Breislak S, (1801) Voyages Physiques et Lythilogiques dans la Campanie. Paris, Dentu, Imprimeur-Libraire. 324 p.

Brocchini D, Principe C, Castradori D, Laurenzi MA, Gorla L, (2001) Quaternary evolution of the southern sector of the Campanian Plain and early Somma-Vesuvius activity: insights from the Trecase 1 well. Mineralogy and Petrology. 73, 67-91

Brown RJ, Orsi G, de Vita S, (2008) New insights into Late Pleistocene explosive volcanic activity and caldera formation on Ischia (southern Italy). Bulletin of Volcanology.70, 583-603

Brown RJ, Civetta L, Arienzo I, D’Antonio M, Moretti R, Orsi G, Tomlinson EL, Albert PG, Menzies MA, (2014) Geochemical and isotopic insights into the assembly, evolution and disruption of a magmatic plumbing system before and after a cataclysmic caldera‑collapse eruption at Ischia volcano (Italy) Contribution to Mineralogy and Petrology. 168:1035

Browne BL, Eichelberger JC, Patino LC, Vogel TA, Dehn J, Uto K, Hoshizumi H, (2006) Generation of porphyritic and equigranular mafic enclaves during magma recharge events at Unzen volcano, Japan. Journal of Petrology. 47, 301–328 doi: 10.1093/petrology/egi076

Brugger CR, Hammer JE, (2010a) Crystallization kinetics in continuous decompression experiments: implications for interpreting natural magma ascent processes. Journal of Petrology. 51, 1941–1965

Brugger CR, Hammer JE, (2010b) Crystal size distribution analysis of plagioclase in experimentally decompressed hydrous rhyodacite magma. Earth and Planetary Science Letters. 300, 246–254

Bruno PPG, de Alteriis, G, and Florio, G, (2002) The western undersea section of the Ischia volcanic complex (Italy, Tyrrhenian Sea) inferred by marine geophysical data: Geophysical Research Letters. 29, 9 doi:10.1029/2001GL013904

Buchner G, (1954), Scavi nella necropoli di Pithecusa (1952–53): Atti Società Magna Grecia. 1, 11–19

Buchner G, Rittmann A, (1948) Origine e Passato dell’Isola d’Ischia (G. Macchiaroli, ed.). Napoli. Macchiaroli. 77 p.

Buchner G, (1969) Mostra degli scavi di Pithecusa. Dialoghi di Archeologia. 3, 85–101

Buchner G, (1986) Eruzioni vulcaniche e fenomeni vulcanotettonici di età preistorica e storica nell’isola d’Ischia, in Centre Jean Bérard, ed., Tremblements de Terre, Eruptions Volcaniques et Vie des Hommes dans la Campanie Antique. Volume 7. Naples, Centre Jean Bérard, Institut Français de Naples. 145–188

Buchner G, Italiano A, Vita-Finzi C, (1996) Recent uplift of Ischia, southern Italy, in McGuire, W.J., Jones, A.P., and Neuberg, J., eds. Volcano Instability on the Earth and Other Planets: Geological Society of London Special Publication. 110, 249–252

Burgisser A, Bergantz GW (2011) A rapid mechanism to remobilize and homogenize crystalline magma bodies. Nature 471, 212-5 doi:10.1038/nature09799

Cappelletti P, Cerri G, Colella A, de' Gennaro M, Langella A, Perrotta A, Scarpati C, (2003) Post-eruptive processes in the Campanian Ignimbrite. Mineralogy and Petrology. 79, 79–97

Capuano P, Russo G, Civetta L, Orsi G, D'Antonio M, Moretti R, (2013) The active portion of the Campi Flegrei caldera structure imaged by 3-D inversion of gravity data. Geochemistry, Geophysics, Geosystems. 14, 4681–4697 doi:101002/ggge20276

Carlino S, Cubellis E, Luongo G, Obrizzo F, (2006) On the mechanics of caldera resurgence of Ischia island (southern Italy), in Troise, C., De Natale, G., and Kilburn, C.R.J., eds. Mechanisms of Activity and Unrest at Large Calderas. Geological Society of London Special Publication. 269, 181–193

Carslaw HS, Jaeger JC, (1959) Conduction of Heat in Solids Oxford: Oxford University Press, 510 p.

Carmichael ISE, (1967) The iron-titanium oxides of sialic volcanic rocks and their associated ferromagnesian silicates: Contribution to Mineralogy and Petrology.14, 36-64

Casalini M, Avanzinelli R, Heumann A, de Vita S, Sansivero F, Conticelli S, Tommasini S (2017) Geochemical and radiogenic isotope probes of Ischia volcano, southern Italy: constraints on magma chamber dynamics and residence time. American Mineralogists. 102, 262–274

Cashman KV, (1988) Crystallization of Mount St. Helens 1980–1986 dacite: a quantitative textural approach. Bulletin of Volcanology. 50, 194–209

Cashman KV, Marsh BD, (1988) Crystal size distribution (CSD) in rocks and the kinetics and dynamics of crystallization II: Makaopuhi lava lake. Contribution to Mineralogy and Petrology. 99, 292–305

Cashman KV, (1992) Groundmass crystallization of Mount St. Helens dacite, 1980–1986: a tool for interpreting shallow magmatic processes. Contribution to Mineralogy and Petrology. 109, 431–449

Cashman KV, (1993) Relationship between plagioclase crystallization and cooling rate in basaltic melts. Contribution to Mineralogy and Petrology. 113, 126–142

Cashman KV, McConnell, SM, (2005) Multiple levels of magma storage during the 1980 summer eruptions of Mount St. Helens, WA. Bulletin of Volcanology. 68, 57–75

Cashman KV, Giordano, G (2014) Calderas and magma reservoirs. Journal of Volcanology and Geothermal Research. 288, 28–45

Cassignol C, Gillot PY, (1982) Range and effectiveness of unspiked potassium–argon dating: experimental ground work and application. In: Odin, G.S. Ed. Numerical Dating in Stratigraphy. Wiley. New York, NY. 160 pp.

Cello G, Mazzoli S, (1999) Apennine tectonics in southern Italy. A review. Journal of Geodynamics. 27, 191-211

Chakraborty S, Ganguly J, (1991) Compositional zoning and cation diffusion in garnets, in Diffusion, Atomic Ordering and Mass Transport: Selected Problems in Geochemistry (ed. J. Ganguly). New York: Springer-Verlag. 121-171

Chakraborty S, Ganguly J, (1992) Cation diffusion in aluminosilicate garnets: experimental determination in spessartine-almandine diffusion couples, evaluation of effective binary diffusion coefficients, and applications. Contribution to Mineralogy and Petrology. 111, 74–86

Chakraborty S, (2006) Diffusion modeling as a tool for constraining timescales of evolution of metamorphic rocks. Mineralogy and Petrology. 88, 7–27

Chakraborty S, (2008) Diffusion in silicates: a tool to track timescales of processes comes of age Annual Review of Earth and Planetary Sciences. 36, 153–190

Chamberlain KJ, Morgan DJ, Wilson CJN, (2014) Timescales of mixing and mobilisation in the Bishop Tuff magma body: perspectives from diffusion chronometry. Contribution to Mineralogy and Petrology.167, 1034

Charlier BLA, Wilson CJN, Lowenstern JB, Blake S, van Calsteren PW, Davidson JP (2005) Magma generation at a large hyperactive silicic volcano (Taupo, New zealand) revealed by U-Th and U-Pb systematics in zircons. Journal of Petrology. 46, 3-32

Charlton D, Kilburn C, Edwards S. (2020) Volcanic unrest scenarios and impact assessment at Campi Flegrei caldera, Southern Italy. Journal of Applied Volcanology. 9, 7 https://doi.org/10.1186/s13617-020-00097-x

Cheng, H., Lemlich, R., (1983) Errors in measurement of bubble size distribution in foam. Industrial & Engineering Chemistry Fundamentals. 22, 105-109 doi: 10.1021/i100009a018

Cherniak DJ, (1996) Strontium diffusion in sanidine and albite, and general comments on strontium diffusion in alkali feldspars. Geochimica and Cosmochimica Acta. 60, 5037-5043

Cherniak DJ, (2002) Ba diffusion in feldspar. Geochimica and Cosmochimica Acta. 66, 1641-1650

Cherniak DJ, Watson EB, Wark DA, (2007) Ti diffusion in quartz. Chemica Geology. 236, 65-74

Chertkoff DG, Gardner JE, (2004) Nature and timing of magma interactions before, during, and after the caldera-forming eruption of Volcán Ceboruco, Mexico. Contribution to Mineralogy and Petrology. 146, 715-735

Chiesa S, Gillot PY, Orsi G, (1985a) The Citara-Serrara formation (Ischia island): Evidence for different explosive eruptions, in IAVCEI (International Association of Volcanology and Chemistry of the Earth’s Interior) 1985 Scientifi c Assembly Abstracts. 16–21. September 1985: Giardini Naxos, IAVCEI

Chiesa S, Gillot PY, Pasquarè G, Vezzoli L, (1985b) Collapse and resurgent calderic movements in a volcano-tectonic area: A new interpretation of the geological history of Ischia island, in IAVCEI (International Association of Volcanology and Chemistry of the

Earth's Interior) 1985 Scientific Assembly Abstracts. 16–21 September 1985: Giardini Naxos, IAVCEI

Chiesa S, Poli S, Vezzoli L, (1986) Studio dell'ultima eruzione storica dell'isola di Ischia: Bollettino del Gruppo Nazionale di Vulcanologia. 153–166

Chiesa S, Civetta L, De Lucia M, Orsi G, Poli S, (1987) Volcanological evolution of the island of Ischia, in Di Girolamo, P., ed., The Volcanoclastic Rocks of Campania (Southern Italy): Geochemical, Geophysical, Geological, Mineralogical, Paleomagnetic, Petrographical and Volcanological Aspects: Rendiconti dell'Accademia di Scienze Fisiche e Matematiche, Napoli (Special Issue). 69–83

Chiodini G, Frondini F, Cardellini C, Granieri D, Marini L, Ventura G (2001) CO_2 degassing and energy release at Solfatara volcano, Campi Flegrei, Italy. Journal of Geophysical Research. 106, 213–221

Chiodini G, Caliro S, De Martino P, Avino R, Gherardi F, (2012) Early signals of new volcanic unrest at Campi Flegrei caldera? Insights from geochemical data and physical simulations. Geology. 40, 943–946

Chiodini G, Vandemeulebrouck J, Caliro S, D'Auria L, De Martino P, Mangiacapra A, Petrillo Z, (2015) Evidence of thermal-driven processes triggering the 2005–2014 unrest at Campi Flegrei caldera. Earth and Planetary Science Letters. 414:58–67

Chiodini G, Paonita A, Aiuppa A, Costa A, Caliro S, De Martino P, Acocella V, Vandemeulebrouck J, (2016) Magmas near the critical degassing pressure drive volcanic unrest towards a critical state. Nature Communications. 7:13712. doi:10.1038/ncomms13712

Christopher T, Blundy J, Cashman K, Cole P, Edmonds M, Smith P, Sparks RSJ, Stinton A, (2015) Crustal-scale degassing due to magma system destabilization and magma-gas decoupling at Soufrière Hills Volcano, Montserrat. Geochemistry, Geophysics, Geosystems. 16, 2797–2811. (doi:10.1002/2015gc005791)

Cinque A, Alinaghi HH, Laureti L, Russo F, (1987) Osservazioni preliminari sull'evoluzione geomorfologica della piana del Sarno (Campania, Appennino Meridionale). Geografia Fisica Dinamica Quaternaria. 10, 161-174.

Cinque A, Patacca E, Scandone P, Tozzi M, (1993) Quaternary kinematic evolution of the Southern Apennines. Relationship between surface geological features and deep lithospheric structures. Annali Geofisica. 36, 249-260

Cioni R, Civetta L, Marianelli P, Metrich N, Santacroce R, Sbrana A, (1995) Compositional layering and syn-eruptive mixing of a periodically refilled shallow magma chamber: the AD 79 Plinian eruption of Vesuvius. Journal of Petrology. 36, 739–776

Cioni R, Marianelli P, Santacroce R, (1999) Temperature of Vesuvius magma. Geology. 27, 443–446

Civetta L, Carluccio E, Innocenti F, Sbrana A, Taddeucci G, (1991a). Magma chamber evolution under the Phlegraean Fields during the last 10 ka: trace element and isotope data. European Journal of Mineralogy. 3 415–428

Civetta L, Gallo G, Orsi G, (1991b) Sr- and Nd- isotope and trace-element constraints on the chemical evolution of the magmatic system of Ischia (Italy) in the last 55 ka. Journal of Volcanology and Geothermal Research. 46, 213–230 doi:10.1016/0377-0273(91)90084-D

Civetta L, Orsi G, Pappalardo L, Fisher RV, Heiken G, Ort M, (1997) Geochemical zoning, mingling, eruptive dynamics and depositional processes - the Campanian Ignimbrite, Campi Flegrei caldera, Italy. Journal of Volcanology and Geothermal Research. 75, 183–219

Clark AH, Pearce TH, Roeder PL, Wolfson RI, (1986) Oscillatory zoning and other microstructures in magmatic olivine and augite: Nomarski interference contrast observations on etched polished surfaces. American Mineralogist. 71, 734–741

Cooper AR, (1968) The use and limitations of the concept of an effective binary diffusion coefficient for multi-component diffusion. In: Wachtman JB, Franklin AD (eds) Mass transport in oxides. NBS special publication. Mineralogical Society of America, Chantilly, Virginia. 296, 79–84

Cooper KM, (2015) Timescales of crustal magma reservoir processes: insights from U-series crystal ages. Geological Society of London Special Publications. 422, SP422-7. (doi:10.1144/SP422.7)

Cooper KM, Reid MR, (2003) Re-examination of crystal ages in recent Mount St. Helens lavas: implications for magma reservoir processes. Earth and Planetary Science Letters. 213, 149–167 (doi:10.1016/S0012-821X(03)00262-0)

Cooper KM, Reid MR, (2008) Uranium-series crystal ages. Review of Mineralogy and Geochemistry. 69, 479–544. (doi:10.2138/rmg.2008.69.13)

Cooper KM, (2019) Time scales and temperatures of crystal storage in magma reservoirs: implications for magma reservoir dynamics. Philosphical Transaction of the Royal Society. 377: 20180009. http://dxdoiorg/101098/rsta20180009

Coombs ML, Eichelberger JC, Rutherford MJ, (2000) Magma storage and mixing conditions for the 1953-1974 eruptions of Southwest Trident volcano, Katmai National Park, Alaska. Contributions to Mineralogy and Petrology. 140, 99–118 doi: 10.1007/s004100000166

Conceição RV, Green DH, (2004) Derivation of potassic (shoshonitic) magmas by decompression melting of phlogopite+ pargasite lherzolite. Lithos 72, 209-229

Condomines M, Sigmarsson O, Gauthier PJ, (2010) A simple model of 222Rn accumulation leading to 210Pb excesses in volcanic rocks. Earth and Planetary Science Letters. 293, 331–338

Condomines M, Gauthier P-J, Sigmarsson O, (2003) Timescales of magma chamber processes and dating of young volcanic rocks. In Uranium Series Geochemistry. Reviews in

Mineralogy and Geochemistry (eds. B. Bourdon, GM. Henderson, CC. Lundstrom and SP. Turner). The Mineralogical Society of America, Washington, DC, pp. 125–174

Conticelli S, D‟Antonio M, Pinarelli L, Civetta L, (2002) Source contamination and mantle heterogeneity in the genesis of Italian potassic and ultrapotassic volcanic rocks: Sr-Nd-Pb Isotopic data from Roman Province and Southern Tuscany. Mineralogy and Petrology. 74, 189-222

Conticelli S, Melluso L, Perini G, Avanzinelli R, Boari E, (2004) Petrologic, geochemical and isotopic characteristics of potassic and ultrapotassic magmatism in central-southern Italy: inferences on its genesis and on the nature of the mantle sources. Periodico di Mineralogia. 73, 153-164

Conticelli S, Carlson RW, Widom E, Serri G, (2007) Chemical and isotopic composition (Os, Pb, Nd, and Sr) of Neogene to Quaternary calc-alkalic, shoshonitic, and ultrapotassic mafic rocks from the Italian peninsula: inferences on the nature of their mantle sources. In: Beccaluva L., et al. (Eds.), Cenozoic Volcanism in the Mediterranean Area. Geological Society of America Special Paper. 418, 171-202

Conticelli S, Guarnieri L, Farinelli A, Mattei M, Avanzinelli R, Bianchini G, Boari E, Tommasini S, Tiepolo M, Prelević D, Venturelli G, (2009) Trace elements and Sr–Nd–Pb isotopics of K-rich, shoshonitic, and calc-alkaline magmatism of the Western Mediterranean Region: Genesis of ultrapotassic to calc-alkaline magmatic associations in a post-collisional geodynamic setting. Lithos 107, 68-92

Conticelli S, Laurenzi MA, Giordano G, Matte M, Avanzinelli R, Melluso L, Tommasini S, Boari E, Cifelli F, Perini G, (2010) Leucite-bearing (kamafugitic/leucititic) and –free (lamproitic) ultrapotassic rocks and associated shoshonites from Italy: constraints on petrogenesis and geodynamics. In: (Eds.) Marco Beltrando, Angelo Peccerillo, Massimo Mattei, Sandro Conticelli, and Carlo Doglioni, Journal of the Virtual Explorer. 36, 20 p. doi: 10.3809/jvirtex.2010.00251

Cornell W, Carey SN, Sigurdsson H. (1983) Computer simulation of transport and deposition of the campanian Y-5 ash. Journal of Volcanology and Geothermal Research. 17, 89–109. doi:10.1016/0377-0273(83)90063-X

Costa A, Folch A, Macedonio G, Giaccio B, Isaia R, Smith VC, (2012) Quantifying volcanic ash dispersal and impact of the Campanian Ignimbrite super-eruption. Geophysical Research Letters. 39 (10). http://dx.doi.org/10.1029/2012GL051605.

Costa F, Chakraborty S, Dohmen R. (2003) Diffusion coupling between trace and major elements and a model for calculation of magma residence times using plagioclase. Geochimica and Cosmochimica Acta 67, 2189–2200 doi:10.1016/S0016-7037(02)01345-5)

Costa F, Chakraborty S, (2004) Decadal time gaps between mafic intrusion and silicic eruption obtained from chemical zoning patterns in olivine. Earth and Planetary Science Letters. 227, 517–530

Costa F, Streck M, (2004) Periodicity and timescales for basaltic magma replenishment at Volcán Arenal (Costa Rica). IAVCEI General Assembly 2004 abstracts

Costa F, Dungan M, (2005) Short timescales of magmatic assimilation from diffusion modelling of multiple elements in olivine. Geology. 33, 837–840

Costa F, Dohmen R Chakraborty S, (2008) Time scales of magmatic processes from modeling zoning patterns of crystals. In: Rosso, JJ. Minerals, Inclusions and Volcanic Processes. Mineralogical Society of America. Reviews in Mineralogy and Geochemistry. 69,545-594

Costa F, Coogan L, Chakraborty S, (2010) The timescales of magma mixing and mingling involving primitive melts and melt-mush interaction at Mid-Ocean Ridges. Contributions to Mineralogy and Petrology. 159, 371–387

Costa F, Morgan D, (2011) Time constraints from chemical equilibration in magmatic crystals. In Timescales of magmatic processes: from core to atmosphere, (eds A. Dosseto, S. Turner, J. Van-Orman). 125–159. Chichester, UK. Wiley.

Couch S, Sparks RSJ, Carroll MR (2001) Mineral disequilibrium in lavas explained by convective self-mixing in open magma chambers. Nature. 411, 1037–1039

Cox KG, Bell JD, Pankhurst RJ, (1979) The Interpretation of Igneous Rocks. London George Allen & Unwin. 450 pp.

Crank J, (1975) The Mathematics of Diffusion, 2nd edn. Oxford: Oxford University Press, 410 pp.

Crisci GM, De Francesco AM, Mazzuoli R, Poli G, Stanzione D, (1989) Geochemistry of recent volcanics of Ischia Island, Italy: Evidences for fractional crystallization and magma mixing. Chemical Geology. 78, 15-33

Cubellis E, (1985) Il terremoto di Casamicciola del 28 luglio 1883: Analisi degli effetti, modellizzazione della sorgente ed implicazioni sulla dinamica in atto: Bollettino della Società dei Naturalisti in Napoli. 94, 157–186

D’Antonio M, Tilton GR, Civetta L, (1996) Petrogenesis of Italian alkaline lavas deduced from Pb-Sr-Nd isotopic relationships. In: Basu, A., Hart, S.R., (Eds.). Isotopic Studies of Crust-Mantle Evolution - American Geophysical Union, Geophysical Monograph. 95, 253-267

D’Antonio M, Civetta L, Di Girolamo P, (1999a) Mantle source heterogeneity in the Campanian region (south Italy) as inferred from geochemical and isotopic features of mafic volcanic rocks with shoshonitic affinity. Mineralogy and Petrology. 67, 163-192.

D’Antonio M, Civetta L, Orsi G, Pappalardo L, Piochi M, Carandente A, de Vita S, Di Vito MA, Isaia R, (1999b) The present state of the magmatic system of the Campi Flegrei caldera based on a reconstruction of its behavior in the past 12 ka: Journal of

Volcanology and Geothermal Research. 91, 247–268 doi:101016/S0377-0273(99)00038-4

D'Antonio M, Tonarini S, Arienzo I, Civetta L, Di Renzo V, (2007) Components and processes in the magma genesis of the Phlegrean Volcanic District, southern Italy. Geological Society of America. 418, 203–220

D'Antonio M, (2011) Lithology of the basement underlying the Campi Flegrei caldera: volcanological and petrological constraints. Journal of Volcanology and Geothermal Research. 200, 91–98

D’Antonio M, Tonarini S, Arienzo I, Civetta L, Dallai L, Moretti R, Orsi G, Andria M, Trecalli A, (2013) Mantle and crustal processes in the magmatism of the Campania region: inferences from mineralogy, geochemistry, and Sr–Nd–O isotopes of young hybrid volcanics of the Ischia island (South Italy). Contribution to Mineralogy and Petrology. 165, 1173–1194

D’Argenio B, Pescatore TS, Scandone P, (1973) Schema geologico dell’Appennino Meridionale. Accademia Nazionale dei Lincei. Quad. 183, 49-72

D’Auria L, Giudicepietro F, Aquino I, Borriello G, Del Gaudio C, Lo Bascio D, Martini M, Ricciardi GP, Ricciolino P, Ricco C, (2011) Repeated fluid-transfer episodes as a mechanism for the recent dynamics of Campi Flegrei Caldera (1989–2010). Journal of Geophysical Research.116 (B4), B04313. http://dx.doi.org/10.1029/2010JB007837.

Davidson JP Tepley FJ, (1997) Recharge in volcanic systems: Evidence from isotope profiles of phenocrysts. Science. 275, 826-829.

Davidson JP, Tepley FJ, Palacz Z Meffan-Main S, (2001) Magma recharge, contamination and residence times revealed by in situ laser ablation isotopic analysis of feldspar in volcanic rocks. Earth and Planetary Science Letters. 184, 427-442

Davidson JP, Morgan DJ, Charlier BLA, Harlou R, Hora JM, (2007) Microsampling and isotopic analysis of igneous rocks: Implications for the study of magmatic systems. Annual Review of Earth and Planetary Sciences. 35, 273-311

De Astis G, Kempton PD, Peccerillo A, Wu TW, (2006) Trace element and isotopic variations from Mt. Vulture to Campanian volcanoes: constraints for slab detachment and mantle inflow beneath southern Italy. Contributions to Mineralogy and Petrology. 151, 331-351

Deecke W, (1901) Geologischer Führer durch Campanien: Berlin, Verlag von Gebrüder Bornträger, 235 p.

de'Gennaro M, Cappelletti P, Langella A, Perrotta A, Scarpati C (2000) Genesis of zeolites in the Neapolitan Yellow Tuff: geological, volcanological and mineralogical evidence. Contribution to Mineralogy and Petrology. 139, 17–35. https ://doi.org/10.1007/s0041 00050 571

Deino A, Orsi G, de Vita S, Piochi M, (2004) The age of the Neapolitan Yellow Tuff caldera-forming eruption (Campi Flegrei caldera Italy) assessed by ^{40}Ar/^{39}Ar dating method. Journal of Volcanology and Geothermal Research. 133, 157–170

Del Gaudio C, Sepe V, (1998) Ischia: Vertical ground movements. Acta Vulcanologica. 10, 110–112

Del Gaudio C, Aquino I, Ricciardi GP, Ricco C, Scandone R, (2010) Unrest episodes at Campi Flegrei: A reconstruction of vertical ground movements during 1905–2009. Journal of Volcanology and Geothermal Research. 195, 48–56

Dellino P, Isaia R, La Volpe L, Orsi G, (2001) Statistical analysis of textural data from complex pyroclastic sequences: implications for fragmentation processes of the Agnano-Monte Spina Tephra (4.1 ka), Phlegraean Fields, southern Italy. Bulletin of Volcanology. 63, 443–461 https://doiorg/101007/s004450100163

Dellino P, Isaia R, La Volpe L, Orsi G, (2004a) Interaction between particles transported by fallout and surge in the deposits of the Agnano–Monte Spina eruption (Campi Flegrei Southern Italy) Journal of Volcanology and Geothermal Research. 133, 193–210. https://doiorg/101016/S0377-0273(03)00398-6

De Lorenzo G, (1904) Geologia e Geografi a Fisica dell'Italia Meridionale. Bari, Ed. Laterza. 241 p.

Demouchy S, Jacobsen SD, Gaillard F, Stern CR, (2006) Rapid magma ascent recorded by water diffusion profiles in mantle olivine. Geology. 34, 429-432

De Natale G, Troise C, Pingue F (2001) A mechanical fluid-dynamical model for ground movements at Campi Flegrei caldera. Journal of Geodynamic. 32, 487–517

De Natale G, Troise C, Pingue F, Mastrolorenzo G, Pappalardo L, Battaglia M, Boschi E, (2006) The Campi Flegrei caldera: Unrest mechanisms and hazard. Geological Society London Special Publications. 269, 25-45 doi:10.1144/GSL.SP.2006.269.01.03

De Novellis V, Carlino S, Castaldo R, Tramelli A, De Luca C, Pino NA, Pepe S, Convertito V, Zinno I, De Martino P, Bonano M, Giudicepietro F, Casu F, Macedonio G, Manunta M, Cardaci C, Manzo M, Di Bucci D, Solaro G, Zeni G, Lanari R, Bianco F, Tizzani P (2018) The 21 August 2017 Ischia (Italy) earthquake source model inferred from seismological, GPS, and DInSAR measurements. Geophysical Research Letters. 45, 2193–2202 https ://doi.org/10.1002/2017GL0763 36

DePaolo DJ, (1979) Implications of correlated Nd and Sr isotopic variations for the chemical evolution of the crust and mantle. Earth and Planetary Science Letters. 43, 201-211

de Vita S, Orsi G, Civetta L, Carandente A, D'Antonio M, Deino A, di Cesare T, Di Vito MA, Fisher RV, Isaia R, Marotta E, Necco A, Ort M, Pappalardo L, Piochi M, Southon J, (1999) The Agnano – Monte Spina eruption (4100 years BP) in the restless Campi Flegrei caldera (Italy). Journal of Volcanology and Geothermal Research. 91, 269–301.

de Vita S, Sansivero F, Orsi G, Marotta E, (2006) Cyclical slope instability and volcanism related to volcano-tectonism in resurgent calderas: the Ischia Island (Italy) case study. Engineering Geology. 86, 148–165

de Vita S, Sansivero F, Orsi G, Marotta E, Piochi M, (2010) Volcanological and structural evolution of the Ischia resurgent caldera (Italy) over the past 10 k.y. Geological Society of America. 464, 193–241

de Vita S, Sansivero F, Marotta E, Di Vito MA, (2013) Assetto geologico-strutturale ed evoluzione vulcanologica dell'isola d'Ischia. In: SCUOLA ESTIVA AIQUA 2013 Napoli 27 | 31 maggio 2013 Miscellanea I.N.G.V. Istituto Nazionale di Geofisica e Vulcanologia, Sezione di Napoli - Osservatorio Vesuviano, Napoli, Italia. 18, ISSN 2039-6651.

De Vivo B, Rolandi G, Gans PB, Calvert A, Bohrson WA, Spera FJ, Belkin HE, (2001) New constraints on the pyroclastic eruptive history of the Campanian volcanic plain (Italy). Mineralogy and Petrology. 73, 47–65

Didier J, Barbarin B, (1991) Enclaves and Granite Petrology. 13. Elsevier, Amsterdam

Di Girolamo P, Ghiara MR, Lirer L, Munno R, Rolandi G, Stanzione D, (1984). Vulcanologia e petrologia dei Campi Flegrei. Bollettino della Società. Geologica Italiana 103, 349-413

Di Girolamo P, Melluso L, Morra V, Secchi FAG, (1995) Evidence of interaction between mafic and differentiated magmas in the youngest phase of activity at Ischia Island (Italy). Period di Mineralogia. 64, 393–411

Dimanov A, Jaoul O, (1998) Calcium self-diffusion in diopside at high temperature: implications for transport properties. Physics and Chemistry of Minerals. 26, 116-127

Dimanov A, Sautter V (2000) "Average" interdiffusion of (Fe,Mn)–Mg in natural diopside. European Journal of Mineralogy. 12, 749–760

Di Napoli R, Martorana R, Orsi G, Aiuppa A, Camarda M, De Gregorio S, Gagliano Candela E, Luzio D, Messina N, Pecoraino G, Bitetto M, de Vita S, Valenza M, (2011) The structure of a hydrothermal system from an integrated geochemical, geophysical, and geological approach: The Ischia Island case study. Geochemistry, Geophysics, Geosystems. 12, 79–85 https://doi.org/10.1029/2010GC003476

Di Napoli R, Federico C, Aiuppa A, D'Antonio M, Valenza M, (2013) Quantitative models of hydrothermal fluid-mineral reaction: the Ischia case. Geochimica and Cosmochimica Acta. 105, 108–129

Di Renzo V, Di Vito MA, Arienzo I, Carandente A, Civetta L, D'Antonio M, Giordano F, Orsi G, Tonarini S, (2007) Magmatic history of Somma–Vesuvius on the basis of new geochemical and isotopic data from a deep borehole (Camaldoli dellaTorre). Journal of Petrology. 48, 753–784

Di Renzo V, Arienzo I Civetta L, D'Antonio M, Tonarini S, Di Vito MA, Orsi G, (2011) The magmatic feeding system of the Campi Flegrei caldera: architecture and temporal evolution. Chemical Geology. 281, 227–241

Di Vito M, Lirer L, Mastrolorenzo G, Rolandi, G, (1985). Volcanological map of Campi Flegrei: Min. Prot. Civ. Univ. degli Studi di Napoli.

Di Vito MA, Isaia R, Orsi G, Southon J, de Vita S, D'antonio M, Pappalardo L, Piochi M, (1999) Volcanism and deformation in the past 12 ka at the Campi Flegrei caldera (Italy) Journal of Volcanology and Geothermal Research. 91, 221–246

Di Vito MA, Acocella V, Aiello G, Barra D, Battaglia M, Carandente A, Del Gaudio C, de Vita S, Ricciardi GP, Ricco C, Scandone R, Terrasi F, (2016) Magma transfer at Campi Flegrei caldera (Italy) before the 1538 AD eruption. Scientific Reports. 6, 32245

Dodson MH, (1986) Closure profiles in cooling systems. Materials Science Forum. 7, 145–154

Dohmen R, Becker HW, Meissner E, Etzel T, Chakraborty S, (2002) Production of silicate thin films using pulsed laser deposition (PLD) and applications to studies in mineral kinetics. European Journal of Mineralogy. 14, 1155-1168

Dohmen R, Faak K, Blundy JD, (2017) Chronometry and speedometry of magmatic processes using chemical diffusion in olivine, plagioclase and pyroxenes. Reviews in Mineralogy and Geochemistry. 83,535–575 doi:10.2138/rmg.2017.83.16

Don Snyder, (2000) Thermal effects of the intrusion of basaltic magma into a more silicic magma chamber and implications for eruption triggering. Earth and Planetary Science Letters. 175, 257–273

Downes MJ, (1974) Sector and oscillatory zoning in calcic augites from Mt. Etna Sicily. Contribution to Mineralogy and Petrology. 47, 187–196

Druitt TH, Costa F, Deloule E, Dungan M, Scaillet B (2012) Decadal to monthly timescales of magma transfer and reservoir growth at a caldera volcano. Nature. 482, 77–80

Duggen S, Hoernle K, van den Bogaard P, Garbe-Schönberg D, (2005) Postcollisional transition from subduction-to intraplate-type magmatism in the westernmost Mediterranean: evidence for continental-edge delamination of subcontinental lithosphere. Journal of Petrology. 46, 1155-1201

Eberl DD, Kile DE, Drits VA, (2002) On geological interpretations of crystal size distributions: constant vs. proportionate growth. American Mineralogist. 87, 1235–1241

Edmonds M, (2008) New geochemical insights into volcanic degassing. Philosophical Transactions of the Royal Society A: Mathematical, Physical and Engineering Sciences. 366, 4559–4579

Edmonds M, Aiuppa A, Humphreys M, Moretti R, Giudice G, Martin RS, Herd RA, Christopher T, (2010) Excess volatiles supplied by mingling of mafic magma at an andesite arc volcano. Geochemistry, Geophysics, Geosystems. 11, Q04005. (doi:10.1029/2009gc002781)

Edmonds M, Cashman KV, Holness M, Jackson M, (2019) Architecture and dynamics of magma reservoirs. Philosophical Transactions of the Royal Society A. 377: 20180298. http://dx.doi.org/10.1098/rsta.2018.0298

Edwards BR, Russell JK (1996) A review and analysis of silicate mineral dissolution experiments in natural silicate melts. Chemical Geology. 130, 233-245

Eichelberger JC (1975) Origin of andesite and dacite: evidence of mixing at Glass Mountain in California and at other circum-Pacific volcanoes. Geological Society American Bulletin. 86, 1381-1391

Eichelberger JC, (1978) Andesitic volcanism and crustal evolution. Nature. 275, 21-27

Eichelberger JC, (1980). Vesiculation of mafic magma during replenishment of silicic magma reservoirs. Nature. 288, 446–450

Ellam RM, Hawkesworth CJ, Menzies MA, Rogers NW, (1989) The volcanism of southern Italy: role of subduction and the relationships between potassic and sodic alkaline magmatism. Journal of Geophysical Research. 94, 4589-4601

Engwell S, Sparks RSJ, CareyS, (2014) Physical characteristics of tephra layers in the deep sea realm: the Campanian Ignimbrite eruption. Geological Society London Special Publications. 398(1) doi: 10.1144/SP398.7

Faccenna C, Funiciello F, Civetta L, D’Antonio M, Moroni M, Piromallo C, (2007) Slab distribution, mantle circulation, and the opening of the Tyrrhenian basin. In: Beccaluva L., et al. (Eds.), Cenozoic Volcanism in the Mediterranean Area. Geological Society of America Special Paper. 418, 153-169

Faure G, (1992) Principles and Applications of Inorganic Geochemistry. Maxwell MacMilan International Editions, New York, 625

Fedele L, Scarpati C, Lanphere M, Melluso L, Morra V, Perrotta A, Ricci G, (2008) The Breccia Museo formation, Campi Flegrei, southern Italy: geochronology, chemostratigraphy and relationship with the Campanian Ignimbrite eruption. Bulletin of Volcanology. 70, 1189–1219

Fedele L, Scarpati C, Sparice D, Perrotta A, Laiena F, (2016) A chemostratigraphic study of the Campanian Ignimbrite eruption (Campi Flegrei, Italy): Insights on magma chamber withdrawal and deposit accumulation as revealed by compositionally zoned stratigraphic and facies framework. Journal of Volcanology and Geothermal Research. 324, 105–117

Fick A, (1855) Uber Diffusion. Annual Review of Physical Chemistry. 94, 59-86

Fisher JC, (1951) Calculation of diffusion penetration curves for surface and grain boundary diffusion. Journal of Applied Physics. 22, 74–77

Fisher RV, Orsi G, Ort M, Heiken G, (1993) Mobility of a large-volume pyroclastic flowemplacement of the Campanian Ignimbrite, Italy. Journal of Volcanology and Geothermal Research. 56, 205–220

Flinders J, Clemens JD, (1996) Non-linear dynamics, chaos, complexity and enclaves in granitoid magmas. Transactions of the Royal Society of Edinburgh: Earth Science. 87, 225–232

Folch A, Martì J, (1998) The generation of overpressure in felsic magma chambers by replenishment. Earth and Planetary Science Letters. 163, 301–314

Foley SF, (1992) Petrological characterization of the source components of potassic magmas: geochemical and experimental constraints. Lithos 28, 187-204

Fonseca F, (1847) Descrizione e carta geologica dell’Isola d’Ischia: Annali dell’Accademia degli Aspiranti Naturalisti, Napoli. 1, 163–200

Fonseca F, (1870) Geologia dell’Isola d’Ischia: Firenze. Tipografi a Cavour.

Fourmentraux C, Mètrich N, Bertagnini A, Rosi M, (2012) Crystal fractionation, magma step ascent, and syn-eruptive mingling: the Averno 2 eruption (Phlegraean Fields, Italy).Contribution to Mineralogy and Petrology. 163, 1121–1137

Forni F, Petricca E, Bachmann O, Mollo S, De Astis G, Piochi M, (2018a) The role of magma mixing/mingling and cumulate melting in the Neapolitan Yellow Tuff caldera-forming eruption (Campi Flegrei, Southern Italy). Contribution to Mineralogy and Petrololgy. 173, 10.1007/s00410-018-1471-4

Forni F, Degruyter W, Bachmann O, De Astis G, Mollo S, (2018b) Long-term magmatic evolution reveals the beginning of a new caldera cycle at Campi Flegrei. Science Advances. 4, eaat9401

Fourcade S, Allegre C, (1981) Trace elements behavior in granite genesis: a case study: the calc-alkaline plutonic association from the Querigut Complex (Pyrenees, France). Contributions to Mineralogy and Petrology. 76, 177–195

Fourier JB, (1822) Theorie Analytique de Ia Chaleur, Envres de Fourier. English translation by A. Freeman. New York: Dover Publications, 1955.

Francalanci L, Avanzinelli R, Petrone CM, Santo AP, (2004) Petrological and magmatological characteristics of the Aeolian Arc volcanoes, southern Tyrrhenian Sea, Italy: inferences on shallow level processes and magma source variations. Periodico di Mineralogia. 73, 75-104

Francalanci L, Avanzinelli R, Tommasini S, Heuman A, (2007) A west-east geochemical and isotopic traverse along the volcanism of the Aeolian Island Arc, southern Tyrrhenian Sea, Italy: inferences on the mantle source processes. In: Beccaluva L., et al. (Eds.). Cenozoic Volcanism in the Mediterranean Area. Geological Society of America Special Paper. 418, 235-263

Freer R, Carpenter M, Long J, Reed S, (1982) “Null result” diffusion experiments with diopside: implications for pyroxene equilibria. Earth and Planetary Science Letters. 58, 285-292

Freymuth H, Brandmeier M, Wörner G, (2015) The origin and crust/mantle mass balance of Central Andean ignimbrite magmatism constrained by oxygen and strontium isotopes and erupted volumes. Contribtion to Mineralogy and Petrology. 169, 58 doi: 10.1007/s00410-015-1152-5

Freundt A, Tait SR, (1986) The entrainment of high-viscosity magma into low-viscosity magma in eruption conduits. Bulletin of Volcanology. 48, 325–339. https://doi.org/10.1007/BF01074464

Friedlander I, (1927) Oggetti preistorici dell’isola d’Ischia: Bollettino di Paleontologia Italiana. 47, 3

Fusi N, Tibaldi A, Vezzoli L, (1990) Vulcanismo, risorgenza calderica e relazioni con la tettonica regionale nell’isola d’Ischia: Memorie della Società Geologica Italiana. 45, 971–980

Gagnevin D, Daly JS, Poli G, Morgan D, (2005) Pb isotopic zoning of K-feldspar megacrysts determined by laser ablation multi-collector ICP-MS: Insights into granite petrogenesis. Geochimica et Cosmochimica Acta. 69, 1899-1915

Ganguly J, Bhattacharya RN, Chakraborty S, (1988) Convolution effect in the determination of compositional profiles and diffusion coefficients by microprobe step scans. American Mineralogist. 73, 901–909

Ganguly J, (2002) Diffusion kinetics in minerals: principles and applications to tectono-metamorphic processes. In EMU Notes in Mineralogy, Energy Modelling in Minerals, ed. CM Gramaccioli. Budapest: Eötvös Univ. Press Eur Mineral Union. 4, 271-309

Garrido CJ, Keleman PB, Hirth G, (2001) Variation of cooling rate with depth in lower crust formed at an oceanic spreading ridge: plagioclase crystal size distributions in gabbros from the Omanophiolite. Geochemistry, Geophysic, Geosystem. 2 (10) 2000GC000136

Gasperini D, Blichert-Toft J, Bosch D, Del Moro A, Macera P, Albaréde F, (2002) Upwelling of deep mantle material through a plate window: evidence from the geochemistry of

Italian basaltic volcanics. Journal of Geophysical Research. 107 doi:10.1029/2001jb000418.

Gauthier P-J, Condomines M, (1999) ^{210}Pb-^{226}Ra radioactive disequilibria in recent lavas and radon degassing: inferences on magma chamber dynamics at Stromboli and Merapi volcanoes. Earth and Planetary Science Letters. 172, 111–126

Gebauer SK, Schmitt AK, Pappalardo L, Stockli DF, Lovera OM (2014) Crystallization and eruption ages of Breccia Museo (Campi Flegrei caldera, Italy) plutonic clasts and their relation to the Campanian ignimbrite. Contribution to Mineralogy and Petrology. 167, 1–18

Gee LL, Sack RO, (1988) Experimental petrology of melilite nephelinites. Journal of Petrology 29, 1235–1255

Giaccio B, Hajdas I, Isaia R, Deino A, Nomade S, (2017) High-precision ^{14}C and ^{40}Ar/^{39}Ar dating of the Campanian Ignimbrite (Y-5) reconciles the time-scales of climatic-cultural processes at 40 ka Scientific Reports. 7, 45940 doi: 101038/srep45940

Giacomoni PP, Coltorti M, Bryce JG, Fahnestock MF, Guitreau M, (2016) Mt. Etna plumbing system revealed by combined textural, compositional, and thermobarometric studies in clinopyroxenes. Contributions to Mineralogy and Petrology. 171, 34

Gialanella C, (1994) Pithecusa: Gli insediamenti di Punta Chiarito. Relazione preliminare: Annali di Archeologia e Storia Antica (A□OIKIA. I.U.O.). 1, 169–204

Gill J, Williams R, Bruland K, (1985) Eruption of basalt and andesite lava degasses ^{222}Rn and ^{210}Po. Geophysical Research Letters. 12, 17–20

Gill JB, Williams RW, (1990) Th isotope and U-series studies of subduction-related volcanic rocks. Geochimica and Cosmochimica Acta. 54, 1427–1442

Gillot PY, Chiesa S, Pasquarè G, Vezzoli L, (1982) < 33,000 yr K-Ar dating of the volcano-tectonic horst of the Isle of Ischia, Gulf of Naples. Nature. 299, 242–245 doi: 10.1038/299242a0

Ginibre C, Kronz A, Worner G, (2002) High-resolution quantitative imaging of plagioclase composition using accumulated back-scattered electron images: new constraints on oscillatory zoning. Contributions to Mineralogy and Petrology. 142, 436–448

Ginibre C, Wörner G, Kronz A (2007) Crystal zoning as an archive for magma evolution. Elements. 3, 261–266

Goldstein SL, Deines P, Oelkers EH, Rudnick RL, Walter LM (2003) Standards for publication of isotope ratio and chemical data in Chemical Geology. Chemical Geology. 202, 1–4

Grasso M, (2001) The Apenninic-Maghrebian orogen in Southern Italy, Sicily and adjacent areas. In: Vai GB, Martini PI (eds) Anatomy of an Orogen. The Apennines and adjacent Mediterranean basins. Kluwer, Dordrecht. 255-286

Grove TL, Bryan WB (1983) Fractionation of pyroxene-phyric MORB at low pressure: and experimental study. Contribution to Mineralogy and Petrology. 84, 293–209

Grove TL, Baker MB, Kinzler RJ, (1984) Coupled CaAl-NaSi diffusion in plagioclase feldspar: experiments and applications to cooling rate speedometry. Geochimica et Cosmochimica Acta. 48, 2113–2121

Grove TL, Brown SM, (2018) Magmatic processes leading to compositional diversity in igneous rocks: Bowen (1928) revisited. American Journal of Science. 318, 1-28. DOI: 10.2475/01.2018.02

Guidarelli M, Saraò A, Panza GF, (2002) Surface wave tomography and seismic source studies at Campi Flegrei (Italy). Physics of the Earth and Planetary Interiors. 134, 157–173

Guidarelli M, Zille A, Saraò A, Natale M, Nunziata C, Panza GF, (2006) Shear-wave velocity models and seismic sources in campanian volcanic areas: vesuvius and phlegraean fields. In: Dobran, F. (Ed.), Vesuvius. Elsevier B.V, Amsterdam, The Netherlands, pp. 287–309

Guidoboni E, Ciuccarelli C, (2011) The Campi Flegrei caldera: historical revision and new data on seismic crises, bradyseisms, the Monte Nuovo eruption and ensuing earthquakes (twelfth century 1582 ad) Bulletin of Volcanology 73, 655–677

Gvirtzman Z, Nur A, (1999) The formation of Mount Etna as the consequence of slab rollback. Nature. 401, 782-785

Hammer JE, Cashman KV, Hoblitt RP, Newman S, (1999) Degassing and microlite crystallization during pre-climactic events of the 1991 eruption of Mt. Pinatubo, Philippines. Bulletin of Volcanology. 60, 355–380

Handley HK, Turner SP, Smith IE, Stewart RB, Cronin SJ, (2008) Rapid timescales of differentiation and evidence for crustal contamination at intra-oceanic arcs: geochemical and U-Th-Ra-Sr-Nd isotopic constraints from Lopevi volcano, Vanuatu, SW Pacific. Earth and Planetary Science Letters. 273, 184–194

Handy MR, Schmid SM, Bousquet R, Kissling E, Bernoulli D, (2010) Reconciling plate-tectonic reconstructions of Alpine Tethys with the geological–geophysical record of spreading and subduction in the Alps. Earth Science Reviews. 102, 121-158

Hansteen TH, Klügel A, (2008) Fluid inclusion thermobarometry as a tracer for magmatic processes. Reviews in Mineralogy and Geochemistry. 69, 143–177

Harangi S, Downes H, Seghedi I, (2006) Tertiary-Quaternary subduction processes and related magmatism in the Alpine-Mediterranean region. In: Gee D.G., Stephenson R. (Eds.) European Lithosphere Dynamics - Geological Society of London’s Memoirs 32, 167-190

Hawkesworth CJ, Turner SP, McDermott F, Peate DW, van Calsteren P, (1997) U-Th isotopes in arc magmas: implications for element transfer from the subducted crust. Science 276, 551–555

Hawkesworth CJ, Blake S, Evans P, Hughes R, Macdonald R, Thomas L, Turner SP, Zellmer G, (2000) Time scales of crystal fractionation in magma chambers—integrating physical, isotopic and geochemical perspectives. Journal of Petrology. 41, 991–1006 doi:10.1093/petrology/41.7.991

Helz RT, (1987) Diverse olivine types in lavas of the 1959 eruption of Kilauea volcano and their bearing on eruption dynamics. In: Decker RW, Wright TL, Stauffer PH, (Eds.). Volcanism in Hawaii. US. Prof. Paper. 1350, 691–722

Henry DJ, Guidotti CV, Thomson JA, (2005) The Ti-saturation surface for low-to-medium pressure metapelitic biotites: implications for geothermometry and Ti-substitution mechanisms. American Mineralogist. 90, 316-328

Henstock TJ, Woods AW, White RS, (1993) The accretion of oceanic crust by episodic sill intrusion. Journal of Geophysical Research. 98, 4143

Hibbard MJ, (1981) The magma mixing origin of mantled feldspars. Contribution to Mineralogy and Petrology. 76, 158–170

Higgins MD, (1996a) Crystal size distributions and other quantitative textural measurements in lavas and tuff from Egmont volcano (Mt. Taranaki), New Zealand. Bulletin of Volcanology. 58, 194–204

Higgins MD, (1996b). Magma dynamics beneath Kameni volcano, Thera, Greece, as revealed by crystal size and shape measurements. Journal of Volcanology and Geothermal Research. 70, 37–48

Higgins MD, (1998) Origin of anorthosite by textural coarsening: quantitative measurements of a natural sequence of textural development. Journal of Petrology. 39, 1307–1323

Higgins MD, (1999) Origin of megacrysts in granitoids by textural coarsening: a crystal size distribution (CSD) study of microcline in the Cathedral Peak Granodiorite, Sierra Nevada, California. In: Castro, A., Fernandez, C., Vigneresse, J.L. (Eds.), Understanding Granites: Integrating New and Classical Techniques: Geological Society of London Special Publication. 168, 207–219. London

Higgins MD, Roberge J, (2003) Crystal size distribution of plagioclase and amphibole from Soufrière Hills Volcano, Montserrat: evidence for dynamic crystallization textural coarsening cycles. Journal of Petrology. 44, 1401–1411

Huber C, Bachmann O, Dufek J, (2011) Thermo-mechanical reactivation of locked crystal mushes: melting-induced internal fracturing and assimilation processes in magmas. Earth and Planetary Science Letters. 304, 443–454. doi:10.1016/j.epsl.2011.02.022

Humphreys MCS, Blundy JD, Sparks RSJ, (2006) Magma evolution and open-system processes at Shiveluch volcano: insights from phenocryst zoning. Journal of Petrology. 47, 2303–2334

Iovine RS, Fedele L, Mazzeo FC, Arienzo I Cavallo A, Wörner G, Orsi G, Civetta L, D'Antonio M, (2017a) Timescales of magmatic processes occurred prior to the ca 47 ka Agnano-Monte Spina eruption (Campi Flegrei caldera Southern Italy) based on diffusion chronometry on sanidine phenocrysts. Bulletin of Volcanology. 79, 18 doi:101007/s00445-017-1101-4

Iovine RS, Mazzeo FC, Arienzo I, D'AntonioM , Wörner G, Civetta L, Pastore Z, Orsi G, (2017b) Source and magmatic evolution inferred from geochemical and Sr-O-isotope data on hybrid lavas of Arso, the last eruption at Ischia island (Italy; 1302 AD). Journal of Volcanology and Geothermal Research. 331, 1–15

Iovine RS, Mazzeo FC, Wörner G, Pelullo C, Cirillo G, Arienzo I, Pack A, D'Antonio M, (2018) Coupled δ^{18}O-δ^{17}O and ^{87}Sr/^{86}Sr isotope compositions suggest a radiogenic and 18O-enriched magma source for Neapolitan volcanoes (Southern Italy). Lithos. 316–317, 199–211

Ippolito F, D'Argenio B, Pescatore T, Scandone P, (1975) Structural-stratigraphic units and tectonic framework of Southern Apennines. In: Squyres CH (ed) Geology of Italy. Petrol Expl Soc Libya, Tripoli. 317-328

Isaia R, D’Antonio M, Dell’Erba F, Di Vito M, Orsi G, (2004). The Astroni volcano: the only example of closely spaced eruptions in the same vent area during the recent history of Campi Flegrei caldera (Italy). Journal of Volcanology and Geothermal Research. 133, 171–192 doi:10.1016/S0377-0273(03)00397-4

Isaia R, Marianelli P, Sbrana A, (2009) Caldera unrest prior to intense volcanism in Campi Flegrei (Italy) at 4.0 ka B.P.: implications for caldera dynamics and future eruptive scenarios. Geophysical Research Letters 36, L21303 doi:10.1029/2009GL040513

Jagoutz E, Palme H, Baddenhausen H, Blum K, Cendales M, Dreibus G, Spettel B, Lorentz V, Wllnke H, (1979) The abundances of major, minor and trace elements in the Earth's mantle as derived from primitive ultramafic nodules. Proceedings of the 10th Lunar and Planetary Science Conference. Geochimica and Cosmochimica Acta. Supp. I. 11, 2031-2050

James DE, (1982) A combined O, Sr, Nd, and Pb isotopic and trace element study of crustal contamination in central Andean lavas, I. Local geochemical variations. Earth and Planetary Science Letters. 57, 47-62

Jancic S, Garside J, (1976) A new technique for accurate crystal size distribution analysis in an MSMPR crystallizer. In: Mullin, J.F. (Ed.), Industrial Crystallization. Plenum Press, New York, p. 472.

Janse EH, deJong EJ, (1976) The occurrence of growth dispersion and its consequences. In: Mullin, J.F. (Ed.), Industrial Crystallization. Plenum Press, New York, p. 472.

Jarosewich E, Nelen JA, Norberg JA (1980) Reference samples for electron microprobe analysis. Geostandards Newsletter. 4, 43-47.

Jerram DA, Davidson JP (2007) Frontiers in textural and microgeochemical analysis. Elements 3, 235-238.

Johnson MC, Rutherford MJ, (1989) Experimental calibration of the aluminium- in-hornblende geobarometer with application to Long Valley caldera (California) volcanic rocks. Geology. 17, 837-841

Johnston-Lavis HJ, (1885) Monograph of the Earthquakes of Ischia: Dulau & Co. Naples and London. 112 p.

Kahl M, Chakraborty S, Costa F, Pompilio M, (2011) Dynamic plumbing system beneath volcanoes revealed by kinetic modelling and the connection to monitoring data: an example from Mt Etna. Earth and Planetary Science Letters. 308, 11–22

Kahl M, Chakraborty S, Costa F, Pompilio M, Liuzzo M, Viccaro M, (2013) Compositionally zoned crystals and realtime degassing data reveal changes in magma transfer dynamics during the 2006 summit eruptive episodes of Mt. Etna. Bulletin of Volcanology. 75, 692

Kahl M, Chakraborty S, Pompilio M, Costa F (2015) Constraints on the nature and evolution of the magma plumbing system of Mt Etna volcano (1991–2008) from a combined thermodynamic and kinetic modelling of the compositional record of minerals. Journal of Petrology. 56, 2025–2068

Kahl M, Viccaro M, Ubide T, Morgan DJ, Dingwell DB, (2017) A branched magma feeder system during the 1669 eruption of Mt Etna: evidence from a time-integrated study of zoned olivine phenocryst populations. Journal of Petrology. 58, 443–472

Kayzar TM., Cooper KM, Reagan MK, Kent AJR, (2009) Gas transport model for the magmatic system at Mount Pinatubo, Philippines: Insights from (^{210}Pb)/(^{226}Ra). Journal of Volcanology and Geothermal Research. 181, 124–140

Kelemen PB, Koga KT, Shimizu N, (1997) Geochemistry of gabbro sills in the crust-mantle transition zone of the Oman ophiolite: Implications for the origin of the oceanic lower crust. Earth and Planetary Science Letters. 146, 475–488

Keller J, Ryan, WBF, Ninkovich D, Altherr R (1978). Explosive volcanic activity in the Mediterranean over the past 200,000 yr as recorded in deep-sea sediments. Bulletin of the Geological Society of America. 89, 591–604. doi:10.1130/0016-7606(1978)89<591:EVAITM>2.0.CO;2

Kent AJR, Darr C, Koleszar AM, Salisbury MJ, Cooper KM, (2010) Preferential eruption of andesitic magmas through recharge filtering. Nature Geoscience. 3, 631–636

Kile DE, Eberl DD, Hoch AR, Reddy MM, (2000) An assessment of calcite crystal growth mechanisms based on crystal size distributions. Geochimica and Cosmochimica Acta 64, 2937–2950

Kile DE, Eberl DD, (2003) On the origin of size-dependent and size-independent crystal growth; influence of advection and diffusion. American Mineralogist. 88, 1514–1521

Knesel KM, Davidson JP, Duffield WA, (1999) Evolution of silicic magma through assimilation and subsequent recharge: evidence from Sr isotopics in sanidine phenocrysts, Taylor Creek Rhyolites, NM. Journal of Petrology. 40, 773–786

Kohn MJ, Penniston–Dorland SC, (2017) Diffusion: Obstacles and opportunities in petrochronology. Reviews in Mineralogy and Geochemistry. 83, 103–152

Kohn SC, Henderson CMB, Mason RA, (1989) Element zoning trends in olivine phenocrysts from a supposed primary high-magnesian andesite: an electron- and ion-microprobe study. Contribution to Mineralogy and Petrology. 103, 242–252

Kouchi A, Sunagawa I, (1985) A model for mixing basaltic and dacitic magmas as deduced from experimental data. Contribution to Mineralogy and Petrology. 89, 17-23

Kress V, (1997) Magma mixing as a source for Pinatubo sulphur. Nature. 389, 591–593

Kroll H, Evangelakakis C, Voll G, (1993) Two-feldspar geothermometry: a review and revision for slowly cooled rocks. Contribution to Mineralogy and Petrology. 114, 510–518 https://doi.org/10.1007/BF00321755

Kuno H (1936) Petrological notes on some pyroxene-andesites from Hakone volcano, with special reference to some types of pigeonite phenocrysts. Jap J Geol Geograph 13, 107-140

Lambert G, Le Cloarec MF, Ardouin B, Le Roulley JC, (1985) Volcanic emission of radionuclides and magma dynamics. Earth and Planetary Science Letters. 76, 185–192

Langella A, Bish DL, Cappelletti P, Cerri G, Colella A, de' Gennaro R, Graziano SF, Perrotta A, Scarpati C, de' Gennaro M, (2013) New insights into the mineralogical facies distribution of Campanian Ignimbrite, a relevant Italian industrial material. Applied Clay Science. 72, 55–73

Langmuir CH, Vocke JrRD, Hanson GN, Hart SR, (1978) A general mixing equation with applications to Icelandic basalts. Earth and Planetary Science Letters. 37, 380–392

Larsen ES, Irving J, Gonyer FA, (1938) Petrologic results of a study of the minerals from the Tertiary volcanic rocks of the San Juan region, Colorado American Mineralogist. 23, 227-257

Lasaga, A.C. (1979) Multicomponent exchange and diffusion in silicates. Geochim. Cosmochim. Acta 43, 455-469

Le Bas MJ, Le Maitre RW, Streckeisen A, Zanettin B, (1986) A chemical classification of volcanic rocks based on the total alkali–silica diagram. Journal of Petrology. 273, 745–750

Le Claire AD, (1963) The analysis of grain boundary diffusion measurments. British Journal of Applied Physics. 14, 351–356

Lentz RCF, McSween HYJ, (2000). Crystallization of the basaltic shergottites: insights from crystal size distribution (CSD) analysis of pyroxenes. Meteoritics and Planetary Science. 35 (5), 919–927

Leonard GS, Cole JW, Nairn IA, Self S, (2002) Basalt triggering of the c. AD 1305 Kaharoa rhyolite eruption, Tarawera Volcanic Complex, New Zealand. Journal of Volcanology and Geothermal Research. 115, 461–486

Liedl A, Buono G, Lanzafame G, Dabagov SB, Della Ventura G, Hampai D, Mancini L, Marcelli A, Pappalardo L, (2019). 3D imaging textural characterization of pyroclastic products from the 1538 AD Monte Nuovo eruption (Campi Flegrei, Italy). Lithos. 340–34.: 316-331 doi.org/10.1016/j.lithos.2019.05.010

Lindsley DH, Andersen DJ, (1983) A two-pyroxene thermometer. Journal of Geophysical Research. 88, 887-90 https://doi.org/10.1029/JB088iS02p0A887

Lindsley DH, Spencer KJ, (1982) Fe—Ti oxide geothermometry: Reducing analyses of coexisting Ti-Magnetite (Mt) and Ilmenite (Ilm) (abst.). Transactions of the American Geophysical Union. 63, 471

Lirer L, Luongo G, Scandone R, (1987) On the volcanological evolution of Campi Flegrei. EOS, 68, 226-234

Locardi E, Nicholich R, (1988) Geodinamica del Tirreno e dell'Appennino centromeridionale: la nuova carta della Moho. Memorie della Società Geologica Italiana. 41, 121-140

Lofgren GE, (1974) An experimental study of plagioclase crystal morphology: isothermal crystallization. American Journal of Science. 274, 243-273

Lofgren GE, (1980) Experimental studies on the dynamic crystallization of silicate melts. In: Physics of Magmatic Processes. Hargraves RB (ed). Princeton University Press. 487-551

Lustrino M, Duggen S, Rosenberg CL, (2011) The Central-Western Mediterranean: anomalous igneous activity in an anomalous collisional tectonic setting. Earth-Science Reviews 104, 1-40

Luongo G, Cubellis E, Di Vito MA, Cascone E, (1995) L’isola d’Ischia: Dinamica e struttura del M. Epomeo, in Bonardi, G., De Vivo, B., Gasparini, P., and Vallario, A., eds.

Cinquant’Anni di Attività Didattica e Scientifi ca del Prof. Felice Ippolito. Napoli, Liguori Editore,. 393–402

MacDonald GA, Katsura T, (1965) Eruption of the Lassen Peak, Cascade Range, California, in 1915: example of mixed magmas. Bulletin of the Geological Society of America. 76, 475–482

Macdonald R., Sumita M, Schmincke HU, Bagiński B, White JC, Ilnicki SS, (2015) Peralkaline felsic magmatism at the Nemrut volcano, Turkey: impact of volcanism on the evolution of Lake Van (Anatolia) IV. Contributions to Mineralogy and Petrology. 169, 34

Maier WD, Arndt NT, Curl EA, (2000) Progressive crustal contamination of the Bushveld Complex: evidence from Nd analysis of the cumulate rocks. Contributions to Mineralogy and Petrology. 140, 316-327

Mangan MT, (1990) Crystal size distribution systematics and the determination of magma storage times: the 1959 eruption of Kilauea Volcano, Hawaii. Journal of Volcanology and Geothermal Research. 44, 295–302

Mangiacapra A, Moretti R, Rutherford M, Civetta L, Orsi G, Papale P, (2008) The deep magmatic system of the Campi Flegrei caldera (Italy) Geophysical Research Letters 35, L21304. https://doiorg/101029/2008GL035550

Mangler MF, Petrone CM, Hill S, Delgado-Granados H. Prytulak J, (2020) A pyroxenic view on magma hybridization and crystallization at Popocatepetl Volcano, Mexico. Frontiers in Earth Science. 8, 362. doi:10.3389/feart.2020.00362

Mantovani E, Babbucci D, Albarello D, Mucciarelli M, (1990) Deformation pattern in the central Mediterranean and behavior of the African/Adriatic promontory. Tectonophysics. 179, 63–79

Marianelli P, Sbrana A, Proto M, (2006) Magma chamber of the Campi Flegrei supervolcano at the time of eruption of the Campanian Ignimbrite. Geology. 34(11), 937– 940 doi: 10.1130/G22807A.1

Mariño PJ, Dobson KJ, Ortenzi G, Kueppers U, Morgavi D, Petrelli M, Hess K, Laeger K, Porreca M, Pimentel A, Perugini D (2017) Enhancement of eruption explosivity by heterogeneous bubble nucleation triggered by magma mingling. Scientific Report. 7, 16897. https://doi.org/10.1038/s41598-017-17098-3

Marsh BD, (1981) On the crystallinity, probability of occurrence, and rheology of lava and magma. Contributions to Mineralogy and Petrology. 78, 85–98 doi: 10.1007/BF00371146

Marsh BD, (1988) Crystal size distribution (CSD) in rocks and the kinetics and dynamics of crystallization; I. Theory. Contributions to Mineralogy and Petrology. 99, 277–291

Marsh BD, (1989) Magma chambers. Annual Review of Earth and Planetary Sciences. 17, 439–472. (doi:10.1146/annurev.ea.17.050189.002255)

Marsh BD, (1998) On the interpretation of crystal size distributions in magmatic systems. Journal of Petrology. 39, 553–599

Martin VM, Holness MB, Pyle DM (2006) Textural analysis of magmatic enclaves from the Kameni Islands, Santorini, Greece. Journal of Volcanology and Geothermal Research. 154, 89–102

Martì A, Folch A, Costa A, Engwell S, (2016) Reconstructiong the plinian and the coignimbrite sources of large volcanic eruptions: a novel approach for the Campanian Ignimbrite. Scientific Report. 6, 21220. http://dx.doi.org/10.1038/srep21220.

Martin VM, Morgan DJ, Jerram DA, Caddick MJ, Prior DJ, Davidson JP, (2008) Bang! Month-scale eruption triggering at Santorini volcano. Science 321, 1178 doi:10.1126/science.1159584

Masotta M, Mollo S, Freda C, Gaeta M, Moore G, (2013) Clinopyroxene–liquid thermometers and barometers specificto alkaline differentiated magmas. Contribution to Mineralogy and Petrology. 166, 1545–1561 doi:101007/s00410-013-0927-9

Mastrolorenzo G, (1994) Averno tuff ring in Campi Flegrei (south Italy). Bulletin of Volcanology. 54, 561-572

Mastrolorenzo G, Brachi L, Canzanella A, (2001) Vesicularity of various types of pyroclastic deposits of Campi Flegrei volcanic field: evidences of analogies in magma rise and vesiculation mechanisms. Journal of Volcanology and Geothermal Research. 109, 41-53

Mastrolorenzo G, Palladino DM, Pappalardo L, Rossano S, (2017) Probabilistic-Numerical assessment of pyroclastic current hazard at Campi Flegrei and Naples city: Multi-VEI scenarios as a tool for “full-scale” risk management. Plos One. doi.org/10.1371/journal.pone.0185756

Matzen AK, Baker MB, Beckett JR, Stolper EM, (2011) Fe–Mg partitioning between olivine and high-magnesian melts and the nature of Hawaiian parental liquids. Journal of Petrology. 52, 1243–1263

Mazzeo FC, D'Antonio M, Arienzo I, Aulinas M, Di Renzo V, Gimeno D, (2014) Subduction-related enrichment of the Neapolitan volcanoes (Southern Italy) mantle source: new constraints on the characteristics of the slab-derived components. Chemical Geology. 386, 165-183

Mazzoli S, Helman M, (1994) Neogene patterns of relative plate motion for Africa–Europe: some implications for recent central Mediterranean tectonics. Geologische Rundschau. 83, 464-468

Mazzoli S, Barkham S, Cello G, Gambini R, Mattion L, Shiner P, Tondi E, (2001) Reconstruction of continental margin architecture deformed by the contraction of the

Lagonegro Basin, southern Apennines, Italy. Journal of the Geological Society. 158, 309-319

Mazzoli S, D'Errico M, Aldega L, Corrado S, Invernizzi C, Shiner P, Zattin M, (2008) Tectonic burial and 'young' (< 10 Ma) exhumation in the southern Apennines fold and thrust belt (Italy). Geology. 36, 243-246

McKenzie D, (1985) The extraction of magma from the crust and mantle. Earth and Planetary Science Letters. 74, 81–91 (doi:10.1016/0012-821X(85)90168-2)

Mele D, Dioguardi F, Dellino P, Isaia R, Sulpizio R, Braia G, (2015) Hazard of pyroclastic density currents at the Campi Flegrei Caldera (Southern Italy) as deduced from the combined use of facies architecture physical modeling and statistics of the impact parameters. Journal of Volcanology and Geothermal Research. 299, 35–53 https://doiorg/101016/jjvolgeores201504002

Melluso L, Morra V, Perrotta A, Scarpati C, Adabbo M, (1995) The eruption of the Breccia Museo (Campi Flegrei, Italy): fractional crystallization processes in a shallow, zoned magma chamber and implications for the eruptive dynamics. Journal of Volcanology and Geothermal Research. 68, 325–339

Melluso L, de'Gennaro R, Fedele L, Franciosi L, Morra V, (2012) Evidence of crystallization in residual, Cl–F-rich, agpaitic, trachyphonolitic magmas and primitive Mg-rich basalt–trachyphonolite interaction, in the lava domes of the Phlegrean Fields (Italy). Geological Magazine. 149, 532–550

Melluso L, Morra V, Guarino V, de' Gennaro R, Franciosi L, Grifa C, (2014) The crystallization of shoshonitic to peralkaline trachyphonolitic magmas in a H_2O–Cl–F-rich environment at Ischia (Italy), with implications for the feeder system of the Campania Plain volcanoes. Lithos. 210-211, 242-259

Melnik O, Sparks RSJ, (2005) Controls on conduit magma flow dynamics during lava dome building eruptions. Journal of Geophysicl Research. 110. B02209, doi:10.1029/2004 JB003183

Melzer S, Foley SF, (2000) Phase relations and fractionation sequences in potassic magma series modelled in the system $CaMgSi_2O_6$-$KAlSiO_4$-Mg_2SiO_4-F at 1 bar to 18 kbar. Contributions to Mineralogy and Petrology. 138, 186-197.

Menand T, (2008) The mechanics and dynamics of sills in layered elastic rocks and their implications for the growth of laccoliths and other igneous complexes. Earth and Planetary Science Letters. 267, 93-99

Mihaljevic M, (1999) Encyclopedia of Geochemistry. Mercury. (ed: Marshall CP and Fairbridge RW) Kluwer Academic Publishers, Encyclopedia of Earth Sciences Series. Dordrechti, Boston, Lonon. 712 p.

Milch L, (1905) Über magmatische Resorption und porphyrische Struktur. Neues Jb Mineral Geol Paläont 22, 1-32

Mollo S, Del Gaudio P, Ventura G, Iezzi G, Scarlato P, (2010) Dependence of clinopyroxene composition on cooling rate in basaltic magmas: implications for thermobarometry. Lithos. 118, 302–312

Mollo S, Putirka K, Misiti V, Soligo M, Scarlato P (2013) A new test for equilibrium based on clinopyroxene-melt pairs: clues on the solidification temperatures of Etnean alkaline melts on clinopyroxene- melt pairs: clues on the solidification temperatures of Etnean alkaline melts at post-eruptive conditions. Chemical Geology. 352, 92–100. https ://doi.org/10.1016/j.chemg eo.2013.05.026

Mollo S, Masotta M, Forni F, Bachmann O, De Astis G, Moore G, Scarlato P (2015) A K-feldspar-liquid hygrometer specific to alkaline differentiated magmas. Chemical Geology. 392, 1–8

Mollo S, Hammer JE, (2017) Dynamic crystallization in magmas: mineral reaction kinetics. Microstructures, textures, chemical and isotopic signatures. 16, 378–418 doi: 10.1180/EMU-notes.16.12.

Monti P, (1980) Ischia. Archeologia e Storia: Napoli. Ed. Fratelli Porzio. 830 p.

Moore G, Roggensack K, Klonowski S, (2008) A low-pressure-high-temperature technique for the piston-cylinder. American Mineralogist. 93, 48–52

Morabito S, Petrosino P, Milia A Sprovieri M, Tamburrino S, (2014) A multidisciplinary approach for reconstructing the stratigraphic framework of the last 40 ka in a bathyal area of the eastern Tyrrhenian Sea. Global and Planetary Change. 123, 121-138

Moretti R, Arienzo I, Orsi G, Civetta L, D'Antonio M, (2013) The deep plumbing system of Ischia: a physico-chemical window on the fluid-saturated and CO^2-sustained Neapolitan volcanism (southern Italy). Journal of Petrology. 54, 951-984

Moretti R, Arienzo I, Di Renzo V, Orsi G, Arzilli F, Brune F, D'Antonio M, Mancini L, Deloule E, (2019) Volatile segregation and generation of highly vesiculated explosive magmas by volatile-melt fining processes: The case of the Campanian Ignimbrite eruption. Chemical Geology. 503, 1-14

Morgan DJ, Blake S, Rogers NW, DeVivo B, Rolandi G, Macdonald R, Hawkesworth J (2004) Timescales of crystal residence and magma chamber volume from modeling of diffusion profiles in phenocrysts: Vesuvius 1944. Earth and Planetary Science Letters. 222, 933–946.

Morgan DJ, Jerram DA, (2006) On estimating crystal shape for crystal size distribution analysis. Journal of Volcanology and Geohermal Research. 154, 1–7

Morgan DJ, Blake S, Rogers NW, DeVivo B, Rolandi G, Davidson J, (2006) Magma recharge at Vesuvius in the century prior to the eruption ad 79. Geology. 34, 845–848

Morgan DJ, Blake S (2006) Magmatic residence times of zoned phenocrysts: introduction and application of the binary element diffusion modeling (BEDM) technique. Contribution to Mineralogy and Petrology. 151, 58-70

Morgavi D, Arzilli F, Pritchard C, Perugini D, Mancini L, Larson P, Dingwell BD (2016) The Grizzly Lake complex (Yellowstone Volcano, USA): mixing between basalt and rhyolite unraveled by microanalysis and X-ray microtomography. Lithos. 260, 457–474

Morgavi D, Arienzo I, Montagna C, Perugini D, Dingwell DB, (2017) Magma Mixing: History and Dynamics of an Eruption Trigger. In: Gottsmann J, Neuberg J, Scheu B. (eds) Volcanic Unrest. Advances in Volcanology. Springer, Cham. https://doi.org/10.1007/11157_2017_30

Müller T, Dohmen R, Becker HW, ter Heege J, Chakraborty S, (2013) Fe–Mg interdiffusion rates in clinopyroxene: experimental data and implications for Fe–Mg exchange geothermometers. Contribution to Mineralogy and Petrology. 166, 1563–1576

Munno R, Petrosino P, (2004) New constraints on the occurrence of Y-3 upper Pleistocene tephra marker layer in the tyrrhenian sea. Il Quaternario, Italian Journal of Quaternary Sciences. 17, 11-20

Murphy MD, Sparks RSJ, Barclay J, Carroll MR, Lejeune AM, Brewer TS, Macdonald R, Black S, Young S, (1998) The role of magma mixing in triggering the current eruption at the Soufriere Hills Volcano, Montserrat, West Indies. Geophysical Research Letters. 25, 3433-3436 doi: 10.1029/98GL00713

Murphy MD, Sparks RSJ, Barclay J, Carroll MR, Brewer TS, (2000) Remobilization of andesite magma by intrusion of mafic magma at the Soufriere Hills Volcano, Montserrat, West Indies. Journal of Petrology. 41, 21-42

Nakamura M, (1995) Continuous mixing of crystal mush and replenished magma in the on going Unzen eruption. Geology. 23, 807-810

Nakamura M, Shimakita S, (1998) Dissoultion origin and syn-entrapment compositional change of melt inclusion in plagioclase. Earth and Planetary Science Letters. 161, 119-133

Naslund H, McBirney A, (1996) Mechanisms of formation of igneous layering. In Developments in petrology. Amsterdam, The Netherlands: Elsevier. 15, 1–43

Neave DA, Putirka KD, (2017) A new clinopyroxene-liquid barometer, and implications for magma storage pressures under Icelandic rift zones. American Mineralogist. 102, 777–794

Neri A, Bevilacqua A, Esposti Ongaro T, Isaia R, Aspinall WP, Bisson M, Flandoli F, Baxter PJ, Bertagnini A, Iannuzzi E, Orsucci S, Pistolesi M, Rosi M, Vitale S (2015) Quantifying volcanic hazard at Campi Flegrei caldera (Italy) with uncertainty assessment: II. Pyroclastic density current invasion maps. Journal of Geophysical Research: Solid Earth. 120:JB011776

Newman S, Lowenstern JB, (2002) Volatile Calc: a silicate melt-H_2O-CO_2 solution model written in Visual Basic for excel. Computers and Geosciences. 28, 597–604

Nikogosian IK, van Bergen MJ, (2010) Heterogeneous mantle sources of potassium-rich magmas in central-southern Italy: melt inclusion evidence from Roccamonfina and Ernici (Mid Latina Valley).Journal of Volcanology and Geothermal Research. 197, 279-302

Nimis P, (1995) A clinopyroxene geobarometer for basaltic systems based on crystal-structure modeling. Contributions to Mineralogy and Petrology. 121, 115-125

Nimis P, Ulmer P, (1998) Clinopyroxene geobarometry of magmatic rocks. Part 1. An expanded structural geobarometer for anhydrous and hydrous basic and ultrabasic systems. Contributions to Mineralogy and Petrology. 133, 122-135

Nimis P, (1999) Clinopyroxene geobarometry of magmatic rocks. Part 2. Structural geobarometers for basic to acid, tholeiitic and mildly alkaline magmatic systems. Contributions to Mineralogy and Petrology. 135, 62-74

Niu Y, Regelous M, Wendt JI, Batiza R, O’Hara MJ, (2002) Geochemistry of near-EPR seamounts: Importance of source vs. process and the origin of enriched mantle component. Earth and Planetary Science Letters. 199, 327-345

Noguchi S, Toramaru A, Shimano T, (2006) Crystallization of microlites and degassing during magma ascent: constraints on the fluid mechanical behavior of magma during the Tenjo eruption on Kozu Island, Japan. Bulletin of Volcanology. 68, 432–449

Nunziata A, Rapolla A, (1987) A gravity and magnetic study of the volcanic island of Ischia, Naples (Italy): Journal of Volcanology and Geothermal Research. 31, 333–344 doi: 10.1016/0377-0273(87)90076-X

Nunziata C, Natale M, Luongo G, Panza, GF, (2006) Magma reservoir at Mt. Vesuvius: size of the hot, partially molten, crust material detected deeper than 8 km. Earth and Planetary Science Letters. 242, 51–57

O’Brien WD, Michael JD, Christiansen EH, Gibson D (2019) Formation of rapakivi feldspar in the Deer Isle Granite Complex, coastal Maine: in situ lead isotope and trace-element analysis. Contributions to Mineralogy and Petrology. 174, 56. https://doi.org/10.1007/s00410-019-1591-5

Onsager L, (1945) Theories and problems of liquid diffusion. Annals of the New York Academy of Sciences. 46, 241–65

Orsi G, Chiesa S, (1988) The uplift of the Monte Epomeo block at the island of Ischia (Gulf of Naples): Geological and geochemical constraints: Eos (Transactions, American Geophysical Union). 69, 1473.

Orsi G, de Vita S, Piochi M, (1994) Ischia: A volcanic island, in Carannante, G., and Tonielli, R., eds., International Association of Sedimentologists 15th Regional Meeting, April 1994, Ischia, Italy, Fieldtrip Guidebook. Napoli, De Frede. 107–123

Orsi G, Gallo G, Zanchi A, (1991) Simple-shearing block resurgence in caldera depression. A model from Pantelleria and Ischia: Journal of Volcanology and Geothermal Research. 47, 1–11 doi: 10.1016/0377-0273(91)90097-J.

Orsi G, Gallo G, Heiken G, Wohletz K, Yu E, Bonani G, (1992a) A comprehensive study of the pumice formation and dispersal: The Cretaio Tephra of Ischia (Italy): Journal of Volcanology and Geothermal Research. 53, 329–354 doi: 10.1016/0377-0273(92)90090-Z

Orsi G, D'Antonio M, de Vita S, Gallo G, (1992b) The Neapolitan Yellow Tuff, a large-magnitude trachytic phrcatoplinian eruption: eruptive dynamics, magma withdrawtd and caldera collapse. Journal of Volcanology and Geothermal Research. 53, 275-287

Orsi G, Civetta L, D'Antonio M, Di Girolamo P, Piochi M, (1995). Step-filling and development of a three-layers magma chamber: the Neapolitan Yellow Tuff case history. Journal of Volcanology and Geothermal Research. 67, 291-312

Orsi G, de Vita S, Di Vito MA, (1996a) The restless, resurgent Campi Flegrei nested caldera (Italy): constraints on its evolution and configuration. Journal of Volcanology and Geothermal Research. 74, 179-214

Orsi G, Piochi M, Campajola L, D'Onofrio A, Gialanella L, Terrasi F, (1996b) ^{14}C geochronological constraints for the volcanic history of the island of Ischia (Italy) over the last 5000 years. Journal of Volcanology and Geothermal Research. 71, 249–257

Orsi G, Patella D, Piochi M, Tramacere A, (1999) Magnetic modelling of the Phlegrean volcanic district with extension to the Ponza Archipelago, Italy. Journal of Volcanology and Geothermal Research. v. 91, 345–360 doi: 10.1016/S0377-0273(99)00043-8.

Orsi G, de Vita S, Di Vito M, Isaia R, Nave R, Heiken G, (2003) Facing volcanic and related hazards in the Neapolitan Area. In: Heiken, G., Fakundiny, R. & Sutter, J. (eds).

Earth Science in the Cities: a Reader. Washington, DC: American Geophysical Union, 121-170

Orsi G, Di Vito MA, Isaia R, (2004) Volcanic hazard assessment at the restless Campi Flegrei caldera. Bulletin of Volcanology. 66, 514–530

Orsi G, Di Vito MA, Selva J, Marzocchi W, (2009) Long-term forecast of eruption style and size at Campi Flegrei caldera (Italy) Earth and Planetary Science Letters. 287, 265–276

Pan Y, Batiza R, (2002) Mid-ocean ridge magma chamber processes: Constraints from olivine zonation in lavas from the East Pacific Rise at 9°30′N and 10°30′N. Journal of Geophysical Research. 107. doi:10.1029/2001JB000435

Paoletti V, D'Antonio M, Rapolla A, (2013) The structural setting of the Ischia Island (Phlegrean Volcanic District, Southern Italy): Inferences from geophysics and geochemistry. Journal of Volcanology and Geothermal Research 249, 155-173

Paone A, (2006) The geochemical evolution of the Mt. Somma-Vesuvius volcano. Mineralogy and Petrology. 87, 53-80

Pappalardo L, Civetta L, D'Antonio M, Deino A, Di Vito M, Orsi G, Carandente A, de Vita S, Isaia R, Piochi M, (1999) Chemical and Sr- isotopical evolution of the Phlegrean magmatic system before the Campanian Ignimbrite and the Neapolitan Yellow Tuff eruptions. Journal of Volcanology and Geothermal Research. 91, 141-166

Pappalardo L, Civetta L, de Vita S, Di Vito M, Orsi G, Carandente A, Fisher RV (2002a) Timing of magma extraction during the Campanian ignimbrite eruption (Campi Flegrei Caldera). Journal of Volcanology and Geothermal Research. 114, 479–497

Pappalardo L, Piochi M, D'Antonio M, Civetta L, Petrini R, (2002b) Evidence for multistage magmatic evolution during the past 60 kyr at Campi Flegrei (Italy) deduced from Sr, Nd and Pb isotope data. Journal of Petrology. 43, 1415-1434

Pappalardo L, Ottolini L, Mastrolorenzo G, (2008) The Campanian Ignimbrite (Southern Italy) geochemical zoning, insight on the generation of a super-eruption from catastrophic differentiation and fast withdrawal. Contribution to Mineralogy and Petrology. 156, 1–26

Pappalardo L, Mastrolorenzo G (2010) Short residence times for alkaline Vesuvius magmas in amulti-depth supply system, Evidence from geochemical and textural studies. Earth Planetary and Science Letters. 296, 133–143

Pappalardo L, Mastrolorenzo G, (2012) Rapid differentiation in a sill-like magma reservoir: a case study from the campi flegrei caldera. Scientific Reports. 2:712. doi:101038/srep00712

Patacca E, Scandone P, (2001) Late thrust propagation and sedimentary response in the thrust-belt-foredeep system of the southern Apennines (Pliocene-Pleistocene). In: Vai GB, Martini PI (eds) Anatomy of an Orogen. The Apennines and adjacent Mediterranean basins. Kluwer, Dordrecht. 401-440

Patacca E, Scandone P, (2007) Geology of the Southern Apennines. In: Patacca E., Scandone P. (Eds.), Results of the CROP Project, Sub-Project CROP-04. Special Issue. 7, 75–119.

Paterson SR, Pignotta GS, Vernon RH, (2004) The significance of microgranitoid enclave shapes and orientations. Journal of Structural Geology. 26, 1465–1481. doi: 10.1016/j.jsg.2003.08.013

Pearce TH, Kolisnik AM, (1990) Observations of plagioclase zoning using interference imaging. Earth Science Reviews. 29, 9-26

Pearce TH, (1994) Recent work on oscillatory zoning in plagioclase. In: Feldspars and their Reactions. Parsons I (ed). Kluwer Academic Publisher. 313-349

Peate DW, Hawkesworth CJ, (2005) U-series disequilibria: insights into mantle melting and the time scales of magma differentiation. Reviews of Geophysics. 43(RG1003), 1–43.

Peccerillo A, (1999) Multiple mantle metasomatism in central-southern Italy: geochemical effects, timing and geodynamic implications. Geology. 27, 315-318

Peccerillo A, Panza GF, (1999) Upper mantle domains beneath central-southern Italy: petrological, geochemical and geophysical constraints. Pure and Applied Geophysics 156, 421-443

Peccerillo A, Dallai L, Frezzotti ML, Kempton PD, (2004) Sr-Nd-Pb-O isotopic evidence for decreasing crustal contamination with ongoing magma evolution at Alicudi volcano (Aeolian arc, Italy): implications for style of magma-crust interaction and for mantle source compositions Lithos. 78, 217-233

Peccerillo A, Lustrino M, (2005) Compositional variations of the Plio-Quaternary magmatism in the circum-Tyrrhenian area: deep- versus shallow mantle processes. In: Foulger G.R., et al. (Eds.), Plates, Plumes and Paradigms. Geological Society of America Special Paper. 388, 421-434

Peccerillo A, Panza GF, Aoudi A, Frezzotti ML, (2008) Relationships between Magmatism and Lithosphere-Asthenosphere Structure in the Western Mediterranean and Implications for Geodynamics. Rendiconti Lincei. 19, 291-309

Pelullo C, Cirillo G, Iovine RS, Arienzo I, Aulinas, Pappalardo, Petrosino P, Fernandez‑Turiel JL, D’Antonio M, (2020) Geochemical and Sr–Nd isotopic features of the Zaro volcanic complex: insights on the magmatic processes triggering a small-scale prehistoric eruption at Ischia island (south Italy) International Journal of Earth Sciences. 109, 2829–2849 https://doi.org/10.1007/s00531-020-01933-6

Perinelli C, Gaeta M Bonechi B, Granati SF, Freda C, D’Antonio M, Stagno V, Sicola S, Romano C, (2019) Effect of water on the phase relations of primitive K-basalts: Implications for high-pressure differentiation in the Phlegraean Volcanic District magmatic system. Lithos .342, 530–541.

Perrotta A, Scarpati C, (1994) The dynamics of Breccia Museo eruption (Campi Flegrei, Italy) and the significance of spatter clasts associated with lithic breccias. Journal of Volcanology and Geothermal Research. 59, 335–355

Perrotta A, Scarpati C, (2003) Volume partition between the plinian and co-ignimbrite air fall deposits of the Campanian Ignimbrite eruption. Mineralogy and Petrology. 79, 67–78

Perrotta A, Scarpati C, Luongo G, Morra V, (2006) The Campi Flegrei caldera boundary in the city of Naples. In: De Vivo, B. (Ed.), Volcanism in the Campania Plain: Vesuvius, Campi Flegrei and Ignimbrites 9. Elsevier, Amsterdam, pp. 85–96 in the series Developments in Volcanology.

Perugini D, Busà T, Poli G, Nazzareni S, (2003) The role of chaotic dynamics and flow fields in the development of disequilibrium textures in volcanic rocks. Journal of Petrology. 44, 733–756.

Perugini D, Valentini L, Poli G, (2007) Insights into magma chamber processes from the analysis of size distribution of enclaves in lava flows: A case study from Vulcano Island (Southern Italy). Journal of Volcanology and Geothermal Research. 166, 193–203

Perugini D, Poli G, (2012) The mixing of magmas in plutonic and volcanic environments: analogies and differences. Lithos, 153, 261–277

Peslier AH, Luhr JF, (2006) Hydrogen loss from olivines in mantle xenoliths from Simcoe (USA) and Mexico: mafic alkalic magma ascent rates and water budget of the sub-continental lithosphere. Earth and Planetary Science Letters. 242, 302-319

Petrone C, Bugatti G, Braschi E, Tommasini S. (2016) Pre-eruptive magmatic processes re-timed using a non-isothermal approach to magma chamber dynamics. Nature Communication. 7, 12946. https://doi.org/10.1038/ncomms12946

Pinilla C, Davis SA, Scott TB, Allan NL, Blundy JD, (2012) Interfacial storage of noble gases and other trace elements in magmatic systems. Earth and Planetary Science Letters. 319, 287–294

Piochi M, (1995) The Ischia magmatic system in the last 10 ka; geochemical and geophysical evidence: Plinius. 13, 190–197

Piochi M, Civetta L, Orsi G, (1999) Mingling in the magmatic system of Ischia (Italy) in the past 5 ka: Mineralogy and Petrology. 66, 227–258 doi: 10.1007/BF01164495

Piochi M, Bruno PP, De Astis G, (2005a) Relative roles of rifting tectonics and magma ascent processes: inferences from geophysical, structural, volcanological, and geochemicaldata for the Neapolitan volcanic region (southern Italy) Geochemistry, Geophysics, Geosystems. 6, Q07005 doi:10,1029/2004GC000885

Piochi M, Mastrolorenzo G, Pappalardo L, (2005b) Magma ascent and eruptive processes fromtextural and compositional features of Monte Nuovo pyroclastic products, Campi Flegrei, Italy. Bulletin of Volcanology. 67, 663–678

Piochi M, Kilburn CRJ, Di Vito MA, Mormone A, Tramelli A, Troise C, De Natale G, (2014) The volcanic and geothermally active Campi Flegrei caldera: an integrated multidisciplinary image of its buried structure. International Journal of Earth Science. 10, 401–421 https://doi.org/10.1007/s00531-013-0972-7

Piromallo C, Morelli A, (2003) P wave tomography of the mantle under the Alpine-Mediterranean area. Journal of Geophysical Research. 108, B2, 2065, doi: 10.1029/2002JB001757

Pistolesi M, Rosi M, Cioni R, Cashman KV, Rossotti A, Aguilera E, (2011) Physical volcanology of the post-XII century activity at Cotopaxi Volcano, Ecuador: behavior of an andesitic central volcano. Geological Society of America Bulletin. 123,1193–1215

Plail M, Barclay J, Humphreys MCS, Edmonds M, Herd RA, Christopher TE (2014) Characterization of mafic enclaves in the erupterd products of Soufriere Hills Volcano, Montserrat, 2009–2010. In Wadge G, Robertson REA, Voight B, (eds) The eruption of Soufriere Hills Volcano, Montserrat from 2000 to 2010. Geological Society, London, Memoirs. 39, 343–360

Poli S, Civetta L, (1987) Magma mixing and chemical zoning in the recent magma chamber of Ischia (Italy): A Sr-isotope study: Terra Cognita. 7, 358

Poli S, Chiesa S, Gillot PY, Gregnanin A, Guichard F, (1987) Chemistry versus time in the volcanic complex of Ischia (Gulf of Naples, Italy): Evidence of successive magmatic cycles: Contributions to Mineralogy and Petrology. 95, 322–335. doi:10.1007/BF00371846

Poli S, Chiesa S, Gillot PY, Guichard F, Vezzoli L, (1989) Time dimension in the geochemical approach and hazard estimation of a volcanic area: The Isle of Ischia case (Italy): Journal of Volcanology and Geothermal Research. 36, 327–335 doi: 10.1016/0377-0273(89)90077-2

Powell M, Powell R, (1977) Geothermometry and oxygen barometry using coexisting iron-titanium oxides: a reappraisal: Mineralogical Magazine. 41, 257-263

Prèlevic D, Foley SF, Romer R, Conticelli S, (2008) Mediterranean Tertiary lamproites derived from multiple source components in postcollisional geodynamics. Geochimica et Cosmochimica Acta. 72(8), 2125-2156.

Press WH, Teukolsky SA, Vetterling WT, Flannery BP, (2007) Numerical Recipes. Cambridge University Press, Cambridge.

Putirka KD, Johnson M, Kinzler RJ, Longhi J, Walker D, (1996) Thermobarometry of mafic igneous rocks based on clinopyroxene-liquid equilibria, 0–30 kbar. Contributions to Mineralogy and Petrology. 123, 92–108

Putirka KD, (1999) Clinopyroxene + liquid equilibria to 100 kbar and 2450 K. Contributions to Mineralogy and Petrology. 135, 151–163

Putirka KD, Mikaelian H, Ryerson F Shaw H, (2003) New clinopyroxene– liquid thermobarometers for mafic, evolved, and volatile-bearing lava compositions, with applications to lavas from Tibet and the Snake River Plain, Idaho. American Mineralogist. 88, 1542–1554.

Putirka KD, (2005) Igneous thermometers and barometers based on plagioclase + liquid equilibria: Tests of some existing models and new calibrations. American Mineralogist. 90, 336–346

Putirka K, Perfit M, Ryerson FJ, Jackson MG (2007) Ambient and excess mantle temperatures, olivine thermometry, and active vs. passive upwelling. Chemical Geology. 241, 177-206

Putirka KD, (2008) Thermometers and barometers for volcanic systems. Reviews in Mineralogy and Geochemistry. 69, 61-120.

Putirka KD, (2017) Down the crater: where magmas are stored and why they erupt. Elements. 13, 11–16

Putirka KD, (2018) Geothermometry and geobarometry. Encyclopedia of Earth Sciences Series. https://doi.org/10.1007/978-3-319-39312-4_322

Pyle DM, Ricketts GD, Margari V, van Andel TH, Sinitsyn, AA, Praslov ND, Lisitsyn S, (2006) Wide dispersal and deposition of distal tephra during the Pleistocene “Campanian Ignimbrite/Y5” eruption, Italy. Quaternary Science Reviews. 25, 2713–2728

Randolph AD, Larson MA, (1971) Theory of Particulate Processes. Academic Press, New York.

Rao DR Choubey V, Rao TVS, (1991) ITHERM: A basic program for magnetite-ilmenite thermometry. Computers & Geosciences 17, 307–314 doi:10.1016/0098-3004(91)90019-A

Reagan MK, Tepley III FJ, Gill JB, Wortel M, Garrison J, (2006) Timescales of degassing and crystallization implied by ^{210}Po–^{210}Pb–^{226}Ra disequilibria for andesitic lavas erupted from Arenal volcano. Journal of Volcanology and Geothermal Research. 157, 135–146

Reagan MK, Cooper KM, Pallister JS, Thornber CR, Wortel M, (2008) Timing of degassing and plagioclase growth in lavas erupted from Mount St. Helens, 2004–2005, from ^{210}Po-^{210}Pb-^{226}Ra Disequilibria. A volcano rekindled: the renewed eruption of Mount St.

Helens, 2004–2006, Edited by David R. Sherrod, William E. Scott, and Peter H. Stauffer. U.S. Geol. Surv. Professional Pap. 1750, 847–856

Renjith ML, Charan SN, Subbarao DV, Babu EVSSK, Rajashekhar VB (2013) Grain to outcrop-scale frozen moments of dynamic magma mixing in the syenite magma chamber, Yelagiri Alkaline Complex, South India. Geoscience Frontiers. 1-20

Rittmann A, (1930) Geologie der Insel Ischia: Berlin, Zeitschrift für Vulkanologie, Erganzungsband. 6, 265 p.

Rittman A, Vighi L, Ventriglia V, Nicotera P, (1950) Rilievo geologico dei Campi Flegrei. Bollettino della Società Geologica Italiana. 69, 117-362

Roach AL, (2005) The Evolution of Silicic Magmatism in the Post-Caldera Volcanism of the Phlegrean Fields, Italy PhD thesis Brown University, Providence USA.

Roeder PL, Emslie R (1970) Olivine-liquid equilibrium. Contribution to Mineralogy and Petrology. 29, 275–289

Rollinson H, (1993) Using geochemical data: evaluation, presentation, interpretation. Longman. London. 352 p

Romano P, (1992) La distribuzione dei depositi marini lungo le coste della Campania. Stato delle conoscenze e prospettive di ricerca. Studi Geologici Camerti. (spec vol) 1992/1, 265-269

Rosi M, Sbrana A, Principe C, (1983) The Phlegraean Fields: structural evolution, volcanic history and eruptive mechanism. Journal of Volcanology and Geothermal Research. 17, 273–288

Rosi M, Santacroce R, (1984) Volcanic hazard assessment in the Phlegraean Fields: a contribution based on stratigraphic and historical data. Bulletin of Volcanology. 47, 359–370

Rosi M, Sbrana A, (1987) Phlegrean Fields. CNR, Quaderni de "La Ricerca Scientifi ca". 114, 1-175

Rosi M, Sbrana A, Vezzoli L, (1988). Correlazioni tefrostratigrafiche di alcuni livelli di Ischia. Procida e Campi Flegrei. Memorie della Società Geologica Italiana. 41, 1015–1027

Rosi M, Vezzoli L, Aleotti P, De Censi M, (1996) Interaction between caldera collapse and eruptive dynamics durino the Campanian ignimbrite eruption, Phlegraean Fields, Italy. Bulletin of Volcanology. 57, 541-554

Rosi M, Vezzoli L, Castelmenzano A, Grieco G, (1999) Plinian pumice fall deposit of the Campanian Ignimbrite eruption (Phlegraean Fields, Italy). Journal of Volcanology and Geothermal Research. 91, 179–198

Ruprecht P, Bergantz GW, Dufek J, (2008) Modeling of gas-driven magmatic overturn: tracking of phenocryst dispersal and gathering during magma mixing. Geochemistry, Geophysics, Geosystems. 9, Q07017. (doi:10.1029/2008gc002022)

Ruprecht P, Bachmann O, (2010) Pre-eruptive reheating during magma mixing at Quizapu volcano and the implications for the explosiveness of silicic arc volcanoes. Geology 38, 919–922. (doi:10.1130/G31110.1)

Ruth DCS, Costa F, Bouvet de Maisonneuve C, Franco L, Cortés JA, Calder ES (2018) Crystal and melt inclusion timescales reveal the evolution of magma migration before eruption Nature. Communication. 9, Article 2657, 10.1038/s41467-018-05086-8

Salisbury MJ, Bohrson WA, Clynne MS, Ramos FC, Hoskin P, (2008) Multiple plagioclase crystal populations identified by crystal size distribution and in situ chemical data: implications for timescales of magma chamber processes associated with the 1915 eruption of Lassen Peak, CA. Journal of Petrology. 49, 1755–1780

Saunders K, Blundy J, Dohmen R, Cashman K, (2012a) Linking petrology and seismology at an active volcano. Science. 336, 1023–1027

Saunders K, Rinnen S, Blundy J, Dohmen R, Klemme S, Arlinghaus HF, (2012b) TOF-SIMS and electron microprobe investigation of zoned magmatic orthopyroxenes: first results of trace and minor element analysis with implications for diffusion modelling. American Mineralogist. 97, 532–542

Saunders K, Buse B, Kilburn MR, Kearns S, Blundy J, (2014) Nanoscale characterisation of crystal zoning. Chemical Geology. 364, 20–32

Sautter V, Jaoul O, Abel F, (1988) Aluminum diffusion in diopside using the 27 Al (p, γ) 28 Si nuclear reaction: preliminary results. Earth and Planetary Science Letters. 89, 109-114

Sbrana A, Fulignati P, Marianelli P, Boyce AJ, Cecchetti A, (2009) Exhumation of an active magmatic–hydrothermal system in a resurgent caldera environment: the example of Ischia (Italy). Journal of the Geological Society. 166, 1061–1073 doi:10.1144/0016-76492009-030

Sbrana A, Biagio G, Cubellis E, Faccenna C, Fedi M, Florio G, Giordano F, Giudetti G, Grimaldi M, Italiano F, Luperini W, Toccaceli RM, (2011) Carta Geologica della Regione Campania, scala 1:10000. Foglio 464 Isola di Ischia. Note Illustrative, aree emerse. Regione Campania. Assessorato Difesa del Suolo, LAC Firenze

Sbrana A, Marianelli P, Pasquini G, (2018) Volcanology of Ischia (Italy). J Maps, 14, 494–503

Scacchi A, (1841) Notizie geologiche sulle conchiglie che si trovan fossili nell’isola d’Ischia e lungo la spiaggia tra Pozzuoli e M. Nuovo. Antologia di Scienze Naturali. Napoli. 1, 33–48

Scarpati C, Cole P, Perrotta A, (1993) The Neapolitan Yellow Tuff - A large multiphase eruption from Campi Flegrei, Southem Italy. Bulletin of Volcanology. 55, 343-356

Scarpati C, Perrotta A, (2012) Erosional characteristics and behaviour of large pyroclastic density currents. Geology 40, 1035–1038

Scarpati C, Perrotta A, Lepore S, Calvert A, (2013) Eruptive history of Neapolitan Volcanoes: Constrains from ^{40}Ar-^{39}Ar dating. Geological Magazine. 150, 412–425

Scarpati C, Sparice D, Perrotta A, (2014) A crystal concentration method for calculating ignimbrite volume from distal ash-fall deposits and a reappraisal of the magnitude of the Campanian Ignimbrite. Journal of Volcanology and Geothermal Research. 280, 67–75

Scarpati C, Sparice D, Perrotta A, (2015a) Facies variation in the Campanian Ignimbrite. Rendiconti Online della Società Geologica Italiana. 33, 83–87

Scarpati C, Sparice D, Perrotta A, 2015b. The ground layer of the Campanian Ignimbrite: an example of deposition from a dilute pyroclastic density current. Bulletin of Volcanology. 77, 97 http://dx.doi.org/10.1007/s00445-015-0985-0

Scarpati C, Perrotta A, (2016) Stratigraphy and physical parameters of the Plinian phase of the Campanian Ignimbrite eruption. Geological Society of America Bulletin. http://dx.doi.org/10.1130/B31331.1

Scarpati C, Sparice D, Perrotta A, (2016) Comparative proximal features of the main Plinian deposits (Campanian Ignimbrite and Pomici di Base) of Campi Flegrei and Vesuvius. Journal of Volcanology and Geothermal Research. 321, 149–157

Scherillo A, (1955) Petrografia chimica dei tufi flegrei (TufoGiallo, Mappamonte, Pozzolana). Rend. Act. Sci. Fis. Mat. Napoli, 22

Schiano P, Clocchiatti R, Ottolini L, Sbrana A, (2004) The relationship between potassic, calc-alkaline and Na-alkaline magmatism in South Italy volcanoes: A melt inclusion approach. Earth and Planetary Science Letters. 220, 121-137.

Schiano P, Monzier M, Eissen JP, Martin H, Koga KT, (2010) Simple mixing as the major control of the evolution of volcanic suites in the Ecuadorian Andes. Contribution to Mineralogy and Petrology. 160, 297–312. doi 10.1007/s00410-009-0478-2

Schmalzried H, (1981) Solid State Reactions. Verlag Chemie, Weinheim.

Schwinger S, Dohmen R, Schertl HP, (2016) A combined diffusion and thermal modeling approach to determine peak temperatures of thermal metamorphism experienced by meteorites. Geochimica and Cosmochimica Acta. 191, 255–276

Self S, (1992) Krakatau revisited: the course of events and interpretation of the 1883 eruption. Geo Journal. 28, 109–121

Selva J, Orsi G, Di Vito MA, Marzocchi W, Sandri L, (2012) Probability hazard map for future vent opening at the Campi Flegrei caldera (Italy), Bulletin of Volcanology. 74, 497–510

Selva J, Acocella V, Bisson M, Caliro S, Costa A, Della Seta M, De Martino P, de Vita S, Federico C, Giordano G, Martino S, Cardaci C, (2019) Multiple natural hazards at volcanic islands: a review for the Ischia volcano (Italy). Journal of Applied Volcanology. 8, 5. https ://doi.org/10.1186/s1361 7-019-0086-4

Serri G, (1990) Neogene-Quaternary magmatism of the Tyrrhenian region: characterization of the magma sources and geodynamic implications. Memorie della Società Geologica Italiana. 41, 219-242

Sevink J, Van Gorp W, Di Vito MA, Arienzo I, (2020) Distal tephra from Campanian eruptions in early Late Holocene fills of the Agro Pontino graben and Fondi basin (Southern Lazio, Italy). Journal of Volcanology and Geothermal Research. https://doi.org/10.1016/j.jvolgeores.2020.107041

Sigmundsson F, Hreinsdottir S, Hooper A, Arnadottir T, Pedersen R, Roberts JM, Oskarsson N, Auriac A, Decriem J, Einarsson P, Geirsson H, Hensch M, Ofeigsson BG, Sturkell E, Sveinbjornsson H, Feigl LK (2010) Intrusion triggering of the 2010 Eyjafjallajokull explosive eruption. Nature. 468, 426–430

Sigurdsson H, Houghton B, Rymer H, Stix J, (2000) Encyclopedia of Volcanoes: New York, Academic. Press, 1389 p.

Silleni A, Giordano G, Isaia R, Ort MH (2020) The Magnitude of the 39.8 ka Campanian Ignimbrite Eruption, Italy: Method, Uncertainties and Errors. Frontiers in Earth Sciences. 8:543399. doi: 10.3389/feart.2020.543399

Simon JI, Hutcheon ID, Simon SB, Matzel JEP, Ramon EC, Weber PK, Grossman L, DePaolo DJ, (2011) Oxygen isotope variations at the margin of a CAI records circulation within the solar nebula. Science. 331, 1175–1178 doi: 10.1126/science.1197970

Sims KWW, Pichat S, Reagan MK, Kyle PR, Dulaiova H, Dunbar NW, Prytulak J, Sawyer G, Layne GD, Blichert-Toft J, Gauthier PJ, Charette MA, Elliott TR, (2013) On the time scales of magma genesis, melt evolution, crystal growth rates and magma degassing in the Erebus volcano magmatic system using the 238U, 235U and 232Th decay series. Journal of Petrology. 54, 235–271

Sisson T, Bacon C, (1999) Gas-driven filter pressing in magmas. Geology. 27, 613–616. (doi:10.1130/0091-7613(1999)027<0613:GDFPIM>2.3.CO;2)

Smith VC, Isaia R, Pearce NJG, (2011) Tephrostratigraphy and glass compositions of post-15 ka Campi Flegrei eruptions: implications for eruption history and chronostratigraphic markers. Quaternary Science Reviews. 30, 3638–3660. doi:101016/jquascirev201107012.

Snyder D (2000)Thermal effects of the intrusion of basaltic magma into a more silicic magma chamber and implications for eruption triggering. Earth and Planetary Science Letters. 175, 257-273.

Solaro C, Balcone-Boissard H, Morgan DJ, Boudon G, Martel C and Ostorero L (2020) A system dynamics approach to understanding the deep magma plumbing system beneath Dominica (Lesser Antilles). Frontiers in Earth Science. 8:574032. doi: 10.3389/feart.2020.574032

Sparks RSJ, Sigurdsson H, Wilson L, (1977) Magma mixing: a mechanism for triggering acid explosive eruptions. Nature 267, 315 - 318.

Sparks RSJ, Marshall, LA, (1986) Thermal and mechanical constraints on mixing between mafic and silicic magmas. Journal of Volcanology and Geothermal Research. 29, 99–124.

Sparks RSJ, Cashman KV (2017) Dynamic magma systems: implications for forecasting volcanic activity. Elements. 13, 35–40. doi: 10.2113/gselements.13.1.35

Sparks RSJ, Annen C, Blundy JD, Cashman KV, Rust AC, Jackson MD, (2019) Formation and dynamics of magma reservoirs. Philosophical Transactions of the Royal Society A . 377: 20180019. http://dx.doi.org/10.1098/rsta.2018.0019

Spencer KJ, Lindsley DH, (1981) A solution model for coexisting iron-titanium oxides: American Mineralogist. 66, 1189-1201

Spera FJ, Bohrson WA, (2001) Energy-constrained open-system magmatic processes I: General model and energy-constrained assimilation and fractional crystallization (EC-AFC) formulation. Journal of Petrology. 42, 999-1018

Stewart ML, Pearce TH, (2004) Sieve-textured plagioclase in dacitic magma: interference imaging results. American Mineralogist 89, 348-351

Stock MJ, Humphreys MCS, Smith VC, Isaia R, Brooker RA, Pyle DM (2018) Tracking volatile behaviour in sub-volcanic plumbing systems using apatite and glass: Insights into pre-eruptive processes at Campi Flegrei, Italy. Journal of Petrology. https://doi.org/10.1093/petrology/egy020

Stormer JCJ, (1983) The effects of recalculation on estimates of temperature and oxygen fugacity from analyses of multicomponent iron-titanium oxides. American Mineralogist. 68, 586-594

Streck MJ, Dungan MA, Malavassi E, Reagan MK, Bussy F, (2002) The role of basalt replenishment in the generation of basaltic andesites of the ongoing activity at Arenal volcano, Costa Rica: evidence from clinopyroxene and spinel. Bulletin of Volcanology. 64, 316–327

Streck MJ (2008) Mineral textures and zoning as evidence for open system processes. Reviews in Mineralogy and Geochemistry. 69, 595–622

Tachibana S, Tamada S, Kawasaki H, Ozawa K, Nagahara H, (2013) Interdiffusion of Mg–Fe in olivine at 1,400–1,600 °C and 1 atm total pressure. Physics and Chemistry of Minerals. 40, 511–519

Tait S, Jaupart C, Vergniolle S, (1989) Pressure, gas content and eruption periodicity of a shallow, crystallising magma chamber. Earth and Planetetary Science Letters. 92, 107–123 doi:10.1016/0012-821X(89)90025-3

Tarasewicz J, White RS, Brandsdottir B, Schoonman CM, (2014) Seismogenic magma intrusion before the 2010 eruption of Eyjafjallajokull volcano, Iceland. Geophysical Journal International. 198, 906–921.

Taylor HP Jr, Giannetti B, Turi B (1979) Oxygen isotope geochemistry of the potassic igneous rocks from the Roccamonfina volcano, Roman comagmatic region, Italy. Earth and Planetary Science Letters. 46-1, 81-106. https://doi.org/10.1016/0012-821X(79)90067-0

Tepley F, Davidson JP, Clynne MA, (1999) Magmatic interactions as recorded in plagioclase phenocrysts of Chaos Crags, Lassen Volcanic Center, California. Journal of Petrology. 40, 787–806 doi: 10.1093/petrology/40.5.787

Tibaldi A, (1996) Distinguishing tectonics faults from lava flow faults in basalts of Mt, Etna and trachyte on Ischia Island, Italy. Acta Vulcanologica. 8, 91–98

Tibaldi A, Vezzoli L, (1997) Intermittenza e struttura della caldera risorgente attiva dell’isola d’Ischia: Il Quaternario: Journal of Quaternary Science. 10, 465–470

Tibaldi A, Vezzoli L, (1998) The space problem of a caldera resurgence:An example from Ischia Island, Italy: Geologische Rundschau. 87, 53–66, doi:10.1007/s005310050189

Tibaldi A, Vezzoli L, (2000) Late Quaternary monoclinal folding induced by caldera resurgence at Ischia, Italy, in Cosgrove, J.W., and Ameen, M.S., eds. Forced Folds and Fractures: Geological Society of London Special Publication. 169, 103–113

Tibaldi A, Vezzoli L, (2004) A new type of volcano fl ank failure: The resurgent caldera sector collapse, Ischia, Italy: Geophysical Research Letters. 31 doi:10.1029/2004GL020419.

Thirlwall MF, Graham AM, Arculus RJ, Harmon RS, Macpherson CG, (1996) Resolution of the effects of crustal assimilation, sediment subduction, and fluid transport in island arc magmas: Pb-Sr-Nd-O isotope geochemistry of Grenada, Lesser Antilles. Geochim. Cosmochim. Acta. 60, 4785-4810

Thunell R, Federman A, Sparks RSJ, Williams D (1979) The age, origin, and volcanological significance of the Y-5 ash layer in the Mediterranean. Quaternary Research. 12, 241–253. doi:10.1016/0033-5894(79)90060-7

Tomkeieff SI, (1939) Zoned olivines and their petrogenetic significance. Mineralogical Magazin. 25, 229-251

Tomlinson EL, Albert PG, Wulf S, Brown R J, Smith VC, Keller J, Orsi G, Bourne AJ, Martin A Menzies MA, (2014) Age and geochemistry of tephra layers from Ischia, Italy: constraints from proximal-distal correlations with Lago Grande di Monticchio Journal of Volcanology and Geothermal Research. 287, 22-39

Tonarini S, Leeman WP, Civetta L, D‟Antonio M, Ferrara G and Necco A, (2004) B/Nb and $\delta^{11}B$ systematics in the Phlegrean Fields District, Italy. Journal of Volcanology and Geothermal Research. 133, 123-139

Tonarini S, D’Antonio M, DiVito MA, Orsi G, Carandente A, (2009) Geochemical and B-Sr-Nd isotopic evidence for mingling and mixing processes in the magmatic system that fed the Astroni volcano (4.1-3.8 ka) within the Campi Flegrei caldera (southern Italy). Lithos. 107, 135-151 doi:10.1016/j.lithos.2008.09.012

Torrente M, Milia A, Bellucci F, Rolandi G, (2010) Extensional tectonics in the Campania Volcanic Zone (eastern Tyrrhenian Sea, Italy): new insights into the relationship between faulting and ignimbrite eruptions. Italian journal of geosciences. 129 (2). pp. 297-315. ISSN 2038-1727

Trasatti E, Bonafede M, Ferrari C, Giunchi C, Berrino G, (2011) On deformation sources in volcanic areas: modeling the Campi Flegrei (Italy) 1982–84 unrest. Earth and Planetary Science Letters. 306, 175–185

Trasatti E, Acocella V, Di Vito MA, Del Gaudio C., Weber G, Aquino I., Caliro S, Chiodini G, de Vita S, Ricco C, Caricchi L, (2019) Magma degassing as a source of longterm seismicity at volcanoes: the Ischia island (Italy) case. Geophysical Research Letters. doi:10.1029/2019GL085371

Triglia R, Battaglia M, Sottili G, Brilli M, (2008) Volcanic eruptions from ghost magma chambers, Geophysics Research Letters. https://doi.org/10.1029/2008GL034579

Troise C, De Natale G, Pingue F, Tammaro U, De Martino P, Obrizzo F, Boschi E (2008) A new uplift episode at Campi Flegrei caldera (Southern Italy): implication for unrest interpretation and eruption hazard evaluation. In: Gottsmann J, Marti J (eds) Developments in Volcanology, Caldera volcanism: analysis, modelling and response, 10, 375–392. Elsevier, Amsterdam

Troise C, De Natale G, Schiavone R, Somma R, Moretti R, (2019) The Campi Flegrei caldera unrest: Discriminating magma intrusions from hydrothermal effects and implications for possible evolution. Earth-Science Reviews. 188, 108–122

Troll VR, (2001) Evolution of large peralkaline silicic magma chambers and associated caldera systems: a case study from Gran Canaria, Canary Islands. Ph.D. thesis, Christian-Albrechts-Universität zu Kiel. 1-143

Tsuchiyama A, (1985) Dissolution kinetics of plagioclase in the melt of the system diopside-albite-anorthite, and origin of dusty plagioclase in andesite. Contributions to Mineralogy and Petrology. 89, 1-16

Turner JS, Campbell IH, (1986) Convection and mixing in magma chambers. Earth Science Reviews. 23, 255–352 doi: 10.1016/0012-8252(86)90015-2.

Turner SP, George RMM, Evans PJ, Hawkesworth CJ, Zellmer GF, (2000) Timescales of magma formation, ascent and storage beneath subduction zone volcanoes. Philosophical Transactions of the Royal Society of London. 358, 1443–1464.

Turner S, Foden JU, (2001) Th and Ra disequilibria, Sr, Nd and Pb isotope and trace element variations in Sunda arc lavas: predominance of a subducted sediment component. Contributions to Mineralogy and Petrology. 142, 43–57. https://doi.org/10.1007/s004100100271

Turner S, George R, Jerram DA, Carpenter N, Hawkesworth C, (2003) Case studies of plagioclase growth and residence times in island arc lavas from Tonga and the Lesser Antilles, and a model to reconcile discordant age information. Earth and Planetary Science Letters. 214, 279–294

Turner S, Costa F, (2007) Measuring timescales of magmatic evolution. Elements. 3, 267–272

Ubide T, McKenna CA, Chew DM, Kamber BS, (2015) High-resolution LA-ICP-MS trace element mapping of igneous minerals: in search of magma histories. Chemical Geology 409, 157–168. doi: 101016/jchemgeo201505020

Ubide T, Mollo S, Zhao JX, Nazzari M, Scarlato P, (2019) Sector zoned clinopyroxene as a recorder of magma history, eruption triggers, and ascent rates. Geochimica and Cosmochimica Acta. 251, 265–283 doi: 101016/jgca201902021

Ubide T, Kamber B, (2018) Volcanic crystals as time capsules of eruption history. Nature Communications. 9, 326–326. doi: 101038/s41467-017-02274-w

Vai GB, Martini PI, (2001) Anatomy of an Orogen. The Apennines and adjacent Mediterranean basins (eds). Kluwer, Dordrecht. 632

Vance JA, (1962) Zoning in igneous plagioclase: normal and oscillatory zoning. American Journal of Science. 260, 76–760

Vance JA, (1965) Zoning in igneous plagioclase: patchy zoning. The Journal of Geology. 73, 636–651

Venezky DY, Rutherford MJ, (1999) Petrology and Fe-Ti oxide reequilibration of the 1991 Mount Unzen mixed magma. Journal of Volcanology and Geothermal Research. 89, 213-230

Ventura G, Del Gaudio P, Iezzi G, (2006) Enclaves provide new insights on the dynamics of magma mingling: A case study from Salina Island (Southern Tyrrhenian Sea, Italy). Earth and Planetary Science Letters. 243, 128–140 doi: 10.1016/j.epsl.2006.01.004

Vezzoli L, (1988) Island of Ischia. Quaderni de La Ricerca Scientifica. Consiglio Nazionale delle Ricerche, Roma. 114. 126 pp.

Vezzoli L, Principe C, Malfatti J, Arrighi S, Tanguy J, Le Goff M, (2009) Modes and times of caldera resurgence: The <10 ka evolution of Ischia Caldera, Italy, from high-precision archaeomagnetic dating. Journal of Volcanology and Geothermal Research. 186, 305-319

Vilardo G, Isaia R, Ventura G, De Martino P, Terranova C, (2010) InSAR permanent scatterer analysis reveals fault reactivation during inflation and deflation episodes at Campi Flegrei caldera. Remote Sensing of Environment. 114, 2373–2383

Vitale S, Ciarcia S, (2013) Tectono-stratigraphic and kinematic evolution of the southern Apennines/Calabria-Peloritani Terrane system (Italy). Tectonophysics. 583, 164-182

Vitale S, R Isaia, (2014) Fractures and faults in volcanic rocks (Campi Flegrei, Southern Italy): Insights into volcano-tectonic processes, International Journal of Earth Science. 103, 801–819 doi:10.1007/s00531-013-0979-0.

von Buch L, (1809) Ischia: Moll’s Neue Jahrbücher der Berg- und Hüttenkunde 1. Nurnberg. 1809, 343–353. reprinted in Gesammelte Schriften 2, Berlin. 1870, 62–68

Waight TE, Maas R, Nicholls IA, (2001) Geochemical investigations of microgranitoid enclaves in the S-type Cowra Granodiorite, Lachlan Fold Belt, SE Australia. Lithos 56, 165-186

Waight TE, Wiebe RA, Krogstad EJ, (2007) Isotopic evidence for multiple contributions to felsic magma chambers: Gouldsboro Granite, Coastal Maine. Lithos. 93, 234-247

Wager L, Brown G, Wadsworth W, (1960) Types of igneous cumulates. Journal of Petrology. 1, 73–85 doi:10.1093/petrology/1.1.73

Wallace GS, Bergantz GW, (2002) Wavelet-based correlation (WBC) of zoned crystal populations and magma mixing. Earth and Planetary Science Letters. 202, 133–145

Wallace GS, Bergantz GW, (2004) Constraints on mingling of crystal populations from off-center zoning profiles: a statistical approach. American Mineralogits. 89, 64–73

Wallace GS, Bergantz GW, (2005) Reconciling heterogeneity in crystal zoning data: an application of shared characteristic diagrams at Chaos Crags, Lassen Volcanic Center California. Contribution to Mineralogy and Petrology. 149, 98–112

Wark DA, Watson EB, (2006) Titaniq: a titanium-in-quartz geothermometer. Contribution to Mineralogy and Petrology. 152, 743-754

Wark DA, Hildreth W, Spear FS, Cherniak DJ, Watson EB, (2007) Pre-eruption recharge of the Bishop magma system. Geology. 35, 235–238

Watson EB, Liang Y, (1995) A simple model for sector zoning in slowly grown crystals: Implications for growth rate and lattice diffusion, with emphasis on accessory minerals in crustal rocks. American Mineralogist. 80, 1179–1187

Watson EB, (1996) Surface enrichment and trace-element uptake during crystal growth. Geochimica and Cosmochimica Acta. 60, 5013–5020

Wilcox RE, (1944) Rhyolite-basalt complex of Gardiner River, Yellowstone Park, Wyoming. Bulltin of the Geologic Society of America. 55, 1047–1080

Wohletz K, Orsi G, de Vita S, (1995) Eruptive Mechanisms of the Neapolitan-Yellow-Tuff Interpreted from stratigraphic, chemical, and granulometric data. Journal of Volcanology and Geothermal Research. 67, 263–290 https ://doi.org/10.1016/0377-0273(95)00002-C

Wolff JA, Balsley SD, Gregory RT, (2002) Oxygen isotope disequilibrium between quartz and sanidine from the Bandelier Tuff, New Mexico, consistent with a short residence time of phenocrysts in rhyolitic magma. Journal of Volcanology and Geothermal Research. 116, 119-135

Woo JY, Kilburn CR, (2010) Intrusion and deformation at Campi Flegrei, southern Italy: sills, dikes, and regional extension. Journal of Geophysical Research: Solid Earth 115(B12).

Woods AW, Cowan A. 2009 Magma mixing triggered during volcanic eruptions. Earth and Planetary Science Letters. 288, 132–137. (doi:10.1016/j.epsl.2009.09.015)

Wörner G, Staudigel H, Zindler A, (1985) Isotopic constraints on open system evolution of the Laacher See magma chamber (Eifel, West Germany). Earth and Planetary Science Letters. 75, 37-49

Wulf S, Kraml M, Brauer A, Keller J, Negendank JFW, (2004) Tephrochronology of the 100 ka lacustrine sediment record of Lago Grande di Monticchio (southern Italy): Quaternary International. 122, 7–30 https:// doi.org/10.1016/j.quaint.2004.01.028

Yang HJ, Kinzler RJ, Grove T, (1996) Experiments and models of anhydrous, basaltic olivine plagioclase-augite saturated melts from 0.001 to 10 kbar. Contribution to Mineralogy and Petrology. 124, 1–18 doi:10.1007/s004100050169

Yang JH, Wu FY, Chung SL, Wilde SA, Chu MF, (2004a) Multiple sources for the origin of granites: geochemical and Nd/Sr isotopic evidence from the Gudaoling granite and its mafic enclaves, NE China. Geochim. Cosmochim. Acta. 68, 4469–4483

Zellmer GF, Blake S, Vance D, Hawkesworth C, Turner S, (1999) Plagioclase residence times at two island arc volcanoes (Kameni Islands, Santorini, and Soufriere, St. Vincent) determined by Sr diffusion systematics. Contribution to Mineralogy and Petrology. 136, 345-357

Zellmer GF, Sparks RSJ, Hawkesworth C, Wiedenbeck M, (2003) Magma emplacement and remobilization timescales beneath Montserrat: insights from Sr and Ba zonation in plagioclase phenocrysts. Journal of Petrology. 44, 1413-1431

Zellmer GF, Clavero JE, (2006) Using trace element correlation patterns to decipher a sanidine crystal growth chronology: an example from Taapaca volcano, Central Andes. Journal of Volcanology and Geothermal Reserch. 156, 291-301

Zellmer GF, Turner SP (2007) Arc dacite genesis pathways: Evidence from mafic enclaves and their hosts in Aegean lavas. Lithos. 95, 346–362

Zhang Y, (2010) Diffusion in minerals and melts: Theoretical background. Review in Mineralogy and Geochemistry. 72, 5–59

Zollo A, Gasparini P, Virieux J, le Meur H, de Natale G, Biella G, Boschi E, Capuano P, de Franco R, dell'Aversana P, de Matteis R, Guerra I, Iannaccone G, Mirabile L, Vilardo G, (1996) Seismic evidence for a low-velocity zone in the upper crust beneath Mount Vesuvius. Science. 274, 592–594

Zollo A, Maercklin N, Vassallo M, Dello Iacono D, Virieux J, Gasparini P, (2008) Seismic reflections reveal a massive melt layer feeding Campi Flegrei caldera. Geophysical Research Letters. 35, L12306. https://doi.org/10.1029/2008GL034242

SUPPLEMENTARY MATERIAL

Supplementary Material 1

Compositional and Sr-isotopic data for Agnano Monte Spina matrix-glasses and minerals

Table 1

Major element contents of matrix-glass samples from A-MS eruption.

Sub-member	A1	A1	A1	A1	A2	A2	A2	A2	A2	B1	B1
SiO_2	58.83	58.31	57.32	59.29	58.11	59.34	58.11	57.75	58.19	58.03	59.60
TiO_2	0.35	0.29	0.64	0.57	0.30	0.64	0.44	0.34	0.55	0.33	0.44
Al_2O_3	18.33	17.97	18.96	18.04	17.35	17.96	17.56	17.77	17.49	17.89	18.40
Fe_2O_3tot	3.15	3.57	3.71	3.19	3.21	3.28	3.34	2.82	2.78	3.31	3.32
MnO	0.24	0.18	0.12	0.02	0.17	0.16	0.05	0.00	0.09	0.23	0.15
MgO	0.73	0.69	0.55	0.46	0.54	0.49	0.47	0.53	0.32	0.60	0.66
CaO	2.42	2.19	2.39	2.20	2.13	2.26	2.35	2.28	2.15	2.52	2.40
Na_2O	4.80	3.84	3.41	4.95	5.25	5.12	4.82	4.12	4.94	4.58	4.75
K_2O	8.35	8.12	8.21	7.97	7.59	7.61	7.65	7.58	8.13	8.35	8.35
P_2O_5	0.19	0.21	0.00	0.08	0.08	0.14	0.14	0.19	0.00	0.08	0.02
F	0.34	0.05	0.00	0.21							
Cl	0.75	0.78	0.57	0.81	0.63	0.70	0.70	0.70	0.79	0.69	0.69
Sum	98.60	96.57	96.10	97.87	95.33	95.40	93.94	96.09	95.69	97.08	98.98

Major and minor oxides as wt%.

B1	B1	B1	B1	B1	B2	B2	B2	B2	B2	B2	B2
58.64	56.76	58.46	57.85	58.41	58.18	59.52	57.95	60.03	57.73	57.18	57.92
0.55	0.36	0.63	0.55	0.42	0.37	0.45	0.45	0.65	0.70	0.64	0.34
18.14	17.79	18.11	17.67	18.30	18.05	18.15	17.92	17.08	17.88	17.11	17.73
3.34	3.42	3.62	2.93	3.23	3.10	2.93	3.22	3.51	3.32	3.33	3.40
0.31	0.00	0.33	0.11	0.07	0.09	0.23	0.00	0.08	0.17	0.11	0.06
0.60	0.56	0.60	0.62	0.54	0.54	0.46	0.46	0.45	0.63	0.85	0.49
2.23	2.16	2.35	2.35	2.38	2.27	2.21	2.14	1.57	2.17	3.39	2.47
4.64	4.57	4.89	4.35	4.61	3.47	4.23	4.55	3.90	4.72	4.23	4.24
8.21	8.24	8.31	8.28	8.30	7.87	7.57	8.18	7.09	7.64	7.44	7.79
0.17	0.13	0.23	0.08	0.04	0.12	0.11	0.08	0.11	0.13	0.00	0.00
					0.14	0.14	0.00	0.28			
0.67	0.60	0.68	0.63	0.69	0.81	0.80	0.65	0.76	0.75	0.65	0.75
97.54	94.94	98.22	95.46	96.99	95.12	96.85	95.70	95.78	95.85	95.27	95.40

B2	D1	D1	D1	D1	D1	D1	D1	D1	D1	D1	D1
57.08	58.98	59.13	57.41	59.62	57.55	57.59	57.99	58.18	58.96	58.08	59.00

0.50	0.55	0.44	0.43	0.59	0.26	0.40	0.52	0.53	0.41	0.33	0.52
18.17	18.77	18.45	17.55	18.75	18.06	18.10	18.24	18.41	18.26	17.98	18.33
3.19	3.74	3.92	4.01	4.07	4.15	3.39	3.70	3.61	3.72	3.26	3.14
0.18	0.15	0.04	0.08	0.19	0.09	0.09	0.16	0.21	0.17	0.22	0.25
0.62	0.83	1.05	0.67	0.87	1.09	0.75	0.70	0.74	0.70	0.67	0.61
2.58	2.84	2.83	2.40	2.68	3.17	2.67	2.73	2.66	2.74	2.60	2.66
4.69	4.45	4.19	4.41	4.46	4.14	4.03	3.98	4.15	4.52	4.37	4.30
7.75	8.96	8.89	8.38	8.78	8.37	8.77	8.74	8.86	8.68	8.64	8.38
0.00	0.25	0.07	0.14	0.10	0.20	0.28	0.24	0.13	0.10	0.07	0.15
0.69	0.59	0.56	0.69	0.64	0.54	0.64	0.62	0.58	0.64	0.74	0.71
95.81	99.52	99.01	95.48	100.11	97.08	96.07	97.00	97.48	98.26	96.22	97.34

D1	D2	D2	D2	D2	D2	D2	D2	E2	E2	E2
58.60	58.66	56.10	57.75	57.69	57.81	57.62	58.24	57.83	57.72	58.63
0.17	0.32	0.47	0.48	0.41	0.31	0.52	0.59	0.64	0.18	0.69
18.62	18.37	17.89	18.13	18.02	18.09	18.34	18.49	17.93	18.10	18.65
3.64	3.44	3.76	3.70	3.88	3.79	3.66	3.79	3.58	3.55	2.68
0.12	0.19	0.16	0.22	0.13	0.19	0.16	0.21	0.00	0.16	0.00
0.83	0.80	0.89	0.91	1.07	0.88	0.90	0.86	0.80	0.68	0.70
2.77	2.75	2.65	2.76	3.15	2.81	2.87	2.95	2.58	2.54	2.64
4.21	4.28	4.00	4.15	3.80	4.16	4.09	4.02	4.05	4.10	3.13
8.63	8.68	8.13	8.61	8.39	8.65	8.83	8.64	7.25	8.57	9.51
0.24	0.13	0.19	0.08	0.11	0.17	0.04	0.12	0.07	0.19	0.11
								0.19	0.22	0.33
0.61	0.58	0.63	0.63	0.56	0.62	0.60	0.59	0.61	0.63	0.45
97.83	98.63	95.48	97.81	97.45	97.62	97.92	98.68	95.75	97.26	97.75

E2	E2	E2	E2
60.06	57.20	56.39	57.06
0.22	0.39	0.64	0.37
19.01	18.11	17.74	17.88
2.51	3.57	3.90	3.46
0.04	0.21	0.00	0.15
0.52	0.75	0.84	0.81
1.87	2.62	2.68	3.01
3.25	4.12	4.08	4.04
9.72	8.50	8.34	8.57
0.06	0.27	0.19	0.30
0.35	0.58	0.58	0.58
98.58	96.38	95.53	96.64

Table 2

Representative EDS analysis of feldspar crystals of investigated rocks

Sub-member	A1	A1	A1	A1	A1	A2	A2	A2	A2
Spot	core	rim	core	rim	gm	core	rim	core	rim
SiO_2	48.39	47.72	54.55	50.25	62.62	64.09	62.58	62.61	61.57
Al_2O_3	31.59	31.74	27.29	30.12	19.44	19.37	18.75	19.2	18.89
FeO_{tot}	0.85	0.64	0.5	0.63	0.05	0.21	0	0.39	0.21
CaO	14.74	15.2	9.74	13.04	0.46	0.69	0.77	0.62	0.78
Na_2O	2.89	2.53	5.28	3.65	2.35	3.25	2.33	2.99	2.3
K_2O	0.39	0.41	1.35	0.77	12.58	11.65	12.82	11.43	12.22
SrO						0.11	0.11	0	0.54
BaO	0	0.05	0	0	0.54	0.19	0.06	0.29	1.09
Sum	99.2	98.33	99.02	98.81	98.54	99.64	97.53	97.59	97.76
Cations performula unit									
Si	2.248	2.231	2.505	2.333	2.935	2.946	2.951	2.938	2.926
Al	1.730	1.749	1.477	1.649	1.074	1.049	1.042	1.062	1.058
Fe	0.033	0.025	0.019	0.024	0.002	0.008	0.000	0.015	0.008
Ca	0.734	0.761	0.479	0.649	0.023	0.034	0.039	0.031	0.040
Na	0.260	0.229	0.470	0.329	0.214	0.290	0.213	0.272	0.212
K	0.023	0.024	0.079	0.046	0.752	0.683	0.771	0.684	0.741
Sr	0.000	0.000	0.000	0.000	0.000	0.003	0.003	0.000	0.015
Ba	0.000	0.001	0.000	0.000	0.010	0.003	0.001	0.005	0.020
Sum	10.057	10.043	10.061	10.059	10.021	10.032	10.040	10.018	10.042
Or	2.3	2.5	7.7	4.5	76.3	67.8	75.2	69.5	74.1
Ab	25.6	22.6	45.7	32.1	21.4	28.9	21.0	27.4	22.1
An	72.1	74.9	46.6	63.4	2.3	3.4	3.8	3.1	3.9

Major oxides as wt.%. gm: groundmass. The cation proportions of feldspars are calculated on the basis of 32 oxygens. An: anorthite; Ab: albite; Or: orthoclase

Sub-member	A2	A2	B1	B1	B1	B1	B2	B2	B2	B2
Spot	gm	gm	core	rim	core	rim	core	rim	gm	core
SiO_2	63.78	50.79	63.89	61.95	63.54	63.49	47.45	53.49	45.96	63.99
Al_2O_3	19.65	30.23	19.21	19.06	19.14	19.28	32.31	28.72	33.34	19.72
FeO_{tot}	0.2	0.88	0.38	0.13	0	0.12	0.75	0.54	0.8	0.19
CaO	0.55	12.44	0.53	0.58	0.38	0.43	15.26	10.93	16.76	0.62
Na_2O	3.31	3.85	2.18	2.12	2.21	2.17	2.37	4.62	1.72	2.6
K_2O	11.36	0.67	12.8	12.55	13.02	12.84	0.27	1.04	0.17	12.39
SrO	0	0.41	0.23	0.34	0.34	0.15				
BaO	0.3	0.16	0.52	1.22	0.43	0.27	0	0.04	0.21	0.42
Sum	99.18	99.45	99.74	98.03	99.07	98.76	98.71	99.5	99.3	100.33
Cations performula unit										
Si	2.939	2.341	2.950	2.931	2.953	2.951	2.214	2.444	2.146	2.938
Al	1.067	1.642	1.046	1.063	1.048	1.056	1.777	1.547	1.835	1.067
Fe	0.008	0.034	0.015	0.005	0.000	0.005	0.029	0.021	0.031	0.007
Ca	0.027	0.614	0.026	0.029	0.019	0.021	0.763	0.535	0.838	0.030
Na	0.296	0.344	0.195	0.195	0.199	0.196	0.214	0.409	0.156	0.231
K	0.668	0.039	0.754	0.758	0.772	0.761	0.016	0.061	0.010	0.726
Sr	0.000	0.011	0.006	0.009	0.009	0.004	0.000	0.000	0.000	0.000

0.005	0.003	0.009	0.023	0.008	0.005	0.000	0.001	0.004	0.008
10.019	10.059	10.003	10.026	10.017	9.999	10.026	10.035	10.040	10.015

67.6	4.2	77.0	77.0	77.4	77.6	1.6	6.1	1.4	73.7
29.7	35.1	20.3	20.1	20.7	20.2	21.6	40.7	15.4	23.3
2.7	60.7	2.6	2.9	1.9	2.2	76.8	53.2	83.2	3.1

B2	D1	D1	D1	D1	D1	D2	D2	D2	D2
rim	core	rim	core	rim	gm	core	rim	gm	gm
64.04	63.44	62.3	62.59	62.83	63.77	62.14	63.16	63.66	48.82
19.27	19.11	19.48	19.38	19.61	19.29	19.61	19.19	19.3	30.69
0.23	0.2	0.2	0.27	0.16	0.02	0.1	0.17	0.25	0.63
0.59	0.56	0.83	0.64	0.68	0.63	0.5	0.45	0.51	13.94
2.52	2.15	2.09	2.24	2.25	2.02	1.92	1.91	1.9	3.03
12.41	13.15	12.67	12.87	12.65	13.27	12.45	13.25	13.37	0.73
	0.23	0.24	0.44	0.58	0.27	0.22	0.33	0	0.33
0.52	0.12	1.06	0.75	1.52	0.25	1.73	0.1	0.22	0.16
99.88	98.96	98.89	99.17	100.35	99.54	98.85	98.65	99.22	98.39

2.952	2.949	2.919	2.923	2.916	2.949	2.921	2.948	2.950	2.284
1.047	1.047	1.076	1.067	1.073	1.051	1.087	1.056	1.054	1.692
0.009	0.008	0.008	0.011	0.006	0.001	0.004	0.007	0.010	0.025
0.029	0.028	0.042	0.032	0.034	0.031	0.025	0.023	0.025	0.699
0.225	0.194	0.190	0.203	0.202	0.181	0.175	0.173	0.171	0.275
0.730	0.780	0.757	0.767	0.749	0.783	0.747	0.789	0.790	0.044
0.000	0.006	0.007	0.012	0.016	0.007	0.006	0.009	0.000	0.009
0.009	0.002	0.019	0.014	0.028	0.005	0.032	0.002	0.004	0.003
10.004	10.028	10.034	10.056	10.047	10.015	9.993	10.010	10.008	10.059

74.4	77.4	76.5	76.0	75.5	78.2	79.1	79.5	80.2	4.5
22.7	19.8	19.4	20.9	21.2	18.7	18.4	18.3	17.2	27.6
2.9	2.8	4.1	3.1	3.3	3.1	2.6	2.3	2.6	67.9

E2	E2	E2	E2	E2	E2	E2	E2	E2
core	rim	core	rim	core	rim	core	rim	gm
45.79	47.67	48.03	44.73	51.68	47.8	48.35	48.38	48.01
32.82	32.98	31.72	34.95	30.44	32.54	32.2	31.89	31.33
0.95	0.81	0.57	0.64	0.58	0.53	0.51	0.52	0.57
16.43	15.92	15.09	18.73	12.94	15.54	15.17	14.87	14.72
1.78	2.17	2.68	0.88	3.77	2.42	2.67	2.57	2.66
0.24	0.36	0.54	0.16	0.88	0.43	0.51	0.55	0.59
								0.3
0.11	0.49	0	0.08	0.06	0.13	0.08	0.11	0
98.64	100.72	99.12	100.64	100.78	99.82	99.76	99.17	98.26

2.156	2.193	2.237	2.070	2.352	2.212	2.233	2.245	2.249

1.821	1.788	1.742	1.907	1.633	1.775	1.752	1.744	1.730
0.037	0.031	0.022	0.025	0.022	0.021	0.020	0.020	0.022
0.829	0.785	0.753	0.929	0.631	0.770	0.751	0.739	0.739
0.162	0.194	0.242	0.079	0.333	0.217	0.239	0.231	0.242
0.014	0.021	0.032	0.009	0.051	0.025	0.030	0.033	0.035
0.000	0.000	0.000	0.000	0.000	0.000	0.000	0.000	0.008
0.002	0.009	0.000	0.001	0.001	0.002	0.001	0.002	0.000
10.044	10.041	10.058	10.041	10.046	10.044	10.052	10.029	10.049
1.6	3.0	3.1	1.1	5.1	2.7	3.1	3.4	3.4
16.1	19.2	23.6	7.8	32.7	21.4	23.4	23.0	24.4
82.2	77.8	73.3	91.2	62.1	75.9	73.5	73.6	72.2

E2	E2	E2	E2	E2
gm	core	rim	core	rim
46.46	62.54	61.65	62.17	62.45
32.49	18.74	19.16	19.49	18.78
0.78	0.3	0.1	0.2	0.3
15.32	0.46	0.59	0.76	0.56
2.36	2	2.02	2.09	1.94
0.37	13.29	12.6	12.59	13.09
0.33	0.1	0.4	0.62	0.59
0.4	0.24	1.41	1.76	0
98.52	97.66	97.98	99.69	97.72
2.182	2.951	2.924	2.910	2.947
1.799	1.042	1.071	1.075	1.045
0.031	0.012	0.004	0.008	0.012
0.771	0.023	0.030	0.038	0.028
0.215	0.183	0.186	0.190	0.178
0.022	0.800	0.762	0.752	0.788
0.009	0.003	0.011	0.017	0.016
0.007	0.004	0.026	0.032	0.000
10.073	10.038	10.029	10.045	10.027
2.9	79.4	77.7	76.2	78.0
21.9	18.3	19.4	20.1	19.2
75.3	2.3	3.0	3.7	2.8

Table 3

Representative EDS analysis of clinopyroxene crystals of investigated rocks

Member	A1	A1	A1	A1	A1	A1	A2	A2	A2	A2
SiO_2	49.58	49.09	50.18	49.10	48.90	45.71	49.86	51.92	48.68	48.75
TiO_2	0.64	0.54	0.26	0.69	0.62	0.88	0.72	0.88	0.70	0.68

Al_2O_3	3.65	3.36	2.73	3.49	3.61	4.59	2.95	4.51	3.21	3.26
FeOtot	8.46	8.23	8.63	8.29	8.30	12.97	9.44	5.70	8.67	7.89
MnO	0.44	0.24	0.49	0.36	0.39	0.67	0.48	0.21	0.52	0.45
MgO	13.48	13.33	13.25	12.89	13.42	9.03	12.59	16.10	13.03	13.54
CaO	22.85	23.15	22.79	23.26	22.78	23.44	22.77	23.55	22.47	22.69
Na_2O	0.28	0.46	0.63	0.43	0.34	0.61	0.66	0.18	0.71	0.49
K_2O	0.12	0.00	0.06	0.09	0.00	0.00	0.11	0.07	0.14	0.00
Cr_2O_3	0.00	0.06	0.00	0.04	0.00	0.03	0.00	0.06	0.00	0.00
Sum	99.52	98.70	99.40	98.85	98.47	97.93	99.73	103.54	98.13	97.90
Cations per formula unit										
Si	1.87	1.87	1.91	1.87	1.87	1.81	1.89	1.86	1.87	1.87
Ti	0.02	0.02	0.01	0.02	0.02	0.03	0.02	0.02	0.02	0.02
Al^{IV}	0.13	0.13	0.09	0.13	0.13	0.19	0.11	0.14	0.13	0.13
Al^{VI}	0.03	0.02	0.03	0.03	0.03	0.02	0.02	0.05	0.02	0.02
Fe	0.27	0.26	0.27	0.26	0.27	0.43	0.30	0.17	0.28	0.25
Mn	0.01	0.01	0.02	0.01	0.01	0.02	0.02	0.01	0.02	0.01
Mg	0.76	0.76	0.75	0.73	0.76	0.53	0.71	0.86	0.75	0.78
Ca	0.92	0.95	0.93	0.95	0.93	0.99	0.93	0.90	0.93	0.93
Na	0.02	0.03	0.05	0.03	0.03	0.05	0.05	0.01	0.05	0.04
K	0.01	0.00	0.00	0.00	0.00	0.00	0.01	0.00	0.01	0.00
Cr	0.00	0.00	0.00	0.00	0.00	0.00	0.00	0.00	0.00	0.00
Sum	4.04	4.05	4.05	4.05	4.05	4.08	4.05	4.03	4.07	4.05
Wollastonite (Ca)	47	48	47	49	47	50	47	47	47	47
Enstatite (Mg)	39	38	38	37	39	27	36	44	38	39
Ferrosilite (Fe)	14	14	15	14	14	23	16	9	15	14
Mg#	74	74	73	73	74	55	70	83	73	75

B1	B1	B1	B1	B1	B1	B1	B1	B1	B1	B1	B1	B1
49.44	48.76	47.30	49.30	49.90	48.43	51.53	51.49	51.08	48.75	49.71	49.35	49.97
0.52	1.14	0.97	0.48	0.59	0.67	0.49	0.51	0.59	0.92	0.63	0.75	0.54
3.60	4.32	6.10	3.46	3.14	3.83	2.99	3.21	2.09	4.44	3.26	3.76	3.43
8.20	8.84	7.83	7.99	8.03	8.65	4.10	4.65	10.14	8.81	8.42	8.59	8.92
0.50	0.43	0.00	0.28	0.36	0.45	0.08	0.20	0.67	0.36	0.47	0.32	0.20
13.61	12.53	12.70	13.33	13.89	12.61	16.49	16.46	12.81	13.08	13.51	13.15	13.59
23.03	22.80	23.39	23.10	22.91	22.67	23.48	23.73	22.36	22.88	23.10	23.57	23.81
0.43	0.59	0.33	0.35	0.52	0.52	0.24	0.15	0.71	0.47	0.52	0.43	0.37
0.00	0.00	0.00	0.00	0.00	0.00	0.00	0.00	0.00	0.00	0.00	0.10	0.00
0.00	0.00	0.00	0.00	0.00	0.00	0.00	0.00	0.00	0.00	0.00	0.00	0.00
99.48	99.62	98.85	98.55	99.35	97.91	99.48	100.52	100.50	99.71	99.80	100.23	100.96

1.87	1.85	1.80	1.88	1.88	1.86	1.90	1.89	1.92	1.84	1.88	1.86	1.87
0.01	0.03	0.03	0.01	0.02	0.02	0.01	0.01	0.02	0.03	0.02	0.02	0.02
0.13	0.15	0.20	0.12	0.12	0.14	0.10	0.11	0.08	0.16	0.12	0.14	0.13
0.03	0.04	0.07	0.04	0.02	0.04	0.03	0.03	0.01	0.04	0.02	0.03	0.02
0.26	0.28	0.25	0.25	0.25	0.28	0.13	0.14	0.32	0.28	0.27	0.27	0.28
0.02	0.01	0.00	0.01	0.01	0.01	0.00	0.01	0.02	0.01	0.02	0.01	0.01
0.77	0.71	0.72	0.76	0.78	0.72	0.91	0.90	0.72	0.74	0.76	0.74	0.76
0.93	0.93	0.95	0.94	0.93	0.94	0.93	0.93	0.90	0.93	0.93	0.95	0.95
0.03	0.04	0.02	0.03	0.04	0.04	0.02	0.01	0.05	0.03	0.04	0.03	0.03
0.00	0.00	0.00	0.00	0.00	0.00	0.00	0.00	0.00	0.00	0.00	0.00	0.00
0.00	0.00	0.00	0.00	0.00	0.00	0.00	0.00	0.00	0.00	0.00	0.00	0.00
4.05	4.04	4.05	4.04	4.05	4.05	4.03	4.03	4.04	4.05	4.05	4.05	4.06
47	48	50	48	47	48	47	47	46	47	47	48	48
39	37	37	39	40	37	46	45	37	38	38	37	38
14	15	13	13	13	15	7	8	17	15	14	14	14
75	72	74	75	76	72	88	86	69	73	74	73	73

B1	B1	B2	B2	B2	B2	B2	B2	B2	B2	B2	D1
46.85	44.00	50.78	50.49	49.94	49.03	49.96	49.24	49.81	50.07	48.40	49.37
1.13	1.69	0.51	0.58	0.55	0.50	0.72	0.67	0.42	0.57	0.61	0.64
8.20	7.48	2.16	2.79	3.00	3.21	2.54	3.99	2.29	3.33	3.74	3.72
6.69	10.60	8.40	7.55	8.30	7.90	8.32	8.14	8.30	7.86	9.12	8.26
0.22	0.53	0.59	0.53	0.55	0.48	0.52	0.30	0.61	0.45	0.50	0.55
13.58	10.59	13.72	13.68	13.51	13.07	13.40	13.35	12.93	13.60	12.52	13.38
22.62	21.97	23.25	22.95	23.04	22.68	22.61	23.33	22.11	22.68	21.92	23.12
0.33	0.44	0.55	0.52	0.59	0.37	0.47	0.46	0.59	0.51	0.65	0.49
0.05	0.13	0.04	0.08	0.04	0.01	0.00	0.10	0.00	0.00	0.04	0.00
0.03	0.16	0.00	0.02	0.09	0.00	0.06	0.00	0.00	0.04	0.04	0.00
100.01	97.82	100.11	99.36	99.61	97.42	98.60	99.61	97.40	99.22	97.59	99.55
1.75	1.72	1.91	1.90	1.89	1.89	1.90	1.86	1.92	1.89	1.87	1.86
0.03	0.05	0.01	0.02	0.02	0.01	0.02	0.02	0.01	0.02	0.02	0.02
0.25	0.28	0.09	0.10	0.11	0.11	0.10	0.14	0.08	0.11	0.13	0.14
0.11	0.07	0.00	0.03	0.02	0.04	0.02	0.04	0.03	0.04	0.04	0.03
0.21	0.35	0.26	0.24	0.26	0.25	0.26	0.26	0.27	0.25	0.29	0.26
0.01	0.02	0.02	0.02	0.02	0.02	0.02	0.01	0.02	0.01	0.02	0.02
0.76	0.62	0.77	0.77	0.76	0.75	0.76	0.75	0.74	0.77	0.72	0.75
0.91	0.92	0.94	0.93	0.93	0.94	0.92	0.94	0.92	0.92	0.91	0.94
0.02	0.03	0.04	0.04	0.04	0.03	0.03	0.03	0.04	0.04	0.05	0.04
0.00	0.01	0.00	0.00	0.00	0.00	0.00	0.00	0.00	0.00	0.00	0.00

0.00	0.00	0.00	0.00	0.00	0.00	0.00	0.00	0.00	0.00	0.00	0.00
4.05	4.07	4.05	4.04	4.05	4.04	4.04	4.05	4.03	4.04	4.05	4.05
48	48	47	48	47	48	47	48	47	47	47	48
40	32	39	39	39	38	39	38	38	39	37	38
12	19	14	13	14	14	14	14	15	13	16	14
78	64	74	76	74	75	74	75	74	76	71	74

D1	D1	D1	D1	D1	D1	D1	D1	D2	D2	D2	D2	D2
49.23	51.03	50.11	51.98	50.63	49.82	48.93	50.34	50.88	50.60	49.77	49.54	49.48
0.66	0.78	0.72	0.41	0.65	0.64	0.83	0.46	0.71	0.46	0.60	0.76	0.32
3.98	2.89	2.79	1.93	3.97	3.50	4.57	2.72	2.66	2.94	2.64	3.08	3.23
8.59	9.10	8.80	2.78	4.71	8.09	8.73	7.30	4.01	8.06	8.97	5.70	7.88
0.49	0.75	0.74	0.07	0.21	0.39	0.16	0.29	0.08	0.51	0.50	0.25	0.40
13.22	13.03	13.26	17.00	15.90	13.50	13.27	14.53	16.30	13.81	13.12	15.00	13.83
23.13	22.93	22.86	23.78	23.58	22.99	22.82	23.33	23.17	22.78	23.13	23.09	22.99
0.36	0.63	0.57	0.20	0.20	0.45	0.53	0.40	0.19	0.50	0.50	0.41	0.38
0.00	0.00	0.00	0.00	0.00	0.00	0.00	0.00	0.00	0.00	0.00	0.00	0.00
0.00	0.00	0.00	0.00	0.00	0.00	0.00	0.00	0.00	0.00	0.00	0.00	0.00
99.66	101.17	99.85	98.92	99.92	99.54	99.90	99.53	98.13	99.79	99.43	97.88	98.60
1.86	1.90	1.89	1.93	1.87	1.88	1.84	1.89	1.90	1.90	1.89	1.88	1.88
0.02	0.02	0.02	0.01	0.02	0.02	0.02	0.01	0.02	0.01	0.02	0.02	0.01
0.14	0.10	0.11	0.07	0.13	0.12	0.16	0.11	0.10	0.10	0.11	0.12	0.12
0.04	0.03	0.01	0.02	0.04	0.03	0.04	0.01	0.02	0.03	0.01	0.02	0.03
0.27	0.28	0.28	0.09	0.15	0.26	0.27	0.23	0.13	0.25	0.29	0.18	0.25
0.02	0.02	0.02	0.00	0.01	0.01	0.01	0.01	0.00	0.02	0.02	0.01	0.01
0.74	0.72	0.75	0.94	0.87	0.76	0.74	0.81	0.91	0.77	0.74	0.85	0.78
0.94	0.91	0.92	0.95	0.93	0.93	0.92	0.94	0.93	0.92	0.94	0.94	0.94
0.03	0.05	0.04	0.01	0.01	0.03	0.04	0.03	0.01	0.04	0.04	0.03	0.03
0.00	0.00	0.00	0.00	0.00	0.00	0.00	0.00	0.00	0.00	0.00	0.00	0.00
0.00	0.00	0.00	0.00	0.00	0.00	0.00	0.00	0.00	0.00	0.00	0.00	0.00
4.05	4.04	4.05	4.02	4.03	4.04	4.05	4.05	4.02	4.04	4.05	4.05	4.05
48	47	47	48	48	48	47	47	47	47	47	48	47
38	37	38	48	45	39	38	41	46	39	37	43	40
15	16	15	4	8	14	14	12	7	14	15	10	13
73	72	73	92	86	75	73	78	88	75	72	82	76

E2	E2	E2	E2	E2	E2	E2	E2	E2	E2
49.59	48.84	48.86	49.17	47.74	49.35	50.32	48.96	48.74	49.22

0.64	0.68	0.88	0.95	1.40	0.67	0.56	1.03	0.73	0.51
3.52	4.26	4.45	3.93	5.73	3.39	2.75	4.01	3.66	3.23
7.73	8.17	8.50	8.41	5.68	7.83	8.01	8.46	8.12	7.67
0.28	0.36	0.44	0.44	0.20	0.23	0.34	0.12	0.38	0.45
13.84	12.96	13.08	13.12	14.92	13.91	13.65	13.05	13.25	13.48
22.82	23.22	23.44	23.07	22.57	22.87	22.88	22.84	22.48	22.21
0.39	0.39	0.43	0.34	0.20	0.52	0.50	0.47	0.49	0.46
0.11	0.00	0.10	0.16	0.10	0.07	0.06	0.07	0.00	0.00
0.04	0.08	0.08	0.00	0.58	0.00	0.00	0.10	0.10	0.00
98.98	99.18	100.57	100.00	99.74	99.03	99.30	99.10	97.94	97.24
1.88	1.85	1.84	1.86	1.79	1.87	1.90	1.86	1.87	1.89
0.02	0.02	0.02	0.03	0.04	0.02	0.02	0.03	0.02	0.01
0.12	0.15	0.16	0.14	0.21	0.13	0.10	0.14	0.13	0.11
0.03	0.04	0.03	0.03	0.04	0.02	0.02	0.04	0.03	0.04
0.24	0.26	0.27	0.27	0.18	0.25	0.25	0.27	0.26	0.25
0.01	0.01	0.01	0.01	0.01	0.01	0.01	0.00	0.01	0.01
0.78	0.73	0.73	0.74	0.83	0.79	0.77	0.74	0.76	0.77
0.92	0.94	0.94	0.93	0.91	0.93	0.93	0.93	0.92	0.92
0.03	0.03	0.03	0.02	0.01	0.04	0.04	0.03	0.04	0.03
0.01	0.00	0.00	0.01	0.00	0.00	0.00	0.00	0.00	0.00
0.00	0.00	0.00	0.00	0.02	0.00	0.00	0.00	0.00	0.00
4.04	4.04	4.06	4.04	4.04	4.05	4.04	4.04	4.05	4.04
47	48	48	48	47	47	47	48	47	47
40	38	37	38	43	40	39	38	39	40
13	14	14	14	10	13	13	14	14	13
76	74	73	74	82	76	75	73	74	76

Table 4

Representative EDS analysis of biotite crystals from investigated rocks

Sub-member	A1	A1	A1	B1	B2
SiO_2	0.12	0.18	0.09	0.11	0.16
TiO_2	7.86	7.8	8.12	8.72	8.7
Al_2O_3	2.8	2.77	2.72	2.69	2.85
FeOtot	79.49	79.78	78.61	78.36	77.69
MnO	0.99	1.15	1.14	1.16	1.26
MgO	2	2.27	2	2.21	2.32
CaO	0.1	0.14	0.1	0.09	0.19
Na_2O	0.11	0.17	0.08		0
K_2O	0.06	0.03	0.11		0.04
P_2O_5	0	0	0.1		0.09
Sum	94.04	94.91	93.75	94.1	93.98

Cations per formula unit					
Si	0.004	0.007	0.003	0.004	0.006
Ti	0.219	0.214	0.227	0.245	0.242
Al	0.122	0.119	0.119	0.118	0.124
Fe2+	1.065	1.041	1.062	1.084	1.060
Fe3+	1.397	1.397	1.378	1.361	1.340
Mn	0.031	0.036	0.036	0.037	0.039
Mg	0.110	0.124	0.111	0.123	0.128
Ca	0.004	0.005	0.004	0.004	0.008
Na	0.008	0.012	0.006	0.000	0.000
K	0.003	0.001	0.005	0.000	0.002
P	0.000	0.000	0.003	0.000	0.003
Sum	3.023	3.028	3.022	2.992	3.018
Mg#	9	11	9	10	11
Ulv (mol.%)	22.33	22.09	23.00	24.88	24.75

Major and minor oxides as wt.%. Ulv: Ulvospinel. The cation proportions of biotites are calculated on the basis of 22oxygens. Mg # = atomic [Mg^{2+}/(Mg^{2+} + Fe$_{tot)}$)]*100.

B2	D1	E2
0.16	0.25	0.47
8.25	6.82	6.87
2.96	3.94	4.17
79.85	79.72	77.7
0.81	0.69	0.69
1.96	2.85	2.61
0	0.04	0.46
0.14		0
0.06		0.04
0		0
94.97	95.4	93.58
0.006	0.009	0.017
0.227	0.186	0.190
0.128	0.169	0.181
1.081	1.014	1.023
1.366	1.409	1.365
0.025	0.021	0.021
0.107	0.154	0.143
0.000	0.002	0.018
0.010	0.000	0.000
0.003	0.000	0.002
0.000	0.000	0.000
3.030	2.988	3.024
9	13	12
23.31	19.55	20.71

Table 5

Representative EDS analysis of opaque oxides crystals of investigated rocks

Sub-member	A1	A1	A1	B1	B2	D1	D1	E2

TiO_2	7.86	7.80	8.12	8.72	8.70	8.25	6.82	6.87
Al_2O_3	2.80	2.77	2.72	2.69	2.85	2.96	3.94	4.17
FeO_{tot}	79.49	79.78	78.61	78.36	77.69	79.85	79.72	77.70
MnO	0.99	1.15	1.14	1.16	1.26	0.81	0.69	0.69
MgO	2.00	2.27	2.00	2.21	2.32	1.96	2.85	2.61
Cr_2O_3	0.00	0.00		0.02	0.00	0.00	0.04	0.00
Sum	94.04	94.91	93.75	94.10	93.98	94.97	95.40	93.58
FeO wt. %	34.39	34.06	34.22	34.75	34.32	35.28	33.36	33.28
Fe_2O_3 wt. %	50.13	50.81	49.34	48.47	48.20	49.53	51.52	49.37
Cations per formula unit								
Ti	0.219	0.214	0.227	0.245	0.242	0.227	0.186	0.190
Al	0.122	0.119	0.119	0.118	0.124	0.128	0.169	0.181
Fe^{2+}	1.065	1.041	1.062	1.084	1.060	1.081	1.014	1.023
Fe^{3+}	1.397	1.397	1.378	1.361	1.340	1.366	1.409	1.365
Mn	0.031	0.036	0.036	0.037	0.039	0.025	0.021	0.021
Mg	0.110	0.124	0.111	0.123	0.128	0.107	0.154	0.143
Cr	0.000	0.000	0.000	0.001	0.000	0.000	0.001	0.000
Sum	3.023	3.028	3.022	2.992	3.018	3.030	2.988	3.024

Major oxides as wt.%. Fe_2O_3 and FeO are calculated on the basis of stoichiometry. The cation proportions of opaque oxides are calculated on the basis of 4 oxygens

Table 6

Representative EDS analysis of apatite crystals of investigated rocks

Sub-member	A1	A1	B2	B2	B2	B2	E2	E2
CaO	53.69	54.98	54.74	51.83	54.13	52.33	53.68	53.13
P_2O_5	40.33	41.69	41.62	39.12	41.28	37.93	40.23	40.64
BaO	0.15	0.00	0.16	0.30	0.00	0.25	0.42	0.27
S	0.49	0.56	0.62	0.91	0.62	1.12	0.41	0.57
Cl	0.93	0.61	0.71	0.89	0.79	0.84	0.96	1.03
F	2.43	2.91	2.91	2.81	2.82	2.34	2.00	2.46
Sum	100.17	102.35	102.28	98.39	102.42	97.86	99.10	99.68
Cations per formula unit								
Ca	4.452	4.479	4.444	4.343	4.390	4.460	4.530	4.390
P	2.643	2.684	2.670	2.590	2.645	2.554	2.683	2.653
S	0.041	0.046	0.050	0.076	0.050	0.095	0.035	0.047
F	0.455	0.293	0.340	0.440	0.378	0.423	0.478	0.502
Cl	0.638	0.750	0.747	0.745	0.724	0.631	0.534	0.643
Sum	8.400	8.389	8.390	8.434	8.394	8.423	8.389	8.376

Major oxides as wt.%. The cation proportions of opaque oxides are calculated on the basis of 13 oxygens

Table 7

Sr- isotopic composition of whole rocks and minerals of A-MS products

Member	**Whole rock**	**Feldspar**	**Clinopyroxene**	**Brown mica**

	^{87}Sr/^{86}Sr	2s	^{87}Sr/^{86}Sr	2s	^{87}Sr/^{86}Sr	2s	^{87}Sr/^{86}Sr
A1	0.707473	0.000006	0.707491	0.000007	0.707445	0.000008	
A2	0.707474	0.000006	0.707483	0.000007	0.707482	0.000008	
B2	0.707493	0.000006	0.707493	0.000007	0.707533	0.000006	
D2	0.70753	0.000006	0.70748	0.000008	0.707556	0.000008	
E2	0.707502	0.000006	0.707498	0.000008	0.707552	0.000008	0.707535

2s is the standard deviation and refers to each measurement.

Supplementary Material 2:

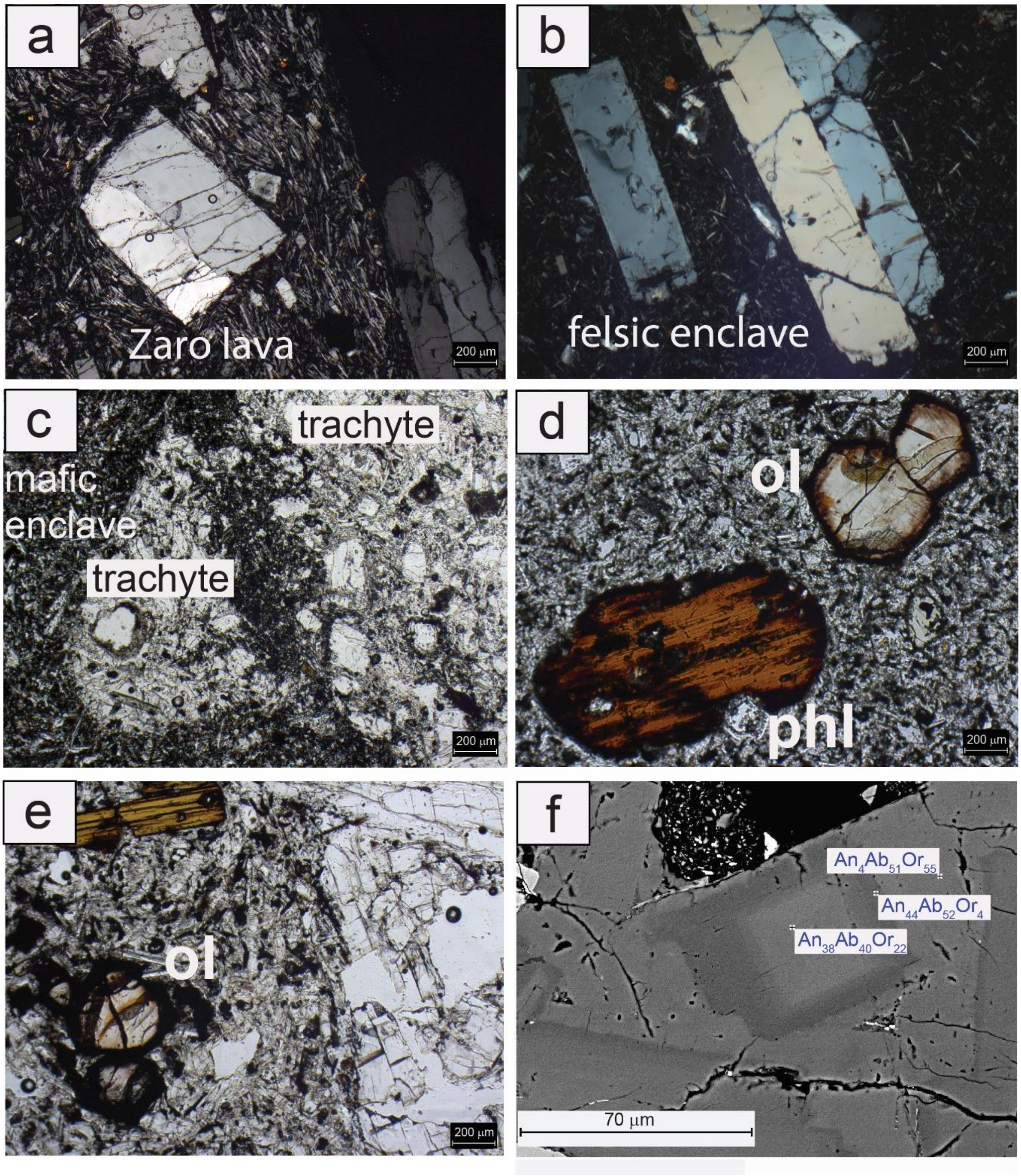

Fig. 1 a-b) microphotographs comparing the trachitic/fluidal texture in Zaro lava (a) with the less crystalline groundmass of a felsic enclave (b); c) microphotograph showing the disruption of a boundary due to infiltration of the mafic magma and engulfment of the host trachyte; d) partial resorption in phlogopite and olivine phenocrysts from mafic enclaves; e) partial resorption in olivine phenocrysts from hybrid enclave; f) plagioclase crystal from hybrid enclave showing a reversely zoned core; ol olivine; phl phlogopite

Sample location, compositional and isotopic data for Zaro whole rocks and minerals

Table 1

Location of analyzed samples

facies	**sample**	**Location**
mafic enclave	**ZR3C**	40°45'27"N - 13°51'44"E
	ZR1C	40°45'09"N - 13°52'06"E
	M4C	40°45'25"N - 13°52'22"E
hybrid enclave	**M6C**	40°45'17"N - 13°52'44"E
felsic enclave	**ZR3B**	40°45'27"N - 13°51'44"E
	ZR1B	40°45'09"N - 13°52'06"E
Zaro lava	**ZR3A**	40°45'27"N - 13°51'44"E
	ZR1A	40°45'09"N -13°52'06"E
	M1	40°44'59"N - 13°52'34"E
	M3	40°45'01"N - 13°53'00"E
	M4	40°45'25"N - 13°52'22"E
	M5	40°45'05"N - 13°52'42"E
	M6N	40°45'20"N - 13°52'32"E
	M7	40°45'30"N - 13°52'25"E
	M8	40°45' 17"N - 13°52'15"E
	M2	40°45'03"N - 13°52'45"E
	M5B	40°45'05"N - 13°52'42"E
	M10	40°45'16" N - 13°52'11"E
	M12B	40°45' 02"N - 13°52'31"E
	M13B	40°45'29" N - 13°52'03"E
	M9	40°45'19"N - 13°52'00"E
pumices	**ZRP1**	40°44'55"N-13°52'23" E
	ZRP2	40°44'55"N-13°52'23" E
	ZRP3	40°44'55"N-13°52'23" E
	ZRP4	40°44'55"N-13°52'23" E

Table 2

Major and trace element contents of whole-rock samples from Zaro eruptive complex.

facies	**mafic enclave**			**hybrid enclave**	**felsic enclave**
sample	ZR3C	ZR1C	M4C	M6C	ZR3B
sampling locality	P.ta caruso	S.Francesco Bay	S.Montano Bay	S. Montano Bay	P.ta caruso
SiO_2	51.81	51.50	51.99	58.11	60.97
TiO_2	1.36	1.36	1.33	0.86	0.63
Al_2O_3	17.79	17.80	17.91	18.35	18.21
Fe_2O_{3tot}	7.15	7.24	7.02	4.56	3.13

MnO	0.14	0.14	0.14	0.11	0.14
MgO	5.00	5.31	4.88	1.81	0.66
CaO	7.90	8.27	7.61	3.69	1.74
Na_2O	4.37	4.45	4.44	5.14	6.39
K_2O	2.88	2.98	3.14	5.90	6.95
P_2O_5	0.37	0.38	0.37	0.27	0.12
L.O.I.	0.80	0.88	0.79	1.15	1.31
Sum	99.58	100.31	99.61	99.93	100.25
Mg#	62.04	63.15	61.85	48.13861575	36.15
Li	24.1	22.4	23.1	27.4	24.4
Be	2.9	3.8	3.4	6.4	8.5
Sc	20.0	20.0	18.9	7.5	3.1
V	169.2	169.0	169.9	91.0	53.2
Cr	117.2	143.8	117.0	40.6	29.5
Co	18.8	19.6	18.2	7.1	2.0
Ni	53.4	61.3	52.8	16.4	9.2
Cu	21.6	23.8	21.7	13.3	12.4
Zn	52.5	52.5	55.4	45.2	62.5
Ga	16.4	15.4	16.9	16.6	19.0
Ge	1.1	1.1	1.2	1.1	1.3
Rb	116.1	111.3	122.1	173.1	287.9
Sr	503.7	519.5	526.2	356.3	132.6
Ba	770.2	779.9	793.0	24.1	303.8
Y	25.2	24.9	24.7	174.1	41.9
Zr	164.7	151.8	150.2	43.5	484.3
Nb	45.3	43.3	41.2	1.8	100.3
Sn	1.7	1.7	1.7	0.3	3.7
Sb	0.2	0.2	0.2	8.2	0.7
Cs	4.4	4.2	4.0	771.1	14.2
La	39.2	37.8	38.3	49.0	93.9
Ce	77.1	72.9	73.2	96.2	172.6
Pr	7.7	7.3	7.5	9.6	16.5
Nd	31.4	30.6	31.1	36.8	55.6
Sm	6.6	6.5	6.6	7.5	10.6
Eu	2.4	2.4	2.5	2.7	1.8
Gd	7.4	7.2	7.1	7.8	12.2
Tb	0.9	0.8	0.8	0.9	1.3
Dy	5.2	5.0	5.0	5.2	8.1
Ho	0.8	0.8	0.8	0.8	1.2
Er	2.5	2.4	2.4	2.4	4.2
Tm	0.4	0.4	0.4	0.4	0.8
Yb	2.7	2.7	2.6	2.6	5.2
Lu	0.4	0.4	0.4	0.4	0.8
Hf	3.8	3.5	3.5	3.9	10.6
Ta	3.1	3.0	2.9	2.6	6.5
Pb	41.8	13.3	29.9	19.4	74.5
Th	8.6	7.5	7.4	12.2	41.8
U	2.4	3.9	2.1	4.7	12.3

Major and minor oxides expressed as wt%. Trace elements expressed as part per million (p.p.m.). L.O.I.: loss of ignition. Mg# : atomic $[Mg^{2+}/(Mg^{2+}+Fe^{2+})]*100$ calculated assuming $Fe_2O_3/FeO = 0,2$ for shoshonites and 0,4 for trachytes.

	Zaro lava				
ZR1B	ZR3A	ZR1A	M1	M3	M4
S.Francesco Bay	P.ta caruso	S.Francesco Bay	Mt. Marecocco	Mezzavia	S.Montano Bay
61.21	61.61	60.68	61.71	60.29	61.60
0.60	0.64	0.57	0.63	0.62	0.59
18.21	18.46	17.99	18.39	18.72	18.30
3.32	3.34	3.33	3.28	3.16	3.21
0.21	0.17	0.23	0.17	0.12	0.19
0.58	0.75	0.50	0.65	0.69	0.58
1.52	1.77	1.45	1.72	2.07	1.55
6.71	5.99	6.83	6.06	5.12	6.66
6.51	6.98	6.43	6.77	6.82	6.64
0.09	0.13	0.08	0.11	0.14	0.10
0.78	0.81	0.85	1.91	2.29	0.73
99.73	100.66	98.93	101.39	100.03	100.15
31.83	37.68	28.72	34.77	37.17	32.84
25.8	23.7	32.1	13.1	8.6	17.6
19.5	11.8	21.0	9.2	2.9	13.5
3.1	3.3	2.9	3.2	3.2	3.1
50.0	49.7	42.3	50.0	47.6	46.6
23.4	12.4	21.9	8.2	10.2	11.9
1.5	1.9	1.4	1.9	2.2	1.5
6.8	4.8	6.8	2.9	3.5	3.8
9.5	11.7	8.9	6.9	13.4	8.0
72.8	69.1	71.7	62.1	48.8	67.8
22.9	20.3	24.7	20.9	18.5	23.4
1.4	1.4	1.6	1.4	1.3	1.5
383.1	309.3	428.9	301.0	236.3	374.4
85.0	126.1	69.4	111.5	143.6	97.9
171.3	268.3	143.4	233.7	287.1	207.6
56.9	42.8	60.1	45.4	41.1	51.5
870.6	539.2	993.4	574.1	400.8	773.1
138.9	108.6	166.1	112.5	91.0	141.3
5.3	3.3	5.6	2.5	1.9	2.8
1.3	0.4	1.5	0.5	0.4	0.8
23.0	15.1	22.9	15.2	7.2	22.5
134.4	95.9	143.3	99.3	88.0	118.5
244.3	182.9	260.5	188.7	166.6	220.1
20.9	16.2	21.5	16.9	16.2	18.7
66.8	57.2	67.4	56.0	55.9	59.3
11.7	10.6	11.6	6.9	7.2	7.6
1.4	1.8	1.3	1.0	1.2	1.0
14.2	12.5	14.3	7.7	7.8	8.9
1.5	1.4	1.6	0.9	0.9	1.0
9.7	8.4	10.0	5.3	5.3	6.1
1.6	1.3	1.7	0.9	0.8	1.0
5.5	4.4	5.9	2.9	2.6	3.4
1.2	0.9	1.3	0.6	0.5	0.7
7.6	5.6	8.5	3.7	3.2	4.7

1.2	0.9	1.4	0.6	0.5	0.8
18.0	12.1	20.0	8.0	5.9	10.9
7.3	6.8	8.7	4.4	4.0	5.4
46.5	48.5	52.8	34.9	38.2	26.0
71.6	46.3	83.8	47.7	34.2	62.5
21.1	13.8	25.2	13.6	8.8	18.2

M5	M6N	M7	M8	M9	M2
Vent area	S.Montano Bay	La Guardiola	La Mortella	La Mortella	Mt. Caccaviello
61.95	61.24	60.78	61.64	61.40	61.42
0.65	0.62	0.60	0.66	0.60	0.65
18.55	18.23	17.94	18.49	18.24	18.41
3.31	3.27	3.19	3.33	3.21	3.26
0.14	0.17	0.18	0.15	0.17	0.14
0.77	0.65	0.65	0.73	0.65	0.75
1.97	1.67	1.67	1.83	1.66	1.88
5.68	6.14	6.28	5.67	6.34	5.52
7.09	6.78	6.57	6.94	6.69	6.99
0.14	0.11	0.10	0.13	0.11	0.13
1.41	0.99	1.88	0.69	0.80	0.86
101.66	99.87	99.84	100.26	99.87	100.01
38.38	34.97	35.47	36.98	35.29	38.15
15.0	25.2	24.9	16.5	23.8	12.5
7.9	13.3	16.1	11.0	14.8	8.2
3.4	3.2	3.1	3.3	2.9	3.5
46.4	45.0	44.0	55.4	50.1	55.1
20.6	21.6	24.7	35.0	33.5	23.4
2.4	1.9	1.7	2.2	1.7	2.4
6.6	6.6	7.2	9.9	10.0	6.2
8.8	8.7	9.8	12.3	11.1	10.5
49.1	65.8	62.9	57.1	59.0	53.1
18.6	20.7	22.3	19.6	20.8	19.5
1.4	1.5	1.5	1.3	1.5	1.3
238.2	313.3	337.6	267.7	320.4	247.6
158.2	102.8	103.4	137.6	104.1	143.7
327.5	213.6	210.6	288.2	226.7	304.2
36.5	45.6	48.0	41.6	47.3	39.5
370.5	580.7	696.9	477.1	644.3	418.2
83.1	117.7	126.0	100.6	120.0	90.7
2.8	3.8	4.4	3.5	3.9	2.6
0.6	0.9	1.0	0.7	1.1	0.4
6.0	12.0	14.6	10.8	17.3	9.3
76.8	102.9	110.6	88.6	109.6	81.3
149.4	195.9	211.5	173.5	205.1	159.9
14.3	17.6	17.9	15.9	18.1	15.0
51.7	59.1	58.4	56.2	59.8	52.4
10.0	10.7	10.7	10.6	10.8	8.4

1.9	1.6	1.5	1.8	1.6	1.5
10.8	12.2	12.5	11.7	12.8	8.9
1.2	1.4	1.4	1.3	1.4	1.0
7.1	8.2	8.4	7.9	8.7	6.1
1.1	1.3	1.4	1.2	1.4	0.9
3.5	4.4	4.7	4.0	4.8	3.1
0.7	0.9	1.0	0.8	1.0	0.6
4.2	5.6	6.2	5.0	6.2	3.7
0.7	0.9	1.0	0.8	1.0	0.6
8.0	12.3	14.6	10.3	13.8	7.4
5.6	6.7	6.8	6.5	6.7	5.1
25.2	39.4	39.9	32.6	35.8	29.0
30.1	50.5	57.8	39.2	55.2	33.9
8.2	15.0	16.6	11.3	16.4	8.8

				pumices			
M5B	M10	M12B	M13B	ZRP1	ZRP2	ZRP3	ZRP4
Vent area	La Mortella	La Mortella	La Guardiola				
61.49	61.62	60.61	61.17	59.83	59.74	59.24	59.32
0.65	0.64	0.63	0.64	0.47	0.45	0.46	0.47
18.33	18.21	18.07	18.27	17.48	17.46	17.38	17.40
3.31	3.39	3.21	3.15	2.91	2.75	2.78	2.87
0.14	0.18	0.14	0.13	0.24	0.23	0.23	0.24
0.76	0.62	0.76	0.71	0.31	0.31	0.31	0.34
1.93	1.60	1.74	1.93	1.09	1.07	1.07	1.14
5.67	6.26	5.00	5.68	7.48	7.48	7.40	7.50
7.04	6.66	7.43	6.99	5.89	5.80	5.81	5.93
0.14	0.11	0.13	0.15	0.04	0.04	0.04	0.04
1.08	0.87	0.83	1.26	2.43	3.18	3.33	3.73
100.53	100.17	98.56	100.07	98.18	98.53	98.06	98.98
38.14	33.14	39.05	37.92	23.03	24.17	24.28	25.12
15.4	22.1	13.1	14.1				
7.9	15.7	6.1	8.5				
3.5	3.1	3.2	3.2				
51.5	52.8	37.4	55.2				
19.7	27.2	35.4	32.9				
2.3	1.8	2.2	2.2				
6.1	8.2	9.5	9.5				
9.0	10.6	14.6	13.4				
48.0	64.5	47.4	53.5				
18.8	21.8	18.8	18.6				
1.2	1.3	1.4	1.2				

243.6	327.9	271.6	254.1
150.1	90.5	138.6	146.7
317.8	188.5	289.6	314.3
37.9	49.4	40.3	38.2
385.7	678.1	433.6	407.9
86.1	119.0	90.8	88.0
3.1	4.2	3.8	3.0
0.6	1.0	0.6	0.6
6.6	17.8	2.7	13.1
80.3	113.4	81.6	81.2
153.3	213.6	171.0	159.6
15.0	19.0	15.3	14.9
53.4	63.0	54.4	52.5
10.4	11.4	8.7	10.1
2.0	1.5	1.5	1.9
11.2	13.2	9.7	11.3
1.3	1.5	1.1	1.3
7.4	9.0	6.5	7.5
1.2	1.5	1.0	1.2
3.7	4.9	3.3	3.8
0.7	1.0	0.6	0.7
4.3	6.5	4.0	4.5
0.7	1.0	0.6	0.7
8.5	14.2	7.9	8.9
6.1	6.3	4.7	6.0
28.9	36.5	28.0	42.1
31.5	56.4	37.1	33.1
8.9	16.4	8.5	10.4

Table 3

Representative EDS analysis of olivine crystals of investigated rocks.

facies	**mafic enclave**								
sample	ZR3C	ZR3C	ZR3C	ZR3C	ZR1C	ZR1C	ZR1C	ZR1C	ZR1C
spot	core	rim	core	gm	core	rim	gm	gm	core
SiO_2	39.90	39.21	39.14	38.10	38.81	38.81	37.15	37.37	39.14
FeO	14.19	21.11	13.86	17.67	18.16	14.87	23.34	22.86	14.17
MnO	0.00	0.79	0.00	0.42	0.55	0.26	0.68	0.76	0.36
MgO	46.12	39.96	46.83	40.90	42.84	45.18	37.66	38.16	45.88
CaO	0.42	0.24	0.22	0.32	0.21	0.29	0.15	0.21	0.29
Sum	101.75	101.71	101.98	98.08	100.72	99.96	99.52	99.79	99.97

Cations per formula unit

Si	0.989	1.001	0.974	0.997	0.987	0.981	0.985	0.985	0.984
Fe	0.294	0.451	0.289	0.387	0.386	0.314	0.517	0.504	0.298
Mn	0.000	0.017	0.000	0.009	0.012	0.006	0.015	0.017	0.008
Mg	1.704	1.521	1.738	1.595	1.623	1.703	1.488	1.500	1.719
Ca	0.011	0.007	0.006	0.009	0.006	0.008	0.004	0.006	0.008
Sum	3.009	2.999	3.024	3.003	3.013	3.019	3.015	3.015	3.016
Forsterite	85.28	77.14	85.76	80.49	80.79	84.41	74.20	74.85	85.23

Major oxides as wt.%. All Fe in olivines as Fe^{2+}; gm: groundmass. The cation proportions of olivines are calculated on the basis of 4 oxygens. Forsterite= atomic [Mg2+/(Mg2+ + Fetot)]*100

hybrid enclave							
M6C	M6C	M6C	M6C	M6C	M6C	M6C	M6C
core	rim	core	rim	core	rim	core	rim
39.80	37.50	39.06	37.55	38.78	38.63	39.42	37.71
15.06	25.07	14.37	21.15	14.11	20.04	14.50	21.97
0.49	0.74	0.25	0.58	0.14	0.44	0.17	0.54
44.50	36.32	46.48	39.40	45.57	42.39	45.31	38.16
0.20	0.17	0.29	0.35	0.25	0.19	0.25	0.14
101.41	100.50	100.63	99.20	99.26	102.03	100.20	98.83
1.000	0.993	0.977	0.986	0.982	0.977	0.991	0.996
0.316	0.555	0.300	0.464	0.299	0.424	0.305	0.485
0.010	0.017	0.005	0.013	0.003	0.009	0.004	0.012
1.667	1.433	1.732	1.542	1.720	1.599	1.698	1.503
0.005	0.005	0.008	0.010	0.007	0.005	0.007	0.004
3.000	3.006	3.023	3.014	3.017	3.021	3.009	3.004
84.05	72.09	85.22	76.85	85.20	79.04	84.78	75.59

Table 4

Representative EDS analysis of opaque oxides crystals of investigated rocks

facies	**mafic enclaves**			**hybrid enclave**			
sample	ZR3C	ZR3C	ZR3C	M6C	M6C	M6C	M6C
phase	mgnt	mgnt	Cr-spinel	Ti-mgnt	Ti-mgnt	ulvöspinel	Cr-spinel
TiO_2	4.14	4.16	0.96	12.81	13.07	30.93	0.61
Al_2O_3	0.66	0.91	35.22	4.10	4.05	2.84	30.48
FeO_{tot}	76.81	77.72	27.90	67.67	69.09	56.31	26.80
MnO	3.30	2.15	0.36	0.93	1.15	1.13	0.78
MgO	2.26	1.09	12.31	4.54	3.78	2.81	12.24
Cr_2O_3	0.31	0.28	22.72	0.33	0.14	0.00	27.55
Sum	87.48	86.31	100.19	90.38	91.28	94.02	98.46

Cations per formula unit							
Ti	0.125	0.129	0.021	0.366	0.373	0.885	0.014
Al	0.031	0.044	1.211	0.184	0.181	0.127	1.083
Fe^{2+}	0.878	0.987	0.479	1.079	1.122	1.689	0.444
Fe^{3+}	1.708	1.689	0.202	1.073	1.069	0.102	0.232
Mn	0.112	0.075	0.009	0.030	0.037	0.036	0.020
Mg	0.135	0.067	0.535	0.257	0.214	0.159	0.550
Cr	0.010	0.009	0.524	0.010	0.004	0.000	0.657
Sum	3.000	3.000	3.004	3.000	3.000	3.000	3.000
Cr#	24.17	17.06	30.20	5.10	2.26	0.00	37.75

Major oxides as wt.%. Fe_2O_3 and FeO are calculated on the basis of stoichiometry. mgnt= magnetite. The cation proportions of opaque oxides are calculated on the basis of 4 oxygens;Cr#: atomic [$Cr^{2+}/(Cr^{2+}+Al_{tot})$]*100.

felsic enclaves		**Zaro lava**		**pumices**			
ZR3B	ZR3B	M1	M1	ZRP1	ZRP2	ZRP2	ZRP4
Ti-mgnt	Ti-mgnt	Ti-mgnt	Ti-mgnt	Ti-mgnt	Ti-mgnt	Ti-mgnt	Ti-mgnt
16.64	14.03	11.10	12.73	11.14	10.65	11.34	11.57
0.61	1.18	2.16	1.93	0.79	0.88	0.84	1.35
67.60	73.84	77.64	74.91	79.83	76.07	76.67	75.56
3.35	3.77	2.14	1.96	3.28	3.15	2.93	1.97
0.12	0.49	2.60	1.66	1.08	1.31	1.21	1.85
0.00	0.17	0.00	0.26	0.07	0.00	0.02	0.00
88.32	93.49	95.64	93.46	96.82	92.83	93.55	92.88
0.516	0.407	0.307	0.364	0.310	0.308	0.327	0.333
0.030	0.054	0.094	0.087	0.034	0.040	0.038	0.061
1.391	1.255	1.098	1.207	1.145	1.134	1.163	1.166
0.939	1.127	1.292	1.177	1.328	1.314	1.292	1.250
0.117	0.123	0.067	0.063	0.103	0.103	0.095	0.064
0.007	0.028	0.143	0.094	0.060	0.075	0.069	0.105
0.000	0.005	0.000	0.008	0.002	0.000	0.001	0.000
3.000	3.000	3.000	3.000	2.997	2.997	3.000	2.996
0.00	9.01	0.00	8.38	5.61	0.00	1.57	0.00

Table 5

Representative EDS analysis of clinopyroxene crystals of investigated rocks

facies	**mafic enclaves**						**hybrid enclave**				
sample	ZR3C	ZR3C	ZR3C	ZR3C	ZR3C	ZR3C	M6C	M6C	M6C	M6C	M6C
spot	gm	core	rim	gm	gm	gm	gm	gm	gm	core	rim
SiO_2	50.72	50.86	51.77	49.04	49.41	52.07	51.83	45.62	46.89	49.04	49.78
TiO_2	0.45	0.86	0.71	1.29	1.19	0.59	1.24	3.22	2.05	1.18	0.88

Al_2O_3	2.36	2.42	2.02	5.09	4.24	2.14	2.69	7.52	7.40	3.51	3.57
FeO	8.24	8.39	8.23	8.14	8.02	7.78	8.14	9.60	7.18	9.28	7.53
MnO	0.39	0.50	0.78	0.26	0.45	0.51	0.55	0.38	0.31	0.59	0.42
MgO	13.78	13.40	13.72	13.70	13.09	14.17	13.89	11.71	12.32	12.62	14.32
CaO	22.48	22.36	21.77	21.16	21.69	22.27	23.45	22.43	22.65	21.88	22.08
Na_2O	0.68	0.76	0.58	0.43	0.81	0.78	0.51	0.41	0.37	0.77	0.62
Cr_2O_3	0.00	0.00	0.00	0.10	0.04	0.06	0.05	0.00	0.00	0.15	0.09
Sum	99.93	99.78	100.29	99.91	99.65	100.51	102.82	101.67	100.99	99.02	99.27
Cations per formula unit											
Si	1.916	1.914	1.940	1.843	1.867	1.934	1.897	1.715	1.767	1.868	1.872
Ti	0.013	0.024	0.020	0.036	0.034	0.016	0.034	0.091	0.058	0.034	0.025
Al^{VI}	0.022	0.022	0.030	0.068	0.056	0.028	0.013	0.048	0.096	0.026	0.030
Al^{IV}	0.084	0.086	0.060	0.157	0.133	0.066	0.103	0.285	0.233	0.132	0.128
Fe	0.260	0.264	0.258	0.256	0.253	0.242	0.249	0.302	0.226	0.296	0.237
Mn	0.013	0.016	0.025	0.008	0.014	0.016	0.017	0.012	0.010	0.019	0.013
Mg	0.776	0.752	0.766	0.767	0.737	0.784	0.758	0.656	0.692	0.717	0.803
Ca	0.910	0.902	0.875	0.852	0.878	0.886	0.920	0.903	0.915	0.893	0.890
Na	0.050	0.055	0.043	0.032	0.059	0.056	0.036	0.030	0.027	0.057	0.045
Cr	0.000	0.000	0.000	0.003	0.002	0.000	0.002	0.000	0.000	0.005	0.003
Sum	4.043	4.035	4.016	4.022	4.034	4.030	4.028	4.043	4.024	4.045	4.045
Wollastonite(Ca)	46.45	46.64	45.46	45.24	46.62	45.96	47.31	48.21	49.63	46.41	45.80
Enstatite(Mg)	13.93	14.47	14.70	14.01	14.22	13.36	13.70	16.76	12.82	16.35	12.88
Ferrosilite(Fe)	39.62	38.89	39.84	40.75	39.16	40.67	38.99	35.03	37.55	37.24	41.32
Mg#	74.89	74.02	74.82	75.00	74.43	76.44	75.25	68.50	75.34	70.79	77.22

Major and minor oxides as wt.%. b.d.l.: below detection limit; micro: microlite; gm: groundmass. The cation proportions of clinopyroxenes are calculated on the basis of 6 oxygens. Mg # atomic [Mg^{2+}/(Mg^{2+} + $Fe_{tot)]}$*100.

felsic enclaves					**Zaro lava**				
ZR3B	ZR3B	ZR3B	ZR3B	ZR3B	M1	M1	M1	M1	M1
core	rim	core	rim	micro	core	rim	gm	gm	gm
51.28	51.27	51.88	50.81	52.10	51.21	51.40	51.74	50.39	51.36
0.72	0.71	0.43	0.68	0.66	0.75	0.75	0.54	1.45	0.88
1.86	2.01	1.44	2.37	2.37	1.88	2.36	2.32	2.23	2.25
7.22	7.49	8.10	7.62	7.78	8.35	7.87	8.33	10.24	10.16
0.64	0.63	1.14	0.69	0.83	0.45	0.93	0.65	1.13	1.13
13.84	13.89	13.04	13.55	13.88	13.38	13.43	13.45	12.09	12.70
22.62	22.96	22.23	22.58	22.83	22.50	22.29	22.73	21.01	21.19
0.26	0.81	0.46	0.44	0.23	0.77	0.46	0.40	0.97	0.88
0.00	0.00	0.14	0.08	0.00	0.00	0.13	0.00	0.00	0.00
100.62	99.81	99.78	101.18		100.26	101.04	100.17	101.31	
1.940	1.922	1.963	1.921	1.930	1.932	1.927	1.932	1.915	1.926

0.020	0.020	0.012	0.019	0.018	0.021	0.021	0.015	0.041	0.025
0.022	0.011	0.028	0.027	0.034	0.015	0.031	0.034	0.015	0.026
0.060	0.078	0.037	0.079	0.070	0.068	0.073	0.068	0.085	0.074
0.228	0.235	0.256	0.241	0.241	0.264	0.247	0.260	0.326	0.319
0.020	0.020	0.036	0.022	0.026	0.014	0.030	0.021	0.036	0.036
0.780	0.776	0.735	0.764	0.766	0.753	0.751	0.748	0.685	0.710
0.917	0.922	0.901	0.915	0.906	0.910	0.895	0.909	0.855	0.851
0.019	0.059	0.034	0.032	0.017	0.056	0.034	0.029	0.071	0.064
0.000	0.000	0.004	0.002	0.000	0.000	0.004	0.000	0.000	0.000
4.008	4.043	4.007	4.022	4.008	4.033	4.018	4.017	4.029	4.031
47.11	47.22	46.71	47.11	46.73	46.88	46.58	46.91	44.98	44.43
12.79	13.05	15.17	13.55	13.77	14.32	14.38	14.49	19.02	18.51
40.10	39.74	38.12	39.34	39.51	38.79	39.04	38.60	36.00	37.06
77.35	76.77	74.16	76.02	76.08	74.07	75.25	74.20	67.78	69.02

pumices

ZRP1 core	ZRP1 rim	ZRP2 core	ZRP2 rim	ZRP3 gm	ZRP4 core	ZRP4 rim
51.29	51.78	49.05	51.62	50.11	50.40	50.93
0.72	0.45	0.78	0.46	0.81	0.51	0.88
1.45	1.22	1.55	1.49	1.71	1.24	2.38
10.29	10.01	12.75	8.62	12.16	10.18	7.55
1.49	1.52	1.50	1.30	1.52	1.51	0.53
11.74	11.87	9.51	12.91	10.31	11.03	13.99
21.64	21.94	20.43	22.11	21.03	21.38	22.48
1.34	1.30	1.77	1.17	1.59	1.19	0.61
0.00	0.02	0.06	0.02	0.06	0.05	0.04
100.09	100.15	97.41	99.84	99.38	97.51	99.50
1.947	1.960	1.939	1.948	1.934	1.962	1.913
0.021	0.013	0.023	0.013	0.024	0.015	0.025
0.012	0.014	0.011	0.015	0.012	0.019	0.018
0.053	0.040	0.061	0.052	0.066	0.038	0.087
0.327	0.317	0.421	0.272	0.393	0.331	0.237
0.048	0.049	0.050	0.042	0.050	0.050	0.017
0.664	0.670	0.560	0.726	0.593	0.640	0.783
0.880	0.890	0.865	0.894	0.870	0.892	0.905
0.099	0.095	0.136	0.086	0.119	0.090	0.044
0.000	0.001	0.002	0.001	0.002	0.002	0.001
4.050	4.048	4.069	4.048	4.062	4.039	4.031
45.86	46.22	45.60	46.23	45.65	46.62	46.59
19.52	18.99	24.86	16.22	23.21	19.93	13.08
34.62	34.79	29.53	37.55	31.14	33.46	40.33
67.04	67.88	57.07	72.75	60.18	65.89	76.76

Table 6

Representative EDS analysis of feldspar crystals of investigated rocks

facies	**mafic enclave**									
sample	ZR3C	ZR3C	ZR3C	ZR3C	ZR3C	ZR3C	ZR3C	ZR3C	ZR3C	ZR3C
spot	gm	core	core	rim	gm	gm	gm	gm	gm	gm
SiO_2	50.8	47.5	47.2	60.7	57.4	52.5	51.7	61.8	65.1	65.1
Al_2O_3	31.2	34.4	34.0	24.0	25.3	28.0	29.0	24.0	19.4	19.5
FeO	0.3	0.9	0.6	0.2	0.7	0.9	1.5	0.6	0.4	0.2
CaO	14.2	17.1	17.3	5.0	7.6	10.8	11.9	5.2	1.2	0.9
Na_2O	3.5	1.9	1.8	7.7	7.2	4.9	4.4	8.3	6.1	5.7
K_2O	0.1	0.1	0.0	1.4	0.6	0.3	0.3	1.0	7.8	8.3
Sum	100.99	103.08	101.24	100.20	100.21	97.91	99.03	101.43	100.42	100.56
Cations per formula unit										
Si	2.309	2.145	2.150	2.728	2.599	2.444	2.387	2.729	2.941	2.942
Al	1.670	1.830	1.827	1.270	1.353	1.535	1.579	1.250	1.030	1.038
Fe	0.013	0.036	0.021	0.007	0.026	0.033	0.057	0.021	0.017	0.008
Ca	0.693	0.826	0.843	0.242	0.369	0.539	0.588	0.247	0.057	0.042
Na	0.311	0.168	0.156	0.673	0.631	0.444	0.398	0.707	0.536	0.497
K	0.003	0.006	0.000	0.079	0.035	0.015	0.015	0.058	0.449	0.478
Sum	5.008	5.027	5.012	5.013	5.052	5.018	5.027	5.022	5.036	5.021
An mol%	0.69	0.83	0.84	0.24	0.37	0.54	0.59	0.25	0.06	0.04
Ab mol%	0.31	0.17	0.16	0.67	0.65	0.44	0.40	0.71	0.54	0.50
Or mol %	0.01	0.01	0.00	0.09	0.04	0.02	0.02	0.06	0.45	0.48

Major oxides as wt.%. ph:phenocryst; micro: microphenocryst; gm: groundmass. The cation proportions of feldspars are calculated on the basis of 32 oxygens. An: anorthite; Ab: albite; Or: orthoclase.

hybrid enclave

M6C	M6C	M6C	M6C	M6C	M6C	M6C	M6C	M6C	M6C	M6C	M6C	M6C
micro	gm	micro	core	rim	core	rim	core	rim	micro	micro	core	rim
64.7	64.3	61.7	51.3	56.7	45.6	46.2	64.8	64.3	64.8	64.8	63.4	66.7
19.7	20.4	24.0	29.4	26.9	33.0	33.0	19.3	19.7	19.7	19.8	19.7	19.7
0.4	0.3	0.3	0.8	0.5	0.5	0.3	0.4	0.1	0.5	0.2	0.3	0.6
0.9	1.0	5.4	12.8	9.1	17.2	16.6	0.7	1.0	1.0	0.8	1.0	0.4
4.4	4.8	7.3	3.7	5.7	1.8	2.0	4.3	4.4	5.7	5.6	4.5	5.2
9.8	9.3	1.7	0.5	0.7	0.3	0.2	10.3	9.6	7.8	8.3	9.4	9.4
100.76	102.54	101.45	99.48	100.05	99.02	98.64	100.03	99.62	99.72	99.82	98.62	102.26
2.932	2.893	2.731	2.365	2.560	2.136	2.162	2.950	2.937	2.936	2.937	2.924	2.961
1.053	1.082	1.253	1.595	1.432	1.825	1.819	1.038	1.059	1.054	1.057	1.069	1.031
0.016	0.011	0.012	0.030	0.017	0.019	0.012	0.016	0.003	0.020	0.008	0.012	0.021
0.044	0.048	0.258	0.633	0.438	0.862	0.832	0.034	0.048	0.048	0.038	0.051	0.017

0.390	0.415	0.630	0.327	0.500	0.160	0.181	0.377	0.392	0.504	0.495	0.404	0.451
0.568	0.535	0.096	0.027	0.041	0.015	0.010	0.597	0.559	0.450	0.478	0.553	0.533
5.013	5.032	5.005	5.007	4.995	5.038	5.024	5.019	5.009	5.014	5.021	5.020	5.016
0.04	0.05	0.26	0.63	0.44	0.86	0.83	0.03	0.05	0.05	0.04	0.05	0.02
0.39	0.45	0.64	0.34	0.51	0.18	0.19	0.38	0.40	0.50	0.50	0.41	0.45
0.57	0.54	0.10	0.03	0.04	0.02	0.01	0.60	0.56	0.45	0.48	0.56	0.54

trachitic lava										**pumices**		
ZR3B ph	ZR3B micro	ZR3B ph	ZR3B core	ZR3B rim	M1 core	M1 rim	M1 micro	M1 core	M1 rim	ZRP1	ZRP1	ZRP1
66.1	66.6	65.7	66.4	65.0	62.7	66.3	66.1	64.4	63.8	66.49	66.09	65.63
19.8	19.2	19.5	19.7	19.7	20.7	19.2	19.9	19.6	18.9	19.89	19.62	19.71
0.1	0.6	0.6	0.8	0.7	0.3	0.3	0.6			0.39	0.45	0.35
0.9	0.0	0.6	0.9	0.9	3.0	0.5	1.1	1.0	0.4	0.53	0.35	0.67
5.0	5.2	5.6	5.4	5.4	7.1	6.3	6.0	5.3	5.5	7.06	6.85	7.2
9.0	9.1	8.1	7.7	8.4	3.3	7.6	6.8	8.5	8.5	6.56	6.92	6.12
101.51	101.5	100.54	101.86	100.25	98.705	101.9	101.76	99.4	97.64	100.92	100.72	100.13
2.952	2.982	2.950	2.950	2.937	2.865	2.958	2.938	2.934	2.955	2.954	2.955	2.946
1.045	1.016	1.032	1.033	1.047	1.114	1.010	1.041	1.055	1.029	1.042	1.034	1.043
0.003	0.024	0.023	0.030	0.025	0.013	0.012	0.024	0.000	0.000	0.014	0.017	0.013
0.044	0.000	0.030	0.042	0.042	0.144	0.022	0.053	0.048	0.021	0.025	0.017	0.032
0.433	0.454	0.486	0.469	0.476	0.631	0.541	0.521	0.467	0.492	0.608	0.594	0.627
0.511	0.521	0.467	0.434	0.482	0.194	0.432	0.387	0.497	0.500	0.372	0.395	0.350
4.992	4.997	5.001	4.977	5.014	4.991	5.015	4.981	5.020	5.027	5.015	5.022	5.021
0.04	0.00	0.03	0.04	0.04	0.14	0.02	0.05	0.05	0.02	0.03	0.02	0.03
0.43	0.45	0.49	0.47	0.48	0.65	0.56	0.52	0.47	0.50	0.61	0.61	0.63
0.51	0.52	0.47	0.44	0.48	0.20	0.43	0.39	0.50	0.50	0.37	0.39	0.35

ZRP2	ZRP2	ZRP2	ZRP3	ZRP3	ZRP3	ZRP4	ZRP4	ZRP4	ZRP4	ZRP4
64.31	65.14	64.57	64.73	64.89	64.69	64.73	64.73	65.31	64.69	63.98
19.84	18.96	19.77	19.55	19	19.15	19.29	19.44	18.99	19.34	19.5
0.61	0.39	0.44	0.33	0.21	0.18	0.19	0.24	0.29	0.36	0.63
0.86	0.23	0.67	0.8	0.34	0.52	0.61	0.83	0.44	0.67	0.91
7.5	6.97	6.23	6.61	6.48	6.52	6.22	5.93	6.8	6.49	5.93
5.35	6.54	7.16	6.82	7.18	7.02	7.33	7.73	6.68	6.89	6.99
98.66	98.57	99.19	98.92	98.47	98.31	98.37	99.31	98.89	98.58	98.75
2.925	2.969	2.936	2.943	2.967	2.960	2.958	2.946	2.969	2.951	2.932
1.064	1.019	1.060	1.048	1.024	1.033	1.039	1.043	1.018	1.040	1.053
0.023	0.015	0.017	0.013	0.008	0.007	0.007	0.009	0.011	0.014	0.024
0.042	0.011	0.033	0.039	0.017	0.025	0.030	0.040	0.021	0.033	0.045
0.661	0.616	0.549	0.583	0.574	0.578	0.551	0.523	0.599	0.574	0.527

0.310	0.380	0.415	0.396	0.419	0.410	0.427	0.449	0.387	0.401	0.409
5.029	5.019	5.017	5.022	5.018	5.018	5.012	5.019	5.016	5.016	5.009
0.04	0.01	0.03	0.04	0.02	0.03	0.03	0.04	0.02	0.03	0.04
0.66	0.62	0.55	0.58	0.58	0.58	0.55	0.53	0.61	0.58	0.54
0.31	0.38	0.42	0.40	0.42	0.41	0.43	0.45	0.39	0.40	0.42

Table 7

Representative EDS analysis of biotite crystals from investigated rocks

facies	**mafic enclaves**		**hybrid enclave**			**felsic enclaves**			
Sample	ZR3C	ZR3C	M6C	M6C	M6C	ZR3B	ZR3B	ZR3B	ZR3B
spot	gm	gm	micro	micro	micro	core	rim	gm	gm
SiO_2	34.38	34.39	36.37	36.34	37.11	36.77	35.92	37.10	40.45
TiO_2	7.12	8.65	8.01	7.56	5.65	6.63	6.79	7.45	4.07
Al_2O_3	13.58	13.73	14.53	14.67	14.39	13.84	12.78	13.41	11.63
FeO	13.25	12.64	11.98	13.26	13.23	12.59	15.94	13.78	10.87
MnO	0.09	0.16	0.42	0.05	0.37	0.44	0.68	0.38	1.02
MgO	16.07	15.18	14.13	14.52	15.33	15.33	15.25	16.08	16.86
CaO	0.33	0.00	0.27	0.30	0.00	0.00	0.00	0.00	0.11
Na_2O	1.08	1.16	0.68	0.92	0.53	0.35	0.77	0.51	0.33
K_2O	8.58	8.17	9.57	9.31	9.78	8.88	8.94	9.23	9.92
BaO	0.59	0.26	0.57	1.37	0.13	0.49	0.47	0.42	0.50
SrO	0.34	0.36	0.39	0.55	0.10	0.05	0.00	0.00	0.32
Cl^-	0.15	0.14	0.17	0.02	0.05	0.08	0.01	0.09	0.05
F^-	4.30	3.83	0.52	1.25	0.48	0.00	3.15	2.69	4.62
Sum	99.84	98.66	97.62	100.15	97.16	95.46	100.71	100.13	100.75
Cations per formula unit									
Si	2.592	2.590	2.678	2.651	2.735	2.734	2.671	2.694	2.970
Ti	0.404	0.490	0.443	0.415	0.313	0.371	0.380	0.407	0.225
Al	1.207	1.219	1.261	1.262	1.250	1.213	1.120	1.148	1.006
Fe	0.835	0.796	0.738	0.809	0.815	0.783	0.991	0.837	0.667
Mn	0.006	0.010	0.026	0.003	0.023	0.028	0.043	0.023	0.063
Mg	1.806	1.704	1.551	1.579	1.684	1.699	1.691	1.741	1.845
Ca	0.027	0.000	0.021	0.023	0.000	0.000	0.000	0.000	0.009
Na	0.158	0.169	0.097	0.130	0.076	0.050	0.111	0.072	0.047
K	0.825	0.785	0.899	0.867	0.920	0.842	0.848	0.855	0.929
Ba	0.017	0.008	0.016	0.039	0.004	0.014	0.014	0.012	0.014
Sr	0.015	0.016	0.017	0.023	0.004	0.002	0.000	0.000	0.014
F	1.025	0.912	0.121	0.288	0.112	0.000	0.741	0.618	1.073
Cl	0.019	0.018	0.021	0.002	0.006	0.010	0.001	0.011	0.006
Sum	7.892	7.788	7.747	7.802	7.824	7.736	7.869	7.789	7.790
Mg#	68.37	68.16	67.77	66.12	67.38	68.46	63.04	67.53	73.44

Major and minor oxides as wt.%. micro: microlite; gm: groundmass. The cation proportions of biotites are calculated on the basis of 22oxygens. Mg # = atomic $[Mg^{2+}/(Mg^{2+} + Fe_{tot})]*100$.

Zaro lava		**pumices**				
M1 micro	M1 micro	ZRP1	ZRP1	ZRP2	ZRP2	ZRP4
35.87	36.08	37.11	38.25	38	37.99	37.21
5.95	7.26	6.2	4.19	4.04	3.3	4.12
13.98	13.95	13.4	12.01	12.26	11.76	12.28
14.91	13.44	13.31	13.97	14.83	13.92	13.51
0.72	0.27	0.45	0.93	0.9	0.81	0.71
15.16	15.30	16.21	15.99	16.04	16.46	15.59
0.00	0.20	0	0.03	0	0.11	0.1
0.71	0.86	0.87	1.07	1.05	0.77	0.83
9.21	9.03	8.84	8.85	8.99	8.75	8.83
1.60	0.68	0.45	0	0	0.38	0.36
0.16	0.10	0	0	0.35	0	0.11
0.08	0.00	0.12	0.06	0	0.08	0.09
2.54	3.32	1.92	2.49	2.8	3.18	1.98
100.87	100.50	98.88	97.83	99.25	97.51	95.74
2.659	2.661	2.729	2.861	2.828	2.878	2.838
0.332	0.403	0.343	0.236	0.226	0.188	0.236
1.222	1.213	1.162	1.059	1.076	1.050	1.104
0.924	0.829	0.819	0.874	0.923	0.882	0.862
0.045	0.017	0.028	0.059	0.057	0.052	0.046
1.675	1.682	1.777	1.783	1.780	1.859	1.773
0.000	0.016	0.000	0.002	0.000	0.009	0.008
0.102	0.123	0.124	0.155	0.152	0.113	0.123
0.871	0.850	0.829	0.845	0.854	0.846	0.859
0.046	0.020	0.013	0.000	0.000	0.011	0.011
0.007	0.004	0.000	0.000	0.015	0.000	0.005
0.596	0.774	0.447	0.589	0.659	0.762	0.478
0.010	0.000	0.015	0.008	0.000	0.010	0.012
7.885	7.816	7.824	7.874	7.910	7.888	7.865
64.44	66.99	68.46	67.11	65.85	67.82	67.29

Table 8

C.I.P.W. norms of Zaro whole-rock samples

facies	**mafic enclave**			**felsic enclave**		**Zaro lava**			
sample	ZR3C	ZR1C	M4C	ZR3B	ZR1B	ZR3A	ZR1A	M1	M3
qz	0.0	0.0	0.0	0.0	0.0	0.0	0.0	0.0	0.0
cor	0.0	0.0	0.0	0.0	0.0	0.0	0.0	0.0	0.0
or	17.0	17.6	18.5	41.0	38.5	41.3	38.0	40.0	40.3
ab	29.0	25.5	28.4	40.1	43.6	42.0	42.3	43.9	42.2
an	20.4	19.8	19.7	0.5	0.4	2.8	0.0	3.0	8.0

ne	4.3	6.6	5.0	7.5	7.1	4.7	7.8	4.0	0.6
lc	0.0	0.0	0.0	0.0	0.0	0.0	0.0	0.0	0.0
ac	0.0	0.0	0.0	0.0	0.0	0.0	0.9	0.0	0.0
di	13.2	15.1	12.6	6.1	5.5	4.3	5.7	4.1	1.2
hy	0.0	0.0	0.0	0.0	0.0	0.0	0.0	0.0	0.0
ol	8.1	8.1	8.0	0.7	1.0	1.7	1.1	1.6	2.6
mt	2.7	2.8	2.7	1.2	1.3	1.3	0.8	1.3	1.2
il	2.6	2.6	2.5	1.2	1.1	1.2	1.1	1.2	1.2
hm	0.0	0.0	0.0	0.0	0.0	0.0	0.0	0.0	0.0
ap	0.9	0.9	0.9	0.3	0.2	0.3	0.2	0.3	0.3
aq	0.8	0.9	0.8	1.3	0.8	0.8	0.9	1.9	2.3
Total	99.1	99.8	99.1	100.0	99.5	100.4	98.7	101.2	99.8

Normative contents were calculated on water-free basis, using Fe_2O_3/FeO ratios = 0,2 for shoshonites and 0,4 for trachytes.

M4	M5	M6N	M7	M8	M9	M2	M5B	M10	M12B
0.0	0.0	0.0	0.0	0.0	0.0	0.0	0.0	0.0	0.0
0.0	0.0	0.0	0.0	0.0	0.0	0.0	0.0	0.0	0.0
39.2	41.9	40.1	38.8	41.0	39.5	41.3	41.6	39.4	43.9
43.5	42.2	42.9	43.2	43.2	43.3	42.7	42.0	44.4	39.9
0.5	4.2	2.2	1.4	4.5	1.6	4.8	3.8	1.9	4.9
6.9	3.2	4.9	5.4	2.6	5.6	2.1	3.2	4.7	1.3
0.0	0.0	0.0	0.0	0.0	0.0	0.0	0.0	0.0	0.0
0.0	0.0	0.0	0.0	0.0	0.0	0.0	0.0	0.0	0.0
5.6	3.9	4.5	5.2	3.1	5.0	3.0	4.1	4.5	2.4
0.0	0.0	0.0	0.0	0.0	0.0	0.0	0.0	0.0	0.0
0.9	1.8	1.4	1.1	2.1	1.2	2.1	1.7	1.5	2.3
1.2	1.3	1.3	1.2	1.3	1.2	1.3	1.3	1.3	1.2
1.1	1.2	1.2	1.1	1.2	1.1	1.2	1.2	1.2	1.2
0.0	0.0	0.0	0.0	0.0	0.0	0.0	0.0	0.0	0.0
0.2	0.3	0.3	0.2	0.3	0.2	0.3	0.3	0.3	0.3
0.7	1.4	1.0	1.9	0.7	0.8	0.9	1.1	0.9	0.8
99.9	101.4	99.6	99.6	100.0	99.6	99.8	100.3	99.9	98.3

	pumices			
M13B	ZRP1	ZRP2	ZRP3	ZRP4
0.0	0.0	0.0	0.0	0.0
0.0	0.0	0.0	0.0	0.0
41.3	34.8	34.3	34.3	35.1
41.8	44.3	45.0	44.1	42.8
3.7	0.0	0.0	0.0	0.0
3.4	6.9	6.8	7.0	7.4
0.0	0.0	0.0	0.0	0.0
0.0	1.0	0.9	1.0	1.0
4.1	4.5	4.4	4.4	4.6
0.0	0.0	0.0	0.0	0.0
1.5	1.8	1.7	1.7	1.7
1.2	0.0	0.0	0.0	0.0
1.2	0.9	0.9	0.9	0.9

0.0	0.0	0.0	0.0	0.0
0.3	0.1	0.1	0.1	0.1
1.3	0.0	0.0	0.0	0.0
99.9	95.5	95.1	94.5	95.0

Table 9

Sr-Nd isotopic composition of whole rocks and minerals of Zaro products

whole rocks

	$^{87}Sr/^{86}Sr$	2s	$^{143}Nd/^{144}Nd$	2s
mafic enclaves				
ZR3C	0.704954	± 0.000006	0.512681	± 0.000006
ZR1C	0.705005	± 0.000005	0.512685	± 0.000006
hybrid enclave				
M6C	0.7058204	± 0.000005		
felsic enclaves				
ZR3B	0.7061	± 0.000007	0.512551	± 0.000006
ZR1B	0.706083	± 0.000006	0.512558	± 0.000006
Zaro lava				
M1	0.706108	± 0.000005		
ZR1A	0.706094	± 0.000006		
M9	0.706094	± 0.000006	0.512552	± 0.000006
M8	0.706078	± 0.000006	0.512553	± 0.000006
M5	0.70608	± 0.000006		
ZR3A	0.706149	± 0.000007		
M6N	0.706088	± 0.000006	0.512567	± 0.000008
M2	0.706071	± 0.000006	0.512557	± 0.000006
M5B	0.706095	± 0.000005	0.512568	± 0.000006
M13B	0.706101	± 0.000006		

minerals

	$^{87}Sr/^{86}Sr$	2s
mafic enclaves		
ZR3C ol	0.704859	± 0.000006
ZR3C cpx	0.705621	± 0.000006
ZR3C cpx2	0.705604	± 0.000011
ZR3C feld	0.706232	± 0.000006
ZR3C feld2	0.706023	± 0.000006
ZR1C ol	0.704933	± 0.000005
ZR1C cpx	0.705804	± 0.000005
ZR1C feld	0.706189	± 0.000005
hybrid enclave		
M6C cpx	0.705897	± 0.000008
M6C feld	0.706207	± 0.000005
felsic enclaves		
ZR3B cpx	0.705972	± 0.000007
ZR3B feld	0.706189	± 0.000007
ZR1B cpx	0.706100	± 0.000006
ZR1B feld	0.706143	± 0.000006
Zaro lava		
M1 cpx	0.706131	± 0.000008
M1 feld	0.706187	± 0.000006
ZR1A cpx	0.706233	± 0.000006
ZR1A feld	0.706193	± 0.000005

pumices	ZRP1 feld	0.70616	± 0.000007

2s is the standard deviation and refers to each measurement.

Table 10

O-isotope composition of minerals of Zaro rocks.

	$\delta^{18}O$ (‰)	±1σ	SiO2 (wt. %)	$\delta^{18}O_{melt}$ (‰)
mafic enclave				
ZR3C			51.50	
ZR1C			51.81	
ZR3C ol	5.44	0.15		6.43
ZR1C cpx	4.82	0.15		5.26
ZR3C cpx	4.75	0.15		5.19
ZR3C feld	5.62	0.15		5.57
felsic enclave				
ZR3B			60.97	
ZR1B			61.21	
ZR1B cpx	4.61	0.15		5.62
ZR3B cpx	4.65	0.15		5.65
ZR1B feld	5.98	0.15		6.18
Zaro lava				
ZR1A			60.68	
M1			61.71	
ZR1A cpx	4.63	0.15		5.61
M1 cpx	4.64	0.15		5.68
M1 feld	5.91	0.15		6.13

The error on each measurement is calculated as standard deviation of the San Carlos olivine standard and is ~ 0.15‰.
Errors for melt values were obtained by measurements errors. $\delta^{18}O$ melt is calculated using the formula Δ(melt-min)= a[SiO_2 wt.%] + b after Bindeman et al., (2004).

Supplementary Material 3

Table 1

Detailed concentration profiles of major and minor elements along transects in the A-MS zoned clinopyroxene crystals

Member	A1	A1	A1	A1	A1	A1	A1	A1
Crystal n°	cpx 3	cpx 3	cpx 3	cpx 3	cpx 3	cpx 3	cpx 3	cpx 3
line n°	line1	line1	line1	line1	line1	line1	line1	line1
Spot n°	1	2	3	4	5	6	7	8
SiO_2	53.67	52.46	52.93	52.98	53.13	52.89	53.05	53.23
TiO_2	-	-	-	-	-	-	-	-
Al_2O_3	1.96	2.05	1.97	2.03	1.96	2.07	2.09	2.05
FeOtot	4.26	4.64	4.57	4.62	4.17	4.33	4.53	4.43
MnO	0.00	0.00	0.00	0.00	0.00	0.00	0.00	0.00
MgO	16.26	15.95	16.01	16.03	16.25	16.22	16.14	16.23
CaO	23.92	23.57	23.29	23.43	24.05	23.62	23.63	23.77
Na_2O	0.16	0.27	0.18	0.23	0.20	0.16	0.18	0.20
K_2O	0.02	0.01	0.00	0.04	0.01	-	-	0.01
NiO	0.10	0.00	0.10	-	0.07	0.16	0.02	0.06
Cr_2O_3	0.12	0.24	0.15	0.21	0.23	0.21	0.17	0.15
	0.00	0.00	0.00	0.00	0.00	0.00	0.00	0.00
Sum	100.55	99.29	99.26	99.62	100.15	99.75	99.87	100.23
distance (μm)	0	2.5	5	7.5	10	12.5	15	17.5
Mg#	87	86	86	86	87	87	86	87
Wollastonite	48	48	47	47	48	48	48	48
Ferrosilite	7	7	7	7	7	7	7	7
Enstatite	45	45	45	45	45	46	45	45
Al IV	0.044	0.058	0.045	0.049	0.054	0.055	0.052	0.052

Al VI	0.040	0.032	0.041	0.039	0.031	0.035	0.039	0.037

A1	A1	A1	A1	A1	A1	A1	A1	A1	A1
cpx 3	cpx 3	cpx 3	cpx 3	cpx 3	cpx 3	cpx 3	cpx 3	cpx 3	cpx 3
line1	line1	line1	line1	line1	line1	line1	line1	line1	line1
9	10	11	12	13	14	15	16	17	18
52.78	52.28	52.82	53.01	53.02	48.98	50.80	51.14	50.88	51.14
-	-	-	-	-	-	-	-	-	-
2.19	1.93	2.12	2.13	2.21	5.23	3.78	3.35	3.10	3.23
4.26	4.27	3.88	4.52	5.38	7.02	6.69	7.17	6.88	7.37
0.00	0.00	0.00	0.00	0.00	0.00	0.00	0.00	0.00	0.00
16.08	16.42	16.39	16.10	15.66	13.54	14.08	14.13	14.19	13.89
23.58	23.89	24.22	23.78	23.65	23.18	23.03	22.99	22.89	23.07
0.20	0.12	0.13	0.18	0.20	0.38	0.37	0.43	0.38	0.43
0.02	0.02	-	0.02	0.03	-	0.01	-	0.03	-
0.11	0.05	0.03	0.03	0.06	0.05	0.08	0.04	0.01	0.03
0.11	0.12	0.11	0.08	0.12	0.04	-	-	-	0.01
0.00	0.00	0.00	0.00	0.00	0.00	0.00	0.00	0.00	0.00
99.42	99.17	99.72	99.93	100.38	98.42	98.94	99.36	98.46	99.24
20	22.5	25	27.5	30	32.5	35	37.5	40	42.5
87	87	88	86	84	77	79	78	79	77
48	48	48	48	48	49	48	48	48	48
7	7	6	7	8	12	11	12	11	12
45	46	46	45	44	40	41	41	41	40
0.054	0.063	0.059	0.054	0.055	0.147	0.095	0.087	0.082	0.083
0.041	0.021	0.032	0.039	0.040	0.087	0.072	0.061	0.056	0.060

A1	A1	A1	A1	A1	A1	A1	A1	A1	A1
cpx 3	cpx 3	cpx 3	cpx 3	cpx 3	cpx 3	cpx 3	cpx 3	cpx 3	cpx 3
line1	line1	line1	line1	line1	line1	line1	line1	line1	line2
19	20	21	22	23	24	25	26	27	1
50.56	51.18	51.29	50.86	50.61	50.65	50.87	50.51	51.39	52.71
-	-	-	-	-	-	-	-	-	-
3.29	3.15	3.17	3.41	3.44	3.06	3.16	3.44	3.40	2.49
7.43	7.40	7.06	7.73	7.60	7.32	7.69	8.05	7.63	3.74

0.00	0.00	0.00	0.00	0.00	0.00	0.00	0.00	0.00	0.00
13.75	13.82	13.77	13.75	13.43	13.55	13.79	13.16	13.52	16.30
22.79	23.18	22.77	22.75	22.83	23.23	22.92	22.98	22.52	24.23
0.42	0.44	0.48	0.51	0.36	0.36	0.52	0.46	0.51	0.13
0.01	0.03	-	-	0.01	0.02	0.02	0.04	0.04	0.02
0.02	0.18	0.13	0.14	0.01	0.16	-	0.06	0.11	0.11
-	-	-	0.11	0.04	0.04	0.08	0.02	0.05	0.17
0.00	0.00	0.00	0.00	0.00	0.00	0.00	0.00	0.00	0.00
98.41	99.42	98.67	99.38	98.46	98.45	99.16	98.83	99.22	99.93
45	47.5	50	52.5	55	57.5	60	62.5	65	0
77	77	78	76	76	77	76	74	76	89
48	48	48	47	48	49	48	48	48	49
12	12	12	13	13	12	12	13	13	6
40	40	40	40	39	39	40	38	40	46
0.087	0.083	0.072	0.091	0.086	0.083	0.087	0.090	0.075	0.068
0.060	0.056	0.069	0.059	0.068	0.054	0.053	0.063	0.075	0.040

A1 cpx 3 line2	A1 cpx 3 line2	A1 cpx 3 line2	A1 cpx 3 line2	A1 cpx 3 line2	A1 cpx 3 line2	A1 cpx 3 line2	A1 cpx 3 line2	A1 cpx 3 line2	A1 cpx 3 line2
2	3	4	5	6	7	8	9	10	11
52.09	52.44	51.98	52.51	52.59	52.25	50.94	50.41	50.30	51.20
-	-	-	-	-	-	-	-	-	-
2.76	2.51	2.30	2.50	2.68	2.46	4.00	3.71	3.50	3.35
3.87	3.69	3.90	3.82	3.87	5.04	6.53	7.21	7.55	7.61
0.00	0.00	0.00	0.00	0.00	0.00	0.00	0.00	0.00	0.00
16.10	16.25	16.13	16.09	16.39	15.30	14.30	13.63	13.38	13.45
24.07	24.18	23.88	23.97	24.25	23.55	23.03	23.14	22.80	22.96
0.11	0.18	0.09	0.15	0.14	0.17	0.37	0.39	0.40	0.40
0.01	-	0.00	-	0.01	-	-	0.04	-	-
0.03	0.02	0.01	0.03	0.06	0.01	0.08	0.13	0.14	0.06
0.22	0.24	0.14	0.08	0.17	0.14	0.15	0.09	0.02	0.04
0.00	0.00	0.00	0.00	0.00	0.00	0.00	0.00	0.00	0.00
99.34	99.59	98.50	99.25	100.25	99.03	99.53	98.80	98.17	99.10
2.5	5	7.5	10	12.5	15	17.5	20	22.5	25
88	89	88	88	88	84	80	77	76	76
49	49	48	49	48	48	48	48	48	48
6	6	6	6	6	8	11	12	12	12
45	46	45	45	46	44	41	40	39	39

0.077	0.070	0.066	0.063	0.076	0.059	0.103	0.100	0.090	0.078
0.043	0.039	0.035	0.046	0.039	0.049	0.073	0.065	0.066	0.070

A1	A1	A1	A1	A1	A1	A1
cpx 3	cpx 3	cpx 3	cpx 3	cpx 3	cpx 3	cpx 3
line2	line2	line2	line2	line2	line2	line2
12	13	14	15	16	17	18
51.10	50.87	51.24	50.20	51.45	49.91	50.64
-	-	-	-	-	-	-
3.57	3.39	3.50	3.46	3.45	4.27	3.49
7.75	7.69	7.78	7.67	7.69	8.12	8.06
0.00	0.00	0.00	0.00	0.00	0.00	0.00
13.52	13.43	13.24	13.26	13.43	12.85	13.36
23.42	23.09	22.64	23.13	22.77	22.59	22.78
0.43	0.42	0.48	0.44	0.34	0.38	0.33
0.00	0.02	-	-	0.02	-	-
0.09	0.03	-	-	0.03	0.02	0.01
0.05	0.03	0.07	-	0.05	0.05	0.05
0.00	0.00	0.00	0.00	0.00	0.00	0.00
99.93	99.01	98.97	98.18	99.23	98.29	98.77
27.5	30	32.5	35	37.5	40	42.5
76	76	75	75	76	74	75
49	48	48	49	48	48	48
13	13	13	13	13	14	13
39	39	39	39	39	38	39
0.093	0.086	0.075	0.093	0.074	0.105	0.088
0.064	0.065	0.080	0.062	0.078	0.086	0.067

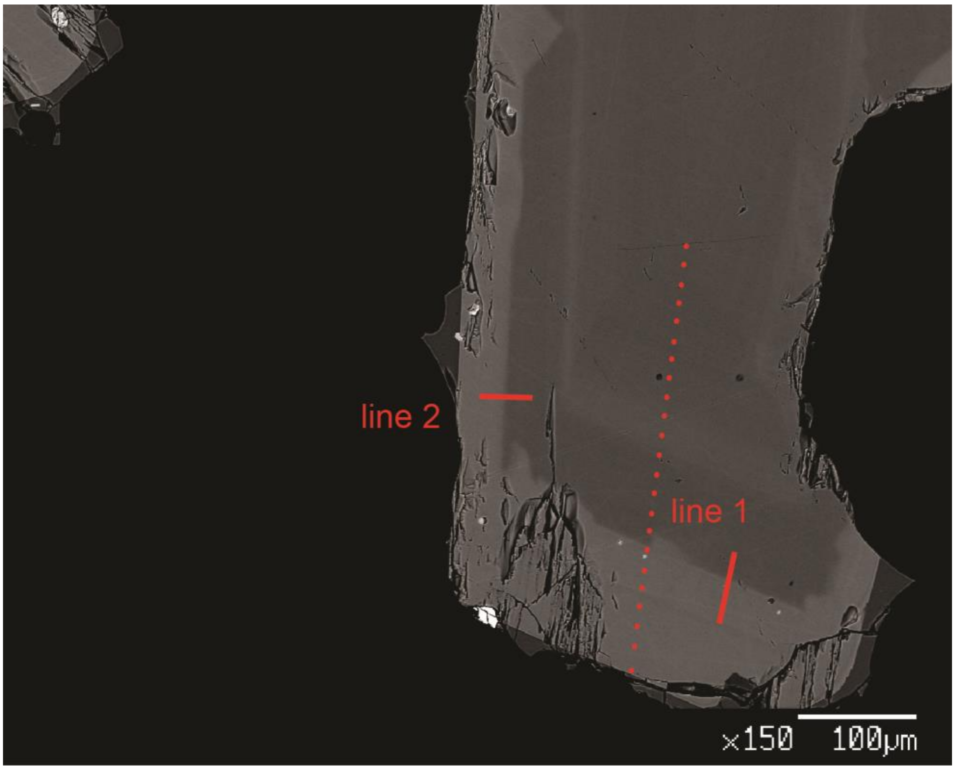

A1	A1	A1	A1	A1	A1	A1	A1	A1	A1
cpx 5	cpx 5	cpx 5	cpx 5	cpx 5	cpx 5	cpx 5	cpx 5	cpx 5	cpx 5
		line1	line1	line1	line1	line1	line1	line1	line1
core	rim	1	2	3	4	5	6	7	8
52.95	49.35	52.65	51.88	52.37	50.83	50.54	50.26	51.96	50.74
0.34	0.99	0.46	0.39	0.48	0.58	0.63	0.60	0.61	0.64
1.76	5.04	2.12	2.20	2.38	2.93	3.80	3.92	2.71	2.74
3.91	8.33	4.59	4.50	5.12	5.77	6.49	7.35	7.77	8.05
0.00	0.00	0.00	0.00	0.00	0.00	0.00	0.00	0.00	0.00
17.05	12.61	16.07	16.06	15.97	15.04	14.33	13.88	14.06	13.73
22.30	22.80	23.43	23.40	23.32	22.71	23.26	23.23	22.26	22.64
0.07	0.53	0.15	0.12	0.11	0.16	0.27	0.34	0.55	0.54
0.02	0.02	-	-	0.00	-	0.02	0.02	0.03	0.01
0.01	-	0.01	0.16	0.14	0.13	0.09	0.07	0.06	0.02
0.32	0.03	0.01	0.11	0.02	-	0.04	0.07	0.01	-
0.00	0.00	0.00	0.00	0.00	0.00	0.00	0.00	0.00	0.00
98.73	99.70	99.55	98.91	99.94	98.23	99.50	99.82	100.05	99.20
		0	7	14	21	28	35	42	49
89	73	86	86	85	82	80	77	76	75
45	49	47	48	47	47	48	48	46	47
6	14	7	7	8	9	10	12	13	13

48	37	45	45	45	43	41	40	41	40
0.046	0.148	0.060	0.072	0.072	0.089	0.115	0.122	0.070	0.089
0.031	0.075	0.032	0.024	0.031	0.041	0.052	0.050	0.048	0.032

A1	A1	A1	A1	A1	A1	A1	A1	A1	A1
cpx 5	cpx 5	cpx 5	cpx 5	cpx 5	cpx 5	cpx 5	cpx 5	cpx 5	cpx 5
line1	line1	line1	line1	line1	line1	line1	line1	line1	line2
9	10	11	12	13	15	16	17	18	1
50.92	50.89	50.67	51.01	49.89	50.32	50.68	51.12	50.98	52.18
0.60	0.60	0.57	0.64	0.68	0.61	0.71	0.74	0.71	0.55
2.84	2.72	3.11	2.98	3.16	3.17	3.03	3.25	3.24	3.04
8.14	8.00	8.04	8.35	8.05	8.10	8.28	8.02	7.98	4.62
0.00	0.00	0.00	0.00	0.00	0.00	0.00	0.00	0.00	0.00
13.71	13.51	13.48	13.68	13.43	13.59	13.22	13.26	13.49	16.07
22.36	22.72	22.52	22.35	22.60	22.20	23.06	22.53	22.92	23.32
0.54	0.56	0.48	0.41	0.48	0.44	0.43	0.41	0.48	0.19
0.04	0.01	-	-	-	-	0.00	0.06	-	-
0.05	0.08	0.11	-	0.05	0.06	0.05	0.07	0.06	0.00
-	0.04	0.01	0.07	0.08	0.06	0.01	0.01	0.04	0.08
0.00	0.00	0.00	0.00	0.00	0.00	0.00	0.00	0.00	0.00
99.21	99.27	99.05	99.57	98.48	98.63	99.58	99.50	99.90	100.12
56	63	70	77	84	98	105	112	119	0
75	75	75	74	75	75	74	75	75	86
47	48	47	47	48	47	48	48	48	47
13	13	13	14	13	13	13	13	13	7
40	39	39	40	39	40	38	39	39	45
0.085	0.085	0.091	0.088	0.105	0.096	0.095	0.086	0.096	0.087
0.041	0.036	0.047	0.043	0.036	0.045	0.039	0.058	0.047	0.044

A1	A1	A1	A1	A1	A1	A1	A1	A1	A1
cpx 5	cpx 5	cpx 5	cpx 5	cpx 5	cpx 5	cpx 5	cpx 5	cpx 5	cpx 5
line2	line2	line2	line2	line2	line2	line2	line2	line2	line2
2	3	4	5	6	7	8	10	11	13
51.36	52.03	52.02	52.12	51.47	50.31	49.93	47.88	51.51	49.47
0.54	0.61	0.39	0.47	0.46	0.64	0.85	0.67	0.54	0.57

2.88	2.93	2.64	2.63	2.65	4.08	4.60	3.13	2.71	3.13
4.64	4.53	4.29	4.57	4.66	5.68	6.23	7.40	7.70	7.71
0.00	0.00	0.00	0.00	0.00	0.00	0.00	0.00	0.00	0.00
16.09	16.44	16.09	16.10	15.97	14.68	14.29	14.65	13.80	12.93
23.23	23.06	23.57	23.28	23.26	22.61	23.19	21.18	22.12	22.08
0.10	0.15	0.19	0.10	0.10	0.23	0.29	0.66	0.49	0.46
0.03	-	0.04	0.00	0.01	-	0.04	0.03	-	0.04
0.01	0.13	0.02	0.14	0.06	0.06	0.04	0.01	0.04	0.09
0.14	0.04	0.14	0.16	0.11	0.13	-	0.07	-	0.13
0.00	0.00	0.00	0.00	0.00	0.00	0.00	0.00	0.00	0.00
99.14	100.01	99.46	99.67	98.82	98.55	99.52	95.78	99.03	96.64
5	10	15	20	25	30	35	40	45	50
86	87	87	86	86	82	80	78	76	75
47	47	48	47	47	48	48	45	47	48
7	7	7	7	7	9	10	12	13	13
45	46	45	45	45	43	41	43	41	39
0.095	0.091	0.080	0.079	0.085	0.115	0.139	0.132	0.067	0.090
0.031	0.036	0.035	0.035	0.031	0.065	0.063	0.011	0.052	0.052

A1 cpx 5 line2	A1 cpx 5 line2	A1 cpx 5 line2	A1 cpx 5 line2	A1 cpx 5 line2	A1 cpx 5 line2	A1 cpx 5 line2
14	15	16	17	18	19	20
51.33	50.63	50.84	51.10	51.21	50.87	49.65
0.67	0.58	0.51	0.54	0.52	0.59	0.71
2.95	2.81	2.72	2.70	2.68	2.94	3.75
8.00	7.91	7.89	7.95	8.07	7.84	8.22

0.00	0.00	0.00	0.00	0.00	0.00	0.00
13.61	13.41	13.50	13.34	13.46	13.40	13.41
22.28	22.14	22.41	22.65	22.46	22.66	22.70
0.48	0.51	0.51	0.50	0.43	0.41	0.44
-	0.01	-	0.01	0.02	-	0.03
0.07	-	0.10	0.05	0.05	0.08	-
0.08	0.05	0.04	0.05	0.05	-	-
0.00	0.00	0.00	0.00	0.00	0.00	0.00
99.55	98.19	98.61	98.89	98.98	98.84	98.91
55	60	65	70	75	80	85
75	75	75	75	75	75	74
47	47	47	48	47	48	48
13	13	13	13	13	13	13
40	40	40	39	39	39	39
0.080	0.078	0.077	0.074	0.072	0.082	0.122
0.050	0.048	0.044	0.046	0.047	0.049	0.045

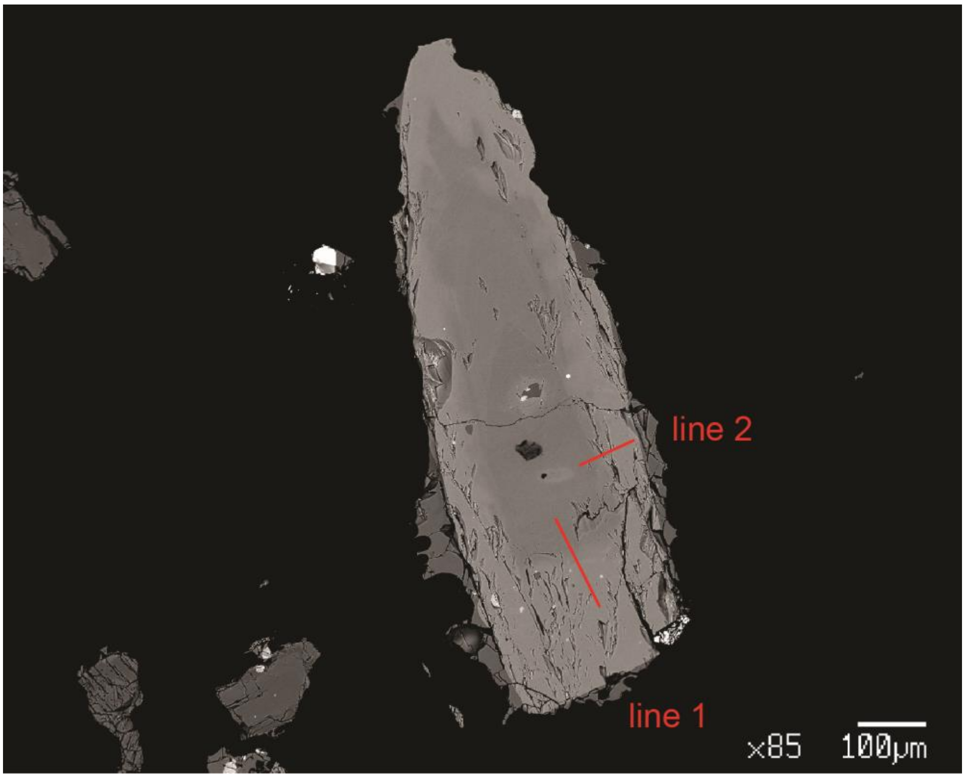

A1	A1	A1	A1	A1	A1	A1	A1	A1	A1
cpx 6	cpx 6	cpx 6	cpx 6	cpx 6	cpx 6	cpx 6	cpx 6	cpx 6	cpx 6

line1	line1	line1	line1	line1	line1	line1	line1	line1	line1
1	2	3	4	5	6	7	8	9	10
51.41	52.18	52.38	52.10	52.06	52.84	52.46	50.71	51.02	50.59
0.45	0.41	0.47	0.38	0.44	0.45	0.39	0.77	0.71	0.70
2.21	2.21	2.09	2.14	2.48	2.34	2.41	3.80	4.25	4.26
3.55	3.73	3.59	3.91	3.85	3.87	4.57	4.97	5.26	5.38
16.53	16.43	16.24	16.43	16.34	16.25	16.27	15.20	15.26	14.92
23.47	23.84	23.87	23.56	23.06	23.61	23.09	22.90	23.10	22.99
0.13	0.22	0.13	0.15	0.14	0.14	0.10	0.23	0.16	0.27
0.02	0.03	0.05	0.02	-	-	0.03	-	0.04	-
0.00	0.02	0.06	0.03	0.01	0.03	0.05	0.06	0.00	0.02
0.46	0.41	0.25	0.25	0.22	0.13	0.17	0.08	0.06	0.10
98.29	99.54	99.13	99.04	98.76	99.81	99.56	98.83	99.90	99.30
0	10	20	30	40	50	60	70	80	90
89	89	89	88	88	88	86	84	84	83
48	48	48	48	47	48	47	48	48	48
6	6	6	6	6	6	7	8	8	9
47	46	46	46	47	46	46	44	44	43
0.083	0.077	0.065	0.071	0.071	0.063	0.068	0.111	0.120	0.121
0.014	0.019	0.026	0.022	0.037	0.038	0.036	0.056	0.065	0.065

A1	A1	A1	A1	A1	A1	A1	A1	A1	A1
cpx 6	cpx 6	cpx 6	cpx 6	cpx 6	cpx 6	cpx 6	cpx 6	cpx 6	cpx 6
line1	line1	line1	line1	line1	line1	line1	line1	line1	line1
11	12	13	14	15	16	17	18	19	20
49.99	50.07	49.85	49.73	50.18	50.46	51.40	50.13	49.76	50.41
0.66	0.85	0.64	0.78	0.73	0.62	0.68	0.79	0.90	0.86
4.42	4.27	4.61	4.72	4.47	4.01	3.99	4.36	4.70	4.54
5.44	5.53	5.72	5.77	5.66	5.21	5.31	5.52	5.60	5.49
15.01	14.95	15.01	14.77	14.93	15.01	15.95	14.88	14.81	14.75
22.88	23.00	22.59	23.07	23.45	23.19	23.09	23.09	22.95	22.53
0.15	0.22	0.30	0.17	0.19	0.14	0.31	0.20	0.22	0.20
-	0.00	-	0.02	-	0.02	0.00	0.01	0.01	0.02
-	0.06	-	0.14	0.10	0.05	-	0.12	-	0.07
0.11	-	-	0.01	-	0.05	0.01	0.04	0.08	-

98.78	99.12	98.80	99.23	99.83	98.88	100.75	99.19	99.10	98.97
100	110	120	130	140	150	160	170	180	190
83	83	82	82	82	84	84	83	82	83
48	48	47	48	48	48	47	48	48	48
9	9	9	9	9	8	8	9	9	9
43	43	44	43	43	43	45	43	43	43
0.132	0.133	0.137	0.145	0.139	0.118	0.121	0.133	0.144	0.124
0.063	0.055	0.066	0.062	0.056	0.059	0.051	0.059	0.062	0.076

A1	A1	A1	A1	A1	A1	A1	A1	A1	A1
cpx 6	cpx 6	cpx 6	cpx 6	cpx 6	cpx 6	cpx 6	cpx 6	cpx 6	cpx 6
line1	line1	line1	line1	line1	line1	line1	line1	line1	line1
21	22	23	24	25	26	27	28	29	30
50.52	51.85	51.13	52.29	53.04	52.54	52.85	52.25	52.30	53.18
0.79	0.51	0.54	0.49	0.45	0.40	0.46	0.43	0.44	0.45
4.75	2.58	2.98	2.18	2.12	2.13	2.41	2.41	2.14	1.90
5.67	5.16	5.81	4.51	4.39	4.09	4.11	4.09	3.74	4.05
14.82	15.80	15.27	16.22	16.47	16.51	16.43	16.65	16.70	16.58
23.09	22.62	22.88	23.43	23.28	23.62	23.24	23.42	23.14	23.51
0.15	0.18	0.12	0.10	0.11	0.12	0.15	0.09	0.14	0.17
0.02	0.02	0.01	-	0.01	-	-	-	0.01	0.01
-	0.02	0.02	-	0.07	0.02	0.07	0.07	0.02	0.15
0.01	0.05	0.05	0.04	0.13	0.08	0.10	0.07	0.12	0.14
99.86	98.86	98.89	99.38	100.23	99.61	99.89	99.53	98.78	100.25
200	210	220	230	240	250	260	270	280	290
82	85	82	87	87	88	88	88	89	88
48	47	47	47	47	47	47	47	47	47
9	8	9	7	7	6	7	6	6	6
43	45	44	46	46	46	46	47	47	46
0.133	0.073	0.091	0.069	0.061	0.067	0.065	0.077	0.065	0.057
0.073	0.040	0.040	0.026	0.031	0.026	0.039	0.028	0.028	0.025

A1	A1	A1	A1	A1	A1	A1	A1	A1	A1	A1
cpx 6	cpx 6	cpx 6	cpx 6	cpx 6	cpx 6	cpx 6	cpx 6	cpx 6	cpx 6	cpx 6
line1	line1	line1	line1	line1	line1	line1	line1	line1	line1	line1
31	32	33	34	35	36	37	38	39	40	41

53.11	52.53	52.50	52.95	52.91	53.12	52.65	53.15	53.06	53.26	52.70
0.52	0.51	0.36	0.47	0.40	0.35	0.33	0.43	0.48	0.35	0.49
2.22	1.83	1.88	1.90	2.05	1.96	1.95	1.91	1.67	1.83	1.60
4.06	4.17	4.03	3.62	3.64	3.59	3.66	3.71	3.86	4.23	3.82
16.45	16.62	16.71	16.77	16.82	16.44	16.55	16.59	16.87	16.71	16.64
23.66	23.63	23.63	23.35	23.34	22.93	23.49	23.16	23.13	23.29	22.75
0.17	0.12	0.06	0.13	0.06	0.14	0.14	0.18	0.13	0.18	0.12
0.02	0.03	0.00	0.01	-	0.01	-	0.01	-	-	-
0.03	0.06	0.12	0.03	-	-	0.09	0.07	0.07	-	-
0.04	0.04	0.21	0.13	0.19	0.23	0.20	0.26	0.08	0.17	0.14
100.28	99.64	99.63	99.46	99.47	98.83	99.15	99.54	99.44	100.08	98.40
300	310	320	330	340	350	360	370	380	390	400
88	88	88	89	89	89	89	89	89	88	89
48	47	47	47	47	47	48	47	47	47	47
6	7	6	6	6	6	6	6	6	7	6
46	46	46	47	47	47	47	47	47	47	47
0.062	0.066	0.067	0.055	0.058	0.042	0.058	0.050	0.050	0.053	0.045
0.033	0.014	0.015	0.027	0.031	0.043	0.027	0.032	0.022	0.026	0.025

A1	A1	A1	A1	A1	A1	A1	A1	A1	A1
cpx 6	cpx 6	cpx 6	cpx 6	cpx 6	cpx 6	cpx 6	cpx 6	cpx 6	cpx 6
line1	line1	line1	line1	line1	line1	line1	line1	line1	line1
42	43	44	45	46	47	48	49	50	51
52.57	52.24	53.09	52.74	53.19	52.19	51.44	52.43	53.02	53.44
0.51	0.29	0.60	0.49	0.50	0.39	0.45	0.45	0.48	0.44
2.00	1.84	2.04	2.27	2.34	2.52	2.63	2.11	2.03	1.88
4.04	4.34	4.41	4.94	5.45	5.55	5.24	4.43	3.79	3.84
16.52	16.38	16.46	16.05	15.95	15.87	15.61	16.44	16.61	16.63
23.24	23.34	22.95	22.72	22.92	23.01	23.08	23.50	23.42	23.67
0.18	0.13	0.10	0.18	0.18	0.15	0.15	0.14	0.15	0.13
-	-	0.06	0.01	-	0.00	0.06	0.02	0.04	0.02
0.14	0.06	0.05	-	-	0.07	0.08	-	0.03	0.05
0.12	0.08	0.07	-	0.04	0.09	0.05	0.06	0.16	0.07
99.41	98.77	99.92	99.52	100.61	99.93	98.90	99.63	99.73	100.35
410	420	430	440	450	460	470	480	490	500

88	87	87	85	84	84	84	87	89	89
47	47	47	46	46	47	47	47	47	48
6	7	7	8	9	9	8	7	6	6
47	46	46	46	45	45	44	46	47	46
0.063	0.060	0.055	0.057	0.059	0.076	0.083	0.069	0.057	0.052
0.024	0.021	0.033	0.041	0.042	0.034	0.033	0.023	0.030	0.029

A1	A1	A1	A1	A1	A1	A1	A1	A1	A1
cpx 6	cpx 6	cpx 6	cpx 6	cpx 6	cpx 6	cpx 6	cpx 6	cpx 6	cpx 6
line1	line1	line1	line1	line1	line1	line1	line1	line1	line1
52	53	54	55	57	58	59	60	61	62
53.02	52.97	52.52	50.74	50.20	50.65	49.82	50.34	50.48	50.68
0.49	0.53	0.37	0.74	0.72	0.66	0.74	0.83	0.67	0.63
1.93	1.92	1.92	3.29	3.29	3.21	3.50	3.97	3.23	3.23
3.99	4.10	4.34	7.36	8.05	8.50	8.00	8.21	7.99	8.10
16.59	16.41	15.93	13.75	13.41	13.09	13.36	13.46	13.40	13.36
23.37	23.39	23.35	23.06	22.77	22.12	22.50	22.86	22.91	22.88
0.09	0.14	0.16	0.43	0.46	0.48	0.41	0.40	0.48	0.40
-	0.02	0.01	-	-	0.05	-	-	-	0.01
0.06	0.07	0.05	0.02	0.05	0.08	0.14	0.01	-	0.08
0.13	0.26	0.18	0.10	0.06	0.04	0.03	0.01	-	-
99.78	99.89	98.83	99.59	99.05	98.97	98.50	100.17	99.27	99.37
510	520	530	540	560	570	580	590	600	610
88	88	87	77	75	73	75	75	75	75
47	47	48	48	48	47	48	48	48	48
6	6	7	12	13	14	13	13	13	13
47	46	45	40	39	39	39	39	39	39
0.056	0.058	0.053	0.102	0.106	0.088	0.110	0.122	0.100	0.096
0.027	0.025	0.031	0.043	0.041	0.055	0.046	0.053	0.043	0.047

A1	A1	A1	A1	A1	A1	A1	A1	A1	A1
cpx 6	cpx 6	cpx 6	cpx 6	cpx 6	cpx 6	cpx 6	cpx 6	cpx 6	cpx 6
line1	line1	line1	line2	line2	line2	line2	line2	line2	line2
63	64	65	1	2	3	4	5	6	7
50.10	50.69	50.25	52.20	52.08	52.19	52.67	52.46	51.90	52.33
0.63	0.66	0.68	0.42	0.47	0.42	0.39	0.51	0.48	0.46

3.29	3.41	3.45	2.49	2.32	2.56	2.42	2.38	2.38	2.48
8.20	7.98	7.81	3.73	3.92	3.66	3.47	3.71	3.82	3.69
13.25	13.61	13.60	16.28	16.44	16.37	16.46	16.39	16.51	16.56
22.65	22.41	22.02	23.26	23.21	23.51	23.42	23.58	23.52	23.21
0.53	0.41	0.44	0.12	0.20	0.13	0.16	0.12	0.14	0.13
0.02	0.04	-	0.00	0.02	-	0.04	0.01	0.02	-
-	0.06	-	0.01	0.04	0.09	0.14	0.04	0.04	-
0.04	-	0.05	0.38	0.48	0.39	0.34	0.40	0.47	0.40
98.82	99.35	98.35	99.02	99.22	99.42	99.54	99.74	99.43	99.37
620	630	640	0	5	10	15	20	25	30
74	75	76	89	88	89	89	89	89	89
48	47	47	48	47	48	48	48	48	47
13	13	13	6	6	6	6	6	6	6
39	40	40	46	47	46	47	46	46	47
0.103	0.098	0.098	0.071	0.076	0.078	0.067	0.074	0.084	0.074
0.044	0.053	0.056	0.037	0.025	0.033	0.038	0.029	0.019	0.033

A1	A1	A1	A1	A1	A1	A1	A1	A1	A1
cpx 6	cpx 6	cpx 6	cpx 6	cpx 6	cpx 6	cpx 6	cpx 6	cpx 6	cpx 6
line2	line2	line2	line2	line2	line2	line2	line2	line2	line2
8	9	10	11	12	13	14	15	16	17
52.61	52.64	52.40	50.38	49.43	49.81	51.05	50.57	49.77	49.89
0.51	0.46	0.63	1.06	0.91	0.69	0.81	0.90	0.96	0.98
2.28	2.24	2.55	4.58	4.60	4.29	4.04	4.70	4.55	5.36
3.78	3.72	4.03	5.43	5.60	5.49	5.28	5.52	5.69	5.56
16.50	16.35	16.34	14.76	14.90	14.80	15.42	14.83	14.73	14.56
23.01	23.48	23.55	23.26	23.25	23.13	23.54	23.33	23.50	23.79
0.14	0.14	0.11	0.19	0.19	0.20	0.23	0.21	0.19	0.24
-	-	0.01	0.01	0.04	-	0.05	0.02	0.02	0.04
0.10	0.01	-	-	0.04	-	-	0.08	0.09	0.11
0.26	0.18	0.19	0.12	0.13	0.07	0.11	0.10	0.01	-
99.25	99.29	99.86	99.85	99.15	98.52	100.58	100.30	99.57	100.60
35	40	45	50	55	60	65	70	75	80
89	89	88	83	83	83	84	83	82	82

47	48	48	48	48	48	48	48	49	49
6	6	6	9	9	9	8	9	9	9
47	46	46	43	43	43	44	43	42	42
0.063	0.062	0.078	0.137	0.153	0.132	0.127	0.138	0.148	0.163
0.036	0.035	0.032	0.062	0.049	0.058	0.048	0.066	0.051	0.070

A1	A1	A1	A1	A1	A1	A1	A1	A1	A1
cpx 6	cpx 6	cpx 6	cpx 6	cpx 6	cpx 6	cpx 6	cpx 6	cpx 6	cpx 6
line2	line2	line2	line2	line2	line2	line2	line2	line2	line2
18	19	20	21	22	23	24	25	26	27
51.12	50.74	52.59	51.76	51.46	52.52	52.09	52.10	51.22	51.27
0.69	0.74	0.51	0.41	0.48	0.54	0.39	0.53	0.57	0.57
3.59	3.46	2.89	2.44	2.44	2.55	2.44	2.56	3.11	2.99
5.02	5.10	4.43	4.21	4.06	4.23	4.01	3.84	4.35	4.53
15.49	15.63	15.83	15.95	15.93	16.05	16.17	16.37	15.82	15.75
23.14	23.53	23.17	23.47	23.55	23.46	23.25	23.64	23.31	23.12
0.10	0.19	0.16	0.13	0.11	0.18	0.11	0.15	0.10	0.14
0.08	0.02	0.01	0.02	-	0.04	-	-	-	0.03
0.05	-	0.06	0.18	-	-	-	0.13	0.16	0.05
0.08	0.08	0.17	0.19	0.12	0.25	0.23	0.30	0.09	0.26
99.37	99.49	99.90	98.84	98.25	99.90	98.74	99.62	98.89	98.80
85	90	95	100	105	110	115	120	125	130
85	85	86	87	87	87	88	88	87	86
48	48	48	48	48	48	48	48	48	48
8	8	7	7	6	7	6	6	7	7
44	44	45	45	45	45	46	46	45	45
0.107	0.118	0.072	0.076	0.078	0.073	0.069	0.083	0.096	0.093
0.050	0.033	0.053	0.030	0.030	0.038	0.038	0.028	0.040	0.039

A1	A1	A1	A1	A1	A1	A1	A1	A1	A1
cpx 6	cpx 6	cpx 6	cpx 6	cpx 6	cpx 6	cpx 6	cpx 6	cpx 6	cpx 6
line2	line2	line2	line2	line2	line2	line2	line2	line2	line2
28	29	30	31	32	33	34	35	36	37

51.12	51.69	51.32	52.33	51.87	52.02	51.98	52.25	51.56	50.53
0.60	0.61	0.88	0.52	0.55	0.48	0.49	0.58	0.56	0.63
3.17	3.19	3.88	2.20	2.31	2.46	2.54	2.64	2.74	3.42
4.80	4.78	5.31	4.26	4.10	4.12	4.28	5.41	7.33	7.77
16.01	15.50	15.14	16.03	16.40	15.85	16.18	15.39	14.15	13.76
22.78	23.41	23.25	23.54	23.70	23.71	23.49	23.24	23.22	22.43
0.10	0.11	0.16	0.17	0.14	0.15	0.07	0.24	0.29	0.46
-	-	-	-	-	0.01	0.05	-	-	-
0.05	0.08	0.13	0.01	0.18	0.09	0.06	0.05	0.09	0.01
0.17	0.09	0.09	0.08	0.22	0.17	0.21	0.29	0.14	0.10
98.87	99.53	100.24	99.25	99.47	99.18	99.40	100.17	100.18	99.19
135	140	145	150	155	160	165	170	175	180
86	85	84	87	88	87	87	84	77	76
47	48	48	48	48	48	48	48	48	47
8	8	9	7	6	7	7	9	12	13
46	44	43	45	46	45	46	44	40	40
0.100	0.091	0.113	0.066	0.084	0.074	0.081	0.078	0.084	0.102
0.039	0.048	0.055	0.030	0.016	0.033	0.030	0.037	0.036	0.050

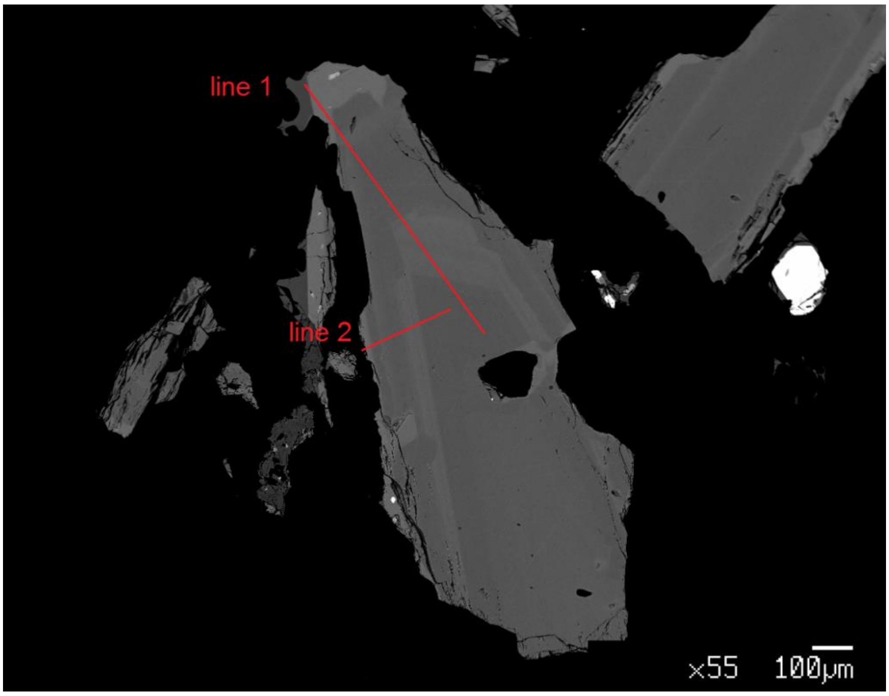

D1	D1	D1	D1	D1	D1	D1	D1	D1	D1
cpx 5	cpx 5	cpx 5	cpx 5	cpx 5	cpx 5	cpx 5	cpx 5	cpx 5	cpx 5
line1	line1	line1	line1	line1	line1	line1	line1	line1	line1
1	2	3	4	5	6	7	8	9	10
52.57	53.95	52.92	53.62	52.59	52.75	52.89	52.88	53.03	53.02
0.48	0.40	0.48	0.46	0.40	0.42	0.39	0.49	0.44	0.45
2.75	2.56	2.33	2.62	2.57	2.56	2.64	2.54	2.62	2.69
4.20	4.16	4.24	4.15	4.65	4.80	4.58	4.74	4.96	4.87
0.21	0.06	0.09	0.09	0.14	0.19	0.09	0.15	0.18	0.21
15.49	15.32	15.48	15.24	15.38	15.12	15.42	15.16	14.95	14.86
23.26	23.00	23.51	23.14	23.21	23.18	23.41	23.25	23.09	22.82
0.14	0.09	0.10	0.08	0.14	0.16	0.16	0.17	0.20	0.24
0.02	-	-	0.05	-	0.05	-	-	0.01	0.06
0.04	0.06	0.06	-	0.08	0.04	0.11	0.04	0.06	-
0.01	0.05	0.02	0.03	0.04	0.07	0.01	0.03	0.02	0.06
0.00	0.00	0.00	0.00	0.00	0.00	0.00	0.00	0.00	0.00
99.17	99.65	99.24	99.47	99.20	99.34	99.71	99.44	99.55	99.27
0.00	2.50	5.00	7.50	10.00	12.50	15.00	17.50	20.00	22.50
86.80	86.78	86.68	86.75	85.50	84.88	85.72	85.08	84.31	84.47
48.20	48.31	48.55	48.56	48.01	48.18	48.26	48.27	48.20	48.08
7.13	6.91	6.98	6.94	7.73	8.10	7.51	7.93	8.38	8.36
44.66	44.77	44.47	44.50	44.26	43.72	44.23	43.79	43.42	43.56

0.10097	0.08179	0.09468	0.08869	0.09729	0.09282	0.09668	0.0915	0.08737	0.08422
0.02321	0.03409	0.01099	0.03027	0.01894	0.02285	0.02203	0.02306	0.03069	0.03722

D1 cpx 5 line1	D1 cpx 5 line1	D1 cpx 5 line1	D1 cpx 5 line1	D1 cpx 5 line1	D1 cpx 5 line1	D1 cpx 5 line1	D1 cpx 5 line1	D1 cpx 5 line1	D1 cpx 5 line1	D1 cpx 5 line1
11	12	13	14	15	16	17	18	19	20	21
52.94	52.64	51.18	51.28	51.97	51.68	51.94	51.53	51.69	50.89	51.59
0.50	0.49	0.69	0.57	0.60	0.55	0.61	0.60	0.59	0.60	0.59
2.83	3.07	4.08	3.49	3.31	2.86	3.13	3.15	3.17	3.42	3.60
4.78	4.97	6.24	6.52	6.96	7.34	7.38	7.52	7.50	7.55	7.42
0.17	0.20	0.25	0.17	0.34	0.40	0.35	0.43	0.38	0.40	0.33
15.07	14.85	13.60	13.79	13.38	13.29	13.33	13.27	13.02	13.08	13.24
23.23	23.49	22.56	22.71	22.45	22.21	21.80	21.98	22.23	21.95	21.84
0.14	0.14	0.27	0.36	0.32	0.42	0.46	0.44	0.47	0.41	0.38
0.02	0.01	0.03	0.00	-	0.01	0.00	0.02	0.02	0.06	-
0.01	0.06	0.03	0.01	-	-	-	0.04	0.04	0.02	0.13
0.14	0.08	0.06	0.05	0.08	0.05	0.08	0.10	0.05	-	0.13
0.00	0.00	0.00	0.00	0.00	0.00	0.00	0.00	0.00	0.00	0.00
99.82	100.01	98.98	98.95	99.41	98.81	99.08	99.07	99.15	98.38	99.24
25.00	27.50	30.00	32.50	35.00	37.50	40.00	42.50	45.00	47.50	50.00
84.89	84.19	79.53	79.04	77.41	76.34	76.30	75.88	75.58	75.54	76.08
48.34	48.75	48.47	48.20	48.01	47.52	47.00	47.12	47.81	47.35	47.16
8.04	8.37	10.89	11.09	12.19	12.93	13.01	13.30	13.23	13.39	13.07
43.62	42.88	40.65	40.72	39.80	39.56	39.98	39.58	38.96	39.26	39.77
0.09688	0.10747	0.13323	0.12496	0.10691	0.10096	0.10603	0.11043	0.10594	0.12015	0.12975
0.03024	0.03048	0.0531	0.0348	0.04392	0.03054	0.03792	0.03414	0.03941	0.03808	0.03701

D1 cpx 5 line1	D1 cpx 5 line1	D1 cpx 5 line2	D1 cpx 5 line2	D1 cpx 5 line2	D1 cpx 5 line2	D1 cpx 5 line2	D1 cpx 5 line2	D1 cpx 5 line2	D1 cpx 5 line2	D1 cpx 5 line2
22	23	1	2	3	4	5	6	7	8	9
51.42	51.17	53.42	53.10	53.31	52.57	52.88	52.90	52.76	53.00	52.64
0.62	0.61	0.48	0.48	0.50	0.45	0.44	0.41	0.48	0.46	0.46
3.50	3.53	2.49	2.58	2.65	2.61	2.67	2.69	2.61	2.60	2.58
7.63	7.53	4.44	4.45	4.34	4.58	4.32	4.35	4.28	4.72	4.51
0.34	0.31	0.09	0.14	0.07	0.11	0.13	0.08	0.13	0.11	0.15
13.34	13.24	15.13	15.32	15.05	15.31	15.31	15.32	15.35	15.34	15.29
22.49	22.32	23.04	23.54	23.34	23.55	23.26	23.47	23.37	23.15	22.97
0.41	0.37	0.18	0.14	0.13	0.15	0.16	0.17	0.15	0.12	0.14

0.02	0.01	0.05	0.01	0.02	0.02	0.01	0.03	0.01	0.03	-
0.04	0.07	0.02	0.05	0.10	0.04	0.08	0.08	0.10	0.06	0.14
0.07	0.05	0.02	0.09	0.13	0.09	0.11	0.07	0.10	0.05	0.06
0.00	0.00	0.00	0.00	0.00	0.00	0.00	0.00	0.00	0.00	0.00
99.87	99.21	99.36	99.89	99.64	99.47	99.37	99.57	99.34	99.63	98.94
52.50	55.00	0.00	2.50	5.00	7.50	10.00	12.50	15.00	17.50	20.00
75.71	75.81	85.86	85.99	86.07	85.63	86.33	86.26	86.47	85.28	85.80
47.57	47.63	48.38	48.60	48.91	48.55	48.43	48.65	48.52	47.96	47.97
13.17	13.07	7.43	7.40	7.22	7.55	7.23	7.17	7.15	7.82	7.60
39.26	39.31	44.20	44.00	43.87	43.91	44.34	44.18	44.33	44.22	44.43
0.1273	0.1256	0.0889	0.09341	0.08416	0.10189	0.09344	0.09535	0.09614	0.09209	0.0927
0.03226	0.0363	0.02442	0.02232	0.03478	0.01591	0.02685	0.02567	0.02157	0.02485	0.02415

D1	D1	D1	D1	D1	D1	D1	D1	D1	D1
cpx 5	cpx 5	cpx 5	cpx 5	cpx 5	cpx 5	cpx 5	cpx 5	cpx 5	cpx 5
line2	line2	line2	line2	line2	line2	line2	line2	line2	line2
10	11	12	13	14	15	16	17	18	19
52.26	52.61	52.32	52.95	51.80	50.92	51.31	51.82	51.56	51.49
0.44	0.46	0.44	0.41	0.52	0.64	0.62	0.64	0.61	0.66
2.69	2.63	2.50	2.48	3.41	3.84	3.44	3.30	3.37	3.24
4.83	4.45	5.43	6.07	6.67	6.44	6.90	7.07	7.26	7.29
0.23	0.16	0.23	0.27	0.31	0.20	0.28	0.37	0.40	0.37
15.10	15.16	14.49	14.43	13.84	13.33	13.64	13.32	13.15	13.12
23.55	23.16	22.82	22.76	22.24	22.18	22.38	22.35	22.08	22.16
0.22	0.16	0.29	0.37	0.28	0.29	0.43	0.43	0.40	0.41
0.02	0.00	-	0.03	-	-	0.02	-	0.00	0.01
0.03	-	-	0.05	-	0.07	0.10	0.03	0.02	-
0.01	0.11	0.14	0.17	0.06	0.14	0.15	0.05	-	0.06
0.00	0.00	0.00	0.00	0.00	0.00	0.00	0.00	0.00	0.00
99.38	98.91	98.65	99.99	99.13	98.05	99.27	99.39	98.85	98.82
22.50	25.00	27.50	30.00	32.50	35.00	37.50	40.00	42.50	45.00
84.78	85.86	82.63	80.91	78.72	78.68	77.89	77.05	76.35	76.24
48.55	48.40	48.15	47.63	47.37	48.31	47.66	47.86	47.63	47.76
8.14	7.53	9.32	10.36	11.61	11.30	11.94	12.45	12.91	12.90
43.31	44.07	42.53	42.01	41.01	40.39	40.41	39.68	39.46	39.34
0.10747	0.09346	0.09026	0.08779	0.11166	0.12429	0.1256	0.1099	0.109	0.10951
0.01435	0.02568	0.02384	0.02411	0.04388	0.05288	0.03172	0.04069	0.04569	0.03938

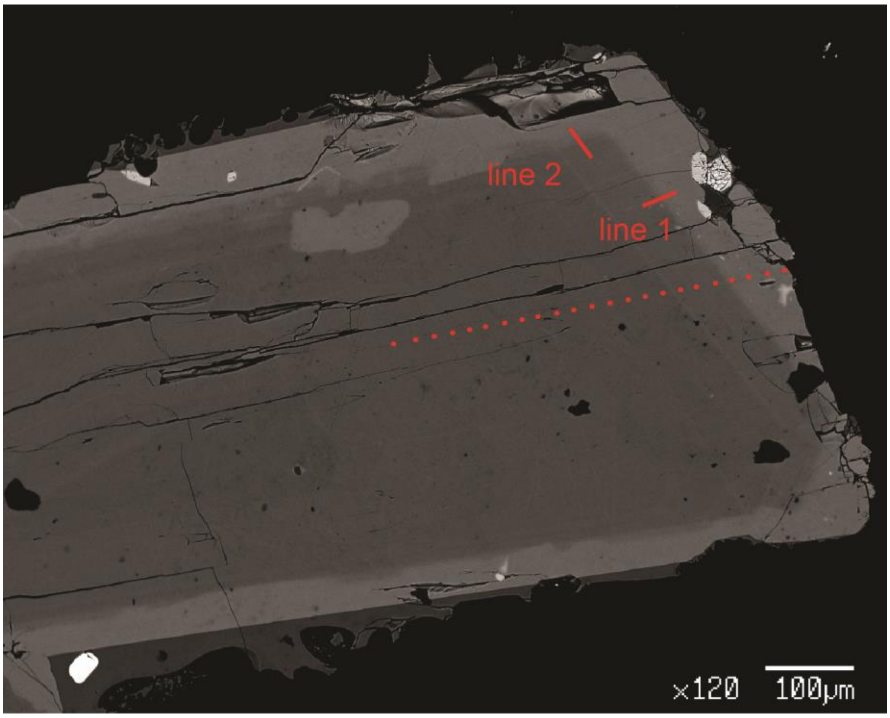

Table 2
Detailed concentration profiles of major and minor elements along transects in the Zaro zoned clinopyroxene crystals

Sample	ZR3A	ZR3A	ZR3A	ZR3A	ZR3A	ZR3A	ZR3A	ZR3A	ZR3A	ZR3A
cpx n°	cpx1	cpx1	cpx1	cpx1	cpx1	cpx1	cpx1	cpx1	cpx1	cpx1
line n°	line1	line1	line1	line1	line1	line1	line1	line1	line1	line1
equidistance (mm)										
texture	core	core	core	core	core	core	core	core	core	core
SiO_2	51.16	51.36	52.38	52.12	51.88	51.73	51.94	51.91	51.51	52.07
TiO_2	0.68	0.64	0.68	0.77	0.65	0.68	0.66	0.68	0.72	0.79
Al_2O_3	2.00	1.83	1.88	1.86	1.91	1.97	1.84	1.75	1.75	1.90
$Fe_2O_{3\ (tot)}$	9.52	9.58	9.58	9.75	9.63	9.28	9.34	9.41	9.46	9.55
MnO	0.67	0.74	0.87	0.80	0.83	0.77	0.88	0.91	0.84	0.76
MgO	12.15	12.05	12.26	11.99	12.28	11.80	12.36	11.93	12.18	12.06
CaO	21.76	21.94	21.85	21.08	21.59	21.29	21.43	21.02	21.51	21.35
Na_2O	1.32	1.28	1.05	1.07	1.08	1.07	1.16	1.16	1.07	1.09
K_2O	-	0.09	0.01	-	0.03	0.02	0.01	-	0.04	0.01
Cr_2O_3	0.11	0.03	0.09	0.10	0.06	0.02	0.07	0.15	0.04	0.04
NiO	-	-	-	-	0.06	0.09	0.02	-	0.11	0.03

Total	99.38	99.55	100.65	99.53	100.00	98.72	99.72	98.92	99.22	99.65
distance (mm)	0.0	10.0	20.0	30.0	40.0	50.0	60.0	70.0	80.0	90.0
Mg#	69.5	69.2	69.5	68.7	69.4	69.4	70.2	69.3	69.7	69.2
Wollastonite	46.67	46.91	46.42	45.82	46.08	46.73	45.97	46.01	46.26	46.23
Ferrosilite	17.07	17.24	17.35	17.92	17.45	17.23	17.14	17.66	17.30	17.43
Enstatite	36.26	35.85	36.23	36.26	36.47	36.04	36.89	36.33	36.44	36.33
AlIV	0.06	0.05	0.04	0.03	0.05	0.03	0.04	0.03	0.05	0.04
AlVI	0.03	0.03	0.04	0.05	0.04	0.05	0.04	0.05	0.03	0.05

ZR3A	ZR3A	ZR3A	ZR3A	ZR3A	ZR3A	ZR3A	ZR3A	ZR3A	ZR3A	ZR3A
cpx1	cpx1	cpx1	cpx1	cpx1	cpx1	cpx1	cpx1	cpx1	cpx1	cpx1
line1	line1	line1	line1	line1	line1	line1	line1	line1	line1	line1
core	core		mantle	mantle	mantle	mantle	mantle	rim	rim	rim
51.74	51.91	51.29	52.03	52.44	51.30	52.10	52.01	52.55	52.44	52.12
0.71	0.71	0.81	0.95	0.92	1.07	0.98	0.99	0.84	0.84	0.83
1.96	1.90	1.96	2.33	2.20	2.50	2.47	2.45	2.31	2.44	2.24
9.39	9.53	9.20	8.38	8.20	8.02	8.26	8.33	7.84	7.73	7.92
0.86	0.81	0.72	0.49	0.63	0.51	0.48	0.56	0.59	0.51	0.49
12.13	11.96	12.42	12.90	13.08	13.03	12.92	13.20	13.62	13.44	13.82
21.71	22.01	21.44	21.40	21.95	21.64	21.73	21.93	21.74	21.52	22.36
1.08	1.20	1.04	0.84	0.98	0.75	1.01	0.93	0.84	0.81	0.77
0.07	0.02	0.02	0.04	0.02	-	0.05	0.05	0.01	0.01	-
0.16	0.19	-	0.04	0.02	0.09	0.08	0.10	0.12	0.06	0.01
0.02	0.05	0.11	0.13	0.12	0.01	0.03	0.06	0.01	0.08	0.01
99.83	100.29	99.01	99.53	100.56	98.92	100.11	100.60	100.47	99.88	100.58
100.0	110.0	120.0	130.0	140.0	150.0	160.0	170.0	180.0	190.0	200.0
69.7	69.1	70.6	73.3	74.0	74.3	73.6	73.9	75.6	75.6	75.7
46.60	47.10	46.14	46.24	46.66	46.61	46.70	46.43	45.99	46.13	46.43
17.18	17.30	16.68	14.97	14.66	14.35	14.67	14.70	13.93	13.79	13.65
36.22	35.61	37.19	38.78	38.68	39.04	38.63	38.88	40.08	40.08	39.92
0.05	0.05	0.05	0.05	0.05	0.07	0.06	0.07	0.05	0.05	0.07
0.04	0.03	0.03	0.05	0.04	0.04	0.05	0.04	0.05	0.06	0.03

ZR3A	ZR3A	ZR3A	ZR3A	ZR3A	ZR3A	ZR3A	ZR3A	ZR3A	ZR3A
cpx1	cpx1	cpx1	cpx1	cpx1	cpx1	cpx1	cpx1	cpx1	cpx1
line2	line2	line2	line2	line2	line2	line2	line2	line2	line2
core	core	core	core	core	core	core	core		
51.74	51.49	51.63	51.99	51.21	51.79	51.47	51.25	51.44	
0.72	0.78	0.75	0.76	0.69	0.70	0.80	0.84	0.72	
1.89	2.00	1.94	1.79	2.05	2.00	2.02	2.03	2.03	
9.37	9.80	9.47	9.49	9.41	9.47	9.64	9.46	8.96	
0.75	0.77	0.77	0.85	0.89	0.86	0.84	0.81	0.84	
11.70	11.98	11.89	12.09	11.99	11.95	12.09	12.02	12.14	
21.82	21.78	21.95	21.50	21.78	21.75	21.31	21.87	22.23	
1.14	1.09	1.14	1.09	1.09	1.00	1.08	1.15	0.98	
0.00	0.04	0.03	0.05	0.07	0.00	0.05	0.03	0.02	
0.10	0.06	0.16	0.10	0.05	0.10	0.04	0.02	0.00	
0.08	0.05	0.05	0.02	0.04	0.04	0.07	0.08	0.01	
99.31	99.85	99.78	99.72	99.27	99.67	99.42	99.56	99.38	
0.00	2.50	5.00	7.50	10.00	12.50	15.00	17.50	20.00	
69.00	68.54	69.12	69.43	69.43	69.22	69.09	69.37	70.72	
47.4318	46.6325	47.2131	46.3346	46.8297	46.8243	46.0071	46.9165	47.5196	
17.185	17.6828	17.2069	17.4171	17.3047	17.3846	17.6798	17.2097	16.3771	
35.3831	35.6847	35.58	36.2484	35.8656	35.7911	36.3131	35.8737	36.1033	
0.04119	0.05616	0.05154	0.04085	0.05659	0.04638	0.05209	0.06029	0.05456	
0.04315	0.03284	0.03476	0.03866	0.03511	0.04254	0.03802	0.03028	0.03593	

ZR3A	ZR3A	ZR3A	ZR3A	ZR3A	ZR3A	ZR3A	ZR3A
cpx1	cpx1	cpx1	cpx1	cpx1	cpx1	cpx1	cpx1
line2	line2	line2	line2	line2	line2	line2	line2
rim	rim	rim	rim	rim	rim	rim	rim
51.29	51.37	51.22	51.44	50.92	51.63	51.84	51.53
0.91	0.89	0.88	0.93	1.01	0.91	0.90	0.94
2.32	2.18	2.24	2.44	2.62	2.31	2.37	2.23
8.57	8.38	8.14	8.58	8.72	8.28	8.33	8.54
0.61	0.60	0.61	0.55	0.55	0.56	0.60	0.57
12.59	12.76	12.70	12.50	12.54	12.59	12.74	12.73

22.16	21.91	22.26	21.96	22.00	22.15	21.82	22.26
0.90	0.83	0.82	0.96	0.85	0.87	0.82	0.93
0.01	0.00	0.04	0.00	0.04	0.00	0.11	0.05
0.03	0.04	0.05	0.06	0.02	0.13	0.05	0.00
0.09	0.05	0.02	0.03	0.08	0.00	0.12	0.00
99.48	99.02	98.97	99.45	99.36	99.43	99.70	99.78
25.00	27.50	30.00	32.50	35.00	37.50	40.00	42.50
72.36	73.08	73.55	72.20	71.94	73.05	73.16	72.65
47.3045	46.9379	47.5996	47.2429	47.1194	47.5626	46.9007	47.2727
15.3057	15.0321	14.6191	15.3452	15.5152	14.8265	15.0025	15.1168
37.3898	38.0301	37.7813	37.4119	37.3654	37.6109	38.0969	37.6105
0.06741	0.05974	0.06377	0.064	0.0781	0.05919	0.05716	0.06519
0.03562	0.03731	0.03604	0.04424	0.03845	0.04316	0.04754	0.0335

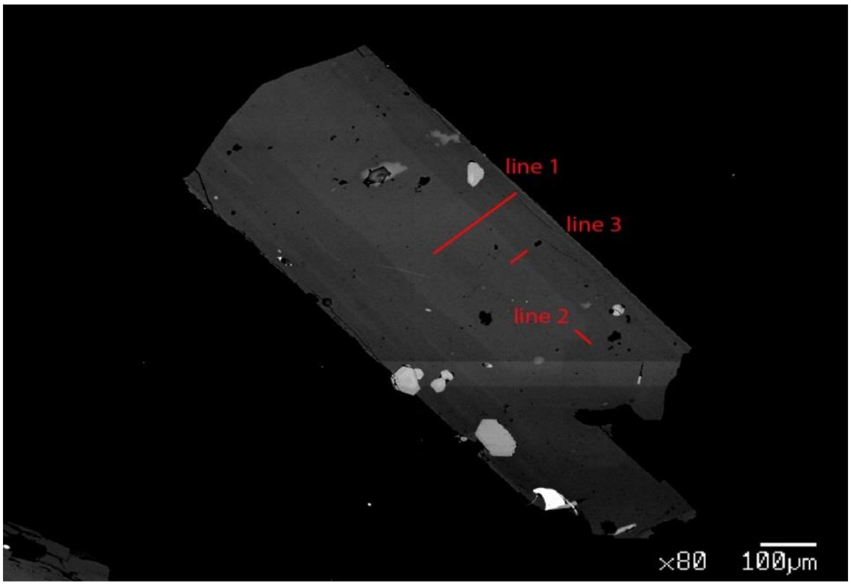

ZR3A	ZR3A	ZR3A	ZR3A	ZR3A	ZR3A	ZR3A	ZR3A	ZR3A	ZR3A
cpx8	cpx8	cpx8	cpx8	cpx8	cpx8	cpx8	cpx8	cpx8	cpx8
line1	line1	line1	line1	line1	line1	line1	line1	line1	line1
core	core	mantle	mantle	mantle	mantle	mantle	mantle	mantle	rim
52.43	52.76	52.47	52.52	52.27	52.33	52.49	52.72	53.49	52.34

0.73	0.71	0.55	0.63	0.60	0.60	0.62	0.48	0.46	0.74
2.19	2.07	1.43	1.41	1.46	1.48	1.44	1.29	1.38	2.04
7.80	7.29	10.72	10.96	10.87	11.15	10.86	11.06	10.50	7.86
0.52	0.50	1.13	1.20	1.22	1.18	1.29	1.20	1.06	0.60
13.33	13.69	10.51	10.86	10.93	11.00	10.82	10.88	11.93	13.67
22.20	22.12	21.03	20.50	20.51	21.12	21.19	20.60	21.26	21.91
0.81	0.73	1.25	1.31	1.36	1.36	1.33	1.34	1.18	0.84
-	0.01	0.03	0.02	-	0.00	-	0.02	-	-
0.07	0.14	0.14	0.13	0.01	0.09	-	-	0.12	0.05
0.04	0.07	-	-	0.01	-	0.05	0.07	-	-
100.12	100.09	99.26	99.54	99.24	100.31	100.10	99.67	101.38	100.06
0.0	10.0	20.0	30.0	40.0	50.0	60.0	70.0	80.0	90.0
75.3	77.0	63.6	63.8	64.2	63.7	64.0	63.7	66.9	75.6
46.99	46.81	46.83	45.44	45.41	45.86	46.33	45.46	45.34	46.09
13.75	12.88	20.62	21.07	20.92	20.91	20.76	21.14	19.26	13.90
39.26	40.31	32.56	33.49	33.67	33.23	32.91	33.40	35.40	40.01
0.05	0.04	0.01	0.01	0.01	0.02	0.02	0.00	0.01	0.05
0.05	0.05	0.06	0.05	0.05	0.04	0.05	0.06	0.05	0.04

ZR3A	ZR3A	ZR3A
cpx8	cpx8	cpx8
line1	line1	line1
rim	rim	rim
50.11	51.28	51.38
0.86	0.84	0.79
1.98	2.11	2.06
8.09	7.87	7.91
0.56	0.61	0.51
13.47	13.88	13.71
21.91	22.08	21.85
0.77	0.84	0.89
0.02	0.00	0.03
0.04	0.04	0.11
0.08	0.01	0.03
97.88	99.58	99.28

110.0	120.0	130.0
74.8	75.9	75.5
46.22	45.98	46.00
14.25	13.80	13.85
39.53	40.21	40.15
0.08	0.08	0.07
0.01	0.02	0.02

ZR3A	ZR3A	ZR3A	ZR3A	ZR3A	ZR3A	ZR3A	ZR3A
cpx8	cpx8	cpx8	cpx8	cpx8	cpx8	cpx8	cpx8
line2	line2	line2	line2	line2	line2	line2	line2
mantle	mantle	mantle				rim	rim
51.52	51.56	51.59	51.80	51.40	51.49	51.35	51.04
0.48	0.57	0.56	0.51	0.65	0.81	0.72	0.85
1.39	1.40	1.40	1.40	1.47	1.71	2.23	2.20
10.71	10.68	10.93	10.21	9.42	8.27	7.88	7.86
1.21	1.09	1.12	1.06	1.00	0.74	0.56	0.64
10.79	10.84	11.01	11.21	11.79	12.66	12.91	13.04
21.21	20.62	20.69	21.06	21.41	21.69	21.65	22.16
1.40	1.42	1.30	1.12	1.02	0.86	0.84	0.86
0.06	0.02	0.08	0.02	0.00	0.03	0.02	0.05
0.05	0.08	0.03	0.00	0.00	0.18	0.00	0.06
0.00	0.00	0.05	0.00	0.04	0.04	0.00	0.00
98.8208	98.2669	98.7489	98.4021	98.1997	98.4832	98.1655	98.7629
0.0	2.0	4.0	6.0	8.0	10.0	12.0	14.0
64.2	64.4	64.2	66.2	69.0	73.2	74.5	74.7
46.58	45.93	45.55	46.32	46.59	46.81	46.86	47.21
20.46	20.48	20.73	19.38	17.72	15.18	14.27	14.15
32.96	33.59	33.72	34.30	35.69	38.01	38.87	38.65
0.02	0.02	0.02	0.02	0.03	0.04	0.05	0.07
0.04	0.05	0.04	0.05	0.04	0.03	0.05	0.03

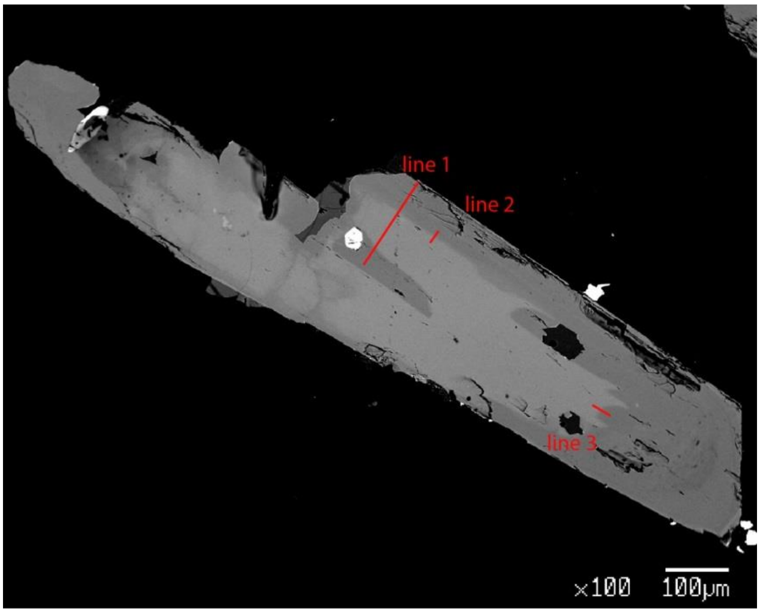

ZR3A cpx9 line2	ZR3A cpx9 line2	ZR3A cpx9 line2	ZR3A cpx9 line2	ZR3A cpx9 line2	ZR3A cpx9 line2	ZR3A cpx9 line2	ZR3A cpx9 line2	ZR3A cpx9 line2	ZR3A cpx9 line2
core	core	core	core		mantle	mantle	mantle	mantle	mantle
52.15	52.11	51.84	52.15	52.58	51.93	52.62	52.16	52.27	52.03
0.60	0.58	0.52	0.52	0.52	0.86	0.83	0.86	0.87	0.98
1.32	1.39	1.26	1.33	1.22	1.72	1.47	1.50	1.62	1.70
11.88	11.92	12.19	11.98	11.50	9.99	9.66	10.00	10.02	10.08
1.39	1.26	1.29	1.37	1.34	1.00	1.09	1.12	1.05	1.07
9.92	10.00	10.05	10.32	10.54	11.11	11.74	11.33	11.42	11.35
20.65	20.79	20.41	20.71	20.67	20.81	20.73	20.76	20.86	20.63
1.50	1.65	1.60	1.57	1.51	1.41	1.48	1.49	1.48	1.40
0.02	-	0.04	0.02	0.02	0.06	0.01	-	-	0.03
-	0.13	-	0.11	0.02	0.08	0.08	-	0.12	0.02
0.03	-	0.06	0.03	0.01	0.03	0.08	0.10	0.12	-
99.45	99.82	99.26	100.10	99.92	98.99	99.79	99.32	99.83	99.29
0.0	1.5	3.0	4.5	6.0	7.5	9.0	10.5	12.0	13.5

59.8	59.9	59.5	60.6	62.0	66.5	68.4	66.9	67.0	66.7
46.07	46.20	45.43	45.52	45.56	46.39	45.59	45.92	45.95	45.71
23.14	22.89	23.44	22.93	22.12	19.15	18.48	19.22	19.05	19.31
30.79	30.92	31.12	31.55	32.32	34.46	35.92	34.86	35.00	34.98
0.01	0.02	0.01	0.02	0.01	0.03	0.02	0.02	0.03	0.03
0.05	0.05	0.05	0.04	0.05	0.05	0.05	0.04	0.04	0.05

ZR3A	ZR3A	ZR3A	ZR3A	ZR3A	ZR3A
cpx9	cpx9	cpx9	cpx9	cpx9	cpx9
line2	line2	line2	line2	line2	line2
mantle			rim	rim	rim
51.87	51.01	51.88	52.25	52.11	51.94
1.09	1.11	1.08	1.10	1.04	1.07
1.88	2.07	2.08	2.04	1.57	1.39
10.26	10.82	11.03	12.21	13.58	14.02
1.27	1.14	1.23	1.41	1.47	1.65
11.19	10.57	9.94	9.01	8.41	7.66
20.62	20.18	19.29	18.87	18.85	18.32
1.61	1.68	1.93	2.11	2.41	2.75
0.00	0.01	0.04	0.04	0.01	0.02
0.06	-	0.09	-	0.10	0.04
-	0.07	0.05	0.19	-	0.05
99.84	98.65	98.63	99.23	99.55	98.92
15.0	16.5	18.0	19.5	21.0	22.5
66.0	63.5	61.6	56.8	52.5	49.3
45.62	45.63	45.18	44.88	44.55	44.44
19.93	21.12	22.43	25.31	27.80	29.71
34.44	33.25	32.39	29.81	27.65	25.85
0.04	0.04	0.04	0.02	0.02	0.01
0.04	0.05	0.05	0.07	0.05	0.05

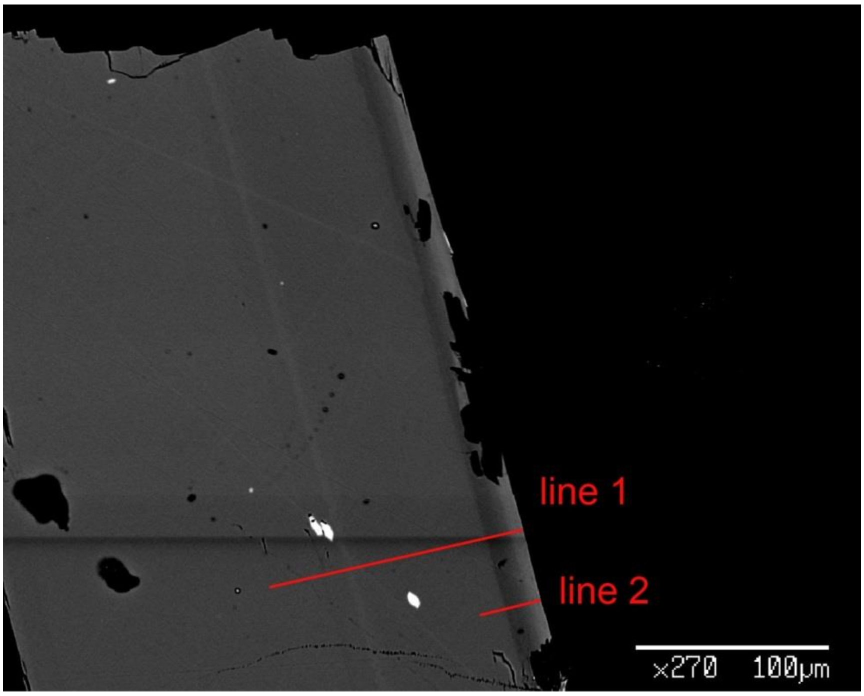

M6C cpx1	M6C cpx1 line1	M6C cpx1 line1	M6C cpx1 line1	M6C cpx1 line1	M6C cpx1 line1	M6C cpx1 line1	M6C cpx1 line1	M6C cpx1 line1	M6C cpx1 line1
core	core	core	core	core	core	core	mantle	mantle	mantle
52.65	50.98	50.97	50.73	50.91	51.03	51.26	50.91	50.14	51.17
0.72	0.88	1.09	0.99	0.92	1.03	1.08	1.28	1.31	1.05
2.42	3.34	3.80	3.63	3.31	3.81	3.60	5.36	5.66	4.65
8.03	7.91	7.94	8.21	8.07	8.25	8.51	4.98	5.03	5.05
0.55	0.42	0.34	0.31	0.36	0.34	0.38	0.10	0.08	0.12
13.32	13.13	12.78	12.98	13.18	12.83	12.79	14.40	14.52	14.87
22.21	22.23	21.54	21.67	21.56	21.86	21.63	21.56	22.38	21.78
0.70	0.64	0.62	0.57	0.65	0.65	0.62	0.36	0.33	0.30
-	-	0.03	0.01	0.04	-	0.00	0.05	0.02	0.01
0.07	0.07	0.05	0.07	0.05	0.11	0.05	0.29	0.26	0.32
0.08	0.03	0.02	0.08	0.02	0.01	0.04	0.02	0.11	0.01
100.75	99.64	99.17	99.25	99.06	99.91	99.97	99.32	99.83	99.34
	0.0	4.0	8.0	12.0	16.0	20.0	24.0	28.0	32.0
74.7	74.7	74.2	73.8	74.4	73.5	72.8	83.8	83.7	84.0

46.82	47.30	47.05	46.72	46.39	47.10	46.65	47.32	48.06	46.84
14.12	13.84	14.12	14.35	14.16	14.44	14.98	8.71	8.56	8.68
39.06	38.87	38.84	38.93	39.45	38.46	38.37	43.97	43.38	44.49
0.05	0.09	0.09	0.09	0.09	0.10	0.09	0.12	0.15	0.11
0.05	0.06	0.08	0.07	0.06	0.07	0.07	0.11	0.09	0.09
M6C	M6C	M6C	M6C	M6C	M6C	M6C	M6C	M6C	M6C
cpx1	cpx1	cpx1	cpx1	cpx1	cpx1	cpx1	cpx1	cpx1	cpx1
line1	line1	line1	line1	line1	line1	line1	line1	line1	line1
mantle	mantle	mantle	mantle	mantle	rim	rim	rim	rim	rim
51.12	51.12	51.34	52.13	51.73	50.42	51.30	51.59	51.93	51.19
0.96	1.07	1.12	0.81	1.06	1.08	0.98	1.05	0.98	0.94
4.40	4.76	4.80	3.57	4.68	4.36	3.89	3.75	3.59	3.33
4.97	4.91	5.24	5.45	5.49	7.65	7.44	7.73	7.44	7.64
0.14	0.21	0.09	0.19	0.14	0.21	0.30	0.23	0.33	0.31
15.03	14.90	14.58	15.13	14.60	13.36	13.79	13.81	13.94	13.90
21.95	22.25	22.15	22.24	21.97	21.91	21.51	21.05	21.40	21.24
0.32	0.31	0.34	0.31	0.34	0.52	0.57	0.55	0.66	0.62
0.02	-	0.04	0.01	-	-	0.02	-	0.02	0.00
0.27	0.15	0.11	0.18	0.22	0.03	0.09	0.05	0.12	0.18
-	0.04	-	0.05	0.09	0.06	0.06	0.05	0.11	0.11
99.18	99.73	99.80	100.07	100.32	99.61	99.96	99.85	100.51	99.47
36.0	40.0	44.0	48.0	52.0	56.0	60.0	64.0	68.0	72.0
84.4	84.4	83.2	83.2	82.6	75.7	76.8	76.1	77.0	76.4
46.85	47.36	47.54	46.63	47.07	46.99	46.02	45.29	45.67	45.40
8.52	8.52	8.93	9.23	9.41	13.15	12.93	13.37	12.95	13.27
44.63	44.12	43.53	44.14	43.52	39.86	41.05	41.34	41.39	41.33
0.11	0.12	0.11	0.09	0.11	0.12	0.10	0.09	0.09	0.09
0.08	0.09	0.09	0.07	0.09	0.07	0.07	0.08	0.07	0.06
M6C	M6C	M6C	M6C	M6C	M6C				
cpx1	cpx1	cpx1	cpx1	cpx1	cpx1				
line1	line1	line1	line1	line1	line1				
rim	rim	rim	rim	rim	rim				
51.35	52.11	52.56	52.75	51.71	48.58				
1.03	0.84	0.96	0.83	1.07	1.39				
3.44	2.53	1.70	1.60	2.47	5.15				

8.85	7.87	8.66	8.12	8.55	10.46
0.41	0.38	0.75	0.69	0.67	0.85
12.33	13.16	12.93	13.32	12.92	11.14
21.42	21.55	20.80	21.07	20.36	19.28
0.83	0.78	0.91	0.97	1.41	2.64
0.01	-	-	0.01	0.02	0.02
0.09	0.03	0.07	0.04	0.11	0.14
0.02	0.08	-	-	-	-
99.79	99.32	99.35	99.40	99.28	99.65
76.0	80.0	84.0	88.0	92.0	96.0
71.3	74.9	72.7	74.5	72.9	65.5
46.76	46.54	45.08	45.32	44.71	44.21
15.79	13.91	15.94	14.81	15.81	20.25
37.45	39.54	38.98	39.86	39.48	35.54
0.08	0.05	0.03	0.03	0.06	0.15
0.07	0.06	0.05	0.04	0.05	0.08

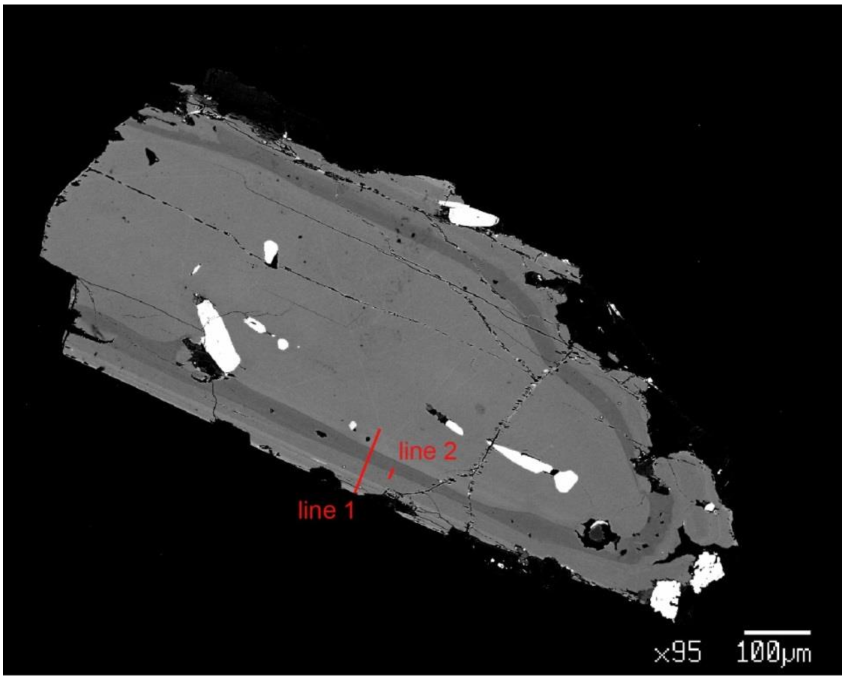

ZR3C	ZR3C	ZR3C	ZR3C	ZR3C	ZR3C	ZR3C	ZR3C	ZR3C
cpx9	cpx9	cpx9	cpx9	cpx9	cpx9	cpx9	cpx9	cpx9
line1	line1	line1	line1	line1	line1	line1	line1	line1

core	core	mantle	mantle	mantle	mantle	mantle	mantle	mantle
50.46	50.13	52.38	52.26	51.88	51.21	51.14	49.79	48.68
1.34	1.30	0.98	0.94	1.04	1.22	1.39	1.38	1.78
5.46	5.34	3.42	3.80	4.17	4.49	5.24	4.96	6.45
5.77	5.65	4.82	5.35	5.20	5.25	5.98	6.07	6.40
0.09	0.10	0.14	0.10	0.09	0.14	0.14	0.12	0.13
14.35	14.77	15.62	15.08	15.14	15.08	14.59	14.68	13.73
21.75	21.93	21.97	22.16	22.19	21.88	22.04	21.55	21.69
0.37	0.40	0.33	0.37	0.37	0.33	0.37	0.40	0.39
0.01	0.00	0.00	0.01	0.01	0.00	0.02	0.01	0.05
0.21	0.18	0.24	0.36	0.45	0.42	0.19	0.22	0.08
0.04	0.03	0.11	0.03	0.06	0.02	0.00	0.03	0.10
99.8542	99.8313	99.9938	100.441	100.587	100.042	101.094	99.2047	99.4732
0.0	13.0	26.0	39.0	52.0	65.0	78.0	91.0	104.0
81.6	82.3	85.2	83.4	83.8	83.7	81.3	81.2	79.3
46.99	46.69	46.18	46.76	46.83	46.49	46.78	46.05	47.27
9.88	9.55	8.13	8.97	8.71	8.94	10.14	10.32	11.10
43.13	43.75	45.68	44.27	44.45	44.57	43.08	43.64	41.63
0.14	0.15	0.08	0.09	0.11	0.12	0.14	0.15	0.19
0.10	0.08	0.06	0.07	0.07	0.07	0.09	0.07	0.09

ZR3C	ZR3C	ZR3C	ZR3C	ZR3C	ZR3C
cpx9	cpx9	cpx9	cpx9	cpx9	cpx9
line1	line1	line1	line1	line1	line1
mantle	mantle	mantle	rim	rim	rim
51.12	50.37	50.60	47.32	47.65	48.97
1.21	1.34	1.26	2.20	2.16	1.99
4.34	4.91	4.63	7.95	7.40	6.63
5.79	5.35	5.78	6.35	6.72	7.10
0.14	0.09	0.11	0.09	0.14	0.09
14.93	14.92	14.70	13.34	13.17	13.27
21.91	22.19	22.26	21.93	21.59	21.49
0.44	0.39	0.37	0.44	0.41	0.45
0.01	0.01	0.05	0.00	0.04	0.03

0.21	0.37	0.18	0.23	0.05	0.12
0.05	0.06	0.08	0.09	0.04	0.04
100.148	99.9964	100.01	99.9364	99.3712	100.183
117.0	130.0	156.0	169.0	182.0	195.0
82.1	83.3	81.9	78.9	77.7	76.9
46.31	47.02	47.06	48.18	47.70	47.16
9.79	8.99	9.71	11.04	11.82	12.33
43.90	43.99	43.23	40.78	40.48	40.51
0.12	0.14	0.13	0.24	0.22	0.19
0.07	0.07	0.07	0.11	0.11	0.10

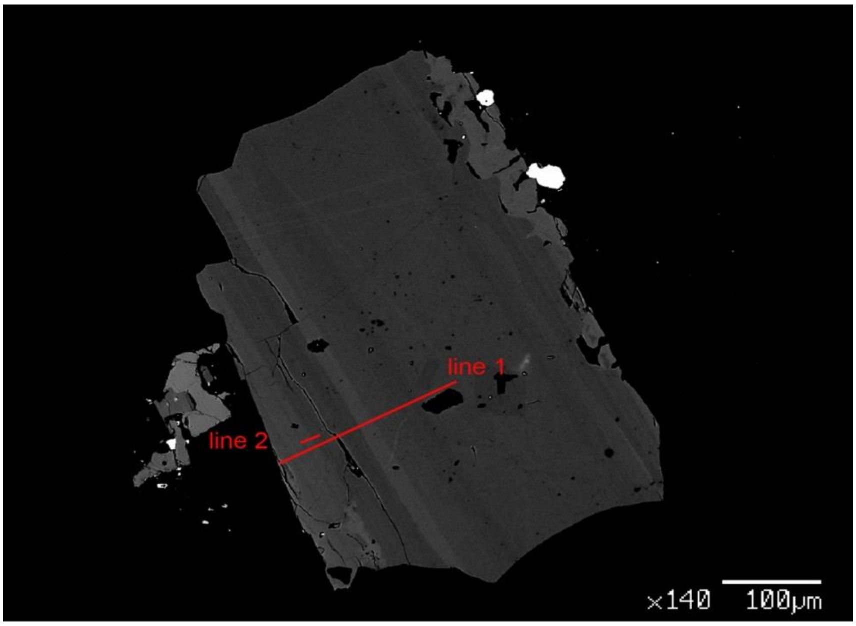

ZR3B	ZR3B	ZR3B	ZR3B	ZR3B	ZR3B	ZR3B	ZR3B	ZR3B	ZR3B
cpx2	cpx2	cpx2	cpx2	cpx2	cpx2	cpx2	cpx2	cpx2	cpx2
line1	line1	line1	line1	line1	line1	line1	line1	line1	line1
core	core	core	core	core	core	core	core	core	core
51.77	52.05	52.30	52.15	51.77	51.77	52.36	52.14	51.97	52.34
0.81	0.76	0.72	0.79	0.75	0.88	0.80	0.78	0.80	0.79
2.14	2.30	2.36	2.25	2.29	2.76	2.38	2.48	2.65	2.33
7.93	7.83	7.91	7.86	7.89	8.06	7.98	8.00	8.00	7.78
0.52	0.51	0.50	0.46	0.54	0.45	0.47	0.52	0.45	0.49

13.57	13.44	13.35	13.44	13.57	13.15	13.68	13.55	13.68	13.48
22.01	21.99	22.01	21.90	22.05	21.63	21.53	22.05	21.97	21.83
0.73	0.82	0.79	0.63	0.73	0.84	0.79	0.80	0.70	0.66
-	0.00	0.01	-	0.04	0.02	-	0.04	-	0.03
0.12	0.02	0.03	0.11	0.00	0.05	0.14	0.03	0.00	0.04
0.08	0.03	0.05	-	-	0.02	0.05	-	0.04	0.08
99.68	99.76	100.03	99.60	99.63	99.64	100.18	100.39	100.28	99.86
11.6	23.2	34.8	46.4	58.0	69.6	81.2	92.8	104.4	116.0
75.3	75.4	75.1	75.3	75.4	74.4	75.3	75.1	75.3	75.5
46.35	46.58	46.68	46.50	46.41	46.44	45.65	46.37	46.15	46.40
13.90	13.81	13.94	13.80	13.85	14.27	14.00	13.99	13.87	13.73
39.75	39.61	39.39	39.70	39.74	39.28	40.35	39.64	39.98	39.86
0.06	0.06	0.05	0.05	0.06	0.07	0.06	0.06	0.07	0.05
0.03	0.04	0.05	0.05	0.04	0.06	0.05	0.04	0.05	0.05
ZR3B	ZR3B	ZR3B	ZR3B	ZR3B	ZR3B	ZR3B	ZR3B	ZR3B	ZR3B
cpx2	cpx2	cpx2	cpx2	cpx2	cpx2	cpx2	cpx2	cpx2	cpx2
line1	line1	line1	line1	line1	line1	line1	line1	line1	line1
	mantle	mantle			rim	rim	rim	rim	rim
50.88	51.18	51.07	51.50	52.06	51.61	52.19	52.33	51.86	51.99
1.00	0.98	0.98	0.98	0.82	0.76	0.73	0.82	0.78	0.85
3.17	3.10	3.01	2.68	2.48	2.53	2.22	2.58	2.78	2.82
8.16	8.52	8.61	8.35	8.15	7.52	7.59	7.50	7.86	7.77
0.53	0.61	0.58	0.49	0.48	0.56	0.54	0.47	0.38	0.48
12.81	12.68	12.74	12.92	13.48	13.31	13.60	13.58	13.56	13.51
21.80	21.75	21.59	21.71	21.85	21.70	22.34	21.78	22.52	22.24
0.97	0.83	0.98	0.96	0.85	0.79	0.81	0.84	0.81	0.74
-	0.05	0.04	0.01	0.08	-	0.07	0.03	-	-
-	0.09	0.06	0.10	0.06	0.08	0.04	0.07	0.10	0.01
0.02	0.01	0.06	0.04	0.05	0.02	-	0.08	-	0.01
99.34	99.80	99.71	99.74	100.37	98.88	100.14	100.07	100.65	100.42
139.2	150.8	162.4	174.0	185.6	197.2	208.8	220.4	232.0	243.6
73.7	72.6	72.5	73.4	74.7	75.9	76.2	76.3	75.5	75.6

46.97	46.75	46.44	46.60	46.15	46.64	46.92	46.44	47.09	46.84
14.63	15.33	15.43	14.82	14.24	13.56	13.34	13.27	13.46	13.57
38.40	37.92	38.12	38.58	39.61	39.80	39.74	40.29	39.45	39.59
0.09	0.08	0.08	0.07	0.07	0.06	0.06	0.06	0.08	0.07
0.05	0.05	0.05	0.05	0.04	0.05	0.04	0.05	0.04	0.05

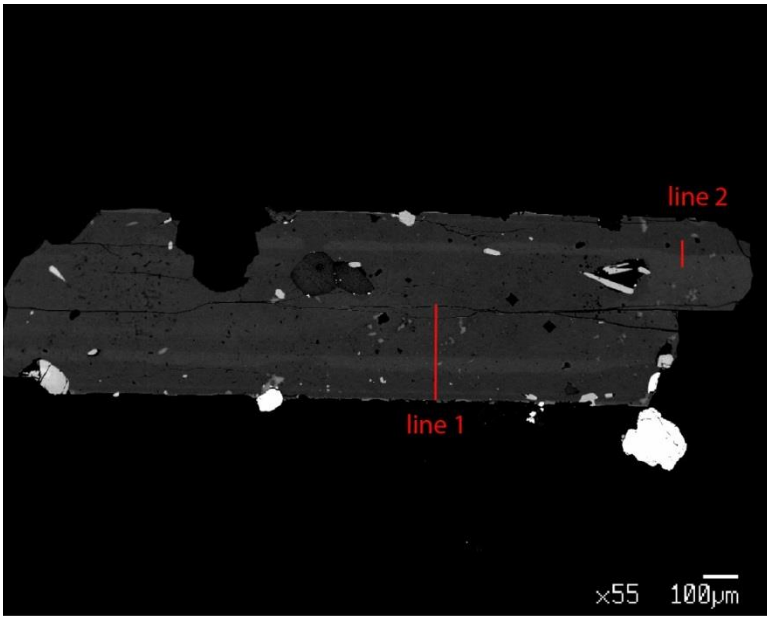

Supplementary Material 4

Table 1

Temperature and pressure estimates obtained through the geothermorometer specific for alkaline liquids (Masotta et al., 2013) on A-MS clinopyroxenes

ME0		ME1		ME2		ME3	
Talk 2012 T-model 11	Palk 2012 P-model 7	Talk 2012 T-model 11	Palk 2012 P-model 7	Talk 2012 T-model 11	Palk 2012 P-model 7	Talk 2012 T-model 11	Palk 2012 P-model 7
1092.2	1.4	1049.8	2.1	989.6	1.4	988.5	1.5
1120.4	1.2	1074.6	1.9	990.4	1.3	982.2	1.7
1104.9	1.3	1064.2	1.7	1001.4	1.1	939.1	1.8
1096.8	1.6	1060.0	2.7	999.9	1.2	966.9	1.5
1083.7	1.6	1067.6	1.6	971.8	1.4	951.0	1.7
1052.9	3.2	1060.1	2.6	1000.0	1.6	934.4	1.5
1085.7	1.8	1053.0	1.9	999.9	1.2	962.5	1.4
1100.7	1.2	1058.4	2.2	977.1	1.1	961.3	1.3
1114.9	3.2	1068.3	1.6	984.1	1.0	940.1	1.2
1115.1	1.1	1078.5	1.3	985.5	1.3	952.8	1.4
1103.7	1.7	1051.6	1.9	989.7	1.8	988.7	1.8
1132.4	1.5	1076.3	1.7	990.6	1.6	982.4	2.0
1116.8	1.6	1066.4	1.5	1001.5	1.5	939.3	2.0
1108.6	1.8	1060.9	2.5	999.9	1.6	967.1	1.8
1095.6	1.8	1068.9	1.4	971.8	1.8	951.2	1.9
1064.3	3.6	1061.6	2.3	1000.1	2.1	934.6	1.7
1097.8	2.1	1053.7	1.7	999.9	1.6	962.6	1.6
1112.5	1.5	1060.3	1.8	977.0	1.4	961.4	1.5
1128.1	3.6	1070.5	1.4	983.9	1.3	940.2	1.4
1126.9	1.4	1080.6	1.1	985.4	1.6	952.9	1.6
1076.8	2.7	1039.5	2.3	981.7	2.0	987.3	2.0
1104.4	2.5	1063.3	2.1	982.4	1.9	980.9	2.1
1089.1	2.5	1055.1	1.8	993.5	1.7	938.0	2.2
1080.9	2.6	1046.3	3.0	992.0	1.8	965.8	1.9
1067.9	2.5	1055.4	1.8	964.5	2.0	949.8	2.1
1037.5	5.4	1048.5	2.8	992.2	2.4	933.4	1.8
1069.4	3.2	1038.8	2.2	992.0	1.8	961.3	1.8
1085.1	2.7	1048.1	2.3	969.8	1.7	960.2	1.7
1096.6	5.1	1059.2	1.8	976.8	1.6	939.1	1.6
1099.4	2.3	1068.8	1.5	977.9	1.9	951.7	1.8
1104.3	0.7	1059.5	1.5	986.3	1.4	987.9	2.0
1132.9		1084.8	1.2	987.1	1.3	981.6	2.2
1117.6	0.6	1073.5	1.1	998.1	1.1	938.6	2.2
1109.6	0.9	1071.0	2.0	996.5	1.2	966.3	2.0
1097.1	1.0	1078.0	0.9	968.8	1.4	950.4	2.2

1066.2	2.0	1070.3	1.8	996.7	1.6	933.8	1.9
1100.0	0.9	1064.0	1.3	996.5	1.2	961.8	1.8
1113.2		1068.1	1.3	974.0	1.1	960.6	1.7
1133.7	2.0	1077.7	1.0	981.0	1.0	939.4	1.6
1127.2		1088.2	0.6	982.3	1.3	952.1	1.8
1096.2	1.8	1053.8	2.1	994.5	1.4	987.0	2.1
1124.5	1.6	1078.9	1.9	995.3	1.3	980.7	2.2
1109.4	1.7	1067.7	1.6	1006.5	1.1	937.7	2.3
1101.6	1.8	1065.1	2.6	1004.9	1.2	965.4	2.0
1089.2	1.8	1072.1	1.6	976.8	1.3	949.5	2.2
1058.7	3.9	1064.5	2.6	1005.1	1.5	933.0	1.9
1092.1	2.2	1058.2	1.8	1004.9	1.2	960.9	1.8
1105.1	1.7	1062.4	2.1	982.2	1.1	959.8	1.8
1125.6	3.7	1071.9	1.6	989.3	0.9	938.6	1.6
1118.9	1.5	1082.3	1.3	990.5	1.2	951.3	1.9
1102.6	1.3	1055.5	1.8	997.6	0.8	975.2	2.5
1131.1	1.1	1080.5	1.5	998.5	0.7	968.4	2.7
1116.2	1.2	1069.9	1.3	1009.7	0.5	926.7	2.7
1108.6	1.4	1066.0	2.3	1008.1	0.6	954.6	2.4
1096.9	1.4	1073.5	1.3	979.8	0.8	938.0	2.6
1066.5	3.2	1066.0	2.2	1008.3	0.7	923.2	2.3
1100.7	1.6	1059.0	1.6	1008.1	0.6	950.3	2.3
1111.7	1.2	1064.2	1.7	985.2	0.5	950.3	2.1
1138.3	3.0	1074.0	1.3	992.3	0.4	929.5	2.0
1125.1	1.0	1084.4	0.9	993.6	0.7	941.2	2.2
1118.0		1060.6	1.6	1003.9	0.9	977.3	2.4
1147.0		1086.1	1.4	1004.8	0.8	970.6	2.6
1131.9		1074.5	1.2	1015.9	0.6	928.7	2.6
1124.4	0.6	1072.6	2.1	1014.2	0.7	956.6	2.3
1112.7	0.6	1079.4	1.1	985.3	0.9	940.0	2.5
1081.8	1.4	1071.7	2.0	1014.4	0.9	925.0	2.2
1116.9		1065.7	1.4	1014.2	0.7	952.3	2.1
1127.3		1069.3	1.5	990.7	0.6	952.2	2.0
1156.9	1.3	1078.6	1.1	997.7	0.5	931.3	1.9
1140.7		1089.3	0.8	999.4	0.8	943.2	2.1
1080.1	2.5	1049.4	2.0	987.0	1.1	975.7	2.6
1107.9	2.3	1074.0	1.8	987.7	1.1	968.9	2.8
1092.4	2.3	1064.1	1.6	998.9	0.9	927.2	2.9
1084.1	2.4	1058.7	2.6	997.4	1.0	955.1	2.6
1070.8	2.4	1066.7	1.5	969.9	1.1	938.5	2.8
1040.2	5.0	1059.4	2.5	997.6	1.2	923.6	2.4
1072.1	3.0	1051.5	1.8	997.4	1.0	950.8	2.4
1088.4	2.4	1058.0	2.0	975.2	0.9	950.8	2.2
1098.2	4.8	1068.2	1.5	982.3	0.7	929.9	2.1
1102.9	2.1	1078.4	1.2	983.3	1.0	941.7	2.4
1112.9	1.4	1048.7	2.1	974.1	1.5	976.9	2.7
1141.6	1.2	1073.0	1.9	974.7	1.5	970.2	2.9

1127.0	1.3	1063.9	1.7	985.9	1.3	928.3	2.9
1119.9	1.4	1056.8	2.8	984.6	1.4	956.2	2.6
1109.0	1.4	1065.4	1.7	958.1	1.5	939.7	2.8
1078.7	3.5	1058.3	2.6	984.8	1.7	924.7	2.4
1113.9	1.7	1049.5	2.0	984.6	1.4	951.9	2.4
1122.4	1.3	1057.4	2.1	963.3	1.2	951.8	2.2
1157.0	3.1	1068.0	1.6	970.6	1.1	930.9	2.1
1135.2	1.1	1078.0	1.3	971.0	1.4	942.8	2.4
1098.5	1.8	1056.5	1.7	987.0	1.1	974.6	2.8
1126.9	1.6	1081.5	1.5	987.7	1.1	967.8	3.0
1111.6	1.7	1070.9	1.3	998.9	0.9	926.2	3.0
1103.6	1.8	1067.0	2.3	997.4	1.0	954.1	2.7
1091.1	1.8	1074.5	1.2	969.9	1.1	937.4	2.9
1060.3	3.9	1067.0	2.1	997.6	1.2	922.8	2.6
1093.7	2.2	1060.0	1.5	997.4	1.0	949.9	2.5
1107.3	1.6	1065.2	1.6	975.2	0.9	950.0	2.3
1126.1	3.7	1075.0	1.2	982.3	0.7	929.2	2.2
1121.3	1.5	1085.4	0.9	983.3	1.0	940.9	2.5

Table 2

Temperature and pressure estimates obtained through the geothermorometer specific for alkaline liquids (Masotta et al., 2013) on Zaro clinopyroxenes

Mafic enclaves		Hybrid enclave		Trachytic lavas		Trachytic lavas	
ME0		ME1		ME1		ME2	
T-model 11	P-model 7	T-model 11	P-model 7	T-model 11	P-model 7	T-model 11	P-model 7
1109.54	2.86	1047.70	1.47	960.86	2.08	953.02	2.70
1109.28	2.97	1041.47	2.06	958.29	2.17	934.63	2.67
1113.29	2.74	1031.39	3.03	963.81	2.17	926.11	2.48
1124.93	2.95	1037.81	2.81	964.98	2.05	942.11	2.54
1122.81	2.11	1049.59	2.52	966.66	2.11	938.69	2.59
1109.54	2.86	1030.10	3.29	965.46	2.13	936.35	2.59
1109.28	2.97	1022.51	3.25	971.91	2.11	939.22	2.48
1113.29	2.74	1040.58	2.52	960.66	2.11	952.96	2.75
1124.93	2.95	1052.29	2.13	958.29	2.17	958.29	2.83
1122.81	2.11	1030.10	3.29	965.46	2.13	943.43	2.83
1116.54	3.06			962.40	2.05	947.30	2.37
1116.55	3.17			959.80	2.14	929.74	2.35
1120.29	2.93			965.38	2.14	921.83	2.18
1132.51	3.19			966.51	2.02	937.14	2.23
1129.47	2.28			968.23	2.08	933.60	2.29

1116.54	3.06	967.03	2.10	931.31	2.29
1116.55	3.17	973.50	2.08	934.77	2.16
1120.29	2.93	962.20	2.08	947.27	2.40
1132.51	3.19	959.80	2.14	951.96	2.46
1129.47	2.28	967.03	2.10	937.61	2.51
1115.64	3.58	961.85	1.98	949.72	2.94
1115.44	3.71	959.27	2.07	931.60	2.89
1119.41	3.44	964.81	2.07	923.27	2.68
1131.26	3.78	965.97	1.95	939.04	2.76
1128.89	2.75	967.67	2.01	935.60	2.81
1115.64	3.58	966.47	2.03	933.27	2.81
1115.44	3.71	972.92	2.00	936.29	2.69
1119.41	3.44	961.65	2.01	949.67	3.00
1131.26	3.78	959.27	2.07	954.82	3.09
1128.89	2.75	966.47	2.03	940.13	3.07
1116.69	3.34	960.87	2.17	942.06	3.09
1116.65	3.46	958.32	2.27	924.88	3.03
1120.44	3.20	963.78	2.26	917.23	2.81
1132.59	3.51	965.01	2.14	932.22	2.90
1129.69	2.53	966.65	2.20	928.64	2.96
1116.69	3.34	965.45	2.22	926.39	2.95
1116.65	3.46	971.86	2.21	930.05	2.82
1120.44	3.20	960.66	2.20	942.04	3.15
1132.59	3.51	958.32	2.27	946.47	3.26
1129.69	2.53	965.45	2.22	932.38	3.23
1125.31	2.92	958.37	1.78	943.58	3.01
1125.41	3.03	955.94	1.84	926.30	2.95
1129.09	2.79	961.13	1.86	918.58	2.74
1141.64	3.02	962.58	1.74	933.65	2.82
1138.20	2.16	964.03	1.80	930.08	2.88
1125.31	2.92	962.84	1.82	927.82	2.87
1125.41	3.03	969.10	1.77	931.43	2.74
1129.09	2.79	958.15	1.80	943.55	3.06
1141.64	3.02	955.94	1.84	948.06	3.16
1138.20	2.16	962.84	1.82	933.89	3.15
1126.15	3.25	955.23	2.02	945.75	2.85
1126.02	3.37	952.76	2.11	928.12	2.81
1129.97	3.12	958.05	2.11	920.15	2.61
1142.11	3.39	959.38	1.99	935.50	2.68
1139.47	2.45	960.91	2.05	932.00	2.73
1126.15	3.25	959.73	2.07	929.71	2.73
1126.02	3.37	966.02	2.05	933.06	2.61
1129.97	3.12	955.02	2.05	945.71	2.91
1142.11	3.39	952.76	2.11	950.49	2.99
1139.47	2.45	959.73	2.07	936.11	2.99
1106.06	3.66	964.91	2.52	958.19	2.16
1105.35	3.80	962.24	2.65	939.66	2.16

1109.84	3.52	967.97	2.63	931.08	2.00
1120.65	3.85	968.98	2.51	947.20	2.04
1120.03	2.82	970.81	2.58	943.75	2.10
1106.06	3.66	969.60	2.59	941.39	2.10
1105.35	3.80	976.18	2.61	944.29	1.98
1109.84	3.52	964.71	2.57	958.12	2.19
1120.65	3.85	962.24	2.65	963.48	2.24
1120.03	2.82	969.60	2.59	948.51	2.30
1093.32	3.34	958.66	2.48	956.74	2.23
1092.45	3.46	956.13	2.60	938.38	2.22
1097.05	3.20	961.54	2.58	929.93	2.06
1107.38	3.48	962.79	2.46	945.91	2.10
1107.35	2.54	964.40	2.53	942.44	2.16
1093.32	3.34	963.21	2.55	940.08	2.16
1092.45	3.46	969.57	2.56	943.10	2.03
1097.05	3.20	958.45	2.52	956.69	2.25
1107.38	3.48	956.13	2.60	961.92	2.31
1107.35	2.54	963.21	2.55	947.05	2.36
1108.10	3.52	958.50	2.26	950.14	1.61
1107.55	3.65	956.00	2.36	932.32	1.64
1111.87	3.38	961.35	2.36	924.24	1.52
1122.99	3.70	962.65	2.24	939.76	1.52
1121.82	2.70	964.22	2.30	936.24	1.60
1108.10	3.52	963.03	2.32	933.93	1.60
1107.55	3.65	969.37	2.31	937.25	1.47
1111.87	3.38	958.28	2.30	950.10	1.61
1122.99	3.70	956.00	2.36	954.98	1.63
1121.82	2.70	963.03	2.32	940.46	1.75
1117.33	3.09	949.86	2.40	952.32	1.34
1117.02	3.20	947.47	2.52	934.48	1.38
1121.12	2.96	952.58	2.50	926.42	1.28
1132.81	3.20	954.03	2.38	941.95	1.27
1130.80	2.31	955.44	2.45	938.40	1.35
1117.33	3.09	954.27	2.46	936.09	1.35
1117.02	3.20	960.44	2.47	939.47	1.22
1121.12	2.96	949.65	2.44	952.27	1.32
1132.81	3.20	947.47	2.52	957.12	1.33
1130.80	2.31	954.27	2.46	942.58	1.48

Supplementary Material 5

Table 1

Mass balance calculations obtained through XLFRAC (Stormer and Nicholls 1978)

	Parent magma	Daughter magma	Subtracted minerals				Difference between parent and daughter magmas	
sample	APR.1	ZR3C	ol	cpx	pl	mgnt		
	Measured (wt.%)	Measured (wt.%)						
SiO2	48.72	52.46	40.16	50.40	47.59		0.01	
TiO2	1.25	1.38		1.01		21.99	0.09	
Al2O3	15.60	18.01		5.26	33.19	2.24	0.00	
FeOt	7.94	7.24	13.32	4.86	0.52	73.44	0.00	
MnO	0.14	0.14	0.23	0.04		0.76	0.00	
MgO	9.61	5.06	45.88	15.60		1.10	0.00	
CaO	12.10	8.00	0.30	22.64	16.64	0.00	0.00	
Na2O	2.87	4.43		0.24	1.72		0.10	
K2O	1.48	2.92			0.16		0.00	
P2O5	0.28	0.37					0.01	
Sum	100	100	99.89	100.05	99.82	99.53	0.215	$\sum R^2$
								0.215

	amounts relative to inizial magma	absolute amounts
	vol. %	vol.%
ol	7.30	14.72
cpx	23.70	47.77
plg	15.81	31.86
mgnt	2.81	5.66
sum	49.62	100.00

	Parent magma	Daughter magma	Subtracted minerals (%)					
Sample	APR.1	ZR3C	ol	cpx	pl	mgnt		
			14.71	47.76	31.85	5.65		
	(ppm)	(ppm)	Kd				D	Calculated magma (ppm)
Rb	46.38	116.08	0.00004	0.00047	0.01600	0.11000	0.01	91.34
Ba	521.2	770.15	0.00004	0.00047	0.01111	0.02800	0.01	1030.76
U	0.98	2.41	0.00001	0.00036	0.06000	0.00764	0.02	1.92
Th	2.88	8.56	0.00000	0.00026	0.00069	0.00069	0.00	5.72
La	14.32	39.17	0.00010	0.10000	0.02200	0.01500	0.06	27.36
Ce	31.92	77.13	0.00010	0.16250	0.00625	0.01600	0.08	59.96
Sr	492.17	503.67	0.01600	0.26000	0.01600	0.01700	0.13	892.03

Nd	18.32	31.36	0.00030	0.28750	0.00278	0.01736	0.14	33.05
Sm	4.36	6.65	0.00060	0.35000	0.00900	0.02400	0.17	7.69
Zr	102	164.67	0.01000	0.10000	0.00090	0.71000	0.09	190.39
Hf	2.7	3.84		0.10940	0.09230	0.14000	0.09	5.04
Eu	1.47	2.41	0.00480	0.38000	0.00900	0.22000	0.20	2.55
Gd	4.58	7.43	0.00900	0.41000	0.00400	0.01800	0.20	7.93
Tb	0.72	0.88	0.01320	0.44000	0.00417	0.01900	0.21	1.23
Dy	4.11	5.19	0.00200	0.04236	0.00208	0.00208	0.02	8.04
Y	20.61	25.25	0.01000	0.48500	0.02300	0.00390	0.24	34.69
Ho	0.77	0.80	0.00160	0.00208	0.01100	0.01700	0.01	1.52
Er	2.13	2.48	0.02580	0.48330	0.01100	0.01800	0.24	3.59
Tm	0.28	0.45	0.00900	0.00139	0.03600	0.01700	0.01	0.55
Yb	1.83	2.73	0.03000	0.46670	0.00400	0.01800	0.23	3.10
Lu	0.27	0.41	0.03420	0.45000	0.00690	0.00972	0.22	0.46

residue liquid (%)
51

Calculations have been performed through the XLFRAC software by Stormer and Nicholls (1978). SR2= sum of the square of residuals. ol= olivine; cpx= clinopyroxene; feld= feldspar; mgnt= magnetite; ap= apatite.

Percentage of subtracted minerals come out from mass balance with major elements obtained by XLFRAC software. Kd= partition coefficient between minerals and liquidus. D= total distribution coefficient. Kd were taken from https://earthref.org.

Table 2

EC-AFC (Spera and Bohrson 2001) model for Zaro products

Parameters used for EC-AFC (Spera and Bohrson 2001) model for Zaro products

Equilibration Parameters		
Teq	900	°C
T_{lm}	1300	°C
$T^0{}_m$	1350	°C
T_{la}	980	°C
$T^0{}_a$	400	°C
T_s	780	°C
Cpm	1484	J/kg K
Cpa	1388	J/kg K
hcry	396000	J/kg

hfus	354000	J/kg

Geochimical Parameters

^{18}O/^{16}O in magma	5.19 ‰	Element	Sr	Nd
^{18}O/^{16}Oin assimilant	12 ‰	Magma: conc. (ppm)	519	30
Oxygenconc magma	47(wt.%)	bulk D_0	4	0.1
Oxygenconcassim	50 (wt.%)	enthalpy	0	0
		Assimilant: conc. (ppm)	280	60
		bulk D_0	0.65	0.1
		enthalpy	0	0
		Isotope	^{87}Sr/^{86}Sr	^{143}Nd/^{144}Nd
		ratio magma	0.705	0.51268
		ratio assimilant	0.713	0.51225

Average O and Sr isotope data of assimilant (Hercynian granodiorite) from Ayuso et al. (1994) and Rottura et al. (1991), respectively.

D0= Bulk distribution coefficient; Teq = Equilibration temperature; Tlm = Magma liquidus temperature; T0m = Initial magma temperature;

Tla= Wall-rock liquidus temperature; T0a = InitialWall-rock temperature; Ts=Solidus, required to be the same formagma and assimilant;Cpm = Magma specific heat capacity; hcry = Crystallization enthalpy; hfus= Fusion enthalpy

Cpa = Assimilant specific heat capacity.